WARSAW UNIVERSITY OF TECHNOLOGY

DISCIPLINE OF SCIENCE – CHEMICAL ENGINEERING/
FIELD OF SCIENCE – ENGINEERING AND TECHNOLOGY

Ph.D. Thesis

Mariusz Tyrański, M.Sc.

Numerical Analyses of Fertiliser Industrial-Scale Unit Operations: Ammonia Synthesis, Ammonia Oxidation and Droplet Removal Using Computational Fluid Dynamics Modelling with Detailed Reaction Kinetics

Supervisor
Professor Łukasz Makowski, Ph.D., D.Sc.

Additional supervisor
Wojciech Orciuch, Ph.D.

WARSAW 2025

I would like to thank my supervisor, Professor Łukasz Makowski, and my auxiliary supervisor, Dr Wojciech Orciuch, for their guidance on my PhD studies and dissertation. Their expertise in chemical engineering and proficiency in process simulations were determinants for the successful completion of this PhD project.

I would like to express my sincere gratitude to Dr Jakub Bujalski, my mentor from the Process Modeling and Control Department in Yara Technology and Projects (Yara International ASA), who supported me throughout my entire PhD studies. His practical knowledge and experience were invaluable contributions to this work.

I would like to thank Kjersti Berglund, director of the Process Modeling and Control Department in Yara Technology and Projects (Yara International ASA). Her and Dr Bujalski's support resulted in my fruitful internship in Norway at Yara Technology and Projects.

I would also like to thank Elin Nilsen and Oskar Bestul from the Ammonia and Nitric Acid Department in Yara Technology and Projects (Yara International ASA), whose experimental work provided unique validation data for this thesis.

Lastly, and most importantly, I wish to thank my family for their untiring support and faith in me.

I dedicate this work to my lovely wife, Barbara, who was always by my side, offering me love and inspiration even in the hardest times.

Abstract

Despite the world's economy's constant growth, many fundamental problems remain unresolved. Undernourishment and food insecurity, now also intensified by global political instabilities and environmental issues, cause pressure on the fertiliser industry to increase its efficiency as much as possible. Existing industrial technologies have excellent potential for improvements since, due to their large-scale character, even minor upgrades can significantly benefit efficiency and reduce operational costs. Furthermore, modifying existing technologies is cheaper and faster than developing new ones, which is incredibly challenging for large-scale production lines. Computational fluid dynamics (CFD) have an excellent potential for supporting experimental work and design processes. Computing Navier-Stokes equations with proper turbulence models using the finite element method allows for simulating the flow field inside the investigated apparatus, which can be extended by adding energy and species transport models and implementing the reaction kinetics.

This thesis is focused on creating and applying CFD models of primary fertiliser industrial-scale unit operations: ammonia synthesis using the Haber-Bosch method and ammonia oxidation in the Ostwald process. The last section is dedicated to droplet removal through wave-plate mist eliminators, a vastly applied supporting process in many industries, including fertilisers. Every analysis contains detailed information about methodology, including geometry, computational setup, boundary conditions, process parameters and applied models such as porous zone or discrete phase modelling. The results include critical parameter fields and functions, including those unavailable to obtain through experimental methods such as reaction rates or particle deposition areas. Novel approaches to the CFD model applications, such as studying the influence of catalyst particle size within the catalytic bed or trajectories and deposition tracking of entrained catalyst particles due to the catalyst gauze degradation phenomenon, were used. The obtained CFD models were the basis of the proposed novel improvements of the considered systems, such as alternative geometries of catalyst beds, catalyst gauze and drainage channels.

The significant contribution of this work was made in cooperation with the Yara Technology and Projects – Technology (Yara International ASA) located in Porsgrunn, Norway, which granted access to geometrical and experimental data of the actual pilot plat ammonia synthesis converter, allowing to fully recreate this apparatus and process in the form of the CFD model including the modification the reaction kinetics to obtain a model with excellent accuracy. The

obtained model was validated using two independent experimental runs, and it gave detailed insight into the process and further experimental research support, providing more control of the converter's geometry and process parameters. The company also offered overall support for the substantive correctness of this dissertation's research regarding ammonia synthesis and oxidation processes.

Keywords: ammonia synthesis, Haber-Bosch Process, ammonia oxidation, Ostwald Process, chemical reactor, wave-plate mist eliminators, droplet removal, computational fluid dynamics, catalyst gauze degradation, heterogeneous catalysis, catalytic bed, multiphase flows

Streszczenie

Pomimo ciągłego wzrostu światowej gospodarki, wiele fundamentalnych problemów pozostaje nierozwiązanych. Niedożywienie i brak bezpieczeństwa żywnościowego, obecnie dodatkowo nasilone przez światowe niestabilności polityczne oraz problemy związane ze środowiskiem naturalnym, wywierają presję na przemysł produkcji nawozów sztucznych, aby zwiększyć jego wydajność tak bardzo jak to możliwe. Istniejące technologie przemysłowe mają doskonały potencjał do ulepszeń, ponieważ ze względu na ich wielkoskalowy charakter, nawet niewielkie poprawki mogą znacznie zwiększyć wydajność oraz zredukować koszty operacyjne. Ponadto modyfikacja istniejących technologii jest tańsza i szybsza niż opracowywanie nowych, co jest niezwykle trudne w przypadku wielkoskalowych linii produkcyjnych. Obliczeniowa mechanika płynów (CFD – ang. computational fluid dynamics) ma świetny potencjał do wspierania prac eksperymentalnych oraz projektowych. Rozwiązywanie równań Naviera-Stokesa z wykorzystaniem odpowiednich modeli burzliwości przy użyciu metody objętości skończonych umożliwia symulację pola przepływu wewnątrz badanego urządzenia, które można rozbudować o modele transportu energii, koncentracji składników oraz kinetykę reakcji chemicznej.

Niniejsza praca skupia się na tworzeniu i stosowaniu modeli CFD kluczowych procesów przemysłu produkcji nawozów sztucznych: syntezy amoniaku metodą Habera-Boscha oraz utleniania amoniaku w procesie Ostwalda. Ostatni rozdział dedykowany jest usuwaniu kropel za pomocą odkraplaczy płytowo-żaluzjowych. Jest to proces pomocniczy szeroko stosowany w wielu gałęziach przemysłu, wliczając produkcję nawozów sztucznych. Każda analiza zawiera szczegółowe informacje na temat metodologii, w tym geometrii, konfiguracji obliczeniowej, warunków brzegowych, parametrów procesowych oraz zastosowanych modeli takich jak model strefy porowatej lub fazy rozproszonej. Wyniki obejmują profile kluczowych parametrów, włączając w to wielkości niemierzalne eksperymentalnie takie jak szybkości reakcji chemicznych lub strefy depozycji cząstek. Wykorzystano nowatorskie zastosowania modeli CFD, takie jak badanie wpływu wielkości cząstek katalizatora w złożu katalitycznym oraz śledzenie trajektorii i osadzania porwanych cząstek katalizatora w wyniku zjawiska degradacji siatki katalitycznej. Uzyskane modele CFD były podstawą do propozycji nowatorskich ulepszeń badanych systemów, takich jak alternatywne geometrie złóż katalizatora, siatek katalitycznych oraz kanałów drenażowych.

Znaczący wkład w tą rozprawę doktorską miała współpraca z firmą Yara Technology and Projects – Technology (Yara International ASA), zlokalizowaną w Porsgrunn, w Norwegii. Firma ta zaoferowała dostęp do danych geometrycznych oraz wyników eksperymentalnych pracy pilotażowego reaktora do syntezy amoniaku. Pozwoliło to stworzyć model CFD całego aparatu, w pełni odwzorowując zachodzący w nim proces. Otrzymane wyniki umożliwiły modyfikację modelu kinetyki reakcji, oraz uzyskanie modelu CFD o bardzo wysokiej dokładności. Walidacja uzyskanego modelu została przeprowadzona używając dwóch niezależnych eksperymentów. Model reaktora zapewnił szczegółowy wgląd w proces oraz dalsze wsparcie badań doświadczalnych, umożliwiając lepszą kontrolę nad geometrią aparatu oraz parametrami procesowymi. Firma Yara Technology and Projects zaoferowała także ogólne wsparcie w celu zapewnienia merytorycznej poprawności badań wchodzących w skład tej rozprawy, dotyczących syntezy oraz utleniania amoniaku.

Słowa kluczowe: synteza amoniaku, Proces Habera-Boscha, utlenianie amoniaku, Proces Ostwalda, reaktor chemiczny, odkraplacze płytowo-żaluzjowe, odkraplanie, obliczeniowa mechanika płynów, degradacja gazy katalitycznej, kataliza heterogeniczna, złoże katalityczne, przepływy wielofazowe

Table of contents

List of figures

List of tables

Nomenclature

Latin symbols

a	drainage channel length, mm
a_i	activity of component i
A	pre-exponential factor, kmol m^{-3} h^{-1}, s^{-1}
A_{face}	area of the computational cell's face, m^2
b	temperature exponent
b_i	constants
$BET_{Nielsen}$	BET surface area of the catalyst used by Nielsen et al. [71], m^2 g^{-1}
$BET_{Nielsen}$	BET surface area of the catalyst used by Yara, m^2 g^{-1}
c	concentration, kg m^{-3}, mol m^{-3}, kmol m^{-3}
c_i, C_i	species concentration, mol m^{-3}, kmol m^{-3}
c_p, C_p	specific heat at constant pressure, J kg^{-1} K^{-1}
C_A, C_B	concentration of species A, B, mol m^{-3}, kmol m^{-3}
C_D	drag force coefficient
$C_{i,j}$, $D_{i,j}$	prescribed matrices
C_{in}	number of droplets injected into the system
C_{out}	number of droplets removed from the system
C_μ	constant
C_1	viscous resistance, m^{-2}
C_2	inertial resistance factor, m^{-1}
$C_{1\varepsilon}$, $C_{2\varepsilon}$, $C_{3\varepsilon}$	constants
d_p	particle/droplet diameter, m
d_h	hydraulic diameter of the inlet, m
D	diffusion coefficient, m^2 s^{-1}
$D_{i,m}$	mass diffusion coefficient (diffusivity) for species i in the mixture
D_t	turbulent diffusivity
$D_{T,i}$	thermal (Soret) diffusion coefficient
D_ω	cross-diffusion term
e	energy concentration, J kg^{-1}
e	internal energy

e_{in}	inlet energy concentration, J kg^{-1}
e_{out}	outlet energy concentration, J kg^{-1}
E, $E_{a,j}$	activation energy, cal mol^{-1}, kJ mol^{-1}
E	total energy, J
E_{pot}	potential energy, J
E_{kin}	kinetic energy, J
f_i	fugacity of component i in a mixture
f_i^0	fugacity of pure component i at temperature and pressure of system
F	surface enlargement factor
F_D	coefficient in drag force acceleration, s^{-1}
F_r	force in r-direction, N
F_s	droplet inertial force, N
F_x	force in x-direction, N
F_2	parameter
$\overrightarrow{F_x}$	external force source term
g	concentration of quantity G
g	gravitational acceleration, m s^{-2}
g_x, g_y, g_z	gravitational acceleration x-, y- and z-components, m s^{-2}
$\vec{g}$	gravitational acceleration vector, m s^{-2}
G	transported quantity
G_b	generation of turbulence kinetic energy due to buoyancy
G^{inV}	"inward" flow of G
G_k	generation of turbulence kinetic energy due to the mean velocity gradients
G_ω	generation of specific dissipation rates due to the mean velocity gradients
$G_{\omega b}$	generation of specific dissipation rate due to buoyancy
h	enthalpy, J kg^{-1}
h_i, h_j	enthalpy of the component i, j, J kg^{-1}
h_j^0	enthalpy of formation of species j
H	catalyst gauze height, m
i, j, k	indexes
I	unit tensor
$\overrightarrow{J_i}, \overrightarrow{J_j}$	diffusion flux of species i, j, kg m^{-2} s^{-1}

k	reaction rate constant, s^{-1}
k	turbulent kinetic energy, $m^2\ s^{-2}$
k	thermal conductivity, $W\ m^{-1}\ K^{-1}$
k_t	turbulent thermal conductivity, $W\ m^{-1}\ K^{-1}$
k_{eff}	effective thermal conductivity, $W\ m^{-1}\ K^{-1}$
$k_{0,j}$	pre-exponential factor, $m^3\ s^{-1}\ mol^{-1}\ K^{-1}$, s^{-1}
K_a	equilibrium constant in terms of activities
L	wave plate mist eliminator's main channel width, mm
m, M	mass, kg
m_p	particle/droplet mass, kg
$\dot{m}_p$	particle/droplet stream, $kg\ s^{-1}$
M_A, M_B	mass of species A, B, kg
M_j	molecular weight of species j
N	total number of species
$N_{particles}$	number of released particles
N_{Pt}	number of released platinum particles
N_{Pt_loss}	number of platinum particles that left the domain without recapturing
$N_{surface\_cells}$	number of computational cells on the catalyst surface
$\dot{n}_i$	mole stream of species i at the domain's outlet, $mol\ s^{-1}$
$\dot{n}_{N_{2_{inlet}}}$	molar flow of nitrogen at the inlet, $kmol\ s^{-1}$
$\dot{n}_{N_{2_{outlet}}}$	molar flow of nitrogen at the outlet, $kmol\ s^{-1}$
$\dot{n}_{NH_{3_{in}}}$	mole stream of NH_3 at the domain's inlet, $mol\ s^{-1}$
$\dot{n}_{NH_{3_{out}}}$	mole stream of NH_3 at the domain's outlet, $mol\ s^{-1}$
p	particle index
p, P	pressure, Pa, atm
p_x, p_y, p_z	momentum components for x-, y- and z-directions, Ns
P_A	net production of substance A, $mol\ s^{-1}$, $kg\ s^{-1}$
P_e	net production of energy, $J\ s^{-1}$
P_G	net production of G per time unit
P_x	net production of momentum in x-direction, $Ns\ s^{-1}$
r	radial coordinate

r	reaction rate, mol m^{-3} s^{-1}, kmol m^{-3} s^{-1}, mol m^{-2} s^{-1}, kmol m^{-2} s^{-1}
r_A	production of species A by chemical reaction, mol m^{-3} s^{-1}, kmol m^{-3} s^{-1}, mol m^{-2} s^{-1}, kmol m^{-2} s^{-1}
r_j	rate of reaction j, mol m^{-3} s^{-1}, kmol m^{-3} s^{-1}, mol m^{-2} s^{-1}, kmol m^{-2} s^{-1}
R	curvature radius of the bending place, m
R	universal gas constant, cal K^{-1} mol^{-1}, kJ mol^{-1} K^{-1}
$R_{accretion}$	accretion rate, kg m^{-2} s^{-1}
$R_{accretion_i}$	local accretion rate, kg m^{-2} s^{-1}
R_{accr_ratio}	percentage of all captured platinum, %
R_i, R_j	net rate of production of species i, j by surface chemical reaction, mol m^{-2} s^{-1}, kmol m^{-2} s^{-1}
R_i, R_j	net rate of production of species i, j by volumetric chemical reaction, mol m^{-3} s^{-1}, kmol m^{-3} s^{-1}
R_{NH_3}	formation/consumption rate of NH_3, mol m^{-3} s^{-1}, kmol m^{-3} s^{-1}
Re	Reynolds number
Re_d	droplet Reynolds number
Re_p	particle Reynolds number
S	strain rate magnitude, s^{-1}
Sc_t	turbulent Schmidt number
S_h	volumetric heat sources
S_i	creation rate for the species i from the dispersed phase or user-defined source
S_i	local selectivity of species i
S_i	momentum source term for the i (x-,y- or z-directions)
S_k	user-defined source term of turbulent kinetic energy
S_m	mass source term
S_v	surface-to-volume ratio, m^{-1}
S_{net_i}	net selectivity of species i
St	Stokes number
S_ε	user-defined source term for a turbulent dissipation rate
S_ω	user-defined source term for a specific dissipation rate
t	contact time, s, ms

t	time, s
T	temperature, °C, K
u	average gas velocity between wires, m s^{-1}
u	continuous phase velocity, m s^{-1}
u_{in}	continuous phase velocity at inlet, m s^{-1}
u_i, u_j, u_k	velocity components, m s^{-1}
u'	continuous phase velocity fluctuation, m s^{-1}
u'_i, u'_i	fluctuating velocity components, m s^{-1}
u_p	particle/droplet velocity, m s^{-1}
U	internal energy, J
$\overline{u}$	average continuous phase velocity, m s^{-1}
$\bar{u}_i$, $\bar{u}_j$	average velocity components, m s^{-1}
$\overline{u'}$	average continuous phase velocity fluctuation, m s^{-1}
$\overline{u'}_i$, $\overline{u'}_j$	average velocity fluctuation components, m s^{-1}
$\vec{u}$	gas velocity vector, m s^{-1}
$\overrightarrow{u_p}$	particle/droplet velocity vector, m s^{-1}
v	velocity, m s^{-1}
v_r	velocity in radial direction, m s^{-1}
v_x	velocity in x-direction, m s^{-1}
$v_{x,in}$	inlet velocity in x-direction, m s^{-1}
$v_{x,out}$	outlet velocity in x-direction, m s^{-1}
v_y	velocity in y-direction, m s^{-1}
v_z	velocity in z-direction, m s^{-1}
v_z	swirl velocity, m s^{-1}
$\|v\|$	magnitude of velocity, m s^{-1}
V	volume, m^{-3}
$\vec{v}$	overall velocity vector, m s^{-1}
v_{ij}	stoichiometric coefficient of species i in reaction j
v_i^N	number of nitrogen atoms in molecule i
W	energy flow resulting from work, J s^{-1}
W_i	efficiency production of species i
x, y, z	coordinates

x_A	mass fraction of species A
$x_{A,in}$	inlet mass fraction of species A
$x_{A,out}$	outlet mass fraction of species A
x_i, x_j, x_k	computational domain dimensions, m
y	distance, m
y_i	mole fraction of component i
y^+	dimensionless wall distance
Y_i	local mass fraction of species i
Y_k	dissipation of turbulence kinetic energy due to turbulence
Y_M	contribution of the fluctuating dilatation in compressible turbulence to the overall dissipation rate
Y_ω	dissipation of a specific dissipation rate due to turbulence
z	vertical coordinate

Greek symbols

α	drainage channel angle, °
α	parameter
α	permeability, m^2
α^*, α_1	coefficients
α_c	angle between wave-plates, °
α_{NH_3}	degree of NH_3 conversion
$\delta_{i,j}$	delta function
γ_i	activity coefficient of component i
Γ	site density, mol m^2
ε	porosity
ε	turbulent dissipation rate, $m^2\ s^{-3}$
η	conversion factor
η	droplet removal efficiency, %
η_{Pt_trap}	platinum recapture efficiency, %
θ_i	surface coverage of adsorbed species i
λ	thermal conductivity coefficient, $J\ m^{-1}\ s^{-1}\ K^{-1}$
μ	continuous phase dynamic viscosity, Pa·s

μ_t	continuous phase turbulent viscosity, Pa·s
ξ	effectiveness factor
π	Archimedes' constant
ρ	continuous phase density, kg m^{-3}
ρ_p	particle/droplet density, kg m^{-3}
σ_k	turbulent Prandtl number for k
σ_ε	turbulent Prandtl number for ε
σ_ω	turbulent Prandtl number for ω
τ_{xx}, τ_{yx}, τ_{zx}	shear stress components, Pa
τ_r	particle relaxation term
$\bar{\bar{\tau}}_{eff}$	effective stress tensor
φ	scalar component
$\bar{\varphi}$	mean scalar component
φ'	fluctuating scalar component
φ	transport (flow) rate
φ_G	flow rate of G
$\varphi_{G,in}$	inlet flow rate of G
$\varphi_{G,out}$	outlet flow rate of G
φ_m	mass flow rate, kg s^{-1}
$\varphi_{m,in}$	inlet mass flow rate, kg s^{-1}
$\varphi_{m,out}$	outlet mass flow rate, kg s^{-1}
φ_q	energy flow due to the heat not involved in mass flows, J s^{-1}
φ_V	volumetric flow rate, m^3 s^{-1}
$\varphi_{V,in}$	inlet volumetric flow rate, m^3 s^{-1}
$\varphi_{V,out}$	outlet volumetric flow rate, m^3 s^{-1}
ψ	sphericity
ω	specific dissipation rate, m^2 s^{-3}

Acronyms

BET	Brunauer–Emmett–Teller
CAD	computer-aided design
CFD	computational fluid dynamics

DPM	discrete phase model
LES	large eddy simulation
RANS	Reynolds-averaged Navier–Stokes
RSM	Reynolds stress model
SEM	scanning electron microscope
SIMPLE	semi-implicit method for pressure-linked equations
SST	shear stress transport
UDF	user-defined function

1. Introduction

In the modern world of 2025, despite continuous global economic growth, undernourishment and food insecurity are still severe problems [1]. This crisis is further increased due to the global climate changes and political instabilities caused by the Russian invasion of Ukraine since both of those countries were large exporters of fertiliser and agricultural products [2]. However, food production needs to be increased while limiting the growth of agrarian areas as much as possible to slow down the ongoing degradation of natural habitats since it negatively impacts wildlife and climate changes [3]. This goal can be achieved by increasing the effectiveness of large-scale fertiliser production. Existing chemical plants have the potential to be numerically simulated and optimised to improve efficiency and reduce energy consumption, leading to reduced running costs and greenhouse gas emissions. Computer-aided modelling closes knowledge gaps and supports experimental investigation, especially in fields requiring enormous financial effort, such as pilot or full-scale chemical apparatus construction. By enabling an in-depth insight into the process and identifying bottlenecks, it can provide invaluable data to improve the existing processes. This approach is relatively easy to implement. Furthermore, it is also much faster and less expensive than developing new technologies.

Fertiliser production is one of the most critical branches of the chemical industry. Multiple market analyses predict increased demand for fertilisers [4–7]. However, the chemical industry sector is a substantial contributor to global greenhouse gas emissions due to the direct emissions, which are the results of chemical conversions and due to the sector's high energy demand [8]. The energy conversion processes still operate primarily on fossil fuels, further increasing net CO_2 emissions due to the chemical production processes. According to the International Energy Agency [9], The chemical industry generates approximately 7% of the total greenhouse gas emissions and consumes about 10% of global energy production. Fertiliser production is a significant sector since ammonia synthesis alone in 2014 (146 million tons) was second among the most extensive production within the chemical industry, only surpassed by sulfuric acid [10], and its production consumes about 1% of total global energy production [11]. About 10% of the worldwide ammonia production is estimated to be oxidised [12]. Ammonia oxide is further used to produce nitric acid, of which about 80% is manufactured into fertilisers, typically through the conversion with ammonia to yield ammonium nitrate. Finally, about 85% of total ammonia produced is converted to fertiliser products such as urea [10]. Ammonia

synthesis in the Haber-Bosch process and ammonia oxidation in the Ostwald process have great potential to significantly reduce greenhouse gas emissions, increasing process efficiency and reducing the intensity of undesired phenomena like secondary reactions or catalyst losses. Due to the large-scale character of those processes, even minor improvements can cause significant benefits, influencing the process costs and the environmental impact.

Industrial-scale ammonia production is primarily manufactured using the Haber-Bosch process, one of the most efficient and widely used methods [13–15], and it is the basis of fertiliser production. The synthesis occurs in beds filled with catalysts, typically made from iron or magnetite [13]. There are several commercial approaches to ammonia synthesis. In the Kellogg process, the converter contains four axial-flow catalyst beds, an integrated heat recovery system, and centrifugal compressors [15]. The Braun Purifier Process uses the steam-reforming route and a significant excess of process air. Ammonia synthesis occurs in a 2-staged adiabatic converter with two axial flow catalyst beds with heat exchange [15]. The Topsoe Ammonia Process is currently the most widely used solution [15]. It is based on the steam-reforming route, and the converter typically contains 2–3 beds with the axial-radial flow. The Topsoe Process is characterised by low pressure drop, and the most influence on the course of the process is obtained through the proper selection of the catalyst (its size, porosity, shape and placement). The Topsoe converter's construction enables smaller catalyst particles to be used in the process, making it possible to obtain the desired conversion using the smaller capacities of the catalyst bed [15]. Due to the large-scale character of ammonia synthesis reactors, smaller, pilot-scale converters are used to experimentally investigate the influence of different catalysts and process conditions before implementing them into a full-scale process [13,16]. Pilot-scale converters also allow the cost-effective validation of numerical models. Experiments can be performed using much lower catalyst capacity (a few grams instead of kilograms) and much smaller gas flows [13], which causes massive cost reduction compared to the industrial scale.

The Ostwald Process is a typical and effective method to oxidise ammonia in short contact times on platinum or platinum-rhodium catalyst gauzes [17]. The ammonia oxide is further secondary oxidised to NO_2 and absorbed into water [8]. Ammonia combustion is the most critical stage, and it determines the course of the process. Besides, NO is a primary product; side reactions cause the formation of undesired products, such as N_2 and N_2O, which determine the efficiency and selectivity of the Ostwald Process [8]. Most notably, N_2O has a greenhouse gas potential, about 300 higher than CO_2 and can be involved in ozone depletion in the stratosphere [18]. Nitrogen formation is less critical due to its natural environment; however, it

affects efficiency by competing with the primary product. Ammonia combustion occurs during harsh conditions with high temperatures oscillating around 900°C [19]. Mass and heat transport determine this process because of its highly exothermic character and short contact times. Although the Ostwald process has been established in the industry for decades and is well described in the literature [19,20], there are still many unresolved problems, and one of the most severe is catalyst gauze degradation due to the high temperature, pressure and interaction with reactants. This phenomenon causes the morphology changes of the catalyst wires during the process campaign and is also observed during other catalytic reactions [21]. The formation of parallel facets is visible on the catalyst's surface after a few hours [22], and it is followed by the growth of so-called "cauliflower structures" on the catalyst wires' surfaces [17,23]. Those structures enlarge the wire's diameter and increase its surface area. Finally, when cauliflower structures grow larger, they start to collapse, and the gas flow lifts catalyst particles in the form of volatile platinum oxide, consequently causing the gauze to degrade. Continuous loss of platinum is caused by abrasion and vaporisation. In the case of Pt–Rh gauzes, the proportion of Pt and Rh in the alloy is constantly changing since platinum oxide is more volatile than rhodium oxide [17].

Industrial-scale processes are usually part of larger installations with various supporting units, which provide utilities (e.g. heat or cooling systems), optimise energy consumption (e.g. heat recuperation systems), prevent apparatus failure or separate the substrates and products. Analogically to large unit operations like ammonia synthesis and oxidation, secondary equipment often works on high-capacity production lines, which makes them potential subjects to optimise, and due to the large-scale character of those processes, even minimal improvements can significantly increase efficiency and reduce running costs. Droplet removal through mist eliminators is an example of such supporting units. The necessity of removing liquid droplets contaminating gas streams is not limited to the fertiliser industry, and it is a common problem in industrial technologies [24,25]. Gas-liquid aerosols' presence in process streams can result from phenomena like spontaneous condensation or desublimation of supersaturated gas-vapour mixtures, and they are undesired in many gas-liquid contact devices such as absorbers, quench coolers-, or condensers [25]. In the fertiliser industry, mist-eliminators can remove water droplets from streams, leading to vulnerable apparatuses such as compressors or units requiring high-purity gas mixtures, and recapture valuable product droplets from recirculation streams to proceed further. To remove very fine droplets with diameters smaller than 2 μm, sophisticated solutions are required, such as glass fibre bed separators [25]. However, in cases of droplets of

size ranging from a few to tens of micrometres, wave-plate type mist eliminators can be effective and relatively inexpensive solutions [24]. Wave-plate mist eliminators have a simple geometry which forces the gas flow to a zig-zag shape, causing sharp changes in flow patterns. The high density of droplets leads to their depletion from the gas motion path due to the forces of inertia and, consequently, their separation on the walls and drainage channels [24,26]. Proper geometry selection depends on the process conditions and droplet size ranges, and numerical methods can provide valuable data without requiring multiple prototype construction and testing.

2. Motivation and scope of this work

This dissertation is focused on investigating different unit operations of fertiliser production using computational fluid dynamics (CFD) methods. This work's sections subsequently investigate the primary fertiliser production stages: ammonia synthesis and oxidation. The last section concerns droplet removal processes, an example of a supporting process, and it is not limited to one industry branch. Each section studies the influence of critical geometrical aspects, process parameters and specific issues associated with the particular process, such as catalyst loss during ammonia oxidation. Detailed kinetic models were implemented into simulations for the models containing chemical reactions, and CFD models were created to provide insight into parameters that were unavailable to be obtained experimentally, such as direct reaction rate values. Such knowledge can fill the knowledge gaps, and obtained CFD models can be used to support and guide experimental research, as well as to assist design choices, by providing the "virtual prototypes" to test different geometries and parameters and use those data to limit the number of physical prototype variants, significantly reducing implementation costs.

Sections 5 and 6 of this work are dedicated to the ammonia synthesis conducted by the Haber-Bosch process. The literature has many examples of numerical simulations of the Haber-Bosch process. In 1977, Singh and Saraf [27] developed a mathematical model for auto-thermal and adiabatic ammonia synthesis reactors. In 1988, Elnashaie et al. [28] created a steady-state, heterogeneous model of a countercurrent tube-cooled fixed-bed ammonia reactor coupled to a heat exchanger. In 2003, Panahandeh et al. [29] elaborated a two-dimensional model for an axial-radial ammonia synthesis converter using the Navier-Stokes and continuity equations to model momentum, energy and mass balance directly. In the same year, Kasiri et al. [30] modelled a four-bed ammonia synthesis reactor in a dynamic state. In 2006, Dashti et al. [31] created a non-homogenous and one-dimensional model of the Kellogg variant of the ammonia synthesis converter with an internal heat exchanger and three axial flow catalyst beds. In 2014, Azarhoosh et al. [32] applied a generic algorithm for modelling and optimising a horizontal-type ammonia synthesis reactor. In 2018, Jorqueira et al. [33] used the mathematical model created by Singh and Saraf [27] for simulation and sensitivity studies of ammonia reactors. Many of those studies use the kinetic models based on variants of the Temkin-Pyzhev equation for modelling the ammonia synthesis reaction. Dyson and Simon developed a versatile kinetic model [34] by modifying the Temkin-Pyzhev equation by adding the diffusion correction factor. In the current literature, there is little information about the CFD modelling of the Haber-Bosch

process. Still, in 2021, Mirvakili et al. [34] obtained a two-dimensional, axisymmetric model using the kinetic model developed by Dyson and Simon [35]. However, no CFD investigations concerning different catalyst bed parameters exist in the literature. Thus far, there has yet to be data regarding CFD simulations of pilot-scale ammonia synthesis reactors in the current literature before this work.

Section 5 of this dissertation uses CFD methods to investigate a large-scale variant of the axial-radial ammonia synthesis converter. The modified Temkin-Pyzhev expression obtained by Dyson and Simon [35] was implemented in the CFD model through a user-defined function (UDF) to model the ammonia synthesis reaction. The analysed reactor is a Topsoe converter with an axial-radial flow pattern through packed beds filled with a magnetite catalyst. This work is focused on the influence of the catalyst bed's parameters on the process, such as catalyst particle size or porosity. The results contained velocity, reaction rate, concentration, and pressure contours, which were used to identify the high and low reaction intensity areas within the catalyst beds. The obtained CFD model allowed relatively easy identification of geometry flaws like dead reaction zones and prediction of the influence of parameter changes. Based on the results, potential modifications to the catalyst bed's geometry were proposed to reduce bed volume capacities without affecting the reactor's performance.

Section 6 of this dissertation was done during the author's 3-month internship at Yara Technology and Projects – Technology (Yara International ASA). Yara possesses two pilot-scale ammonia synthesis converters at Yara research facilities in Porsgrunn, Norway. This study aimed to recreate the geometry, conditions, and chemical reaction course in the pilot ammonia converters by creating a CFD model to simulate the process accurately. Yara Technology and Projects – Technology provided the experimental data and detailed geometrical information of physical converters, which were the basis for creating and validating the CFD model. The reactor was simulated in a 3-dimensional domain that covers its entire geometry, and the catalyst beds were modelled using a porous zone model with the reaction kinetics developed by Dyson and Simon [35] implemented as a user-defined function. The results include the velocity, temperature, pressure, concentration, and reaction rate profiles, and the motivation of this research was to obtain an insight into the process and more control of the converter's geometry and process parameters.

Sections 7 and 8 focus on the Ostwald ammonia oxidation process and the issue of catalyst degradation and platinum losses. Several numerical studies concerning the surface character of ammonia oxidation are available in the current literature. In 1991, Hickman et al. [36] simulated

the ammonia burner with catalyst gauzes using rate equations acquired from surface experiments. In 1994, Aparicio and Dumesic [37] investigated the microkinetic surface chemistry of ammonia combustion over the iron catalyst. In 2008, Kraehnert and Baerns [38] studied ammonia oxidation in a microstructured quartz reactor using pure platinum as a catalyst and developed a 10-reaction surface kinetic model. In the same year, Novell-Leruth et al. [39] studied the microkinetics of ammonia oxidation by applying Density Functional Theory calculations. In 2009, Scheuer et al. [40] compared experimental data with mechanistic modelling. In 2012, Rafti et al. [41] conducted numerical simulations of ammonia combustion using mean field equations. In 2013, Warner [17] created mechanistic models for ammonia oxidation kinetics in industrial conditions. In 2018, Otomo et al. [42] proposed an improved mechanism of ammonia oxidation after studying this process regarding flame speed and ignition delay time. In the literature, examples of successful simulations of the Ostwald process using the CFD methods exist. In 2020, Wiser [22] implemented and investigated different surface mechanisms using CFD simulations. In 2022, Haas et al. [43] used CFD methods to study the influence of the effects of local mass transfer on N_2O selectivity, and later, in the same year, he expanded this research in his PhD dissertation [8]. In 2022, Pottbacker et al. [44] conducted a combined experimental and CFD study on temperature and concentration gradients. Although there are several CFD studies in the currently available literature, there is little or no information concerning the surface gradients of reaction rates or entrained catalyst particle behaviour and their secondary recapture, which are examples of the primary issues investigated in this work.

Section 7 of this work concerns using the CFD methods for an in-depth analysis of the ammonia oxidation process with 3-layered platinum catalyst gauze. The detailed surface microkinetic model developed by Kraehnert and Baerns [38] was implemented into the simulation using the user-defined function, allowing the plotting surface parameters unavailable to obtain experimentally, such as reaction rate or selectivity gradients. This work also studied the influence of critical parameters like contact times or catalyst gauze temperature on process efficiency and product concentration.

Section 8 uses the CFD model developed in Section 7 to investigate the problem of catalyst degradation and entrainment of its particles. Contact time and gauze temperature are critical parameters that prompt that undesired phenomenon. The CFD model was used to identify the factors directly influencing the degradation process, such as stagnation zones and temperature gradients on the catalyst wire's surface. Zones of increased platinum release were designated after determining the catalyst surface temperature gradient. Based on those results, the

trajectories of entrained platinum particles were simulated to estimate the platinum losses and entrapment areas on subsequent gauze layers, and the results met the experimentally observed tendencies described in the literature [45–47]. This section investigated and compared two different catalyst gauze geometries, including the typical and modified gauze.

Section 9 is dedicated to the supporting process, which is droplet removal by wave-plate mist eliminators. This versatile subject matter is relatively well documented in the literature, including publications concerning CFD modelling. In 1939, Houghton and Radford [48] experimented with mist eliminators at high gas velocities. In 1998, Wang and James [49] applied the k-ε turbulence model to simulate the flow field and droplet motion within wave-plate demisters. In 1999, Wang and James [50] used The Eulerian-Lagrangian method and eddy-interaction model of CFX solver to simulate droplet deposition in wave-plate demisters. In 2002, Azzopardi et al. [51] studied the re-entrainment phenomenon in wave-plate mist eliminators using experimental methods. In 2003, James et al. [52] investigated the influence of drainage channels by conducting simulations of wave-plate plate mist eliminators in the CFX solver. In 2008, Galletti et al. [24] used experimental and CFD methods to develop Eulerian-Lagrangian models of wave-plate mist eliminators with drainage channels. In 2011, Estakhrsar and Rafee [53] studied the influence of the dimensions of drainage channels using the eddy interaction model and the Eulerian-Lagrangian method and tested different turbulence models. In 2013, Rafee et al. investigated the airflow and droplet deposition using the eddy interaction, Eulerian-Lagrangian models and the Reynolds Stress Transport Model for turbulence modelling. In 2017, Liu et al. [54] conducted an experimental and numerical performance study of a novel wave-plate compound demister with higher resistance to droplet re-entrainment. In 2018, Yuan et al. [26] numerically studied the influence of droplet coalescence and breakup with the discrete phase simulated as an unsteady process in wave-plate separators. Current literature proves that computational fluid dynamics play a unique role in understanding this process since it allows the simulation of the system's conditions and quickly estimates the influence of geometry and process parameter changes. Furthermore, the influence of drainage channel geometry on droplet removal efficiency has a vast impact on the process, and this field has great potential for further improvement. Motivated by this knowledge, the primary aim of this work was to create the CFD model of a wave-plate mist eliminator and use it to propose a novel variant of drainage channels that increase the droplet removal performance without increasing the pressure drop.

Section 9 investigates the droplet removal in wave-plate mist eliminators using CFD methods. It contains a numerical study of different aspects of the geometry of drainage pockets, such as length, angle and shape, that influence the droplet removal efficiency and pressure drop. The simulations were conducted for different process velocities. Since mist eliminators are versatile equipment used in many industries, different droplet media were investigated, such as water, diesel fuel, n-octane, sulphuric acid or aqueous ammonia solution. The first part of this work focused on selecting and validating turbulence and turbulent dispersion models most suitable for the simulated process conditions. The influence of drainage channels' presence, width, and slope angle on the mist eliminator separation efficiency and pressure drop were investigated using the most appropriate turbulence and turbulent dispersion models. Based on the results, a new, streamlined shape of drainage channels was proposed, characterised by excellent droplet separation efficiency and reasonably low pressure drop.

This PhD thesis was made with substantial cooperation with dr Jakub Bujalski, a global expert in fluid dynamics from the Process Modeling and Control Department in Yara Technology and Projects (Yara International ASA) Yara Technology and Projects – Technology (Yara International ASA), who provided practical support for the ammonia synthesis and oxidation issues in Sections 5–8.

3. Theoretical background

This section is focused on the theoretical part of this work. Since this dissertation approaches the analysed issues from the chemical and process engineering's point of view, the theoretical section is focused primarily on historical and modern known and used solutions in large-scale industries. Still, it should be noted that many literature publications analysed the detailed chemistry and catalytic aspects of the Haber-Bosch [14,55,56] and Ostwald processes [19,20,57], which substantially contributed to the development of the fertiliser industry.

3.1. Haber-Bosch process

3.1.1. Historical background

The synthesis of ammonia is arguably one of humanity's most extensive volumetric catalytic chemical reactions [12,14]. As a strategic, essential component of the nitrogen industry, it is required for fertiliser production, contributing significantly to the survival of humankind, accounting for 40% of the nitrogen content within the global human diet [14].

The direct synthesis of ammonia from its elements has been known as the Haber-Bosch process since the beginning of the 20th century. At that time, scientists disputed that synthesising ammonia using this approach was possible since the equilibrium point was yet to be determined [13]. Industrial applications require the equilibrium to lie not too far from the side of the elements at reaction temperatures to make the conversion high enough to be viable to implement in large-scale production [13]. The conversion is exothermic, and the total number of molecules is reduced to half during the process, considering the combined number of nitrogen and hydrogen molecules. This necessitates conducting conversion at as low temperatures and as high pressures as possible [13]. Implementing the process required the development of catalysts for molecular nitrogen's activation at low process temperatures. Furthermore, the reactor had to be designed to work under high-pressure conditions and conversion temperatures [13].

Fritz Haber started his research on the thermodynamic equilibrium between ammonia, hydrogen and nitrogen in 1904, obtaining the ammonia by performing the hydro generation of the nitride and its formation in steady-state conditions [13]. His study contained the thermodynamics and rate of approaching the equilibrium point from nitrogen and hydrogen. Haber's first interest was to measure the gas composition at equilibrium since the catalyst does not affect the composition and maximum yield [13]. Before his research, some of the attempts in the 19th century had been successful in converting small amounts of the product since the

nitrogen's behaviour is too inert at moderate temperatures, and at high temperatures, where conversion becomes possible, the ammonia decomposition occurs [13]. A catalyst that allows conversion at high temperatures was required to avoid this. Perman [58] tried to use iron as a catalyst. Still, his experiments failed to achieve an equilibrium due to moisture contamination. Haber used his research as an entry point, assuming that moisture should be eliminated since it hinders the reaction [13].

Haber conducted his experiments using the iron catalyst at an equilibrium point at temperatures around 1026°C and atmospheric pressure [13]. He used two reaction tubes to measure the equilibrium composition by approaching it from opposite directions: synthesis and decomposition of ammonia. At the equilibrium point, the catalyst should stabilise and obtain an actual equilibrium value [13]. Haber obtained only a small amount of ammonia, estimating that the temperature necessary for atmospheric pressure in a commercial system should be lower than 300°C, far from the required minimum. However, this proved that ammonia synthesis could be possible at room temperature if the proper catalyst was discovered [13].

Walter Nernst suggested that Haber's approach is not feasible on the industrial scale since his experiments and theorem indicate that ammonia output would be three times smaller than Haber's predictions [13]. However, Haber's group extended the process by adopting the closed circulating system with a converter and heat exchanger to heat the reaction gas mixture using the heat generated from the reaction itself. In this circulating system, ammonia was produced continuously in the liquid state using the stoichiometric nitrogen-hydrogen mixture at the inlet, proving that this method can be feasible commercially [13].

The BASF (Badische Anilin- und Soda-Fabrik) company noticed Haber's efforts, and in 1909, they sent the Bosch and Mittasch engineers to visit Haber's laboratory and see the demonstration of his process using osmium as a catalyst at the pressure 175 bar, obtaining an ammonia production rate of 80 g per hour [13]. Bosch later created the high-pressure system, and Mittasch focused on commercial catalyst research. In 1910, they demonstrated successful ammonia synthesis from the elements, and BASF started its industrial development, assigning Bosch responsible for this project to solve substantial problems regarding converting this process to a full industrial scale [13]. Those problems involved obtaining cheaper, stable catalysts to enable production at lower temperatures and pressures, improving the high-pressure apparatus, and obtaining an affordable large-scale pure nitrogen-oxygen reactant mixture. After extensive research by Mittasch's team, the magnetite catalyst with high stability and activity was proposed. This material contains iron promoted by alumina and potash and is still widely

used in the ammonia oxidation industry [13]. However, the research was hindered by the reduction of carbon steel by hydrogen, which resulted in damaging the early experimental converters and causing the life of the vessel to last only for a few days of the conducted process. Bosch solved this problem by using the soft iron with a pressure-resistant steel shell from the outside with small holes, allowing the release of the hydrogen to diffuse through the inside soft iron lining [13]. The novel double-tube converter was fully operational in 1911. The first ammonia plant was built with a production capacity of 30 tons of ammonia per day, and this value increased to 230 tons per day by 1917. In this installation, hydrogen was initially obtained from water gas and further replaced by the water-gas shift reaction over an iron oxide catalyst [13]. Nitrogen was obtained through air liquefaction and later by the air reaction with red hot coke, producing the gas mixture of 60% nitrogen and 40% CO, which was used in shift reaction for hydrogen production [13]. The CO_2 was removed by water scrubbing, and residual CO was dissolved in ammoniacal copper liquors.

The developed Haber-Bosch process was applied in Germany and other countries, replacing the calcium cyanamide and electric arc methods of ammonia production. In the late 1950s, technological developments allowed the building of large ammonia plants with production capacity exceeding 1000 tons per day [13], and modern installations can yield up to 1800 tons of ammonia per day [59]. In the 1960s, synthesis gas started being produced from naphtha and natural gas, replacing previously used coal and reducing running costs [13]. Those innovations reduced ammonia costs, substantially contributing to famine risk elimination in most parts of the modern world [13].

3.1.2. Modern commercial practises

In modern industrial ammonia synthesis installations using the Haber-Bosch method, significant roles have primary raw materials since they directly affect the purity of the ammonia synthesis gas. Furthermore, in most commercial systems, ammonia synthesis is an integral part of the overall installation [15]. Hydrogen production for ammonia synthesis is typically made by one of two methods: steam-reforming and partial oxidation [15].

The steam-reforming route is based on the light hydrocarbon stream, like natural gas and liquified petroleum gas naphtha. The process is performed in several steps, including catalytic reaction: desulfurisation, primary reforming, secondary reforming, shift conversion, CO_2 removal, and methanation. The obtained mixture is compressed and proceeds to the ammonia synthesis unit [15]. The nitrogen is introduced to the gas mixture by adding the air in the

secondary reformer. The amount of air is controlled to give a 3:1 hydrogen-to-nitrogen ratio in the subsequent gas mixture. The residual CO is removed in the methanation step to prevent catalyst poisoning. Aside from hydrogen and nitrogen, the feed gas contains about 0.6–1% methane and 0.3% argon and is cooled to recuperate the heat and condensate water before entering the ammonia converter [15].

The partial oxidation route uses heavy hydrocarbons, which are not suitable for steam reforming, including naphtha, crude oil, heavy fuel oil, tar and asphalt [15]. The feed stream is burned in the presence of steam with a limited amount of oxygen in the gasifier. Further steps are carbon removal, high-temperature shift conversion, acid gas removal and nitrogen wash [15]. The nitrogen is added in the latest step in the liquid form, and it is controlled to achieve a stochiometric mixture of hydrogen and nitrogen at the outlet. At this stage, other components like CO, CO_2, methane, and argon are removed from the liquid nitrogen stream [15].

The industrial ammonia process is constrained by the thermodynamic equilibrium, meaning that only a fraction of nitrogen and hydrogen is converted in the single-pass-through reactor. The unreacted substrates are recycled after the removal of ammonia from the converter outlet stream, which is called an “ammonia synthesis loop” and is a typical feature in all commercial ammonia plants [15]. The loop contains a converter with the catalyst, cooler, purge unit, synthesis gas injection, liquid ammonia catchpot (separator) and circulator (compressor) [15]. Converters are designed to contain large catalyst volumes and operate at temperatures up to 530°C and in the 100–350 bar pressure range. They are typically made from stainless steel to resist hydrogen reduction and nitriding [15]. Converters usually have outer shells made from non-stainless steel, which is less expensive, more resistant to pressure and does not come in contact with the medium. For temperature control, converters contain internal heat exchangers, pre-heating gas mixtures, and cooling reacting gas to increase the ammonia concentration at equilibrium [15]. After leaving the converter, the gas mixture is cooled, the ammonia is separated at the liquid state, a purge is required to remove accumulating inerts, and the pressure is usually kept by two compressors to ensure the process continuity during the maintenance periods [15]. Modern ammonia loops can recover up to 90% of the reaction heat, primarily for preheating feed water for high-pressure steam production. The hydrogen recovery efficiency reaches 98% from purge gas, while the remaining 2% is utilised as fuel [15].

The following sections describe the four most typical methods of ammonia synthesis approaches used in the industry, the start-up issues and the basic principles of ammonia loop operation.

3.1.3. Kellog ammonia process

This approach, introduced by Kellogg in the 1960s, uses centrifugal compressors and can be achieved from single-steam plants [15]. As a gas feed, desulfurised naphtha or natural is used, and the inlet stream is pre-heated to 450°C. The primary reformer uses the nickel-based catalyst; its exit conditions are 800°C and 32 bar [15]. The secondary reformer also uses a nickel-based catalyst and introduces air, which is also a source of nitrogen for further ammonia synthesis. The output gas has 1000°C temperature and about 0.3% of methane. The gas mixture is then cooled and forwarded to the shift conversion unit, where the CO concentration is reduced to 0.3%. CO_2 is removed by the liquid solvent to 0.1% [15]. The methanation stage of residual CO and CO_2 is the last step during feed gas preparation, and it occurs on nickel-based catalysts at a temperature of 300–350°C. The output gas has a stoichiometric concentration of H_2 and N_2 with around 0.8% methane and 0.3% argon. The gas stream is compressed to the synthesis pressure and mixed into the ammonia loop with the recycled gas before the final compression within the loop, which is about 150 bar for ammonia plants with a 600–1100 tons capacity per day [15]. The gas is cooled to −25°C to condense and separate ammonia and then pre-heated to 140°C with a residual ammonia concentration of 2% [15].

The converter with 1000 tons per day capacity contains four axial-flow catalyst beds with interchangers below the beds, as shown in Figure 3.1. Before entering the first bed, the gas enters the reactor from the bottom and is pre-heated in the mantle between the outer shell and the cartridge. Bed temperatures are controlled by the heat exchanger's bypasses, mixing the gas and leaving each bed with the quench gas not heated by the reaction heat [15]. The gas mixture leaving the last bed contains about 10–12% ammonia and flows up through the central pipe and to the heat exchanger before leaving the converter from the top. The Kellog converter uses a commercial iron-based catalyst with particle sizes 6–10 mm [15]. After leaving the reactor, the gas mixture is cooled in heat recuperation systems, and the purge stream removes the accumulating inerts from the loop. The purge gas is further utilised as a hydrogen recovery fuel [15].

The Kellogg approach reduced heat waste through the integrated heat recovery system, reusing heat from different process streams and reforming flue gas for earlier processes, such as raising the high-pressure superheated steam that drives the synthesis gas compressor [15]. In some Kellogg synthesis loops, horizontal ammonia converters are used, reducing the pressure drop and allowing smaller catalyst particles to be used [15].

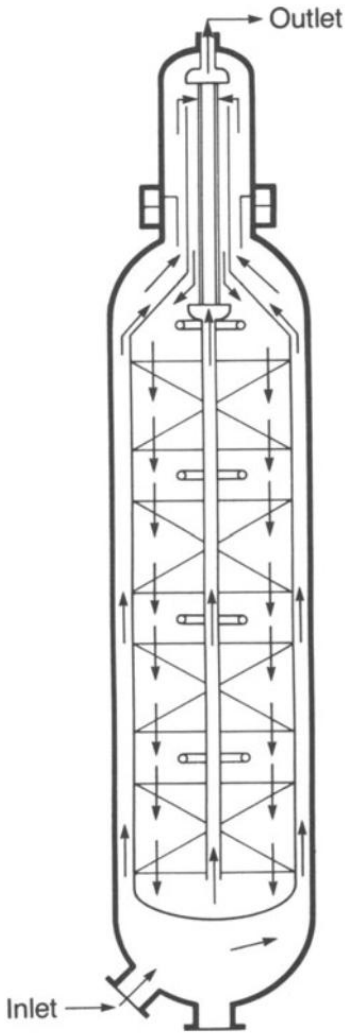

Figure 3.1. Kellog ammonia converter scheme [15]

3.1.4. Braun purifier process

The Braun purifier process uses the steam-reforming route with the gas stream purified before entering the synthesis loop [15]. This approach uses a significant excess of air feed (50% more than the stoichiometric nitrogen requirement) into the secondary reformer, coupled with removing the nitrogen surplus in the cryogenic separator after the methanation step. This arrangement reduces the size and cost of the primary reformer, consequently reducing the amount of fuel needed due to the small heat load of the primary reformer [15]. Similarly to the Kellogg process, the feedstock is naphtha or natural gas, and the primary reforming takes place at 30 bar and 700°C, which is lower than in the Kellogg approach [15]. Process air is added into the secondary reformer after being compressed. Due to its excess, this process produces more heat. Still, the gas exiting the second reformer has a relatively low temperature of 900°C, resulting in the higher methane concentration being further removed before entering the ammonia loop [15].

The characteristic point of the Braun process is purification, where all impurities are removed before the feed stream is introduced into the ammonia synthesis loop [15]. Water is removed in the sieve dryers, and dried gas enters the cryogenic purifier with a heat exchanger, gas expander and rectifier column. The gas stream is cooled to about −175°C [15]. The cooled stream is processed in the rectifier, where the top product is pure synthesis gas while the bottom product is a waste stream used further as fuel [15]. The synthesis gas has a stoichiometric concentration of substrates with a trace of methane and 0.2% argon.

The synthesis gas is compressed to 140–200 bar and enters the ammonia loop, where it is mixed with the recycled gas, and the mixture flows through the circulator compressor. Thanks to the purifying step, the gas enters the rector directly. After conversion, the ammonia is condensed and separated, and only a tiny purge to remove argon is needed within the loop. The purge gas is recycled to the purifier after being scrubbed with water [15]. The ammonia converter is a two-stage adiabatic reactor with two beds enclosed in separate pressure shells and an axial gas flow (Figure 3.2).

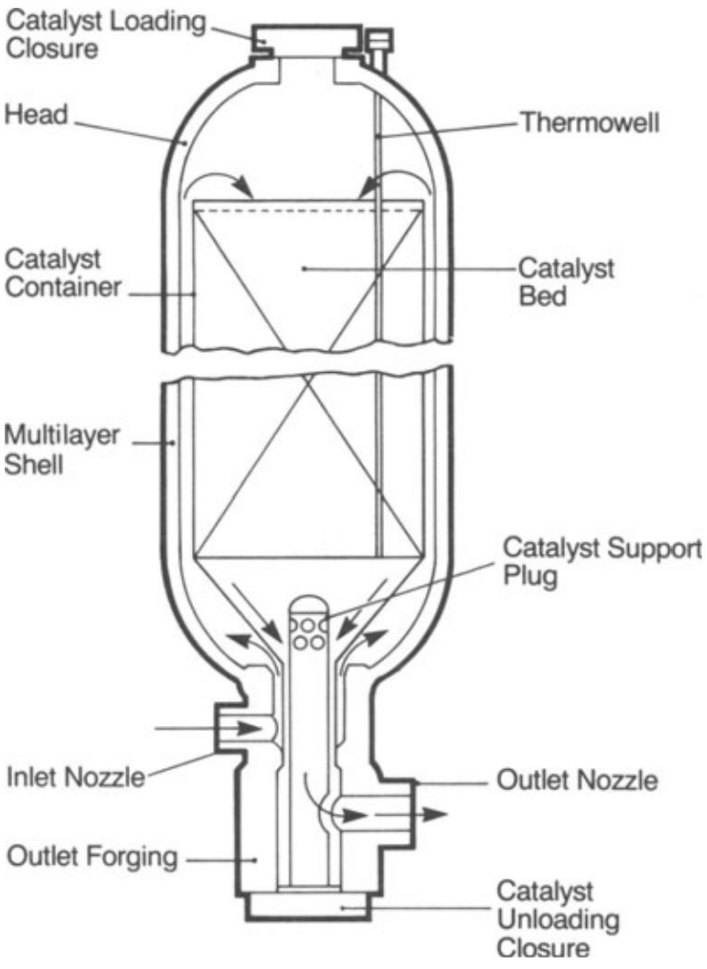

Figure 3.2. The Braun ammonia converter scheme [15]

The synthesis gas enters the reactor from the bottom, flows upwards between the catalyst container and the pressure shell, and enters the catalyst bed. The outlet nozzle is also located at the bottom of the converter. This reactor's design allows simple and easy catalyst replacement. Fresh catalyst is loaded from the top, and the old catalyst is gravitationally discharged at the bottom through the support plug and bottom closure [15]. The drawback of a separate-vessel converter is the requirement for higher temperatures and ammonia concentrations [15]. The inlet bed temperature is 400°C, considerably higher than the typical used values of 50–250°C. Due to the higher temperature, the pressure shell's thickness is higher. The nozzles and inner heat exchanger also need to be designed for higher temperatures since the maximum bed exit temperature is 530°C [15]. High concentrations of ammonia increase the rate of nitriding, which, combined with higher temperatures, requires proper material selection [15].

In the Braun process, waste heat is also recycled to generate high-pressure steam. Due to the reduced heat load on the primary reformer, there is insufficient waste heat to fulfil the total plant compression needs. Because of that, the gas turbine is integrated to balance the steam and power requirements [15]. This turbine drives the process air compressor, and its exhaust gas delivers the combustion air to the furnace of the primary reformer [15].

3.1.5. Topsoe ammonia process

The Topsoe approach also follows the typical steps of the steam-reforming route, and the feedstock is naphtha or natural gas [15]. The significant differences that characterise the Topsoe process are equipment design and catalysts. The primary reformer's furnace is designed with several burners set in furnace walls in contrast to the usually used top-fired design [15]. Topsoe company also produces the catalysts for all steps in the Topsoe ammonia process [15].

The synthesis gas contains the stoichiometric ratio of nitrogen and hydrogen with 0.8% methane and 0.3% argon and is produced by the typical steam-reforming route. The compressed feed gas enters the loop, the mixture is cooled, and liquid ammonia is separated at a temperature of −5°C [15]. Trace amounts of water and CO are removed with the liquid ammonia. The Topsoe process does not use molecular sieves, eliminating the risk of dust carryover [15]. After ammonia separation, the gas is reheated, enters the compressor, and proceeds to the converter containing two or three catalyst beds [15]. The gas flow is typically radial, resulting in low-pressure drops and enabling the usage of small catalyst particles of diameters in the range of 1.5–3 mm, eliminating the diffusional limitations and effectively reducing the required volume of the

catalyst beds [15]. After exiting the converter, the gas mixture is cooled in the heat recovery system, and the purge gas is removed before fresh synthetic gas is added.

The typical model of the Topsoe converter is S-200m, which contains two radial-flow catalyst beds and internal heat exchangers used to control the temperature of the second bed (Figure 3.3).

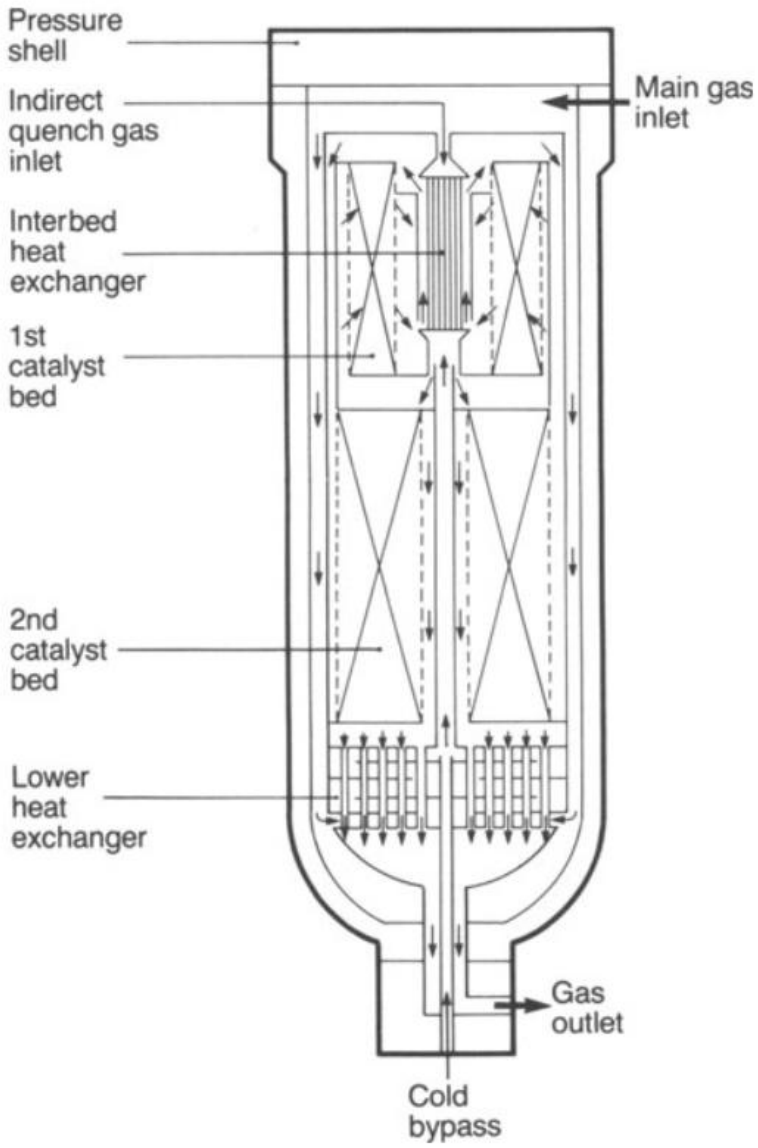

Figure 3.3. Topsoe S-200 radial ammonia converter scheme [15]

The indirect cooling in the Topsoe S-200 converter allows for higher conversion per pass for a given catalyst volume [15]. Topsoe company produces different versions of their converters, such as a variant without a lower heat exchanger, where converted gas leaves the reactor directly to the heat recovery system at a higher temperature [15]. However, this design requires a higher inlet temperature.

The ammonia synthesis process is limited by the reaction's thermodynamic equilibrium, meaning that converters with three inter-cooled beds will obtain higher conversion per pass, increasing the dew point of the converted gas. This will result in the possibility of using cooling water instead of the refrigeration system to condense ammonia [15]. Topsoe also provides the three-bed converter variant by coupling the two-bed S-200 model with a boiler and additional one-bed converter, which enables the higher temperatures heat recovery before the final bed, which can be used in plants requiring heat recovery for high-pressure boilers [15].

3.1.6. ICI AMV ammonia process

Similarly to other discussed processes, this approach is based on the steam-reforming of naphtha or natural gas, using the same steps as the Kellogg or Topsoe approaches [15]. However, the ICI AMV process uses considerably different process conditions. Primary reforming is conducted at mild temperatures, and secondary reforming uses excess process air. After subsequent steps of the steam-reforming route, the synthesis gas contains a surplus of nitrogen and a relatively high methane concentration [15]. After compression, the gas enters the ammonia loop, where ammonia is converted. Methane, argon and nitrogen excess are removed using the cryogenic treatment, which can be applied within a loop due to the low synthesis pressure, and the recovered hydrogen is returned to the circulator [15].

In the ICI AMV approach, the feed gas is mixed with the recovered hydrogen and desulfurised before saturation by contact with circulating process condensate. The feed gas is mixed with steam and, after preheating, enters the primary reformer. The exit conditions of the primary reformer are 750–800°C and 30–40 bar [15]. In the second reformer, gas is reformed with an excess process air, with an exit temperature of 900–950°C and a methane concentration of 1% [15]. The gas mixture then enters high and low-temperature shift converters. The excess heat from the process stream is reused for steam generation and other utilities [15].

After shift conversion, the carbon dioxide is removed, and then the gas mixture is compressed to 80–100 bar. and methanated before entering the ammonia loop before the circulator unit. In the loop, gas is heated and transferred to the ammonia converter. The exit gas is cooled with heat recovery, and the ammonia is separated by the mechanical refrigeration unit [15]. The rest of the gas circulates within the loop with inerts and nitrogen excess removed by the purge. The hydrogen is cryogenically removed from the purge gas and recycled into the circulation [15].

3.1.7. Ammonia synthesis loop's start-up

The commercial catalysts are usually in the form of magnetite, which needs to be reduced to metallic iron before use [15]. The reduction phase lasts 3–5 days, depending on the plant design and specific catalyst variant obtained from the supplier. The critical factors for ammonia plants are water concentration in the loop, flow rate, reduction temperature and reduction pressure [15].

Water content is a factor severely hindering ammonia synthesis, meaning it must be kept to a minimum (less than 100 ppm) [15]. Low water is necessary to prevent the re-oxidation of the already reduced catalyst. The water concentration is reduced in refrigeration systems if the ammonia content of the reduced water is higher than 20% to avoid freezing [15]. During catalyst reduction, the water presence lowers the final activity of the reduced catalyst; in practice, exit water concentration should not exceed 5000 ppm, and 10000 is the maximum limit [15].

Catalyst reduction is performed at the highest possible gas flow rate [15]. This speeds up the process and better distributes the gas within the bed, which is critical since it prevents uneven reduction of the catalyst. This undesired phenomenon results in high local concentrations of water and activity losses [15]. The initial gas rate is limited by start-up heaters, which are externally heated by fuel. Larger heaters have higher initial costs but lower catalyst reduction times at start-up. In multibed reactors, the first bed is reduced initially, and its reaction heat supplements the start-up heater, allowing the increased gas rate during the later reduction phase [15].

During catalyst reduction, the temperature rises about 50°C per hour to reach the values of 320–330°C, and after this level, the heating rate is reduced to 10°C per hour until reaching 370–380°C [15]. Temperature strongly influences the reduction rate and exit water content. During the reduction, the synthesis initiates, which could result in rapid temperature growth. Precise temperature control is needed since peak temperatures should not exceed 500°C until the reduction is complete [15]. To avoid simultaneous reduction of multiple beds, unreduced catalysts must be kept below 350°C [15]. The reduction pressure has less influence on the reduction process, although the higher pressures increase the ammonia synthesis rate, consequently increasing the bed's temperature. Because of that, the reduction is performed using the 100 bar pressure in the case of a typical operating pressure of 150 bar [15].

The producers supply pre-reduced catalyst in a partially oxidised stable form (less than 10% oxidised). The pre-reduced catalyst required a short activation period and allowed handling and charging to the converter [15].

3.1.8. Ammonia synthesis operation principles

Despite many industrial approaches, there are several general operating principles applied in most plants which need to be considered while selecting the optimum loop operation design and process parameters:

- Higher temperature increases the reaction rate, although it gives a less favourable equilibrium. The optimum temperature is balanced between equilibrium and reaction rate [15].
- Inert gases (mainly methane and argon) accumulate in the synthesis loop, suppressing the reactants' partial pressures, and their excess must be removed in the purge stream. The optimum inert concentration is between power consumption due to inert concentration and reduced efficiency due to the increased purge rate [15].
- Increased flow within the circulation loop increases the production rate but requires more energy for circulator and refrigeration [15].
- Higher loop pressures improve the ammonia concentration in equilibrium and increase the reaction rate. However, higher gas pressure requires compression power and more pressure-resistant apparatus [15].

3.2. Ostwald process

3.2.1. Historical background

The history of the selective ammonia oxidation to nitric oxide at high temperatures has been known since the 19th century [57,60]. In 1839, Charles Frédéric Kuhlmann discovered that platinum shows excellent catalytic properties for this purpose. He passed the mixture of ammonia and air over a platinum sponge heated to 300°C [60]. This process was not commercially profitable at that time since the saltpetre was relatively cheap and available [60]. Over a century later, at the turn of the 19th and 20th centuries, scientists realised that the only available source of saltpetre in Chile might be depleted within a short period and started to look for alternative ways for nitric acid production. Kuhlmann's achievement was an entry point for Wilhelm Ostwald, who was working with his assistant at that time, Eberhard Brauer, to develop a way to large-scale ammonia oxide production [60]. The first experiments used a few-millimetre glass tube with platinised asbestos as a catalyst. However, the platinised asbestos

produced minimal amounts of NO. The new approach was performed using a 20 cm heated glass platinum-lined tube with a diameter of 2 mm, obtaining a conversion reaching about 50% [60]. The laboratory setup used by Ostwald and Brauer for their first experiments is presented in Figure 3.4.

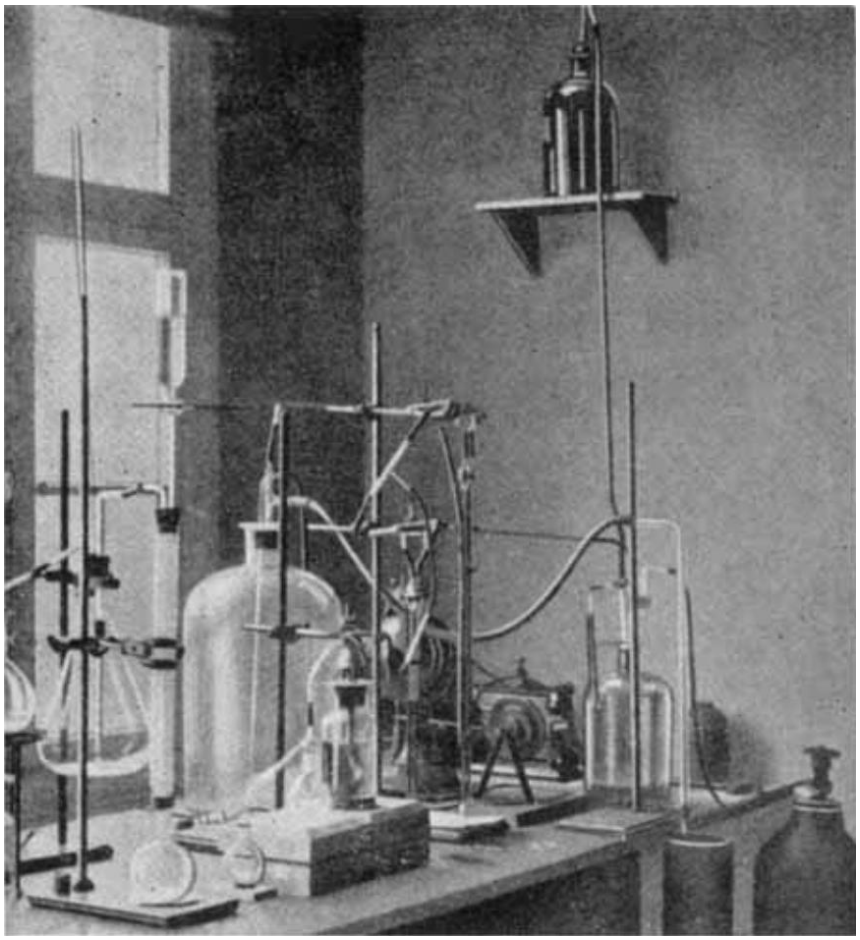

Figure 3.4. Historical experimental laboratory apparatus used by Ostwald and Brauer [60]

In his experiments, Ostwald found that increased contact time (lower velocities) caused a decrease in the ammonia oxide yield, and reduced contact time gave the opposite effect, giving the conversion reaching even 85% [60]. After analysing this "anomaly", Ostwald concluded that the product decomposes to nitrogen and oxygen due to the longer contact time since no ammonia was detected behind the contact zone [60]. Even at this early research stage, those conclusions pointed out the possible complexity of ammonia oxidation and the importance of contact time. Ostwald and Brauer's further experiments investigated the influence of various parameters like inlet ammonia-to-air ratio, catalyst temperature or contact time [60]. In 1902, Ostwald applied for a patent where he outlined the ammonia oxidation conditions, which were 10.6% of inlet gas preheated to 300°C and a short contact time, keeping the platinum catalyst at the temperature around 775°C [57].

In 1904, Ostwald and Brauer developed a small pilot plant containing three ammonia oxidation reactors (Figure 3.5). This installation was a basis for a larger-scale plant with a nitric acid production capacity of 300 kg per day constructed in 1906 [60]. After its success, the larger plant was built in 1908 and could produce 3000 kilograms per day of 53% nitric acid [60]. In those installations, the applied catalyst was platinum in the form of corrugated and rolled platinum strips of 2 cm width and 50 g weight. That catalyst lifespan was about 4–6 weeks due to significant platinum losses and uncertain temperature control [60]. Initially, industrial ammonia oxidation plants were linked with coal-coking industries, providing them with ammonia liquor, which was a byproduct of coking [57]. However, successful ammonia oxidation expansion prompted the research of ammonia synthesis (see Section 3.1.1), which was more technically challenging to obtain. The successful Haber-Bosch method provided large quantities of ammonia, without catalyst poisons from coal coke or cyanamide processes, for the ammonia oxidation industry [13,57].

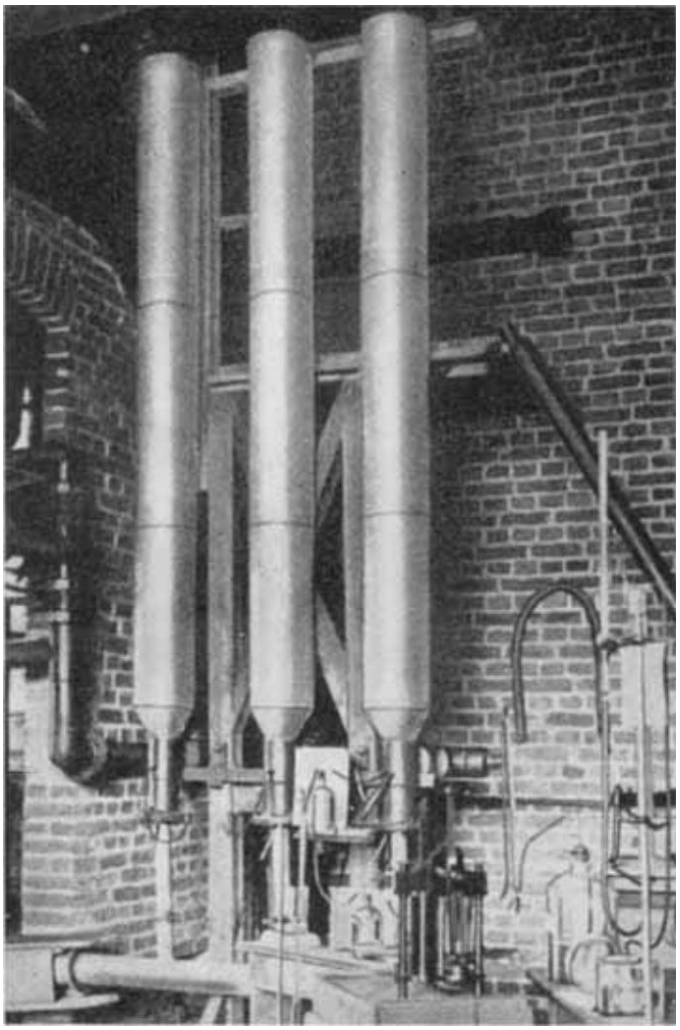

Figure 3.5. Ammonia oxidation pilot plant with three converters constructed by Ostwald and Brauer in 1904 [60]

In 1909, Karl Kaiser approached this problem by pre-heating the air to 300–400°C and applying the platinum catalyst in the form of four-layered woven gauze [60]. The gauze was made of wires with diameters of 0.06 mm woven to 1050 meshes per cm^2, a typical solution even nowadays [19,20]. Kaiser built the pilot plant using his gauze design in 1912 [60].

In 1916, the Berlin-Anhaltische Maschinenbau A. G. company constructed a converter of 20-inch diameter, using multiple platinum gauzes to supply nitric acid for the explosives industry in Germany during the First World War [15]. This converter used the three platinum gazes with wires of 0.006-inch diameter and 80 meshes per linear inch, operating at 700°C [60]. Those gauzes were welded to a platinum grid and immobilised by embedding in asbestos. This converter's design extended the possible catalyst lifespan up to 6 months of work in uniform conditions without catalyst poisoning [60].

In the first quarter of the 20^{th} century, the nitric acid plants were small, struggling with problems like corrosion of the absorption section [57]. The demand for nitrogen fertilisers fuelled the development of acid-resistant steels and improved the nitrogen industry. Still, the main unit operations such as ammonia oxidation, nitric oxide oxidation sec and absorption remain key processes. Furthermore, platinum remains the primary material for ammonia oxidation catalysts despite many improvements, such as replacing the foils, ribbons and sponges into fine mesh gauzes and incorporating the rhodium into the gauze in the form of Pt-Rd alloy wires [57]. Other catalysts, such as iron or cobalt oxides, have been tested. However, platinum gauzes with rhodium additives still provide the most cost-efficient solution overall despite their high material costs [19,20,57].

Ammonia oxidation plants initially operated at atmospheric pressures. Modern plants are designed for different operation conditions based on individual requirements such as heat recovery, gas compression, output acid concentration and other factors [57]. The higher pressures are used since they are beneficial for further processes of nitrogen oxide oxidation and nitrogen peroxide absorption efficiencies. However, higher pressures slightly reduce burner efficiencies and notably increase platinum losses, shortening the lifespan of platinum gauzes [57].

3.2.2. Modern ammonia oxidation plants

Nowadays, there are three basic types of ammonia burners regarding the operating pressure: atmospheric (1–1.4 bar), intermediate (3–6 bar) and pressure-operated (7–10 bar) [8,57]. Some plants compromise that by using the dual-pressure approach by installing the compressor

between the burner and absorption sections, which allows the reduction of operating pressures for intermediate (0.8–1 bar) and pressure-operated (4–5 bar) ammonia burners [57].

Process conditions are different depending on the plant design and can vary even between plants of the same type [57]. Still, the principles of the ammonia burners remain similar for all cases. The inlet mixture typically contains 10–11% ammonia and enters the burner after being preheated to a temperature between 120–300°C [57], and the final gauze temperature results from inlet gas temperature, ammonia concentration, and heat loss. Ammonia burners operating at 96% efficiency and optimum contact times, show a gauze temperature increase of about 40°C per 1% of the increase in ammonia concentration near 8% and about 60°C per 1% analogical ammonia concentration increase near 12% [57]. Typically, the ammonia concentration is fixed, and the higher concentrations are not used to avoid exceeding the explosive mixture limit (16% of ammonia at 1 bar and 12.4% at 10 bars) [57].

With the constant ammonia concentration, preheat temperature, and number of catalyst gauzes, the gas rate is the main factor affecting the efficiency. [57]. Very low gas rates result in long contact times and gauze's low temperature. Those conditions favour the ammonia oxide decomposition into free nitrogen and oxygen [57]. Increased gas rates result in higher gauze temperature, and the efficiency rises to its maximum and then falls due to lowered NO selectivity since a reaction of direct oxidation of ammonia to nitrogen and water is becoming dominant. This factor, combined with the ammonia slip caused by the increased gas velocity and the secondary reaction of unreacted ammonia with NO, sharply lowers the process efficiency [57]. Those trends are illustrated in Figure 3.6.

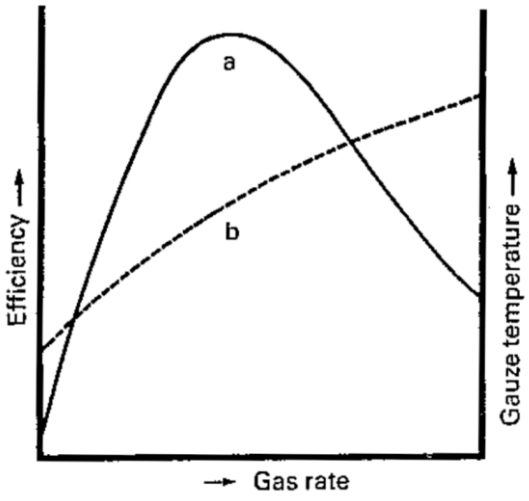

Figure 3.6. Generalised NO efficiency variation (a) and gauze temperature (b) as a function of gas flow rate [57]

In the case of fixed gas flow rate and the preheat temperature, the number of catalyst gauzes may be used to affect the efficiency, and its influence differs depending on the gas rates, illustrated in Figure 3.7. At low gas rates, the efficiency continuously decreases with the number of gauzes [57]. Medium gas rates cause efficiency initially to increase with the number of gauzes, then reach its maximum and sharply fall [57]. This function is similar to the high gas rates, although with sharper initial growth and a sifted and more flattened extremum [57].

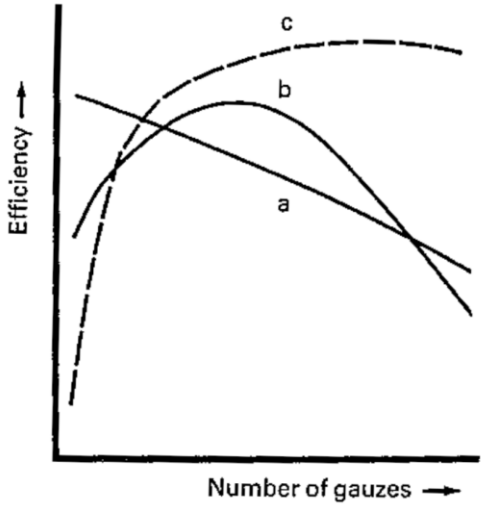

Figure 3.7. Generalised NO efficiency variation for low (a), medium (b), and high (c) gas rates [57]

In atmospheric burners, three to six gauzes are used for maximum efficiency, while pressure plants with higher gas rates use 35 to 45 catalyst gauzes [57]. The maximum obtainable NO efficiencies are 98.5% for atmospheric, 96.5% for intermediate and 95.0% for pressure-operated burners [57].

3.2.3. Catalyst gauze activation, operation and degradation

The number of catalyst gauzes used in industrial burners depends on the plant type. Inside the converter, gauzes are supported on a large open high-chrome steel mesh [57]. Originally, Ostwald used pure platinum [60], although nowadays, the platinum-rhodium alloys are commonly used for the durability reasons [57]. Typical gauzes contain 5–10% of rhodium. The rhodium addition also reduces the catalyst loss and increases the conversion efficiency [57]. Fresh mesh is typically made of wires with a diameter of 0.06 mm or 0.076 μm with 1024 meshes per cm^2 [19]. The gauzes are laid flat on the supporting mesh in the burner pad. Folds and creases had to be avoided to uniformly distribute gas and reduce the possibility of unreacted ammonia slip. During the start-up, the gauze pad is lit by the hydrogen torch or electrically

heated, which activates the fresh gauze's surface [57]. This process usually lasts several hours to reach the desired activity level [57].

During the activation, the first signs of etching start to be visible, observing the crystals' growth and etch pits occurrence. The activated gauze has an increased metal area with reduced clearance sizes in the mesh [57]. The activation process is not uniform since the front side facing the gas inflow is activated more quickly. In a fully activated gauze pad, the whole gauze is roughened almost uniformly [57].

The catalytic etching results in the pits and islands on the catalyst surface, and this phenomenon deepens during the process. With time, the wires become thinner and weaker. The volatilised platinum is entrained, and some amount deposes on the further wires, forming delicate excrescences resembling cauliflowers [17,57]. Those structures temporarily increase the area and activity on those wires. However, due to their delicate shape and increased activity, those excrescences are easily detached, which contributes to the degradation process, and those broken structures have been found in sludges [57]. The differences in platinum losses between pressure and atmospheric converters indicate that more platinum is lost by an additional phenomenon, which is most likely vaporisation [57].

3.2.4. Catalyst gauze maintenance and deactivation

Fresh gauzes are supplied in the precleaned state [57]. The contamination, mostly lubricants and iron, is removed by the suppliers before delivery. Used gauzes are sometimes cleaned in cases of loss of their efficiency due to contamination or physical damage [57]. The maintenance of washed gauze also includes the patching of minor tears. The catalyst gauzes are then returned to a burner or stored for future use [57].

The gauze rejuvenation starts with removing common contaminants such as iron oxide and refractory dust. Then, the remaining contaminations (mainly iron oxide) are dissolved in hydrochloric acid by putting the gauze into baths. The fused refractory is more challenging to remove, and contaminants like molybdenum disulphide can destroy the gauze [57]. Chemical deactivation can be caused by catalyst poisons like sulphur, zinc, iron, molybdenum, and other materials that can be present in specific large-scale chemical plant conditions [57].

The typical activity loss in pressure burners is caused by the rhodium oxide physical blanketing of the gauze. This substance is insoluble in hydrochloric acid and can removed by thermal decomposition in temperatures of 1050°C, hydrogen reduction or slow decomposition during lower pressure operation [57]. The increased amount of rhodium oxide is observed in pressure-

operated burners, which may result in increased platinum loss due to the formation of volatile platinum oxide and, consequently, an increase of the rhodium fraction in the alloy; however, this phenomenon is still debatable [57].

3.2.5. Entrained catalyst recovery

The catalyst losses are caused by entraining the alloy particles, solid rhodium oxide or volatile platinum oxide [57]. This undesired phenomenon significantly contributes to fertiliser production's running costs. There are several approaches to recovering the costly metal, either from the absorber sludges or by gas filtration [57]. The glass or ceramic filters are placed downstream to recapture the platinum dust particles and can achieve up to 60% recovery level. Still, their efficiency is unstable, generating additional pressure drops [57]. Other approaches are Raschig rings or marble chips below the gauze. However, their usage is less efficient and causes other problems, such as rehydration of lime [57].

The most efficient metal recovery is obtained using a getter gauze system. The "recapturing" gauze is made from gold and palladium and is located downstream behind the burner [57]. Its platinum and rhodium recovery rate reaches 60%, although the costs of fabrications and reprocessing are high due to the expensive materials used. Because of these issues, getter gauzes are not used universally in ammonia oxidation plants [57].

The catalyst deactivation and losses due to the rhodium oxidation in pressure-operated and intermediate converters are significant, but there are still unresolved drawbacks. Still, the careful temperature control of the catalyst gauze can reduce the rhodium oxide formation, increasing the catalyst lifespan [57]. However, setting the optimal operating conditions is always a compromise between loss of activity, loss of catalyst and product efficiency [57].

3.3. Mist eliminators

3.3.1. Principles of operation and types of mist eliminators

Mist eliminators, also called mist extractors, are devices designed to remove liquid droplets or solid particles from the gas streams [61]. There are different types of mist eliminators, and the selection of the proper one is based on several factors, such as droplet size, pressure drop, plugging risk (especially in cases with solid particles), or liquid handling capacity [61]. Furthermore, it had to be decided whether the mist eliminator must be installed as a standalone apparatus or inside the other vessel (e.g. internal demisters). An important role is to have the

availability and price of the required construction materials and design/construction costs, including all side equipment like piping, instrumentation, utilities, etc.)

Mist eliminators' operation is based on the natural balance between gravitational and drag forces [61]. This can be accomplished in various ways depending on the type of mist extractor applied. Gravity separators and settling chambers overcome the drag force. Impingement-type separators increase the droplet size to boost the gravitational forces. Venturi scrubbers, cyclones, electrostatic precipitators and wave-plate separators add additional forces [61]. Mist eliminators are often put in the vessels or lines, where gas flows upwards since two opposing forces act on droplets in these places: gravitational (negative buoyant force) and drag force, which slows the droplets' fall rate [61]. Drag force depends on the gas velocity. When the negative buoyant force equals it, the droplet acceleration becomes zero. Further gas velocity increases will move droplets upward to achieve the gas velocity [61]. The same principle applies to horizontal-flow mist eliminators, although the drag forces operate at 90° to gravitational forces [61].

3.3.2. Droplet removal mechanisms in impingement mist eliminators

Impingement-type mist eliminators are widely used because of their high efficiency and operating costs, along with the low pressure drops and initial production and installation costs [61]. The impingement mist extractors contain baffles (wave-plates), wire meshes (demisters) and microfiber pads. There are three primary mechanisms for capturing droplets using the impingement mist eliminators (Figure 3.8).

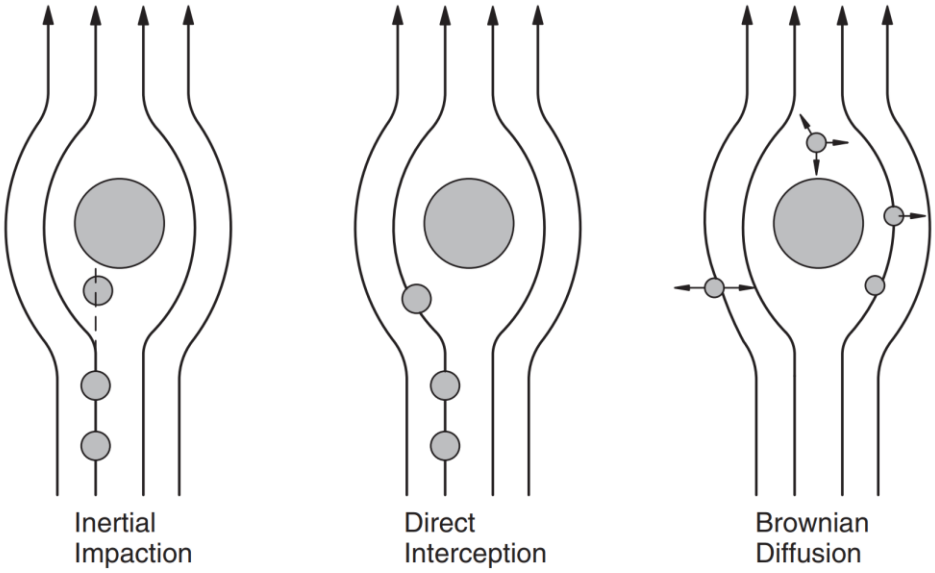

Figure 3.8. Three primary mechanisms of droplet/particle capture in impingement-type mist eliminators [61]

The inertial impactions use the mass and momentum of larger droplets (1–10 μm) to break through the gas flow and impinge on the target. This mechanism has the primary role in wire-mesh demisters and impingement plates, including wave-plate mist eliminators [61]. The direct interception mechanism primarily applies to the smaller droplets (0.3–1 μm), whose momentum is too weak to be removed from the gas streamlines. Direct interception occurs when the gas pathlines lie in such a close vicinity of the target to reduce the distance between the droplet's centre and target to less than half of the droplet's diameter. The droplets that touched the target were collected from the gas stream [61]. The diffusion mechanism mainly affects the smallest (less than 0.3 μm) droplets. They exhibit random Brownian motion resulting from collisions with gas molecules. Those random movements lead the droplets to strike the target and be collected. This mechanism occurs even when gas velocity is zero and is favoured by high-concentration gradients and low velocity [61].

3.3.3. Wave-plate mist eliminator design and application

Wave-plate mist eliminators are the impingement type of mist eliminators. They contain multiple vanes, baffled or plates, usually in a zig-zag shape, as presented in Figure 3.9.

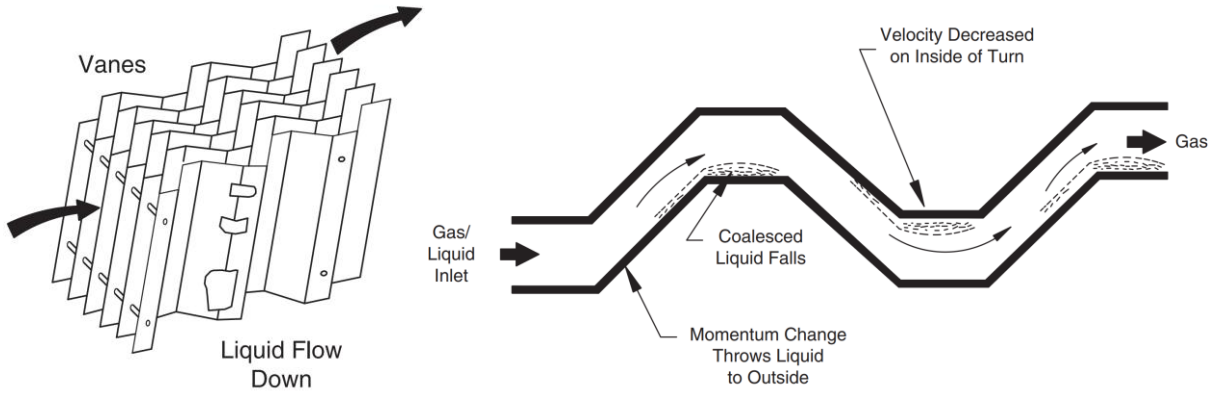

Figure 3.9. Typical wave-plate mist eliminator (a) and detailed flow scheme through the vanes (b) [61]

The vanes cause the gas to change the flow direction multiple times between the plates. The surface of the plates acts as a target for droplet impingement and collection. Those plates are often equipped with drainage channels that increase the droplet removal efficiency, as shown in Figure 3.10. The distances between plates vary between 5 to 75 mm, and the total length of the device is typically 150–300 mm [61].

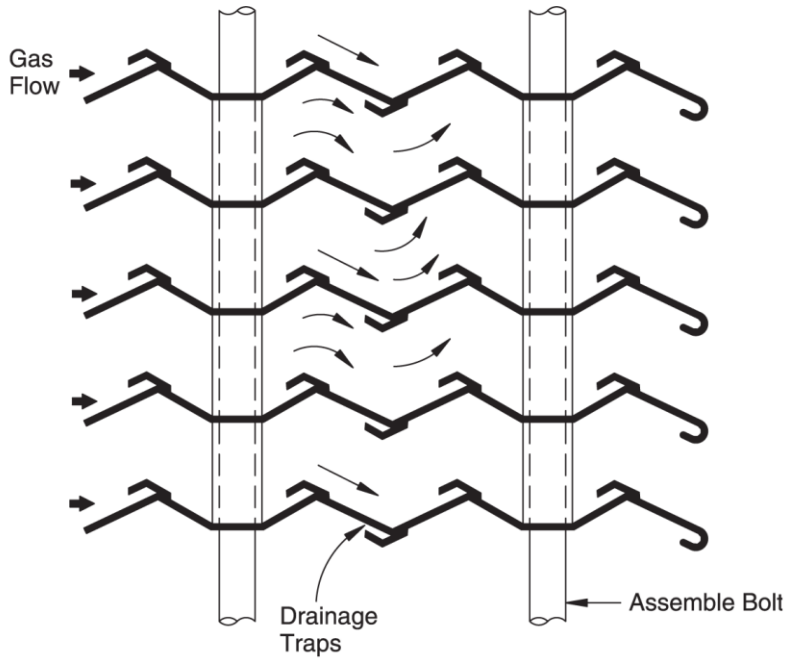

Figure 3.10. Wave-plate mist eliminator with drainage channels [61]

In industrial apparatus, wave-plate separators can be installed both in vertical and horizontal vessels, as shown in Figures 3.11 and 3.12.

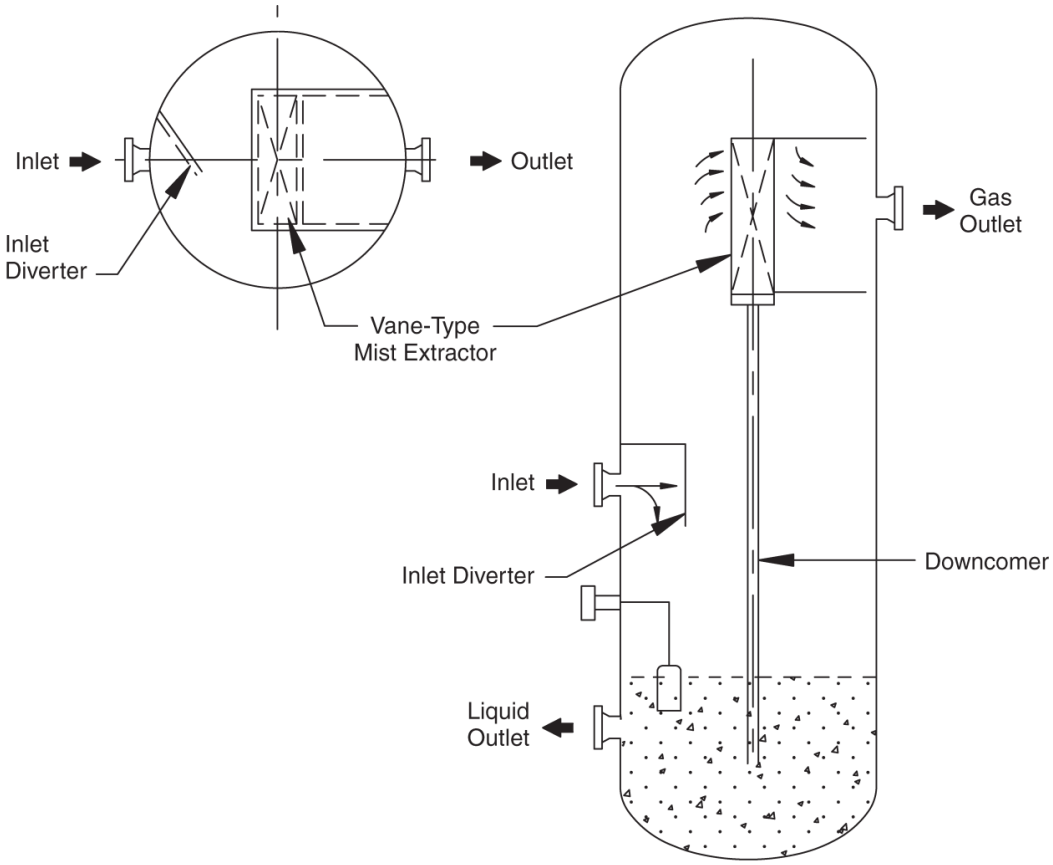

Figure 3.11. Example of vertical vessel equipped with wave-plate mist extractor [61]

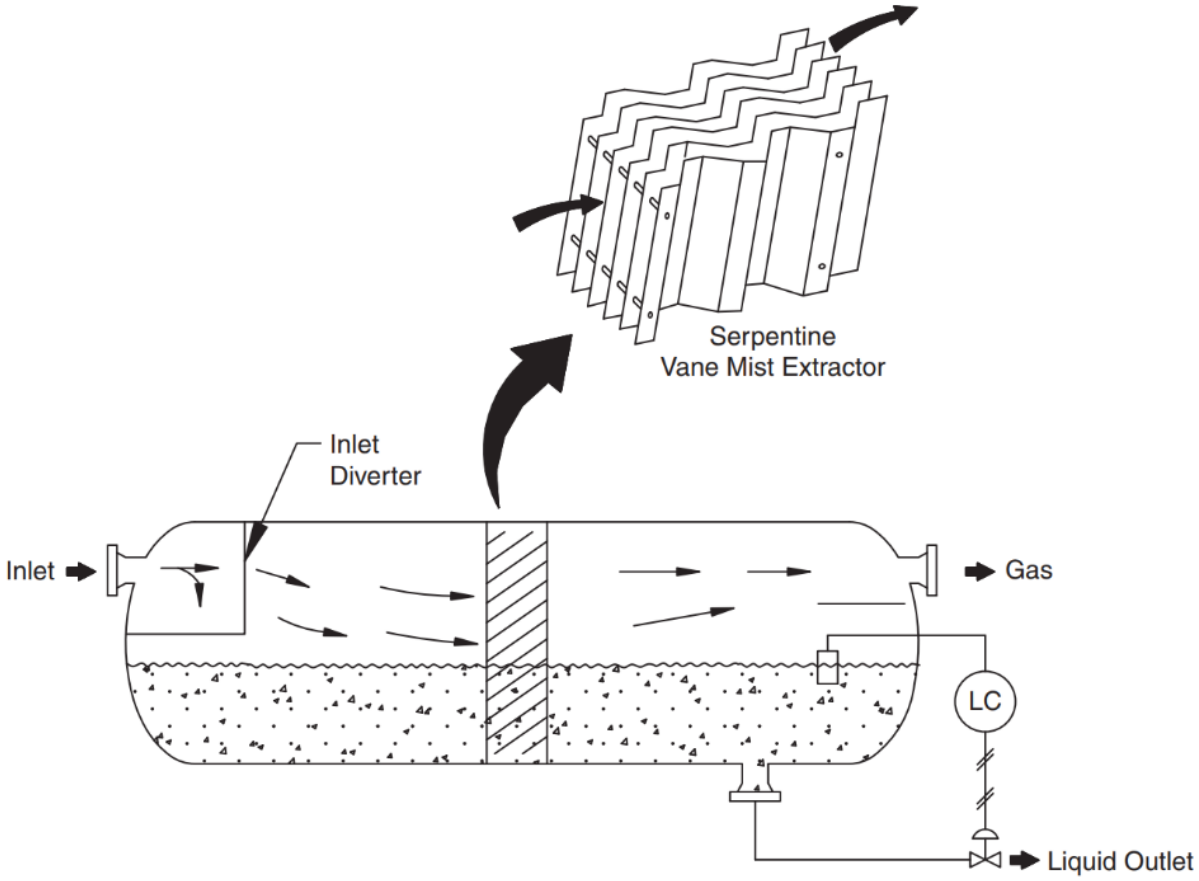

Figure 3.12. Example of horizontal vessel equipped with wave-plate mist extractor [61]

Wave-plate mist eliminators installed within a horizontal gas flow pattern allow higher gas velocities since the captured liquid can easily flow downward due to the gravity forces. This construction removes the liquid from the gas pathway faster, minimising the risk of re-entrainment of liquid droplets [61]. Due to their construction, the wave-plate type of mist extractors can be used when liquid droplets are also contaminated with sold particles [61]. Historically, this type of mist eliminator is used to remove larger droplets (>40 μm). However, modern designs allow obtaining high droplet removal efficiency for droplets of diameters less than 10–15 μm [61,62].

Due to the high differences in densities between gas and liquid droplets, the latter are subject to inertial forces, causing deflection of their trajectories from the gas motion patch. Inertial forces depend on velocity, droplet mass and the geometry of the mist eliminator, as written in the following expression [26]:

$$F_s = \frac{m_p {u_p}^2}{R} = \frac{\pi {d_p}^3 \rho_p {u_p}^2}{6R} \quad (1)$$

where F_s is inertial force, R is a bending place curvature radius, m_p is droplet mass, u_p is droplet velocity, d_p is droplet diameter, and ρ_p is droplet density. According to Equation (1), the inertial force is proportional to the ${d_p}^3$, causing a sharp efficiency decrease for smaller droplets. Not re-entrained droplets can adhere, coalesce, form a film, and gravitationally flow down to be removed from the process stream. A relatively low-pressure drop characterises inertial droplet separators. They can be used for foam-forming and high-viscosity liquids without the risk of clogging, which can be a problem for mesh and fibre separators. Moreover, most wave-plate separators provide relatively higher resistance to droplet re-entrainment than mesh-type separators. However, they cannot obtain high efficiency under low continuous phase velocities or/and fine droplets. The advantage of inertial droplet separators is a low-pressure drop. They can be used to remove foam-forming and high-viscosity liquids, which in the case of mesh and fibre separators is ineffective due to the robust clogging spaces between wires or fibres by liquid droplets. Furthermore, most wave-plate separators have relatively higher resistance to droplet re-entrainment than wire mesh separators. However, they cannot obtain high efficiency under low gas velocities or/and fine droplets [54]. The essential parameters affecting droplet removal efficiency in inertial separators are gas linear velocity, the separator's channel's width and the presence and shape of drainage channels. The inertial force is proportional to the square of velocity, making this parameter critical regarding the influence of separation efficiency. Usually, below the value of 6 m s^{-1}, the increase of velocity is beneficial, although, for higher velocities, the re-entrainment phenomenon increases, which has a negative impact on the separation efficiency. However, in inertial separators with multiple bends of the wave-plate section, the re-entrainment does not occur for velocities below 8 m s^{-1} [54]. High velocities may also cause a flooding phenomenon for vertically positioned separators when an upward gas flow prevents the gravitational downflow of liquid droplets [26]. Applying drainage channels allows for maintaining high efficiency even at higher linear gas velocities. The shape and type of drainage channels substantially affect the separation efficiency. The droplet removal equipment on this stream can protect vulnerable units, such as compressors, and recover more ammonia, which can proceed to further processes.

4. State of the art and methodology

This section describes the general principles and balances of the momentum, energy and mass transport phenomena, which are the foundations of modern computational fluid dynamics.

The mathematical models of computational fluid dynamics applied in this work are described further in this section. This includes the governing equations, critical parameters, and additional models for specific cases such as species transport, porous zones, and disperse phase modelling.

4.1. Mass, energy and momentum transport phenomena

In every study of the transport phenomena of any physical or chemical process, three primary quantities are of fundamental importance: mass, energy, and momentum [63]. This field is the basis for chemical engineering disciplines like fluid mechanics, reactor engineering or separation processes. The transport phenomena field is also useful for other professions, such as civil, mechanical, mining, and construction engineering, as well as chemistry, physics, and material science [63].

In chemical engineering, flow phenomena, mass and heat transfer are treated in terms of continuum properties [63]. In the process scale, references to molecular processes are only occasional for specific cases [63]. The continuous approach is the basis for designing and improving processes in which the transport of substances, heat and momentum have a substantial role. [63]. The transport phenomenon is described by balances and concepts used to analyse the physical processes and phenomena, such as the deviation from equilibrium and resistances to heat and mass transfer, basically concerning a quantitative description of cause and effect [63].

4.1.1. Balance equation and conservation law

The balances are used to describe the transport of any quantity. Their primary principle is to track the selected physical quantity. This concept is particularly useful for conserved quantities (like energy or mass) known not to be lost during the process [63]. The processes can be studied in steady-state or time-dependent (transient) states, where momentum, energy and mass are exchanged between domains. The transport results from driving forces, which are gradients of pressure, momentum, energy or concentration [63].

The balances are performed over control volumes, which are open or closed boundary domains, usually with transport exchange across them. Depending on the approach, the domains vary

from large (macro-balances) to very small volumes at a local scale (micro-balances) [63]. Figure 4.1 presents a sketch of the generalised balance using symbols instead of numerical values.

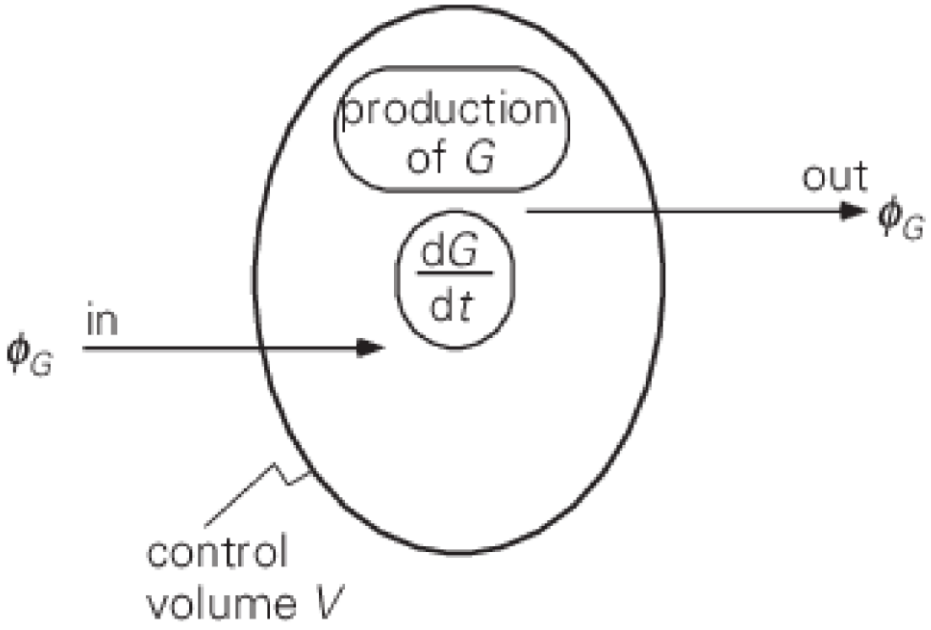

Figure 4.1. The general structure of balance [63]

In the balance shown in Figure 4.1, G is the transported quantity in the process, which changes in the control volume V during the brief period of time Δt. The change of the quantity G during the Δt is a sum of the quantity that flows into volume V, the negative quantity leaving volume G, and the net quantity of G produced in V. Negative production (e.g. destruction or consumption) is also possible in cases such as balancing reaction substrates [63]. The symbol φ denotes a transport (flow) rate, which is the quantity of G per time unit. The general balance presented in Figure 4.1 can be written as [63]:

$$G^{inV}(t + \Delta t) - G^{inV}(t) = \varphi_{G,in} \cdot \Delta t - \varphi_{G,out} \cdot \Delta t + P_G \cdot \Delta t \qquad (2)$$

where G^{inV} is the "inward" flow of G, and P_G is a net production of G per time unit.

If the period of time Δt is very short ($\Delta t \rightarrow 0$), Equation (2) can be divided by to obtain its differential form:

$$\frac{d}{dt} G^{inV} = \varphi_{G,in} - \varphi_{G,out} + P_G \qquad (3)$$

Equation (3) is called the "balance equation", and it is the most basic form of the balance [63]. It describes the incremental change of quantity G in volume V (left-handed side, unsteady-state

term) and the three ways of changing the quantity of G in volume V (right-side). All terms in the balance equation have the dimensions of the quantity of G per time unit [63].

For the cases where a net production is always 0, like mass balances, Equation (3) is simplified to the following form:

$$\frac{d}{dt}G^{inV} = \varphi_{G,in} - \varphi_{G,out} \tag{4}$$

A balance equation in this form is called a "conservation law", and it is used for quantities that are only transported and distributed [63], such as the continuity equation (described in Section 4.2.1) used in CFD models as a most fundamental convergence criterion [64].

4.1.2. Mass balance

The total mass is considered a typical conserved quality governed by the conservation law. Except for very specific cases of nuclear reactions, the production or destruction of mass is impossible and can only be transported [63]. The conservation of total mass (M) is governed by the following expression [63]:

$$\frac{d}{dt}M = \varphi_{m,in} - \varphi_{m,out} \tag{5}$$

The typical units of all terms in Equation (5) are kilograms per second.

The mass balance of specific species in the multiple-species system is described by the following equation:

$$\frac{d}{dt}M_A = \varphi_{m,A,in} - \varphi_{m,A,out} + P_A \tag{6}$$

In this case, the balanced quantity is the mass of the substance A present in the control volume. The balance of species is not a conservation law due to chemical reactions. The preferred units of species balance are moles (or kilomoles) per second [63]. The production term is P_A, and it describes the amount of produced or consumed species in the reaction. The production term for volumetric reactions proceeds as follows:

$$P_A = r_A \cdot V \tag{7}$$

where r_A is a production of the species A per unit of volume (kmol m^{-3} s^{-1}). In the case of surface reaction, the reaction rate unit is the production of species production per surface unit (kmol m^{-2} s^{-1}) and the production term is the multiplication of the reaction rate and surface.

The species concentration is also the quantity that can be balanced. This approach can be useful, especially in cases where concentration gradients significantly determine mass transport [63]. Concentration (g) is defined as the specified quantity G per unit of volume:

$$g = \frac{G}{V} \tag{8}$$

The concentration of total mass is called a density (ρ), and a concentration of species is usually represented by the C, which, for the species A, can be expressed as:

$$C_A = \frac{M_A}{V} \tag{9}$$

And total mass concentration (density) is a sum of the species' mass concentrations:

$$\rho = \frac{M}{V} = \frac{M_A + M_B + \cdots}{V} = C_A + C_B + \cdots \tag{10}$$

If the control volume V is constant in time, the concentration balance can be written as [63]:

$$V \frac{d}{dt} C_A = \varphi_{V,in} \cdot C_{A,in} - \varphi_{V,out} \cdot C_{A,out} + r_A \cdot V \tag{11}$$

where φ_V is a volumetric flow rate. After dividing Equation (11) by the control volume, the equivalent equation is obtained:

$$\frac{d}{dt} C_A = \frac{\varphi_{V,in}}{V} \cdot C_{A,in} - \frac{\varphi_{V,out}}{V} \cdot C_{A,out} + r_A \tag{12}$$

The overall mass balance obtained through concentration balances can be expressed as:

$$\frac{d}{dt}(C_A + C_B + \cdots) = \frac{\varphi_{V,in}}{V} \cdot (C_A + C_B + \cdots)_{in} - \frac{\varphi_{V,out}}{V} \cdot (C_A + C_B + \cdots)_{out} + (r_A + r_B + \cdots) \tag{13}$$

In Equation (13), the right-hand side of the equation should be equal to zero because the production of one species must result in the consumption of the other due to chemical reactions [63]. The exceptions to rule this are nuclear reactions since conservation law does not govern overall mass balance in those cases. A practical example of the application of the concentration balance is a chemical reactor with a volumetric reaction and constant volume [63].

In the case of mass fractions, the mass balance proceeds as follows [63]:

$$\frac{d}{dt} M \cdot x_A = \varphi_{m,in} \cdot x_{A,in} - \varphi_{m,out} \cdot x_{A,out} + P_A \tag{14}$$

where x_A is a mass fraction of species A, which is dimensionless (kg/kg).

Analogous mass balances can be written using other concentration quantities like mole fractions or mole concentrations.

4.1.3. Energy balance

The energy balance exploits the same technique of general balancing presented in Equation (3). Energy is present in many forms that are convertible to each other, which is somehow similar to a chemical reaction, where one species is converted into more others. [63]. However, the transformation process always generates some losses, usually in the form of heat.

The most common forms of energy concentration are kinetic energy, potential energy, internal (thermal) energy, pressure energy and enthalpy [63]. The typical unit of energy concentration is Joule per kg, although the joule per mole is preferable in the cases with chemical reactions. Internal energy is the effect of molecules' thermal movements and short-range interaction between molecules, meaning that it depends on the composition and form of molecules and can be treated as a physical property [63].

Typically, the total system's energy is a sum of internal, potential and kinetic energy [63]:

$$e = u + gz + \frac{1}{2} v^2 \tag{15}$$

The energy concentrations are determined according to the selected reference. For example, it is necessary to include enthalpy changes (Δh) for phase transitions. In cases with chemical reactions, the chemical enthalpy must be considered. This quantity refers to the energy cumulated in the atomic structures of the molecules and the pertinent interactions of electrons and nucleus [63].

The energy dissipation is another phenomenon crucial to balancing the energy. Energy is dissipated due to the friction loss in the form of heat in every transformation from one energy to another [63]. This energy dissipation is mostly no longer "useful" and usually increases minor temperature [63].

Similarly to the mass, the total energy is a conserved quantity [63], meaning that in a given volume, the through energy can change only through inflow and outflow through the boundaries. In the case of a specific type of energy, the production term also must be considered due to the transformation of energy to other types (for example, to heat in the burning process). The commonly used energy unit is Joule. Similarly to the concentration of energy, the total energy is typically defined as a sum of internal, potential and kinetic energy [63]:

$$E = U + E_{pot} + E_{kin} \tag{16}$$

While balancing the energy, several forms of transport must be taken into consideration [63]:

- An energy flow into and out of the control volume due to the mass flows ($\varphi_{m,in} \cdot e_{in}$ and $\varphi_{m,out} \cdot e_{out}$)
- An energy flow as a result of heat not involved in mass flows (φ_q) (for example, due to the heating or cooling elements)
- An energy flow as a result of work "delivered" from the outside to control volume (e.g. compressors, pumps) or "performed" by the control volume (e.g. powering the piston or turbine) (W)

The energy production (P_e) in the interior of the control volume V is also possible (e.g. heat production inside the reactor due to the exothermic reaction). It should be noted that the term "energy production" only contains the other types of energy that are not included in E from Equation (16) (internal, potential and kinetic). Without this simplification, there would be no energy production since energy is a conserved quantity [63].

The unsteady-state term of the energy can be written as:

$$\frac{d}{dt}E = \frac{d}{dt}(\rho V e) \tag{17}$$

This term shows how quickly the total energy changes in control volume [63]

The general form for the total energy balance can be written as follows:

$$\frac{d}{dt}E = \frac{d}{dt}(\rho V e) = \varphi_{m,in} \cdot e_{in} - \varphi_{m,out} \cdot e_{out} + \varphi_q + W + P_e \tag{18}$$

Energy transport through work is usually a result of mechanical devices such as stirrers, pistons, pumps, compressors, turbines, etc. In some cases, like phase transitions under constant pressure with the density changes and work performed, the terms of specific enthalpies are used in the balance [63].

4.1.4. Momentum balance

The momentum $\vec{P}$ is a quantity conceived as a result of moving mass times velocity [63]. The unit of momentum is typically Ns. Unlike mass and energy, which are scalar quantities, momentum is a vector quantity. Therefore, the three balances are needed to establish three components of the momentum [63]. In the case of the Cartesian coordinate system, the three momentum components refer to the system's axes (p_x, p_y, p_z), which represent the momentum concentrations per unit of mass or volume. In classical mechanics, the x-momentum of mass m equals $m \cdot v_x$, which means that the x-momentum concentration per mass unit can be written as [63]:

$$p_x = \frac{m \cdot v_x}{m} = v_x \tag{19}$$

In Equation (19), it can be seen that x-momentum concentration is basically the velocity component of the direction x; thus, the momentum inflows and outflows from the control volume are respectively $\varphi_{m,in} \cdot v_{x,in}$ and $\varphi_{m,out} \cdot v_{x,out}$ [63]. The production of the x-momentum term can be defined using Newton's second law [63]:

$$\frac{d}{dt}(mv_x) = \sum F_x \tag{20}$$

The left-hand side of Equation (20) describes the change of the x-momentum of the body due to the x-components of forces acting on this body [63], and the right-hand side is the sum of x-direction forces, which represents the momentum-production term [63]. Two primary types of forces produce the momentum. First, are body forces acting on the mass in the control volume, such as gravity. The second type of forces affect the control volume's surface. Their examples include pressure and frictional or shear stress [63]. In the case of mass and energy, the production always occurs inside the control volume, and in the case of momentum, it is possible for production to take place on its surfaces.

The general form of x-momentum balance can be written as follows [63]:

$$\frac{dP_x}{dt} = \frac{d}{dt}(M \cdot v_x) = \varphi_{m,in} \cdot v_{x,in} - \varphi_{m,out} \cdot v_{x,out} + \sum F_x \tag{21}$$

In a steady state with transport terms compensating each other, the x-momentum balance is reduced to force balance [63]:

$$0 = \sum F_x \tag{22}$$

Balances for the momentum in y and z dimensions can be written analogously [63].

4.2. General equations of motion

Since fluid mechanics is actually a momentum transport, the fluid motion can be described as a system of momentum balance equations. The Navier-Stokes equations of motion describe the flow in a three-dimensional domain using the "momentum housekeeping" [63]. The Navier-Stokes equations are also mathematically identical to heat and mass transport balances [63].

In modern chemical engineering, the Navier-Stokes equations are a starting point for numerical calculation techniques to give a local insight into various transport and transfer phenomena in all kinds of process equipment. They provide a way to quickly understand and manage the effects of different parameters, geometrical modifications, selectivity or scale on the yield of chemical reactions [63]. This approach allows tracking the intensity and effectiveness of mass and heat transfer through variations of flow patterns, contact times, residence time distributions, etc. [63].

4.2.1. Continuity equation

Every flow field must comply with the overall mass balance, which is derived using the cubic volume element method [63]. In the Cartesian coordinate system, the control volume dx-dy-dz is randomly positioned in the three-dimensional and time-dependent flow field [63]. In this approach, the density and velocity components of v_x, v_y, and v_z are functions of their corresponding coordinates, as shown in Figure 4.2.

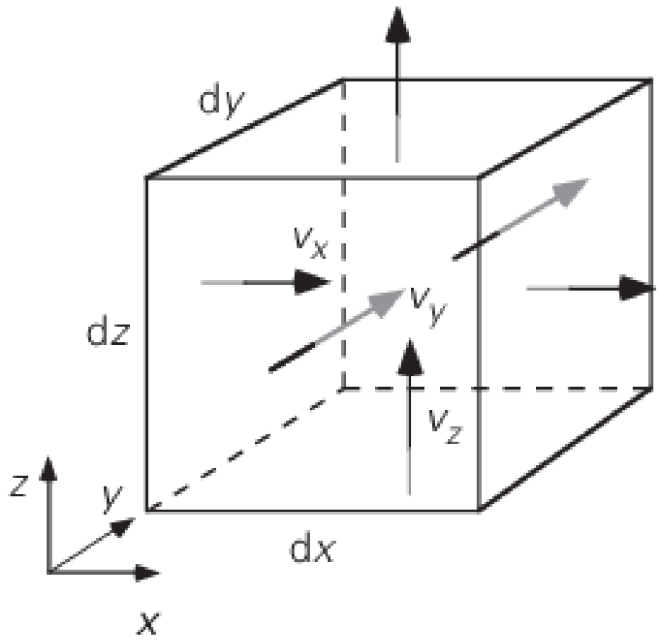

Figure 4.2. Control volume used in the cubic volume element method [63]

The mass balance for the control volume (Figure 4.2) contains the accumulation term [63]:

$$\frac{\partial}{\partial t}\rho \, dxdydz \tag{23}$$

and convective transport terms through all six boundaries. The mass enters through the left-hand boundary plane [63]:

$$[\rho v_x]|_{x,y,z} \, dydz \tag{24}$$

and leaves through the right-hand boundary [63]:

$$[\rho v_x]|_{x+dx,y,z} \, dydz \tag{25}$$

The net convective mass transport in the x-direction proceeds as follows [63]:

$$[\rho v_x]|_{x,y,z} \, dydz - [\rho v_x]|_{x+dx,y,z} \, dydz = -\frac{\partial}{\partial x}(\rho v_x) \, dxdydz \tag{26}$$

The convective mass flows in directions y and z can be written analogously [63]:

$$[\rho v_y]|_{x,y,z} \, dxdz - [\rho v_y]|_{x,y+dy,z} \, dxdz = -\frac{\partial}{\partial y}(\rho v_y) \, dxdydz \tag{27}$$

$$[\rho v_z]|_{x,y,z} \, dxdy - [\rho v_z]|_{x,y,z+dz} \, dxdx = -\frac{\partial}{\partial z}(\rho v_z) \, dxdydz \tag{28}$$

The continuity equation is a combination of the convective mass flow equations in all directions (Equations (26)–(28)) with the accumulation term (Equation (23)) divided by the fixed magnitude $dxdydz$ [63]:

$$\frac{\partial \rho}{\partial t} = -\frac{\partial \rho v_x}{\partial x} - \frac{\partial \rho v_y}{\partial y} - \frac{\partial \rho v_z}{\partial z} \tag{29}$$

The continuity equation results from mass conservation law (Equation (4)), which still applies to the cases with constant density [63]:

$$0 = \frac{\partial v_x}{\partial x} + \frac{\partial v_y}{\partial y} + \frac{\partial v_z}{\partial z} \tag{30}$$

When density is constant, and no nuclear reactions occur, the amount of mass entering the boundary of control volume always has to exit it through one or more other boundaries [63]. For this reason, the continuity equation is an elementary convergence criterion in every CFD simulation [64].

4.2.2. Navier-Stokes equations

The Navier-Stokes equations are basically the equation system of micro-balances of momentum transport described in Section 4.1.4. They use the three velocity components of the coordinate system's directions, which are also the momentum concentrations [63]. Like the continuity equation, the cubic volume element method (Figure 4.2) is used as a reference for momentum balance [63].

The flow domain contains the actual velocity distributions (also called the flow field). The momentum is distributed by the molecular and convective flows caused by the forces exerted on the domain's boundaries and mass inside the domain [63]. This section mainly focuses on Navier-Stokes terms and balance techniques for x-direction, although momentum and force are vector quantities, meaning that they have to be balanced in every direction.

The unsteady-state term corresponds to the momentum accumulation [63]:

$$\frac{\partial}{\partial t} \rho v_x \, dxdydz \tag{31}$$

The velocity's x-component brings mass and momentum into the cubic control volume [63]:

$$[\rho v_x]|_{x,y,z} \, dydz \tag{32}$$

and transport momentum out of the control volume through the opposite plane [63]:

$$[\rho v_x]|_{x+dx,y,z}\, dydz \tag{33}$$

The net contribution of the convective x-direction flow can be written as [63]:

$$[\rho v_x]|_{x,y,z}\, dydz - [\rho v_x]|_{x+dx,y,z}\, dydz = -\frac{\partial}{\partial x}(v_x \rho v_x)\, dxdydz \tag{34}$$

The net contributions of convective transport in other directions are analogous [63]:

$$[\rho v_y]|_{x,y,z}\, dxdz - [\rho v_y]|_{x,y+dy,z}\, dxdz = -\frac{\partial}{\partial y}(v_y \rho v_y)\, dxdydz \tag{35}$$

$$[\rho v_z]|_{x,y,z}\, dxdy - [\rho v_z]|_{x,y,z+dz}\, dxdx = -\frac{\partial}{\partial z}(v_z \rho v_z)\, dxdydz \tag{36}$$

The molecular transport of the x-momentum into the control volume in the y-direction can be expressed as follows [63]:

$$-\mu \left[\frac{\partial v_x}{\partial y}\right]_{x,y,z} dxdz \tag{37}$$

the case of leaving the control volume can be written as [63]:

$$-\mu \left[\frac{\partial v_x}{\partial y}\right]_{x,y+dy,z} dxdz \tag{38}$$

and the accumulation of the molecular momentum term is expressed as [63]:

$$\frac{\partial}{\partial y}\left[\mu \frac{\partial v_x}{\partial y}\right] dxdydz \tag{39}$$

The net molecular transport contribution of x-momentum in the y-direction [63]:

$$-\mu \left[\frac{\partial v_x}{\partial y}\right]_{x,y,z} dxdz - \left\{-\mu \left[\frac{\partial v_x}{\partial y}\right]_{x,y+dy,z}\right\} dxdz = \frac{\partial}{\partial y}\left[\mu \frac{\partial v_x}{\partial y}\right] dxdydz \tag{40}$$

The analogous balances can be written for the molecular transport of the x-momentum in the z-direction and y- and z-momentum molecular transports. The molecular momentum transport balances assume that on each plane of a control volume, either only shear stress or normal stress prevails, and Newton's law can be applied [63].

The production term of x-momentum results from all the forces' x-components acting on the control volume. In the case of the pressure, balanced according to the x-direction, a force is exerted from the left- and right-hand sides of the control volume, which can be written as [63]:

$$p|_x \, dydz + \{-p|_{x+dx} \, dydz\} = -\frac{\partial p}{\partial x} \, dxdydz \tag{41}$$

In Equation (41), the $[-\partial p/\partial x]$ term is a source term, that expresses a certain amount of x-momentum per unit of volume and per unit of time transported to the control volume [63].

Gravity is a body force where pressure is exerted on a plane. The x-component of gravity, which affects the mass in the control volume by adding x-momentum per mass unit per time unit, can be written as [63]:

$$g_x \rho \, dxdydz \tag{42}$$

For the constant viscosity cases, the combined and divided by $dxdydz$ Equations (31), (34)–(36), and (40)–(42) (also including molecular x-momentum transport in other directions) can be written in the following form [63]:

$$\frac{\partial \rho v_x}{\partial t} = -\frac{\partial}{\partial x}(v_x \rho v_x) - \frac{\partial}{\partial y}(v_y \rho v_x) - \frac{\partial}{\partial z}(v_z \rho v_x) + \mu\left(\frac{\partial^2 v_x}{\partial x^2} + \frac{\partial^2 v_x}{\partial y^2} + \frac{\partial^2 v_x}{\partial z^2}\right) - \frac{\partial p}{\partial x} + \rho g_x \tag{43}$$

The Equation (43) can be also presented in another form [63]:

$$\rho \frac{\partial v_x}{\partial t} + \rho v_x \frac{\partial v_x}{\partial x} + \rho v_y \frac{\partial v_x}{\partial y} + \rho v_z \frac{\partial v_x}{\partial z} = \mu\left(\frac{\partial^2 v_x}{\partial x^2} + \frac{\partial^2 v_x}{\partial y^2} + \frac{\partial^2 v_x}{\partial z^2}\right) - \frac{\partial p}{\partial x} + \rho g_x \tag{44}$$

The analogue equations for the x- and y-components of velocity can be expressed as follows [63]:

$$\rho \frac{\partial v_y}{\partial t} + \rho v_x \frac{\partial v_y}{\partial x} + \rho v_y \frac{\partial v_y}{\partial y} + \rho v_z \frac{\partial v_y}{\partial z} = \mu\left(\frac{\partial^2 v_y}{\partial x^2} + \frac{\partial^2 v_y}{\partial y^2} + \frac{\partial^2 v_y}{\partial z^2}\right) - \frac{\partial p}{\partial y} + \rho g_y \tag{45}$$

$$\rho \frac{\partial v_z}{\partial t} + \rho v_x \frac{\partial v_z}{\partial x} + \rho v_y \frac{\partial v_z}{\partial y} + \rho v_z \frac{\partial v_z}{\partial z} = \mu\left(\frac{\partial^2 v_z}{\partial x^2} + \frac{\partial^2 v_z}{\partial y^2} + \frac{\partial^2 v_z}{\partial z^2}\right) - \frac{\partial p}{\partial z} + \rho g_z \tag{46}$$

Equations (44)–(46) are denoted as the Navier-Stokes equations of motion. Along with the continuity equation (Equation (29)), They govern the flow of any Newtonian fluid (with constant viscosity), and they are the backbone of the fluid mechanics [63].

In the vector notation, the equations of motion are written as follows:

$$\rho \frac{\partial \vec{v}}{\partial t} + \rho \vec{v} \cdot \nabla \vec{v} = \mu \nabla^2 \vec{v} - \nabla p + \rho \vec{g} \tag{47}$$

In the cases where viscous effects are negligible, the Equation (47) is simplified to Euler equation [63]:

$$\rho \frac{\partial \vec{v}}{\partial t} + \rho \vec{v} \cdot \nabla \vec{v} = -\nabla p + \rho \vec{g} \tag{48}$$

In laminar flows, the inertial terms may be disregarded, and for steady-state cases, Equation (47) is simplified to the following form [63]:

$$0 = \mu \nabla^2 \vec{v} - \nabla p + \rho \vec{g} \tag{49}$$

It should be noted that Navier-Stokes equations are not limited to the Cartesian coordinate system. They can also be defined for the cylindrical and spherical coordinate systems [63,65].

The momentum balances can also be derived in terms of shear stresses, which is also valid and useful for non-Newtonian fluids [63]. This approach does not contain molecular transport terms. Instead, shear stresses on the six planes are included in the production terms [63]. In the case of x-direction fluid flow, the local shear stress is a result of the local velocity gradient, and the fluid exerts a force [63]:

$$\tau_{yx}|_{x,y,z}\, dxdz \tag{50}$$

The similar force on the opposite plane is generated as a result of the fluid flow [63]:

$$-\tau_{yx}|_{x,y+dy,z}\, dxdz \tag{51}$$

Due to those forces, the net force is produced in the x-direction [63]:

$$-\frac{\partial \tau_{yx}}{\partial y}\, dxdydz \tag{52}$$

In the x-direction, analogical forces are exerted in the remaining four planes [63]:

$$-\frac{\partial \tau_{xx}}{\partial x}\, dxdydz \tag{53}$$

$$-\frac{\partial \tau_{zx}}{\partial z}\, dxdydz \tag{54}$$

The Equations (31), (34)–(36), (41), (42), and (52)–(54) can be merged and divided by $dxdydz$:

$$\frac{\partial \rho v_x}{\partial t} = -\frac{\partial}{\partial x}(v_x \rho v_x) - \frac{\partial}{\partial y}(v_y \rho v_x) - \frac{\partial}{\partial z}(v_z \rho v_x) - \frac{\partial \tau_{xx}}{\partial x} - \frac{\partial \tau_{yx}}{\partial y} - \frac{\partial \tau_{zx}}{\partial z} - \frac{\partial p}{\partial x} + \rho g_x \tag{55}$$

In vector notation, the motion equations in terms of shear stresses can be written as:

$$\rho \frac{\partial \vec{v}}{\partial t} + \rho \vec{v} \cdot \nabla \vec{v} = -\nabla \cdot \bar{\bar{\tau}} - \nabla p + \rho \vec{g} \tag{56}$$

The Navier-Stokes equations of motion apply in a general sense to three-dimensional, time-dependent flows, and their simplified versions can be used for different specific cases [63].

The general equations of motion can also be rearranged to the similar equation governing the heat transport [63]:

$$\rho \frac{\partial c_p T}{\partial t} + \rho v_x \frac{\partial c_p T}{\partial x} + \rho v_y \frac{\partial c_p T}{\partial y} + \rho v_z \frac{\partial c_p T}{\partial z} = \lambda \left(\frac{\partial^2 T}{\partial x^2} + \frac{\partial^2 T}{\partial y^2} + \frac{\partial^2 T}{\partial z^2} \right) + q \tag{57}$$

In Equation (57), the $c_p T$ is regarded as an energy concentration, and its unit is Joule per kilogram [63]. In the case of constant $c_p T$, Equation (57) changes form to [63]:

$$\frac{\partial T}{\partial t} + v_x \frac{\partial T}{\partial x} + v_y \frac{\partial T}{\partial y} + v_z \frac{\partial T}{\partial z} = \lambda \left(\frac{\partial^2 T}{\partial x^2} + \frac{\partial^2 T}{\partial y^2} + \frac{\partial^2 T}{\partial z^2} \right) + \frac{q}{\rho c_p} \tag{58}$$

Finally, the Navier-Stokes equations can be rewritten to analogous equations governing the species concentration transport [63]:

$$\frac{\partial c}{\partial t} + v_x \frac{\partial c}{\partial x} + v_y \frac{\partial c}{\partial y} + v_z \frac{\partial c}{\partial z} = D \left(\frac{\partial^2 c}{\partial x^2} + \frac{\partial^2 c}{\partial y^2} + \frac{\partial^2 c}{\partial z^2} \right) + r \tag{59}$$

The general equations of motion illustrate the analogy between momentum, heat and species transport [63]. The three equations balancing the momentum components, the equations governing the heat and species transport, and the continuity equation create a system of six partial differential equations. These equations are nonlinear and firmly linked internally [63]. Providing sufficient initial and boundary conditions, the velocity (3 components), temperature, pressure, and species concentrations can be computed as a function of time [63].

4.3. Computational fluid dynamics

Equation systems described in the previous section are the basis of modern computational fluid dynamics (CFD). The CFD can be exploited to achieve detailed pieces of information about local variables (velocity, pressure, temperature, concentration, etc.) inside the process equipment [63]. The computational resources provided by modern computers allow the use of CFD simulations in place of the classical phenomenological approach to transport phenomena, which uses concepts such as heat and mass transfer coefficients [63].

Still, classical chemical engineering and CFD-based modern chemical engineering both use the same concepts and laws and rely strongly on balances. Although the phenomenological approach allows for quick and decent results, CFD gives access to significantly more detailed information, including local quantities and parameters unobtainable experimentally [63]. It should be noted, though, that the current state of CFD requires experimental validation, especially for cases with turbulent flows [63].

All calculations in this dissertation were performed in Ansys Fluent solver (versions 2021 R2–2024 R1).

4.3.1. Computational domain and mesh

The motion equations are all derived by a small cube (control volume) without specified dimensions. Those dimensions must be small compared to the flow domain's dimensions to achieve the gradient of internal local values [63]. However, there is an absolute lower limit for the dimensions of the control volume cube, which is the molecules' free path length. A sufficiently larger cube is essential since such small dimensions make the continuum terms of mean velocity and conceptive transport lose their significance [63]. If the cubic volume element is considerably larger than the molecules' free path length, velocity components, temperature, and concentration can be regarded as point properties in the centre of the cubic volume [63].

The CFD is based on the finite volume method. This approach divides the flow domain into a large number of small-volume elements called "computational cells". The flow domain is called the computational domain. It is usually the three-dimensional isolated volume in the shape of the investigated process apparatus (like the chemical reactor interior) with precisely defined boundaries (inlet, outlet, wall, symmetry, etc.). The computational cells (typically tetrahedral, hexahedral or polyhedral shaped) form a three-dimensional "computational mesh", which refinement limits the degree of detail (resolution) [63]. This causes the need for mesh refinement in places where steep gradients are expected. As mentioned before, the smallest cell

size must be larger than the length of the molecule's free path; however, in practice, it is limited mainly by the computer's capacity, memory and computational power since smaller cells generate larger meshes [63]. In some specific cases, the computational domain and mesh may be simplified to a two-dimensional variant, like planar or axisymmetric domains. In these cases, the mesh contains cells in the form of small-surface elements instead of volumes (usually triangular or quadrilateral cells). In those cases, the velocity is balanced using its only x- and y-components, without z-component. This simplification significantly reduces the required computational resources since it reduces the number of differential equations in the system and the computational mesh size.

Computational cells contain the grid points (nodes) spanning across the flow domain [63]. The grids are located inside corresponding cells, preferably close to their centres. The momentum, mass, heat and species concentration are solved in each grid point; the variables have only values in those points [63]. The micro-balances' terms with derivatives in the grid points are discretised using the values of adjacent cell nodes. Several differential schemes are used to support this, using interpolation techniques to calculate the values between the grid points, which helps to change partial differential equations into algebraic equations [63,64]. Each cell produces algebraic equations for every balance set-up. That means the whole flow domain generates a large amount of algebraic equations, which are solved simultaneously through iterations [63]. The iterations are performed until all micro-balances are converged with a desired level of accuracy [63].

In this dissertation, the computational meshes are densest in the regions with the critical influence on the process, such as areas where the highest gradients of temperature or concentrations are anticipated and close to the expected high mass and heat transfer values like chemical reaction zones. The mesh independence was checked by two quantities: the wall shear stress value at the walls and the system's average turbulence energy dissipation rate. The y^+ ~1 condition was met by setting the near-wall cell sizes. Different meshes were tested until the difference between those two quantities was no higher than 3% compared to those with a denser mesh.

4.3.2. Continuous phase modelling – continuity and momentum

The basic principle of Ansys Fluent is solving the conservation equations of mass and momentum [64]. An additional energy equation is added in simulations of flows involving heat transfer or compressible gases. In cases of flows with species transport, species conservation

equations are also solved [64]. Analogously, other additional models (turbulence, combustion, etc.) require their specific balances added to the calculations [64]. All conservation equations presented in this section are applied to cases with no moving reference frames since no such cases were solved in this dissertation.

The following expression governs the continuity [64]:

$$\frac{\partial \rho}{\partial t} + \nabla \cdot (\rho \vec{v}) = S_m \tag{60}$$

Equation (60) is the general equation of conservation of mass used by Ansys Fluent, valid for both compressible and incompressible flows [64]. The difference from Equation (29) is the presence of the source term S_m, which was added since Fluent can model the dispersed phase independently or coupled with the continuous phase. The source term S_m represents the mass added to the continuous phase from the dispersed phase (e.g. from vaporisation) or by any other user-defined sources [64]. Although this dissertation investigates cases with dispersed phases, no mass exchange with continuous phase is modelled, meaning the S_m term in this work will always equal zero.

The conservation of momentum solved by Fluent is governed by the following expression [64]:

$$\frac{\partial}{\partial t}(\rho \vec{v}) + \nabla \cdot (\rho \vec{v} \vec{v}) = -\nabla p + \nabla \cdot (\bar{\bar{\tau}}) + \rho \vec{g} + \vec{F} \tag{61}$$

It can be noted that the momentum balance solved in Fluent solver is a slightly modified version of the general equations of motion derived in terms of shear stresses described in Section 4.2.2. The primary difference is the presence of external body forces term $\vec{F}$, used while using model-dependent source terms like porous zones, interactions with the dispersed phase or other user-defined sources [64]. Since this dissertation exploits the porous zone model in some investigated cases (Sections 5 and 6), this model is further described in detail in Section 4.3.6.

The stress tensor $\bar{\bar{\tau}}$ can be written as follows [64]:

$$\bar{\bar{\tau}} = \mu \left[(\nabla \vec{v} + \nabla \vec{v}^T) - \frac{2}{3} \nabla \cdot \vec{v} I \right] \tag{62}$$

where μ is the molecular viscosity and I is the unit tensor. The second term of the right-hand side of Equation (62) is the volume dilatation's effect [64].

Some cases of this work are calculated in the 2D flow domain. Section 9 uses the planar 2D domain. In this case, the same governing equations of continuity and momentum conservation are applied with the z-components of vector and tensor values equal to zero. However, in Section 5, calculations were performed in the 2D axisymmetric domain, which requires continuity and momentum conservation equations to be transformed into the radial coordination system. The continuity equation for 2D axisymmetric geometries is given by [64]:

$$\frac{\partial \rho}{\partial t} + \frac{\partial}{\partial x}(\rho v_x) + \frac{\partial}{\partial r}(\rho v_r) + \frac{\rho v_r}{r} = S_m \tag{63}$$

where r is the radial coordinate, x is the axial coordinate, v_r is the radial velocity, and v_x is the axial velocity. The conservation of momentum equation for the 2D axisymmetric domain must be expressed for axial direction [64]:

$$\begin{aligned}\frac{\partial}{\partial t}(\rho v_x) + \frac{1}{r}\frac{\partial}{\partial x}(r\rho v_x v_x) + \frac{1}{r}\frac{\partial}{\partial r}(r\rho v_r v_x) \\ = -\frac{\partial \rho}{\partial \mathrm{x}} + \frac{1}{r}\frac{\partial}{\partial x}\left\{r\mu\left[2\frac{\partial v_x}{\partial x} - \frac{2}{3}(\nabla \cdot \vec{v})\right]\right\} + \frac{1}{r}\frac{\partial}{\partial r}\left[r\mu\left(\frac{\partial v_x}{\partial r} + \frac{\partial v_r}{\partial x}\right)\right] + F_x\end{aligned} \tag{64}$$

and radial direction [64]:

$$\begin{aligned}\frac{\partial}{\partial t}(\rho v_r) + \frac{1}{r}\frac{\partial}{\partial x}(r\rho v_x v_r) + \frac{1}{r}\frac{\partial}{\partial r}(r\rho v_r v_r) \\ = -\frac{\partial \rho}{\partial \mathrm{r}} + \frac{1}{r}\frac{\partial}{\partial x}\left[r\mu\left(\frac{\partial v_r}{\partial x} + \frac{\partial v_x}{\partial r}\right)\right] + \frac{1}{r}\frac{\partial}{\partial r}\left\{r\mu\left[2\frac{\partial v_r}{\partial r} - \frac{2}{3}(\nabla \cdot \vec{v})\right]\right\} \\ - 2\mu\frac{v_r}{r^2} + \frac{2}{3}\frac{\mu}{r}(\nabla \cdot \vec{v}) + \rho\frac{{v_z}^2}{r} + F_r\end{aligned} \tag{65}$$

where:

$$\nabla \cdot \vec{v} = \frac{\partial v_x}{\partial x} + \frac{\partial v_r}{\partial r} + \frac{v_r}{r} \tag{66}$$

where v_z is a swirl velocity [64].

4.3.3. Continuous phase modelling – turbulence

In chemical and process engineering, most fluid flows have a turbulent character. In theory, to capture turbulence, the computational mesh should be finer than the smallest visible eddies [63]. However, in most cases, the computer technologies are not advanced enough to directly model turbulence. This is especially true for higher Reynolds numbers, where eddies are smaller, significantly increasing mesh refinement to capture them. Furthermore, in most cases,

it is not required to simulate all eddies precisely in the flow field since the knowledge of mean quantities with their variations is sufficient [63]. Consequently, calculations are mainly performed using a coarser mesh than the turbulence vortexes [63]. One of the most robust solutions to this problem, available in Ansys Fluent, is the Reynolds (Ensemble) averaging, where variables in instantaneous Navier-Stokes equations are decomposed into the mean (ensemble- or time-averaged) and fluctuating components [64]. The velocity components can be expressed as [64]:

$$u_i = \bar{u}_i + u'_i \tag{67}$$

where $\bar{u}_i$ and u'_i are mean and fluctuating components of velocity. Scalar components such as pressure are calculated analogously [64]:

$$\varphi = \bar{\varphi} + \varphi' \tag{68}$$

Where φ is a scalar (pressure, energy, species concentration, etc.)

The ensemble-averaged momentum equations are obtained by substituting Equations (67) and (68) for the flow variables into instantaneous continuity and momentum conservation equations taking a time average [64]. Those can be written in the Cartesian tensor form as follows [64]:

$$\frac{\partial \rho}{\partial t} + \frac{\partial}{\partial x_i}(\rho u_i) = 0 \tag{69}$$

$$\frac{\partial}{\partial t}(\rho u_i) + \frac{\partial}{\partial x_j}(\rho u_i u_j) = -\frac{\partial p}{\partial x_i} + \frac{\partial}{\partial x_j}\left[\mu\left(\frac{\partial u_i}{\partial x_j} + \frac{\partial u_j}{\partial x_i} - \frac{2}{3}\delta_{ij}\frac{\partial u_l}{\partial x_l}\right)\right] + \frac{\partial}{\partial x_j}\left(-\rho\overline{u'_i u'_j}\right) \tag{70}$$

where $-\rho\overline{u'_i u'_j}$ are Reynold stresses. Equations (69) and (70) are called Reynolds-averaged Navier-Stokes equations (RANS). Their general form is the same as the instantaneous Navier-Stokes equations, although the velocities and other variables now represent time-averaged (ensemble-averaged) values [64]. The additional terms appearing in those equations represent the turbulence effects [64]. The RANS approach requires the Reynolds stresses in Equation (70) to be appropriately modelled, which is obtained using a Boussinesq hypothesis to relate the mean velocity gradients and Reynolds stresses [64]:

$$-\rho\overline{u'_i u'_j} = \mu_t\left(\frac{\partial u_i}{\partial x_j} + \frac{\partial u_j}{\partial x_i}\right) - \frac{2}{3}\left(\rho k + \mu_t\frac{\partial u_k}{\partial x_k}\right)\delta_{ij} \tag{71}$$

where μ_t is a turbulent viscosity. The Boussinesq hypothesis is used in many turbulence models such as Spalart-Allmaras, k-ε and k-ω. This approach is characterised by the low computational cost associated with the turbulent viscosity computation [64]. However, the Boussinesq hypothesis assumes turbulent viscosity as an isotropic scalar quantity, and this assumption is valid for flows dominated by only one of the turbulent shear stresses. Still, this covers most of the flows in chemical engineering, such as wall boundary layers, mixing layers, jets, etc. [64]. In the Spalart-Allmaras model, turbulent viscosity is calculated directly. In most cases, however, two-equation turbulence models are applied, where μ_t is computed as a function of turbulent kinetic energy and turbulent dissipation rate (or specific dissipation rate).

In two-equation turbulence models, the momentum resulting from eddies is calculated as separate equations contributing to momentum conservation on a scale between convection and molecular transport [63]. The arguably most well-known two-equation turbulence model is k-ε (and its variations). In this approach, eddies transport momentum via convection, which is modelled in terms of two concepts. First is the concentration of turbulent kinetic energy (k) with the unit of [$m^2\ s^{-2}$] or [$J\ kg^{-1}$]. This is a measure of the strength and magnitude of velocity fluctuations resulting from turbulent eddies [63]. The second concept is the dissipation of k into heat due to the viscosity of the smallest eddies, also called Kolmogorov eddies. This value is denoted as ε with the unit of [$m^2\ s^{-3}$] or [$W\ kg^{-1}$]. The ε corresponds to the density of the smallest vortexes in which the energy dissipation occurs [63]. Since k and ε are regarded as concentrations, they can also be calculated in the form of transport equations, similar to the Navier-Stokes equations. However, it should be noted that k and ε are not conserved quantities [63]. In the standard k-ε model, the turbulent kinetic energy (k) is governed by the following expression [64]:

$$\frac{\partial}{\partial t}(\rho k) + \frac{\partial}{\partial x_j}\left(\rho k u_j\right) = \frac{\partial}{\partial x_j}\left[\left(\mu + \frac{\mu_t}{\sigma_k}\right)\frac{\partial k}{\partial x_j}\right] + G_k + G_b - \rho\varepsilon - Y_M + S_k \qquad (72)$$

and the specific dissipation rate (ε) can be written as [64]:

$$\frac{\partial}{\partial t}(\rho\varepsilon) + \frac{\partial}{\partial x_i}(\rho\varepsilon u_i) = \frac{\partial}{\partial x_j}\left[\left(\mu + \frac{\mu_t}{\sigma_\varepsilon}\right)\frac{\partial \varepsilon}{\partial x_j}\right] + C_{1\varepsilon}\frac{\varepsilon}{k}(G_k + C_{3\varepsilon}G_b) - C_{2\varepsilon}\rho\frac{\varepsilon^2}{k} + S_\varepsilon \qquad (73)$$

In Equations (72) and (73), G_k is a generation of turbulent kinetic energy by mean velocity gradients, G_b is a generation of turbulent kinetic energy by buoyancy, Y_M is a contribution of the fluctuating dilatation in compressible turbulence to the overall dissipation rate, $C_{1\varepsilon}$, $C_{2\varepsilon}$, $C_{3\varepsilon}$

are constants, σ_k, σ_ε are turbulent Prandtl numbers for k and ε, and S_k, S_ε are user-defined source terms [64].

In the standard k-ε model, turbulent viscosity is calculated as follows [64]:

$$\mu_t = \rho C_\mu \frac{k^2}{\varepsilon} \tag{74}$$

where C_μ is a constant.

The k-ε model has different variations called "standard", "RNG", and "realizable" k-ε. All those models have similar forms with the transport equations. The differences between them include the method of calculating turbulent viscosity, turbulent Prandtl numbers and generation and destruction terms in the ε equation [64]. It should be noted that k-ε models work poorly close to the walls, especially for coarser meshes, and require near-wall treatment functions that increase their accuracy in those regions. The commonly used example is the Enhanced Wall Treatment for ε equation [64].

In most calculations, this dissertation uses the SST k-ω model, which is the default turbulence model recommended by Ansys [64]. This approach uses the k-ε model for the high-Reynolds number flows in the outer part of the domain, outside of the boundary layer and the k-ω model for the inner region of the boundary layer [64]. The k-ω model is based on the turbulent energy (k) and specific dissipation rate (ω), which is defined as a ratio of ε to k, and its unit is [s^{-1}]. The k-ω model is characterised by improved accuracy for predicting the flow in the shear layer close to the walls [64]. However, outside the shear layer, the accuracy of this model falls due to the so-called "freestream sensitivity" [64]. Thanks to the combination of advantages of k-ε and k-ω, the SST k-ω model is highly versatile and can be applied to most cases in the chemical engineering field.

In the SST k-ω model, the turbulence in the shear layer is modelled by two additional equations: the turbulent energy (k) and its specific dissipation rate (ω) [64]. The turbulent energy is calculated slightly differently than in the k-ε model and can be written as follows:

$$\frac{\partial}{\partial t}(\rho k) + \frac{\partial}{\partial x_i}(\rho k u_i) = \frac{\partial}{\partial x_j}\left[\left(\mu + \frac{\mu_t}{\sigma_k}\right)\frac{\partial k}{\partial x_j}\right] + G_k - Y_k + S_k + G_b \tag{75}$$

and the specific dissipation rate is governed by the following expression:

$$\frac{\partial}{\partial t}(\rho\omega) + \frac{\partial}{\partial x_i}(\rho\omega u_i) = \frac{\partial}{\partial x_j}\left[\left(\mu + \frac{\mu_t}{\sigma_\omega}\right)\frac{\partial \omega}{\partial x_j}\right] + G_\omega - Y_\omega + D_\omega + S_\omega + G_{\omega b} \qquad (76)$$

In equations (75) and (76), G_k is the turbulence kinetic energy production, G_ω is the generation of ω, Y_k, Y_ω are dissipation of k and ω due to the turbulence, D_ω is a cross-diffusion term, S_k, S_ω are user-defined source terms, and G_b, $G_{\omega b}$ are buoyancy terms [64].

SST k-ω model uses the modified turbulent viscosity formulation to account for the transport effects of the principal turbulent shear stress [64]:

$$\mu_t = \frac{\rho k}{\omega} \cdot \frac{1}{\max\left[\frac{1}{\alpha^*}, \frac{SF_2}{\alpha_1 \omega}\right]} \qquad (77)$$

where S is the strain rate magnitude, α^* and α_1 are coefficients, and parameter F_2 is calculated from the following expression:

$$F_2 = \tanh\left\{\left[\max\left(2\frac{\sqrt{k}}{0.09\omega y}, \frac{500\mu}{\rho y^2 \omega}\right)\right]^2\right\} \qquad (78)$$

where y is the distance to the wall surface.

As mentioned before, most simulations in this dissertation were performed using the SST k-ω. The exception is a modelling of the droplet removal process (Section 9), where two more turbulence models were tested: standard k-ε and Reynolds Stress Model.

The Reynolds Stress Model is the most complicated of the RANS turbulence models since it uses the anisotropic Reynolds stress tensors [64], which is an alternative approach to the Boussinesq hypothesis. This turbulence model requires an additional scale-determining equation (typically for ε or ω). The RSM model requires significant computational resources since it requires five additional transport equations for the 2D domain and seven for the 3D domain, and it is applied mainly for cases where mean flow is dominated by anisotropy or turbulence [64]. This work used it only as a reference in Section 9.7.1. Still, the SST k-ω was used in the main simulations since it was found to be the most accurate for wave-plate mist-eliminator modelling.

It should be noted that this work exploits only a small portion of CFD possibilities, and there are many different approaches to turbulence modelling, most noticeably the large eddy simulations (LES) or hybrid RANS-LES formulations [64].

4.3.4. Heat transfer modelling

Heat transfer is basically the flow of thermal energy from the matter of one region to another. Three main mechanisms govern the heat transfer: conduction, convection and radiation. In Ansys Fluent, heat transport can be calculated using conduction/convection physical models, natural convection/buoyancy-driven flow models, and radiation models. Fluent solves a variation of the energy equation corresponding to the specified heat transfer issue [64]. This work contains cases where heat transfer occurs through convection in fluids and conduction in both fluid and solid regions. The heat sources resulting from chemical reactions also make a critical contribution to heat transfer, as modelled in this work.

In Ansys Fluent, the energy balance is governed by the following equation [64]:

$$\frac{\partial}{\partial t}\left[\rho\left(e+\frac{v^2}{2}\right)\right]+\nabla\cdot\left[\rho\vec{v}\left(h+\frac{v^2}{2}\right)\right]=\nabla\cdot\left(k_{eff}\nabla T-\sum_j h_j\overrightarrow{J_j}+\bar{\bar{\tau}}_{eff}\cdot\vec{v}\right)+S_h \qquad (79)$$

where e is the internal energy, h is the enthalpy, $\overrightarrow{J_j}$ is the diffusion flux of species j, and k_{eff} is the effective conductivity, which is defined as [64]:

$$k_{eff}=k+k_t \qquad (80)$$

where k_t is the turbulent thermal conductivity defined based on the turbulence model.

The first three terms of the right-hand side of Equation (79) represent heat transport due to conduction, species diffusion and viscous dissipation. Term S_h represents defined heat sources, including heat generation rate from chemical reactions, which can be written as follows [64]:

$$S_{h,rxn}=-\sum_j\frac{h_j^0}{M_j}R_j \qquad (81)$$

where h_j^0 is the enthalpy of formation of species j, R_j is the reaction rate of species j, and M_j is the molecular weight of species j.

In solid regions, the energy transport equation has the following form:

$$\frac{\partial}{\partial t}(\rho h) + \nabla \cdot (\vec{v}\rho h) = \nabla \cdot (k\nabla T) + S_h \tag{82}$$

where ρ is the density, k is the conductivity, T is the temperature, S_h is a volumetric heat source, and h is a sensible enthalpy, which can be written as:

$$h = \int_{T_{ref}}^{T} C_p dT \tag{83}$$

The second term of the right-hand side of Equation (82) represents the convective energy transfer due to the motion of solids (rotational or translational), and the terms on the right-hand side represent the heat flux due to the conduction and volumetric heat sources within the solid region [64].

4.3.5. Species transport modelling

In Ansys Fluent, the transport and mixing of chemical species is modelled by solving the conservation equations of diffusion, convection and reaction sources [64]. The chemical reactions can be modelled within the fluid phase (volumetric reactions), within the porous regions, and on the wall or particle surface [64]. In Fluent, conserved quantity is a mass fraction of corresponding species. Species transport is modelled by solving the convection-diffusion conservation equations for each species, which can be written as [64]:

$$\frac{\partial}{\partial t}(\rho Y_i) + \nabla \cdot (\rho \vec{v} Y_i) = -\nabla \vec{J_\iota} + R_i + S_i \tag{84}$$

where Y_i is the mass fraction of species i, ρ is the mixture density, $\vec{v}$ is the diffusing species velocity, $\vec{J_\iota}$ is the diffusion flux of species i, R_i is the net production of species i through a chemical reaction, and S_i is the rate of creation of species i by addition from the dispersed phase and other user-defined sources [64].

Species transport is calculated by solving N–1 species, where N is the total number of fluid chemical species in the domain [64]. The mass fraction of the "last" species (N^{th} species) is determined as 1 minus the sum of other species. This species is considered a "default" in the domain. To minimise errors, it is recommended to select the species with the largest mass fraction value as the "last" species [64].

In laminar flows, the diffusion flux of species i is calculated from Fick's law from a gradient of concentration and temperature, which can be written as [64]:

$$\vec{J_i} = -\rho D_{i,m} \nabla Y_i - D_{T,i} \frac{\nabla T}{T} \tag{85}$$

where $D_{i,m}$ is the mass diffusion coefficient (diffusivity) for species i in the mixture, Y_i is a mass fraction of species i, $D_{T,i}$ is the thermal (Soret) diffusion coefficient, and T is the temperature [64]. In Fluent, the laminar mass diffusivity ($D_{i,m}$) can be defined in various ways. This work uses the Unity Lewis Number approach, where the laminar mass diffusivity of all species is computed as [64]:

$$D_{i,m} = \frac{k}{\rho C_p} \tag{86}$$

where $D_{i,m}$ is the mass diffusivity of species i in the mixture, k is thermal conductivity, ρ is the mixture density, and C_p is the mixture's specific heat [64].

In turbulent flows, the mass diffusion is governed by the following expression [64]:

$$\vec{J_i} = -\left(\rho D_{i,m} + \frac{\mu_t}{Sc_t}\right) \nabla Y_i - D_{T,i} \frac{\nabla T}{T} \tag{87}$$

where μ_t is the turbulent viscosity, and Sc_t is the turbulent Schmidt number defined as [64]:

$$Sc_t = \frac{\mu_t}{\rho D_t} \tag{88}$$

where D_t is the turbulent diffusivity. The Sc_t has a default value of 0.7. In turbulent flows, the total diffusion is the sum of the laminar and turbulent diffusion, although the turbulent diffusion typically overwhelms laminar diffusion, meaning that the specification of detailed laminar diffusion properties is not necessary in those cases [64].

The gas mixture's physical properties (density, specific heat, thermal conductivity, viscosity) are simulated based on the mixing laws based on the individual species' properties. The species model allows the simulation of the chemical reactions based on species transport. There are Fluent's models for modelling reaction rates; however, in this work, reactions were implemented through the user-defined functions manipulating the species conversion, and their kinetics are described in corresponding sections.

4.3.6. Porous zone modelling

This work uses the Ansys Fluent porous zone model for modelling catalyst beds in ammonia synthesis reactors (Sections 5 and 6). The flow through the porous regions is simulated by adding the momentum source term to the fluid flow standard equations [66]:

$$S_i = -\left(\sum_{j=1}^{3} D_{ij}\mu v_j + \sum_{j=1}^{3} C_{ij}\frac{1}{2}\rho|v|v_j\right) \tag{89}$$

where S_i is the source term for the i (x, y, or z) momentum equation, C_{ij} and D_{ij} are prescribed matrices, and $|v|$ is the magnitude of the velocity. In the porous zone model, the pressure drop is proportional to the fluid velocity in the cells [66]. Equation (89) contains two terms. The first is the viscous loss term (left part of right-hand side), while the second is the inertial loss term (right part of right-hand side). In this work, porous media are considered simple and homogenous, and in this case, the momentum source term can be calculated from the following expression [66]:

$$S_i = -\left(\frac{\mu}{\alpha}v_i + C_2\frac{1}{2}\rho|v|v_i\right) \tag{90}$$

where α is the permeability, and C_2 is the inertial resistance factor.

Since the catalyst in the ammonia reactors is in the form of packed beds, the Ergun Equation [66] was used to calculate the input parameters for the Ansys Fluent, which are the viscous resistance (inverse permeability) and the inertial resistance. The viscous resistance can be calculated from the following expression [66]:

$$C_1 = \frac{150}{{d_p}^2}\cdot\frac{(1-\varepsilon)^2}{\varepsilon^3} \tag{91}$$

The inertial resistance can be written as [66]:

$$C_1 = \frac{3.5}{d_p}\cdot\frac{(1-C_2)}{\varepsilon^3} \tag{92}$$

In Equations (91) and (92), ε [-] is a porosity, and d_p [m] is a mean catalyst particle diameter.

In Fluent's porous media model, the energy transport is solved using the standard energy equation (Equation (79)). Since this work's simulations are in steady-state mode, no modification to conduction flux is required [66].

4.3.7. Discrete phase modelling

In Sections 8 and 9 of this work, the dispersed phase was modelled to track the lifted platinum particles (Section 8) and fluid droplets (Section 9). A discrete phase model (DPM) [64] was applied to model their trajectories. Since this work assumes that modelled discrete phase behave as hard spheres, both considered droplets and platinum particles will be referred to as "particles". The DPM model applies the Lagrangian approach to simulate particle motion. This work considers the one-way coupling between gas and discrete phases. The particles' motion is computed after continuous flow, and it is assumed that their movement does not affect the continuous phase flow. The trajectories are tracked using Newton's second law. The force balance equates the particle's inertia with forces acting on the particles, and it can be written as follows [64]:

$$m_p \frac{\mathrm{d}\overrightarrow{u_p}}{\mathrm{d}t} = m_p \frac{\left(\vec{u} - \overrightarrow{u_p}\right)}{\tau_r} + m_p \frac{\vec{g}\left(\rho_p - \rho\right)}{\rho_p} + \overrightarrow{F_x} \tag{93}$$

where m_p is a particle mass, $\vec{u}$ and $\overrightarrow{u_p}$ are gas and particle velocities; ρ and ρ_p are gas and particle densities; $\vec{g}$ is a gravitational acceleration, and $\overrightarrow{F_x}$ is an additional force. The term $m_p \frac{(\vec{u}-\overrightarrow{u_p})}{\tau_r}$ corresponds to the drag force, and τ_r is a particle relaxation term [67], which can be calculated from the following expression [64]:

$$\tau_r = \frac{\rho_p {d_p}^2}{18\mu} \frac{24}{C_D Re} \tag{94}$$

where C_D is the drag force coefficient, μ is a molecular viscosity, and Re is a relative Reynolds number. C_D can be calculated from the Equations (95) and (96):

$$C_D = 0.44 \qquad \text{for} \qquad Re_p > 1000 \tag{95}$$

$$C_D = \frac{1 + 0.15{Re_p}^{0.687}}{{Re_p}^{-24}} \qquad \text{for} \qquad Re_p \leq 1000 \tag{96}$$

where Re_p is the particle's Reynolds number, which can be written as:

$$Re_p = \frac{\rho|u - u_p|d_p}{\mu} \tag{97}$$

It should be noted that several additional assumptions need to be met to apply the DPM model, such as the lack of coalescence between particles, no interaction between particles, and the mass fraction of the dispersed phase should not exceed 0.1 [64].

In the discrete phase model, the turbulent dispersion term can included in simulating particle motion. To achieve that, the stochastic model was used, which computes the particle motion trajectories using instantaneous velocity as follows:

$$u(t) = \overline{u} + u'(t) \tag{98}$$

where: $\overline{u}$ is a continuous phase average velocity, and $u'(t)$ is a continuous phase velocity fluctuation function. Turbulent dispersion was applied in the DPM modelling in Sections 8 and 9 of this work.

In Section 8, the computed particle trajectories were used to identify the regions of the entrained platinum particle's deposition. This was achieved by applying the accretion modelling within the DPM model. In Fluent, the accretion rate is computed as follows [64]:

$$R_{accretion} = \sum_{p=1}^{N_{particles}} \frac{\dot{m}_p}{A_{face}} \tag{99}$$

where A_{face} is the area of the cell face at the wall and $\dot{m}_p$ is the particle stream.

In this work, the accretion rate was used to calculate a ratio of the local accretion rate to the sum of the accretion rate on the corresponding surface:

$$R_{accr\_ratio} = \frac{R_{accretion_i}}{\sum_{i=1}^{N_{surface\_cells}} R_{accretion_i}} \cdot 100\% \tag{100}$$

where $N_{surface\_cells}$ is a number of computational cells of the catalyst surface's model, and $R_{accretion_i}$ is a local accretion rate on the surface of the computational cell i. This approach allowed the transformation of the accretion rate contours into the contours of the percentage of all captured platinum particles, which were used in Section 8 to visualise the regions of increased platinum deposition.

5. Industrial ammonia synthesis in axial-radial ammonia reactor – CFD modelling of the catalyst bed using Temkin and Pyzhev kinetic model

The motivation of this part of the dissertation is to apply computational fluid dynamics methods to give an in-depth insight into parameters that are unavailable for experimental measurement and to use this advantage to improve the ammonia synthesis converters. Section 3.1 describes in detail the types of industrial ammonia synthesis converters and the principles of the Haber-Bosch process.

In this section, the modified Temkin-Pyzhev expression developed by Dyson and Simon [35] was implemented into the numerical model to simulate the ammonia synthesis process. The investigated reactor is the Topsoe converter with axial-radial flow through the catalyst beds, and the examined catalyst is magnetite. This work focused on using the CFD tools to investigate the influence of different catalyst particle sizes on the process. The contours of velocity, reaction rate, concentration and pressure were obtained to determine the gradient of the ammonia formation rate and identify the dead zones with negligible reaction rates. Based on the results, the potential geometry modifications were proposed to reduce the catalyst bed's volume without affecting the converter's performance. This section was made based on the results published in the manuscript "Computational Fluid Dynamics of Ammonia Synthesis in Axial-Radial Bed Reactor" [68], which was a coherent part of this PhD project.

5.1. Geometry

The investigated ammonia reactor is the Topsoe axial-radial reactor with three catalyst beds. In this work, the first bed of the reactor was simulated, including the inflow and outflow zones. The catalyst's bed geometry was created based on the dimensions reported by Panahandeh et al. [29], and the inflow and outflow areas were modelled based on Mirvakili et al. [34]. The converter's geometry was created as a two-dimensional, axisymmetric model, as shown in Figure 5.1. It should be noted that there is limited data about the converter's geometry in the literature. Because of that, the geometry of the catalyst bed's vicinity had to be simplified, and its dimensions were estimated.

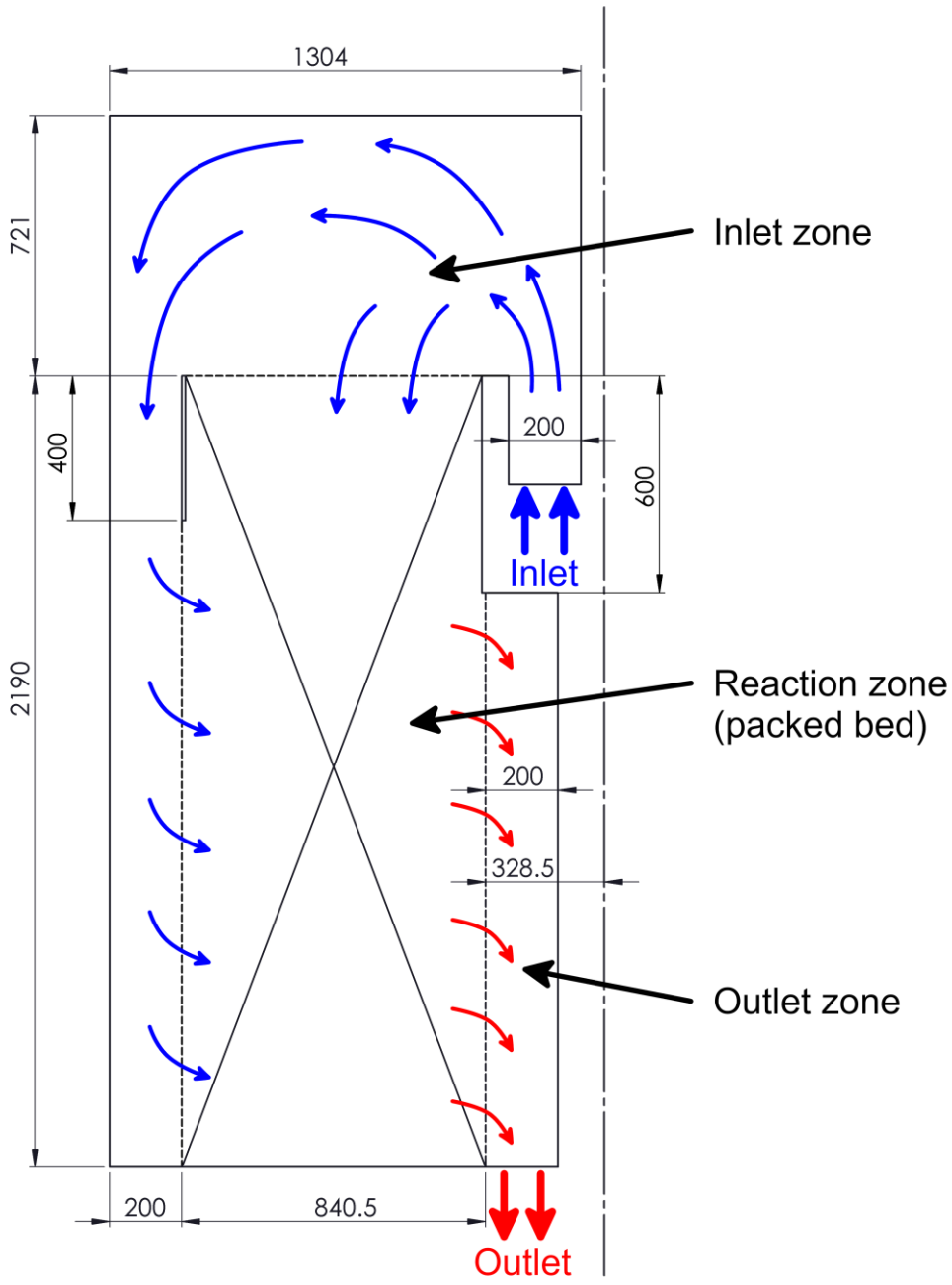

Figure 5.1. Flow patterns and geometry of the investigated axial-radial ammonia synthesis, dimensions in mm. Flow patterns are for reference and do not illustrate phenomena such as circulation zones. [68]

The catalyst beds are annulus-shaped. In the inner part, the converter contains a heat recovery system using shell-and-tube heat exchangers to pre-heat the feed gas mixture. The top of the catalyst bed's walls is non-perforated, forcing the axial gas flow. There is 400 mm of the non-perforated outer wall and 600 mm of the inner wall. The rest of the catalyst bed's walls are perforated. Due to this construction, radial gas flow is dominant at the middle and lower levels of the bed. After leaving the first bed, gas enters the heat recovery system before entering the second catalyst bed.

5.2. Catalyst beds

The gas flow through the catalyst beds was calculated using Ansys Fluent's porous zone model described in Section 4.3.6. In this work, the catalyst magnetite [13] is considered in the form of a packed bed with particles with a diameter range of 1–10 mm (equivalent sphere). The catalyst parameters are listed in Table 5.1.

Table 5.1. Catalyst parameters [68]

Parameter	*Unit*	*Value*	*Source*
particle diameter	mm	1–10	[59,69]
porosity	-	0.52	[69]
sphericity	-	0.65	[59]

Since, in this section, the chemical reaction model was implemented using surface kinetics, the surface-to-volume ratio is an essential parameter, calculated using the following expression:

$$S_v = \frac{6}{\psi d_p} \tag{101}$$

where ψ is the sphericity, and d_p is the particle diameter. Other parameters critical for the porous zone model, such as viscous and inertial resistances, were calculated from the Ergun Equation for packed beds, as described in Section 4.3.6. Table 5.2 lists the calculated viscous and inertial resistance values and surface-to-volume ratios for every particle diameter.

Table 5.2. Calculated catalyst bed's parameters (bed's porosity 0.52) [68]

Particle diameter [mm]	*Viscous resistance [m^{-2}]*	*Inertial resistance [m^{-1}]*	*Surface-to-volume ratio [m^{-1}]*
1	$2.46 \cdot 10^8$	11948	9231
1.5	$1.09 \cdot 10^8$	7965	6154
2	$6.14 \cdot 10^7$	5974	4615
3	$2.73 \cdot 10^7$	3983	3077
4	$1.54 \cdot 10^7$	2987	2308
5	$9.83 \cdot 10^6$	2390	1846
6	$6.83 \cdot 10^6$	1991	1538
8	$3.84 \cdot 10^6$	1494	1154
10	$2.46 \cdot 10^6$	1195	923

5.3. Computational setup

The computational domain is two-dimensional and contains the geometry model presented in Figure 5.1. The gas inlet is located close to the axis, and the gas outlet is at the bottom part of the outlet zone. The numerical mesh contains approximately 90000 quadrilateral cells and was generated using the Ansys Workbench's meshing module. All calculations were performed using the Ansys Fluent solver. Second-order discretisation schemes were used for all variables, and the SIMPLE method was used for pressure-velocity coupling. Calculations were conducted in steady-state mode with applied gravity force. The SST k-ω turbulence model was chosen for turbulence modelling.

5.4. Boundary conditions

This work used the typical process parameters widely used in the industry [15,29,34,70]. Experimental data published by Panahandeh et al. [29] were applied for the simulation, and their results were used for validation. Table 5.3 lists the process conditions used as boundary conditions for the CFD model.

Table 5.3. Axial-radial ammonia converter's CFD model's boundary conditions [29,68]

Parameter	*Unit*	*Value*
flow rate	kmol h^{-1}	19622.17
flow rate	kg s^{-1}	57.72
gas inlet temperature	°C	342
operating pressure	atm	220
inlet N_2 mole fraction	-	0.2093
inlet H_2 mole fraction	-	0.6280
inlet NH_3 mole fraction	-	0.0347
inlet CH_4 mole fraction (inert)	-	0.0939
inlet Ar mole fraction (inert)	-	0.0341

5.5. Reaction kinetics

The reaction of the ammonia synthesis proceeds as follows:

$$N_2 + 3\,H_2 \rightarrow 2\,NH_3$$

To simulate the ammonia synthesis reaction, this work uses the theoretical kinetic model developed by Dyson and Simon [35], which was created from the experimental data of Nielsen

et al. [71]. This kinetic model has been widely used in the literature [27,29,33] and is reportedly implemented in CFD simulations [34,68].

In their kinetic model, Dyson and Simon [35] use a modified Temkin and Pyzhev expression to calculate the reaction rate:

$$R_{NH_3} = 2k\left[{K_a}^2 a_1 \left(\frac{{a_2}^3}{{a_3}^2}\right)^{\alpha} - \left(\frac{{a_3}^2}{{a_2}^3}\right)^{1-\alpha}\right] \tag{102}$$

In Equation (102), the corresponding component subscripts are 1-Nitrogen, 2-Hydrogen, and 3-Ammonia, parameter α has a value of 0.5 [35], and K_a is the equilibrium constant from the equation developed by Gillespie and Beattie [72], which can be written as:

$$\begin{aligned}\log_{10}K_a = {} & -2.691122\log_{10}T - 5.519265\cdot 10^{-5}T + 1.848863\cdot 10^{-7}T^2 \\ & + 2001.6\cdot T^{-1} + 2.6899\end{aligned} \tag{103}$$

The activities can be calculated from the following expression [35]:

$$a_i = f_i = y_i {f_i}^0 \tag{104}$$

where ${f_i}^0$ is the pure component's fugacity at the system's pressure and temperature, and it can be calculated using the activity coefficients, which can be written as follows [35]:

$${f_i}^0 = \gamma_i P \tag{105}$$

where γ_i are activity coefficients that can be calculated from the following expressions [35]:

$$\begin{aligned}\gamma_1 = {} & 0.93431737 + 0.3101804\cdot 10^{-3}T + 0.295896\cdot 10^{-3}P \\ & - 0.2707279\cdot 10^{-6}T^2 + 0.4775207\cdot 10^{-6}P^2\end{aligned} \tag{106}$$

$$\begin{aligned}\gamma_2 = \exp\Big\{ & \exp(-3.8402\cdot T^{0.125} + 0.541)P \\ & - \exp(-0.1263\cdot T^{0.5} - 15.980)P^2 \\ & + 300\cdot[\exp(-0.011901T - 5.941)]\cdot\left(\exp\left(\frac{-P}{300}\right) - 1\right)\Big\}\end{aligned} \tag{107}$$

$$\begin{aligned}\gamma_3 = {} & 0.1438996 + 0.2028538\cdot 10^{-2}T - 0.4487672\cdot 10^{-3}P \\ & - 0.1142945\cdot 10^{-5}T^2 + 0.2761216\cdot 10^{-6}P^2\end{aligned} \tag{108}$$

In Equations (106)–(108), the temperature and pressure units are Kelvin degrees and atmospheres. The rate constant k is calculated from the Arrhenius expression, which proceeds as follows:

$$k = A \cdot \exp\left(\frac{-E}{R \cdot T}\right) \tag{109}$$

Table 5.4 lists the values and units of the constants used in Equation (109):

Table 5.4. Parameters for the Arrhenius equation constants [35,68]

Parameter	*Symbol*	*Unit*	*Value*
pre-exponential factor	*A*	kmol m^{-3} h^{-1}	$8.849 \cdot 10^{14}$
activation energy	*E*	cal mol^{-1}	40765
universal gas constant	*R*	cal K^{-1} mol^{-1}	1.987

Therefore, the ammonia formation rate in the units of kmol per cubic meter of the catalyst bed per hour can be written as [35]:

$$R_{NH_3} = 1.7698 \cdot 10^{15} \exp\left(\frac{-40765}{RT}\right)\left[{K_a}^2 a_1 \left(\frac{{a_2}^3}{{a_3}^2}\right)^{0.5} - \left(\frac{{a_3}^2}{{a_2}^3}\right)^{0.5}\right] \tag{110}$$

According to Dyson and Simon [35], Equation (110) is valid for the catalyst particles with diameters lower than 6 mm, which are sufficiently small to exclude the transport and kinetic effect interaction. In this range, no correction factor is required. Still, larger particles (6–10 mm in size) are subject to diffusion restriction in their pores' structures [35]. To solve this issue, the effectiveness factor is added to Equation (110), which is a function of conversion (η) and temperature, with pressure as a parameter [35]:

$$\xi = b_0 + b_1 T + b_2 \eta + b_3 T^2 + b_4 \eta^2 + b_5 T^3 + b_6 \eta^3 \tag{111}$$

where b_i are constants, and their values are listed in Table 5.5.

Table 5.5. Values of b_i constants used in Equation (111) [35,68]

Pressure [atm]	b_0	b_1	b_2	b_3	b_4	b_5	b_6
150	−17.539096	0.076978	6.900548	$-1.082790 \cdot 10^{-4}$	−26.42469	$4.927648 \cdot 10^{-8}$	38.93727
225	−8.2125534	0.037741	6.190112	$-5.354571 \cdot 10^{-5}$	−20.86963	$2.379142 \cdot 10^{-8}$	27.88403
300	−4.6757259	0.023549	4.687353	$-3.463308 \cdot 10^{-5}$	−11.28031	$1.540881 \cdot 10^{-8}$	10.46627

The pressure effects are such that higher values cause a lower effectiveness factor. In Equation (111), the conversion factor (η) refers to the nitrogen and can be calculated from the following expression:

$$\eta = \frac{\dot{n}_{N_{2_{in}}} - \dot{n}_{N_{2_{out}}}}{\dot{n}_{N_{2_{in}}}} \tag{112}$$

where $\dot{n}_{N_{2_{in}}}$ and $\dot{n}_{N_{2_{out}}}$ are molar flows of the nitrogen at the inlet and outlet respectively. Summarising, the reaction rate for the cases with catalyst particle diameter of 6–10 mm can be written as:

$$R_{NH_3} = 1.7698 \cdot 10^{15} \exp\left(\frac{-40765}{RT}\right)\left[{K_a}^2 a_1 \left(\frac{{a_2}^3}{{a_3}^2}\right)^{0.5} - \left(\frac{{a_3}^2}{{a_2}^3}\right)^{0.5}\right] \cdot \xi \tag{113}$$

It should be noted that Equations (110) and (113) are valid for the fresh catalyst, and additional correction factors may be needed in cases that consider catalyst reduction, poisoning or ageing [35]. Although this kinetics is designed as a volumetric (per volume of the catalyst bed), the surface-to-volume ratio parameter allowed the implementation of this kinetics Ansys Fluent using a user-defined function (UDF) for surface kinetics approach within the catalyst bed.

5.6. Results

This section focused on investigating the influence of the catalyst particle size on the process. As a result, the contours of velocity, reaction rate, concentration and temperature were obtained. The received results allowed to investigate the intensity of the reaction rate among the catalyst bed and identify zones with a negligible reaction rate.

5.6.1. Flow field and velocity

The velocity field is the basis of most CFD simulations. This parameter directly influences mass and heat transfer, which is crucial for the reaction intensity. Figure 5.2 presents velocity magnitude contours (a) and pathlines (b) in the investigated reactor for the case with a catalyst particle diameter of 2 mm.

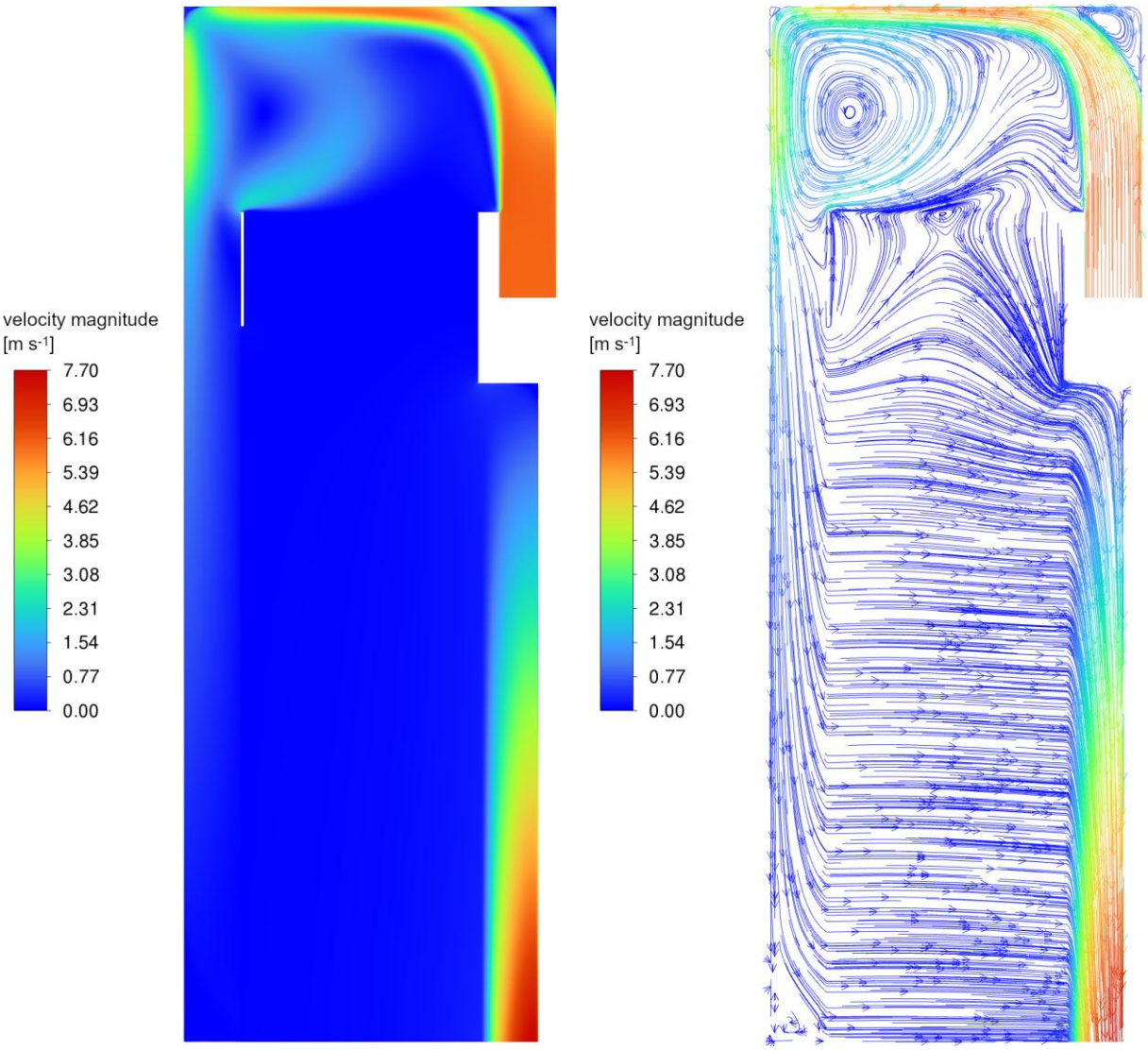

(a) (b)

Figure 5.2. Velocity magnitude contours (a) and pathlines (b) [m s^{-1}] in the investigated axial-radial ammonia converter (catalyst particle diameter of 2 mm) [68]

Velocity profiles have similar patterns regardless of the catalyst particle sizes. Figure 5.2 shows that two "flow zones" formed inside the catalyst bed. As expected, the upper part is dominated by the axial flow due to the lack of a porous wall in this region. Radial flow dominates in the lower parts of the catalyst beds, and it can be noted that the flow there is primarily uniform. In Figure 5.2 (b), the large recirculation area can be observed over the catalyst bed. This phenomenon results from the centrifugal gas inlet location, which causes the gas flow path to curve. After entering the chamber above the bed, part of the gas falls directly into the space between the outer reactor's and the bed's walls. The rest of the inlet gas stream is returned to form a vortex, which also causes the gas entrainment from the upper part of the catalytic bed. This causes the gas to flow in opposite directions in the upper part of the bed, where axial flow

dominates, which can be observed in Figure 5.3. The gas flows downwards closer to the centre of the reactor, while the gas flows upwards in the vicinity of the outer bed's wall.

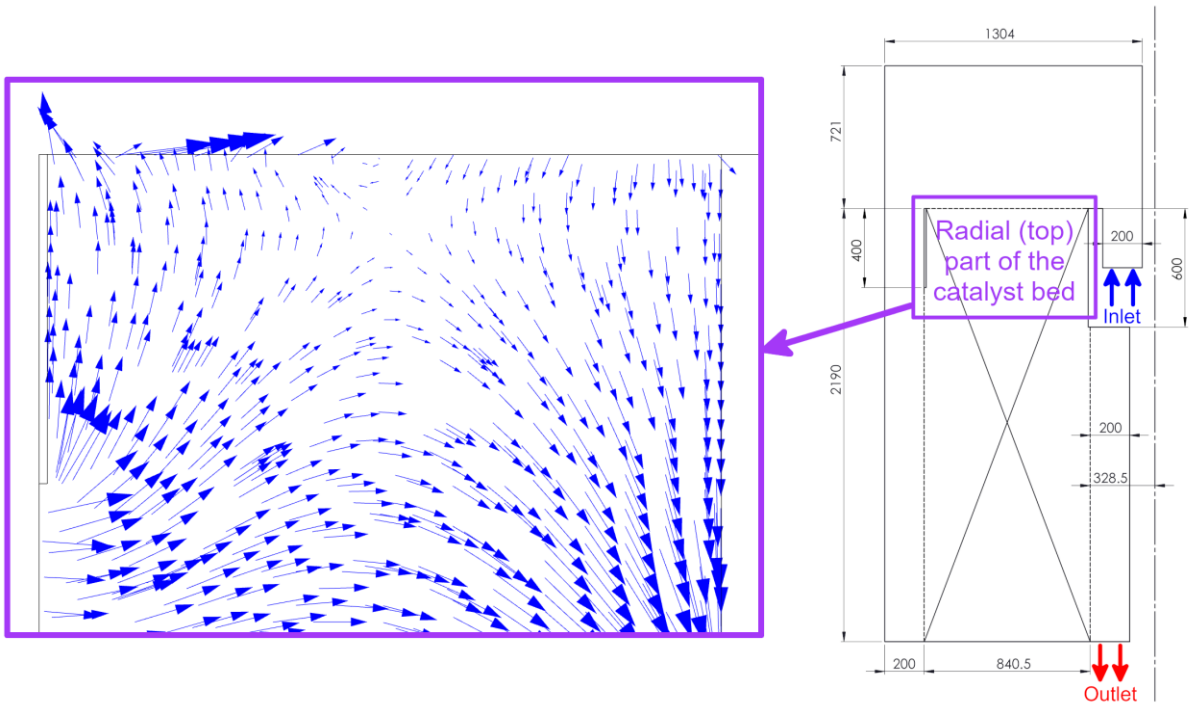

Figure 5.3. Gas flow pattern in enlargement of the "axial-flow" part of the bed in the investigated reactor (catalyst particle diameter of 2 mm) [68]

5.6.2. Particle size influence on the reaction rate and concentration

The primary aim of this section of the dissertation is to determine the influence of the catalyst bed's parameters on the process. Particle diameter is the most essential and evident parameter since it directly affects the reaction's efficiency and causes pressure losses in the gas flow. In modern reactors, high-activity beds with smaller catalyst particles (1–2 mm diameter) are preferred [69]. Figure 5.4 shows the reaction rate of ammonia formation contours, and Figure 5.5 presents contours of ammonia mole fraction for different catalyst particle sizes.

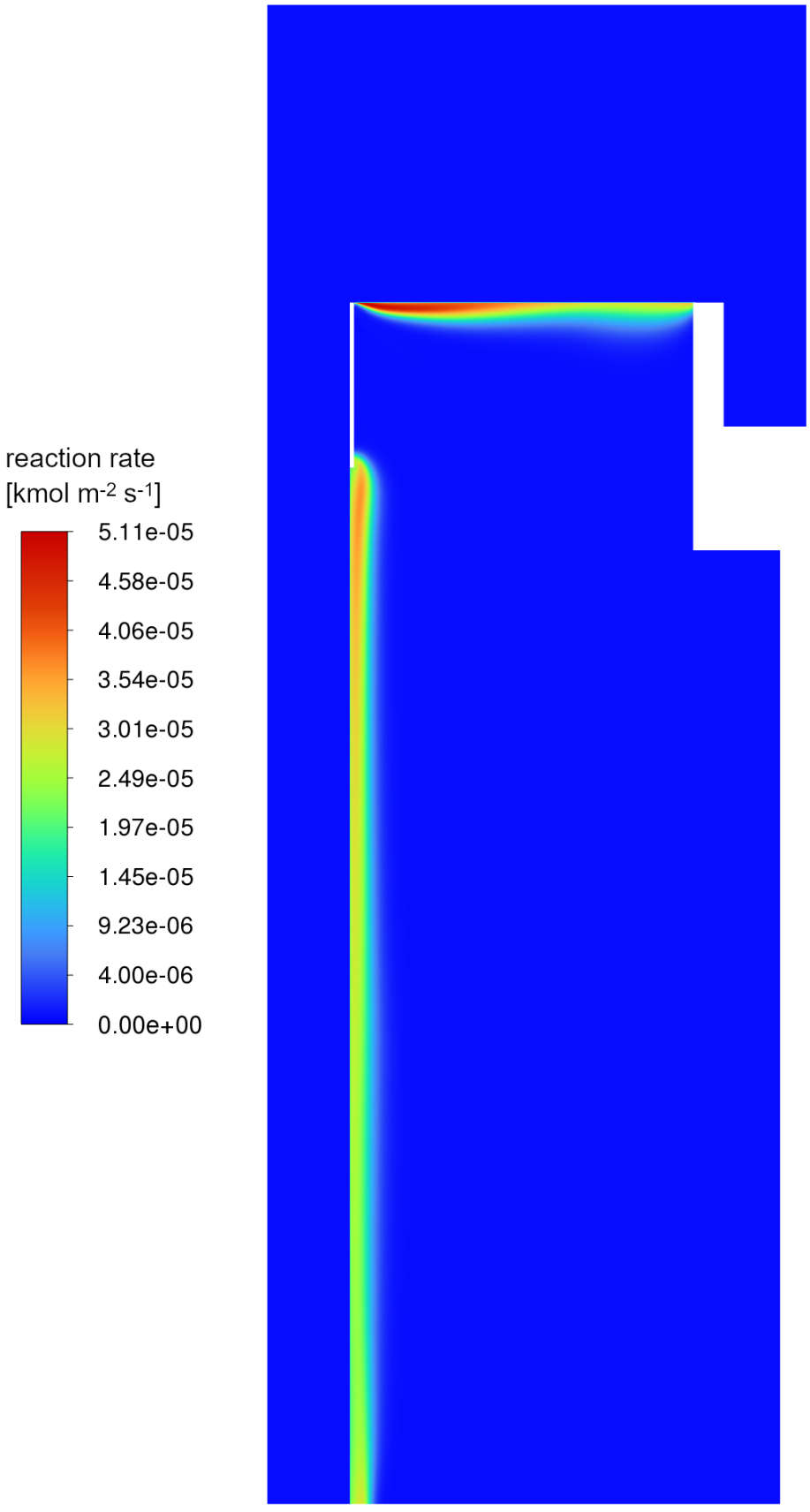

(a) d_p 1 mm

Figure 5.4. Cont.

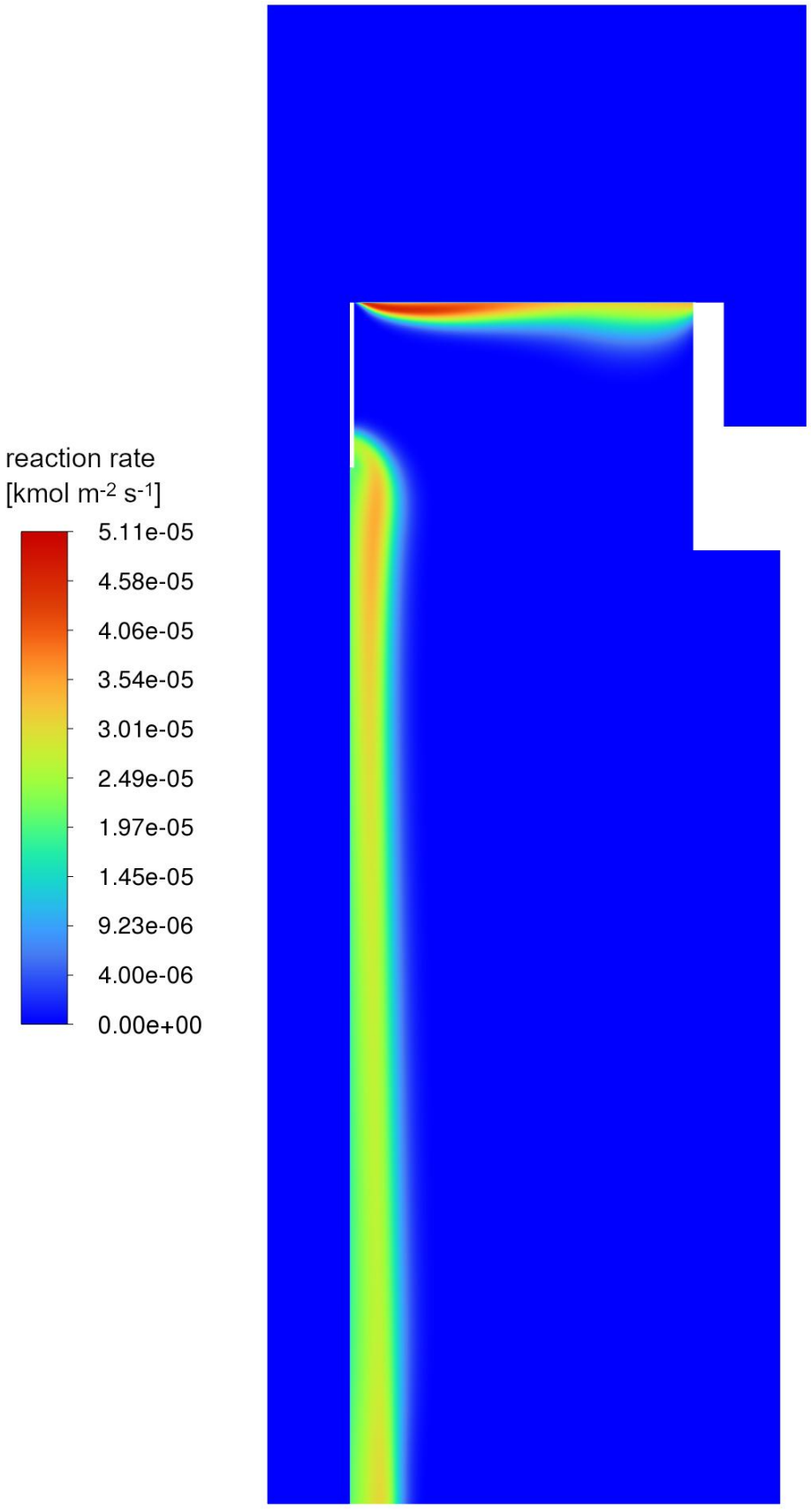

(b) d_p 2 mm

Figure 5.4. Cont.

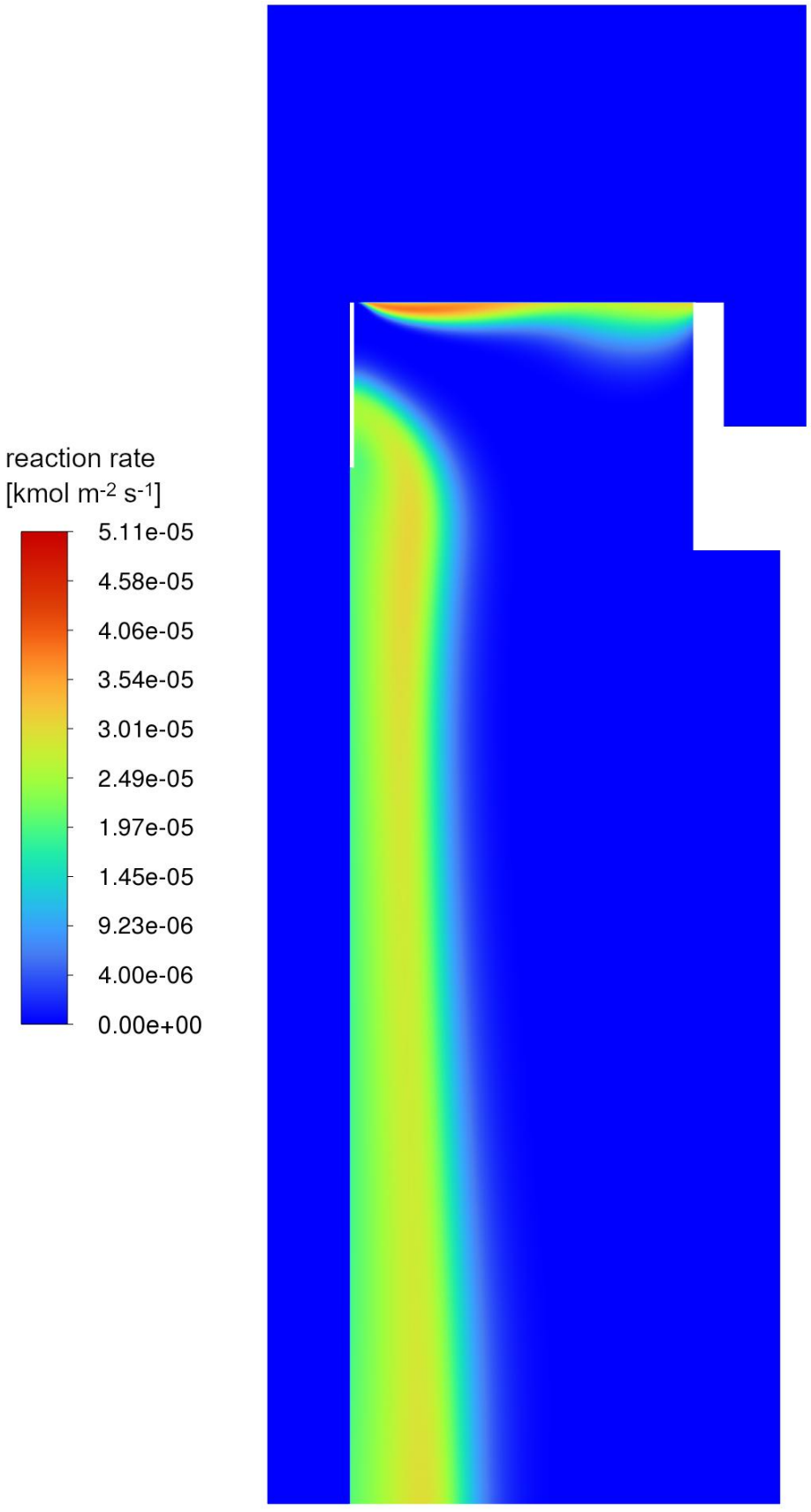

(c) d_p 4 mm

Figure 5.4. Cont.

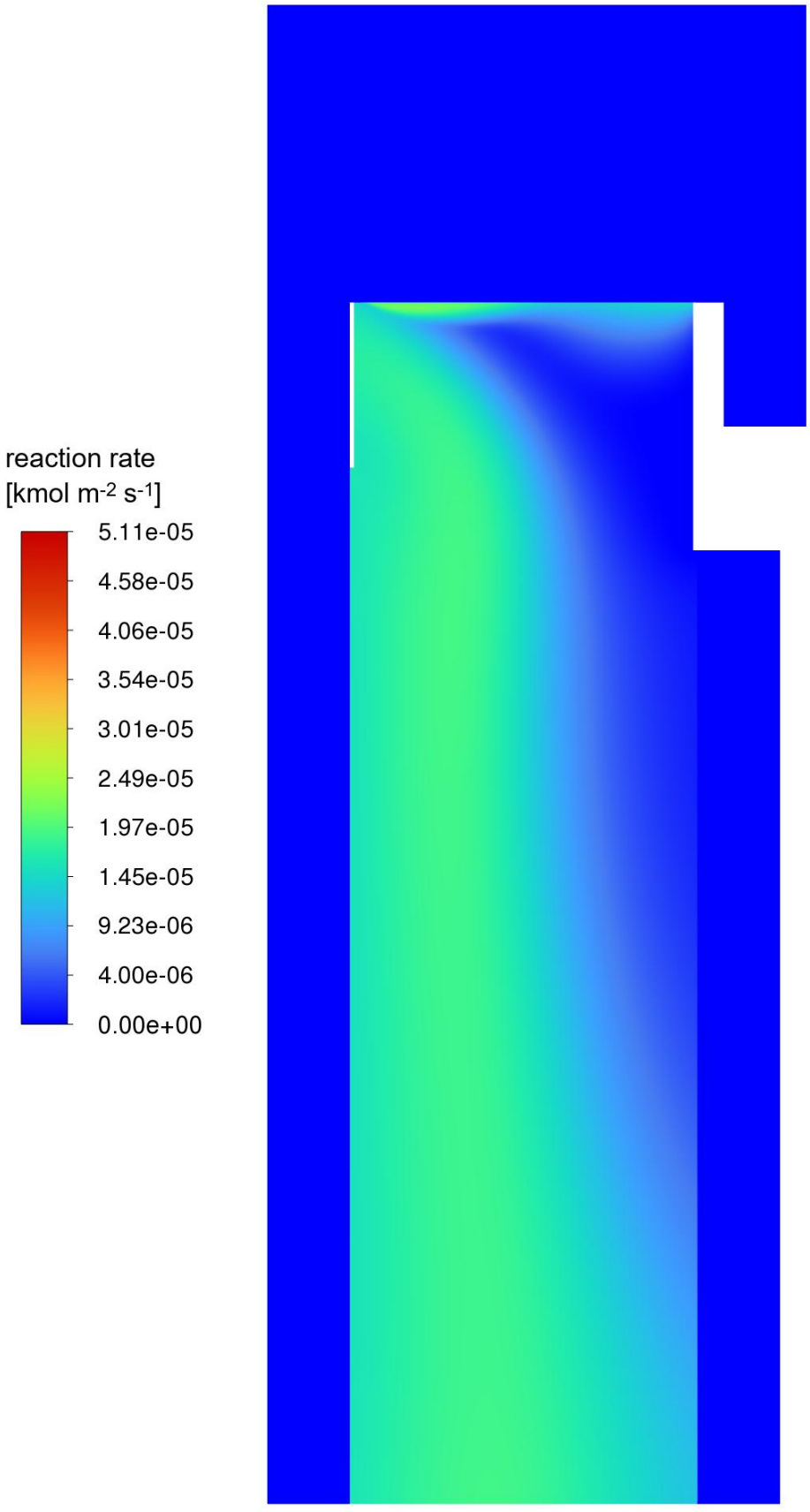

(d) d_p 6 mm

Figure 5.4. Cont.

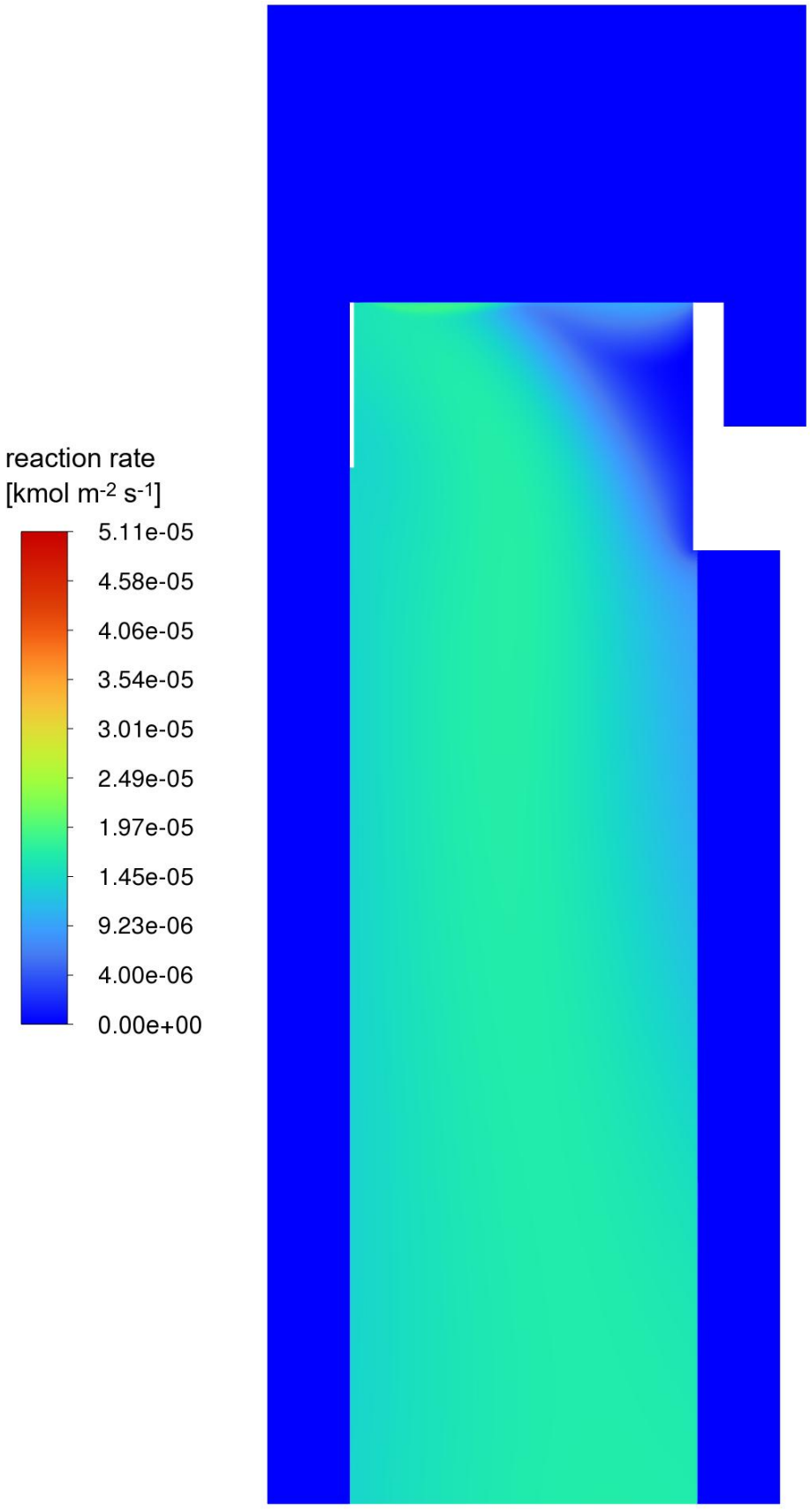

(e) d_p 8 mm

Figure 5.4. Cont.

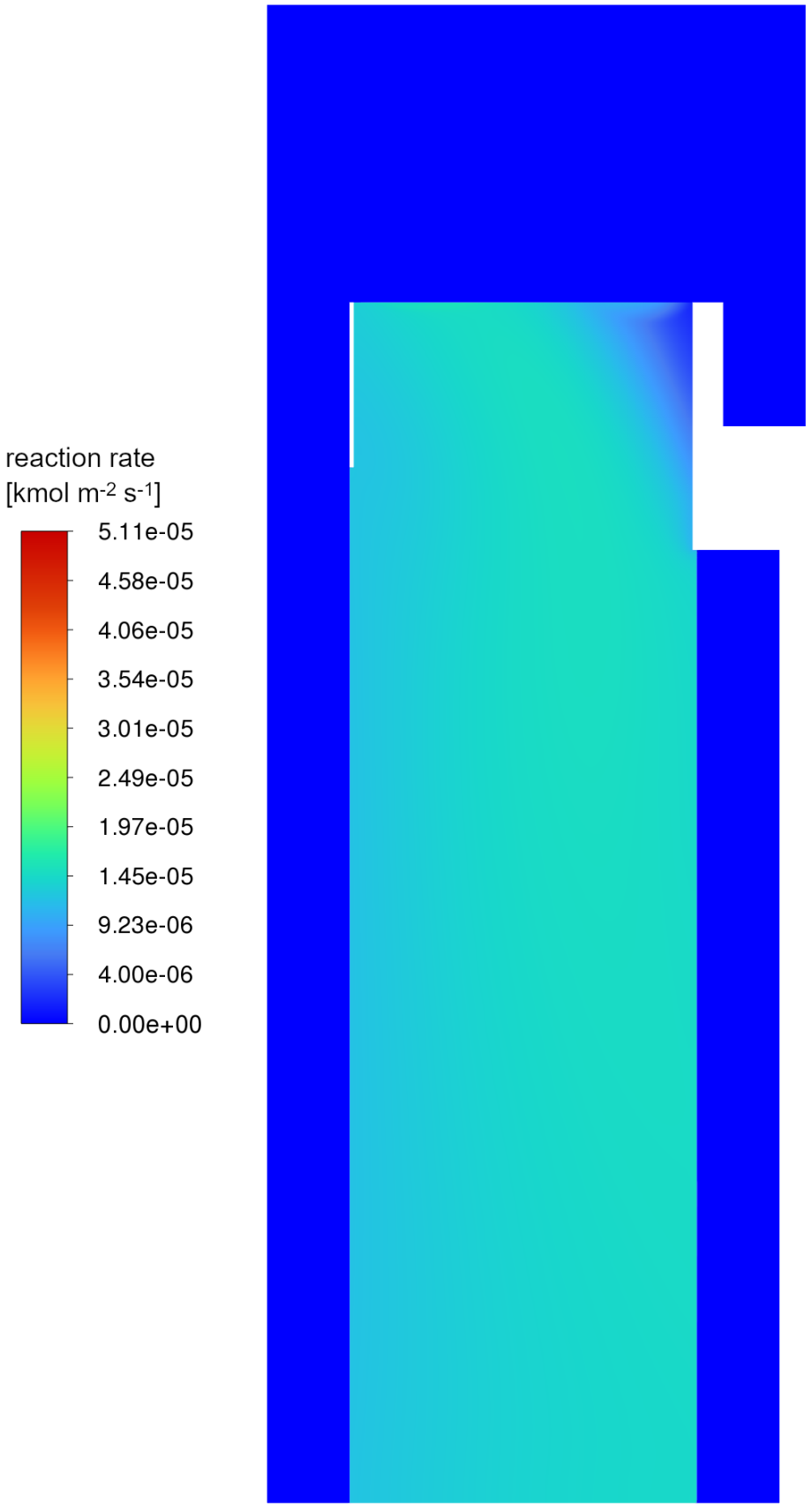

(f) d_p 10 mm

Figure 5.4. Reaction rate contours [kmol m^{-2} s^{-1}] for the investigated reactor with a catalyst particle diameter of 1mm (a), 2 mm (b), 4mm (c), 6 mm (d), 8 mm (e) and 10 mm (f) [68]

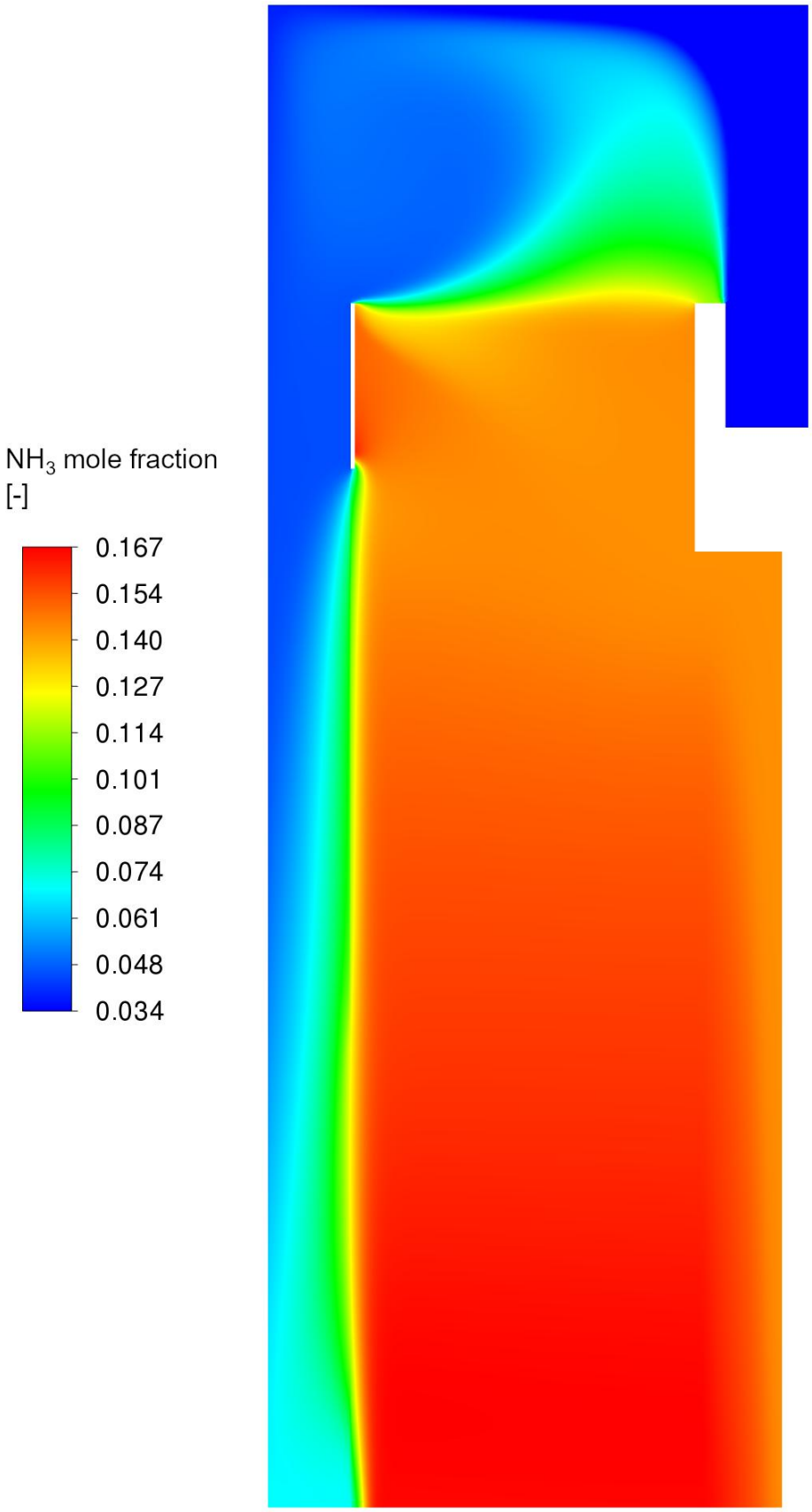

(a) d_p 1 mm

Figure 5.5. Cont.

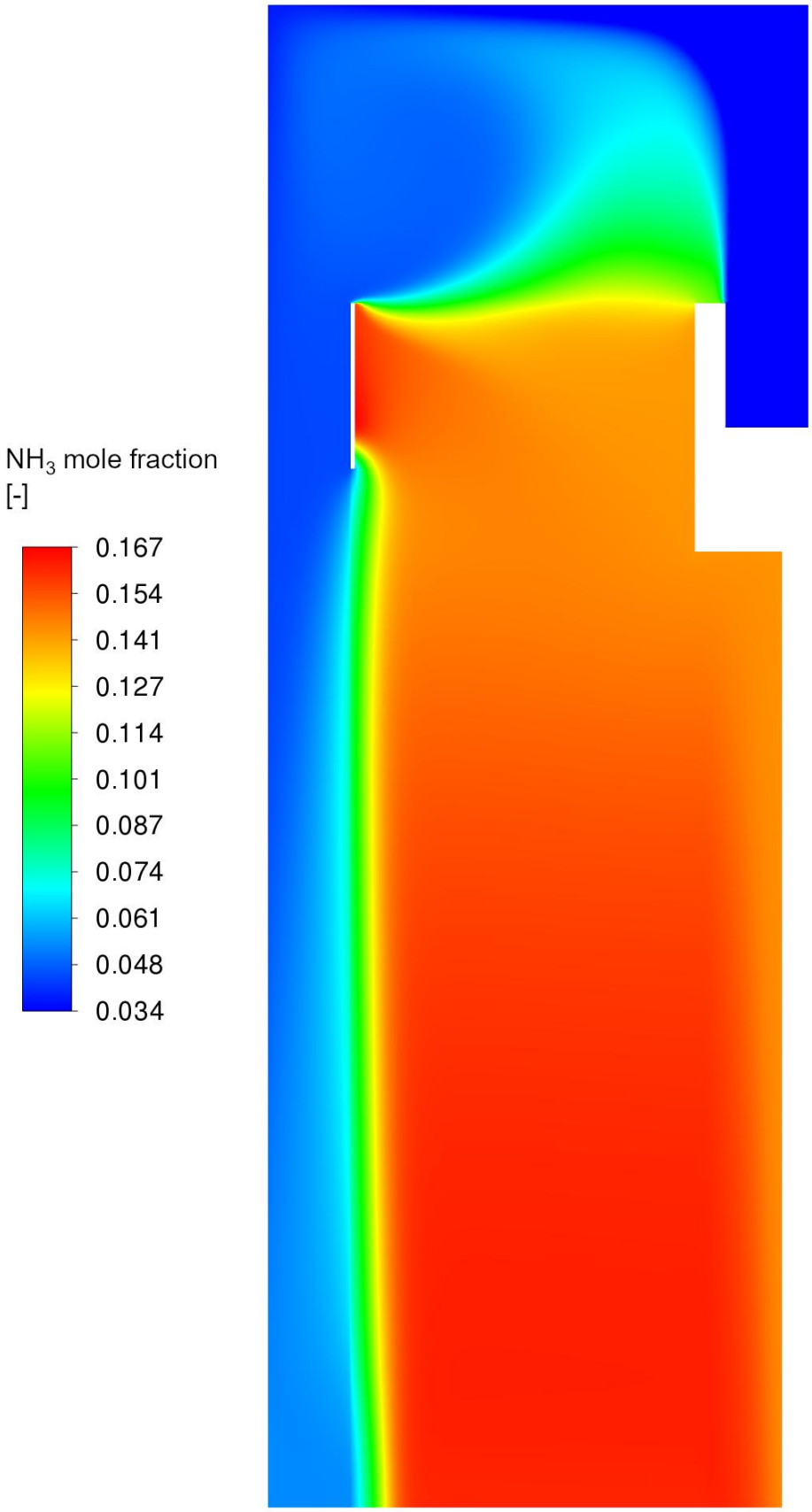

(b) d_p 2 mm

Figure 5.5. Cont.

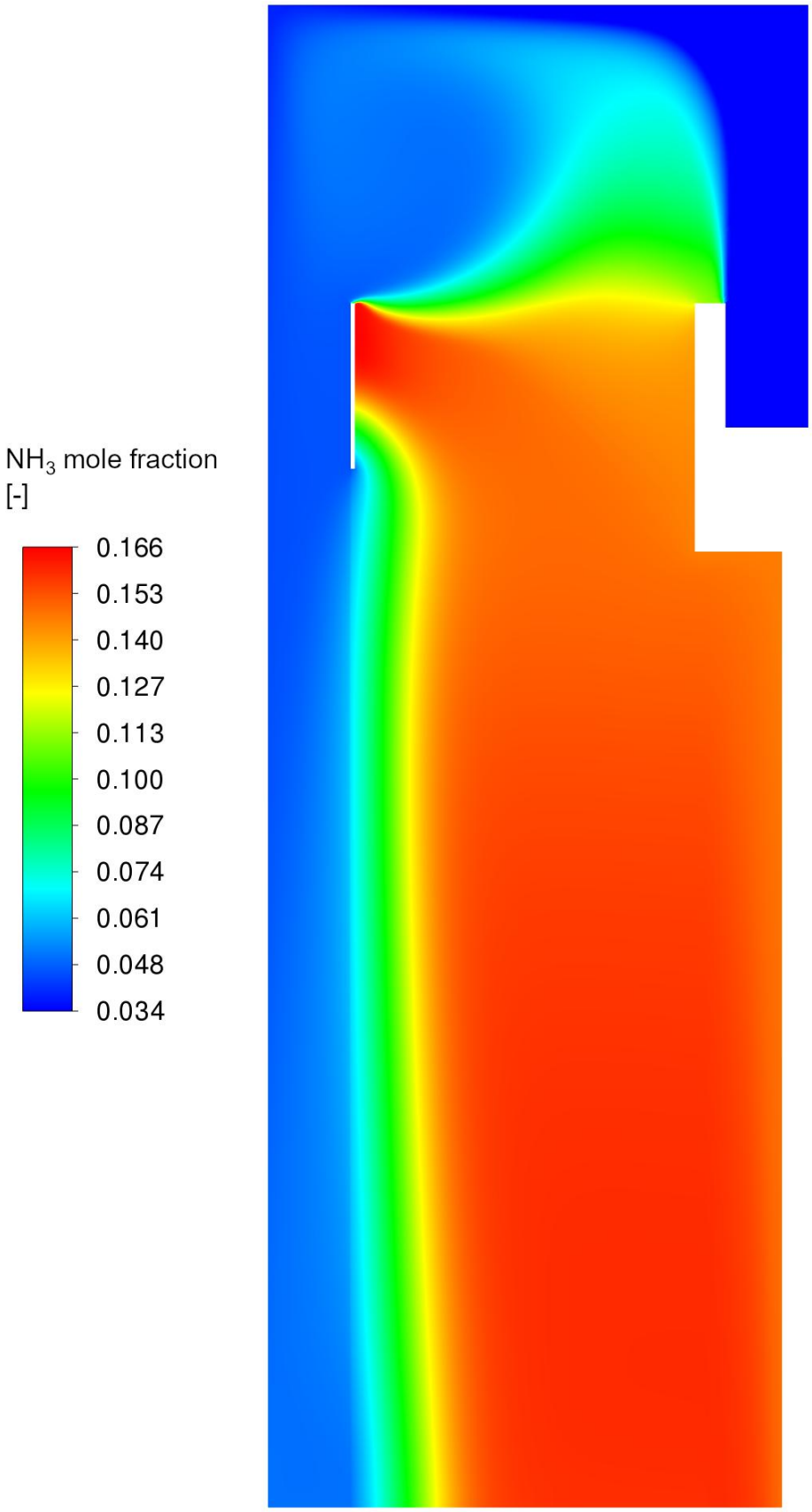

(c) d_p 4 mm

Figure 5.5. Cont.

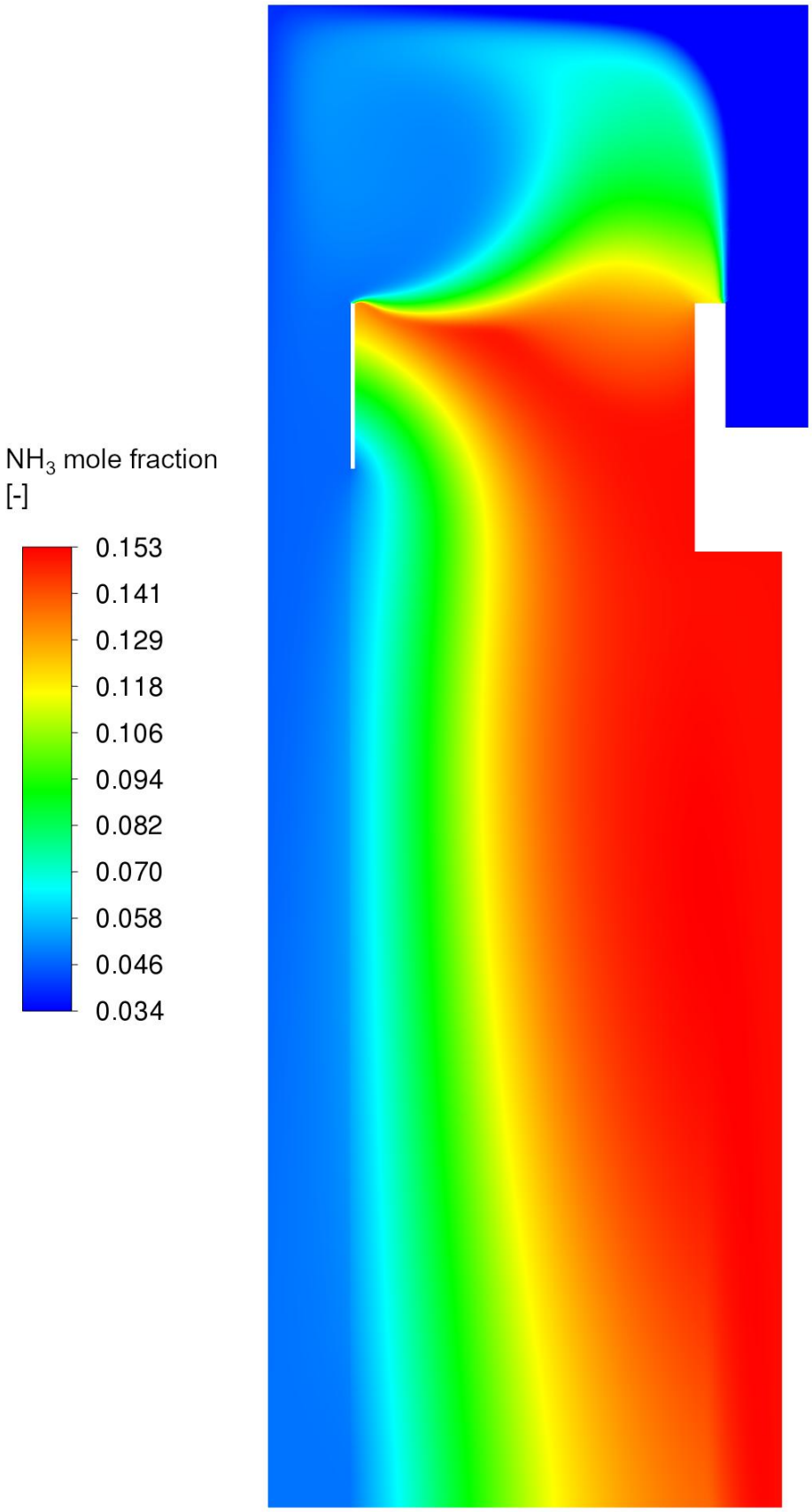

(d) d_p 6 mm

Figure 5.5. Cont.

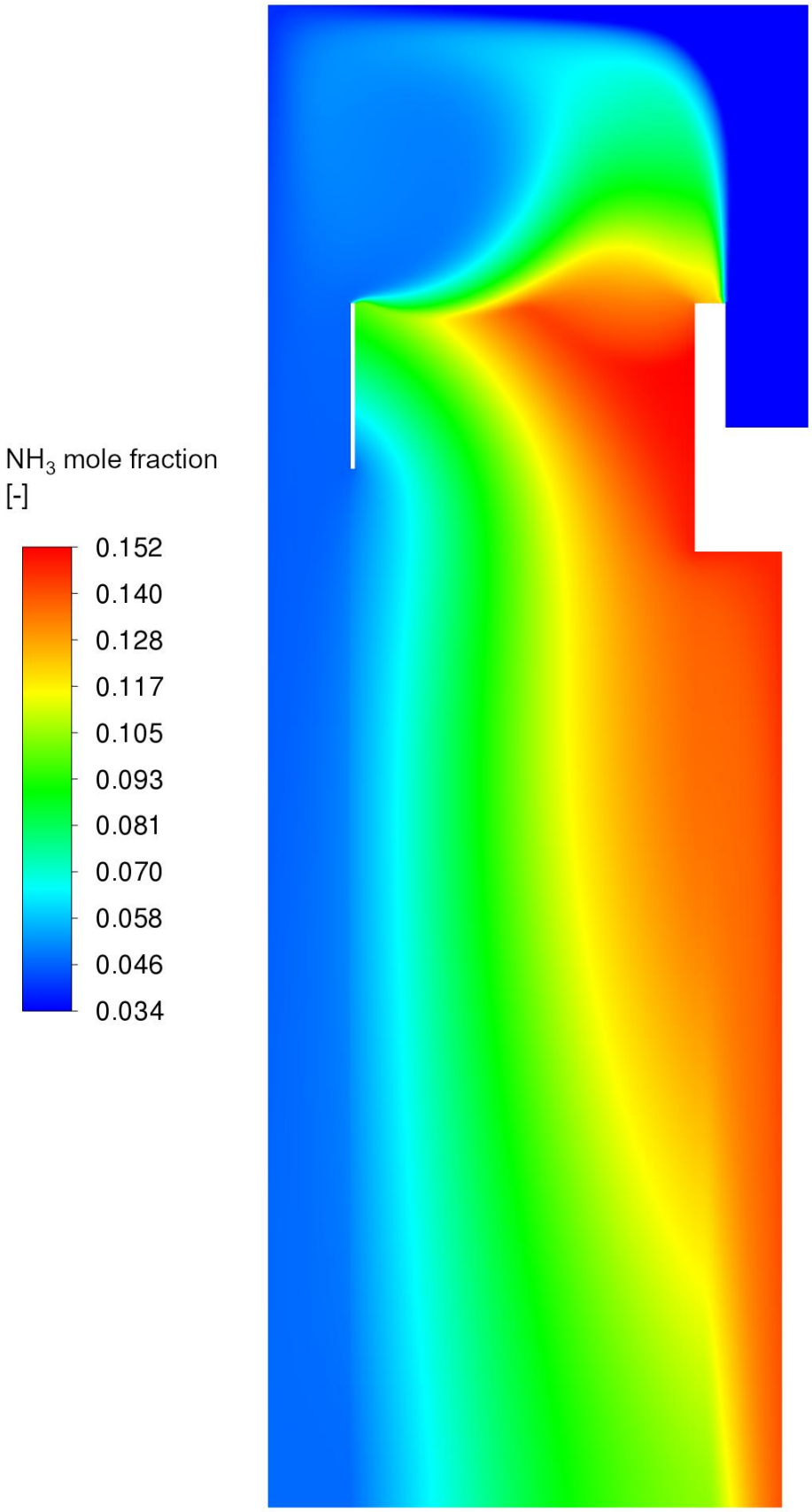

(e) d_p 8 mm

Figure 5.5. Cont.

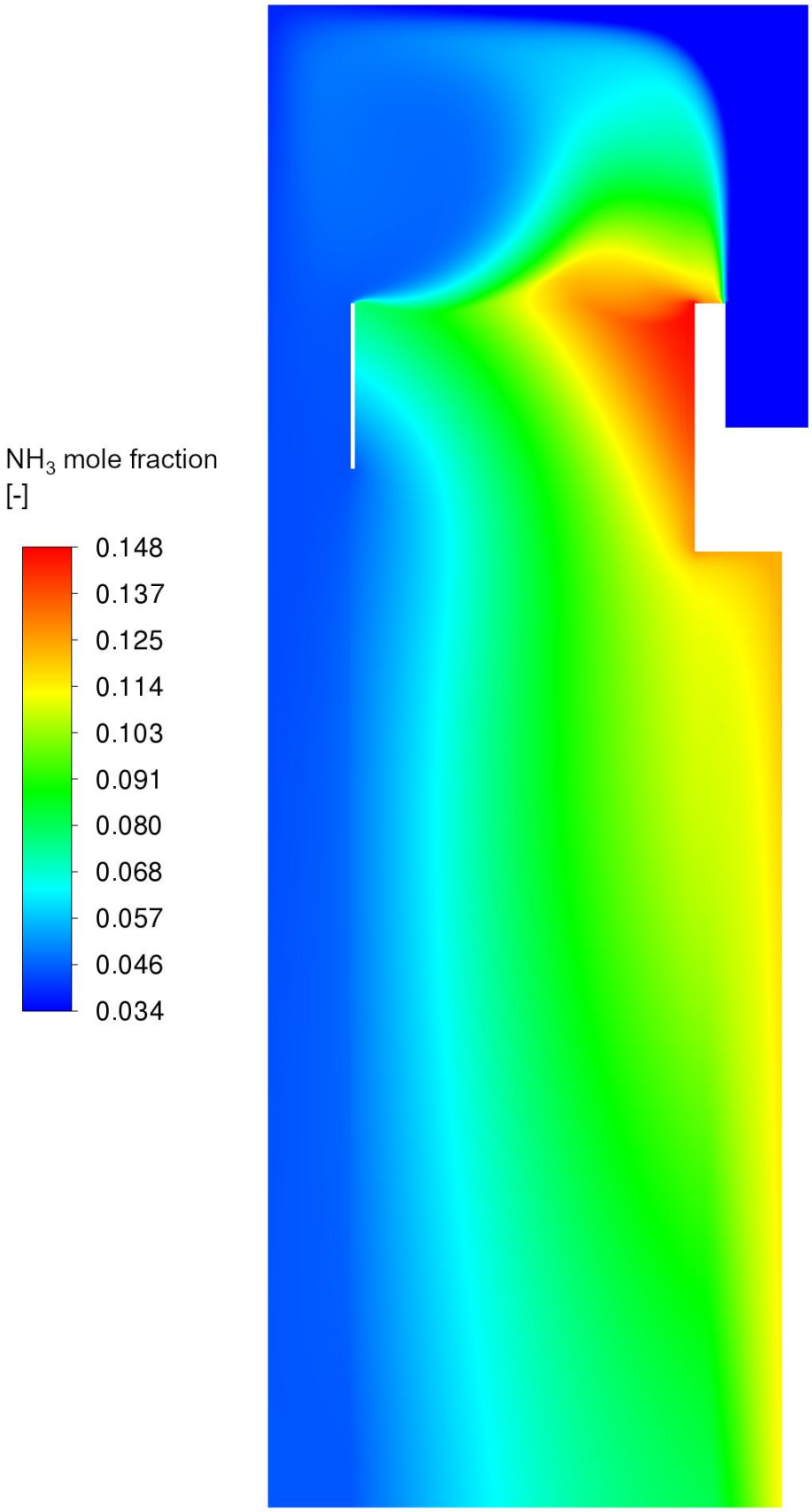

(f) d_p 10 mm

Figure 5.5. Ammonia mole fraction contours [-] for the investigated reactor with a catalyst particle diameter of 1mm (a), 2 mm (b), 4mm (c), 6 mm (d), 8 mm (e) and 10 mm (f) [68]

The reaction is much more intense for the catalyst with smaller diameters (1–4 mm). In those cases, as shown in Figure 5.4, the reaction rate instantly intensifies after the gas enters the catalyst bed. However, after the initial leap, the reaction rate quickly reaches negligible values, which is caused by obtaining the state close to equilibrium since the ammonia synthesis is reversible. For larger catalyst particles (6–10 mm), the ammonia formation rate is much less intense, does not reach the equilibrium and occurs in the entire bed. Those differences are further enlarged due to the diffusion restriction in the particle's pore structure, which was included in the reaction rate (Equation (113)) by adding the modifier ξ, as described in Section 5.5. The ammonia concentration profiles in Figure 5.5 directly result from the reaction rate. The ammonia mole fraction quickly rises to its maximum value for the smaller catalyst particles, which is determined by the equilibrium in current process conditions. In the cases with particle diameters of 1–4 mm, the ammonia concentration is uniform and strives for its equilibrium, while for higher, the outlet concentration is far from equilibrium, which is an unwanted phenomenon.

Although the reaction occurs in the whole bed, its intensity is not uniform. As shown in Figure 5.4, there are zones where the reaction rate is negligible, reaching the near-equilibrium state. To better illustrate this phenomenon, the value of 3% of the maximum value of the reaction rate was assumed as a threshold, below which the reaction is considered negligible. Because of this simplification, the cases with different particle diameters can be compared regarding the bed's percentage of "working" and "dead" volumes. Please note that the 3 % of the maximum reaction rate's value is for reference only, and this assumption can be different depending on the selected threshold, below which the reaction rate is considered negligible. Figure 5.6 presents the dependence of the "working" volume of the catalyst bed in relation to catalyst particle diameter (a) and the ammonia mole fraction at the outlet as a function of catalyst particle diameter (b).

Figure 5.6 presents the irregularity of the ammonia formation intensity in the catalyst bed for the different catalyst particle sizes, which is plotted as dependences of the "working" volume percentage of the bed and ammonia concentration to particle diameters. Those values are firmly connected, and the highest product concentration is obtained if the close-to-equilibrium state is reached before leaving the bed. However, if this state is quickly achieved, a large portion of a catalyst bed is redundant, which is especially visible for the smaller catalyst diameters. The proper volume of the bed should be just enough to achieve the near-equilibrium state just before leaving the bed.

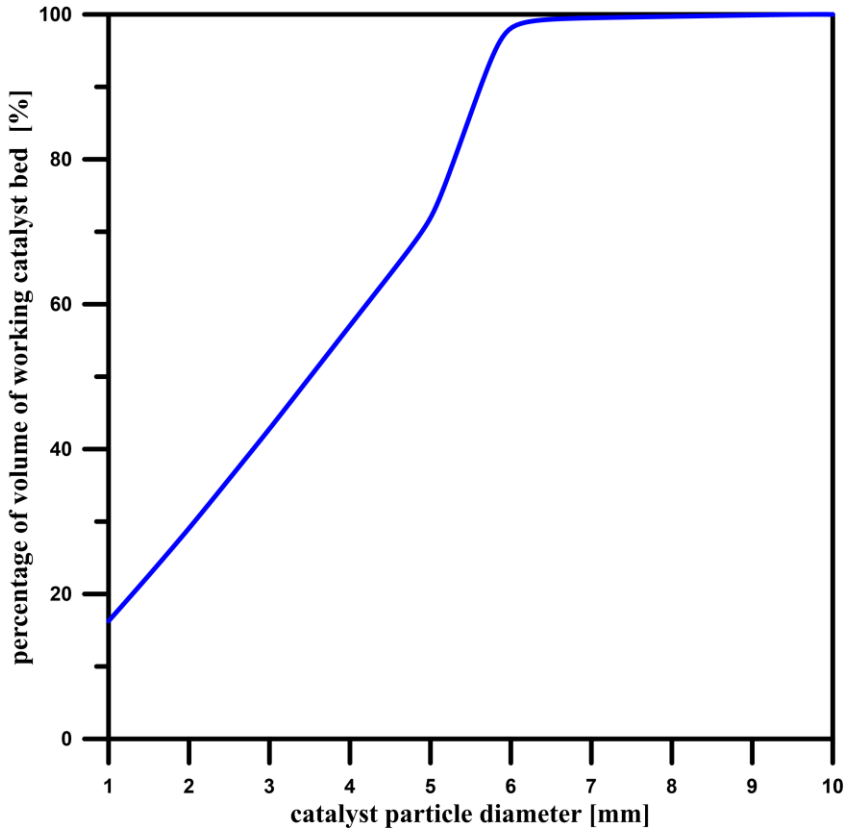

(a)

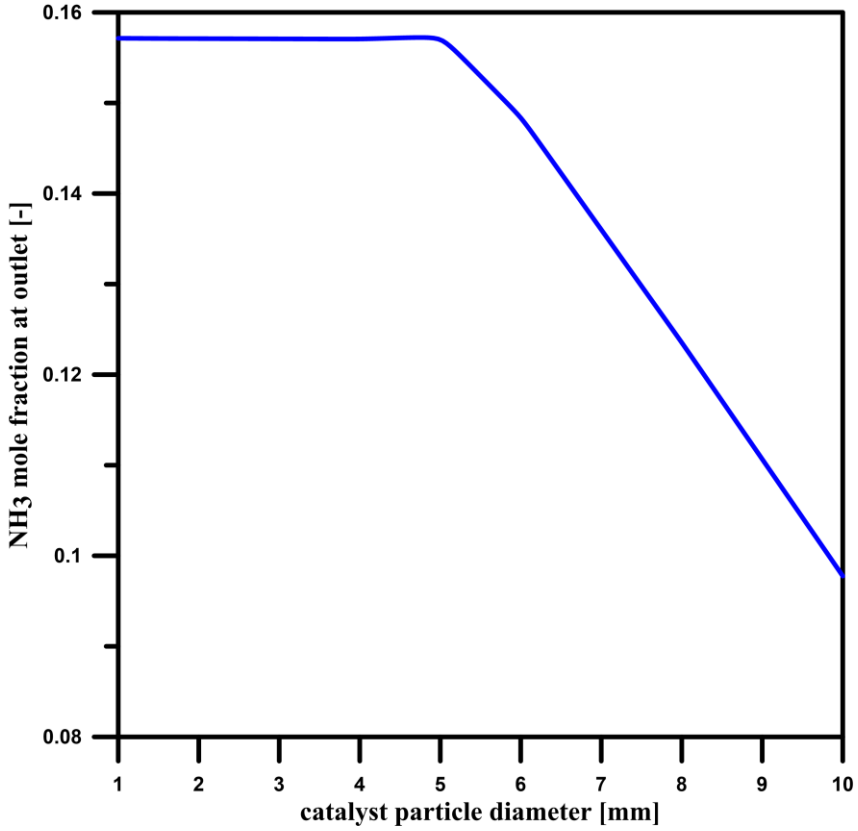

(b)

Figure 5.6. The percentage of the "working" part of the catalyst bed (< 3% of maximum reaction rate) (a) and NH_3 mole fraction at the outlet (b) in relation to catalyst particle diameters [68]

5.6.3. Particle size influence on the temperature

Since ammonia synthesis is an exothermic reaction, the reaction rate is firmly connected to the temperature. Figure 5.7 shows the temperature contours comparison for the cases with 2 mm and 6 mm catalyst particle diameters. It can be observed that temperature contours have a similar pattern to concentration contours. In the case of lower values of the particle diameters, the temperature quickly rises after the gas enters the catalyst bed, which is consistent with reaction rate profiles since the highest values of the reaction rate are there. After reaching the near-equilibrium state, the temperature is homogenous. The temperature gradient is visible through the entire bed for larger particle sizes since the reaction occurs in the entire volume.

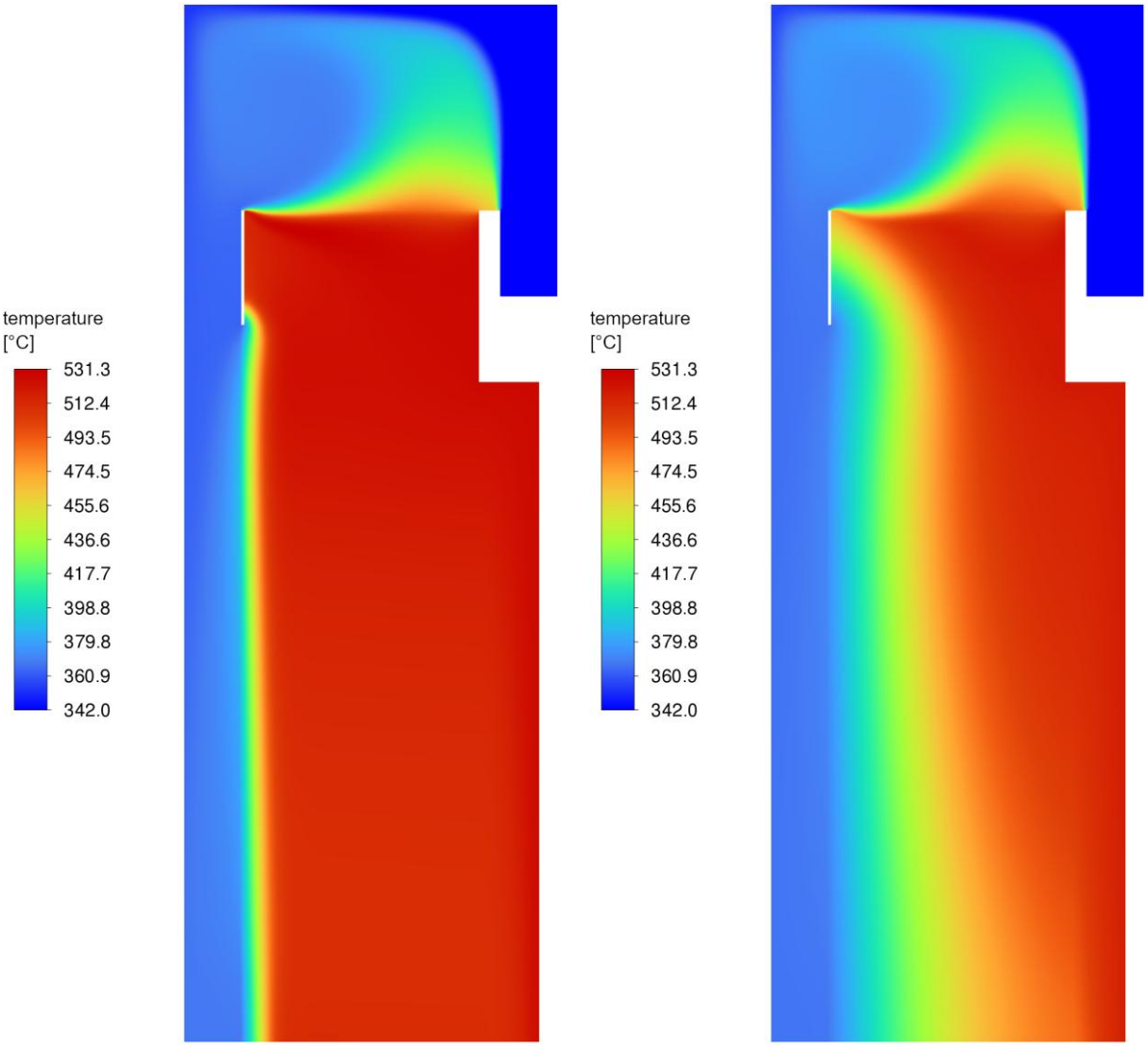

(a) (b)

Figure 5.7. Temperature contours [°C] for the investigated reactor with a catalyst particle diameter of 1 mm (a) and 6 mm (b) [68]

5.6.4. Particle size influence on the pressure drop

Pressure has a significant role in the ammonia synthesis process, and due to the large volumes of catalyst beds, pressure drops are generated. This work investigated the influence of the particle diameter on the bed's pressure drop, which is presented in Figure 5.8. It can be observed that smaller particles generate noticeably higher pressure drop, although it has a minor effect on the process due to the enormous operating pressure in the reactor compared to the pressure drop.

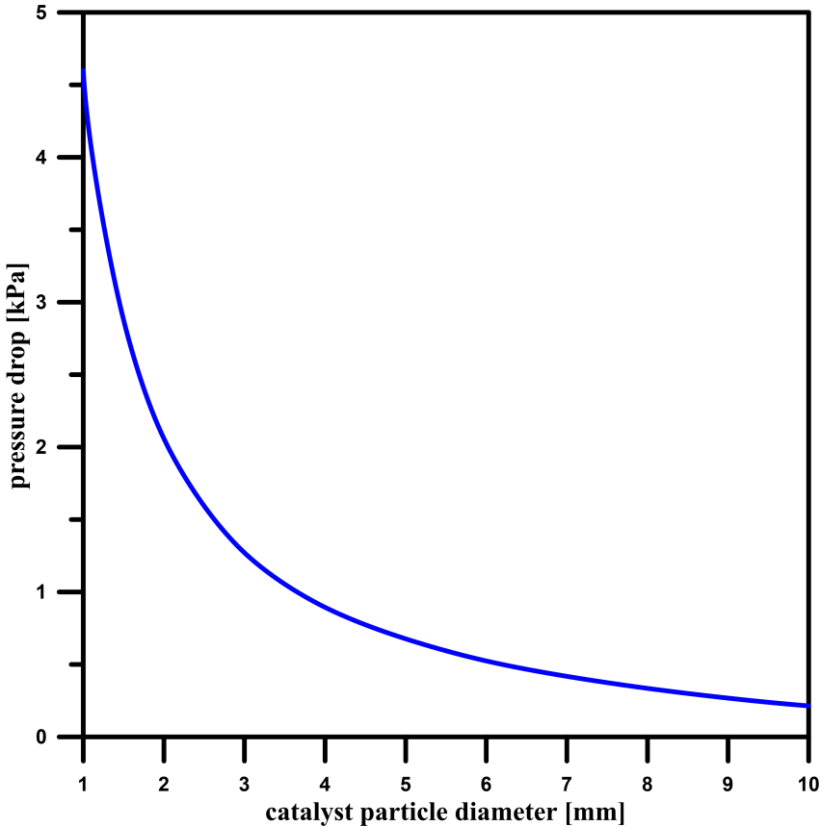

Figure 5.8. Pressure drop of the catalyst bed in relation to the catalyst parameter in the investigated reactor [68]

5.6.5. Catalyst bed's porosity influence on the reaction rate and concentration

Another investigated parameter is the inter-particle porosity of the catalyst bed. This work used a porosity value typical for the magnetite catalyst, which is 0.52 [69]. However, this parameter can vary due to factors like catalyst ageing, which can cause a drop in the porosity to 0.38 [59]. In this section, the results for fresh and aged catalysts were simulated and compared, and for both cases, the sphericity was set to 0.65 [59]. Hence, surface-to-volume ratios remain the same for the corresponding diameters of catalyst particles. Table 5.6 presents the calculated values of

porous zone model parameters for the catalyst bed with a porosity value of 0.38. The parameters of the catalyst bed with a porosity of 0.52 are listed in Table 5.2.

Table 5.6. Calculated catalyst bed's parameters (bed's porosity 0.38) [68]

Particle diameter [mm]	*Viscous resistance* $[m^{-2}]$	*Inertial resistance* $[m^{-1}]$	*Surface-to-volume ratio* $[m^{-1}]$
1	$1.05 \cdot 10^{9}$	39547	9231
1.5	$4.67 \cdot 10^{8}$	26364	6154
2	$2.63 \cdot 10^{8}$	19773	4615
3	$1.17 \cdot 10^{8}$	13182	3077
4	$6.57 \cdot 10^{7}$	9887	2308
5	$4.20 \cdot 10^{7}$	7909	1846
6	$2.92 \cdot 10^{7}$	6591	1538
8	$1.64 \cdot 10^{7}$	4943	1154
10	$1.05 \cdot 10^{7}$	3955	923

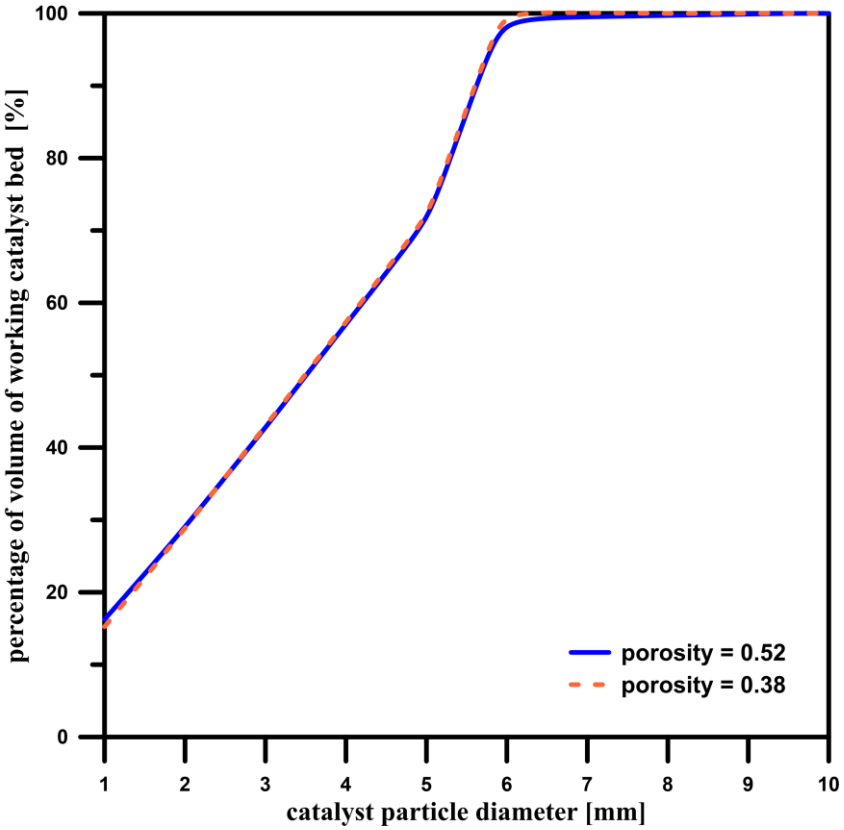

(a)

Figure 5.9. Cont.

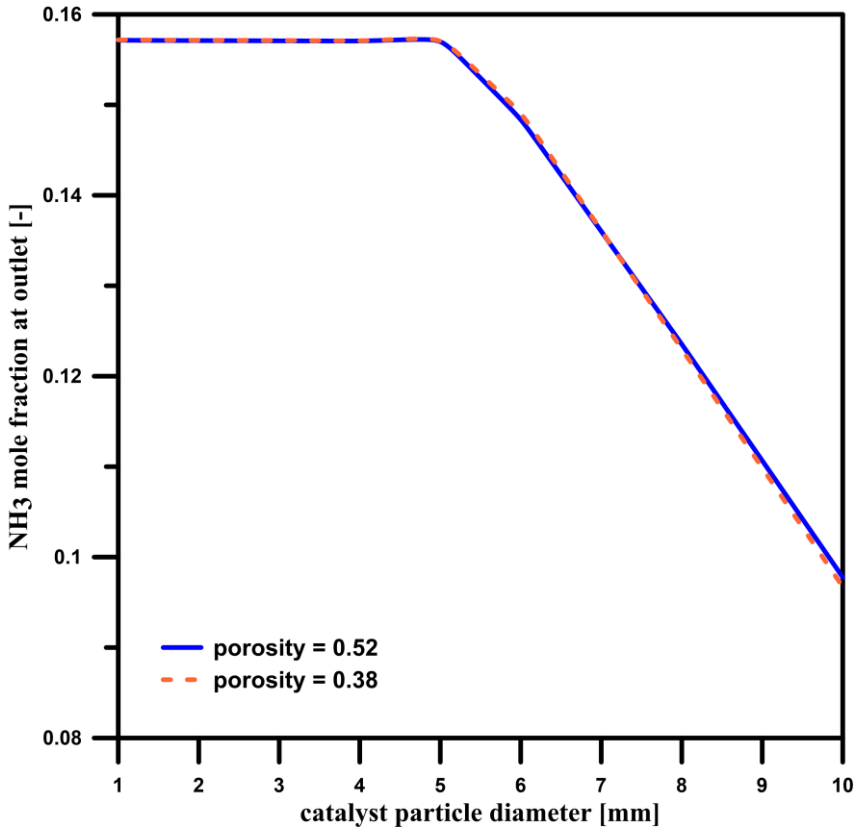

(b)

Figure 5.9. The percentage of the "working" part of the catalyst bed (< 3% of maximum reaction rate) (a) and NH_3 mole fraction at the outlet (b) in relation to catalyst particle diameters – comparison between catalyst beds with 0.52 and 0.38 porosity [68]

Figure 5.9 compares the values of the percentage of "working" catalyst beds and outlet ammonia mole fraction in relation to particle diameters. It can be noted that the other parameters coincide with each other, and their values are almost the same, which suggests that the catalyst bed's porosity has a minor influence on the ammonia synthesis process. It should be noted that in this section, only porosity differences were considered. Other factors associated with the catalyst ageing phenomenon, such as activity reduction or poisoning, may require additional correction.

5.7. Validation

The CFD model was validated using the data published by Panahandeh et al. [29]. The ammonia synthesis reactor's investigated geometry and input process parameters are based on the experimental data presented in this work. Since Panahandeh et al. [29] do not provide data about catalyst particle size, the catalyst particle diameter was estimated based on the experimental outlet ammonia concentration and the calculated relationship between the outlet ammonia fraction and catalyst particle diameter (Figure 5.6 (b)). The estimated diameter is 6.8 mm. Using

this value, a simulation was performed to calculate other parameters. Table 5.7 lists CFD model results with the experimental data [29].

Table 5.7. Outlet parameters' comparison between the experimental data [29] and the CFD model [68]

Outlet parameter	*unit*	*Experiment*	*CFD model*	*Error [%]*
NH_3 mole fraction	-	0.1403	0.1401	0.11
N_2 mole fraction	-	0.1796	0.1796	0.04
H_2 mole fraction	-	0.5390	0.5391	0.03
CH_4 mole fraction	-	0.1035	0.1034	0.03
Ar mole fraction	-	0.0376	0.0375	0.07
temperature	°C	494.7	493.1	0.32

The CFD model's results converge with the experimental data. The maximum error does not exceed 0.32 %, which indicates that the catalyst particle size used by Panahandeh et al. [29] was adequately estimated. It should be noted that this validation was performed for cases that are far from the chemical equilibrium state, which improves its accuracy.

5.8. Improvement proposals

The main challenge of the ammonia synthesis process is obtaining the highest possible ammonia outlet concentration using the smallest possible catalyst volume in the operating conditions. This requires finding the catalyst bed size where the near-equilibrium state is achieved by minimising the "dead" volumes of the bed where the reaction rate is negligible. As shown in Figures 5.4 and 5.5, beds with smaller particle diameters are desirable since they allow for the quick achievement of the near-equilibrium state and the highest possible concentration. However, as presented in Figure 5.6, there is a high risk that a large portion of the bed will be redundant in those cases. The CFD tools allow for the simulation of the investigated process and relatively easy estimation of the required catalyst bed's volume. In the case of the investigated ammonia synthesis reactor, a large part of the "dead" bed is in the lower particle diameter range. In this work, modified variants of the reactor were proposed for the catalyst particle size of 2 mm, which allows the reduction of the bed's volume without losing the efficiency. The models of three novel proposed variants containing about half of the original catalyst bed's volume were obtained only by altering the bed's geometry without any changes to the outer shell of the reactor. Hence, potential improvements could be implemented without replacing the existing apparatus. The changed dimensions are presented in Figure 5.10 in the form of letters A, B, and H, respectively, and their values are listed in Table 5.8.

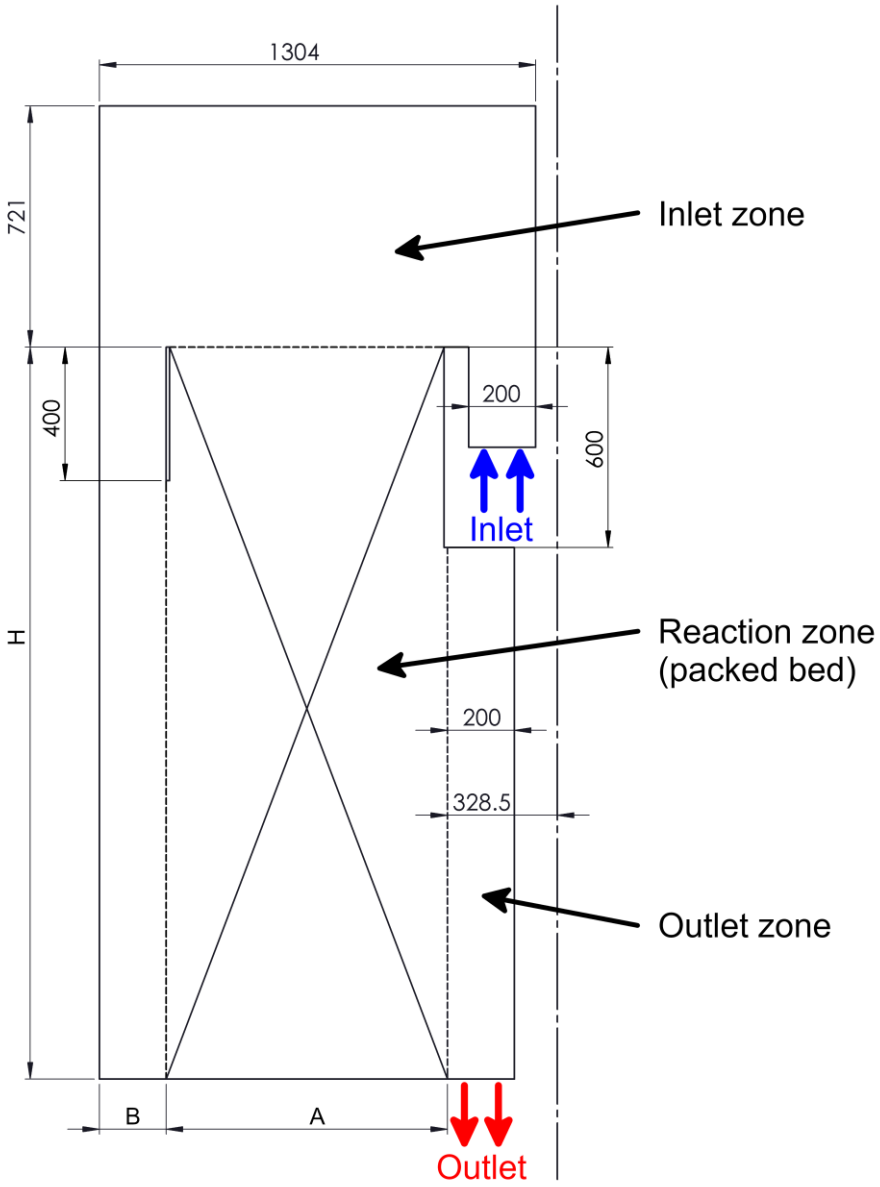

Figure 5.10. Dimensions (A, B and H) changed in the modifications of the investigated axial-radial ammonia synthesis (dimensions in mm) [68]

Table 5.8. Dimensions (in mm) changed in proposed modification variants [68]

Modification	*A*	*B*	*H*
original	840.5	200	2190
variant 1	840.5	200	1455
variant 2	530	510	2190
variant 3	645	396	2183

The reaction rate and concentration contours calculated from the CFD models of proposed variants are shown in Figures 5.11 and 5.12. The comparison of the results between the original and modified variants is presented in Table 5.9.

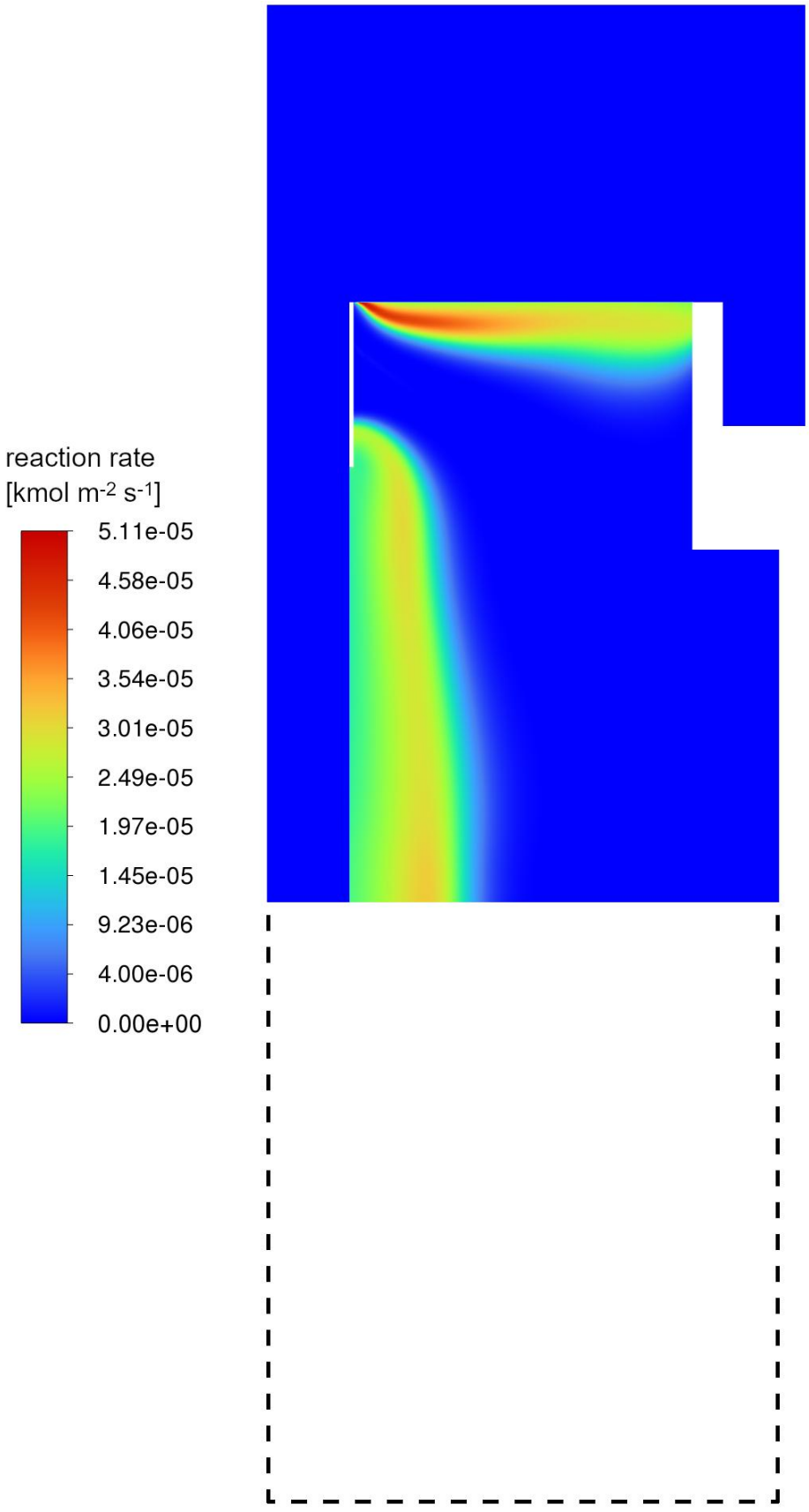

(a) variant 1

Figure 5.11. Cont.

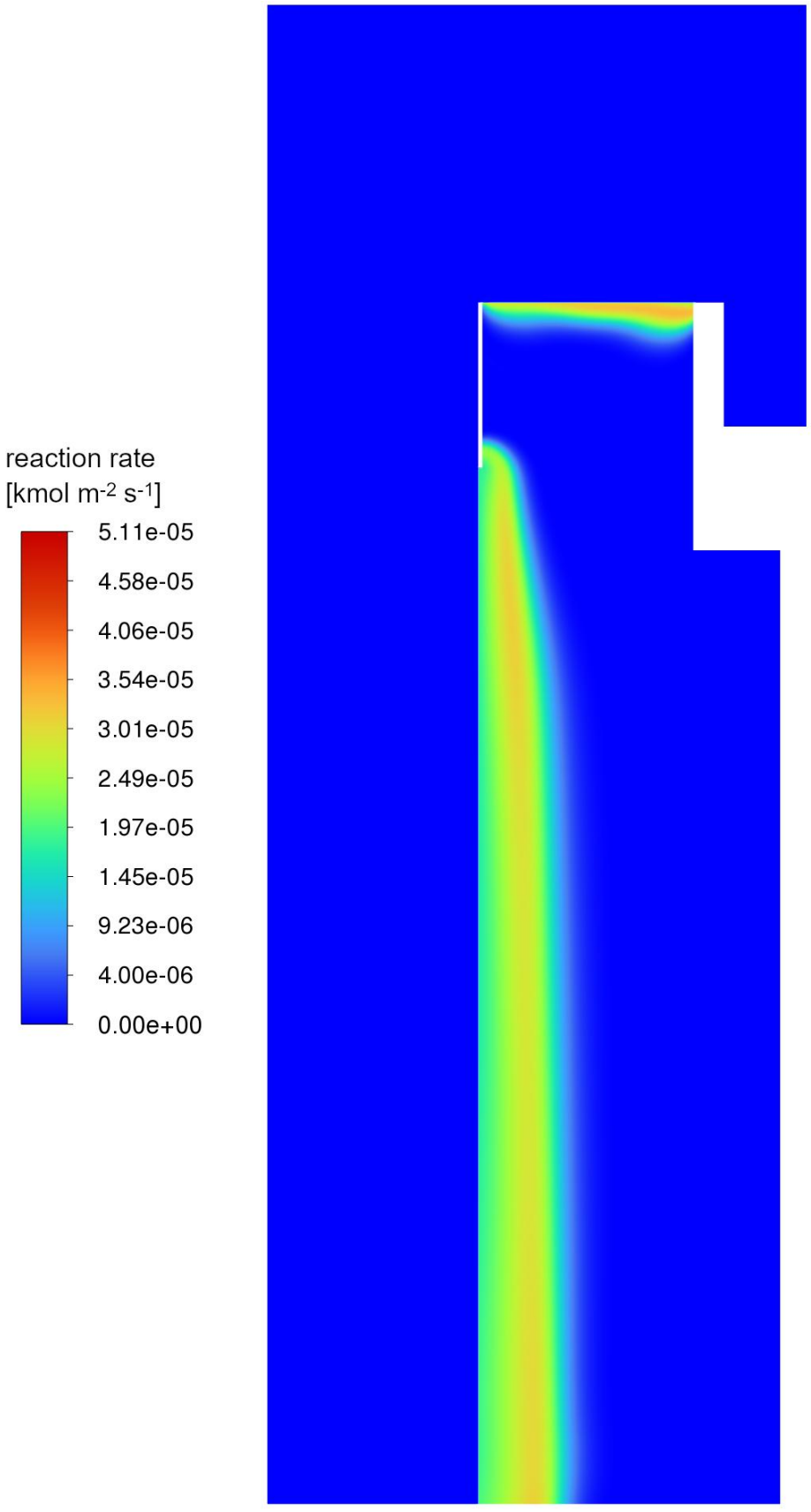

(b) variant 2

Figure 5.11. Cont.

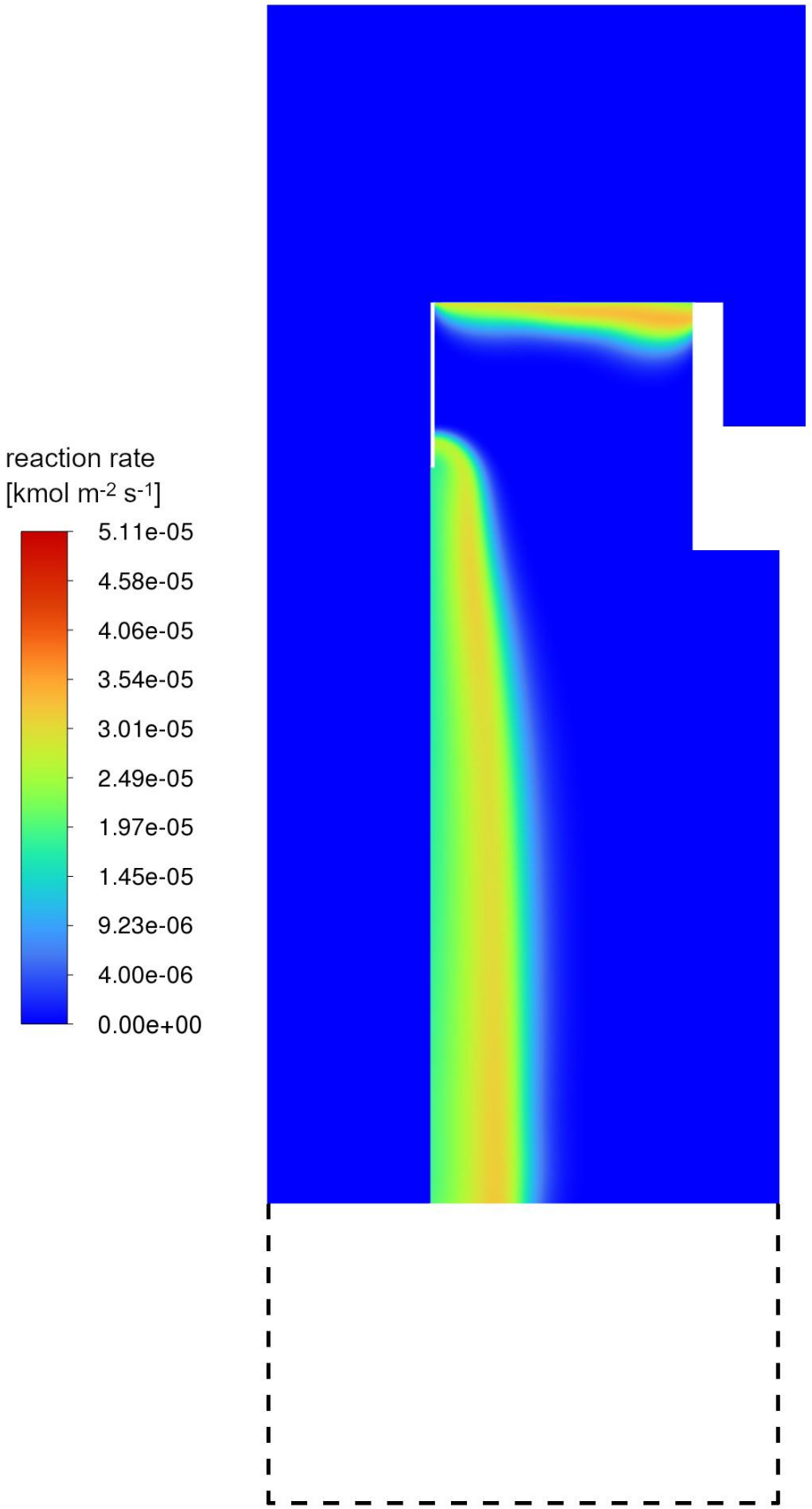

(c) variant 3

Figure 5.11. Reaction rate contours [kmol m^{-2} s^{-1}] for the investigated reactor's proposed modification of variant 1 (a), variant 2 (b), and variant 3 (c) (catalyst particle diameter of 2 mm) [68]

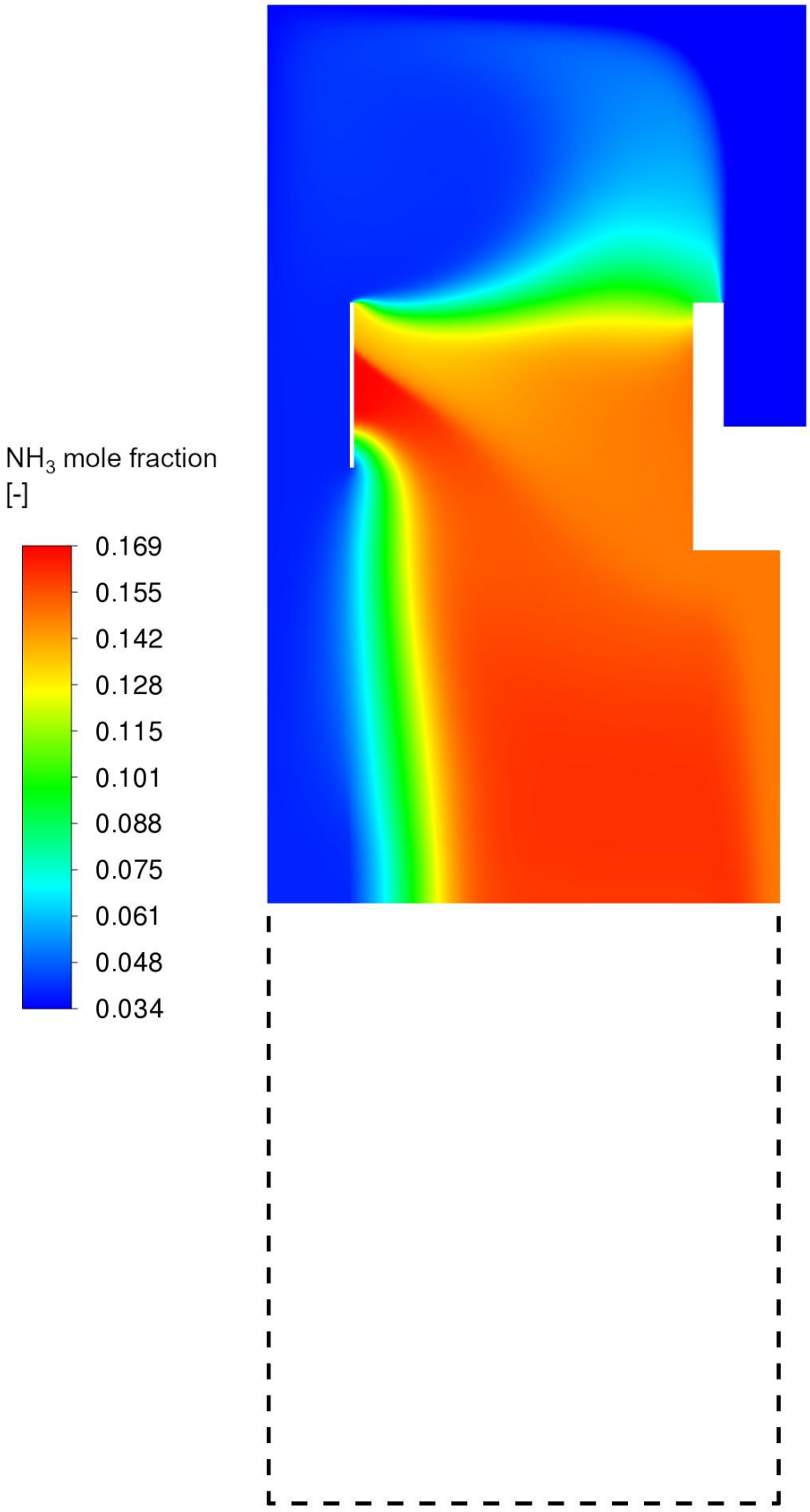

(a) variant 1

Figure 5.12. Cont.

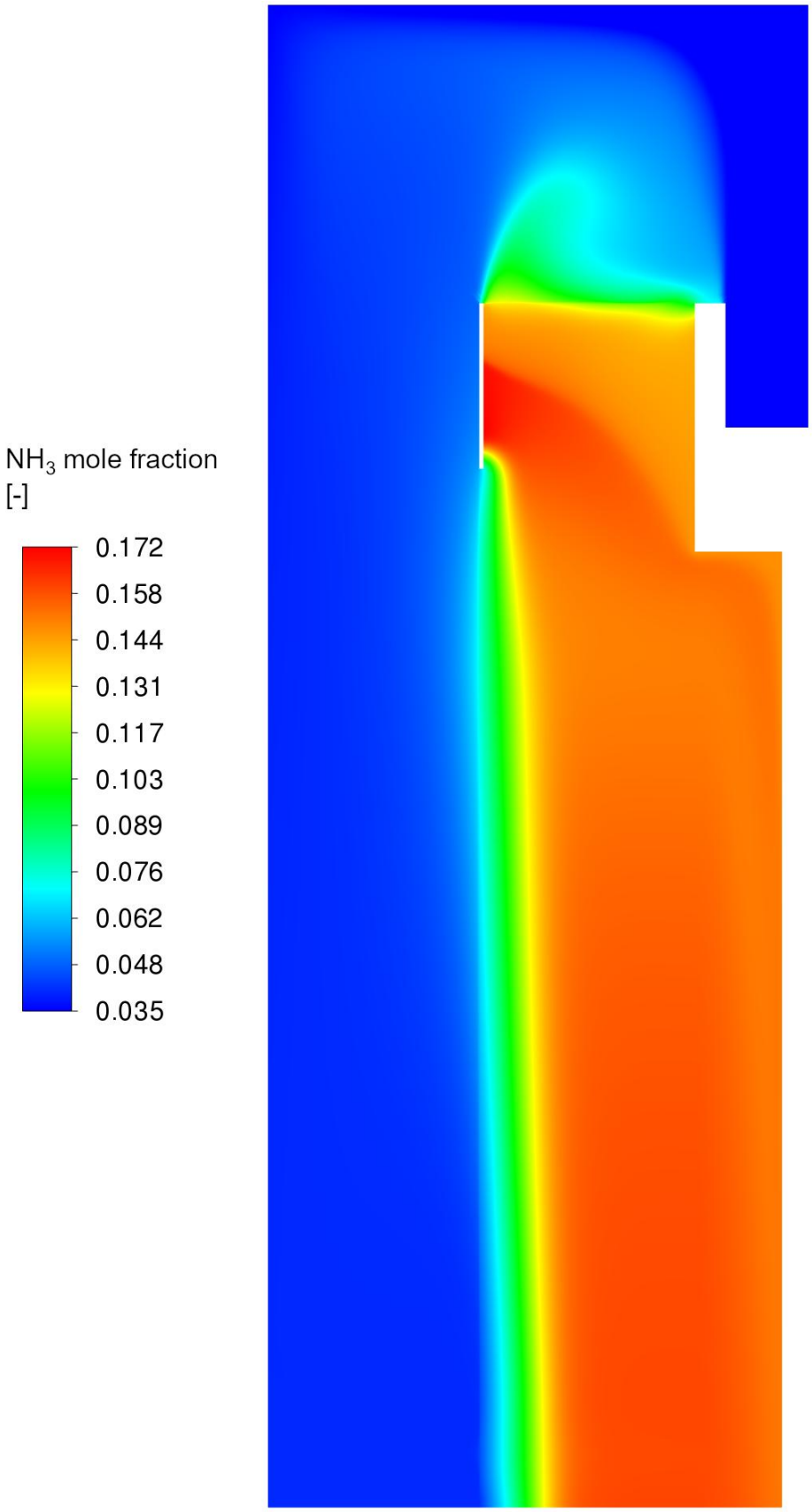

(b) variant 2

Figure 5.12. Cont.

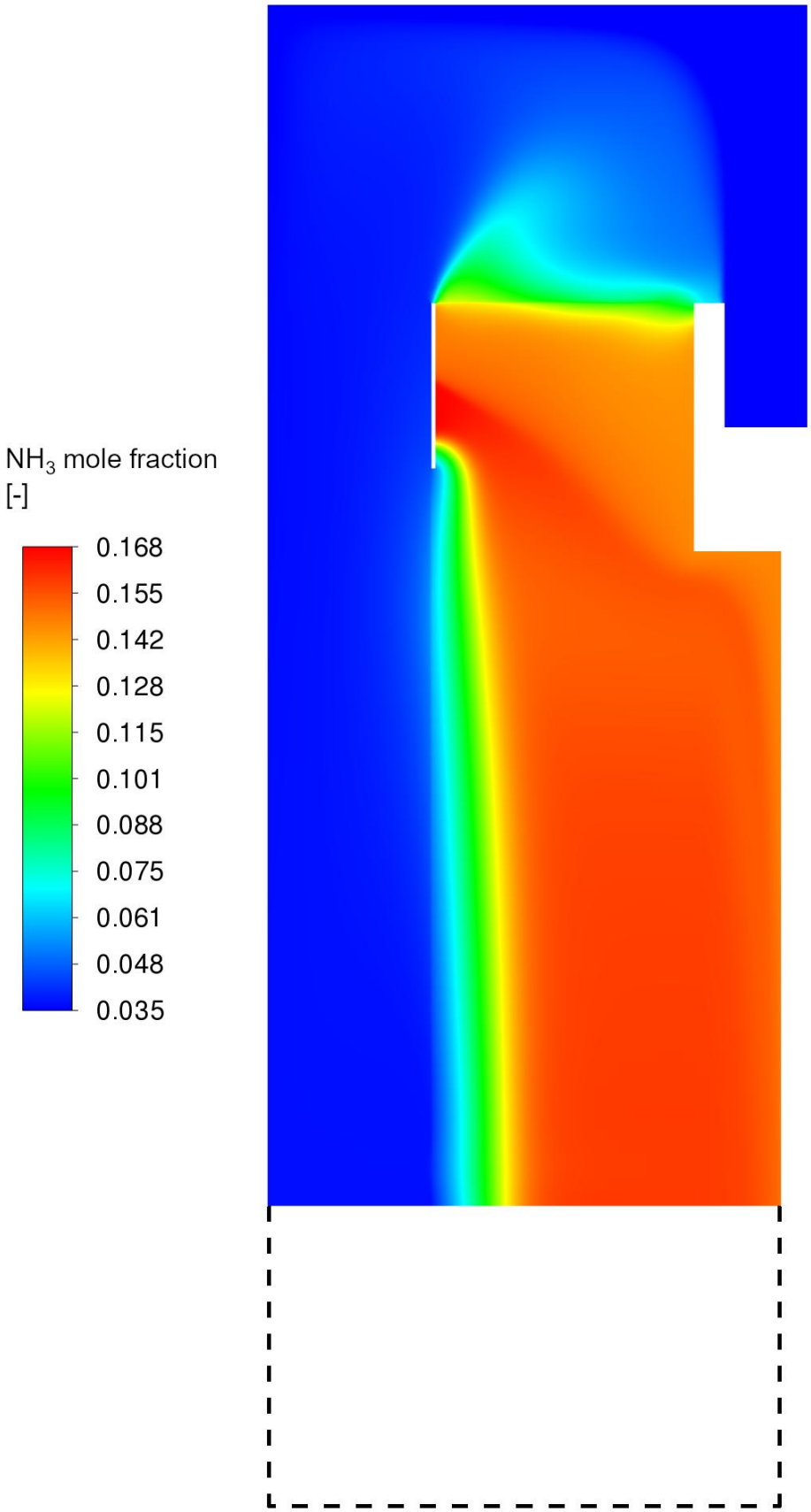

(c) variant 3

Figure 5.12. Ammonia mole fraction's contours [-] for the investigated reactor's proposed modification of variant 1 (a), variant 2 (b) and variant 3 (c) (catalyst particle diameter of 2 mm) [68]

Table 5.9. Results' comparison between the original and proposed modified variants of the investigated ammonia synthesis reactor [68]

Modification	*Catalyst bed's volume [m^3]*	*Percentage of "working" catalyst bed [%]*	*NH_3 mole fraction at the outlet [-]*
original	11.47	29.1	0.157
variant 1	5.71	55.1	0.157
variant 2	5.72	56.3	0.157
variant 3	5.72	54.9	0.157

As shown in Table 5.9, every modification variant can maintain the process's efficiency despite having reduced the bed's volume by half. The CFD model can relatively easily and quickly estimate the minimal volume of the catalyst bed without losing the output amount of product. The existing apparatus can be modified only by altering the catalyst bed's dimensions, and new reactors can be designed in reduced size, consequently reducing the initial installation costs. Another benefit is the smaller amount of catalyst needed, effectively decreasing running costs. Still, it should be noted that a proper catalyst amount surplus should be included in beds to maintain efficiency during the reactor's operation due to catalyst ageing and poisoning.

5.9. Conclusions

Section 5 investigated the Topsoe axial-radial ammonia converter. The CFD model included the two-dimensional geometry of the first catalyst bed. The reaction kinetics was modelled by implementing the modified Temkin-Pyzhev expression [35] through a user-defined function. The results were obtained in the form of velocity, reaction rate, concentration, and temperature, and the influence of the catalyst bed parameters, such as particle diameter, porosity, and pressure drop, was analysed.

The results illustrate that catalyst particle size substantially influences the process. This parameter governs how quickly the state close to equilibrium is reached. Smaller particle sizes in the catalyst bed are desired since they can significantly increase the reaction rate values. In this work, simulations allow for identifying zones where the reaction rate is near zero. Based on those results, the possible geometry modifications of the catalyst bed were proposed to reduce their volumes significantly, maintaining process efficiency.

This section shows that CFD is a proper tool for estimating the appropriate catalyst bed's volume without affecting the process performance. The results show that using the obtained CFD model, one can relatively easily predict the easy-to-implement catalyst bed's geometry changes. It should be noted that simulations do not include operational factors like catalyst poisoning and ageing, which may need additional correction while modelling an actual ammonia converter unit.

6. Pilot plant ammonia reactor – CFD modelling of actual apparatus with experimental validation

This section was done in cooperation with Yara Technology and Projects – Technology (Yara International ASA), which owns two physical pilot plant reactors for the ammonia synthesis process. The reactors are located in Yara research facilities in Porsgrunn, Norway. The experiments were done uniquely for this section's project during the author's 3-month internship in Yara's facilities, which provided data and computational resources for this section.

This study aims to use CFD tools to create virtual models of the pilot plant ammonia reactor using actual geometry and process conditions. The detailed geometry was obtained, and experimental data provided by the Yara were the basis of the CFD model. The theoretical kinetic model developed by Dyson and Simon [35], which uses a modified Temkin and Pyzhev expression, was used to simulate the ammonia synthesis reaction. The obtained CFD simulation was validated by two additional "blind" experiment data sets. The geometry of the reactor is 3-dimensional, and the computational domain covers its entire geometry. The results include velocity, reaction rates, temperature, concentration and pressure profiles. This section was made based on the results presented in the manuscript "Pilot Plant Reactor for Ammonia Synthesis – Computational Fluid Dynamics Analysis with Experimental Validation" [73], which was a consistent part of this PhD project.

6.1. Geometry

Figure 6.1 presents the CAD geometry of the investigated reactor. The six reactor beds are located in the middle part of the reactor. The catalyst beds' dimensions are 70 mm in height and 9 mm in diameter. There is one inlet located at the bottom of the apparatus and six outlets at the top, one per catalyst bed. Figure 6.2 presents the expected gas flow pattern inside the reactor. Figure 6.2 (a) shows the top cross-section with the location of the thermocouples' channels used to measure the temperature along the catalyst beds. The thermocouples are located at different heights, and their detailed positions are presented in Section 6.2. Figure 6.2 (b) presents the A-A cross-section, demonstrating the gas flow through the reactor. The feed gas enters at the bottom of the side of the reactor and is distributed to the mantle in the pre-heating zone, which contains the heating electric cables at the mantle's external wall. The gas enters the inner part at the top of the apparatus. Then, it flows towards the bottom chamber, from where it is

distributed into the six separate reaction beds where the ammonia synthesis reaction occurs. The gas leaves the reactor through six separate outlets at the top.

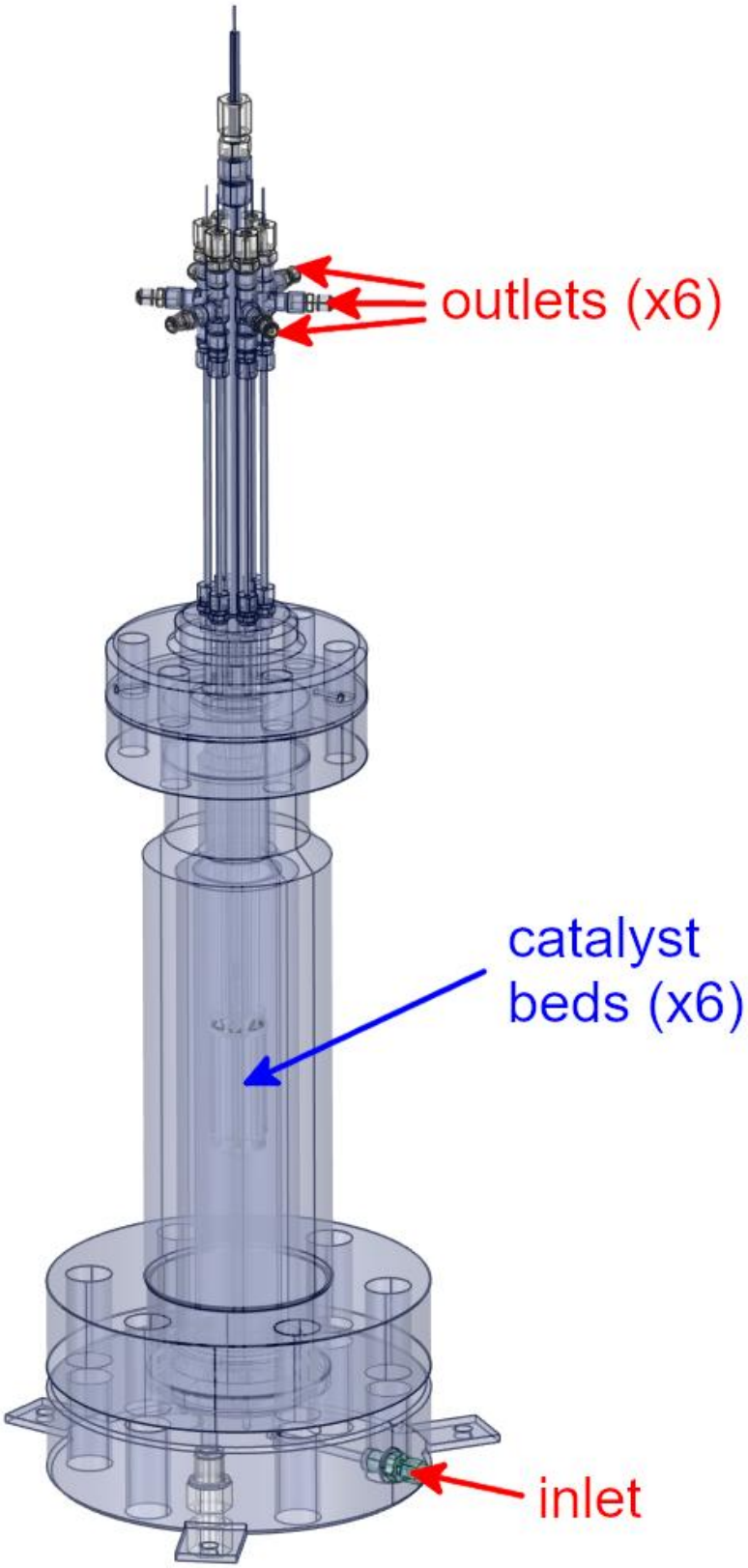

Figure 6.1. CAD geometry of Yara's experimental pilot-scale ammonia synthesis reactor [73]

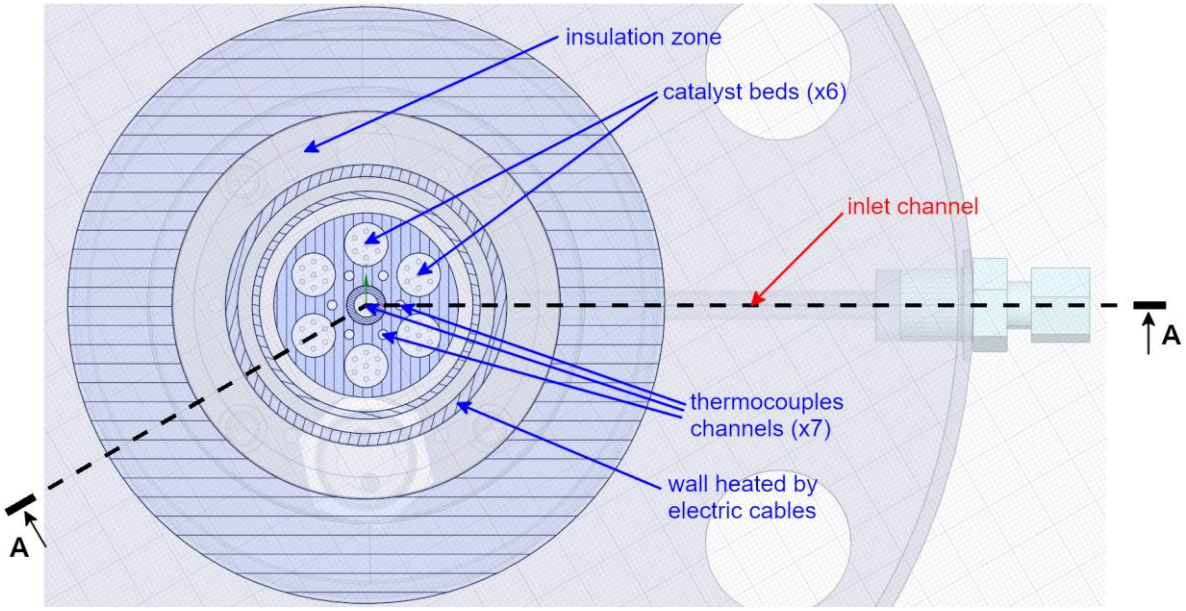

(a)

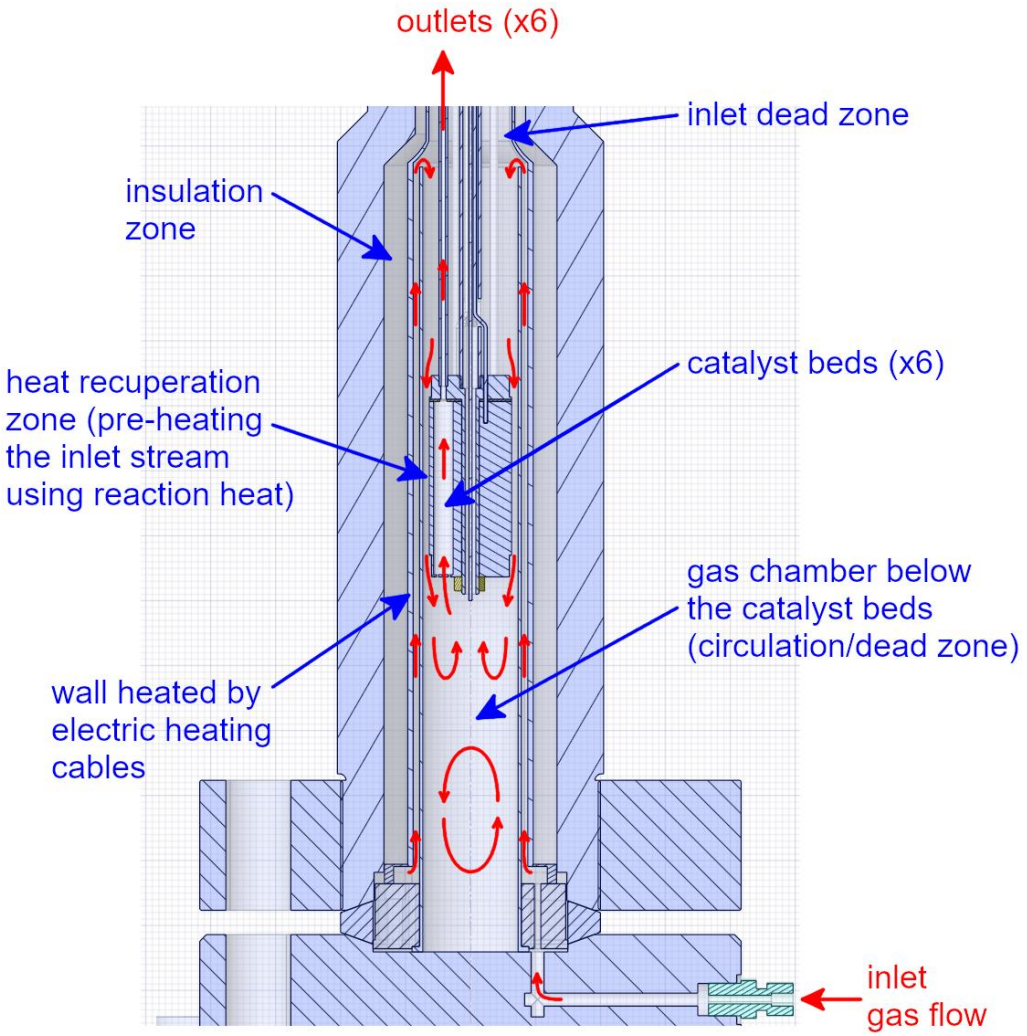

(b)

Figure 6.2. Top cross-section (a) and A-A cross-section (b) schemes of the pilot-scale ammonia synthesis reactor [73]

6.2. Experimental data

The CFD model of the ammonia pilot plant reactor was created and validated based on the experimental data obtained from the Yara Technology and Projects – Technology, which possesses two pilot-scale reactors in the laboratory named “Micro 1” and “Micro 2”. The experimental data and CAD geometry used to create the CFD simulation were obtained from the “Micro 1” reactor. In the validation section, the experimental data from both reactors was from “blind” runs. Since all data was measured continuously during experiments, the time-average values from the steady-state run were used in this work. Outlet parameters were measured separately at each of the six reactor outlets. Therefore, the mean values of them were used. Table 6.1 lists the experimental parameters obtained from the “Micro 2” reactor.

Table 6.1. Experimental data from “Micro 2” used as a basis for the CFD model [73]

Parameter	*Unit*	*Value*
feed ammonia concentration	mole %	2.58
outlet ammonia concentration	mole %	8.71
H_2:N_2 mole ratio in the feed stream	-	3:1
outlet flow from each bed	Nml min^{-1}	1000
inlet pressure	barg	49.06

During the experimental runs, temperature was measured by the seven thermocouples near the catalyst beds in the channels shown in Figure 6.2 (a). Six thermocouples are placed in a circle around the reactor’s axis, while the bottom thermocouple (named “bottom inlet”) is placed in the centre. The time-averaged experimentally measured temperatures are listed in Table 6.2. The “bottom inlet” thermocouple’s height is negative since it is located below the catalyst beds.

Table 6.2. Temperature experimental time-averaged values. The catalyst beds’ height is along the Z-axis, as presented in Figure 6.3. [73]

Thermometer (block)	*Height [mm]*	*Temperature [°C]*
F	70	424.73
E	56	434.36
D	42	445.50
C	28	454.52
B	14	456.15
A	0	456.82
Bottom inlet	−6	443.77

Figure 6.3 presents the detailed positions of the thermocouples in the reactor. The temperature measurements were critical parameters since they were used as a basis to create the CFD model.

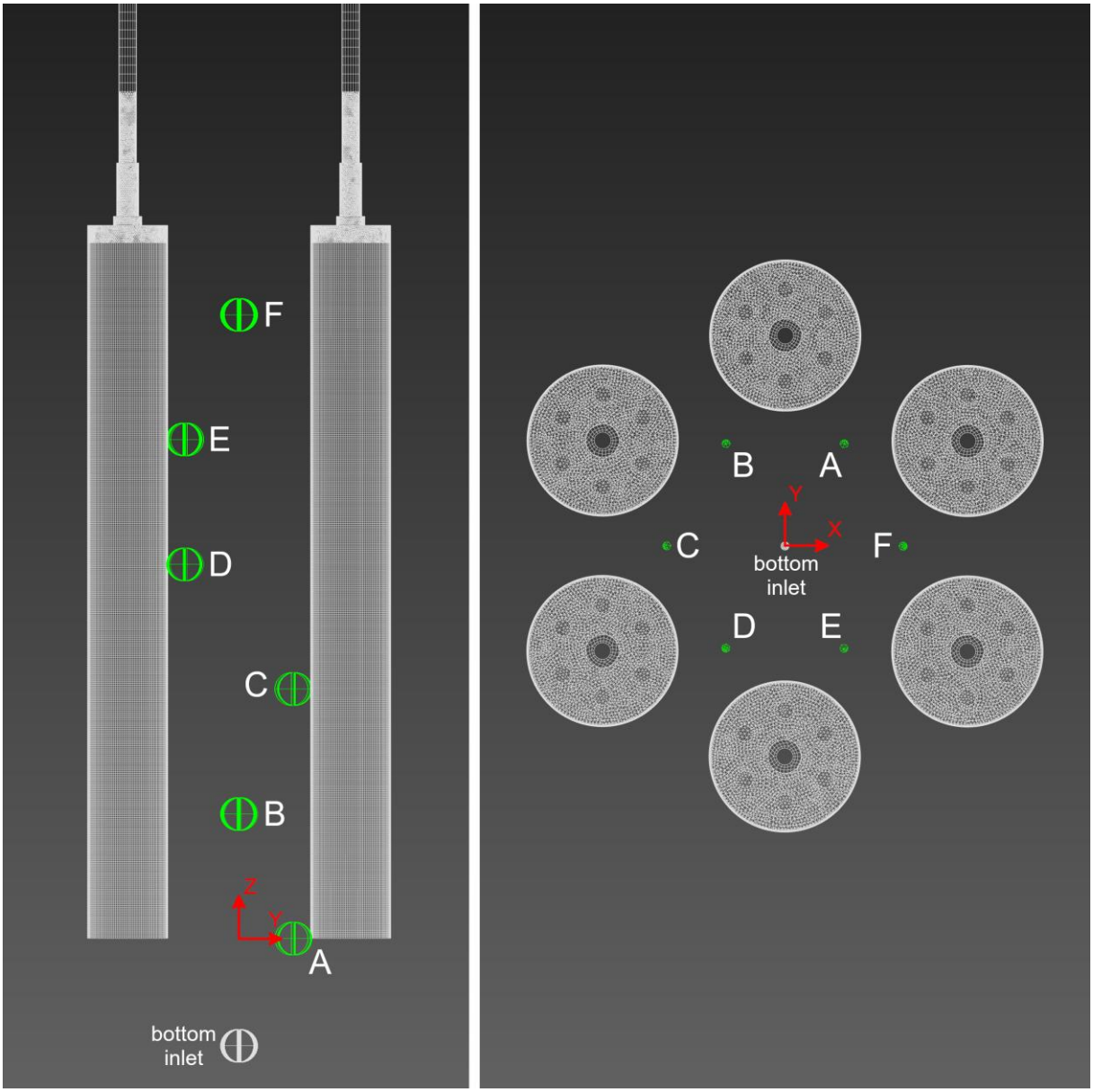

Figure 6.3. Thermocouples' locations within the ammonia synthesis reactor in relation to catalyst beds' locations [73]

6.3. Catalyst beds

Catalyst beds were modelled using the Ansys Fluent porous zone model described in Section 4.3.6. Table 6.3 lists the input parameters used for the calculations.

Table 6.3. Input parameters for the catalyst bed modelling using porous zone model [73]

Parameter	*Symbol*	*Unit*	*Value*
porosity	ε	-	0.574
viscous resistance	C_1	m^{-2}	573083371
inertial resistance	C_2	m^{-1}	15712

6.4. Computational setup

The computational domain (Figure 6.4 (a)) was created based on the CAD model. Figure 6.4 (b) shows the reactor mantle's external wall. The heating cable is located inside the mantles, and because of that, the mantle's clearance was reduced by 2 mm (heating cable's diameter).

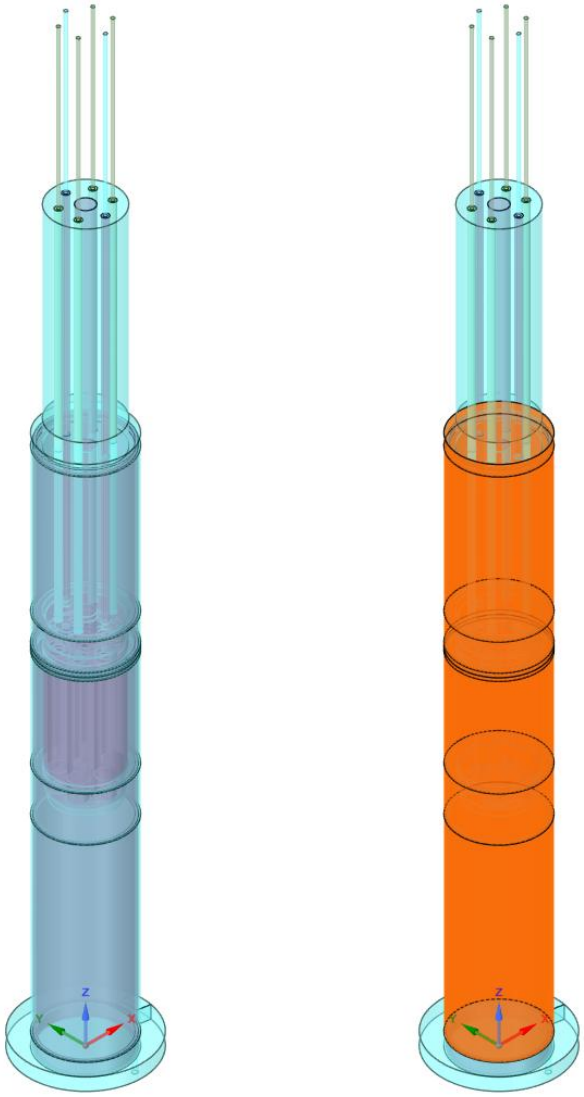

(a) (b)

Figure 6.4. Computational domain of the modelled reactor (a) and the heated external wall (orange) (b) [73]

The domain contains the complete geometry of the reactor to avoid approximation errors and increase the accuracy of the CFD model. The domain contains fluid zones, porous zones, and solid zones, which are internal walls, to simulate heat conduction. Figure 6.5 presents the cross-section of the middle part of the reactor containing the catalyst beds.

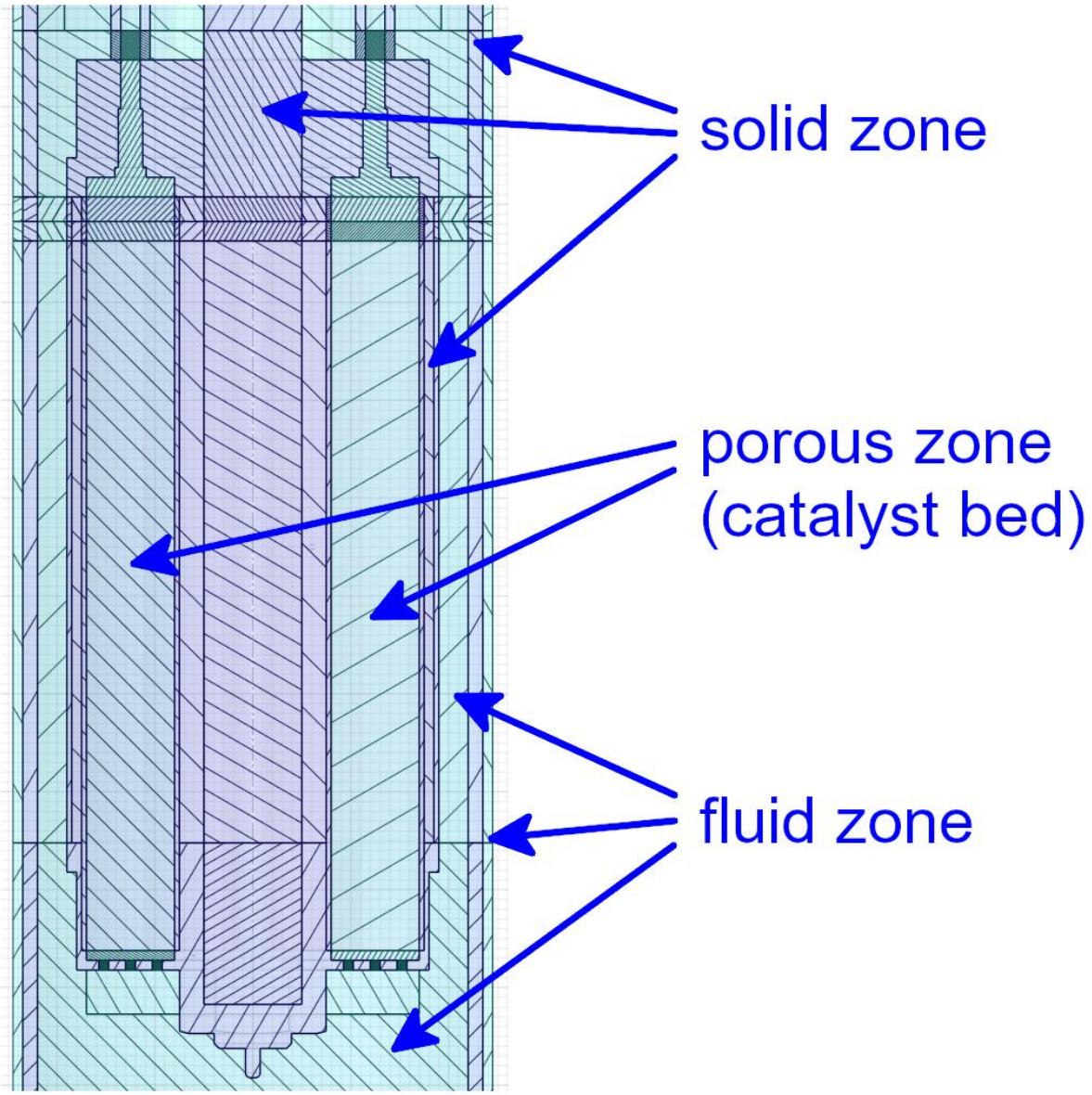

Figure 6.5. Cross-section of the middle part of the computational domain [73]

The computational mesh was generated using the Meshing module of Ansys Workbench 2024 R1, with approximately 24 million computational cells (including 14 million cells in fluid and porous regions). The mesh is more refined and fully hexahedral in catalyst beds and their vicinities. Fluid regions are meshed mostly with hexahedral mesh combined with tetrahedral cells. Figure 6.6 presents the cross-section of the computational mesh at the top and bottom of the catalyst bed.

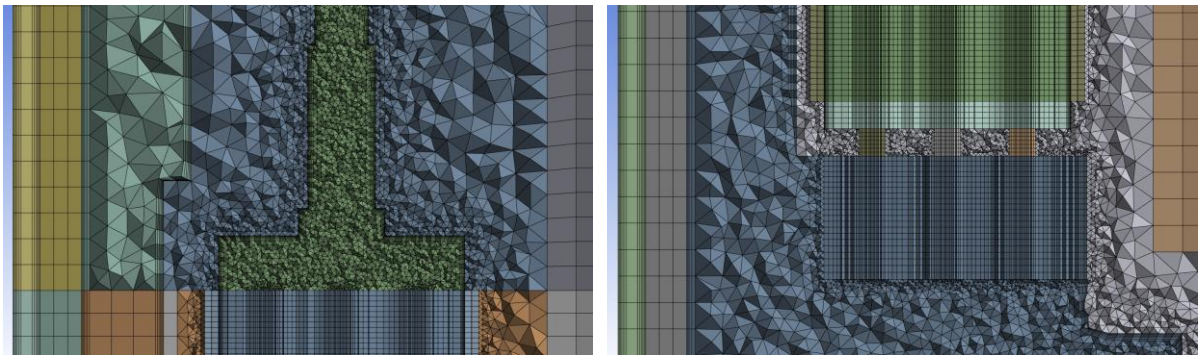

(a) (b)

Figure 6.6. Computational mesh at the vicinity of the top (a) and the bottom (b) of the catalyst bed [73]

Calculations were conducted using Ansys Fluent solver. A steady-state condition with gravity force and negative z-direction was used. The Pseudo-Transient mode was enabled with a low Time-Scale Factor, and pressure-velocity coupling was set to Couple and the PRESTO! The scheme was set for the pressure. The hybrid initialisation method started iterations, and the Second Order Upwind discretisation scheme was applied. First calculations were performed using First Order Upwind schemes before changing to Second Order Upwind. Since the reactor has turbulent flow regions, especially at the catalyst bed's inlet areas and outlets, the SST k-ω model was used for the turbulence modelling.

6.5. Boundary conditions

The boundary conditions used as the input for the CFD simulation in the units required by Ansys Fluent are listed in Table 6.4.

Table 6.4. Ammonia pilot plant reactor's CFD model's boundary conditions [73]

Parameter	*Unit*	*Value*
mass flow inlet	kg s^{-1}	$3.897 \cdot 10^{-5}$
inlet temperature	°C	25
pressure outlet	Pa	4906356
heated wall temperature (estimated)	°C	426
inlet ammonia mole fraction	-	0.0258
inlet nitrogen mole fraction	-	0.2436
inlet hydrogen mole fraction	-	0.7307

The heated wall temperature was unknown due to the measurement limitations. This parameter was estimated to match the Block A temperature, which was selected as a reference to estimate the heated wall temperature. This thermocouple's location is the closest to the catalyst beds'

inlets, where the strongest influence of heat generated by the reaction is expected. The heated wall temperature was obtained by trial and error to ensure that Block A calculated in the simulation agrees with the experimental value.

6.6. Reaction kinetic model modification

The calculations use the kinetic model developed by Dyson and Simon [35], which is described in Section 5.5. The reaction rate can be calculated using Equation (110). Since the investigated pilot plant ammonia synthesis reactor uses catalyst particles with sufficiently small diameters (0.5 mm), there is no need to use a particle size correction factor. However, due to the catalyst parameter differences between the theoretical model and the experimental catalyst, the kinetic model was modified to improve the accuracy of the CFD model. The BET (Brunauer-Emmett-Teller) surface area of the catalyst used by Nielsen et al. [71], which was the basis of the Dyson and Simon kinetics, has a value of 8.57 $m^2\ g^{-1}$, while the BET surface area of the catalyst used by Yara has the value of 11.9 $m^2\ g^{-1}$. To compensate for that, the multiplier was added to Equation (110), which is the ratio between the BET surfaces of the Yara and Nielsen et al. [71] catalysts, as shown in Equation (114).

$$R_{NH_3} = 1.7698 \cdot 10^{15} \exp\left(\frac{-40765}{RT}\right)\left[{K_a}^2 a_1 \left(\frac{{a_2}^3}{{a_3}^2}\right)^{0.5} - \left(\frac{{a_3}^2}{{a_2}^3}\right)^{0.5}\right] \cdot \frac{BET_{Yara}}{BET_{Nielsen}} \qquad (114)$$

The access to the detailed Yara's catalyst parameters, such as BET surface, allowed the modelled reaction to be implemented as a volumetric (per volume of the catalyst bed) reaction within the porous zone model of the investigated pilot-scale ammonia reactor. Because of this, the surface-to-volume ratio is not a required parameter in this case, given that the catalyst difference correction factor is already included in the reaction rate equation. Since Ansys Fluent uses the actual fluid volume in porous media as a reaction zone [64], the reaction rate has to be divided by the bed porosity value, in this case of 0.574:

$$R_{NH_3} = \frac{1.7698}{0.574} \cdot 10^{15} \exp\left(\frac{-40765}{RT}\right)\left[{K_a}^2 a_1 \left(\frac{{a_2}^3}{{a_3}^2}\right)^{0.5} - \left(\frac{{a_3}^2}{{a_2}^3}\right)^{0.5}\right] \cdot \frac{BET_{Yara}}{BET_{Nielsen}} \qquad (115)$$

The unit of the reaction rate in Equation (115) is kmol per cubic meter of the catalyst bed per hour. The reaction rate from the modified kinetics was implemented to Ansys Fluent as a user-defined function (UDF) using a volumetric reaction approach.

6.7. Results

This section presents various results, such as velocity, reaction rate, concentration, temperature and pressure contours. The model was verified by the temperature and outlet concentration experimental measurements.

6.7.1. Flow field and velocity contours in the converter

Velocity magnitude is illustrated as a contour, as shown in Figure 6.7. It can be noted that maximum velocity in the domain occurs inside the outlet pipes and in the vicinity of catalyst beds' inlets, where the most turbulent flow is expected.

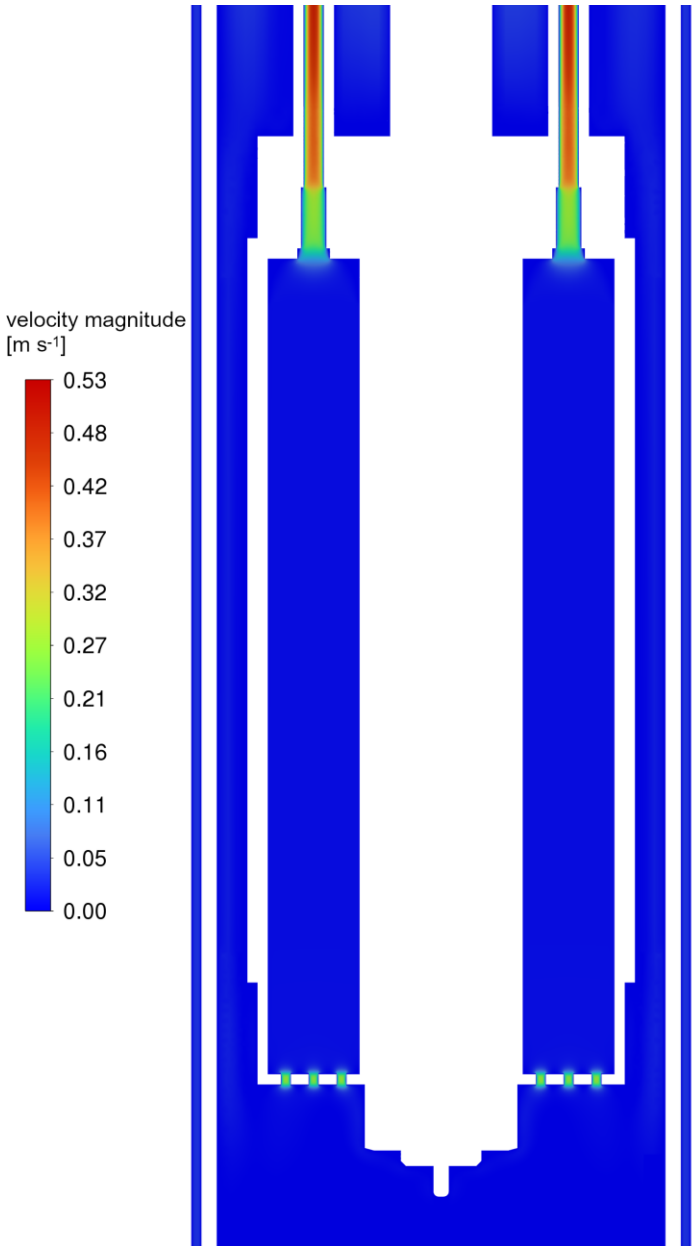

Figure 6.7. Velocity magnitude contours [m s^{-1}] in the cross-section of the investigated reactor (full range) [73]

Velocity magnitude contours presented in the full range do not illustrate the velocity gradients inside the catalyst beds. Figure 6.8 shows the velocity contours with the clipped range from 0 to 0.05 m s^{-1}. It can be observed that inside the catalyst beds, the gas flow is uniform and mostly plug-type.

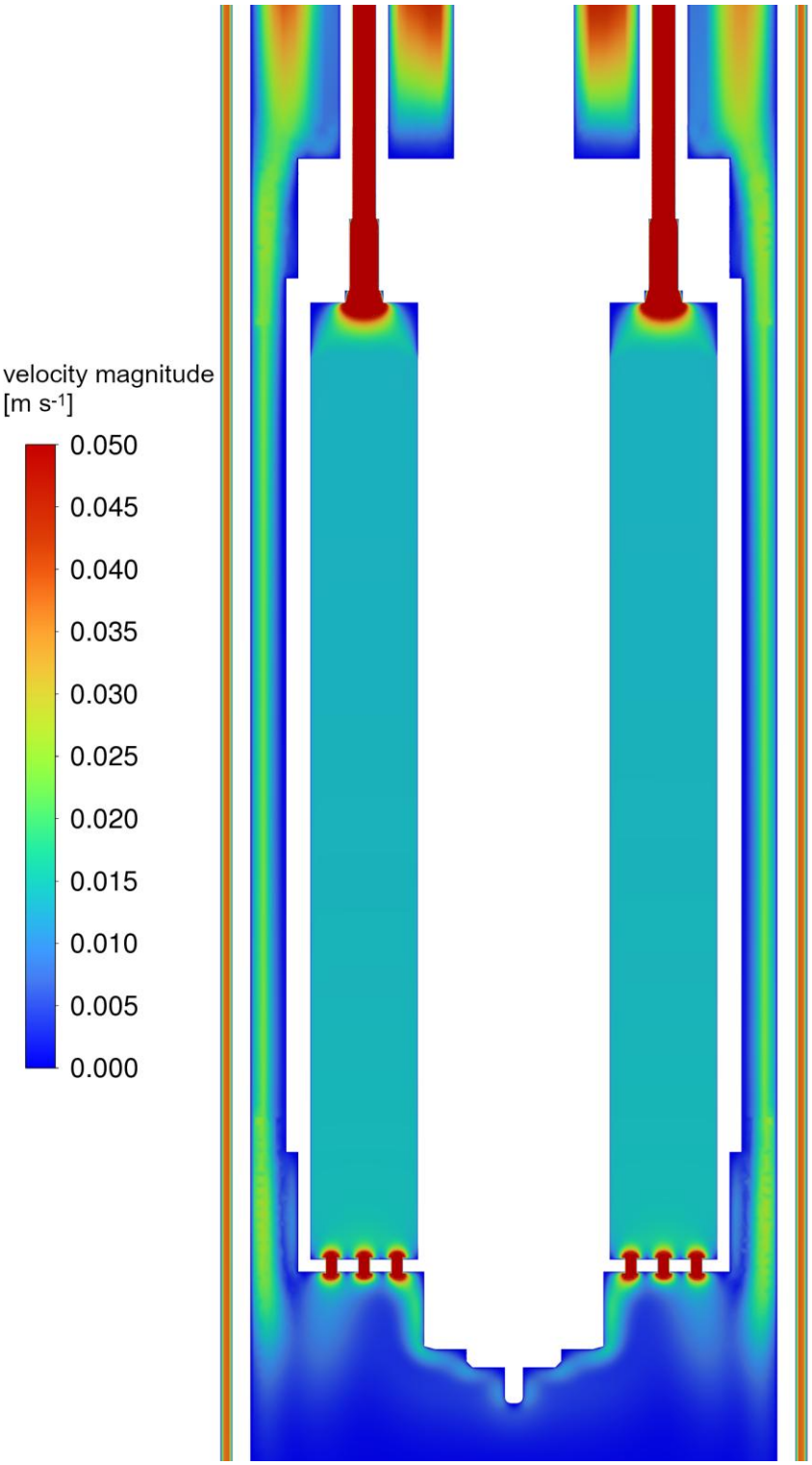

Figure 6.8. Velocity magnitude contours [m s^{-1}] in the cross-section of the investigated reactor (clipped range) [73]

6.7.2. Reaction rate contours inside the catalyst beds

The reaction rate is a parameter that is not possible to measure experimentally. CFD simulations provide the advantage of measuring and plotting this parameter in contours. This allows for identifying the reaction rate intensity inside the investigated system. Reaction rate contours allow finding the highest-intensity reaction zones and localising the areas with negligible reaction rates. Figure 6.9 presents the reaction rate contours in the reactor.

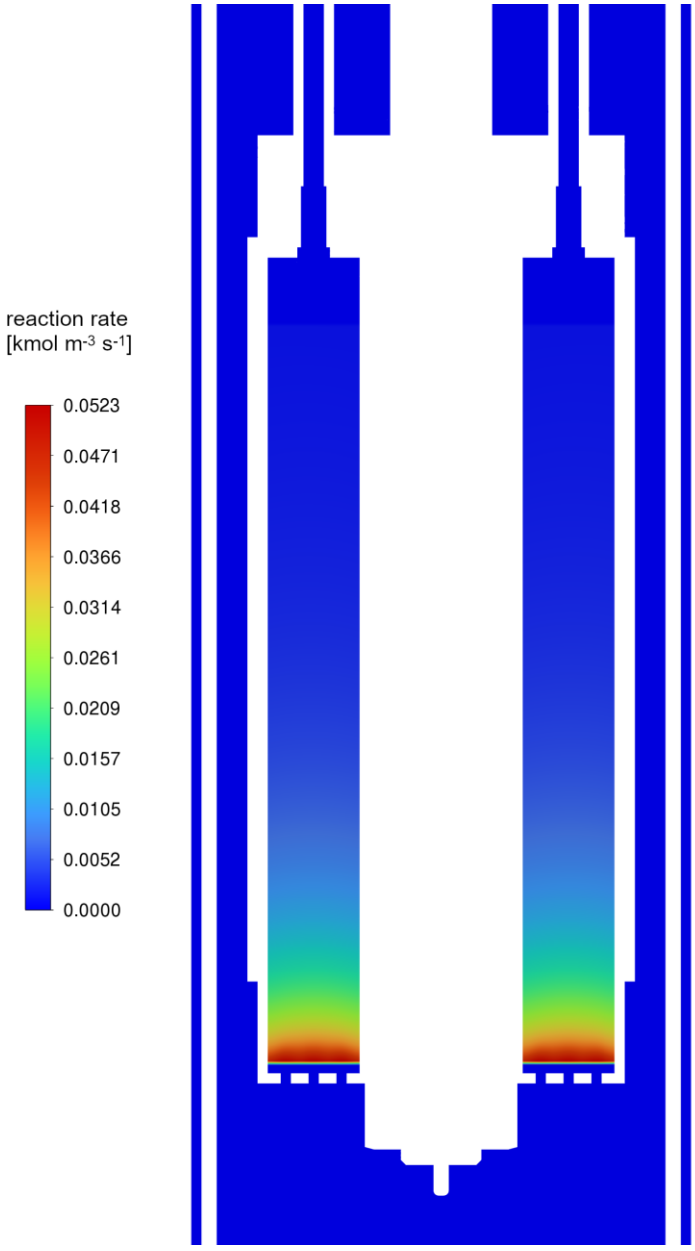

Figure 6.9. Reaction rate contours [kmol m^{-3} s^{-1}] in the cross-section of the investigated reactor (full range) [73]

One can observe that reaction rate values approach zero before leaving catalyst beds. This suggests that the state of the chemical equilibrium was reached. Ammonia synthesis is

considered a reversible reaction, reaching its equilibrium relatively quickly at the current experimental setup. However, the ideal equilibrium cannot be reached, which is visible in Figure 6.10, presenting the reaction rate contours with a clipped range from 0 to 0.0052 kmol m^{-3} s^{-1}.

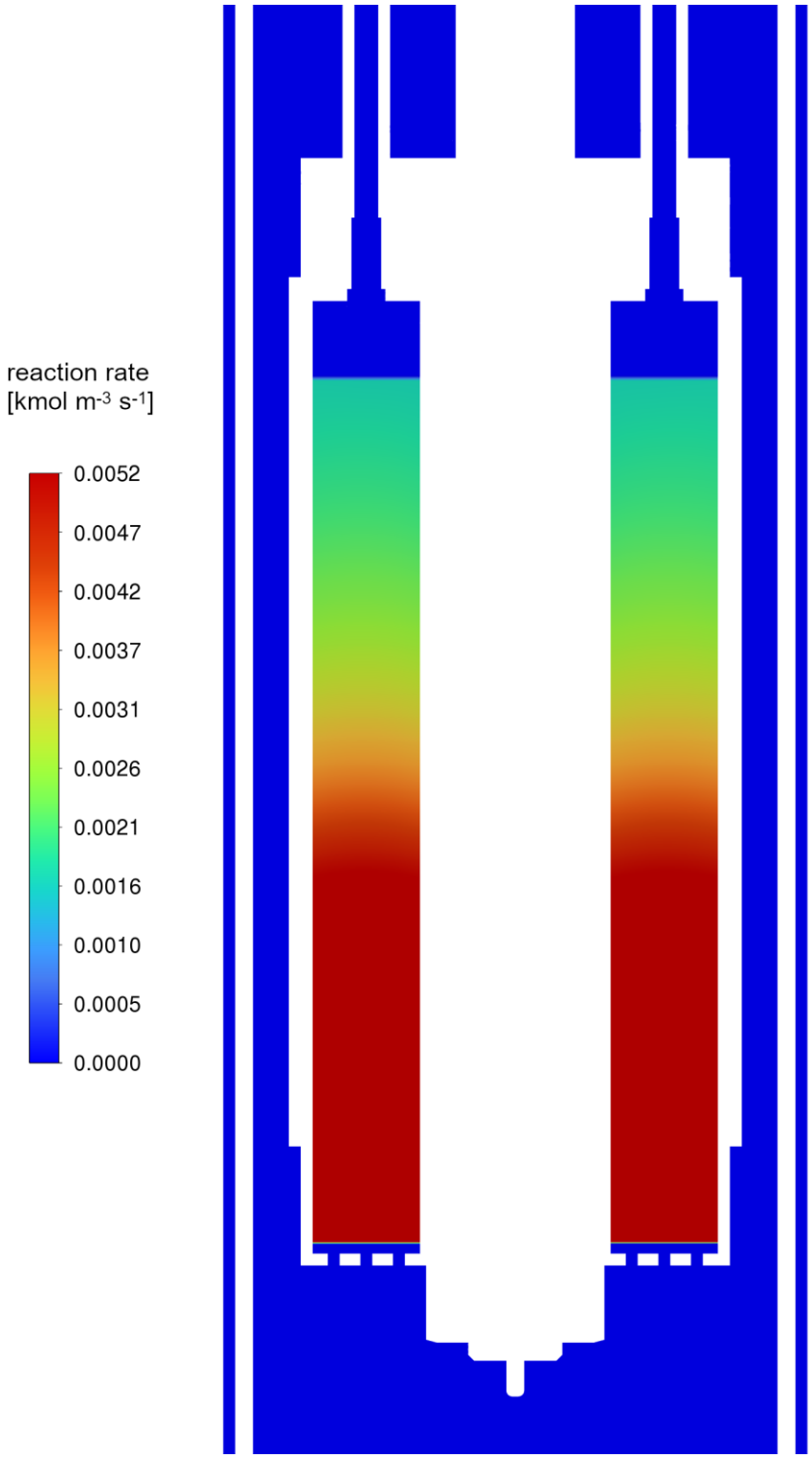

Figure 6.10. Reaction rate contours [kmol m^{-3} s^{-1}] in the cross-section of the investigated reactor (clipped range) [73]

6.7.3. Concentration contours in the converter

Ammonia concentration is relatively easy to measure experimentally, especially at the inlets and outlets of the investigated system. This parameter, directly derived from the reaction rate, is excellent for validation. Figure 6.11 presents the concentration contours of the NH_3 mole fraction.

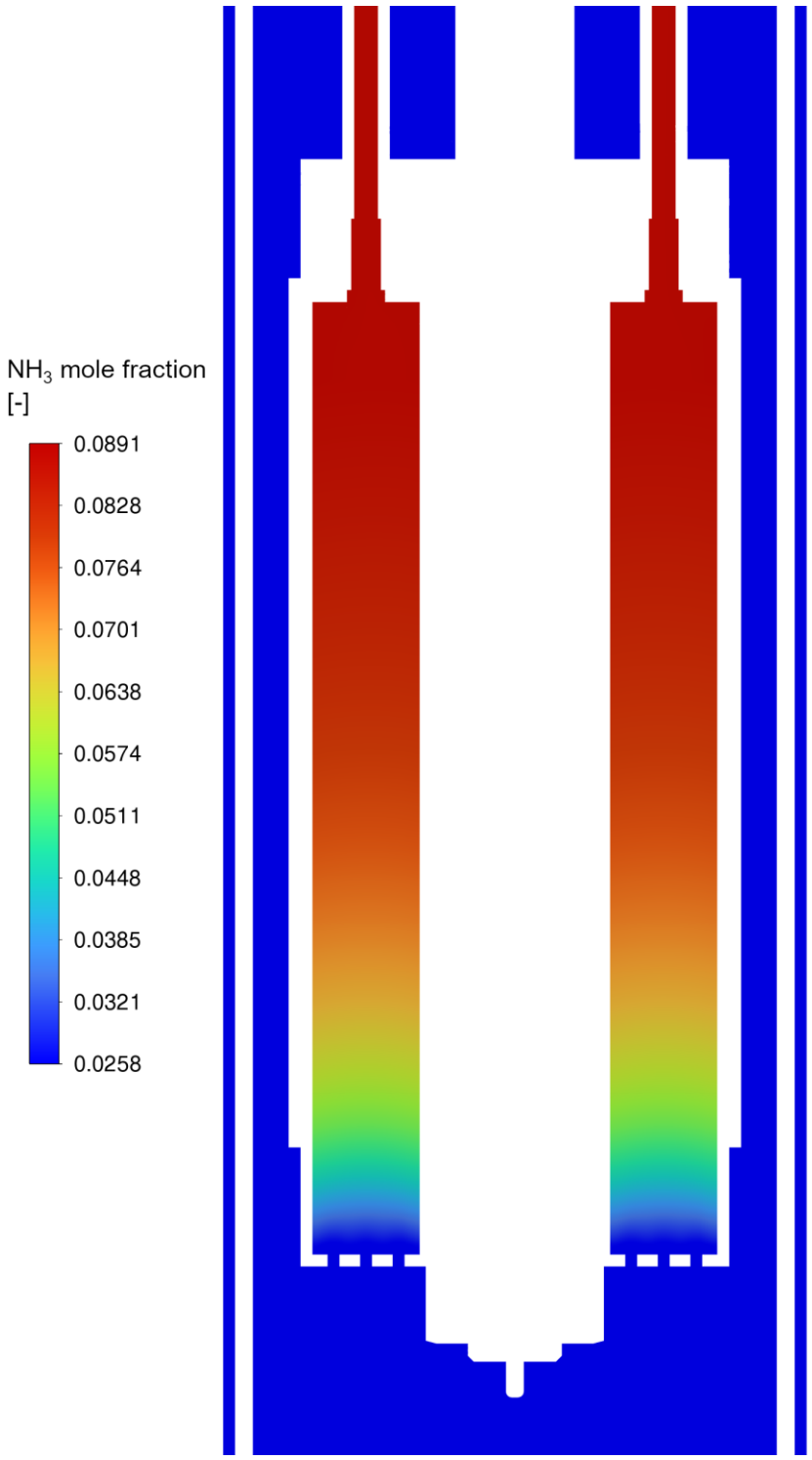

Figure 6.11. Ammonia mole fraction contours [-] in the cross-section of the investigated reactor [73]

Table 6.5 presents the experimental results compared to the CFD simulations results. This data was used to check the accuracy of the simulation.

Table 6.5. The experiment and simulation differences in values of the mean NH_3 mole % at the outlets [73]

Simulation	*NH_3 [outlet mole %]*	*Error [%]*
Experiment	8.71	-
CFD simulation	8.79	0.92

The experimental measurements were performed continuously during the experimental run. The values of ammonia mole fractions listed in Table 6.5 are time-averaged. It should be noted that experimental measurements vary between 8,59–8,78 NH_3 mole %. The simulation results agree with the experimental data with the maximum error between outlet ammonia concentrations of 0.92%.

6.7.4. Temperature contours in the converter and comparison with the experimental measurements

Due to the exothermic nature of the ammonia synthesis reaction, there is a significant relationship between reaction rate and temperature. Therefore, easy-to-measure temperature is a natural parameter for verifying calculations. There are seven block temperature measurement points inside the investigated reactor. The temperature was measured using thermocouples, as described in detail in Section 6.2. It should be noted that temperature measurement from "Block A" was used to estimate the heated wall temperature; thus, its value is the same as in experimental measurements. Table 6.6 compares experimental and simulation results, and Figure 6.12 presents the temperature contours and vertical thermocouples' locations.

Table 6.6. The comparison between the experimental and simulation values of temperature [73]

Block	*Unit*	*Experiment*	*CFD simulation*	*Error %*
F	°C	424.73	448.91	5.69
E	°C	434.36	450.97	3.82
D	°C	445.50	453.12	1.71
C	°C	454.52	455.36	0.18
B	°C	456.15	457.09	0.21
A	°C	456.82	456.78	−0.01
Bottom inlet	°C	443.77	451.02	1.63

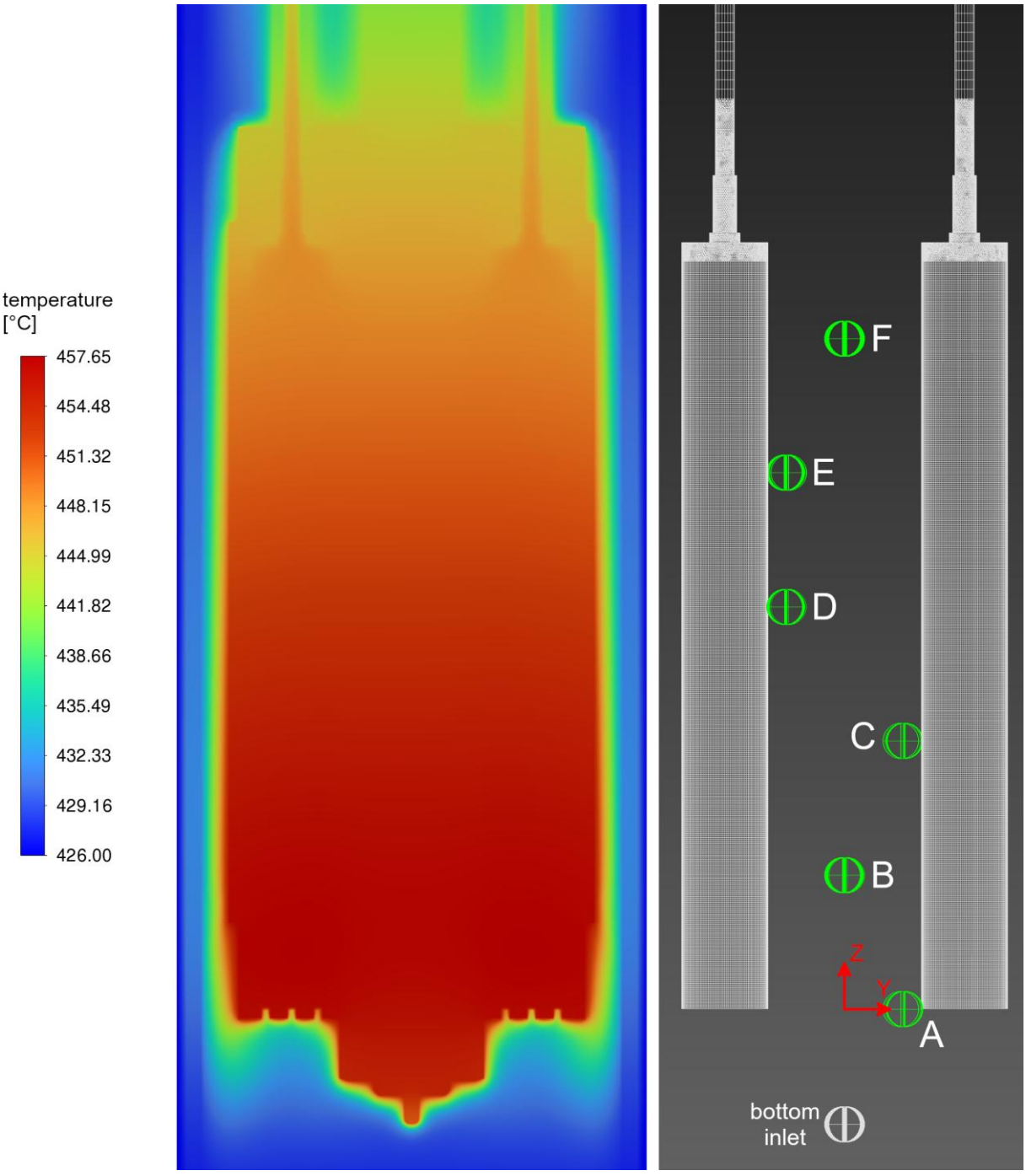

Figure 6.12. Temperature contours [°C] in the cross-section of the investigated reactor (right) and thermocouples' vertical locations (left) [73]

The temperature calculated in the CFD model fits the experimental data with a little error for thermocouple blocks A–C. For blocks D–F, the difference is more noticeable, although it is not higher than 5.69%, which still is a good agreement between the experimental and simulation results. These differences can result from assuming a constant temperature on the heated wall. Another potential source of uncertainty can be the presence of the thermocouples' channels containing the empty spaces with the air acting like insulation, while the model temperature

was taken from the points within the solid body. Similarly to other parameters, the experimental temperature measurements are timely-averaged with no fluctuation above 1.74. Figure 6.13 plots the experimental and modelled temperature values along the catalyst beds based on the data presented in Table 6.6.

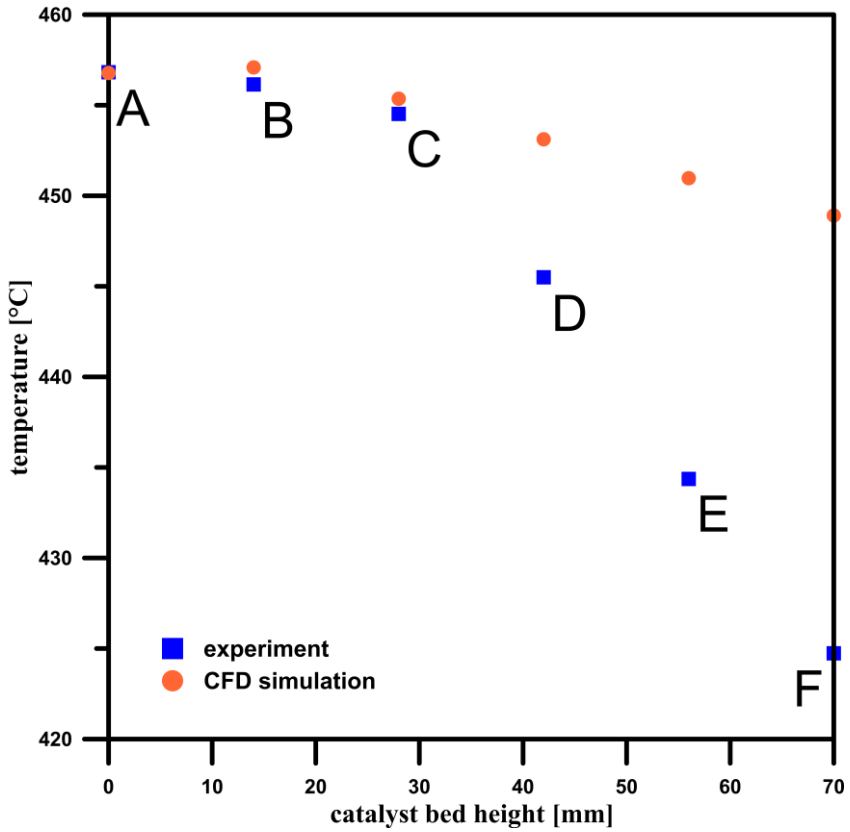

Figure 6.13. The experimental and calculated temperature profiles along the catalyst beds [73]

6.7.5. Pressure drop along the beds and pressure contours inside the converter

Pressure gradients play little role in the process since the pressure drop along the catalyst bed is only 14 Pa, as presented in Figure 6.14. The pressure profiles are shown in Figure 6.15, and the total pressure drop through the reactor is 74 Pa, which means that there is almost no effect on the reaction rate due to the pressure drop.

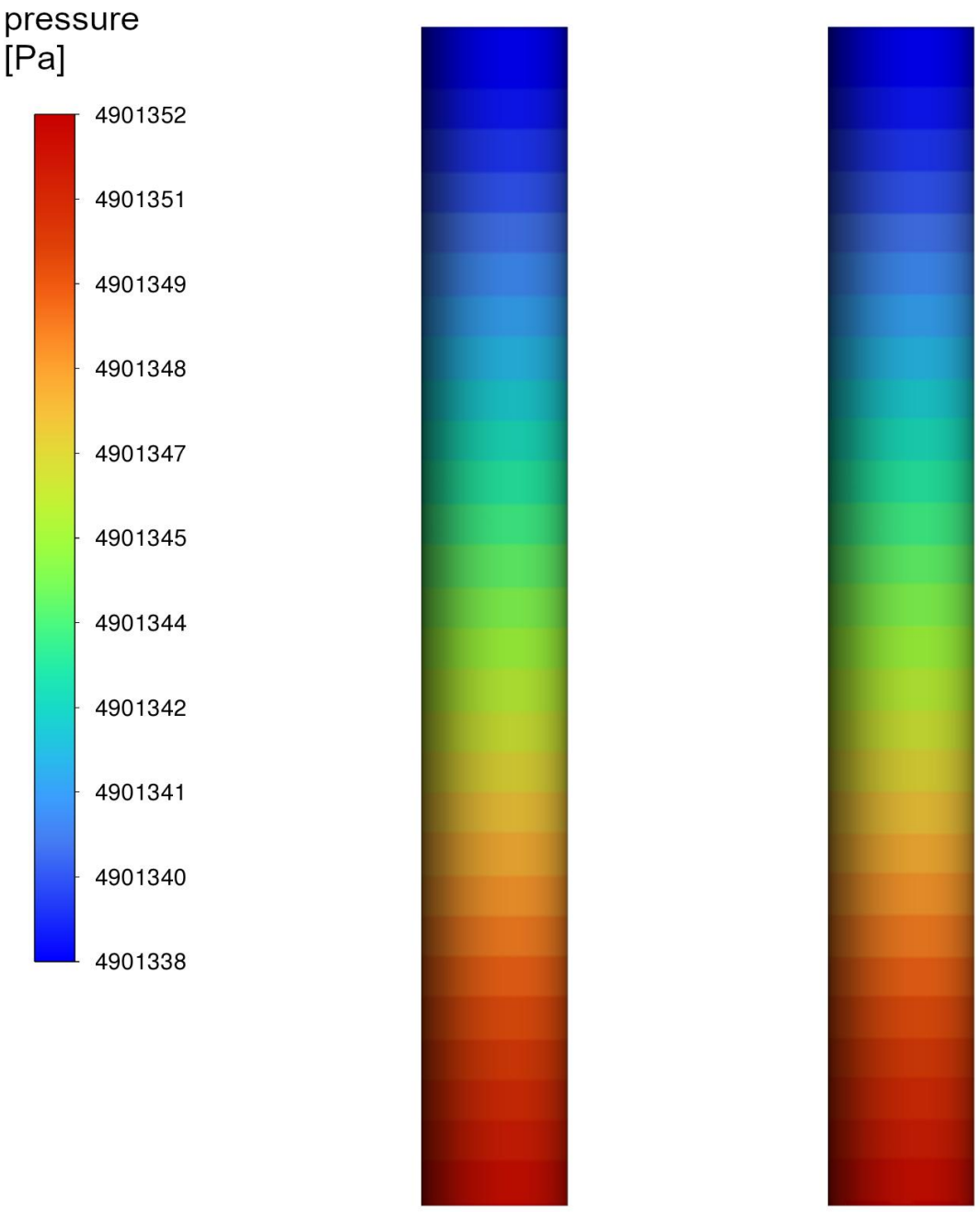

Figure 6.14. Pressure contours [Pa] in the cross-section of the catalyst beds in the investigated reactor [73]

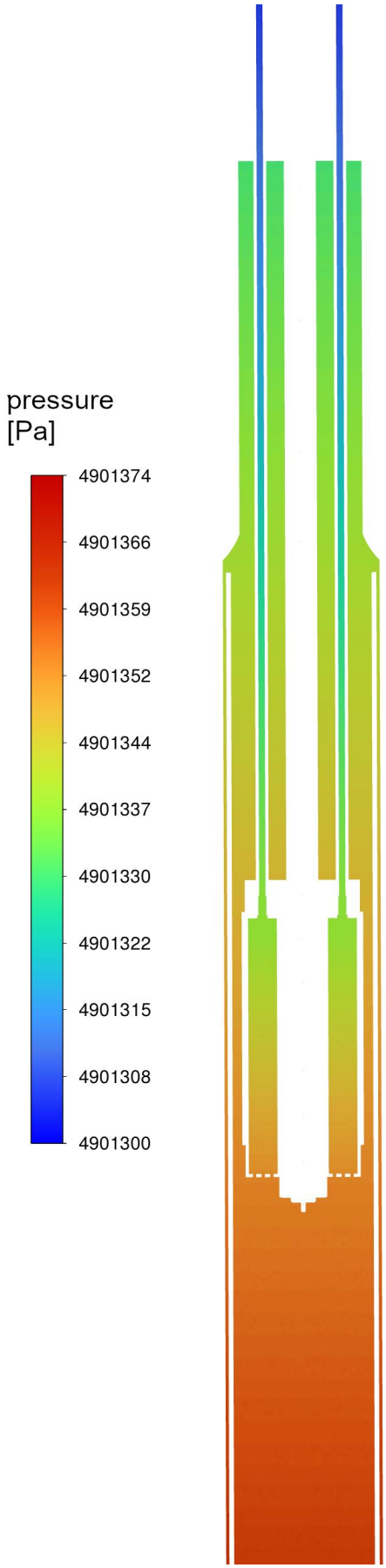

Figure 6.15. Pressure contours [Pa] in the cross-section of the investigated reactor [73]

6.8. Validation

The results of two independent runs of the ammonia pilot-scale reactor were used to validate the CFD model. For this purpose, those experiments are treated as "blind" runs, using only their input parameters to Fluent and comparing the results.

In this section, the experimental data that was the basis of the CFD model is referred to as "Run 1" and the "blind" runs were named "Run 2" and "Run 3", as shown in Table 6.7. It should be noted that "Run 2" was performed on different physical reactor ("Micro 1"), while the other runs were performed on the "Micro 2" reactor. Due to this, slightly larger differences between the model and experiments are expected in the case of "Run 2".

Table 6.7. Physical pilot plant reactor names on which experimental runs were performed [73]

Results	*Data usage*	*Reactor*
Run 1	Basis of the CFD model	Micro 2
Run 2	Validation data	Micro 1
Run 3	Validation data	Micro 2

The validation parameters were the mean mole % of ammonia at the outlet and block temperatures measured by the thermocouples. The CFD model's input data is listed in Table 6.8. Table 6.9 compares the concentration results, and Table 6.10 compares the temperature results. Table 6.11 contains the temperature errors between the experiments and the CFD model. Figure 6.16 presents the comparison between the experimental and modelled temperature profiles along the catalyst beds for validation runs.

Table 6.8. Input data for validation [73]

Parameter	*Unit*	*Run 1 (basis)*	*Run 2 (val.)*	*Run 3 (val.)*
Feed ammonia concentration	mole %	2.58	2.47	2.47
H_2:N_2 ratio in the feed stream	-	3:1	3:1	3:1
Outlet flow from each bed	Nml/min	1000	1000	1000
Inlet pressure	barg	49.06356	48.93162	49.65318
Heating cable temperature (estimated)	°C	426	433	431

Table 6.9. The comparison between experimental and simulation mean NH_3 mole % values at the outlets [73]

		NH_3 outlet mole %	*Error %*
Run 1 (basis)	Experiment	8.71	-
	CFD simulation	8.79	0.92
Run 2 (validation)	Experiment	8.68	-
	CFD simulation	8.48	–2.30
Run 3 (validation)	Experiment	8.60	-
	CFD simulation	8.57	–0.35

Table 6.10. The comparison between experimental and simulation temperature values measured by the thermocouples [73]

Block	*Unit*	*Run 1, Experiment (basis)*	*Run 1, CFD simulation (basis)*	*Run 2, Experiment (val.)*	*Run 2, CFD simulation (val.)*	*Run 3, Experiment (val.)*	*Run 3, CFD simulation (val.)*
F	°C	424.73	448.90	425.42	453.54	425.79	453.71
E	°C	434.36	450.92	441.21	455.58	436.33	455.78
D	°C	445.50	453.19	451.63	457.78	448.07	458.03
C	°C	454.52	455.43	457.60	460.14	457.50	460.43
B	°C	456.15	457.24	463.21	462.07	460.08	462.40
A	°C	456.82	457.03	464.17	461.93	461.54	462.26
Bottom inlet	°C	443.77	450.60	453.33	455.60	448.99	455.86

Table 6.11. The comparison between experimental and simulation temperature values differences measured by the thermocouples [73]

Block temperature	*Run 1 (basis) error %*	*Run 2 (val.) error %*	*Run 3 (val.) error %*
F	5.69	6.61	6.56
E	3.82	3.26	4.46
D	1.71	1.36	2.22
C	0.18	0.55	0.64
B	0.21	−0.25	0.50
A	−0.01	−0.48	0.16
Bottom inlet	1.63	0.50	1.53

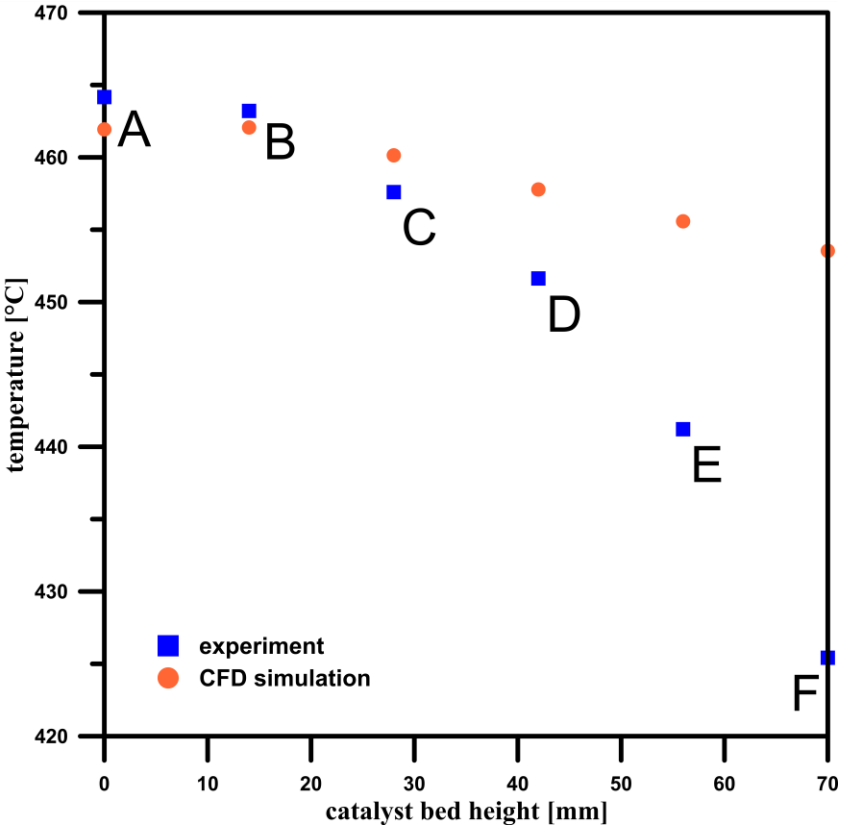

(a)

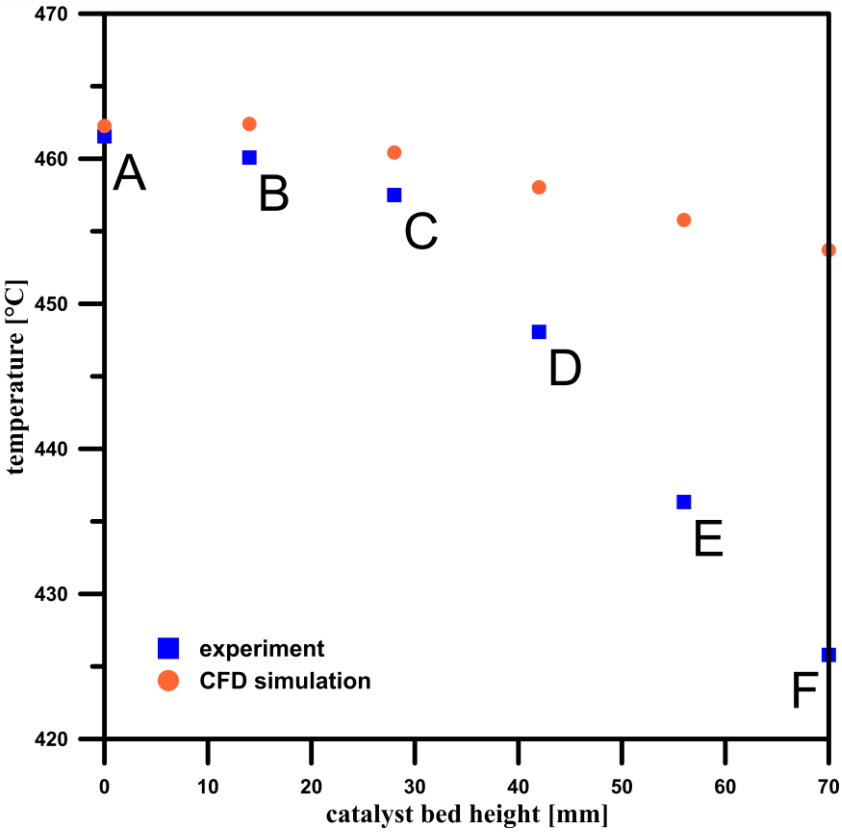

(b)

Figure 6.16. Comparison of the experimental and calculated temperature profiles along the catalyst beds' height for validation cases: "Run 2" (a) and "Run 3" (b) [73]

The simulation results are in good agreement with the experimental data. The maximum differences between outlet ammonia mole fractions do not exceed 2.3%. The temperature errors are slightly larger; however, the difference is no higher than 6.61%, which still matches the experiments well. In validation runs, error trends in the temperature are similar to those in "Run 1", which confirms the excellent simulations' repeatability. Minor and similar errors between "blind" cases with two different reactors ("Micro 1" and "Micro 2") also signify the excellent convergence of the results.

6.9. Conclusions

The CFD model of the pilot-scale ammonia synthesis reactor calculates velocity, reaction rate, concentration, temperature and pressure profiles. This allows for relatively easy identifying areas, such as zones with high or low reaction rates. The obtained model can be a "virtual prototype" for simulating the effects of geometry or parameter changes in the process.

Three experimental runs were conducted on physical ammonia synthesis pilot plant reactors in parallel with CFD modelling. The first was used as a basis of the CFD model, while the other was used as "blind" tests for validation. The simulation results agree with the experimental data. The maximum error between ammonia mole fraction measurements at the outlet is 2.3%. The calculated temperature differences are slightly higher, although they do not exceed 6.61%, indicating that the CFD model is well aligned with the experimental data. In higher parts of the beds, higher temperature differences can be noticed. Still, it can be caused by the simplification of assuming the constant temperature of the heating cables due to the lack of the possibility to measure the generated heat flux or direct temperature of those cables in the experiments. Those differences have a minor influence since the state close to the reaction equilibrium is reached before the gas leaves the catalyst beds. However, for cases where the gas mixture leaves the catalyst beds in a state far from equilibrium, more precise input data from the heating cables may be required to maintain the model's accuracy.

This work proves that computational fluid dynamics is a proper tool for creating a model for steady-state simulation, which allows the study of multiple cases without the necessity of building new prototypes or testing parameter changes in the equipment. Using this model to conduct the time-dependent simulation should be considered as the next step in the potential further validation of this model.

It should be noted that this model has excellent potential for simulating and validating numerical models of pilot-scale ammonia synthesis reactors. However, using this model to simulate cases with significant parameter or geometry differences, such as full-scale industrial reactors, may require additional modifications and validation with proper experimental data.

7. Industrial ammonia oxidation – CFD modelling using detailed kinetic surface reaction model

The Ostwald Process is an effective industrial large-scale nitrogen oxide production method widely used worldwide [8,17,19,20,22,57]. The principles, implementation and issues of the industrial ammonia oxidation are described in Section 3.2.

This section investigates this process, emphasising the influence of the critical parameters such as reaction rates, selectivity, concentration and process efficiency. In the Ostwald Process, ammonia is oxidised to ammonia oxide on the solid catalyst, typically made of 95% platinum and 5% rhodium alloy, to maximise the NO conversion rate and minimise the catalyst loss [19,20,74]. However, this work considered the catalyst pure platinum since it uses the Kraehnert and Baerns [4] surface kinetic model designed for pure platinum gauze. Nevertheless, this kinetic model is accurate and widely used in the literature [8,22,43,44]. This section was made based on the results presented in the manuscript "Study of the Ammonia Oxidation Process on Platinum Gauze and Catalyst Degradation Phenomenon – CFD Simulation with Surface Reaction Kinetics and Catalyst Entrained Particles Motion and Deposition Tracking" [75], which was a coherent part of this PhD project. This section also used the catalyst gauze geometry from the author's previous publication: "Computational Fluid Dynamics of Influence of Process Parameters and the Geometry of Catalyst Wires on the Ammonia Oxidation Process and Degradation of the Catalyst Gauze" [74].

7.1. Geometry

In industrial ammonia burners, the typical catalyst geometry is woven gauze with 1024 meshes per cm^2 and a wire diameter of 0.06 mm [19,20,44]. Catalyst gauzes with thicker diameters of 0.076 mm are also present in modern industry, especially in high-pressure burners [19,20]. In this work, the 3-layer gauze was modelled as a 3D CAD geometry. The first and third layers have the same layout, and the second layer is shifted in two axes by half of the mesh size. The model was simplified to nine meshes, and boundary wires of the first and third layers were cut in their symmetry planes to minimise the simplification error. Figure 7.1 shows the catalyst mesh's dimensions, and Figure 7.2 presents its visualisation.

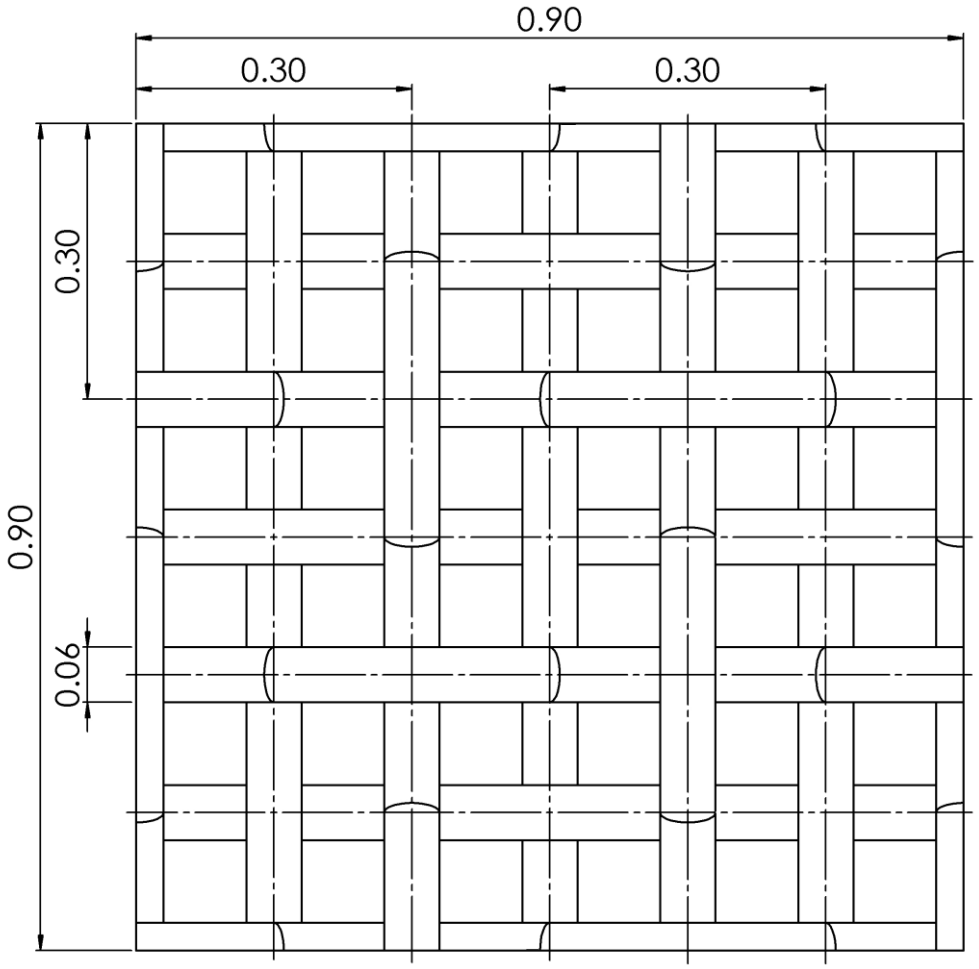

Figure 7.1. Dimensions (in millimetres) of the catalyst gauze [74,75]

(a) (b)

Figure 7.2. Catalyst gauze's model visualisation [74,75]

7.2. Computational setup

The computational domain is a clipping of the ammonia burner containing the catalyst gauze of 3 x 3 meshes, and it is presented in Figure 7.3.

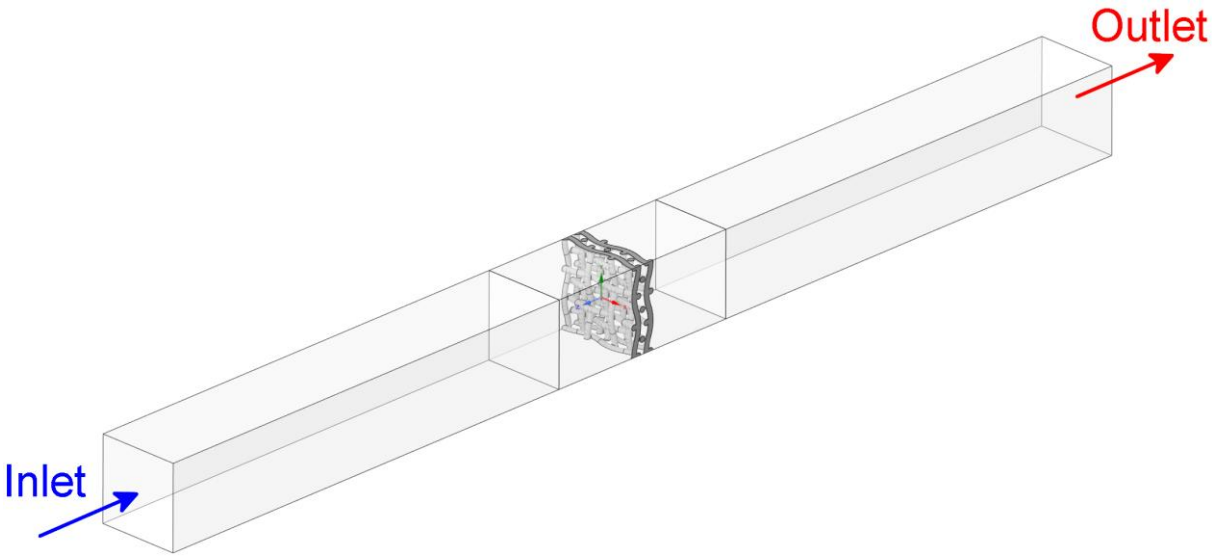

Figure 7.3. Computational domain used for calculations [74,75]

The shape of the domain is a cuboid with gauze in its centre. Its width and height match the gauze model (Figures 7.1 and 7.2), and the distance between the inlet and outlet planes equals 12 mm. The inlet and outlet boundary conditions are at the outermost ends, and the rest of the boundaries are set as symmetry conditions. Walls between solid and fluid phases are set as stationary walls without slip. Since heat transfer is critical in the investigated process, both fluid and solid bodies are meshed, and the coupled fluid-solid thermal conditions are used. The simulations did not use heat radiation modelling since, according to the literature, its influence is negligible [22,44].

The computational mesh was generated in the Ansys Fluent meshing module for both fluid and solid phases. The conformal mesh was applied on the fluid-solid contact wall with a boundary layer in the fluid region adjacent to the gauze's wall. The number of cells in the mesh is approximately 775000, and its type is native polyhedral with inlet and outlet zones generated using the extrude method.

Calculations were performed using Ansys Fluent solver in steady-state mode. The SIMPLE method was used for pressure-velocity coupling, and the Second-Order Upwind discretisation scheme was applied for all variables. Since expected wall temperature gradients are relatively

high, the SST k-ω turbulence model was chosen for calculations. The advantages of turbulent models in the modelling of ammonia oxidations are also reported by Wiser [22].

7.3. Boundary conditions

Ammonia oxidation takes place in the converter called ammonia burners. In the fertiliser industry, three types of burners are most commonly used, distinguished by operating pressure: low (1–2 bar), medium (3–7 bar), and high (>8 bar) pressure types [19]. The investigated reactor is the typical medium-pressure ammonia burner. The operating conditions of the investigated ammonia burner are listed in Table 7.1, and they are used as default boundary conditions in this work if not stated otherwise.

Table 7.1. Typical operating parameters of medium-pressure ammonia burners [75]

Parameter	*Unit*	*Value*	*Source*
contact time	ms	1	[19,44]
gas inlet temperature	°C	150	[8]
operating pressure	bar	5	[8,19]
inlet NH_3 mole fraction	-	0.1	[8]
inlet O_2 mole fraction	-	0.189	[8]
inlet N_2 mole fraction	-	0.711	[8]

This work investigated cases with different contact times and temperatures (ranges listed in Table 7.2) to obtain various results, such as selectivity, reaction rate and efficiency. Different values of contact times were obtained by assigning corresponding inlet gas velocities, listed in Table 7.5 in Section 7.5.

Table 7.2. Investigated parameters' ranges [75]

Parameter	*Unit*	*Range*
contact time	ms	1–0.05
gas inlet velocity (calculated from contact time)	m s^{-1}	0.221–4.416
gas inlet temperature	°C	100–250

7.4. Reaction kinetics

The kinetics of the ammonia oxidation reaction proceeds as follows:

$$4\ NH_3 + 5\ O_2 \rightarrow 4\ NO + 6\ H_2O$$

However, this is merely a stoichiometric simplification, not considering the numerous surface-based reactions in this process. This work uses the surface microkinetic model developed by Kraehnert and Baerns [38] for ammonia oxidation on the pure platinum catalyst. This model is relatively accurate and widely used in the literature [8,22,44,76]. In their model, Kraehnert and Baerns [38] elaborated ten surface reactions with two adsorption sites: "a" – hollow site (with adsorbed nitrogen and oxygen) and "b" – top site (with adsorbed ammonia), listed in Table 7.3.

Table 7.3. Reactions of the microkinetic surface model developed by Kraehnert and Baerns [38] and reported by Haas [8] for the ammonia oxidation process on platinum catalyst [75]

R1	$NH_3 + b \rightarrow NH_3\text{-}b$
R2	$NH_3\text{-}b \rightarrow NH_3 + b$
R3	$O_2 + 2\ a \rightarrow 2\ O\text{-}a$
R4	$2\ O\text{-}a \rightarrow O_2 + 2\ a$
R5	$NH_3\text{-}b + 1.5\ O\text{-}a \rightarrow N\text{-}a + 1.5\ H_2O + 0.5\ a + b$
R6	$NO\text{-}a \rightarrow NO + a$
R7	$NO + a \rightarrow NO\text{-}a$
R8	$2\ N\text{-}a \rightarrow N_2 + 2\ a$
R9	$N\text{-}a + O\text{-}a \rightarrow NO\text{-}a + a$
R10	$NO\text{-}a + N\text{-}a \rightarrow N_2O + 2\ a$

According to Haas [8], the rates of the individual elementary steps can be calculated from the following expression:

$$r_j = k_{0,j} T^b \exp\left(-\frac{E_{a,j}}{RT}\right) \prod_i c_i^{|v_{ij}|} \prod_i \theta_i^{|v_{ij}|} \tag{116}$$

where v_{ij} is the stoichiometric coefficient of species i in reaction j, c_i is gas species concentration at the catalyst wall, θ_i is the surface coverage of adsorbed species, $k_{0,j}$ is the pre-

exponential factor, $E_{a,j}$ is the activation energy, and b is the temperature exponent. The kinetic constants used in Equation (116) are listed in Table 7.4.

Table 7.4. Kinetic constants used in Kraehnert and Baerns [38] ammonia oxidation kinetics, reported by Haas [8,75]

Reaction number	*Pre-exponential factor (k_0) [units vary*]*	*Activation Energy (E_a) [kJ mol^{-1}]*	*Temperature exponent (b) [-]*
R1	$1.95 \cdot 10^{2}$	0.0	1
R2	$5.45 \cdot 10^{9}$	60.9	0
R3	$8.99 \cdot 10^{1}$	0.0	1
R4	$9.37 \cdot 10^{8}$	181.0	0
R5	$1.72 \cdot 10^{15}$	99.5	0
R6	$8.87 \cdot 10^{16}$	155.0	0
R7	$8.84 \cdot 10^{6}$	63.5	1
R8	$2.56 \cdot 10^{17}$	139.0	0
R9	$1.93 \cdot 10^{16}$	135.0	0
R10	$4.00 \cdot 10^{17}$	155.0	0

*k_0 has units of [m^3 s^{-1} mol^{-1} K^{-1}] for R1, R3, R7 and [s^{-1}] for R2, R4, R5, R6, R8, R9, R10

The overall reaction rates of all surface-adsorbed and gas-phase species can be written as a sum of every individual reaction, as shown in Equation (117) [8].

$$R_i = \Gamma F \sum_j v_{ij} r_j \tag{117}$$

where Γ is the site density with a value of $2.71 \cdot 10^{-5}$ mol m^{-2} [8], and F is a surface enlargement factor with a value of 10 [8]. The surface enlargement factor is required due to the differences between the geometrical and actual surface area of platinum wires, which increase during the process in the industry due to the formation of cauliflower structures [8]. The kinetic model was implemented to Ansys Fluent using a user-defined function (UDF) for surface reactions.

7.5. Contact time

Contact time is a parameter that has an essential role in the ammonia oxidation process. Its values should be as low as possible to minimise catalyst wires' degradation. However, short contact times decrease the efficiency of the process and increase the selectivity of undesirable N_2O production [8,22].

As a reference parameter for the results, this work used mean contact time, which can be written as follows:

$$t = \frac{H}{u} \tag{118}$$

where u is the average velocity between wires, and H is the catalyst gauze height. Typical ammonia burners are designed for a contact time of 1 ms, although shorter contact times are also used in the industry [8,17,22]. Nilsen et al. [46] reported that surface reactions in the Ostwald Process are controlled by active centres and limited by mass transport; hence, the lowest required contact time is 0.1 ms. In this work, calculations were performed for 13 different contact times, presented with their corresponding gas inlet velocities in Table 7.5. It can be noted that the lowest contact time value (0.05 ms) is below the minimal value reported by Nilsen et al. [46]; still, it was used as a reference to illustrate the trends in obtained results.

Table 7.5. Investigated contact times with corresponding inlet velocities [75]

Contact time [ms]	0.05	0.1	0.15	0.2	0.25	0.3	0.4	0.5	0.6	0.7	0.8	0.9	1
Inlet velocity [m s^{-1}]	4.416	2.208	1.472	1.104	0.883	0.736	0.552	0.442	0.368	0.315	0.276	0.245	0.221

7.6. Selectivity

Selectivity is a parameter that measures the percentage of key substrate converted to a specific product. In the case of surface reactions, it can be described as a local value on the catalyst surface and the net value of the gas leaving the system. The local selectivity of species *i* on the catalyst surface can be calculated from the following expression [8]:

$$S_i = 100 \cdot v_i^N \frac{R_i}{R_{NH_3}} \tag{119}$$

where R_i is a production rate of species i, v_i^N is number of nitrogen atoms in the molecule i, and R_{NH_3} is the consumption rate of ammonia.

The net selectivity of products at the outlet of the computational domain is calculated from Equation (120).

$$S_{net_i} = 100 \cdot v_i^N \frac{\dot{n}_i}{\dot{n}_{NH_{3_{in}}} - \dot{n}_{NH_{3_{out}}}} \tag{120}$$

where $\dot{n}_{NH_{3_{in}}}$ and $\dot{n}_{NH_{3_{out}}}$ are mole streams of NH_3 at the inlet and the outlet respectively, and $\dot{n}_i$ is a mole stream of species i at the domain's outlet.

7.7. Efficiency

Efficiency is a parameter similar to net selectivity, considering the amount of unreacted substrate. Maximising the desired product's efficiency is always the crucial process aspect. The product efficiency of the ammonia oxidation can be calculated from the following equation:

$$W_i = \alpha_{NH_3} \cdot S_{net_i} \tag{121}$$

where S_{net_i} is a net selectivity of product species i conversion, and α_{NH_3} is a degree of NH_3 conversion (percentage of inlet amount of NH_3 consumed during the process), which was calculated from the following expression:

$$\alpha_{NH_3} = 100 \cdot \frac{\dot{n}_{NH_{3_{in}}} - \dot{n}_{NH_{3_{out}}}}{\dot{n}_{NH_{3_{in}}}} \tag{122}$$

where $\dot{n}_{NH_{3_{in}}}$ and $\dot{n}_{NH_{3_{out}}}$ are mole streams of ammonia at the inlet and outlet of the system respectively.

7.8. Results

This section aimed to determine the influence of critical parameters such as contact time and inlet temperature on the reaction rates, selectivity and product efficiencies. Volumetric profiles of velocity magnitude, temperature and concentration were obtained using the CFD model. The simulations also allowed to investigate crucial surface contours of local reaction rates, selectivity on gauze surface, and the net efficiency of NO and N_2O production.

7.8.1. Flow field and velocity contours in the catalyst gauze's vicinity

Velocity magnitude is an essential parameter in every CFD simulation. They directly influence heat and mass transfer, critical phenomena in cases considering surface reactions. Fluid flow in the catalyst wires' vicinity delivers the reactants and collects the products, determining the contact time between the gas phase and the catalyst surface. Figure 7.4 compares the velocity profiles for the cases using 1 ms and 0.2 ms contact time values.

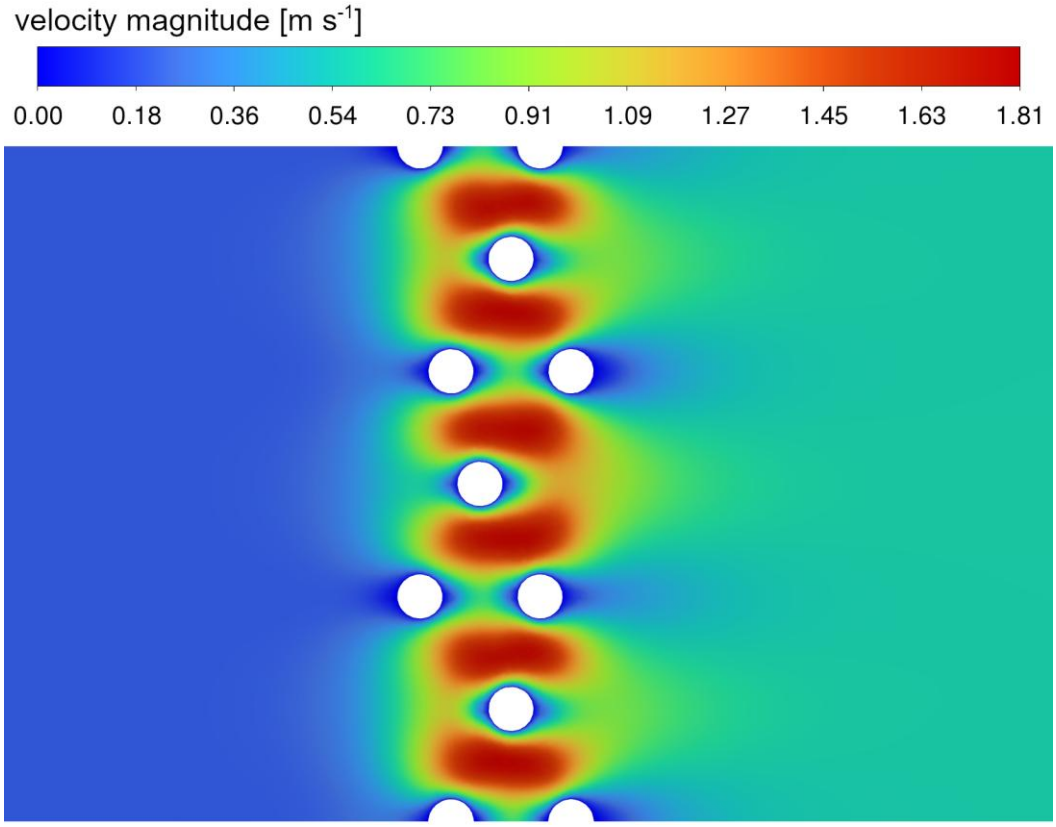

(a)

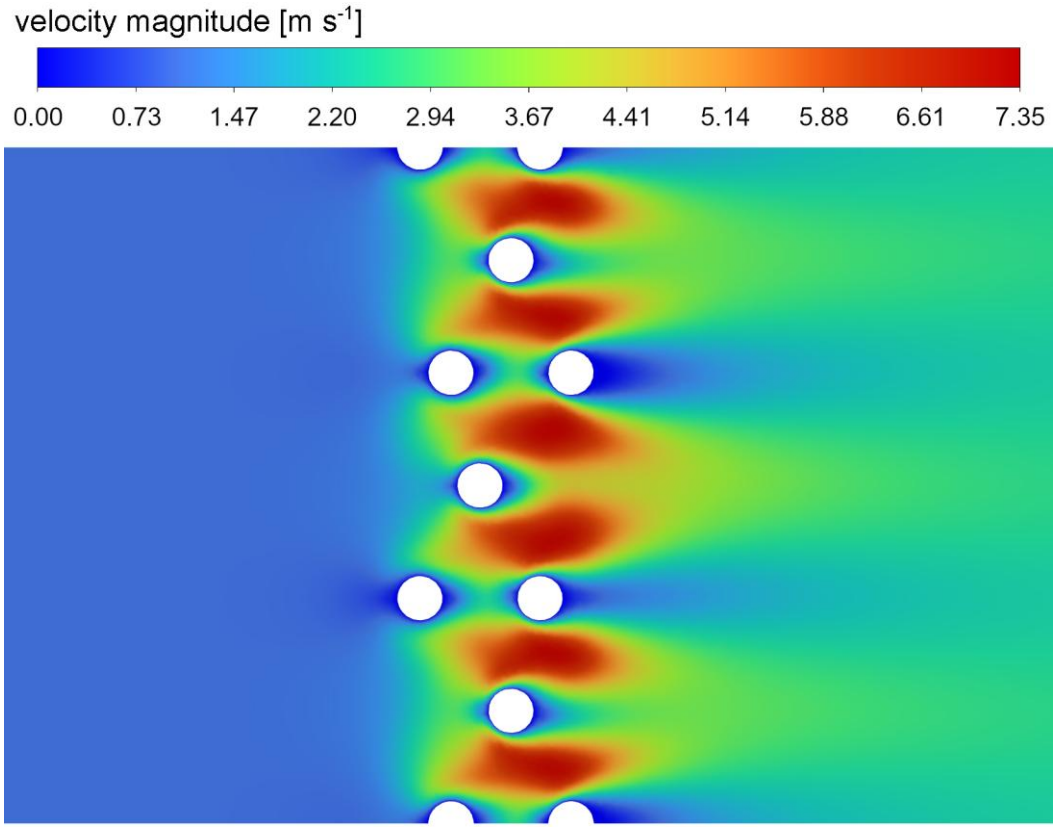

(b)

Figure 7.4. Velocity magnitude contours [m s^{-1}] for 1 ms (a) and 0.2 ms (b) contact times in the cross-section of the investigated domain (inlet temperature 150 °C) [75]

In the ammonia oxidation study, contact time is a crucial parameter due to its influence on numerous parallel and subsequent reactions. The velocity is increased in the catalyst gauze region, which is caused by the reduced flow clearance, and this difference is more visible for shorter contact times. This phenomenon affects heat and mass transfer and, consequently, reaction rates and product selectivity, which are investigated further in the following sections. The velocity field is also suitable for studying stagnation zones, as described in Section 8.2.1.

7.8.2. Reaction rate – surface-averaged trends and surface gradients

Plotting contours of experimentally unmeasurable parameters is an exceptional advantage of CFD modelling. Direct insight into surface reaction rate profiles provides a better understanding of the process. This dissertation implemented the detailed kinetics with ten surface reactions (described in Section 7.4) into the CFD simulation.

Figure 7.5 shows surface-averaged reaction rates in relation to contact times for each reaction and gauze layer.

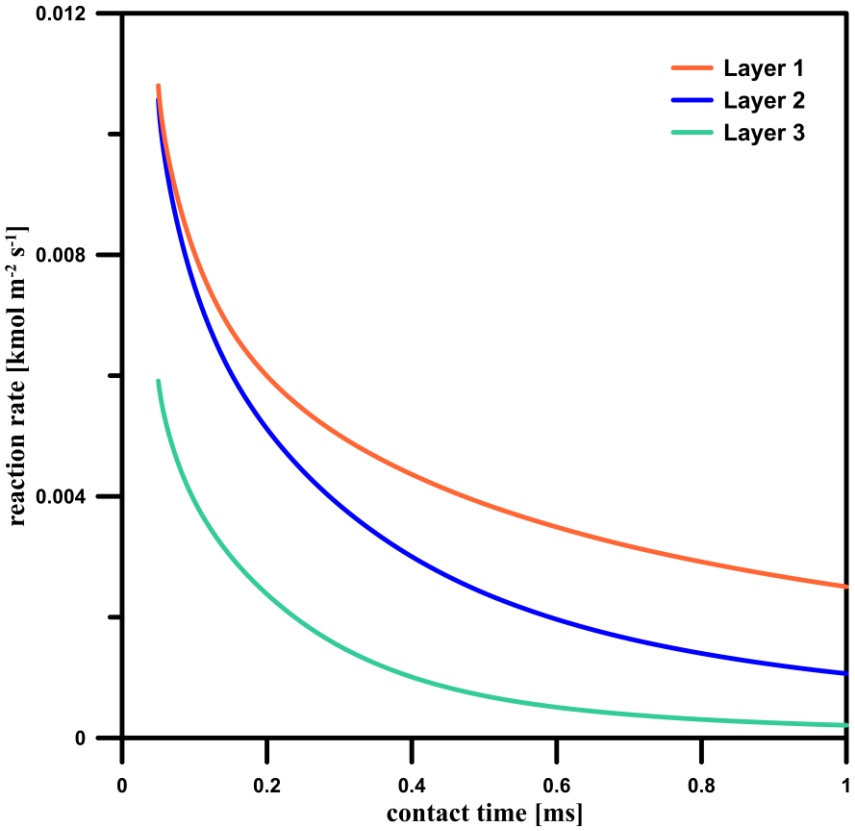

R1

Figure 7.5. Cont.

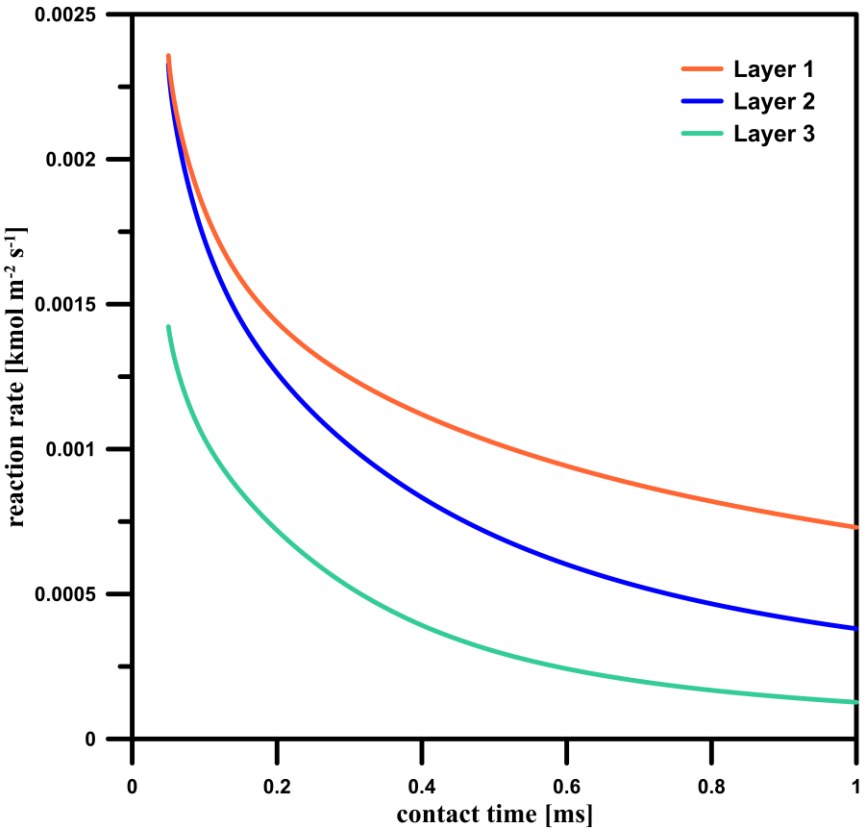

R2

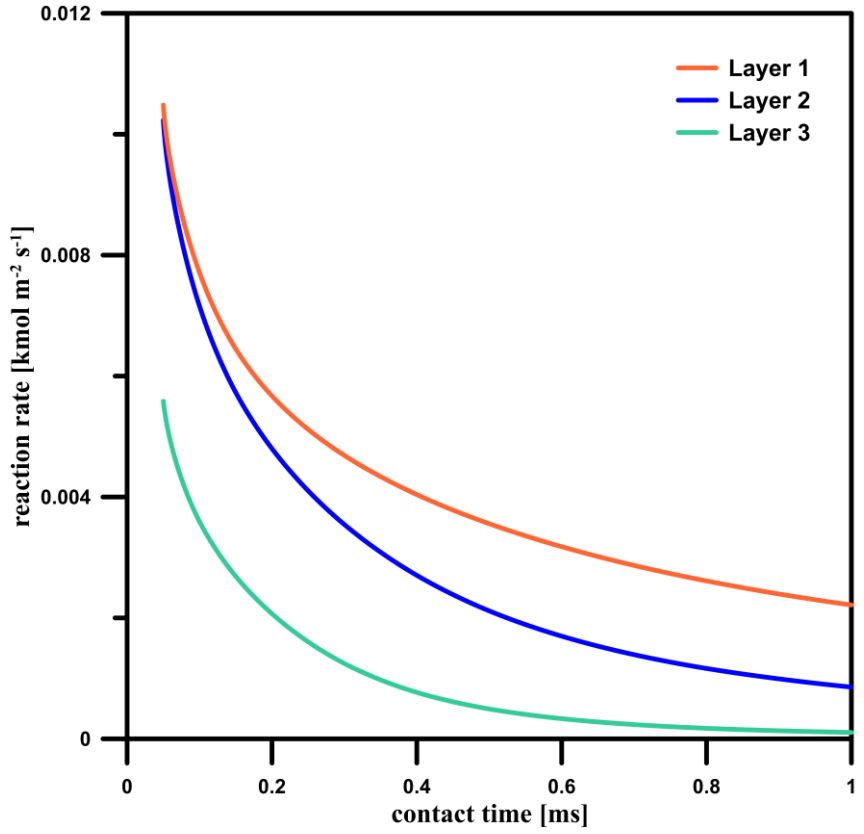

R3

Figure 7.5. Cont.

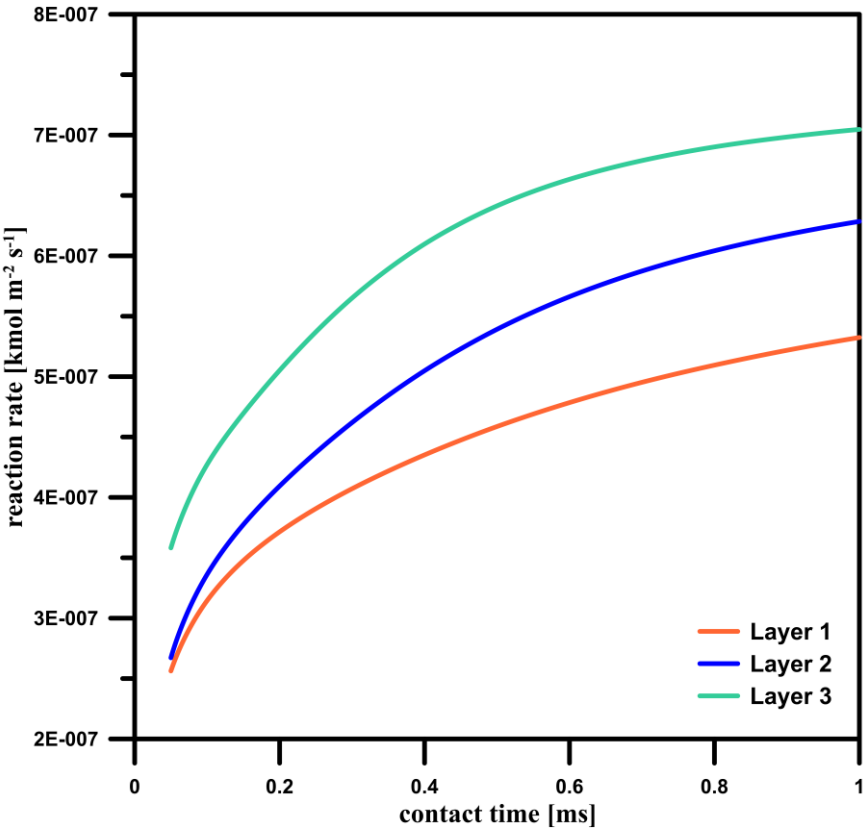

R4

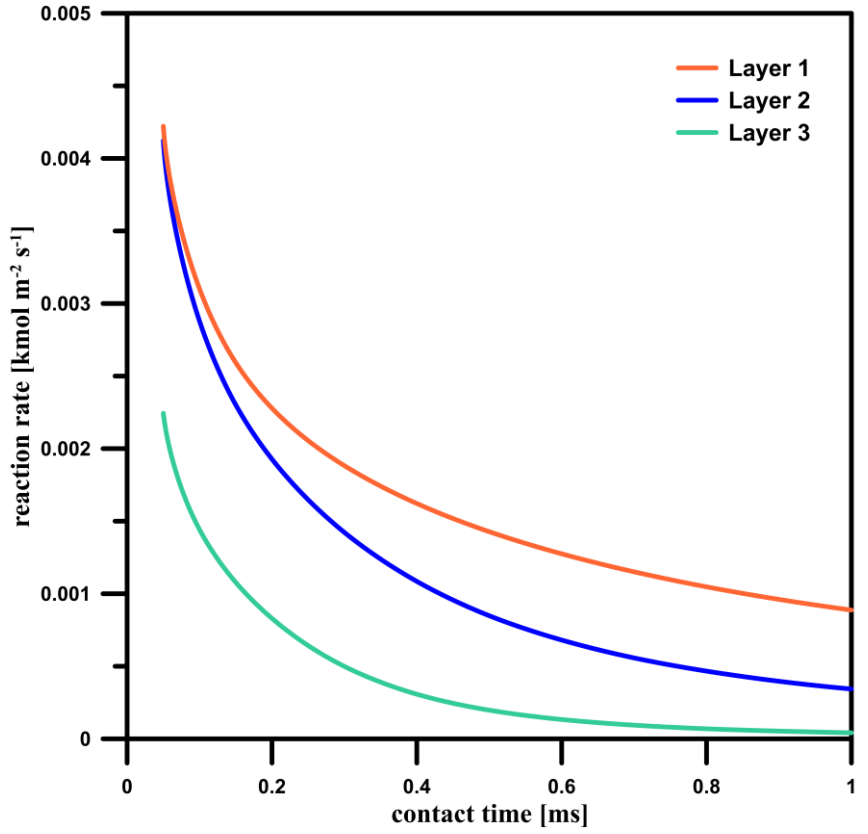

R5

Figure 7.5. Cont.

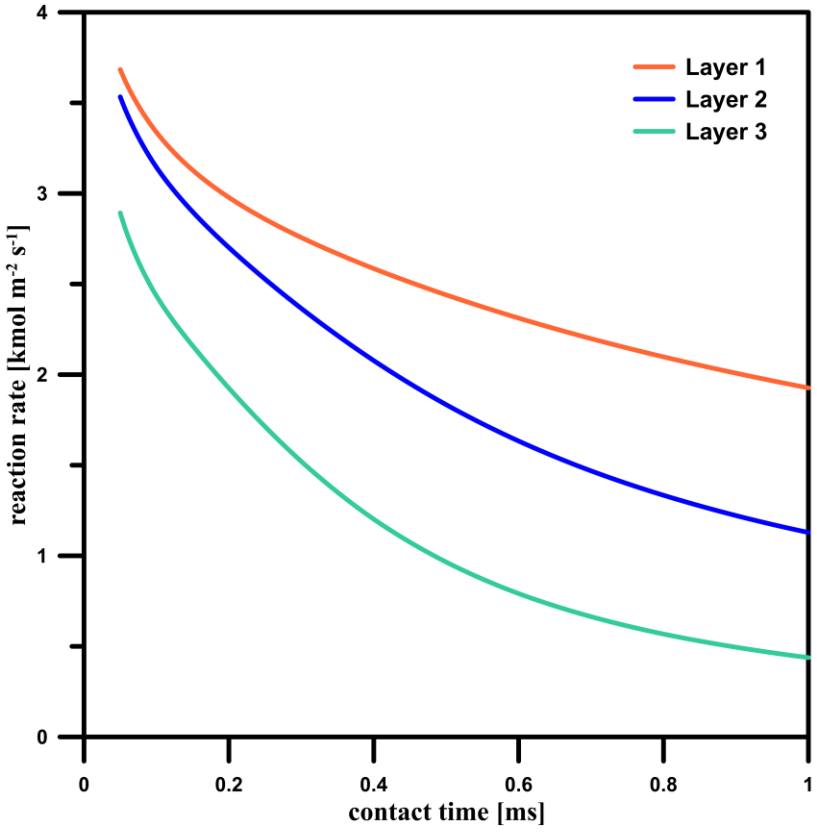

R6

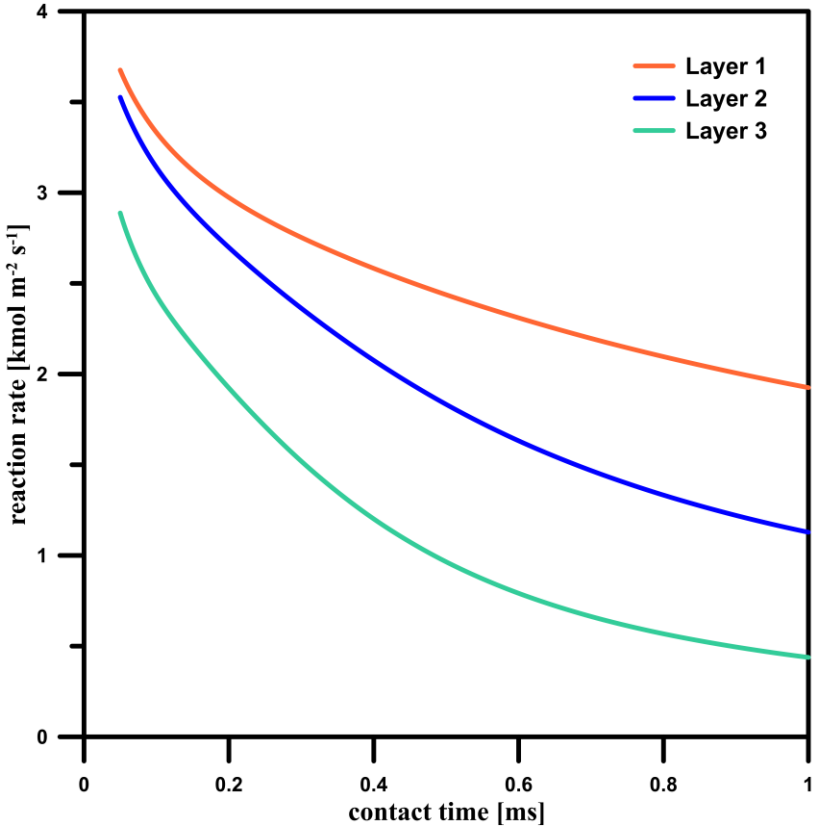

R7

Figure 7.5. Cont.

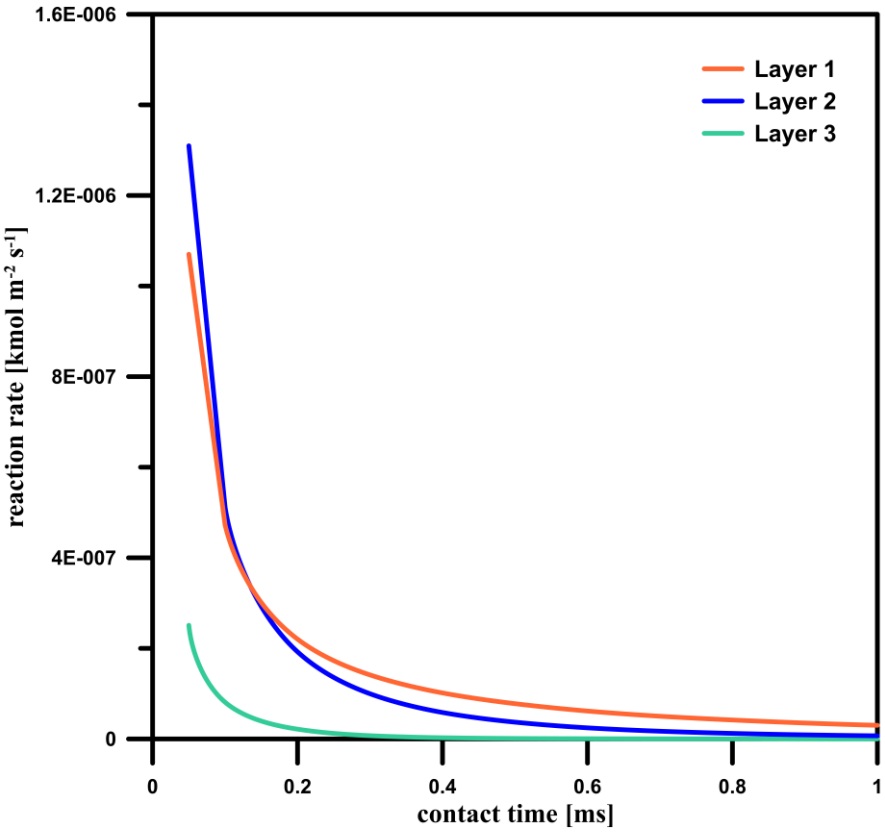

R8

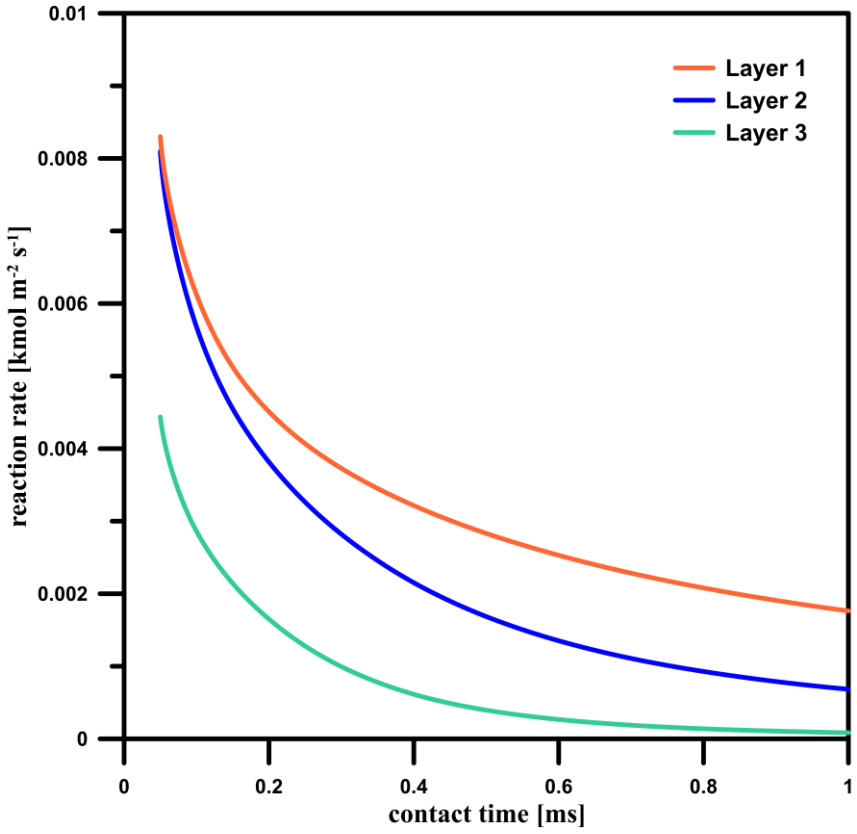

R9

Figure 7.5. Cont.

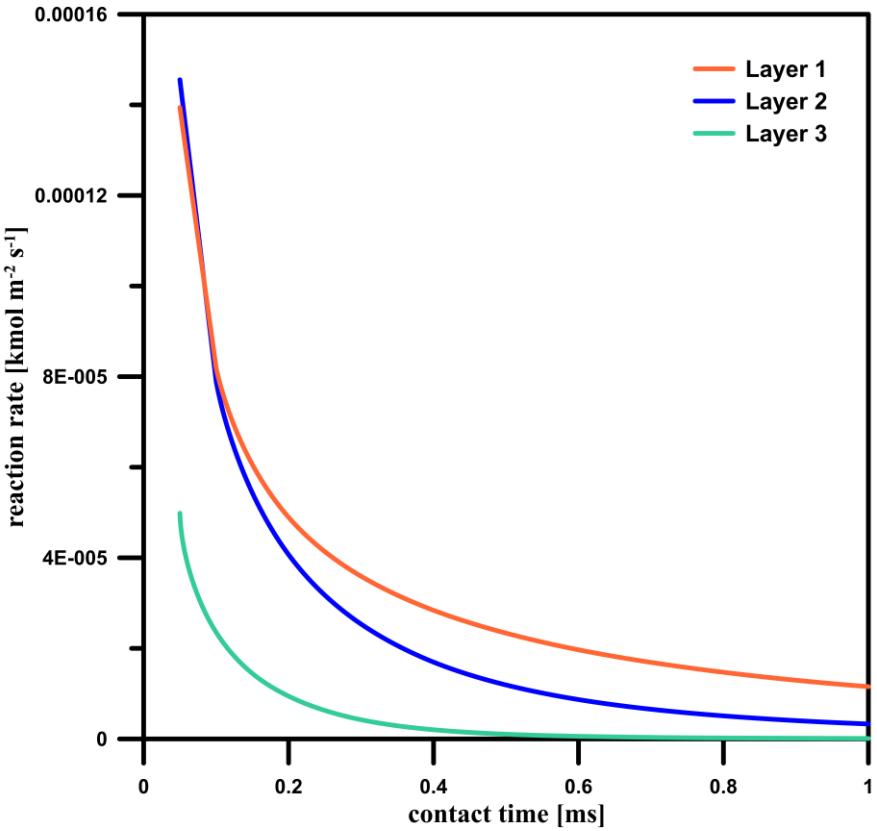

Figure 7.5. Surface-averaged reaction rates as functions of contact time on different catalyst gauze layers (inlet temperature 150°C) [75]

As presented in Figure 7.5, most of the reaction rates slow down on subsequent layers. The only case where the trend is the opposite is reaction R4, yet its rate is significantly lower than other reactions. Reactions R6 and R7 demonstrate a few orders of magnitude higher reaction rate values than the rest. However, these reactions counteract each other, basically representing a single reversible reaction, where NO is a product adsorbing and desorbing from the catalyst surface. R1–R2 (adsorption/desorption of ammonia) and R3–R4 (adsorption/desorption of oxygen) are analogous examples of counteracting reactions in the implemented kinetic model. However, the oxygen desorption rate (R4) is negligibly small compared to its adsorption (R3), indicating that almost no oxygen is desorbed in the process. Figure 7.6 shows ammonia's net adsorption rate and nitrogen oxide's net desorption rate as a function of contact times. It can be noted that both functions are nearly identical, which suggests high NO selectivity. This topic is further investigated in Section 7.8.3.

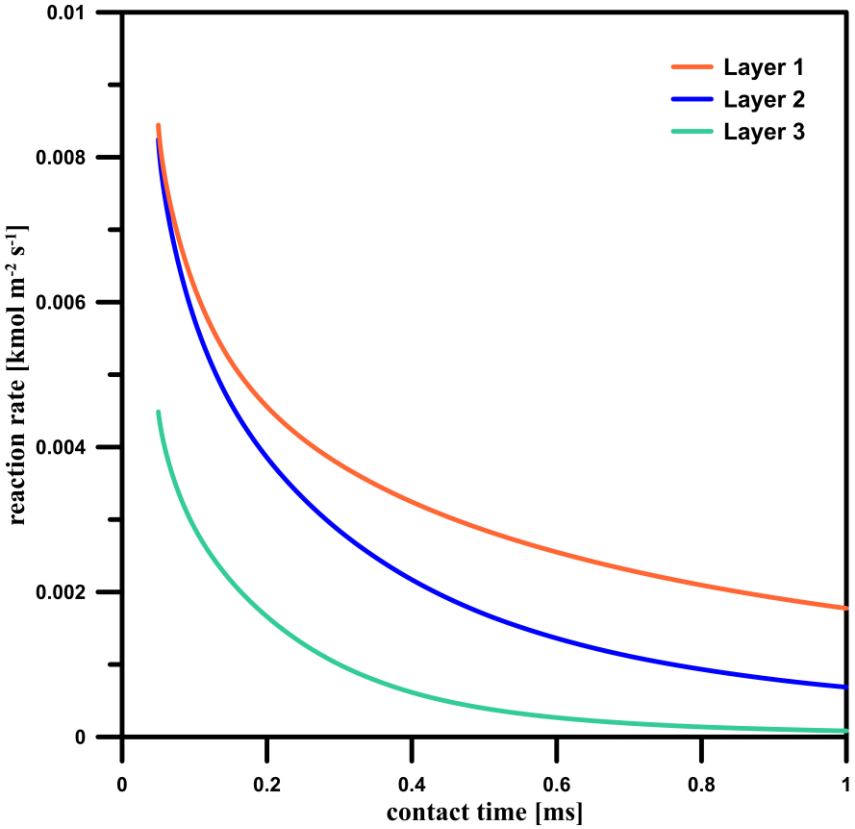

R1–R2

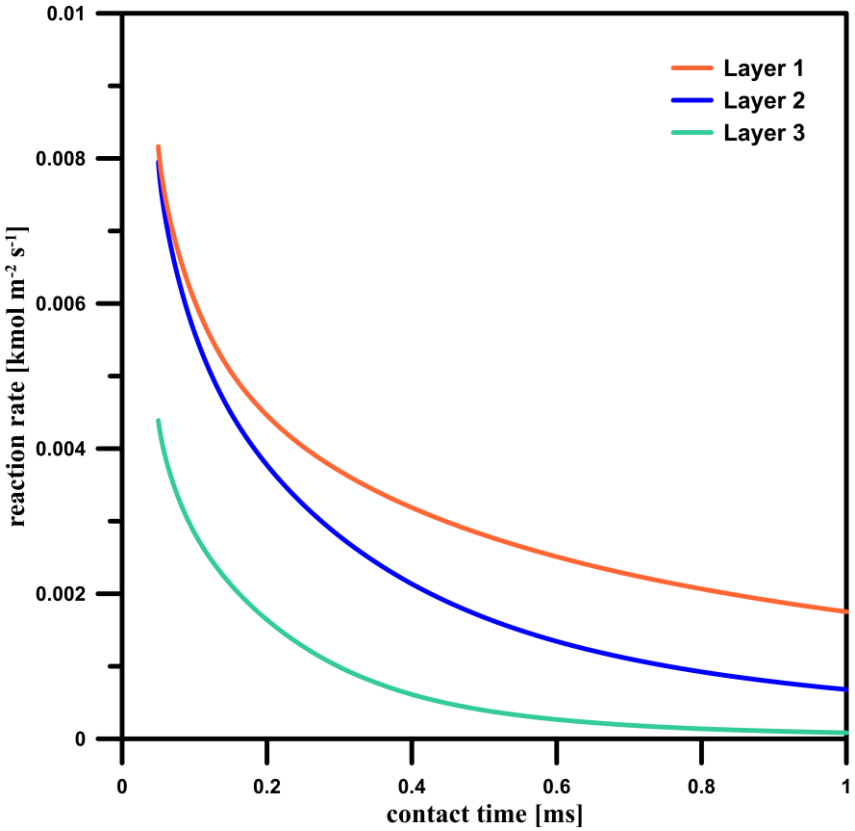

R6–R7

Figure 7.6. Surface-averaged NH_3 net adsorption rate (R1–R2) and NO net desorption rate (R6–R7) as functions of contact time on different catalyst gauze layers (inlet temperature 150°C) [75]

Although Figure 7.5 presents surface-averaged reaction rates, those do not provide information about the gradients of those values within the wire's surfaces. Figure 7.7 shows reaction rate contours plotted on the surface of the first layer of gauze for reactions R1 (adsorption of ammonia), R5 (adsorbed ammonia oxidation), R6 (desorption of NO), and R10 (desorption of N_2O). Analysing those profiles, it can be observed that reaction rate gradients are not uniform and differ for each reaction. This non-uniformity occurs for every reaction on every layer, which is a direct result of the gas flow pattern and formation of stagnation zones, further described in Section 8.2.1.

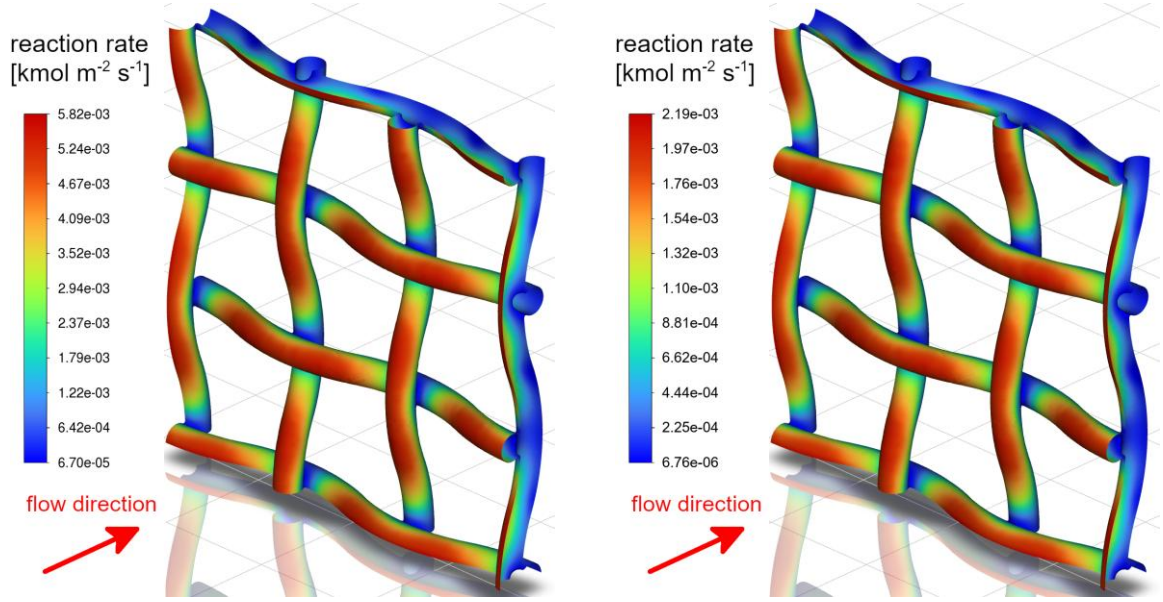

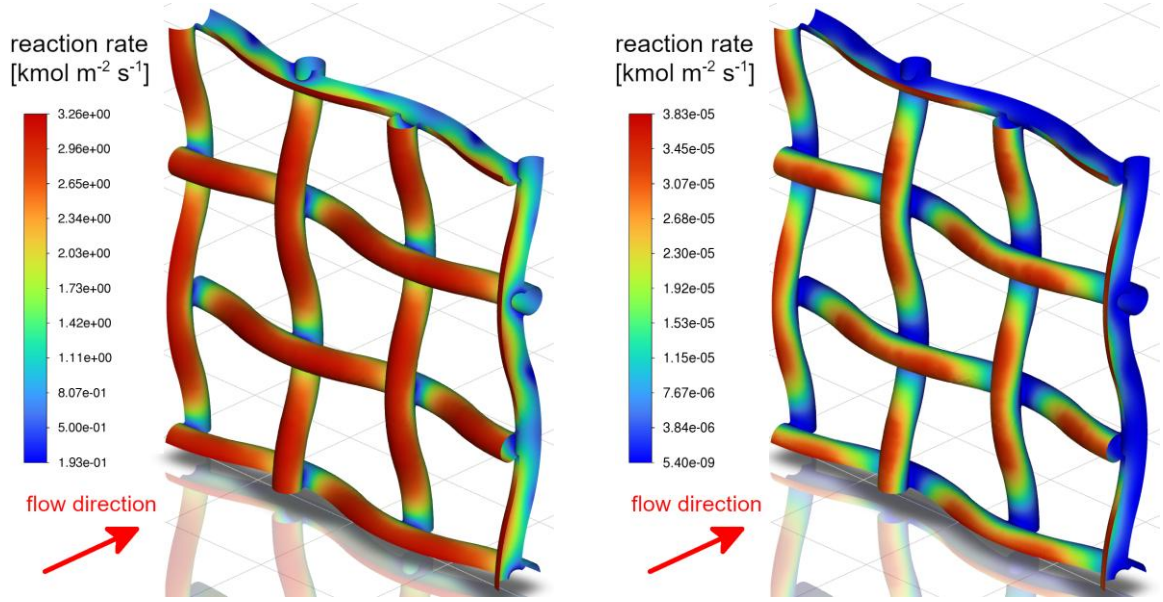

Figure 7.7. Reaction rate contours [kmol m^{-3} s^{-1}] on the surface of the catalyst gauze's first layer for reactions R1, R5, R6 and R10 (contact time 1 ms, inlet temperature 150 °C) [75]

7.8.3. Selectivity – surface-averaged trends and surface gradients

Selectivity is a critical parameter in cases with competing multiple reactions. In ammonia oxidation, it is a percentage of the converted substrate (ammonia) into a specific product. Since maximising the production of desired NO and minimising the conversion of unwanted secondary N_2O is essential for process efficiency, selectivity has a significant role in the Ostwald Process. This work analysed how contact times influence the selectivity of NO and N_2O yielded from different layers of catalyst gauze. Figure 7.8 presents the function of the surface-averaged selectivity of both products. The selectivity of nitrogen is negligible when compared to its other product values since its value did not exceed 0.035% in all investigated cases.

Similarly to the reaction rate, the selectivity can be plotted on the wire's surface as contours. Figures 7.9 and 7.10 show selectivity gradients of NO and N_2O on the catalyst gauze in each layer for a contact time of 1 ms and an inlet gas temperature of 150°C. It can be noted that both products have their selectivity gradients opposite to each other since the selectivity of the N_2 product is negligible. Like reaction rate, selectivity gradients are also highly non-uniform, with the highest values of N_2O selectivity in the locations with the expected lowest contact times. At the third layer, the selectivity of N_2O is much lower, indicating that this secondary product is yielded mainly on the front layers in multi-layered gauze.

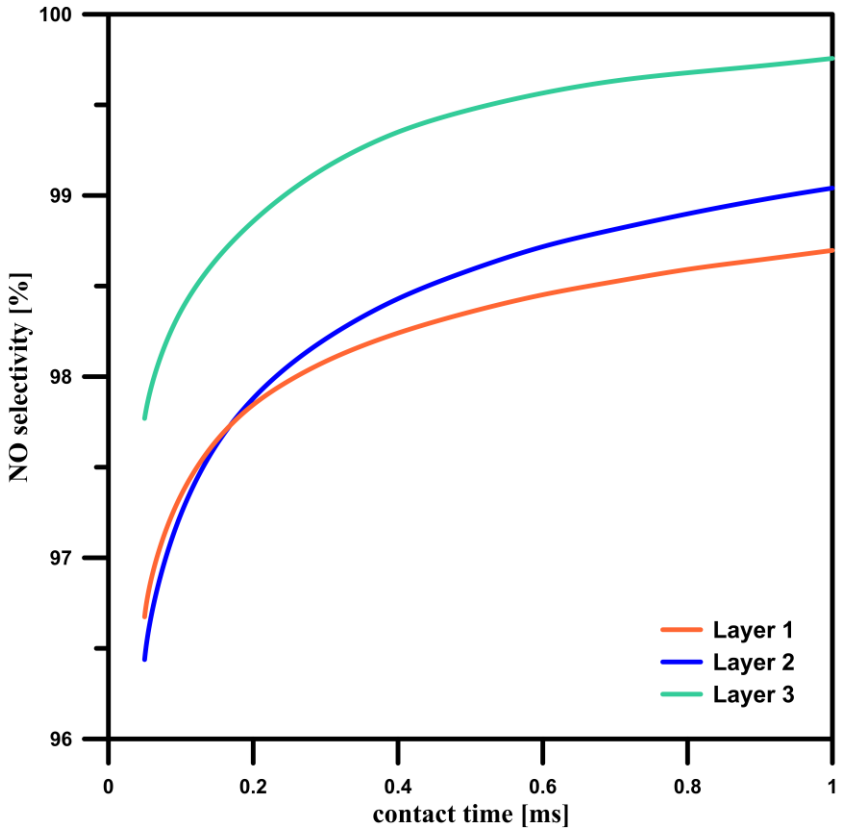

(a)

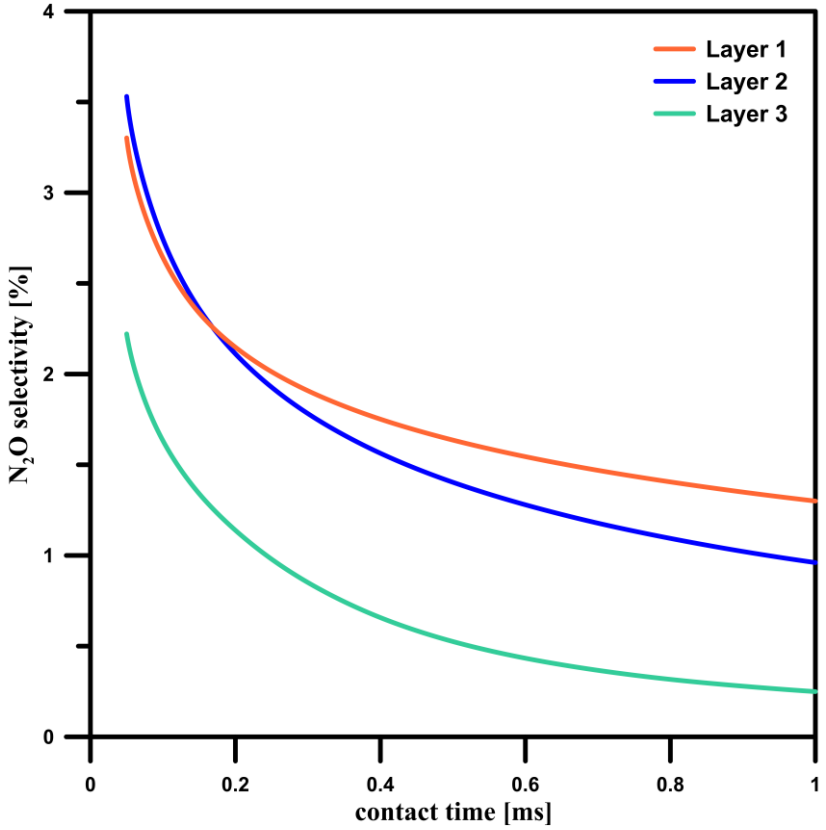

(b)

Figure 7.8. Surface-averaged NO (a) and N_2O (b) selectivity as functions of contact time on different catalyst gauze layers (inlet temperature 150°C) [75]

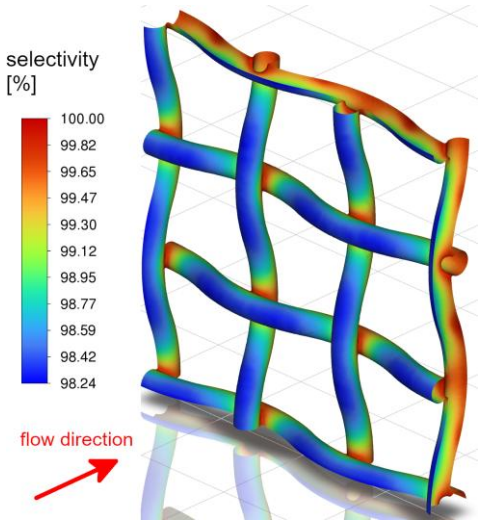

(a) 1st layer

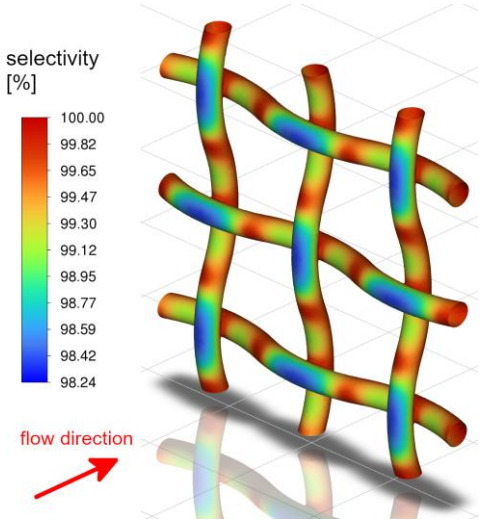

(b) 2nd layer

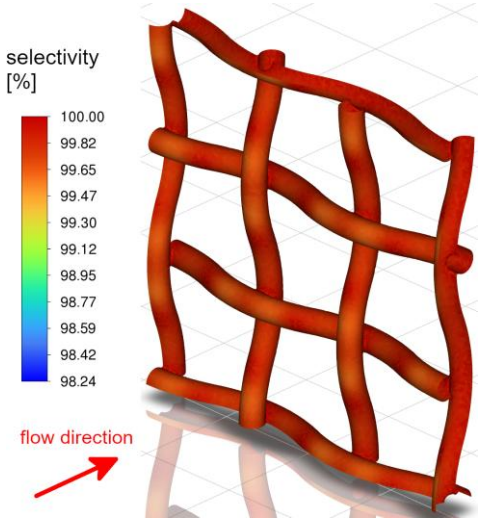

(c) 3rd layer

Figure 7.9. NO selectivity contours [%] on layer 1 (a), layer 2 (b) and layer 3 (c) (contact time 1 ms, inlet temperature 150 °C) [75]

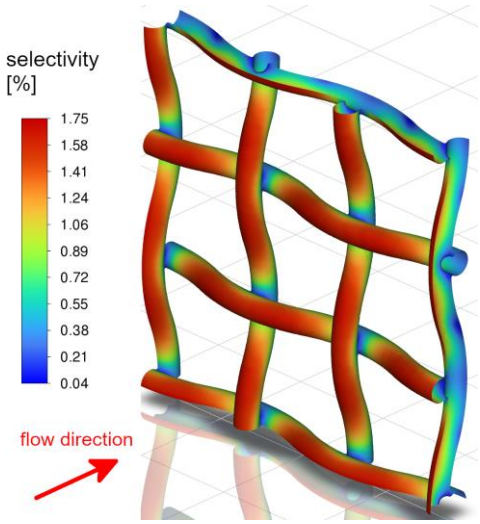

(a) 1st layer

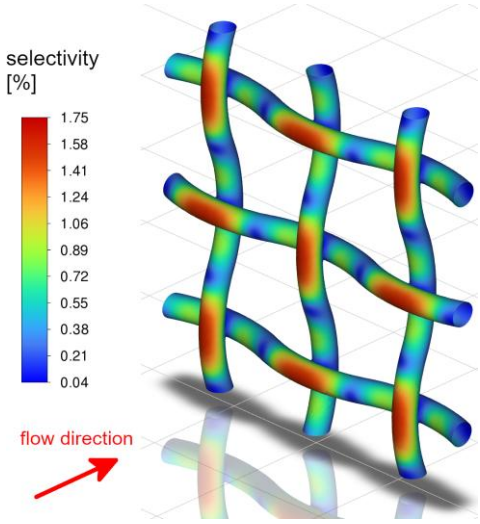

(b) 2nd layer

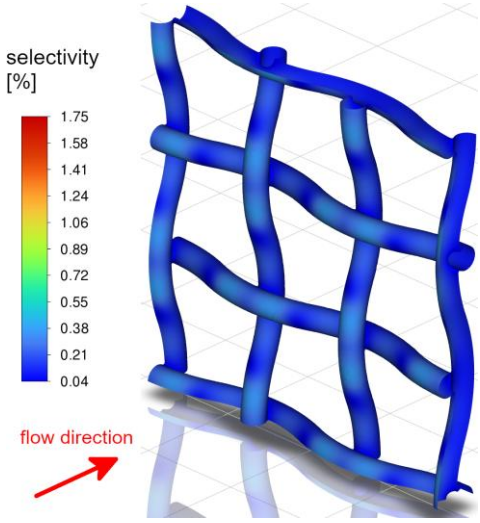

(c) 3rd layer

Figure 7.10. N_2O selectivity contours [%] on layer 1 (a), layer 2 (b) and layer 3 (c) (contact time 1 ms, inlet temperature 150 °C) [75]

7.8.4. Concentration contours in the catalyst gauze's vicinity

Species concentration profiles in the continuous phase directly result from the reaction rates at the catalyst gauze surface. The process efficiency depends on maintaining the highest possible concentration of NO and the lowest fraction of byproducts. Figures 7.11 and 7.12 present the NO and N_2O contour profiles for the cases with a contact time of 1 ms and inlet temperature of 150°C. The nitrogen oxide mole fraction quickly rises close to the catalyst surface. It can be noted that NO production occurs mainly on the first two layers, while the third layer yields only tiny amounts of this product. Those observations align well with the mean net desorption rates on different layers presented in Figure 7.6 (b) for 1 ms contact time.

Figure 7.11 (b) presents the NO mole fraction profiles with clipped range to show the effects of selectivity gradients on the wires' surfaces. The ammonia concentration is highest behind the wires, resulting from slightly longer contact times caused by the small stagnation zones. On the surface of the last layer, the concentration of NO is almost uniform, which is caused by the negligible selectivity of N_2O. Figure 7.12 shows the contours of the N_2O mole fraction. The highest concentration is close to the first two layers, yet the gradient is opposite since the highest fraction of N_2O is in front of the wires of the first layer, where the local contact times reach the lowest values. Also, there is no change in the concentration of N_2O around the third layer, which agrees with the selectivity gradients from the previous section.

Figures 7.13 and 7.14 show the contours of NO and N_2O mole fractions for the contact time of 0.2. Due to the much lower local contact time values, all three layers yield both species. Concentration gradients show the same trends, yet they are significantly larger. The N_2O selectivity is noticeably higher for each layer, and its outlet concentration is higher.

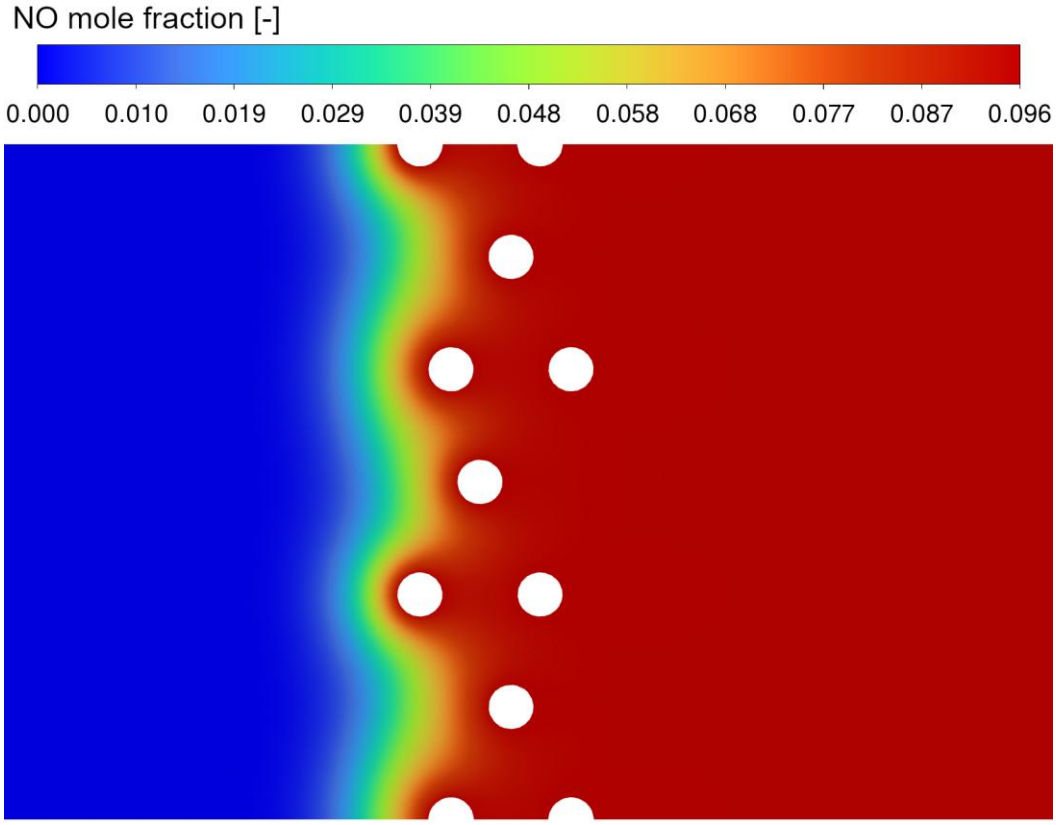

(a)

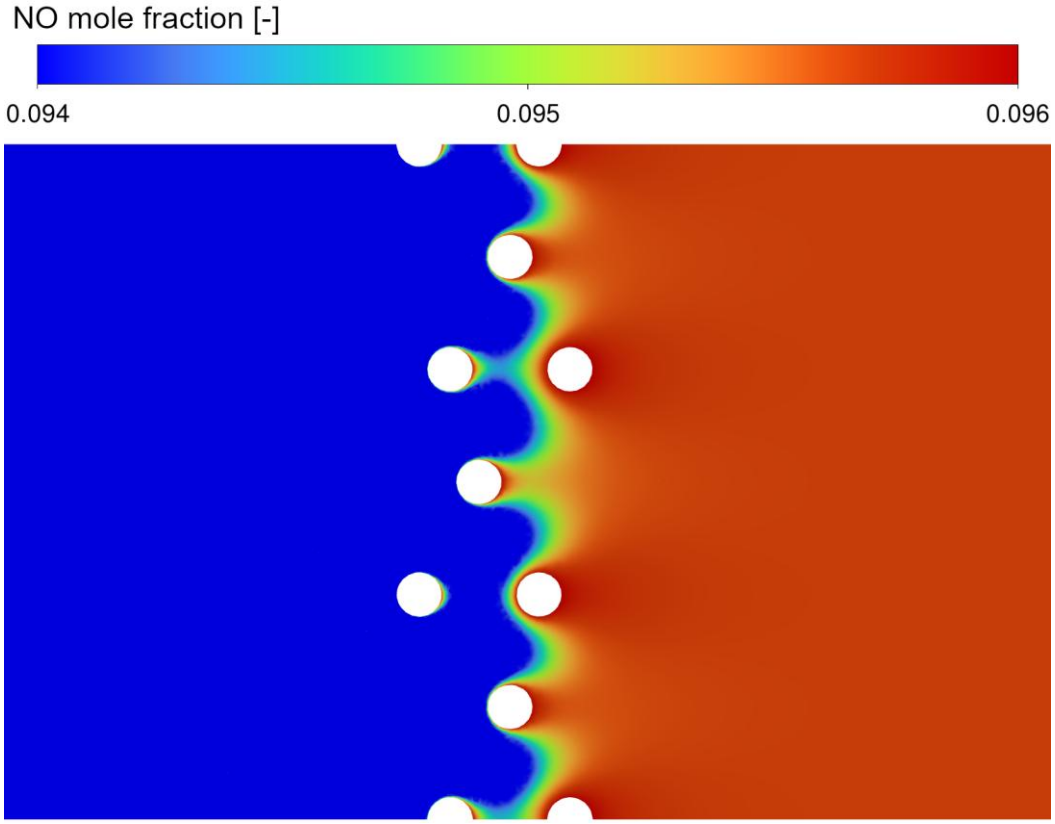

(b)

Figure 7.11. NO mole fractions contours [-] in full range (a) and clipped range (b) in the cross-section of the investigated domain (contact time 1 ms, inlet temperature 150 °C) [75]

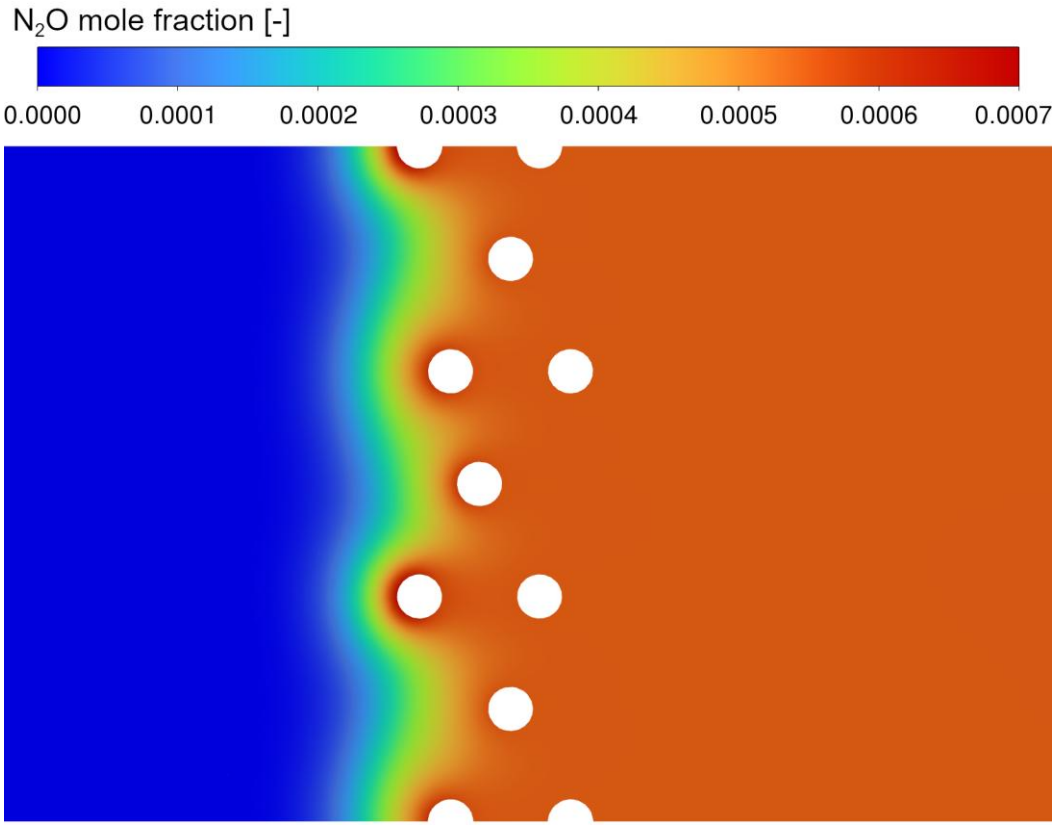

(a)

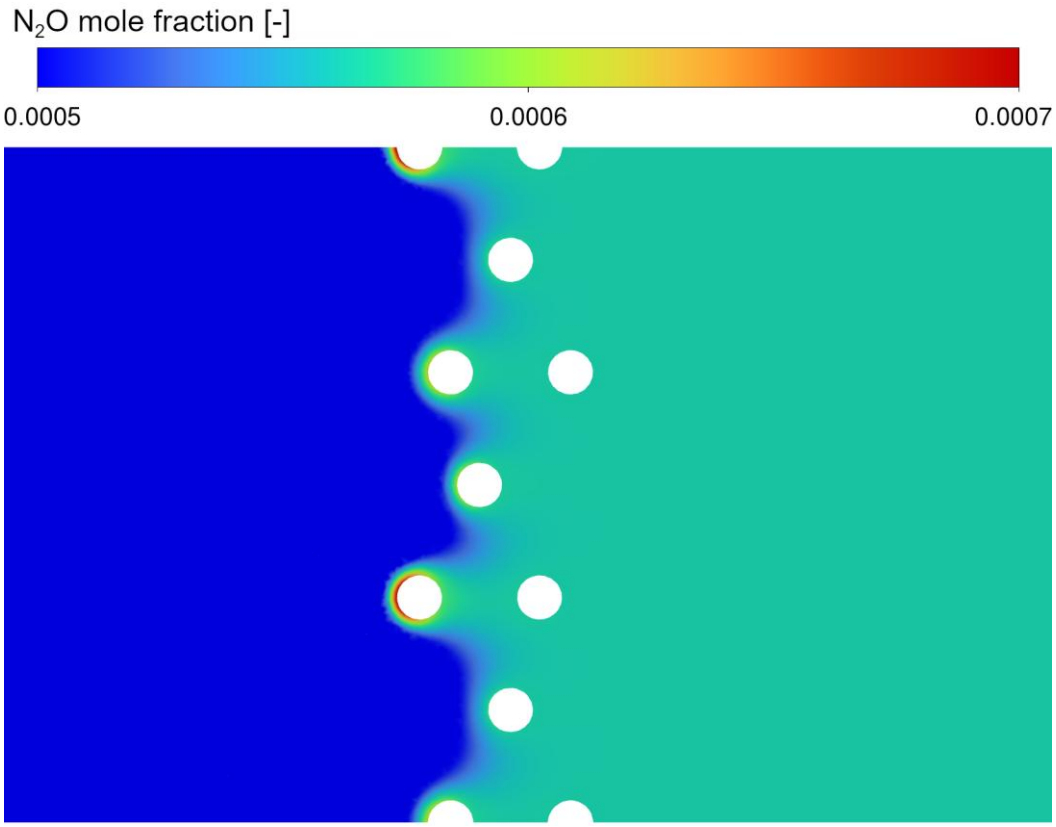

(b)

Figure 7.12. N_2O mole fractions contours [-] in full range (a) and clipped range (b) in the cross-section of the investigated domain (contact time 1 ms, inlet temperature 150 °C) [75]

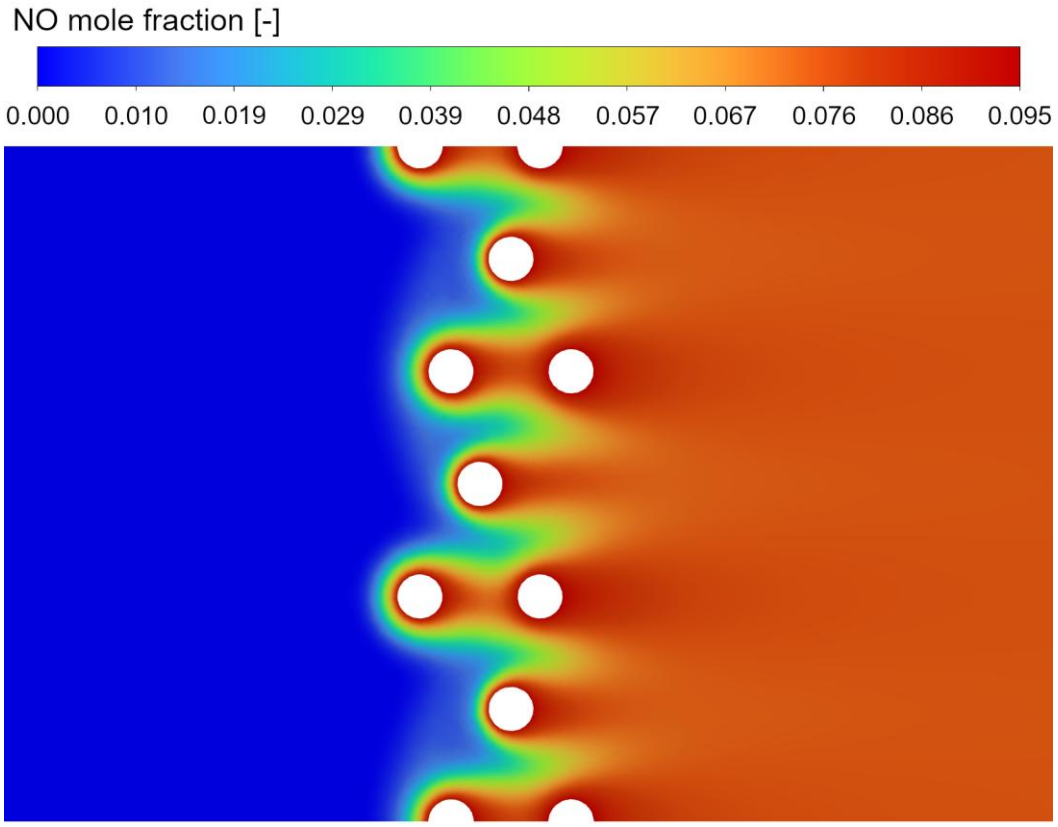

(a)

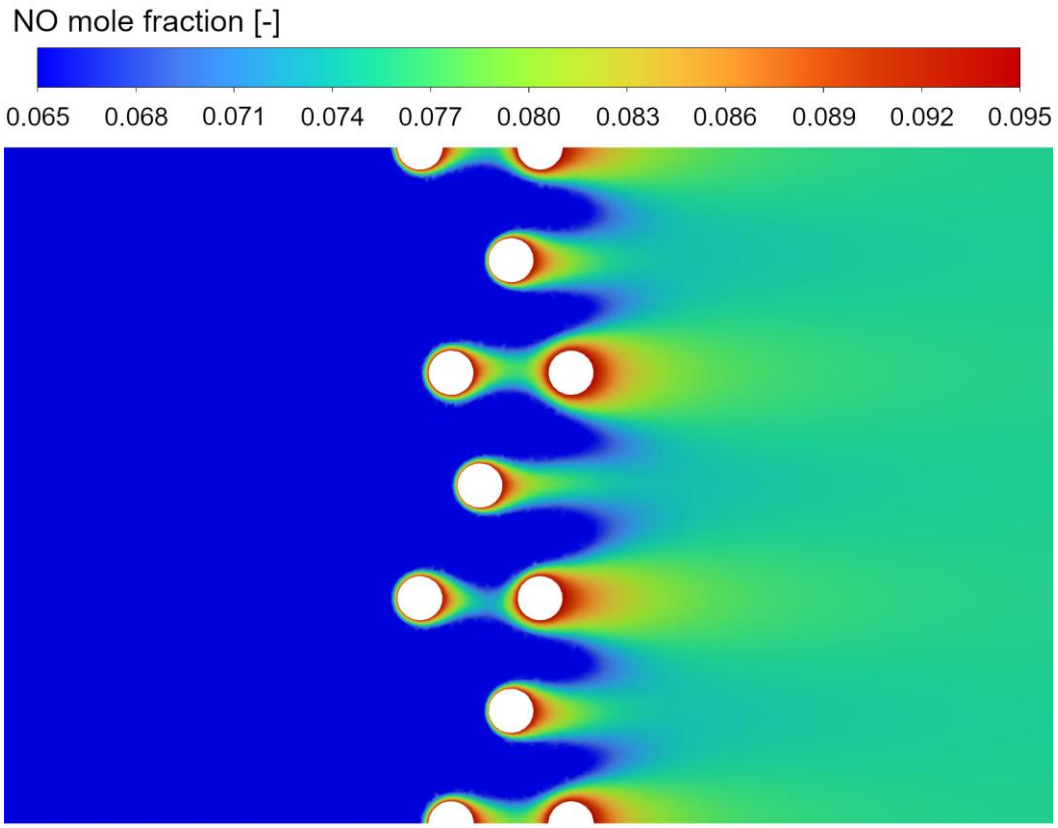

(b)

Figure 7.13. NO mole fractions contours [-] in full range (a) and clipped range (b) in the cross-section of the investigated domain (contact time 0.2 ms, inlet temperature 150 °C) [75]

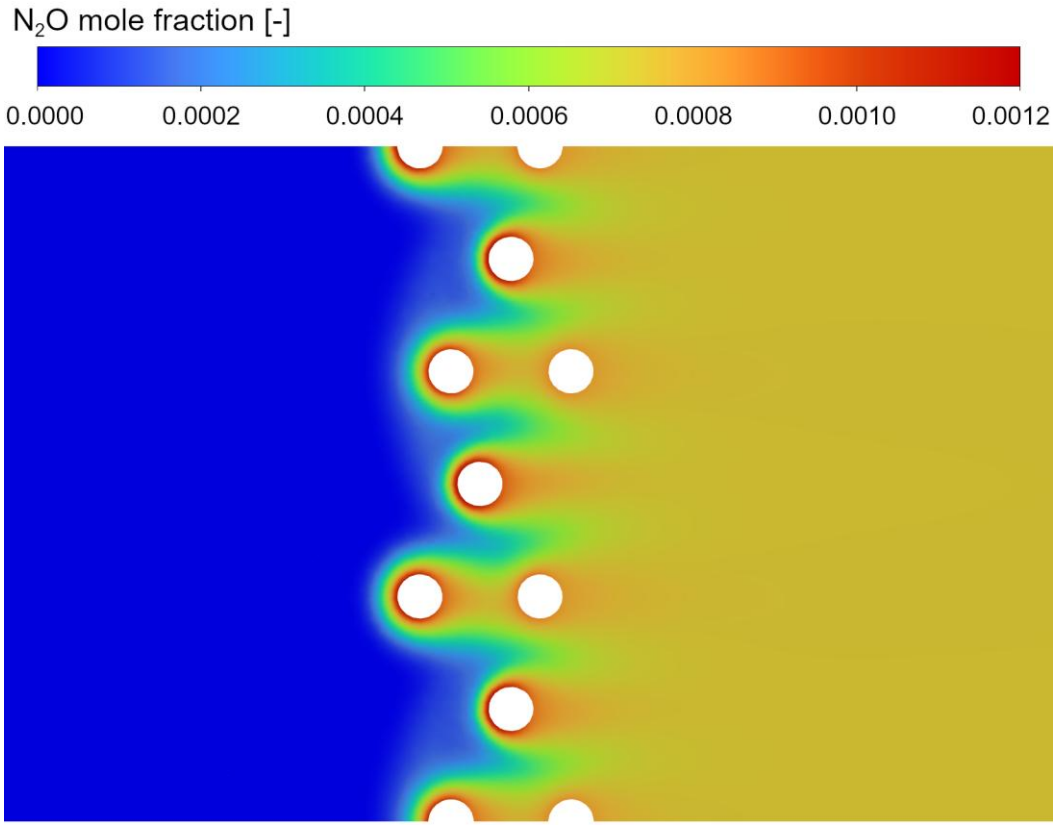

(a)

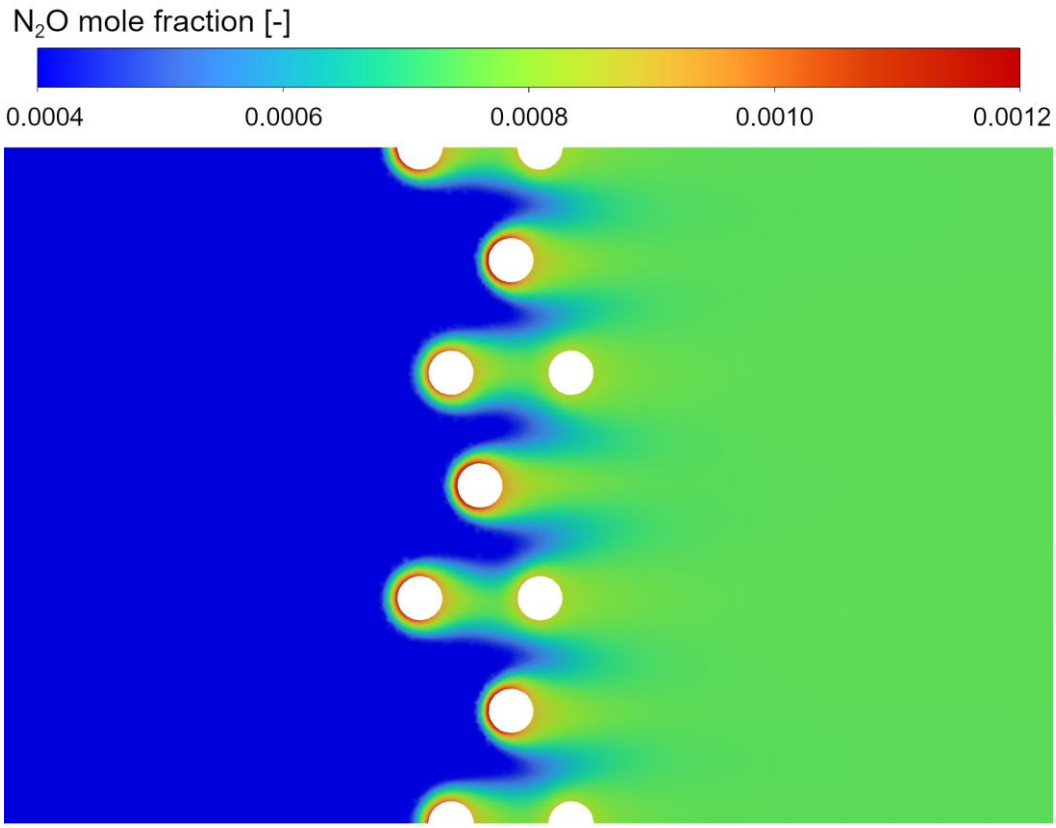

(b)

Figure 7.14. N_2O mole fractions contours [-] in full range (a) and clipped range (b) in the cross-section of the investigated domain (contact time 0.2 ms, inlet temperature 150 °C) [75]

Figure 7.15 shows the mole fractions of NO and N_2O at the outlet as functions of contact time. In the case of ammonia oxide, longer contact times always result in higher product concentration. However, the differences become minor with the increase in contact times. This is why there is no need to increase contact time over 1 ms since, above this value, the concentration gains would be negligible, and longer contact times increase the catalyst degradation intensity during the process. On the contrary, shorter contact times cause an increase in N_2O yield and significantly reduce the process efficiency, as described in Section 7.8.6. Interestingly, reducing contact times does not cause a constant increase in N_2O production. As shown in Figure 7.15 (b), while contact times decrease, the mole fraction of N_2O reaches its maximum and then quickly decreases. This trend results from high gas velocity in exceedingly short contact time ranges, where substrates are washed away before the reaction occurs. Such low contact times are not used in industry since they drastically reduce the outlet concentration and can potentially damage the catalyst gauze, resulting in even more Pt loss.

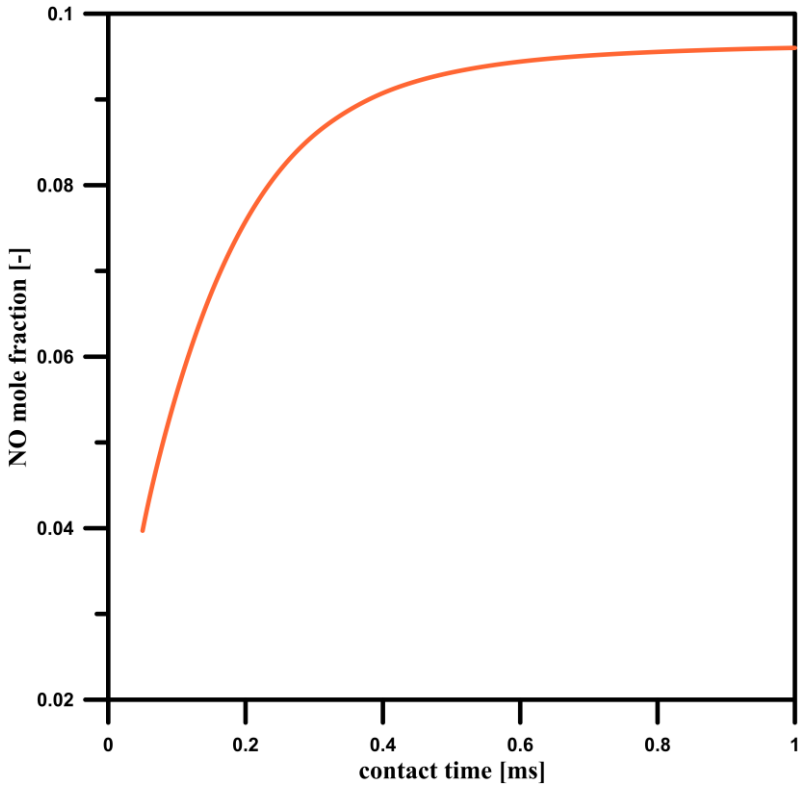

(a)

Figure 7.15. Cont.

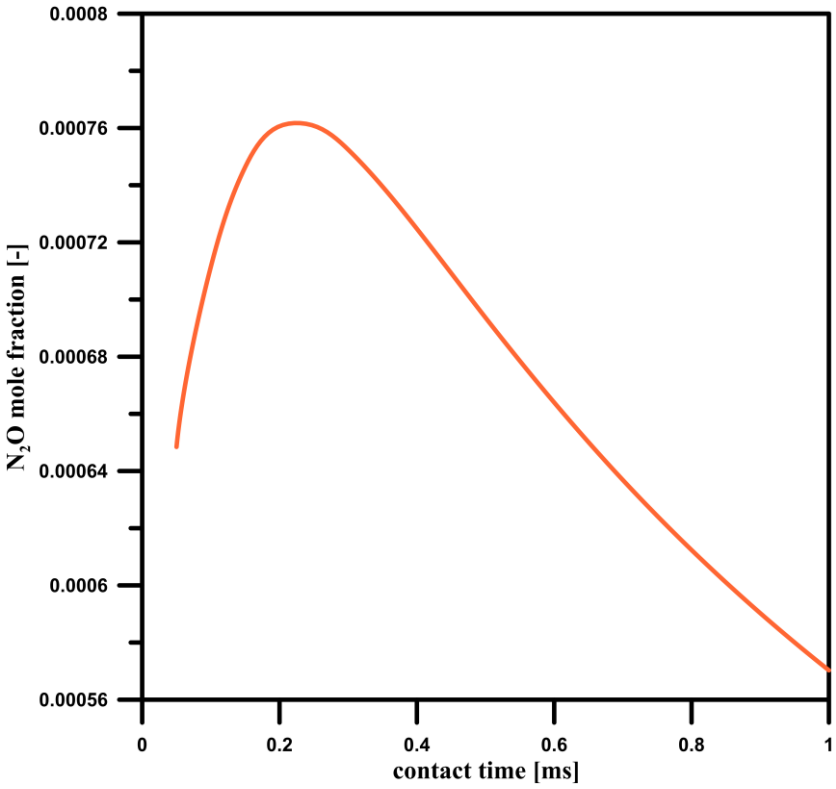

(b)

Figure 7.15. NO (a) and N_2O (b) mole fractions at the domain's outlet as functions of contact time (inlet temperature 150°C) [75]

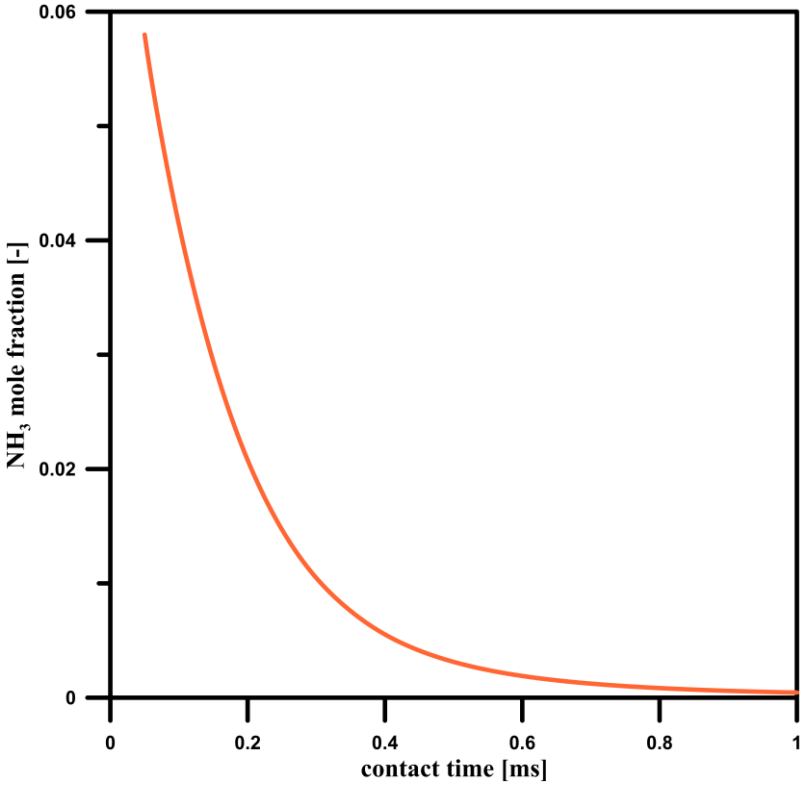

(a)

Figure 7.16. Cont.

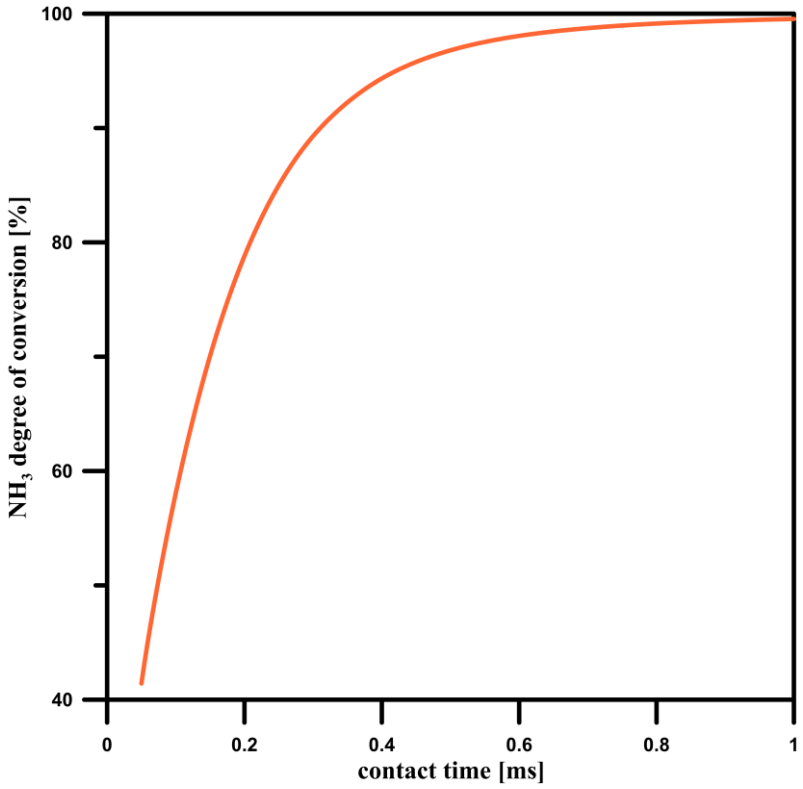

(b)

Figure 7.16. NH_3 mole fraction at the domain's outlet (a) and NH_3 degree of conversion (b) as functions of contact time (inlet temperature 150°C) [75]

Figure 7.16 presents the outlet NH_3 mole fraction and its degree of conversion as functions of contact times. This shows the concentration of unreacted ammonia that leaves the converter depending on contact time. It should be noted that the amount of unreacted ammonia should be kept to a minimum since it can further react with nitrogen oxide.

7.8.5. Influence of the temperature on the process

Temperature profile results from both reaction rates and flow field. The strong exothermic character of ammonia oxidation makes this process firmly associated with temperature. Figure 7.17 compares the temperature field for the cases with contact time values of 1 ms and 0.2 ms for an inlet gas temperature of 150°C.

After the gas comes into contact with the gauze's surface, the temperature rises quickly and reaches its maximum. In Figure 7.17, one can observe that the maximum temperature is comparable in both cases, which corresponds to concentration profiles. This indicates that those parameters are strongly related to each other. In the cases with shorter contact times, the gas phase "washing out" effect is also visible while observing the temperature contours.

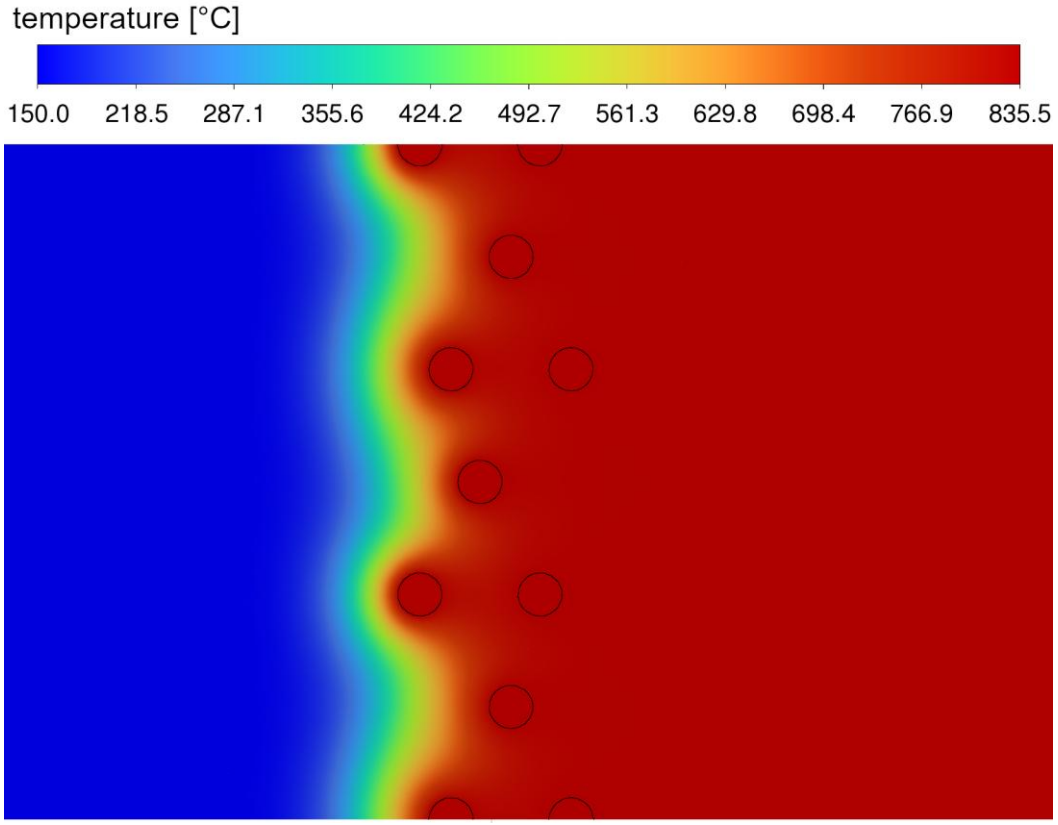

(a)

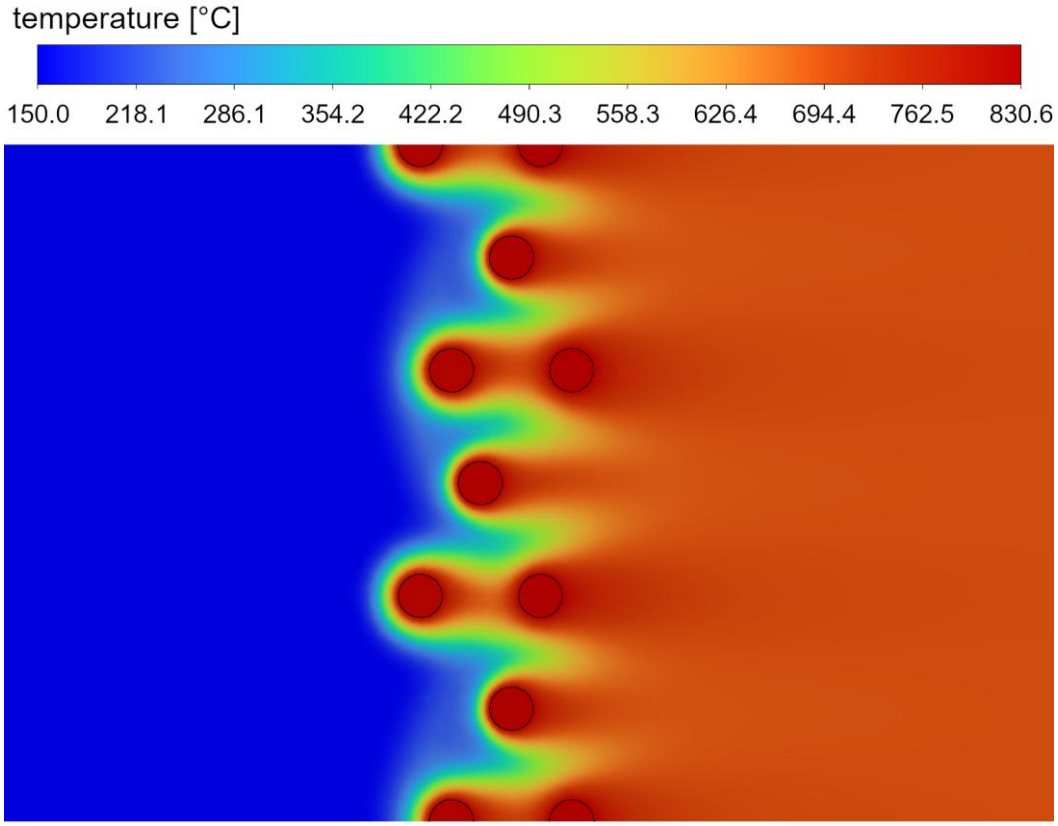

(b)

Figure 7.17. Temperature contours [°C] for 1 ms (a) and 0.2 ms (b) contact times in the cross-section of the investigated domain (inlet temperature 150 °C) [75]

Figure 7.18 presents the surface-averaged temperature in relation to the contact time for the inlet gas temperature of 150°C. It can be observed that the subsequent layers have higher surface temperatures than those preceding them. Shorter contact times cause the temperature values of the first two layers to be closer to each other. This effect of high continuous phase velocity increases the likelihood of gas passing the first layer. Longer contact times, however, caused the temperatures of the second and third layers to be closer, which results from the longer contact time of the first layer, which consequently causes fewer substrates to pass to the subsequent layers. Those trends are also visible in reaction rate (Figure 7.5) and selectivity (Figure 7.8) functions of contact time.

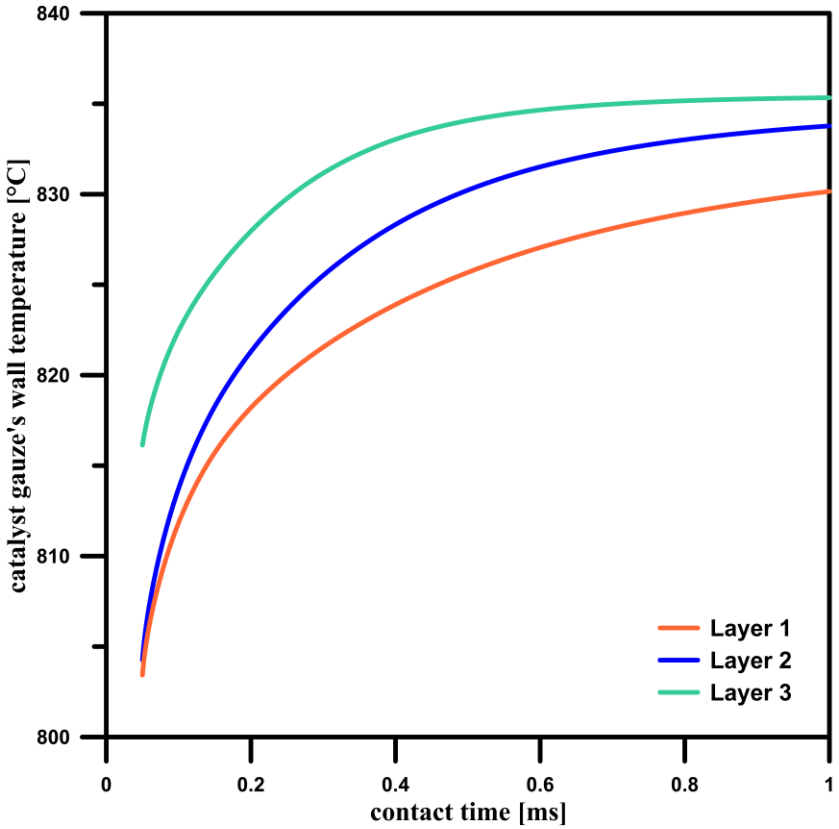

Figure 7.18. Surface-averaged catalyst wall temperature as a function of contact time on different catalyst gauze layers (inlet temperature 150°C) [75]

Figure 7.19 compares the temperature gradients for the cases with 100°C and 200°C inlet gas temperatures for 1 ms contact time.

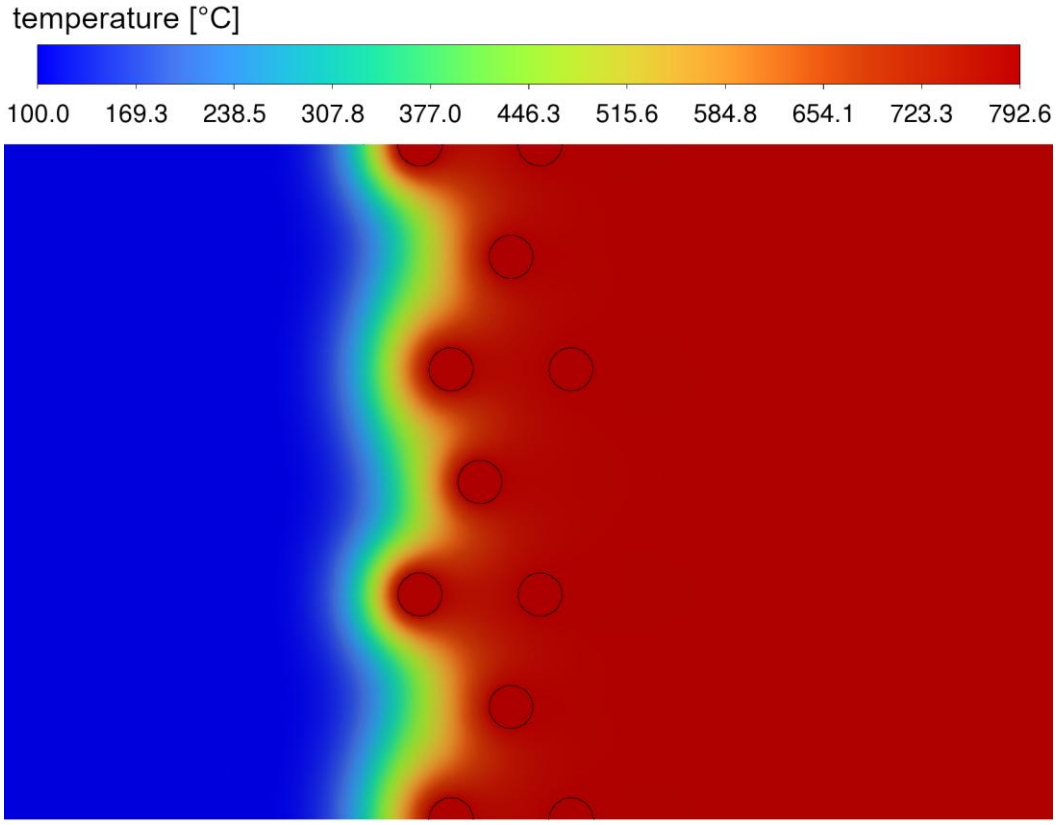

(a)

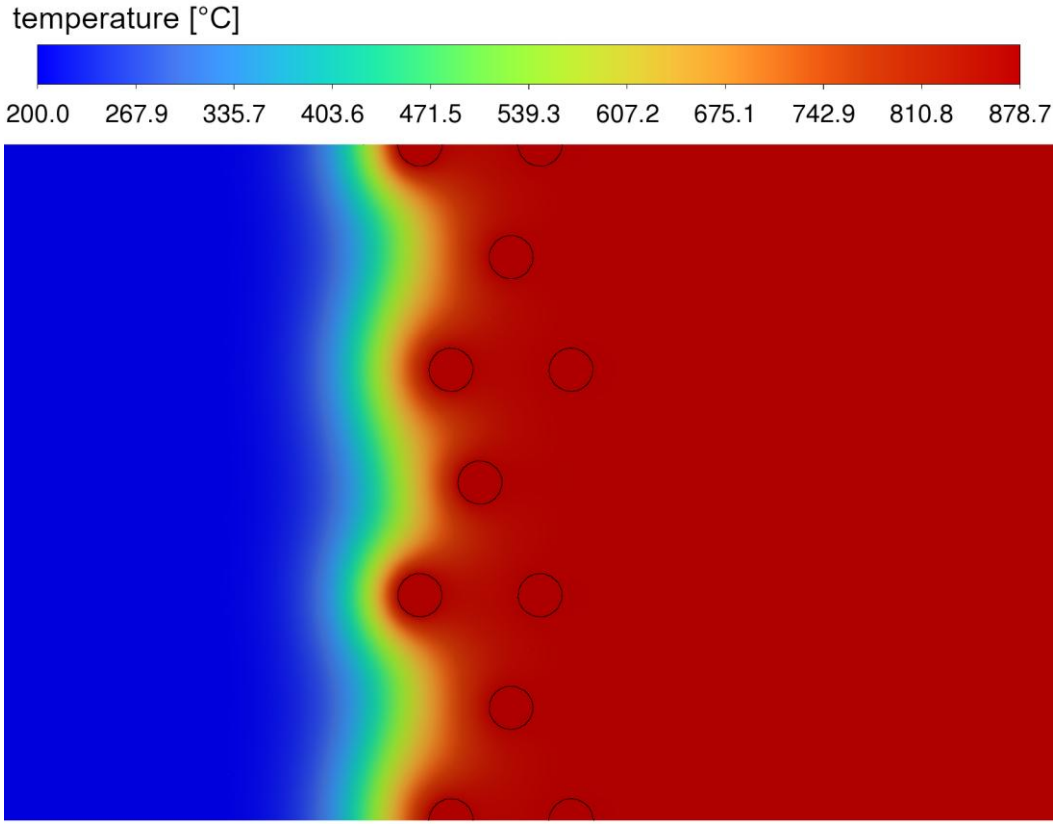

(b)

Figure 7.19. Temperature contours [°C] for gas inlet temperature of 100°C (a) and 200°C (b) in the cross-section of the investigated domain (contact time 1 ms) [75]

The process maximum temperature is firmly influenced by the inlet gas temperature. Figure 7.20 shows the function of surface-averaged temperature and inlet gas temperature. It should be noted that, similarly to reaction rates and selectivity, the surface temperature is not uniform, and its gradient has a crucial role in the degradation process, which is further described in Section 8.2.2.

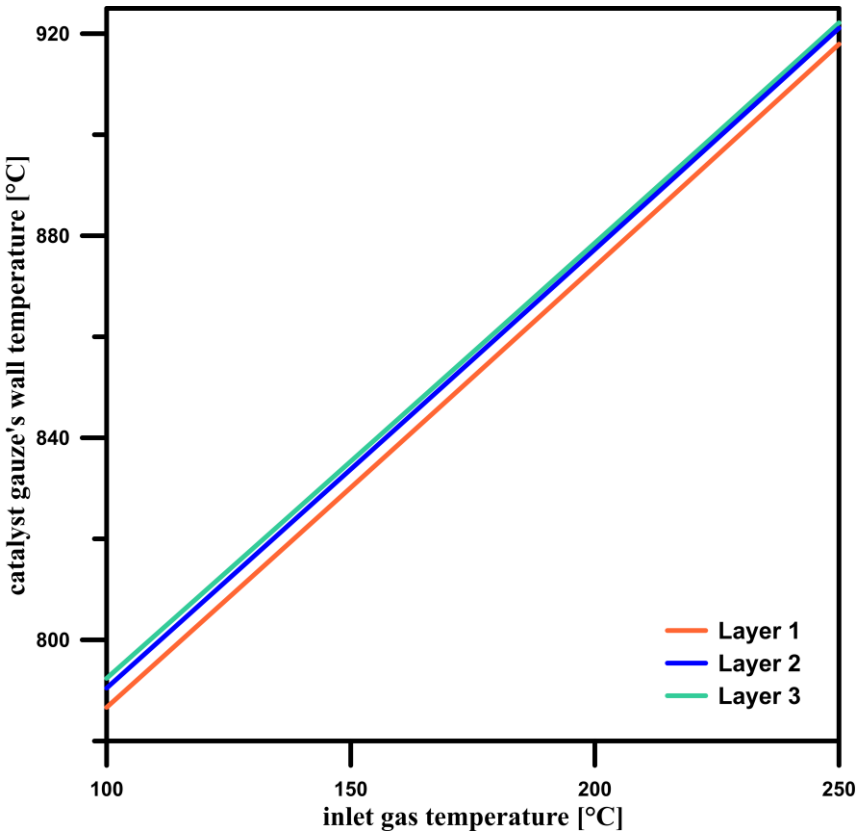

Figure 7.20. Surface-averaged catalyst wall temperature as a function of inlet gas temperature on different catalyst gauze layers (contact time 1 ms) [75]

Figure 7.20 shows that mean wall temperature forms the linear function with the inlet gas temperature, which is valid for all layers. Temperature values of all layers are also relatively similar. Figure 7.21 presents the mole fractions of NO and N_2O at the outlet in relation to the first layer's mean temperature. It can be noted that the trends are opposite for those species. Higher surface temperatures increase NO and decrease N_2O mole fractions. Catalyst wall temperature also affects the efficiency of the process, which is investigated in the next section.

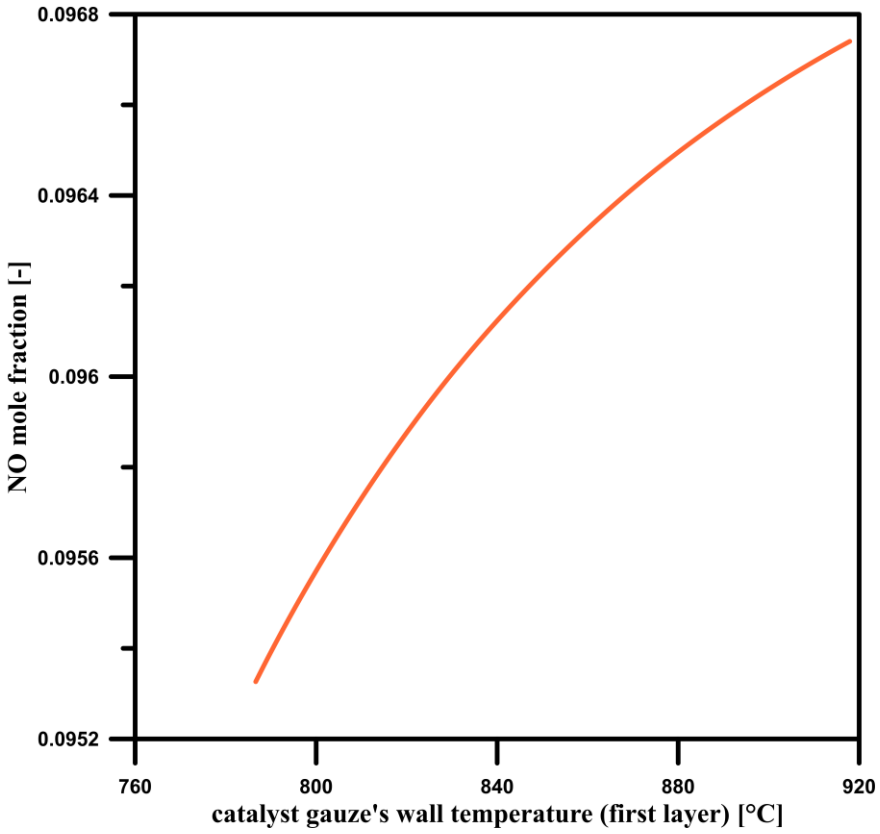

(a)

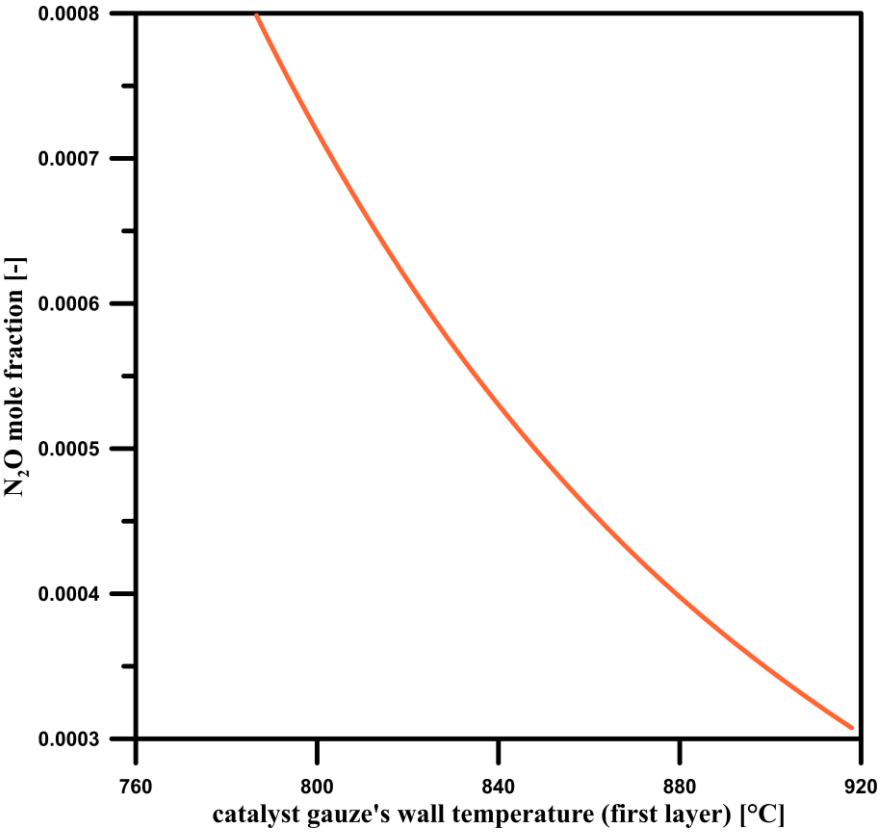

(b)

Figure 7.21. NO (a) and N_2O (b) mole fractions at the domain's outlet as functions of surface-averaged wall temperature on the first layer (contact time 1 ms) [75]

7.8.6. Influence of number of layers, temperature and contact time on efficiency

Obtaining the maximum possible efficiency of ammonia oxide production is a key to the Ostwald Process. This section analysed the influence of inlet temperature and contact time on NO and N_2O production efficiency.

Figure 7.22 compares the cumulative efficiencies of NO and N_2O production in relation to contact time for different layers. First-layer efficiency was obtained by conducting a simulation with reactions active only on the first layer. The second layer's cumulative efficiency was computed with reactions active on the first two layers, and the third layer's cumulative efficiency was calculated with reactions active on the whole gauze. It can be observed that the cumulative efficiencies of all layers have similar patterns to the concentration plots shown in Figure 7.15.

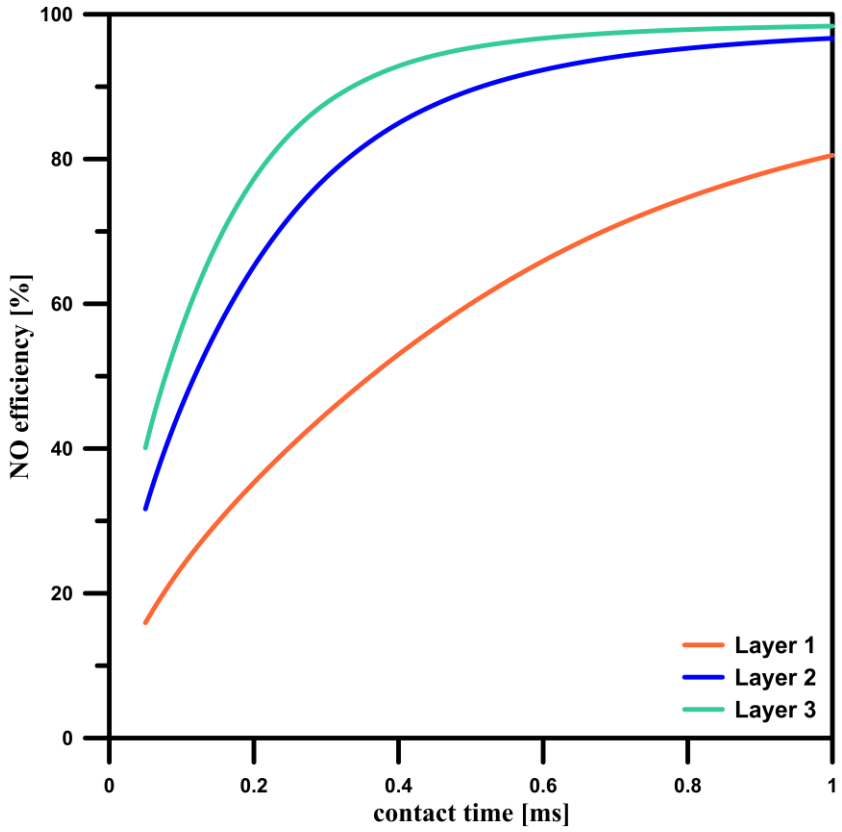

(a)

Figure 7.22. Cont.

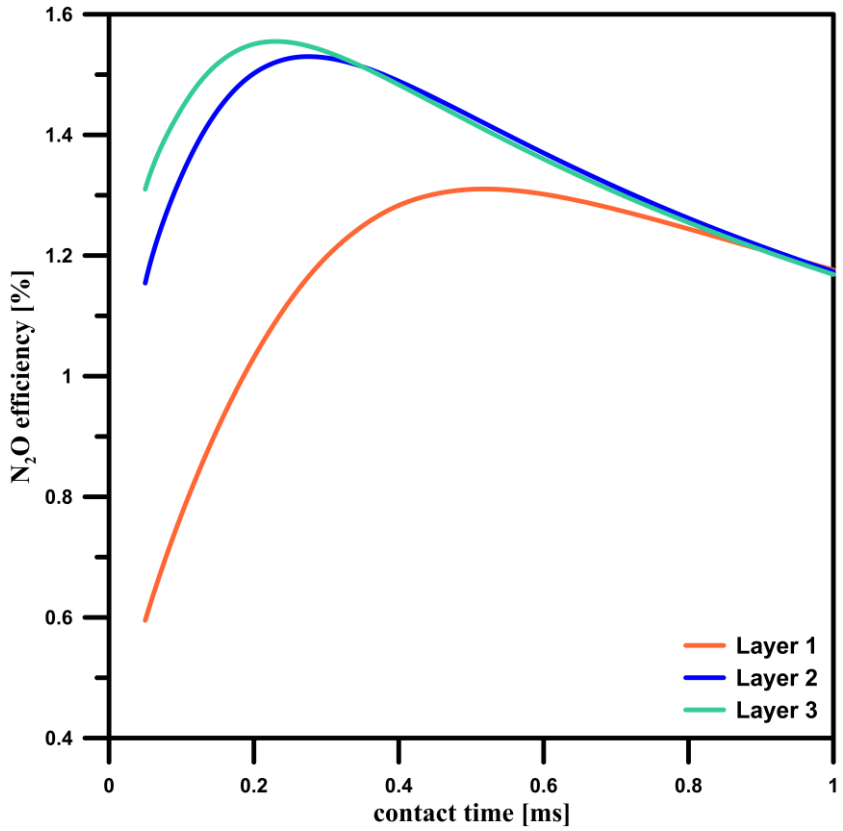

(b)

Figure 7.22. Cumulative NO (a) and N_2O (b) efficiencies as functions of contact time after different catalyst gauze layers (inlet temperature 150°C) [75]

Figure 7.23 compares the efficiencies of NO and N_2O production in relation to the first layer's mean wall temperature. In this case, trends similar to mole fraction plots (Figure 7.21) are also noticeable. It can be observed that product efficiency strongly depends on the contact time: higher NO and lower N_2O production efficiency results from longer contact times. The gauze's temperature also noticeably influences efficiency; its higher values are more favourable. Still, longer contact times and higher temperatures can increase catalyst degradation, which needs to be considered while selecting the proper process conditions.

Efficiency functions provide helpful information for determining process parameters since efficiency and concentration plots allow the estimation of the maximum possible outlet mole fraction in specific process conditions.

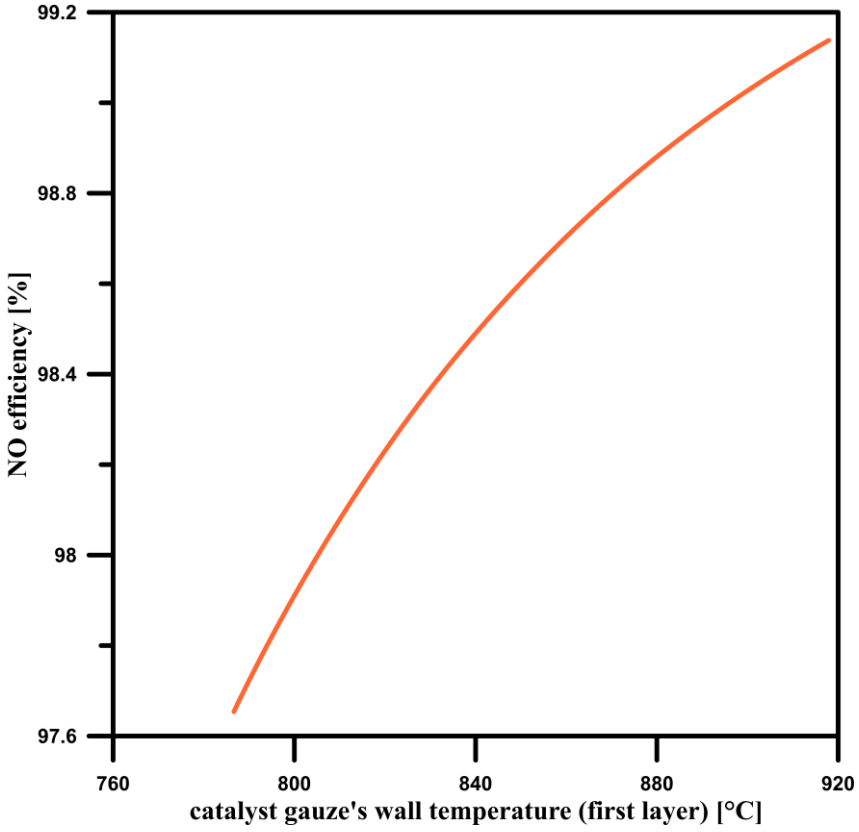

(a)

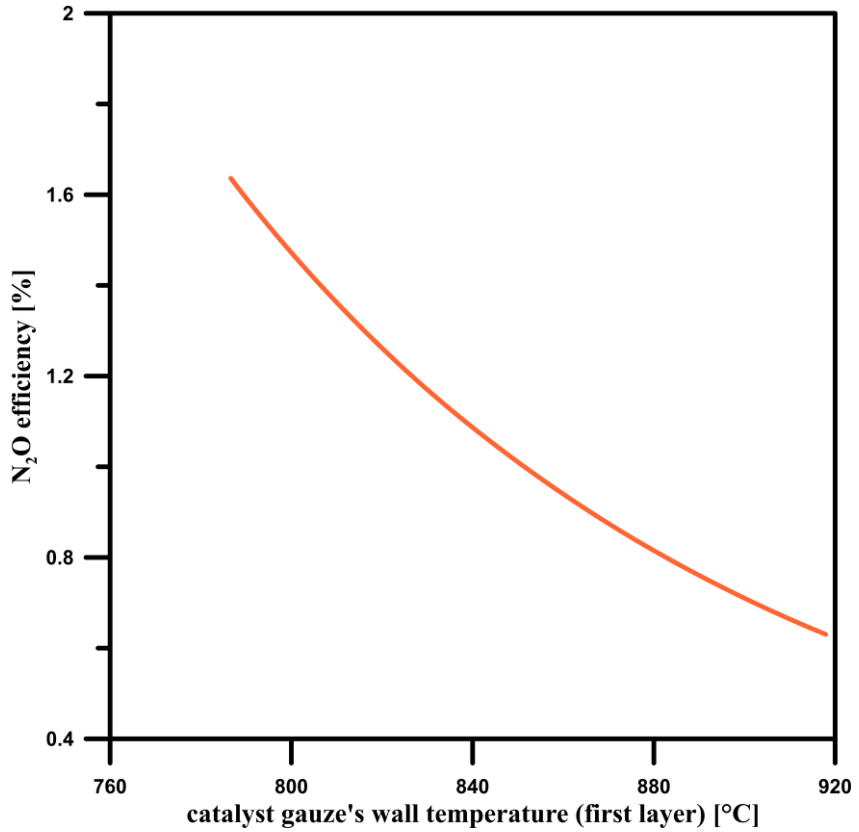

(b)

Figure 7.23. Cumulative NO (a) and N_2O (b) efficiencies as functions of surface-averaged wall temperature on the first layer (contact time 1 ms, reactions on all layers) [75]

7.9. Validation

The CFD model was validated using the experimental data reported by Handforth and Tilley [77], listed in Table 7.6. This section used the pure platinum data to validate the CFD model since the implemented kinetics was designed for this specific case.

Table 7.6. Experimental data obtained by Handforth and Tilley [75,77]

Rate of NH_3 per 1 troy oz. of exposed catalyst [pounds per day]	*Rate of NH_3 per 1 g of exposed catalyst [kg s^{-1}]*	*NH_3 in gas feed [vol. %]*	*Gauze temperature [°C]*	*Conversion efficiency [%]*
100	$1.69 \cdot 10^{-5}$	9.6	810	92.3
100	$1.69 \cdot 10^{-5}$	9.6	870	94.6
100	$1.69 \cdot 10^{-5}$	9.5	900	96.1
100	$1.69 \cdot 10^{-5}$	9.5	920	97.5

Handforth and Tilley [77] carried out the ammonia oxidation process in actual commercial conditions using atmospheric pressure. They investigated different factors like capacity, conversion efficiency and platinum losses. Figure 7.24 shows the geometrical dimensions of Handforth and Tilley's [77] gauze geometry, and Figure 7.25 presents its visualisation.

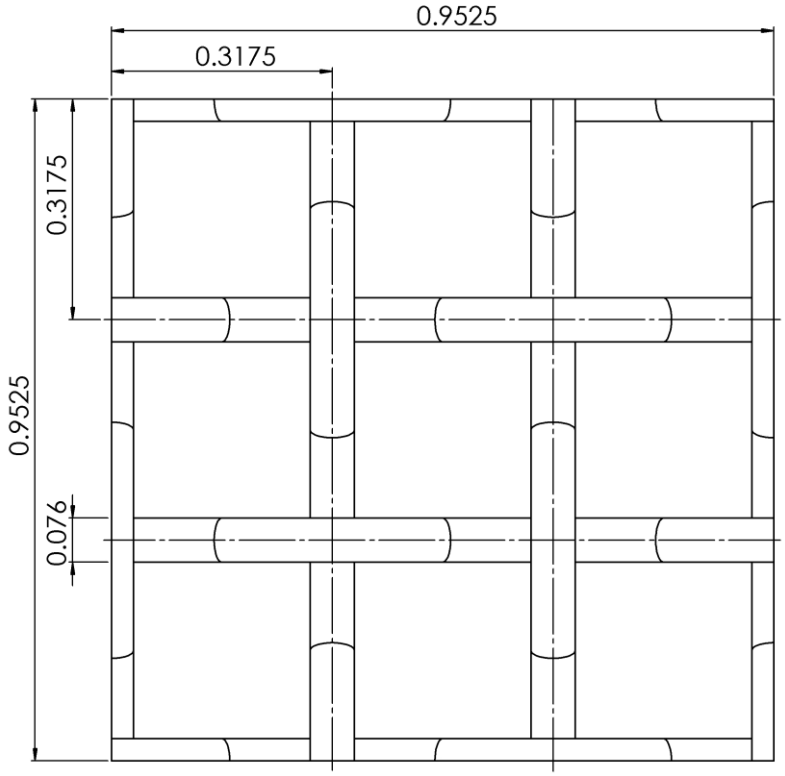

Figure 7.24. Dimensions (in millimetres) of the catalyst gauze used by Handforth and Tiley [75,77]

(a) (b)

Figure 7.25. Catalyst gauze (visualisation) used by Handforth and Tiley [75,77]

In their experiments Handforth and Tilley [77] applied one-layer flat catalyst gauze with an exposed area of 101.6 x 139.7 mm (4 x 5.5 inches). They used an ammonia-air mixture as a feed stream [77]. The gauze was knitted using wires with a diameter of 0.0762 mm (0.003 inches), forming 80 meshes per linear inch [77]. In this work, Handforth and Tilley's [77] gauze geometry was replicated as a CAD model for validation.

The domain and numerical mesh were created analogically to those in the main simulations with the same solver setup. Figure 7.26 shows the computational domain used for validation.

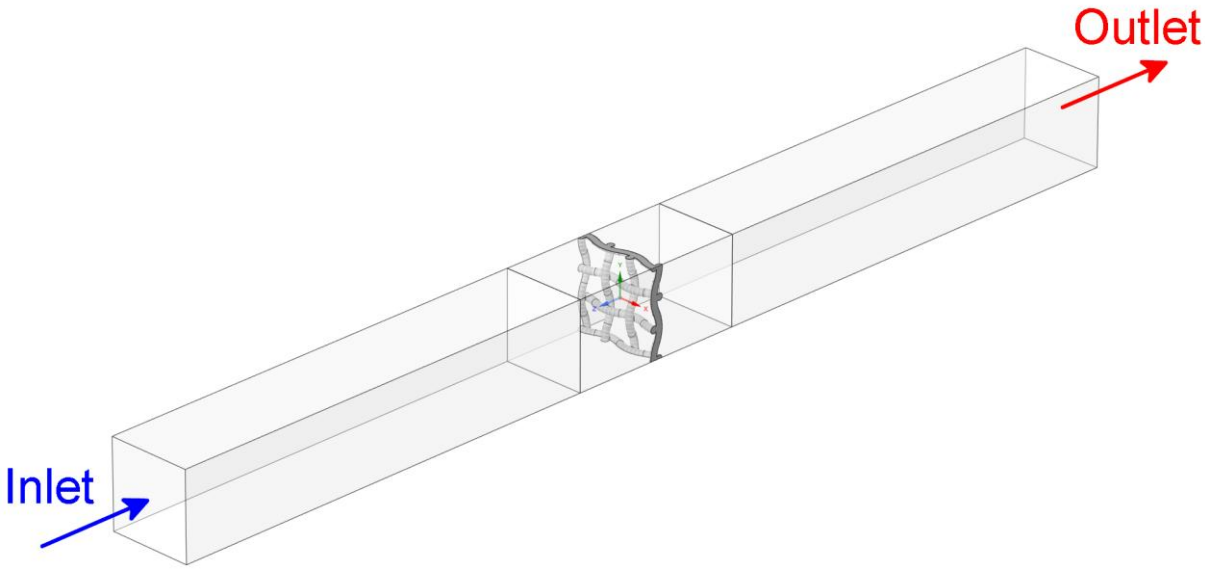

Figure 7.26. Computational domain used for validation [75]

The selected validation parameter is the effect of gauze temperature on the NO conversion efficiency. Simulations were conducted using the same conditions as Handforth and Tilley's experiments [77]. Gauze temperatures in the CFD model were obtained by adjusting the gas inlet temperatures. The comparison of experimental and simulation results is presented in Table 7.7.

Table 7.7. Comparison of the effect of gauze temperature on NO conversion efficiency between experimental data [77] and CFD simulation [75]

Gauze temperature [°C]	*Conversion efficiency, experiment [%]*	*Conversion efficiency, CFD simulation [%]*	*Error [%]*
810	92.3	95.9	3.88
870	94.6	96.7	2.23
900	96.1	97.0	0.95
920	97.5	97.2	−0.32

The results show that the maximum error in NO conversion between experimental [77] and simulation results is 3.88%. This difference is more noticeable in the lower gauze temperature ranges since actual process efficiency is lower than values obtained in the CFD model. However, this difference is even more minor for higher analysed parameters. In the case with the highest catalyst temperature, the experimental efficiency is slightly higher than the simulated one. Nevertheless, the modelled and experimental [77] results in the operating condition ranges are close in values and trends, indicating that the CFD model is relatively accurate. It should be noted that Handforth and Tilley [77] provided no information about the external geometry of the used experimental converter, such as the inflow zone's length before catalyst gauze, which may cause potential errors.

7.10. Conclusions

Section 7 was focused on an in-depth investigation of various aspects of ammonia oxidation on the 3-layered platinum gauze. The simulation used the surface kinetics developed by Kraehnert and Baerns [38], which contains ten reactions. In this analysis, the author investigated the influence of contact time and gauze's temperature on crucial surface parameters like reaction rate, selectivity, and net parameters such as efficiency and outlet concentrations. The model was validated using Handforth and Tilley's [77] experimental data.

Simulation results illustrate how surface parameters change on different catalyst gauze layers in surface-averaged values and local gradients. The CFD model shows the changes in reaction rates and selectivity while adding more layers to the net gauze under different process conditions. The results allow for directly identifying higher and lower reaction rates and selectivity areas on the catalyst wires' surface, which are impossible to measure experimentally, proving that CFD is a valuable tool for this purpose. It should be noted that this work analyses 3-layer gauze, and estimation of the influence of additional layers may require additional calculations.

Summarising, the obtained CFD model allows for studying critical volume and surface parameters and their gradients in potential cases with different catalyst geometries and process parameters. This allows to predict the efficiency and concentration changes for various scenarios, which can be invaluable support for experimental research. The CFD model can also be used as a basis for further study of ammonia oxidation issues, such as catalyst degradation, as investigated in Section 8.

8. Catalyst degradation during ammonia oxidation – trajectories and deposition of entrained catalyst particles

The catalyst degradation, also called “catalyst etching”, is arguably the most severe drawback of the Ostwald Process. This phenomenon is widely discussed in the literature, yet scientists are still not sure about the nature of this process [8,19,45–47,57,78,79]. During the production campaign, the morphology of catalyst wires is directly changed due to the entrainment of the catalyst particles and their partial recapturing on the subsequent layers of the catalyst gauzes, resulting in so-called “cauliflower structures” [23]. The degradation process results in continuous loss of the platinum and, in the case of platinum-rhodium gauzes, the alloy’s composition changes that affect the gauze’s physical and catalytical properties [45–47].

In industry, some measures can be applied to capture the entrained platinum. Examples are glass, quartz or metal wool filters and “recovery gauzes” placed in the gas flow after the catalyst gauze [19,20,57]. Yet, those solutions provide a limited capture efficiency and must be replaced frequently [19,20,57]. Because of that, recapturing as much as possible platinum on the subsequent layers of catalyst gauze is highly desirable since it allows the gauze to operate for more extended periods before the replacement, consequently reducing the running costs. Modelling the particle motion and locating their deposition zones gives the unique possibility of selecting proper gauze geometry for specific process conditions. This can lead to increased recapture efficiency within the gauze itself, even before reaching the other recapture measures.

This section uses the CFD model created in Section 7 to calculate the entrained particles’ trajectories and the regions of their deposition on the subsequent layers, which are the possible initial forming spots of cauliflower structures. The results agree with the tendencies observed in experiments [45–47]. This section was made based on the results presented in the manuscript “Study of the Ammonia Oxidation Process on Platinum Gauze and Catalyst Degradation Phenomenon – CFD Simulation with Surface Reaction Kinetics and Catalyst Entrained Particles Motion and Deposition Tracking” [75], which was part of this PhD project. Similarly to Section 7, this section also used the catalyst gauze geometries from the author's previous publication: “Computational Fluid Dynamics of Influence of Process Parameters and the Geometry of Catalyst Wires on the Ammonia Oxidation Process and Degradation of the Catalyst Gauze.” [74].

8.1. Modification of the catalyst gauze geometry

This section investigates the influence of geometry changes on the catalyst degradation phenomenon. For this purpose, the author proposed an altered version of mesh geometry. The authors' previously published results [74] indicated that this novel variant of catalyst gauze could potentially increase the platinum recapture rate in operating conditions using shorter contact times. In Section 8, the typical geometry is referred to as "Geometry A", and the altered version is called "Geometry B". The novel gauze variant is the modified version of typical catalyst gauze described in Section 7.1 with the same first and third layers and second layer rotated by 45° and shifted by half of the mesh's size. This shift is made along one axis regarding the rest of the layers. Table 8.1 lists the differences between the investigated gauze's geometrical variants.

Table 8.1. Geometrical differences between investigated catalyst gauze's geometry variants [75]

Variant	*Wire diameter [mm]*	*1st and 3rd layer mesh size [mm]*	*2nd layer mesh size [mm]*	*2nd layer angle relative to the 1st and 3rd layers*	*2nd layer shift relative to the 1st and 3rd layers [mm]*
A	0.06	0.3 × 0.3	0.3 × 0.3	90°	0.15; two axes
B	0.06	0.3 × 0.3	0.42 × 0.42	45°	0.15; one axis

Geometry B has larger flow clearances in the second layer, causing reduced flow velocity through the gauze. Those changes require higher inlet gas to maintain the exact gas contact times (Equation (118)) with the catalyst. Table 8.2 compares the inlet gas velocities between Geometry A and Geometry B for investigated contact times.

Table 8.2. Contact time values and corresponding inlet velocities for Geometry A and Geometry B [75]

Contact time [ms]	0.05	0.1	0.15	0.2	0.25	0.3	0.4	0.5	0.6	0.7	0.8	0.9	1
Inlet velocity, Geom A [m s^{-1}]	4.416	2.208	1.472	1.104	0.883	0.736	0.552	0.442	0.368	0.315	0.276	0.245	0.221
Inlet velocity, Geom B [m s^{-1}]	6.335	3.167	2.112	1.584	1.267	1.056	0.792	0.633	0.528	0.452	0.396	0.352	0.317

Dimensions and visualisations of the novel Geometry B gauze variant are presented in Figures 8.1 and 8.2.

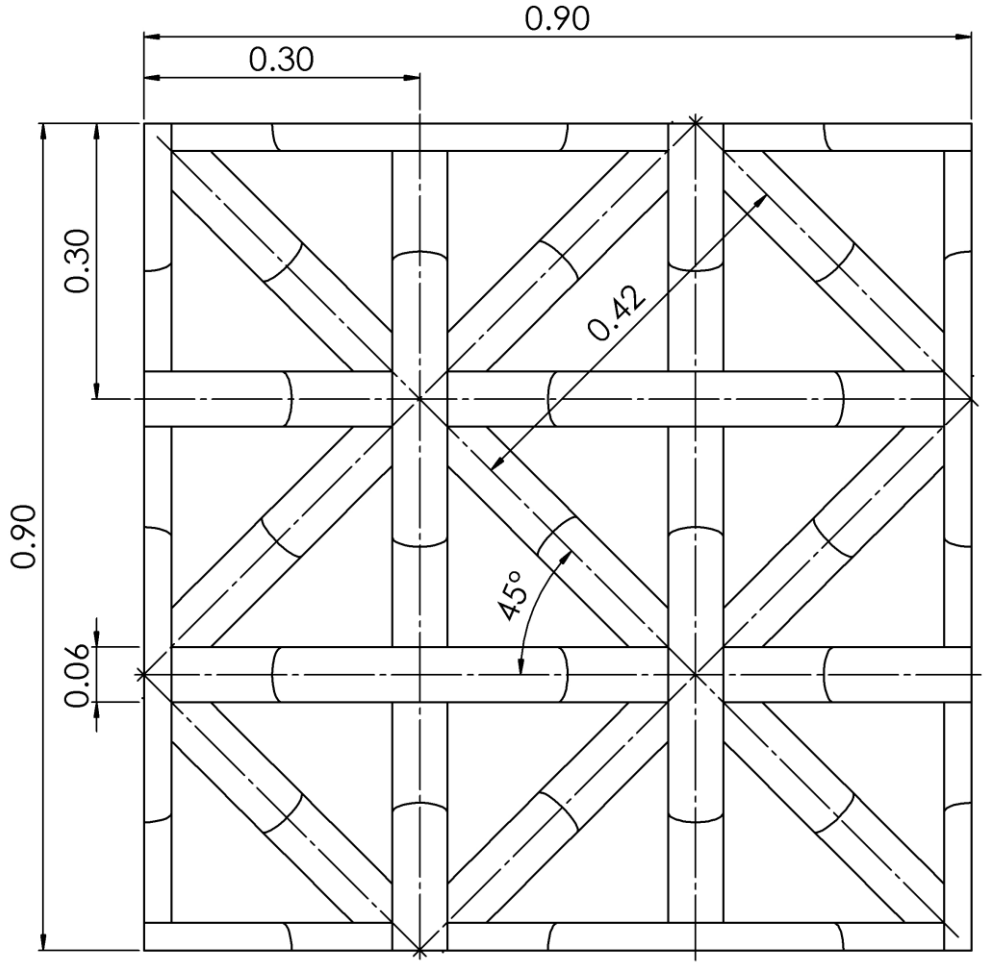

Figure 8.1. Dimensions (in millimetres) of the Geometry B variant of the catalyst gauze [74,75]

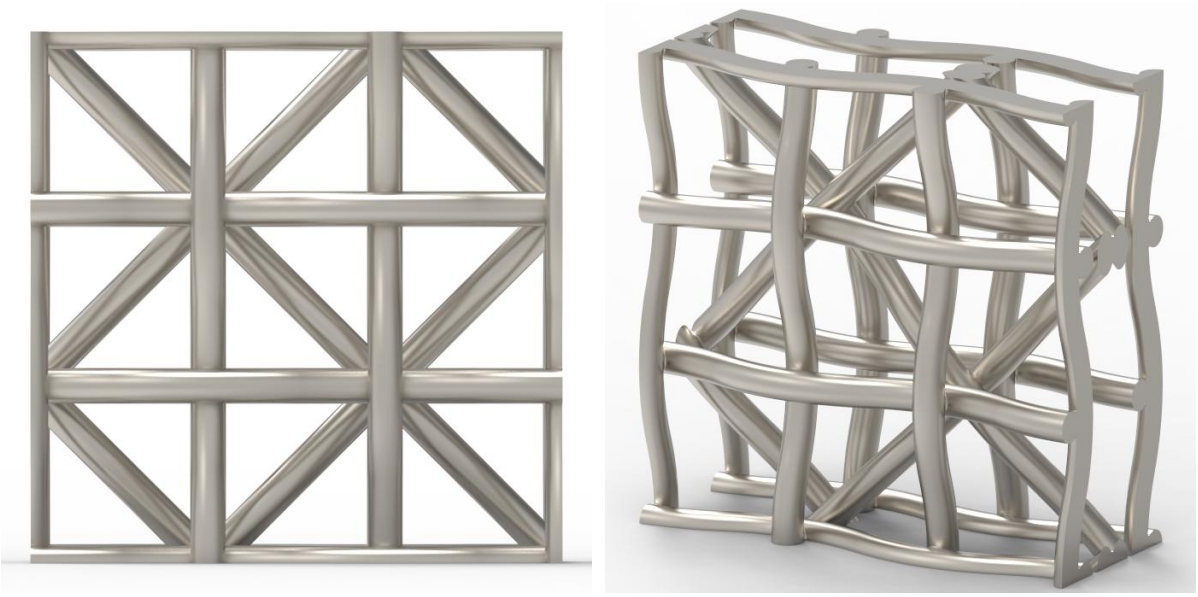

(a) (b)

Figure 8.2. Geometry B variant of catalyst gauze's model visualisation [74,75]

8.2. Identification of catalyst particles' injection areas

In this work, the first layer of catalyst gauze was considered as a source releasing the entrained platinum particles. It should be noted that every layer is degraded in the ammonia oxidation process. Furthermore, the deposition of entrained particles causes the degradation process to be firmly non-uniform. Some layers degrade significantly faster than others [78,79]. The surface temperature gradients estimated the platinum release on the first layer areas. Higher temperature spots are expected to have an increased degradation rate, as observed in the experiments reported in the literature [45–47]. Calculations were performed using different contact times and inlet gas temperature of 150°C.

8.2.1. Stagnation zones

The velocity streamlines (pathlines) can be plotted from the flow fields in CFD calculations. They allow to identify the stagnation zones formed behind the gauze's wires. This undesired phenomenon is formed due to the gauze interrupting the gas flow. Velocity pathlines are presented in Figure 8.3 for Geometry A and Figure 8.4 for Geometry B in cases of 1 ms and 0.2 ms of contact times.

Formation of stagnation areas is strongly associated with contact times since higher velocities required to obtain shorter contact times cause an increase in the sizes of the backflow zones. As seen in Figures 8.3 and 8.4, stagnation zones are significantly smaller for contact times of 1 ms than for contact times of 0.2 ms. Although this trend is valid for both geometries, the stagnation areas in Geometry B are noticeably smaller compared to Geometry A.

Stagnation zones are undesired phenomena that negatively affect the ammonia oxidation process. Backflow zones cause reduced reactivity on the back side of the catalyst wires, which can be observed in Figure 7.7, which is an effect of differences in local contact times and temperatures caused by the zero or very low values of fluid velocity close to the catalyst surface. Velocity pathlines also provide insight into the patterns of possible trajectories of entrained platinum particles. Observing the streamlines presented in Figures 8.3 and 8.4, it can be assumed that most particles should bypass the second layer and settle mainly on the third one.

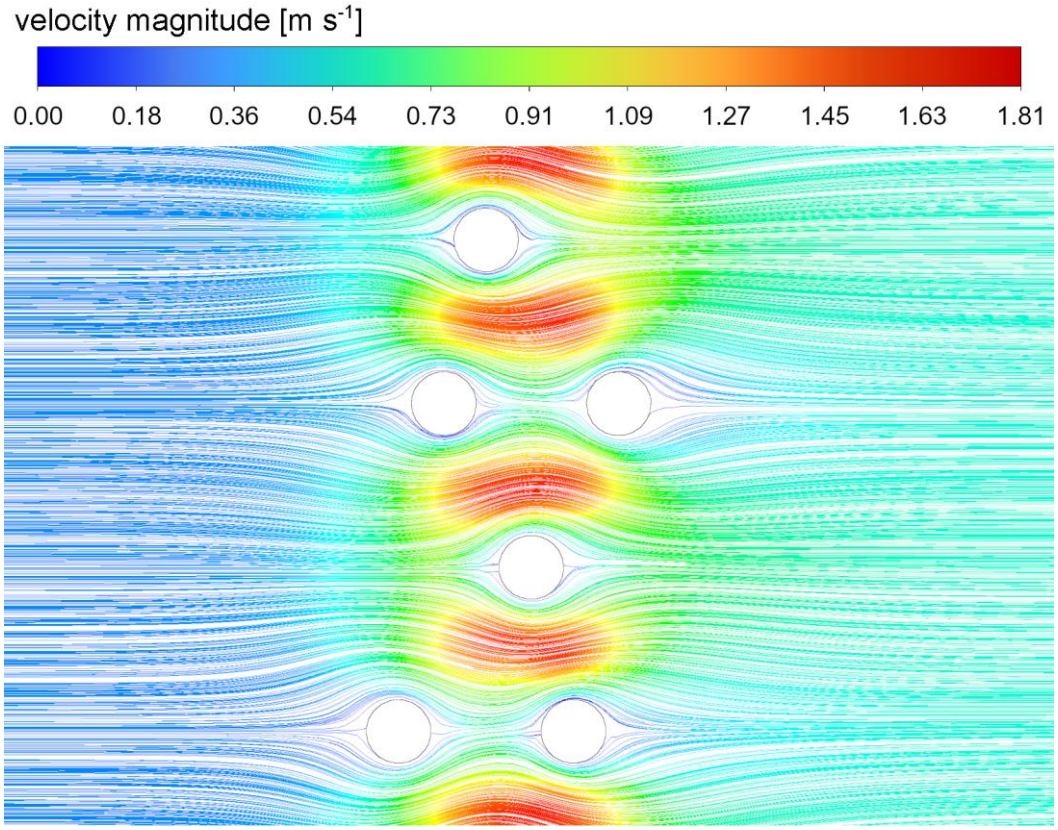

(a)

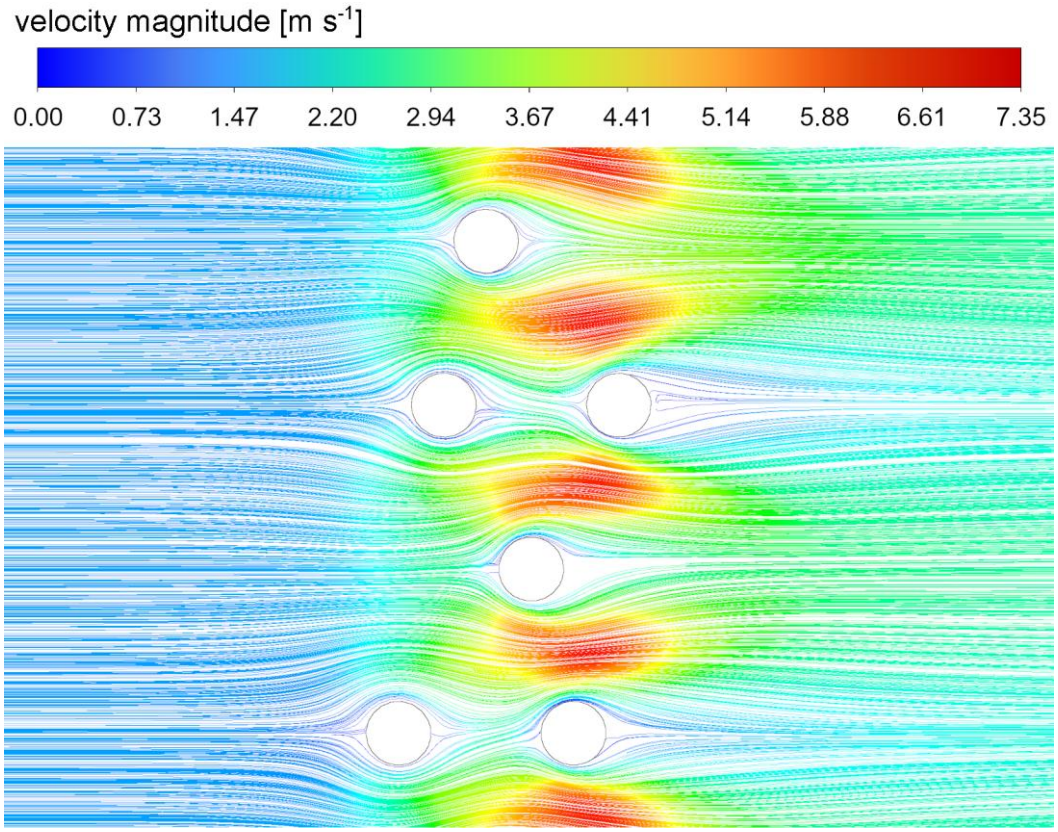

(b)

Figure 8.3. Velocity streamlines [m s^{-1}] for 1 ms (a) and 0.2 ms (b) contact times in the cross-section of the investigated domain (Geometry A) [75]

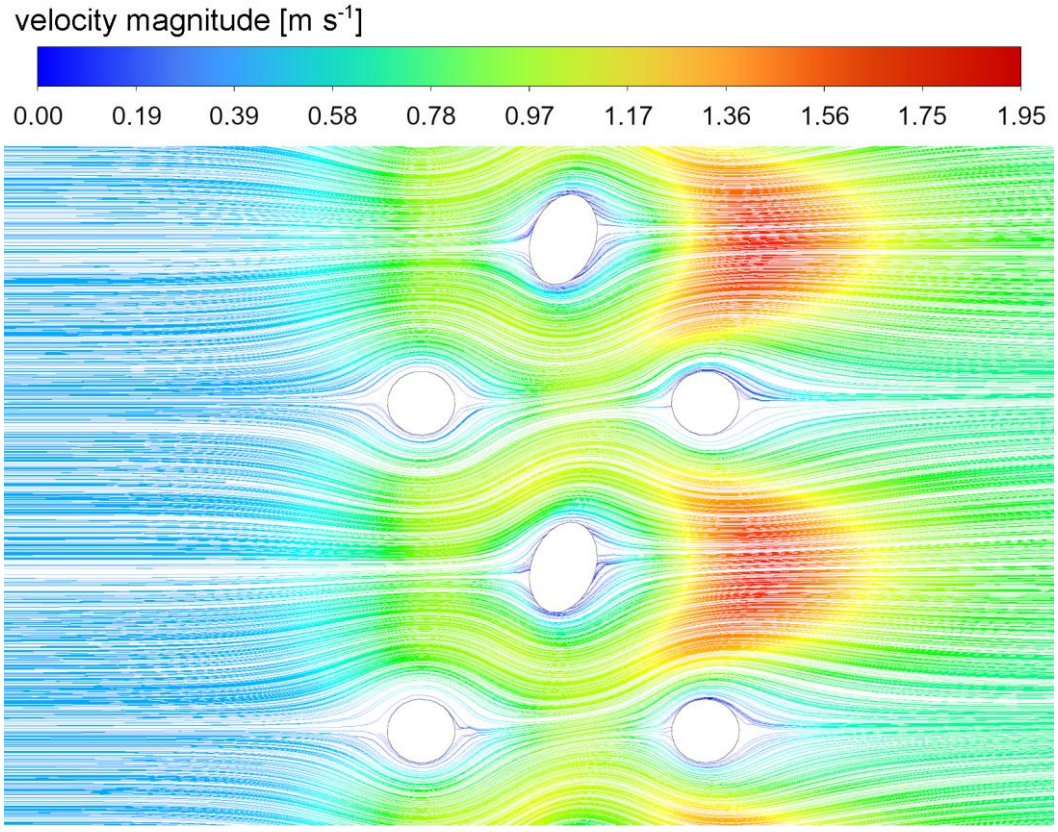

(a)

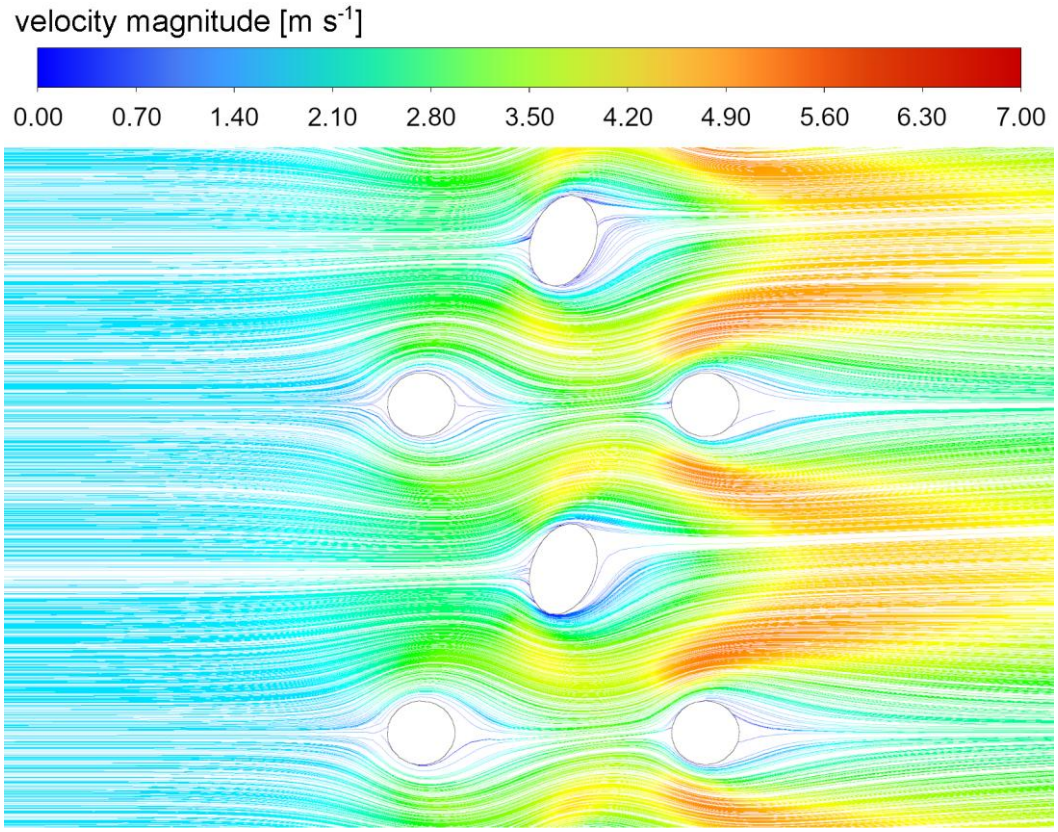

(b)

Figure 8.4. Velocity streamlines [m s^{-1}] for 1 ms (a) and 0.2 ms (b) contact times in the cross-section of the investigated domain (Geometry B) [75]

8.2.2. Catalyst surface temperature gradients

Stagnation zones are phenomena that substantially influence catalyst gauze degradation. They directly cause the gauze's surface temperature gradients, which have a crucial role in the degradation intensity since regions of higher temperature (so-called hotspots) are proven to be zones of increased platinum particles' release rate [45–47]. Figures 8.5 and 8.6 show the temperature profiles on the gauze's first layer for analysed geometries for the cases with contact times of 1 ms and 0.2 ms.

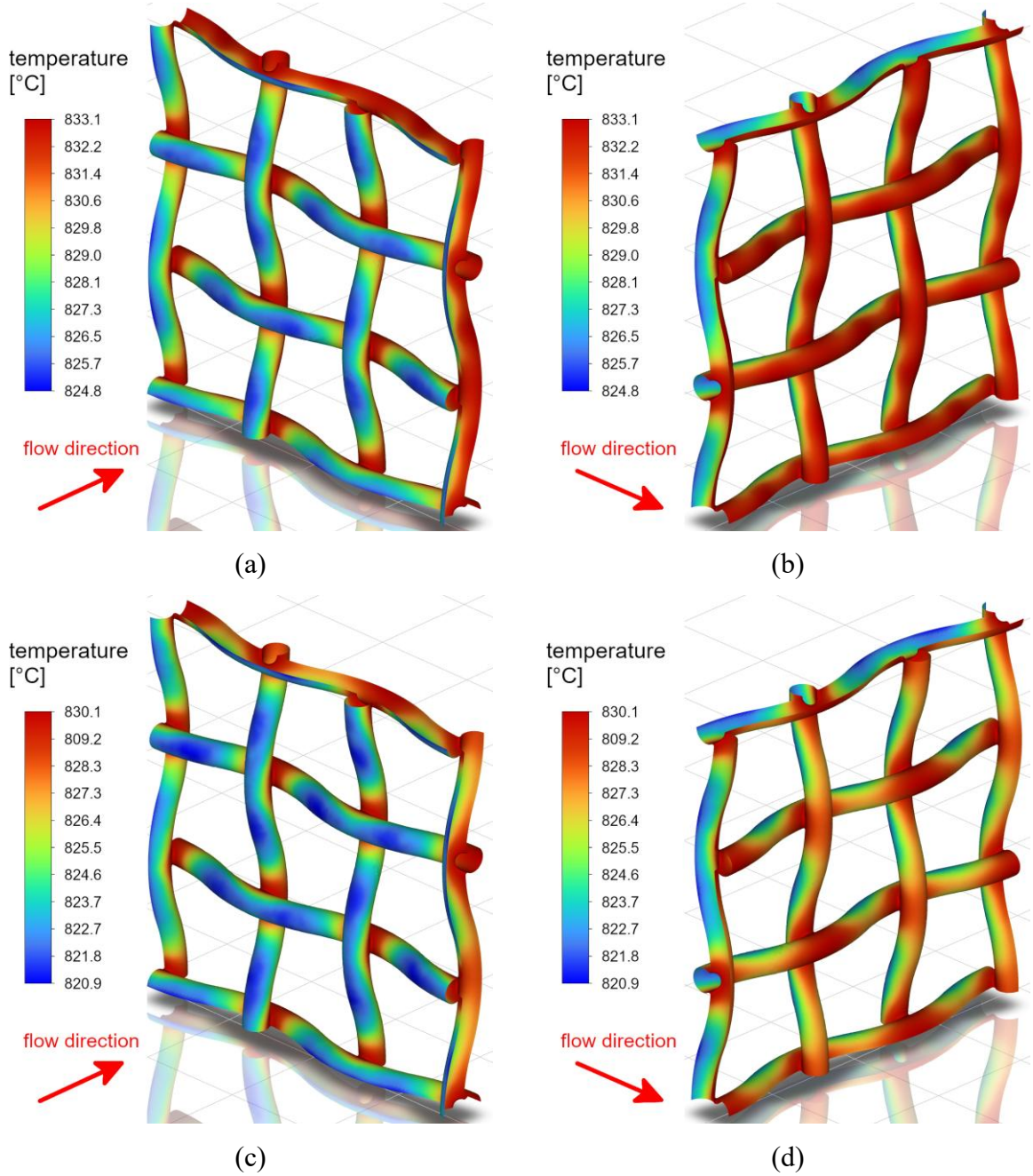

Figure 8.5. Surface temperature contours [°C] on: Geometry A first layer front side (a), Geometry A first layer back side (b), Geometry B first layer front side (c) and Geometry B first layer back side (d) (contact time 1 ms) [75]

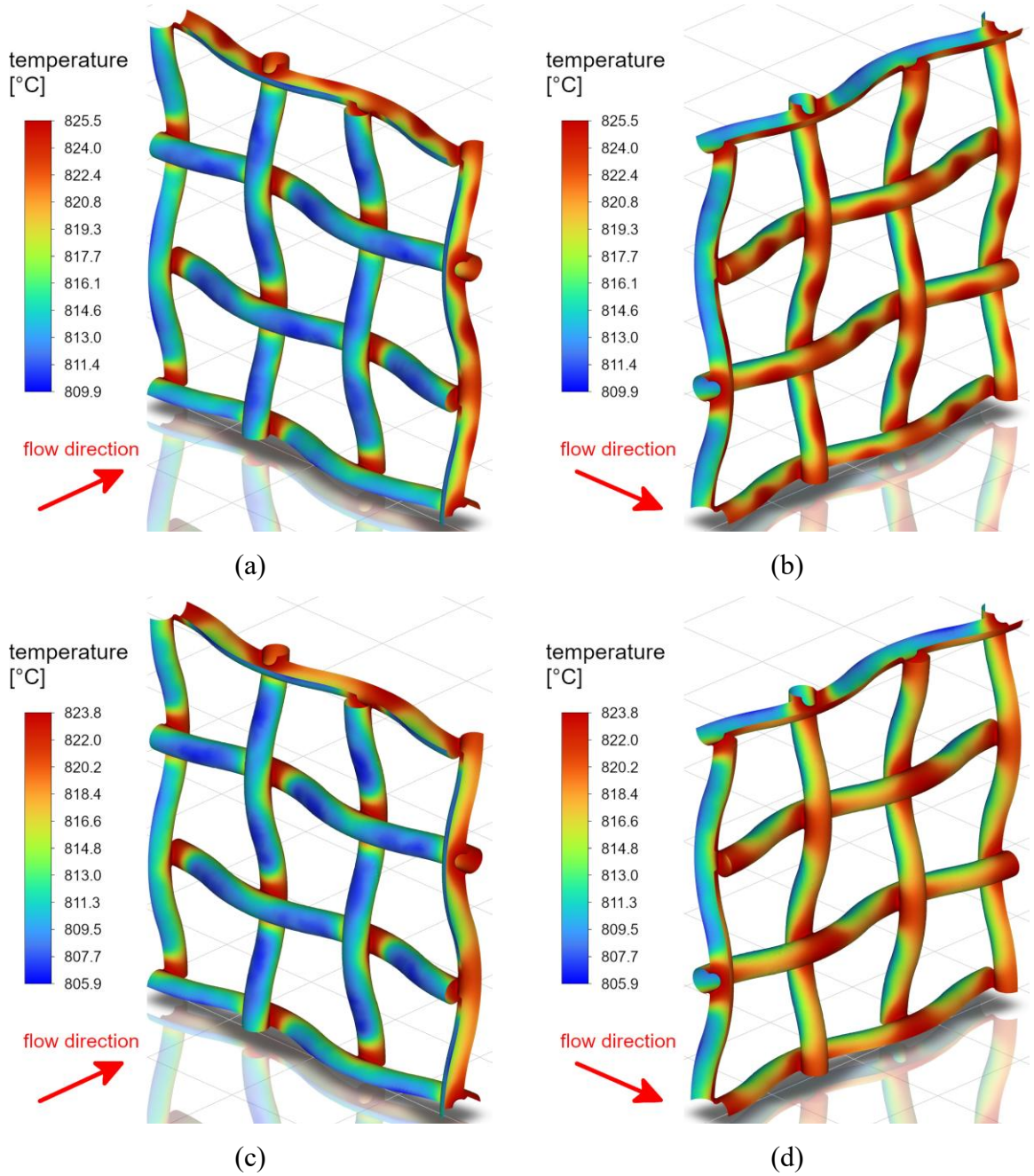

Figure 8.6. Surface temperature contours [°C] on: Geometry A first layer front side (a), Geometry A first layer back side (b), Geometry B first layer front side (c) and Geometry B first layer back side (d) (contact time 0.2 ms) [75]

This work used the temperature gradient contours on the catalyst surface to "extract" the hotspots on the gauze's first layer. Those zones were used as injection areas of platinum particles, assuming that their initial velocity is equal to the fluid velocity in the injection areas' vicinity. It can be observed in Figures 8.5 and 8.6 that temperature values vary between 8.3°C to 17.9°C, which are considerable differences since the wire's diameter has a value of only 0.06 mm. Shorter contact times result in higher gradients, which corresponds to larger stagnation zones described in the previous section. The highest temperature primarily occurs

close to the expected zones of most disrupted gas flow (highest backflows), which are the vicinities of contact spots between the gauze's wires.

8.2.3. Particle injection areas extraction

The particle injection areas were determined by identifying the boundary between "hotspots" and regions with lower temperatures. This boundary was defined at half of the temperature gradient. The computational domain's borders are set as symmetry boundary conditions, which provides a potential risk of numerical errors due to that simplification. Because of that, the platinum release areas were restricted to half of the mesh size from the symmetry boundaries. The methodology of "extraction" of the injection areas for the DPM model is shown in Figure 8.7.

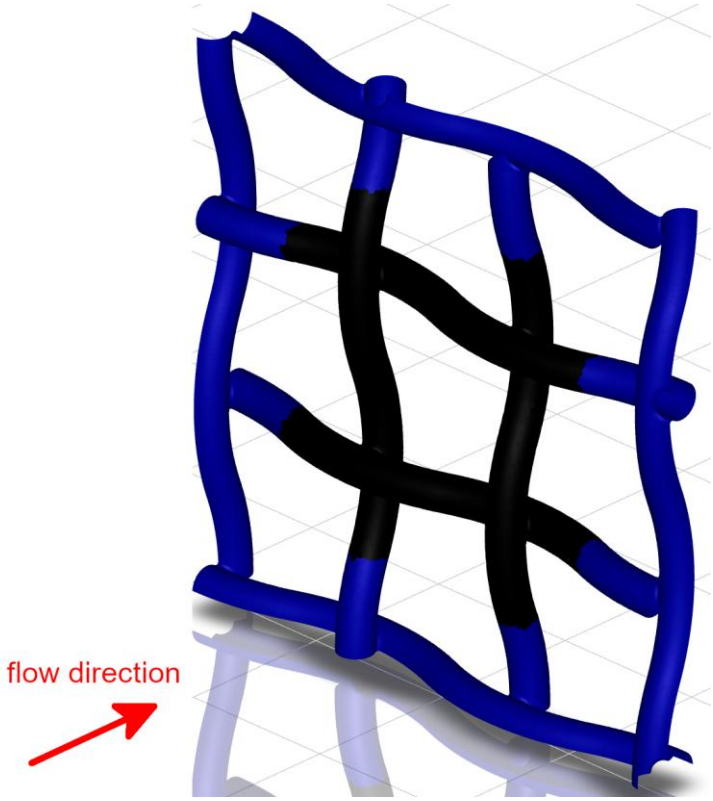

(a)

Figure 8.7. Cont.

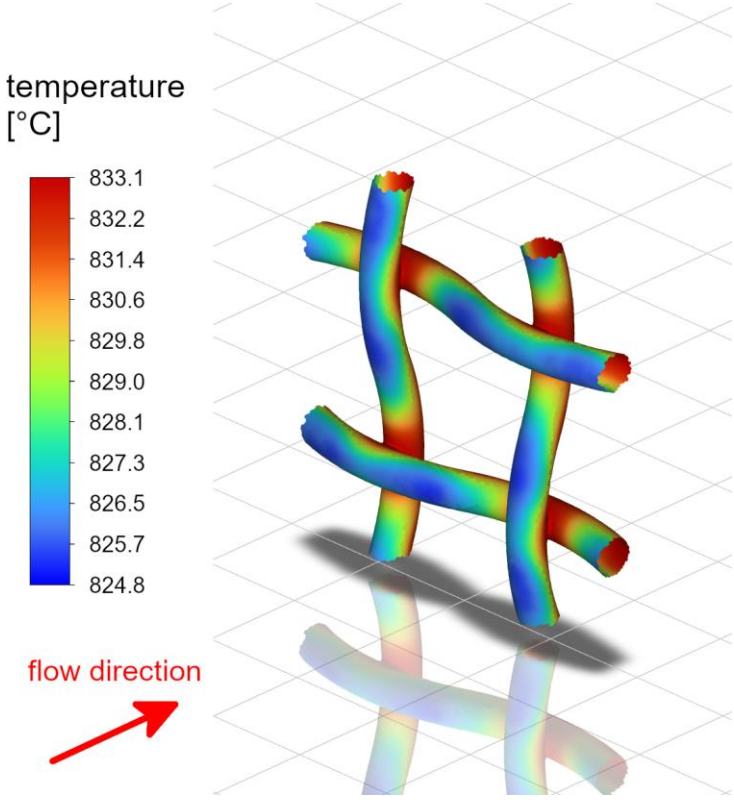

(b)

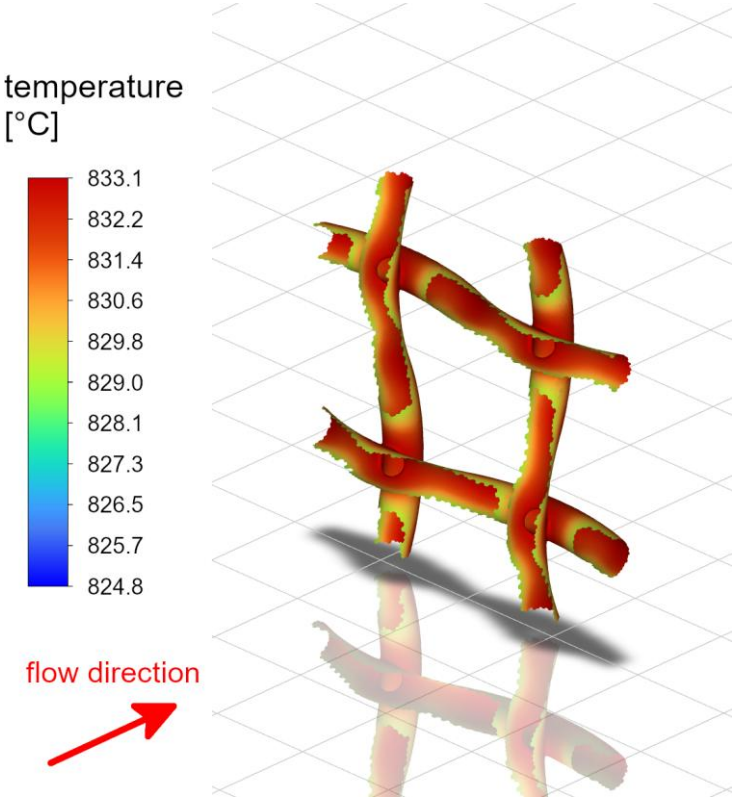

(c)

Figure 8.7. Procedure of determining the platinum particle's injection area (Geometry A, 1 ms contact time, first layer). The initial injection zone (black) was separated from the vicinity of symmetry boundary conditions (a). Then, based on surface temperature gradients (b), the applied injection area (c) was determined by "cutting" the catalyst wire's surface at half of the temperature gradient. [75]

8.3. Catalyst particles' motion and recapture modelling

Catalyst particles' motion was modelled using the discrete phase model (DPM) with the turbulent dispersion model, and deposition areas were calculated using the accretion model described in Section 4.3.7.

The recapture efficiency was calculated as follows:

$$\eta_{Pt\_trap} = \frac{N_{Pt} - N_{Pt\_loss}}{N_{Pt}} \cdot 100\% \tag{123}$$

where N_{Pt} is the number of released platinum particles from the injection areas, and N_{Pt_loss} is the number of platinum particles leaving the domain without recapturing on the gauze.

This work analysed cases for entrained particle diameters in the range between 0.1–10 μm for the particle diameter values in Table 8.3.

Table 8.3. Values of the investigated entrained catalyst particles' diameters [75]

Particle size [μm]	0.1	0.5	0.75	1	1.25	2	3	4	5	10

For setting up the platinum particle recapture conditions, two scenarios were considered:

Scenario 1 – in this case, entrained particles depose on each layer (including the first "releasing" layer). This scenario simulates the initial decomposition of the gauze, where substantial changes alter the gauze, as observed by Pura et al. [78,79] on SEM images. This scenario uses the "trap" boundary conditions for all gauze layers.

Scenario 2 – this case starts to occur during the later loading stage, when the first layer of gauze changes, causing the dead zone behind it to decrease. This causes the entrained particles to settle only on the subsequent layers. In this scenario, the "reflect" boundary condition was applied for the first layer, while the "trap" condition was set for the second and third layers.

8.4. Results

This section focuses on calculating platinum particle trajectories released from areas of increased temperatures for different contact times and particle diameters. Particles' motions were computed using the DPM model described in Section 4.3.7. Based on calculated trajectories, the recapture efficiency and deposition spots were estimated.

8.4.1. Catalyst particles' recapture efficiency

The recapture efficiency represents the recaptured percentage of released platinum particles from the injection areas (Equation (123)). Figures 8.8 and 8.9 show the platinum recapture efficiency in relation to contact time for Geometry A.

Interestingly, the results show that the same recapture mechanisms govern the catalyst particle's behaviour as in impingement mist eliminators described in Section 3.3.2. Depending on particle size and process condition, the inertial impaction and direct interception mechanisms are visible in the results. As shown in Figure 8.8, particles with diameters of 2 μm and larger tend to behave comparably since the inertial impaction mechanism dominates their motion and deposition.

Differences between Scenarios 1 and 2 are also minor. The recapture efficiency is increased for longer contact times, which results from the slower gas-phase velocity and inertial forces acting on particles. In those cases, inertial forces are significant enough to break platinum particles away from gas pathlines, causing them to depose the subsequent layer. However, larger particles' inertia alters their motion even more, increasing the chance of bypassing the subsequent gauze layers. This phenomenon results from the large mesh clearance of the gauze, especially when compared to typical demisters. The recapture rate drops quickly for shorter contact times, resulting in increased velocity (and much higher particle momentum). Particles are lifted and almost immediately removed from gas streamlines and spread out, causing a large portion of them to omit the subsequent layers.

Figure 8.9 shows the capture efficiency in relation to contact time for particles with a smaller diameter range (0.1–1.25 μm). It can be observed that those particles behave substantially differently than those with larger diameters (2–10 μm). Smaller particles, especially those with diameters below 1 μm, are dominated by the direct interception mechanism. Large gauze clearances compared to particle sizes and the character of the direct interception significantly reduce their deposition chances. Platinum particles' mass and velocity do not provide enough momentum to be effectively removed from the gas pathlines, which is particularly visible in Scenario 2 for the diameters of 0.5 and 0.75 μm (Figure 8.9 (b)). Still, even for such small particles, shorter contact times provide enough velocity (and momentum) for them to escape the gas trajectories, which results in increased recapture efficiency.

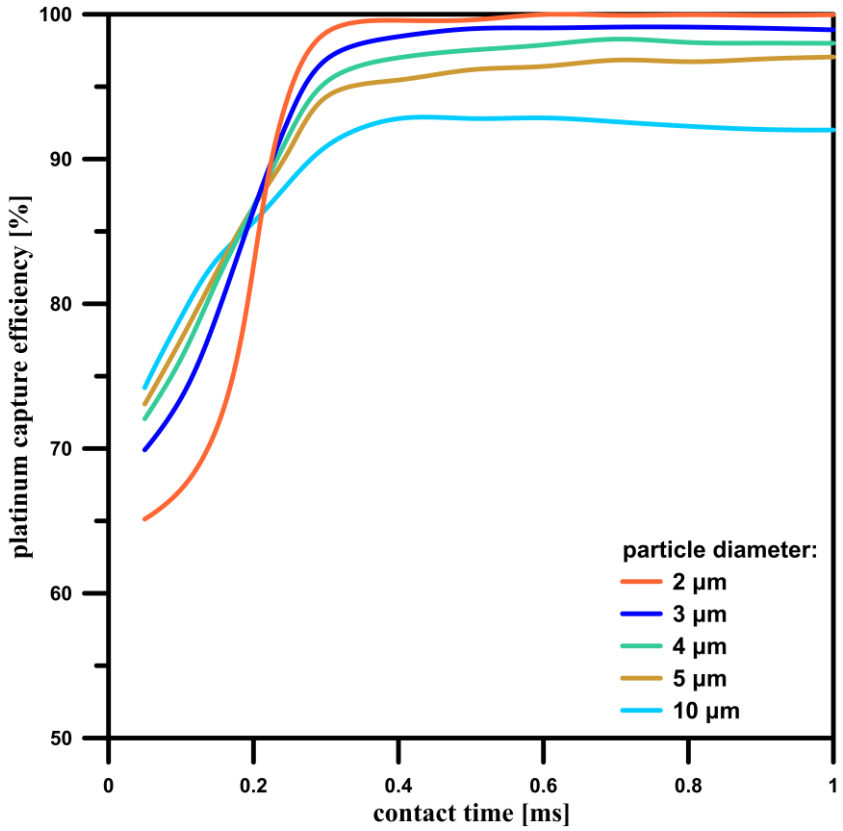

(a)

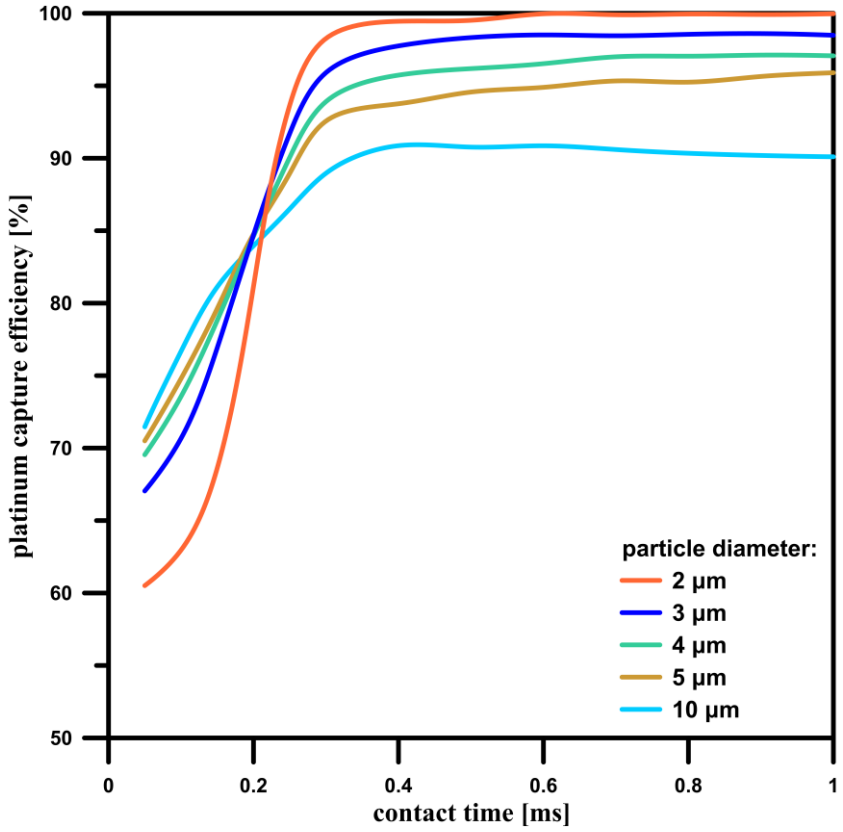

(b)

Figure 8.8. Platinum capture efficiencies as functions of contact time for Scenario 1 (a) and Scenario 2 (b) (platinum particle diameters range: 2–10 µm, Geometry A) [75]

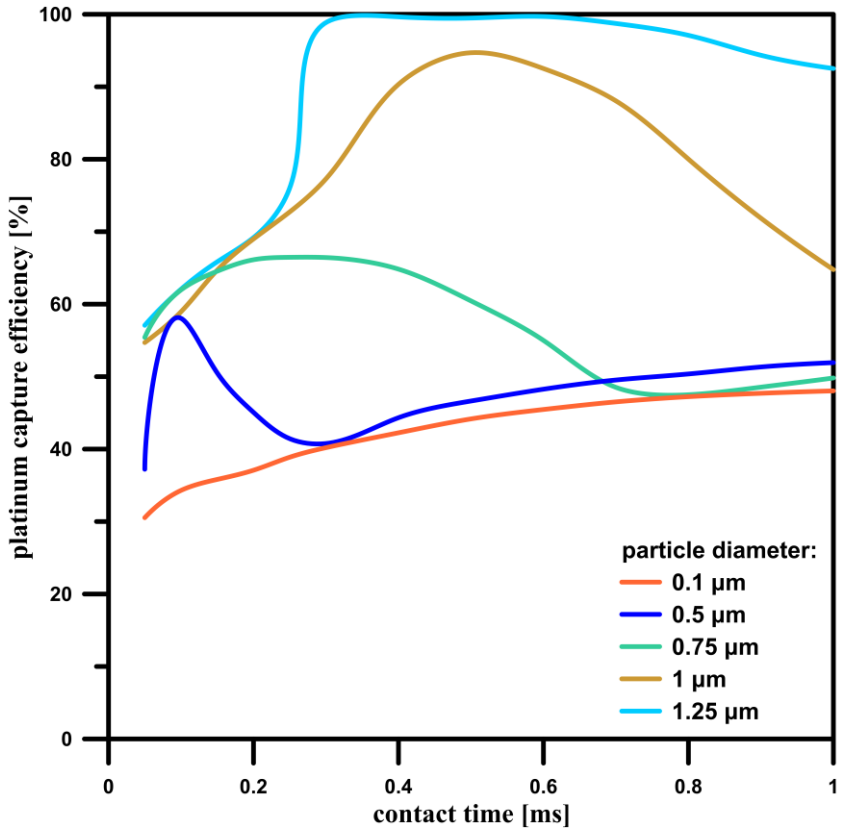

(a)

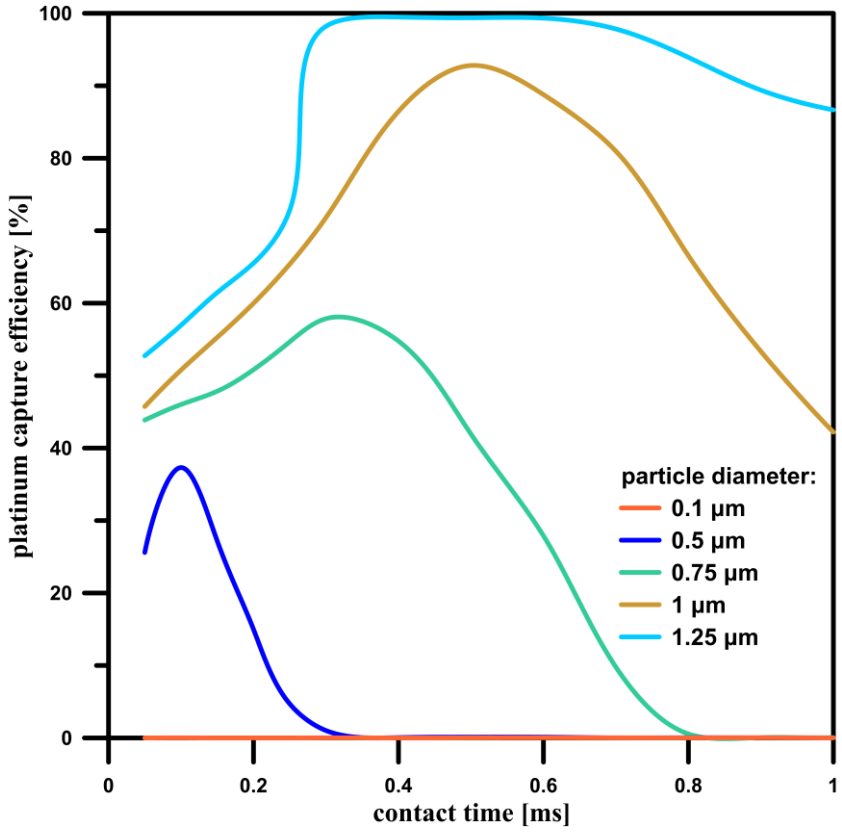

(b)

Figure 8.9. Platinum capture efficiencies as functions of contact time for Scenario 1 (a) and Scenario 2 (b) (platinum particle diameters range: 0.1–1.5 µm, Geometry A) [75]

The smallest particles (0.1 μm) do not depose in Scenario 2, which indicates that particles of this size and smaller do not depose on subsequent layers in industrial conditions. Such small particles are even in the Brownian diffusion effect range, which may increase the possibility of their immediate recapture in Scenario 1, where the first layer also takes part in the deposition process. It can be noted that a significant amount of particles from the size range of 0.1–1.25 μm depose on the first layer in Scenario 1, and this phenomenon is more visible for smaller diameters and longer contact times.

The efficiency plot for particles of 1 μm (Figure 8.9 (b)) is the most interesting case since it is visible there that both inertial impaction and direct interception mechanisms are competing with each other. For longer contact times, particles flow along the gas flow pattern like smaller particles, and only a tiny amount is recaptured. Shorter contact times provide high momentum, causing the particles to be thrown away from the gas and spread by inertia forces, also resulting in capture efficiency loss. However, in this case, there is a recapture efficiency maximum at contact times of about 0.5 ms. At this point, inertia forces are sufficient to remove particles from gas pathlines, but they are still not as high to spread them enough to bypass the subsequent layers.

Figure 8.10 presents the calculated platinum particle trajectories coloured by the velocity for the contact times of 1 ms and 0.2 ms and diameters of 0.5, 1 and 5 μm (Scenario 2). Those trajectories directly show the effects of the deposition mechanisms described above. It can be noted that particles of 0.5 μm move along the gas streamlines for the contact time of 1 ms, and inertial effects are more significant in the 0.2 contact time case where the stagnation zone's influence is also visible on particles' trajectories. Similarly, particles with 1 μm diameter mostly flow along the gas flow pattern for 1 ms contact time, while for 0.2 ms, they are subject to more significant inertia forces. Large particles of 5 μm diameter inertia forces are dominant for both contact times. In the case of 1 ms contact time, most of the particles depose on the third layer, while for 0.2 ms contact time, very high inertia results in large particle spread and low recapture efficiency.

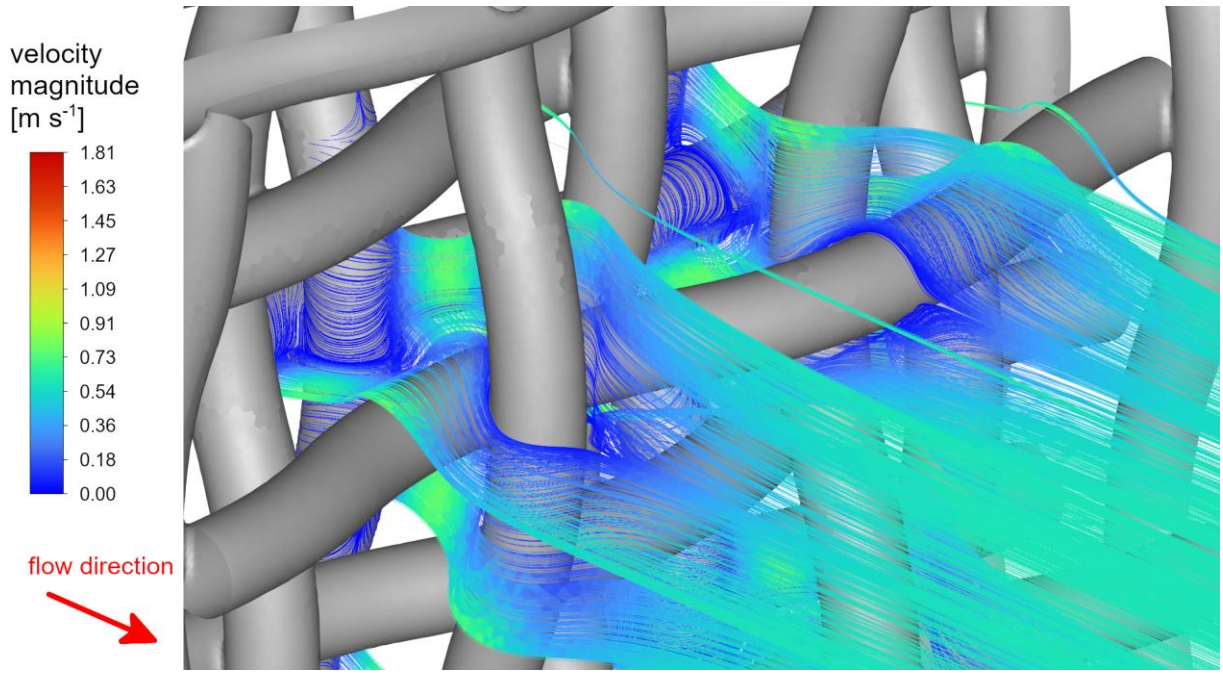

(a) 0.5 μm, 1 ms

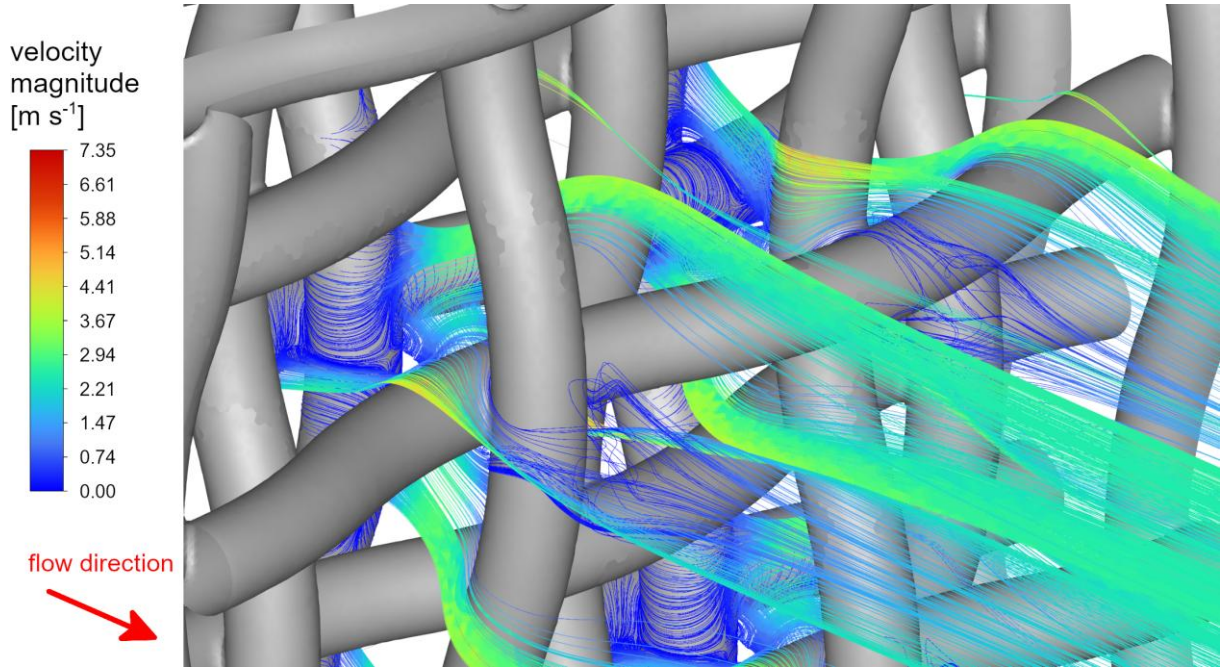

(b) 0.5 μm, 0.2 ms

Figure 8.10. Cont.

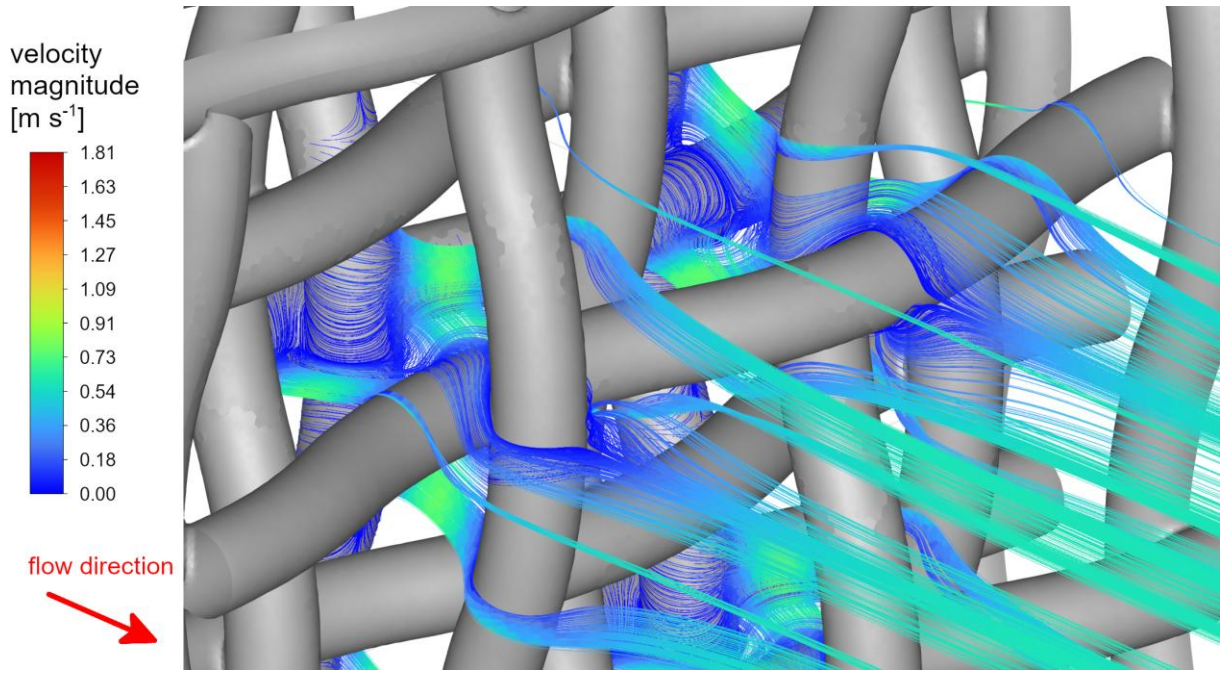

(c) 1 μm, 1 ms

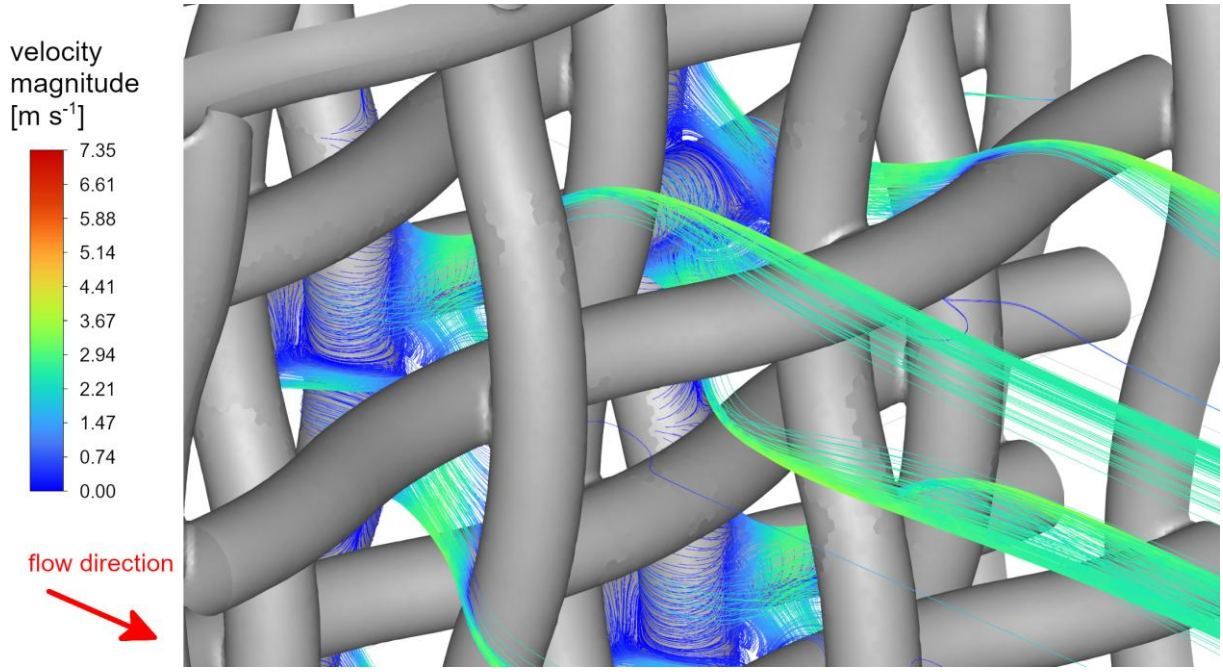

(d) 1 μm, 0.2 ms

Figure 8.10. Cont.

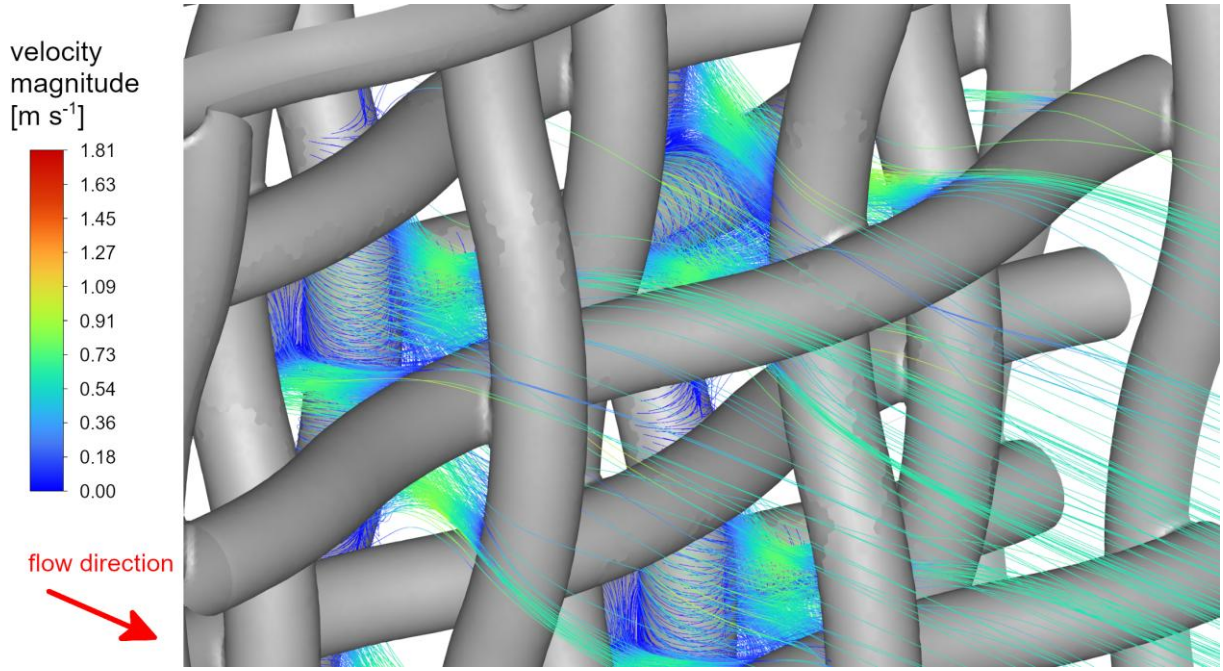

(e) 5 µm, 1 ms

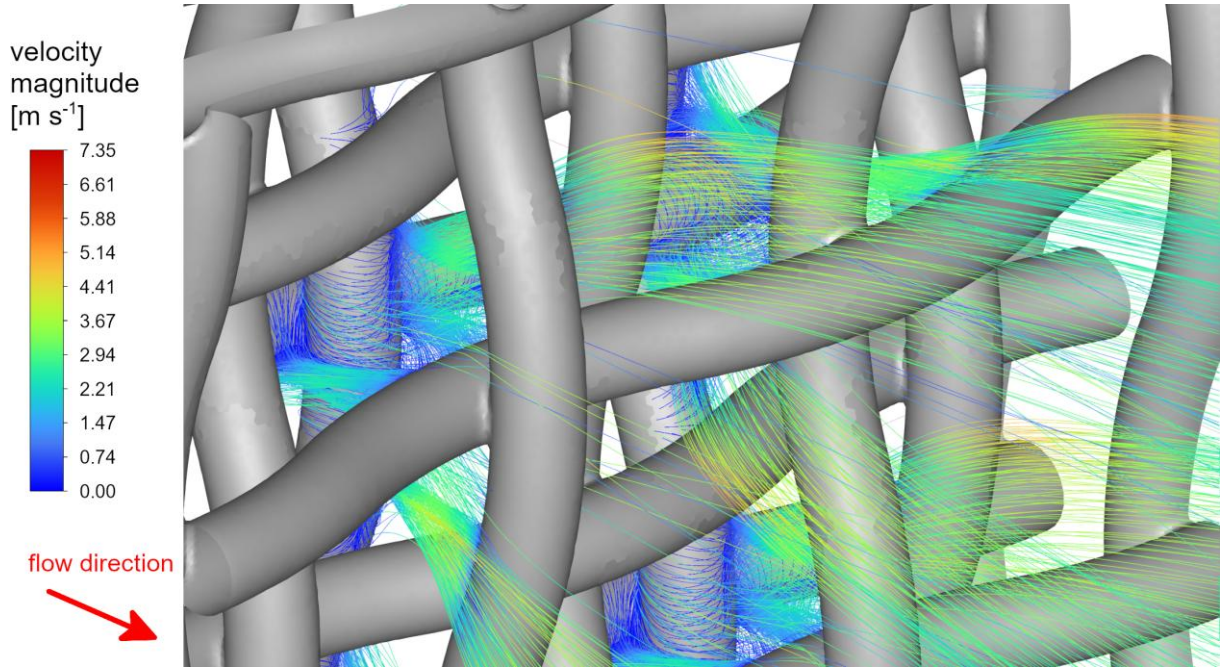

(f) 5 µm, 0.2 ms

Figure 8.10. Platinum particles' trajectories for particle diameters of 0.5 µm (a, b), 1 µm (c, d) and 5 µm (e, f) for contact times of 1 ms (a, c, e) and 0.2 ms (b, d, f) (Scenario 2, Geometry A) [75]

Figures 8.11 and 8.12 show the platinum recapture in relation to contact time for Geometry B.

It can be observed that the altered geometry of the middle layer (in Geometry B) firmly affects the particle's motion and recapture rate. For larger particles above 2 μm (Figure 8.11), the highest recapture efficiency is observed for shorter contact time, while in Geometry A, this parameter drops sharply for shorter contact times. However, in Geometry B, recapture efficiency for longer contact times is much lower than in Geometry A. Differences between Scenarios are significantly more visible for Geometry B, especially for the cases with longer contact times. Still, for shorter contact times, where capture efficiencies reach their maximum, both scenarios give comparable results.

The differences between investigated mesh variants are also substantial for the particle diameter range of 0.1–1.25 μm (Figure 8.12). Geometry B has a much higher recapture performance for shorter contact times. Those results show how geometry changes, even those small and easy to implement, could affect critical parameters.

Figure 8.13 compares the entrained particle's trajectories (coloured by velocity values) for Geometry B analogically to those presented in Figure 8.10. It can be seen how the altered second gauze layer "bends" the particle motion. This geometrical difference significantly increases deposition efficiencies for shorter contact times while doing the opposite in the cases of longer contact times.

Industrial ammonia oxidation plants are designed to operate at different contact times. The typical, most commonly used contact time is 1 ms. Yet, converters using shorter contact times are also applied since they have higher gas capacities and shorter contact times, factors that decrease the gauze degradation rate and platinum losses during production. Altered geometry, such as Geometry B, has the potential to reduce the degradation process even more by the increased recapture rate on subsequent layers, which allows the extension of the operation campaign between gauze replacements. This section shows that the particle's motion modelling provides insight into the process, which can assist the researcher with manipulating the gauze's geometry. Such modifications can reduce platinum losses under specific process operating conditions, contributing to a higher yield from a single campaign.

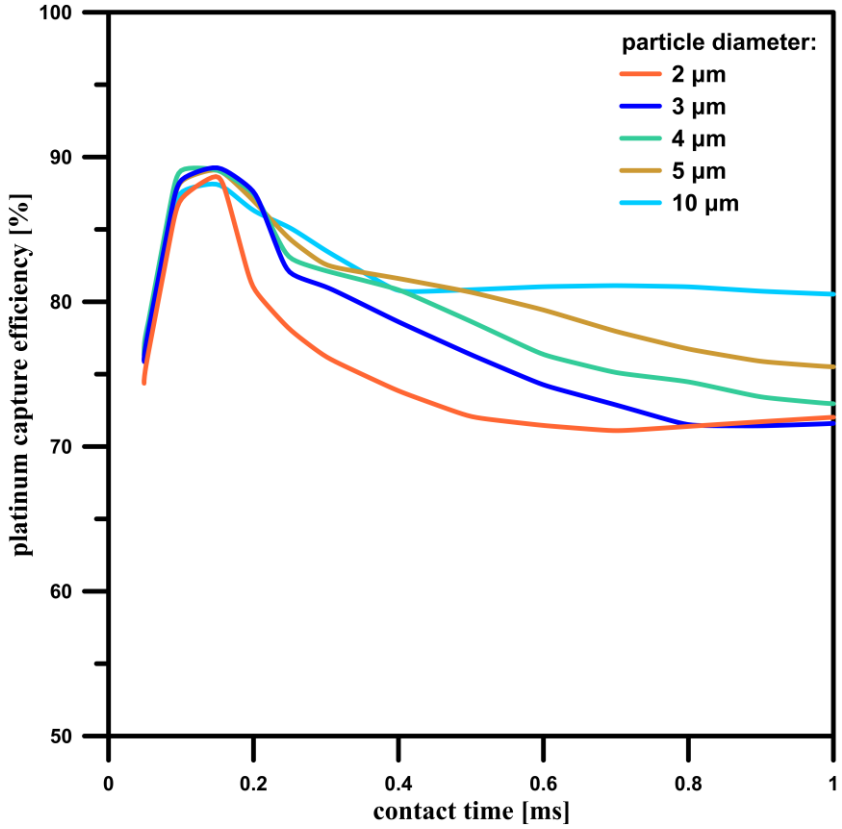

(a)

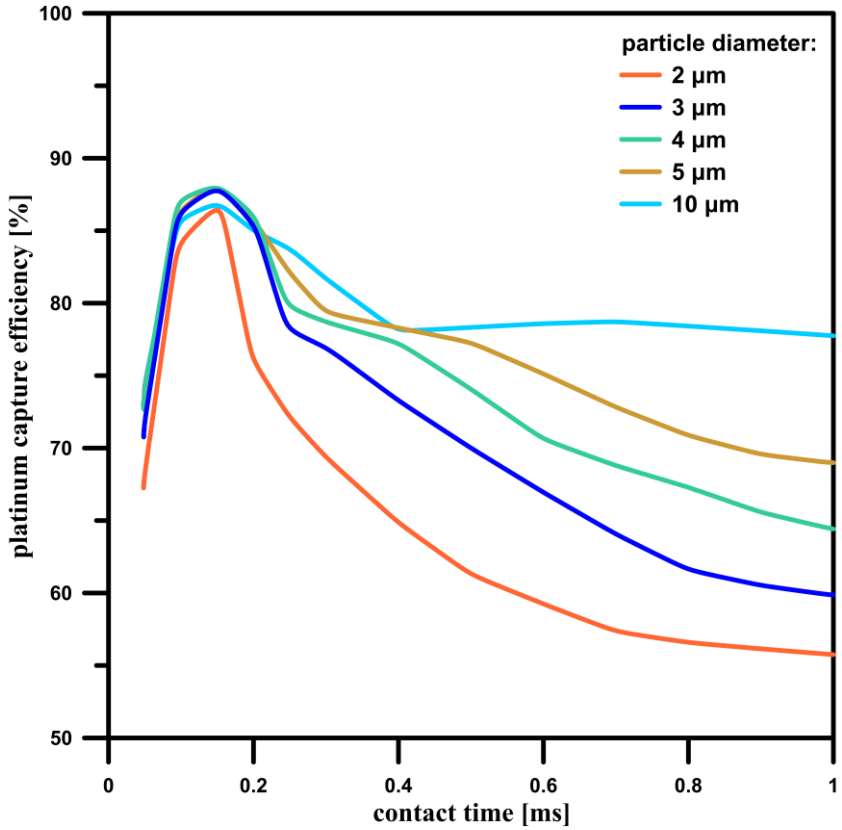

(b)

Figure 8.11. Platinum capture efficiencies as functions of contact time for Scenario 1 (a) and Scenario 2 (b) (platinum particle diameters range: 2–10 µm, Geometry B) [75]

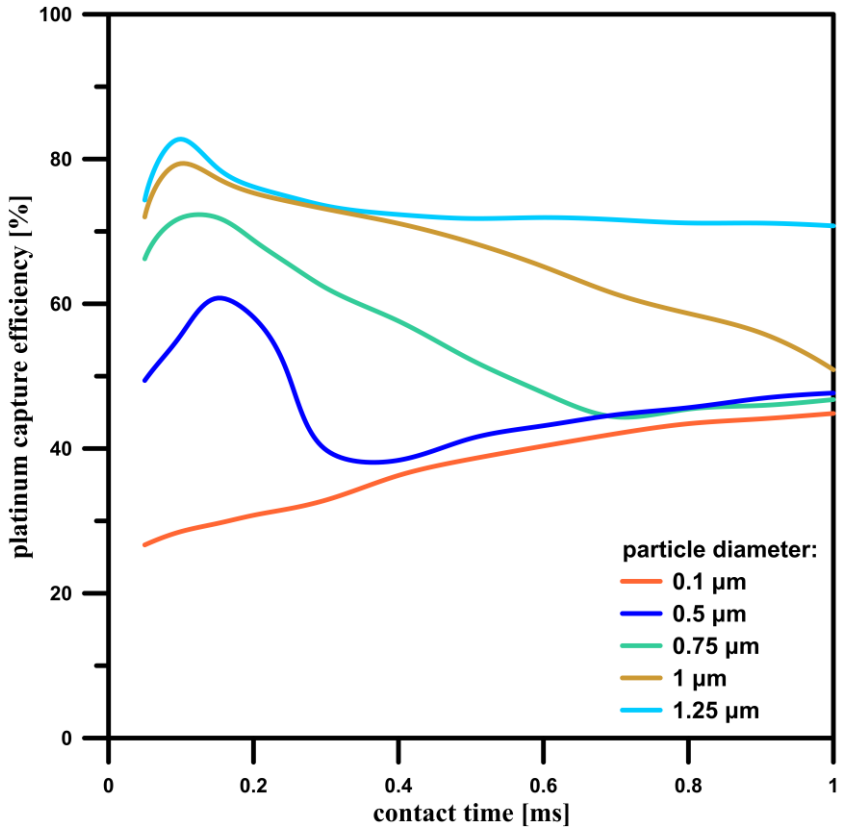

(a)

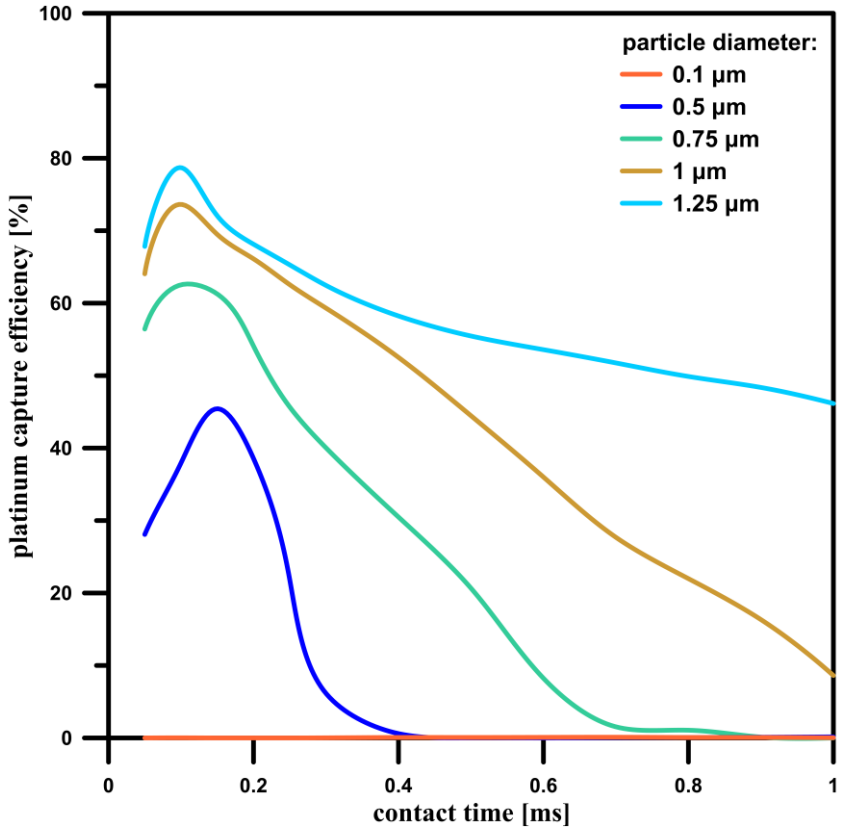

(b)

Figure 8.12. Platinum capture efficiencies as functions of contact time for Scenario 1 (a) and Scenario 2 (b) (platinum particle diameters range: 0.1–1.5 µm, Geometry B) [75]

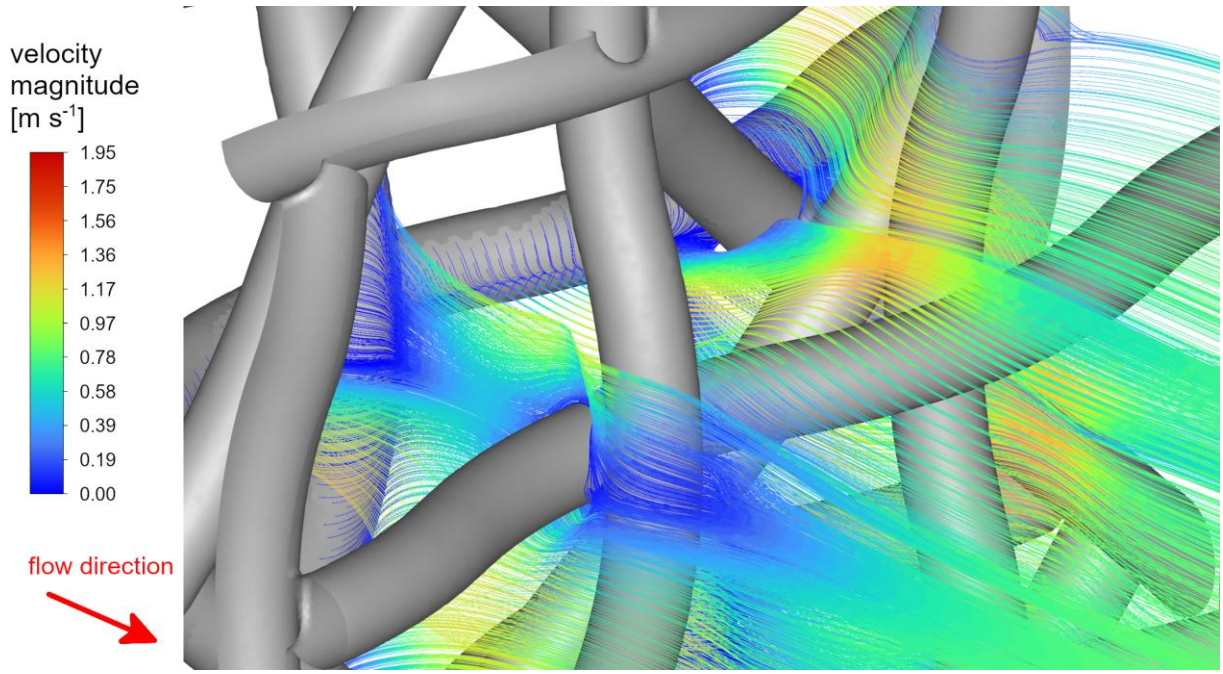

(a) 0.5 μm, 1 ms

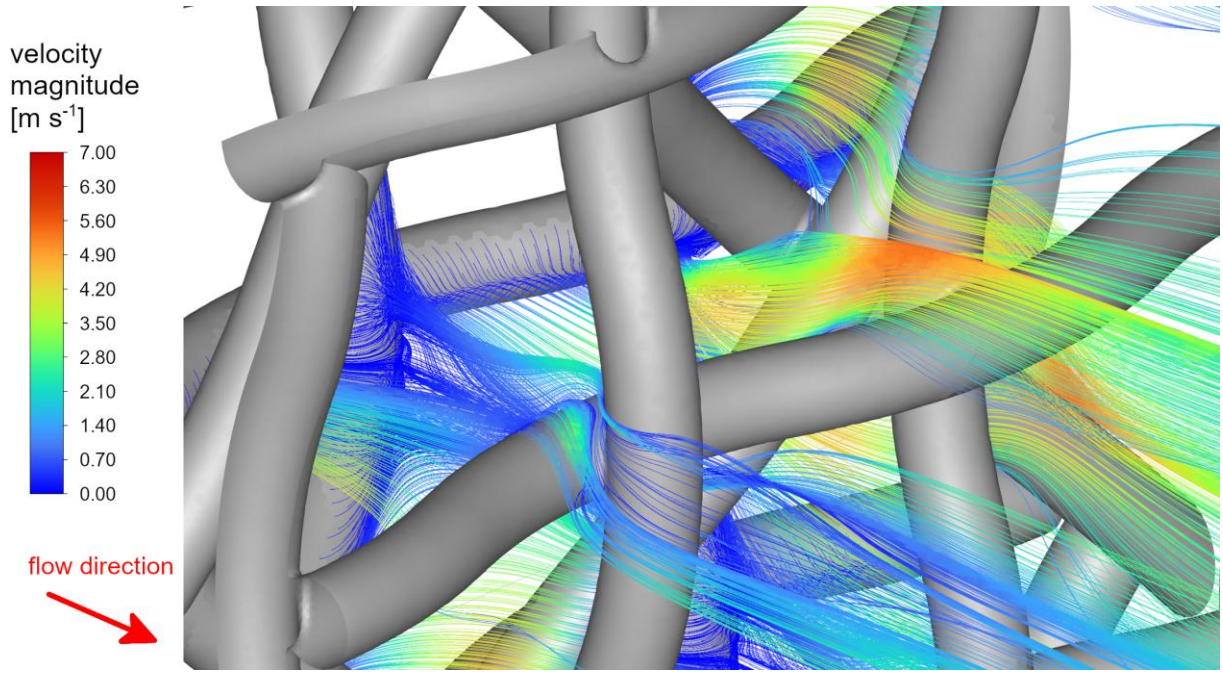

(b) 0.5 μm, 0.2 ms

Figure 8.13. Cont.

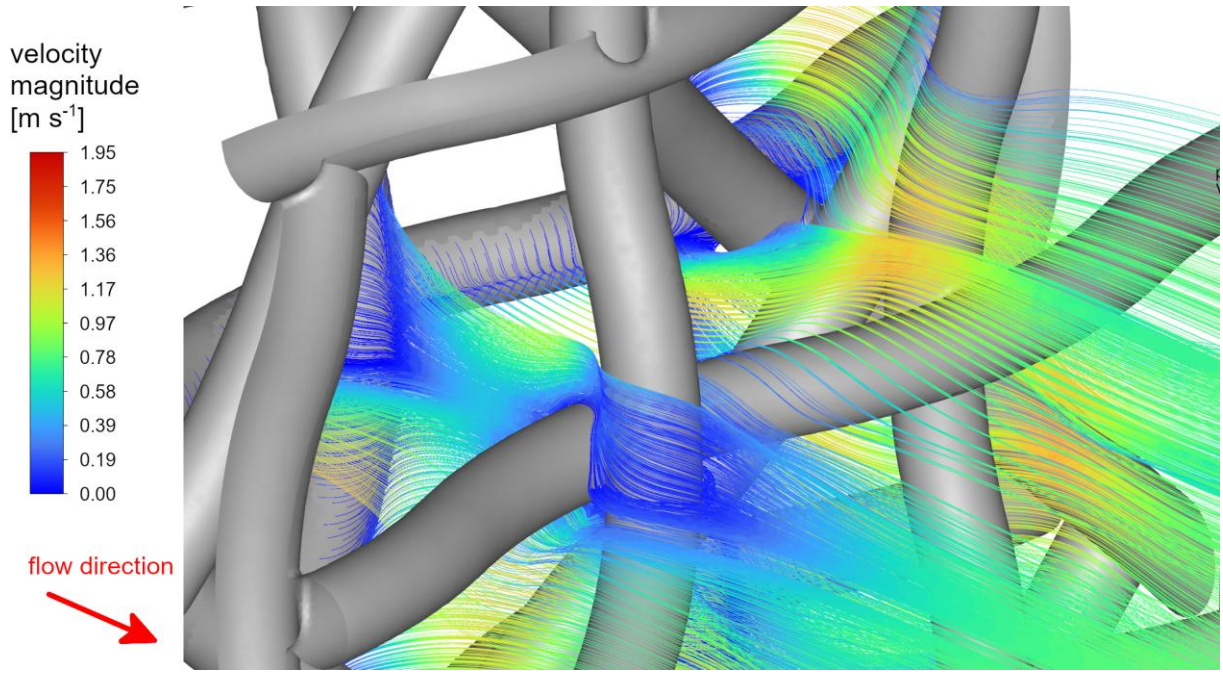

(c) 1 μm, 1 ms

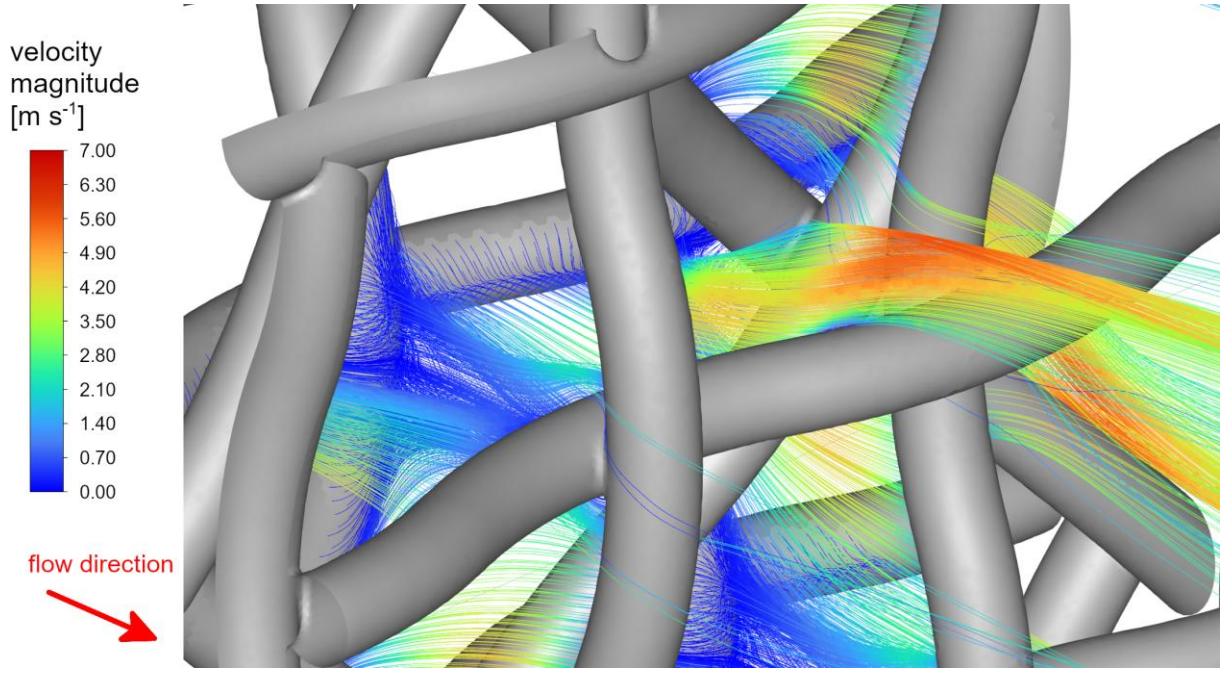

(d) 1 μm, 0.2 ms

Figure 8.13. Cont.

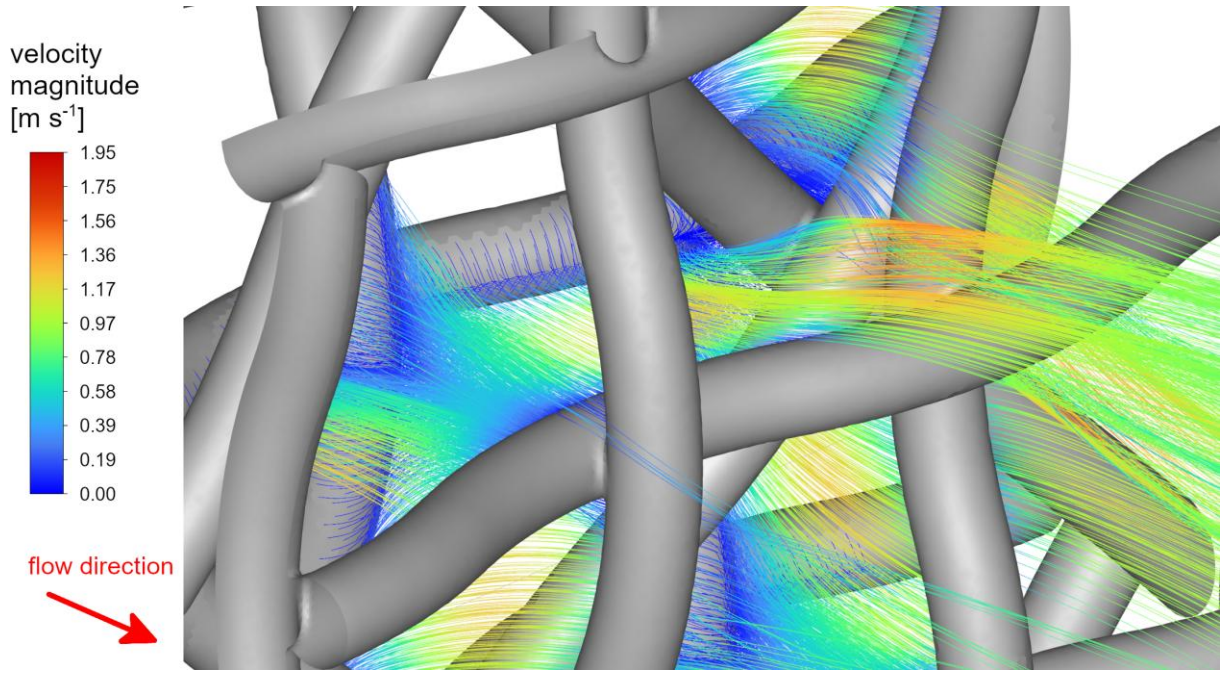

(e) 5 µm, 1 ms

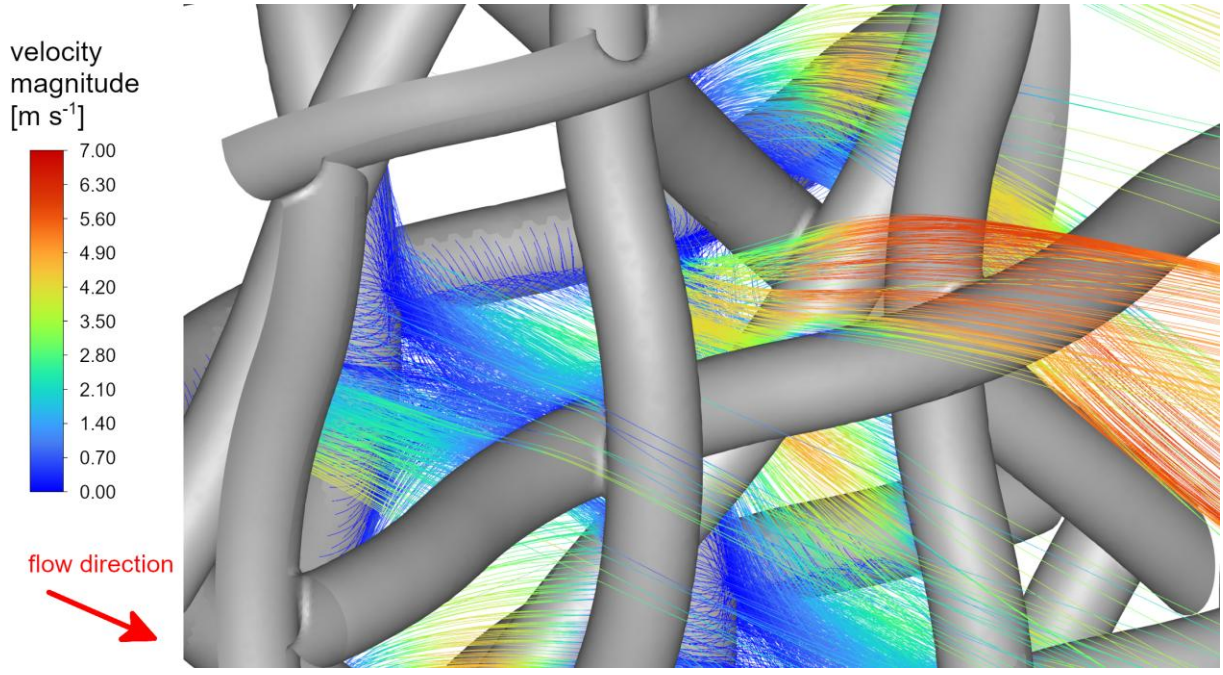

(f) 5 µm, 0.2 ms

Figure 8.13. Platinum particles' trajectories for particle diameters of 0.5 µm (a, b), 1 µm (c, d) and 5 µm (e, f) for contact times of 1 ms (a, c, e) and 0.2 ms (b, d, f) (Scenario 2, Geometry B) [75]

8.4.2. Catalyst particles' deposition areas

This section is focused on estimating the areas of increased deposition on the third layer of catalyst gauze in Scenario 2. The second layer firmly influences the gas flow pattern and, consequently, particles' motion and deposition rate, yet the platinum deposition on this layer is almost non-existent for all cases. In Scenario 1, the first layer captures mostly smaller particles (<1 μm) almost immediately after release from injection areas. However, larger particles exhibit similar behaviour in both scenarios. Figures 8.14 to 8.21 show the deposition (accretion) contours in full and clipped range to 0.1% and temperature contours as a reference since, according to the literature [45–47], the deposition locations correlate with lower temperature spots at the catalyst surface. The deposition contours represent the ratio of the local accretion rate to the sum of the accretion rate on the corresponding surface (Equation (100)), as described in Section 4.3.7. This approach allowed to obtain the contours of the percentage of captured platinum particles. Figures 8.14–8.17 present those contours for the third layer of Geometry A, Scenario 2, contact times of 1 and 0.2 and platinum particle's diameters of 1 and 5 μm.

The percentage of captured platinum contours in full range allows to assess how spread are areas of high recapture rate. It can be noted that the capture zones are most concentrated for the case with particle diameters of 1 μm and contact time of 1 ms, where the amount of platinum captured by a single computational cell reaches up to 2.97%. Larger particles cause larger recapture areas with lower maximum values. This trend agrees with the computed trajectories (Figure 8.10), showing that larger particles are subject to inertial forces, making them more likely to spread out. The effect of inertial forces is also more visible for higher gas velocities (shorter contact times). Clipped ranges of recapture contours, where red colour indicates cells with values over 0.1% and 0.01%, better illustrate the favoured deposition spots. Those have a significant role in the process since they are potential places of platinum mass buildup, where formations called "cauliflower structures" are most likely to start growing.

The accuracy of deposition contours can be verified by comparing their profiles with temperature contours. According to the experimental observations [45–47], particles are expected to have increased deposition rates in colder zones. The results agree with this trend since increased deposition areas exhibit a similar pattern as colder and mid-temperature spots visible in surface temperature contours. This indicates the reasonable accuracy of the results. Still, if possible, experimental validation using precisely the same geometry and process conditions is always recommended in computational fluid dynamics.

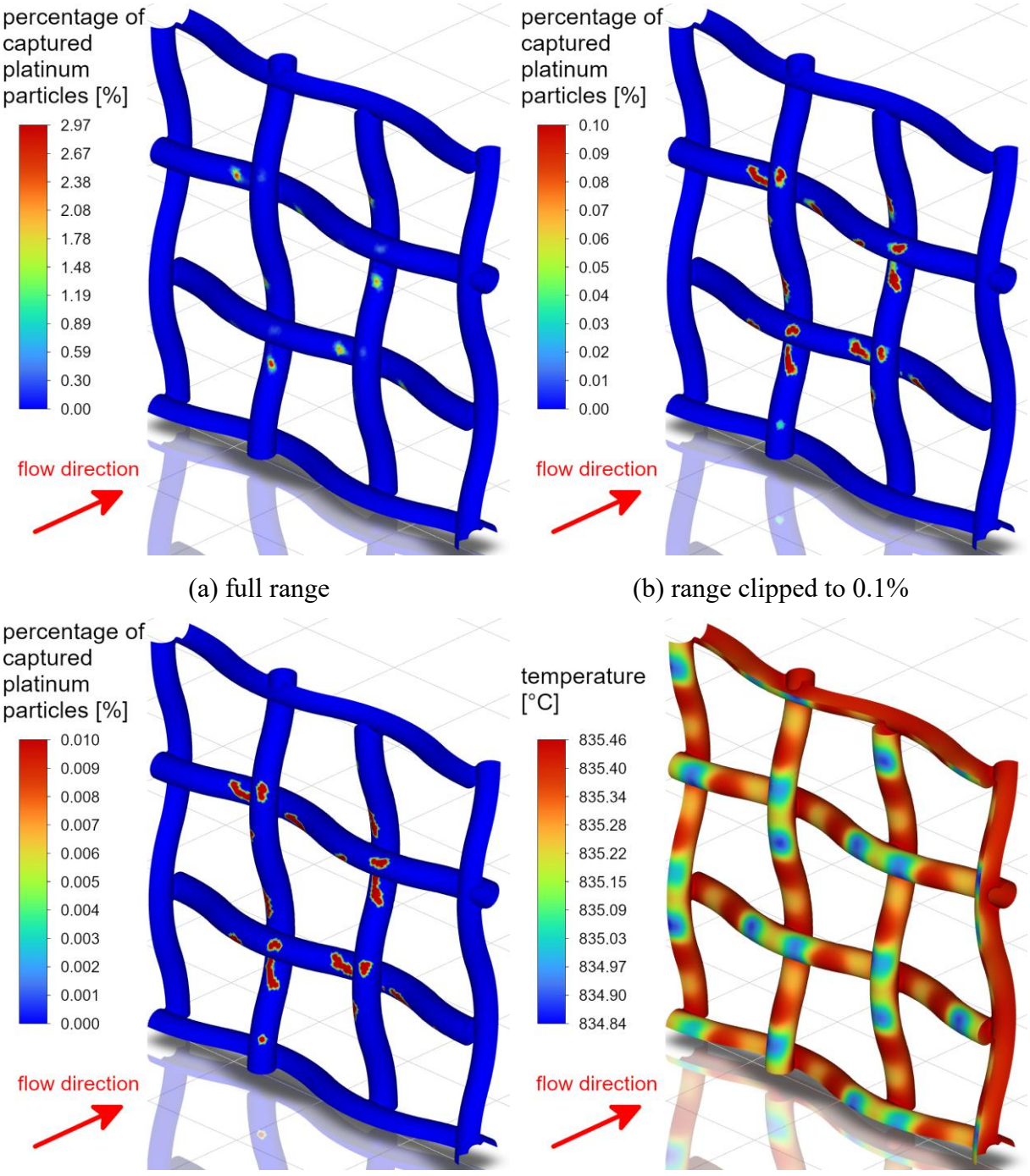

(a) full range

(b) range clipped to 0.1%

(c) range clipped to 0.01%

(d) temperature

Figure 8.14. Contours of the percentage of captured platinum particles of the gauze's third layer: full range (a), clipped range (b, c), and temperature contours (d) (Geometry A, contact time 1 ms, particle diameter 1 µm, Scenario 2) [75]

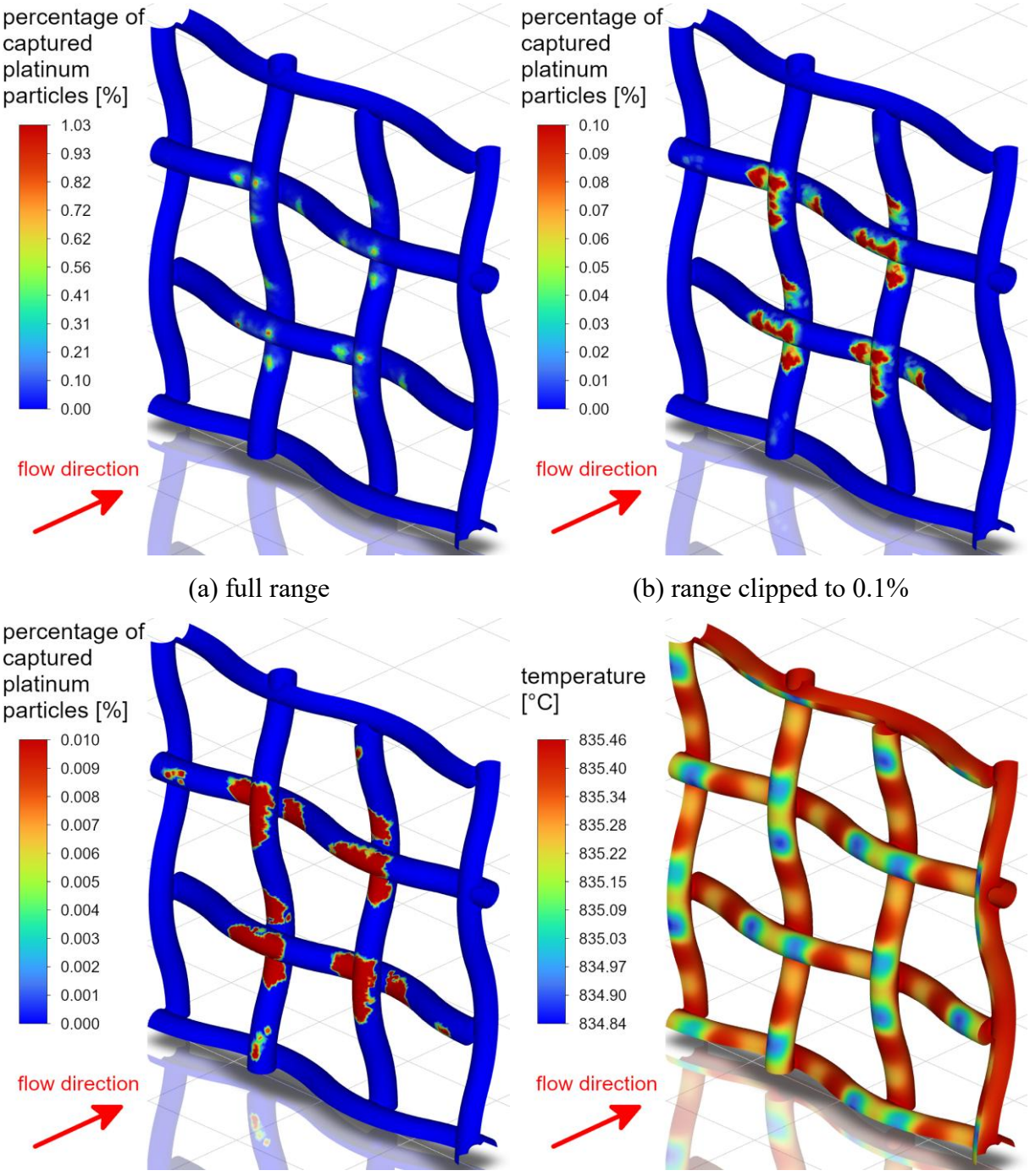

(a) full range

(b) range clipped to 0.1%

(c) range clipped to 0.01%

(d) temperature

Figure 8.15. Contours of the percentage of captured platinum particles of the gauze's third layer: full range (a), clipped range (b, c), and temperature contours (d) (Geometry A, contact time 1 ms, particle diameter 5 µm, Scenario 2) [75]

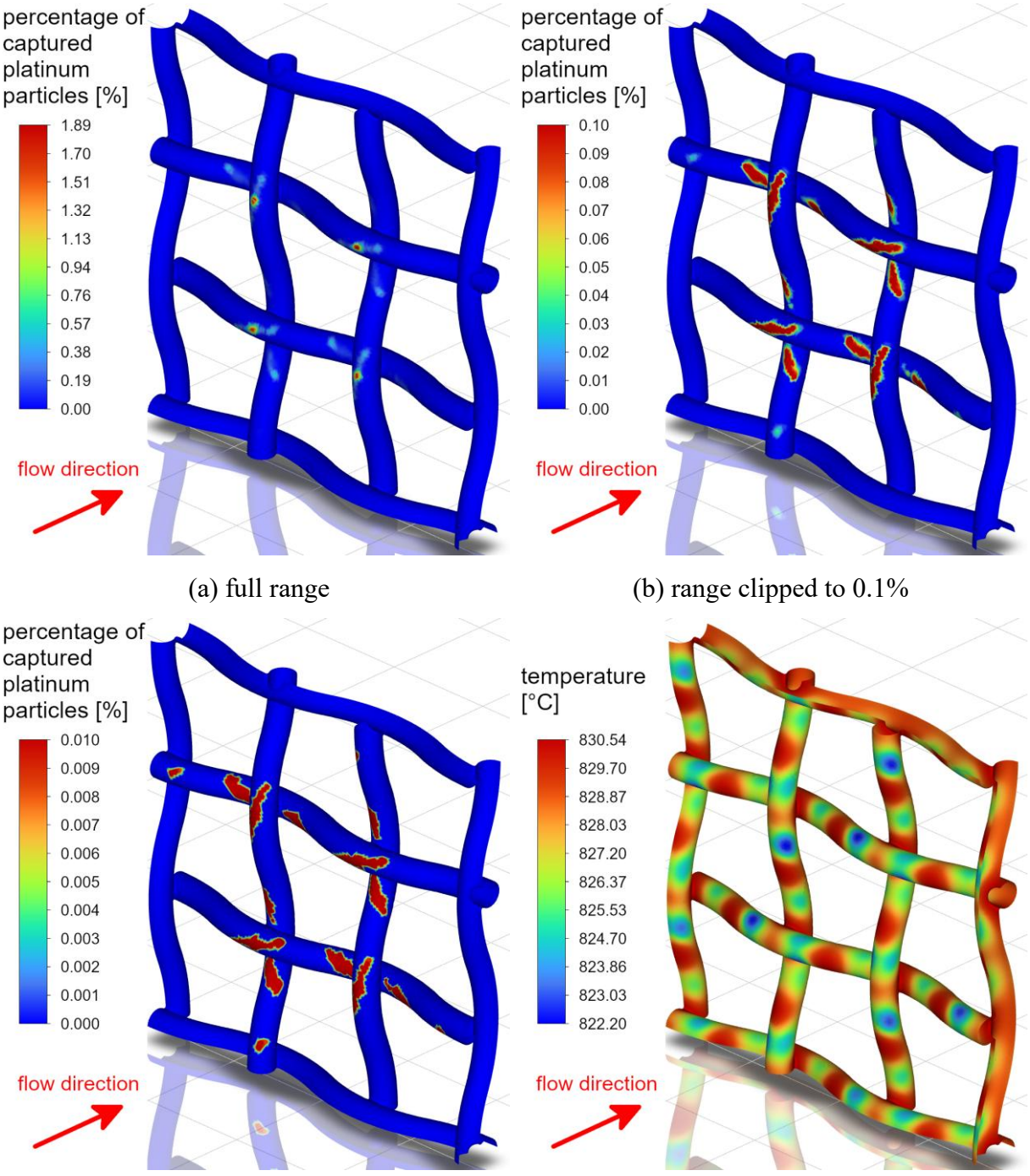

(a) full range

(b) range clipped to 0.1%

(c) range clipped to 0.01%

(d) temperature

Figure 8.16. Contours of the percentage of captured platinum particles of the gauze's third layer: full range (a), clipped range (b, c), and temperature contours (d) (Geometry A, contact time 0.2 ms, particle diameter 1 µm, Scenario 2) [75]

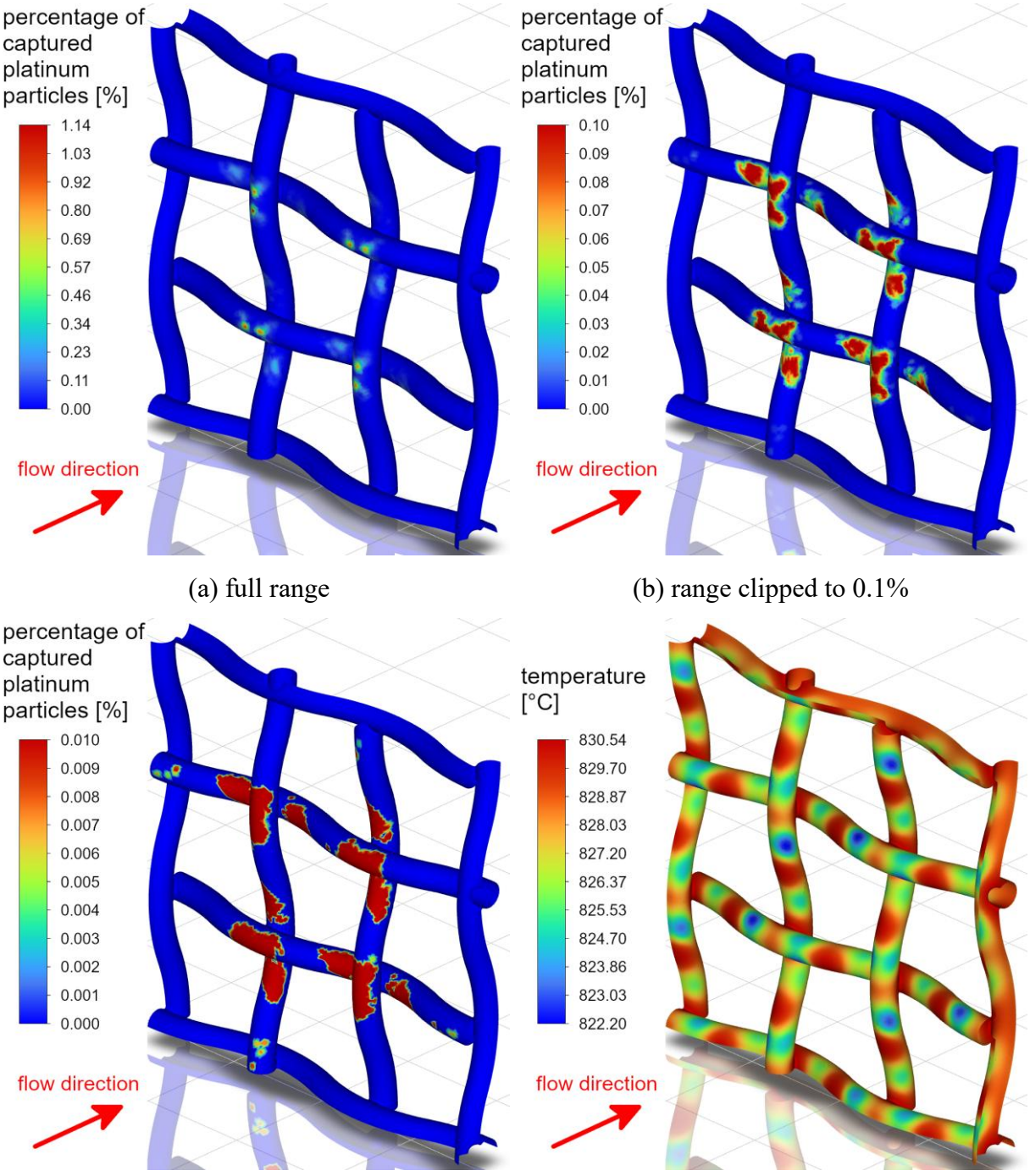

(a) full range

(b) range clipped to 0.1%

(c) range clipped to 0.01%

(d) temperature

Figure 8.17. Contours of the percentage of captured platinum particles of the gauze's third layer: full range (a), clipped range (b, c), and temperature contours (d) (Geometry A, contact time 0.2 ms, particle diameter 5 µm, Scenario 2) [75]

Figures 8.18–8.21 present the contours of platinum deposition for the third layer of Geometry B for Scenario 2, contact times of 1 and 0.2 and platinum particle's diameters of 1 and 5 μm.

In Geometry B, the third layer's surface temperature gradients substantially differ from those in Geometry A, resulting from altered second-layer geometry in the Geometry B gauze variant. Continuous zones of lower temperatures are more extensive, and the trends of platinum deposition in colder spots are even more visible.

The recapture rate is also more concentrated in the case of an article diameter of 1 μm and contact time of 1 ms, where peak capture rates are significantly larger (7.68%) and have smaller areas than in the corresponding case of Geometry A. Those observations suggest that Geometry B has the potential to exhibit more concentrated initial spots of "cauliflower structures" than Geometry A in the analogous cases.

It should be noted that these deposition gradients were computed in steady-state mode without interaction between continuous and discrete phases or dynamic mesh changes. Because of those simplifications, the results indicate initial spots of "cauliflower structures" growth. Modelling further development of those structures requires transient simulations with coupled continuous and discrete phases and dynamic computational mesh changes. However, those simulations would be time-consuming and require enormous computational resources. Still, the steady-state CFD model obtained in this work provides valuable insight into the critical process of catalyst gauze degradation and recapture of entrained particles. It allows the study of those phenomena with relatively low computational resources, granting the opportunity to estimate the influences of geometrical and process parameter changes accurately.

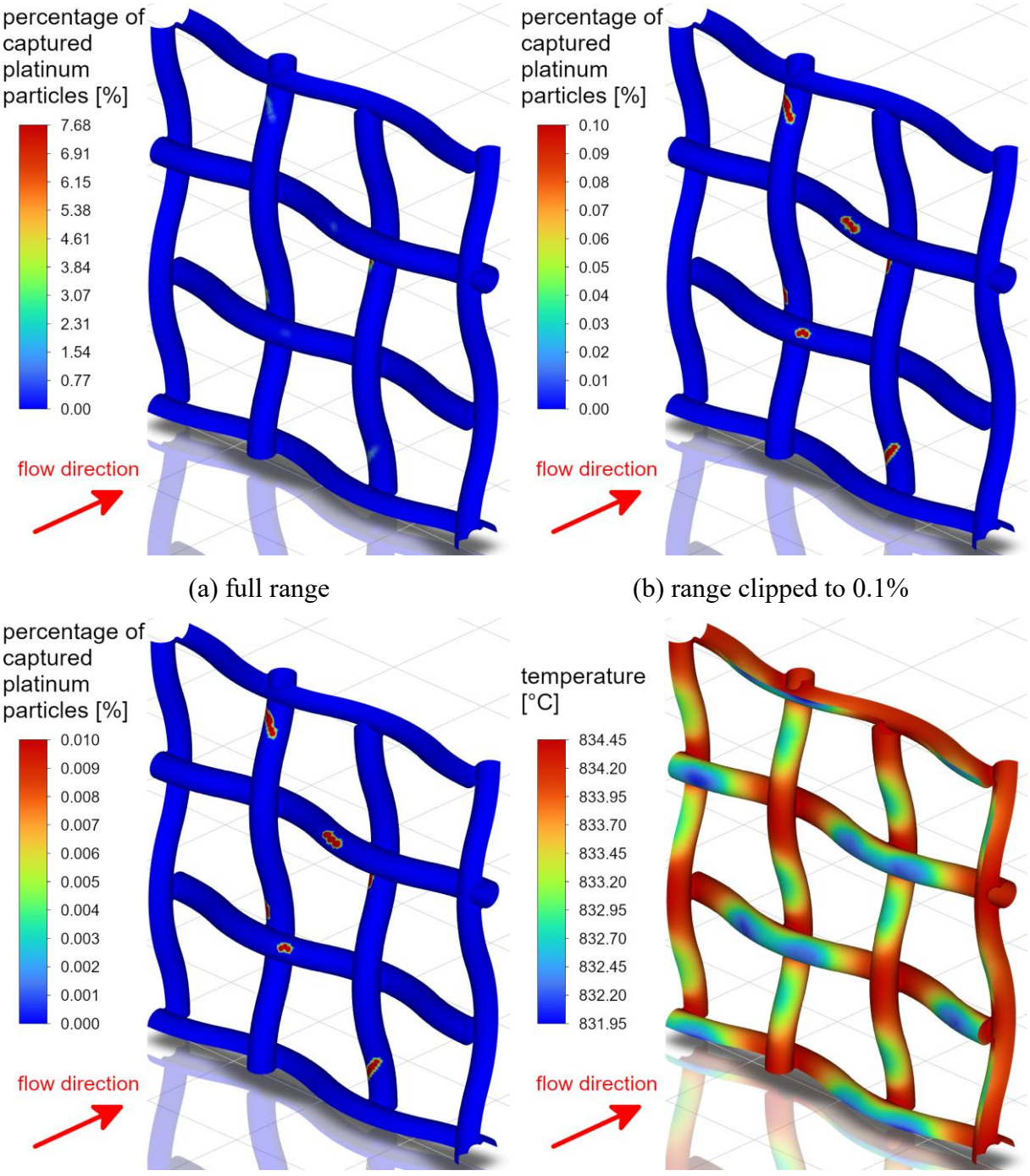

(a) full range

(b) range clipped to 0.1%

(c) range clipped to 0.01%

(d) temperature

Figure 8.18. Contours of the percentage of captured platinum particles of the gauze's third layer: full range (a), clipped range (b, c), and temperature contours (d) (Geometry B, contact time 1 ms, particle diameter 1 µm, Scenario 2) [75]

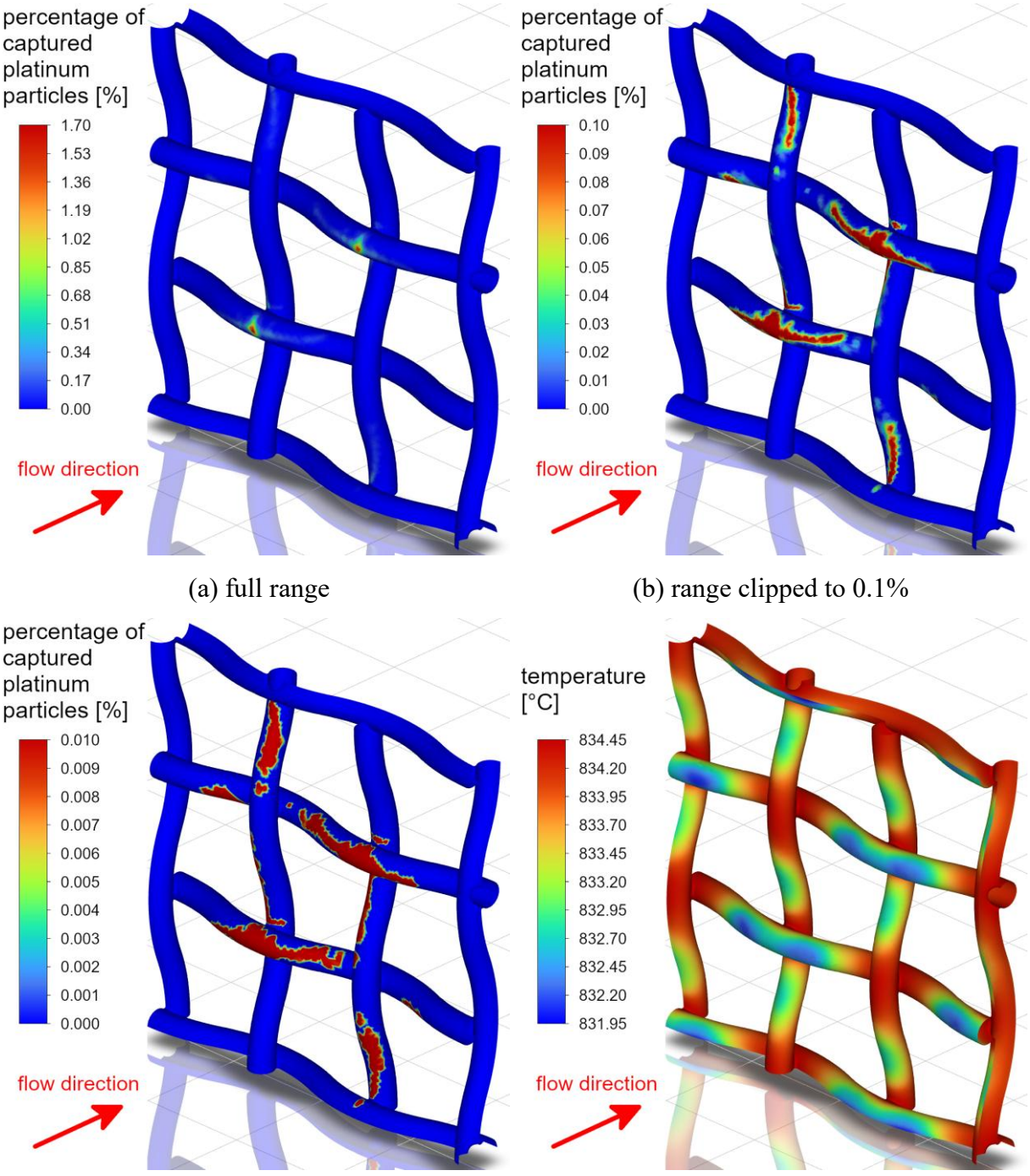

(a) full range

(b) range clipped to 0.1%

(c) range clipped to 0.01%

(d) temperature

Figure 8.19. Contours of the percentage of captured platinum particles of the gauze's third layer: full range (a), clipped range (b, c), and temperature contours (d) (Geometry B, contact time 1 ms, particle diameter 5 µm, Scenario 2) [75]

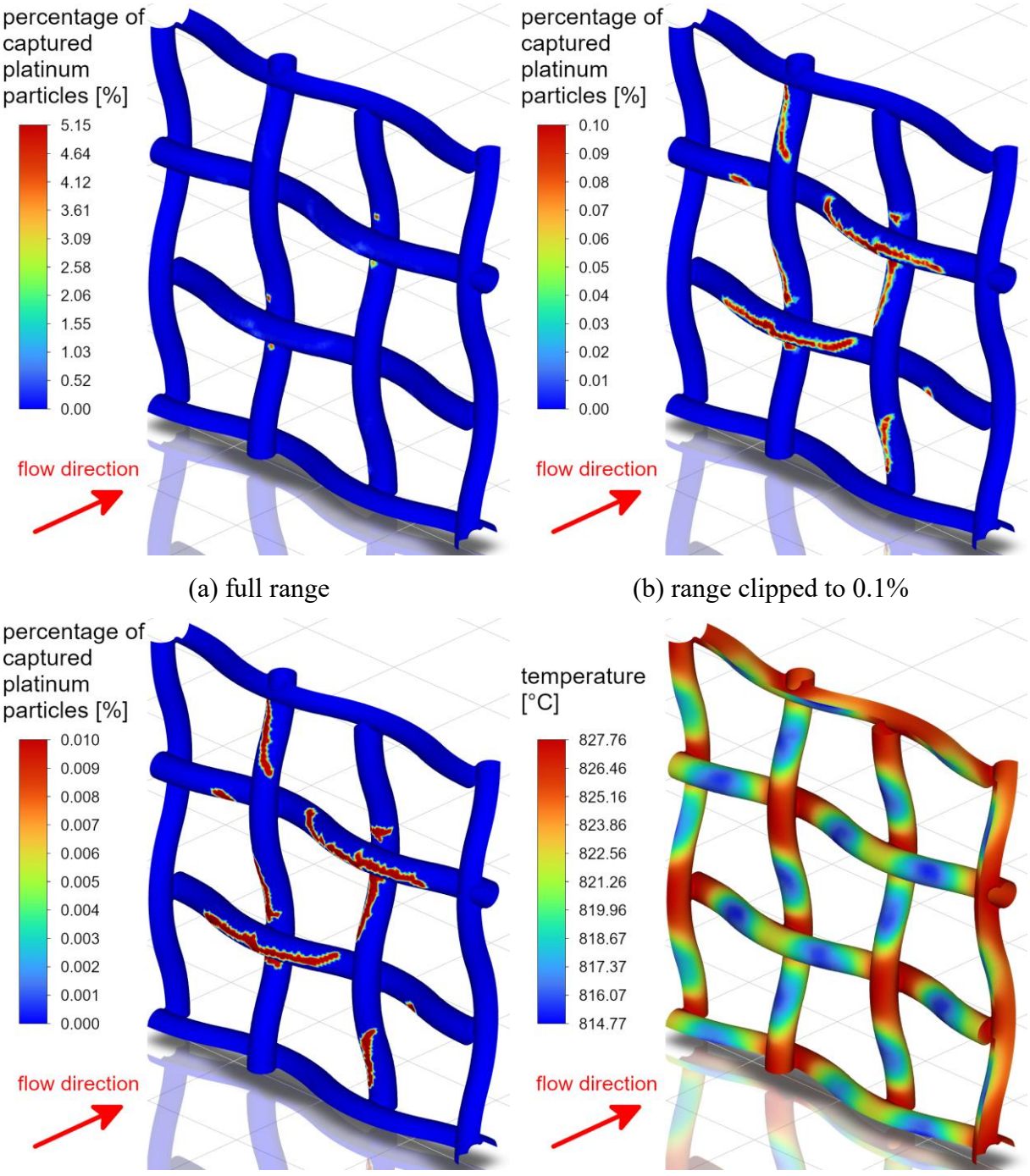

(a) full range

(b) range clipped to 0.1%

(c) range clipped to 0.01%

(d) temperature

Figure 8.20. Contours of the percentage of captured platinum particles of the gauze's third layer: full range (a), clipped range (b, c), and temperature contours (d) (Geometry B, contact time 0.2 ms, particle diameter 1 μm, Scenario 2) [75]

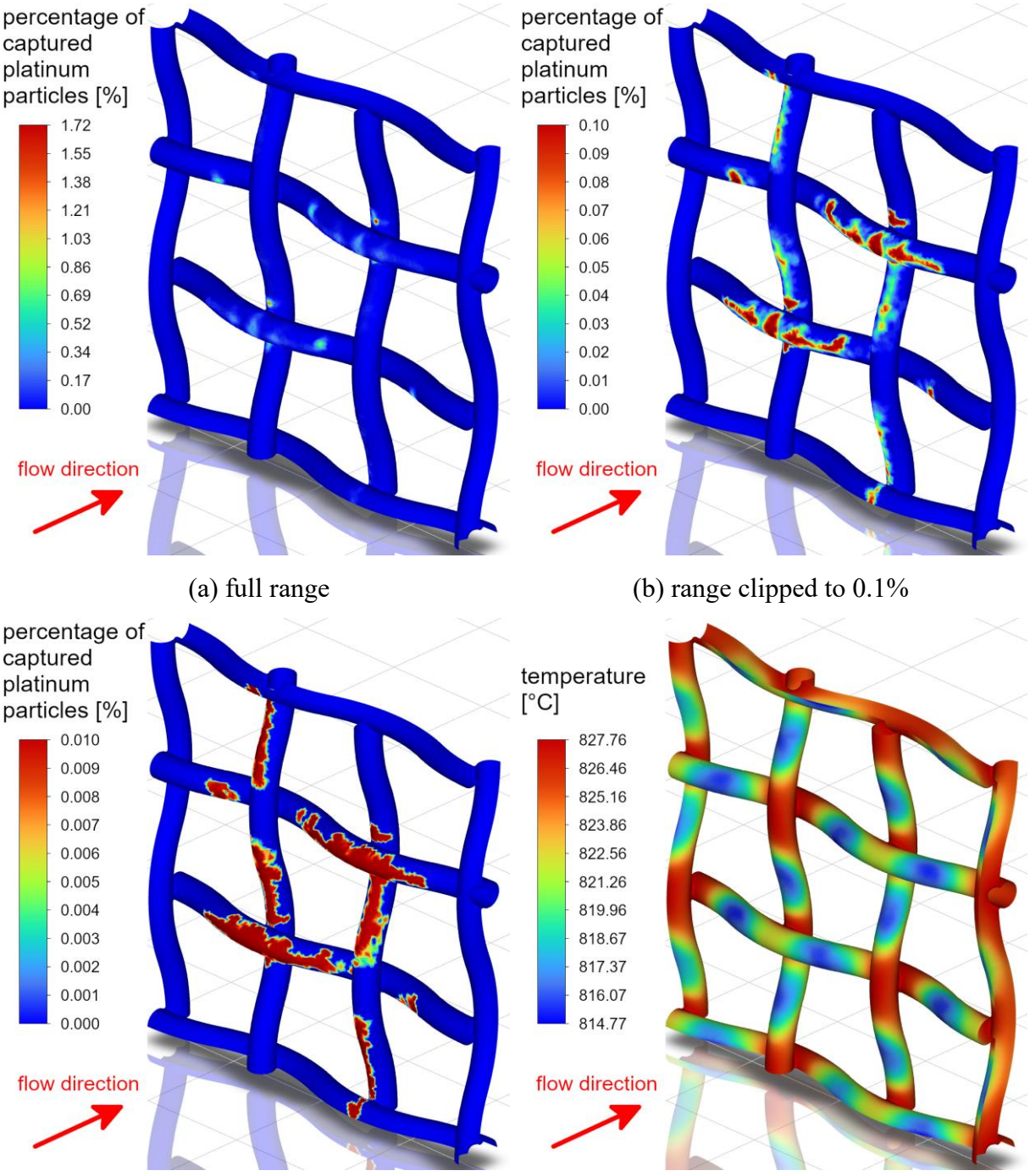

(a) full range

(b) range clipped to 0.1%

(c) range clipped to 0.01%

(d) temperature

Figure 8.21. Contours of the percentage of captured platinum particles of the gauze's third layer: full range (a), clipped range (b, c), and temperature contours (d) (Geometry B, contact time 0.2 ms, particle diameter 5 μm, Scenario 2) [75]

8.5. Reaction efficiency differences between gauze geometrical variants

The alternate variant of catalyst gauze (Geometry B) has noticeably larger clearances in the second layer. This feature directly affects the gas velocity, which needs to be higher due to the importance of maintaining proper contact time, which should be the same as in analogous cases for Geometry A. However, those changes affect the overall process product efficiencies, which are the factors that must be considered while estimating the running costs of the process using the Geometry B gauze variant. Figure 8.22 compares the efficiencies of both geometries in relation to contact time.

It can be noted that the net NO efficiency is lower by 3–30% for Geometry B. The differences are more significant for shorter contact times, where its application would benefit most since the platinum recapture is significantly increased in these conditions compared to Geometry A. Still, the net production efficiency of undesired N_2O is also much lower for shorter contact times, and this difference exceeds 20%, which is highly desirable.

There is also another essential factor concerning the Geometry B gauze variant. Due to the less dense second layer, it requires less platinum for construction (approximately 10% less mass than Geometry A). Since platinum is a costly material, this difference may significantly affect the installation costs of the new gauze. While considering reduced platinum demand for construction, increased catalyst recapture rate, and reduced N_2O production efficiency, Geometry B can be a viable choice for converters designed to operate in shorter contact times. Moreover, improved platinum recapture consequently allows for a longer time for production campaigns, which consequently translates into increased production and cost efficiency, making the direct reduction of net NO efficiency acceptable. It should be noted that this consideration depends on current platinum and rhodium prices since the gains from reducing catalyst loss need to compensate for lower reaction efficiency.

The modified second layer of the Geometry B gauze variant can also be used as a penultimate layer in converters using more than three layered gauzes. This could lead to significant platinum loss reduction in shorter contact time operations. In those cases, the net NO production efficiency would be noticeably smaller.

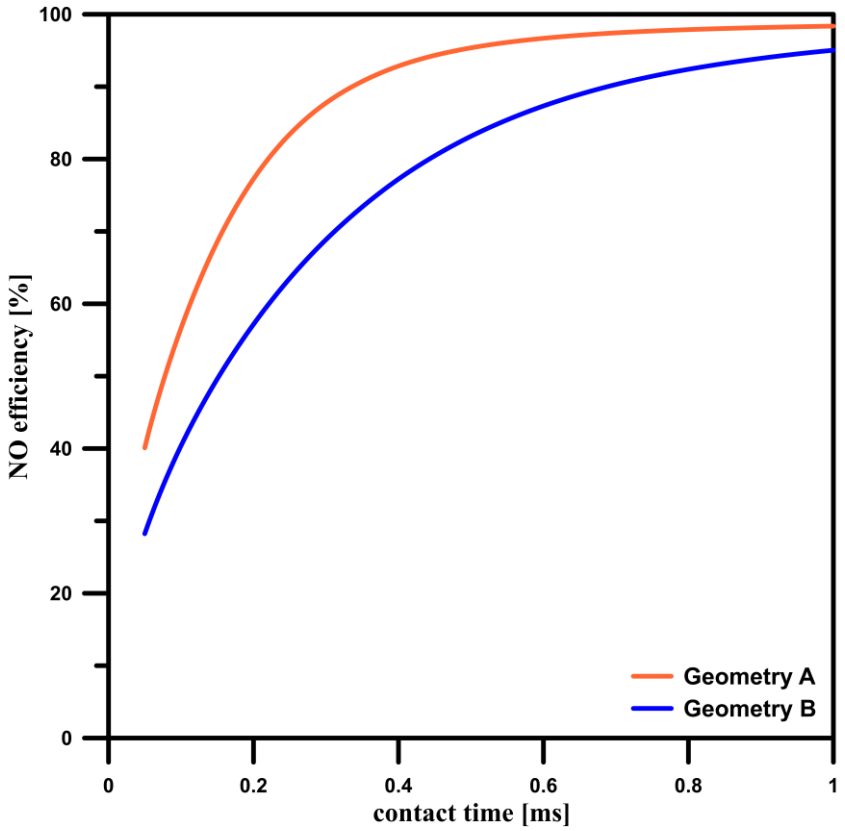

(a)

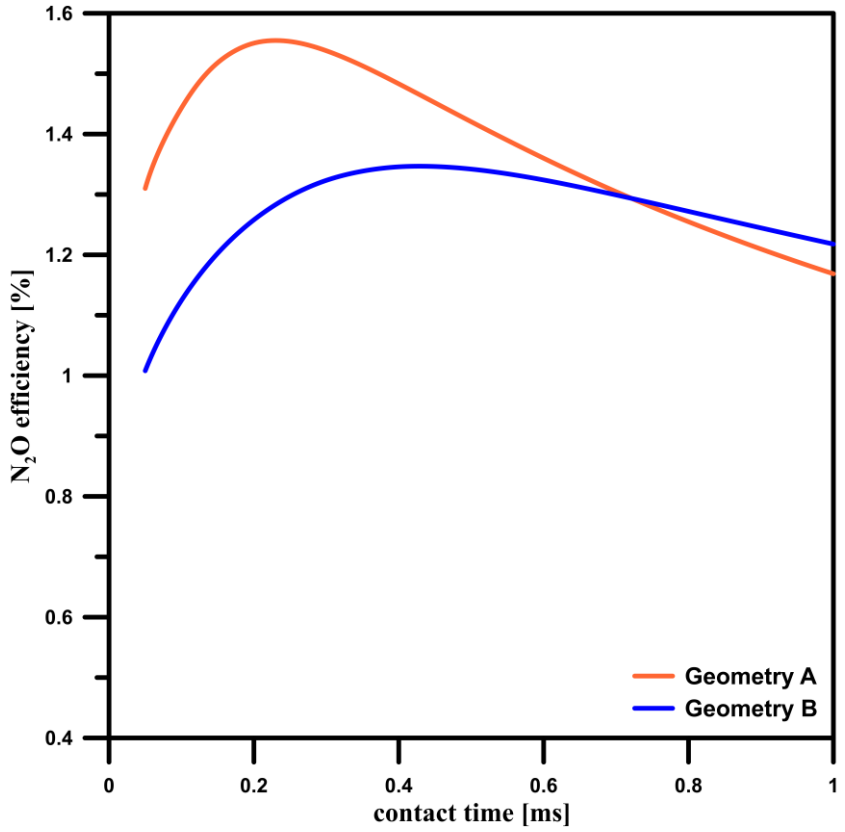

(b)

Figure 8.22. Comparison of cumulative NO (a) and N_2O (b) efficiencies as functions of contact time for investigated catalyst gauze geometry variants [75]

8.6. Conclusions

This section applied the CFD model created in Section 7 to analyse the catalyst degradation issue. The temperature gradients were the basis for defining the entrained catalyst particles' injection areas, and the discrete phase model was used to compute the particles' trajectories and deposition.

The calculated particles' trajectories provide the possibility to estimate the particle recapture efficiencies of the subsequent layers within the same catalyst gauze. The obtained model allows the investigation of different contact times and entrained particle sizes. Results show that the particles mainly depose on the last layer of the 3-layered gauze. However, the geometry and arrangement of the second layer substantially influence the entire recapture efficiency. The analysed typical industrial gauze exhibits reasonable recapture rates for the higher contact times. In contrast, the gauze with the altered middle, rotated by 45° and shifted by half of the mesh size (Geometry B), has better recapture performance for shorter contact time conditions. These results can also be valuable for the gauzes with more than three layers, where the altered gauze from Geometry B can act as a penultimate layer, improving the recapture efficiency.

The obtained results illustrate the particle deposition trends that correlate with the temperature gradients. In the analysed case, the favoured deposition areas covered the areas of cooler or mid-range surface temperatures, corresponding with experimentally observed trends reported in the literature [45–47]. This convergence indicates that steady-state CFD models with uncoupled continuous and discrete phases can accurately estimate the initial spots of "cauliflower structures" growth using low computational resources. Furthermore, those results can be a reliable basis for transient modelling of catalyst degradation phenomenon with dynamic changes of the "cauliflower structures".

Obtained CFD simulations agree with literature reports and have the potential to be fully experimentally validated. They allow for cost-efficient and relatively easy investigation of geometrical and process changes without building physical prototypes and can act as a support numerical tool for experimental research.

9. Supporting process – droplet removal through a mist eliminator

Ammonia synthesis and oxidation processes are primary unit operations of the more extensive industrial technological line which aims to produce fertilisers. However, supporting units also have essential roles, such as preventing equipment failure, helping to reduce running costs, or optimising the process. Droplet removal is an example of supporting unit operation, which, in the case of fertiliser production lines, can be used to remove water droplets contaminating the process stream and residual ammonia droplets from the gas stream recirculating to the ammonia synthesis reactor. A detailed description of wave-plate design and operation principles is presented in Section 3.3.3.

The motivation of this section is to use CFD tools to investigate and improve the wave-plate mist eliminators. Since the droplet removal problem is not limited to the ammonia industry, the other droplet materials were also investigated as a reference. The obtained CFD model was validated using experimental data from the literature [24]. This section was made based on the results published in the manuscript "Influence of Modification of the Geometry of the Wave-Plate Mist Eliminators on the Droplet Removal Efficiency—CFD Modelling" [80], which was part of this PhD project.

9.1. Geometry

Wave-plate mist eliminators have a typical geometry in the form of channels of zig-zag shape, forcing sharp changes in the gas flow pattern a few times. The droplets collide with the walls, which causes their separation from the gas. The separation's efficiency can be increased by adding drainage channels at the cost of increased pressure drop.

For CFD modelling purposes, geometry was created as a planar two-dimensional model, as shown in Figure 9.1.

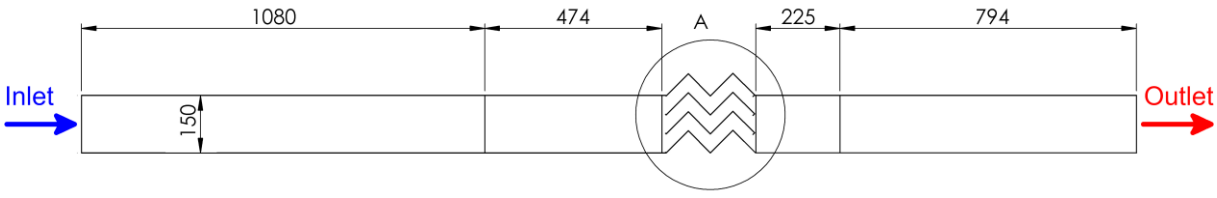

Figure 9.1. Geometry of investigated wave-plate mist eliminator (Geometry A) with inflow and outflow area [80]

Figure 9.1 presents the geometry variant without drainage channels (further called "Geometry A"). In this work, several different variants of wave-plate mist eliminators were investigated. The various configurations include the presence of their length and the angle of drainage channels. Figure 9.2 presents the visualisation of the typical wave-plate mist eliminator with drainage channels.

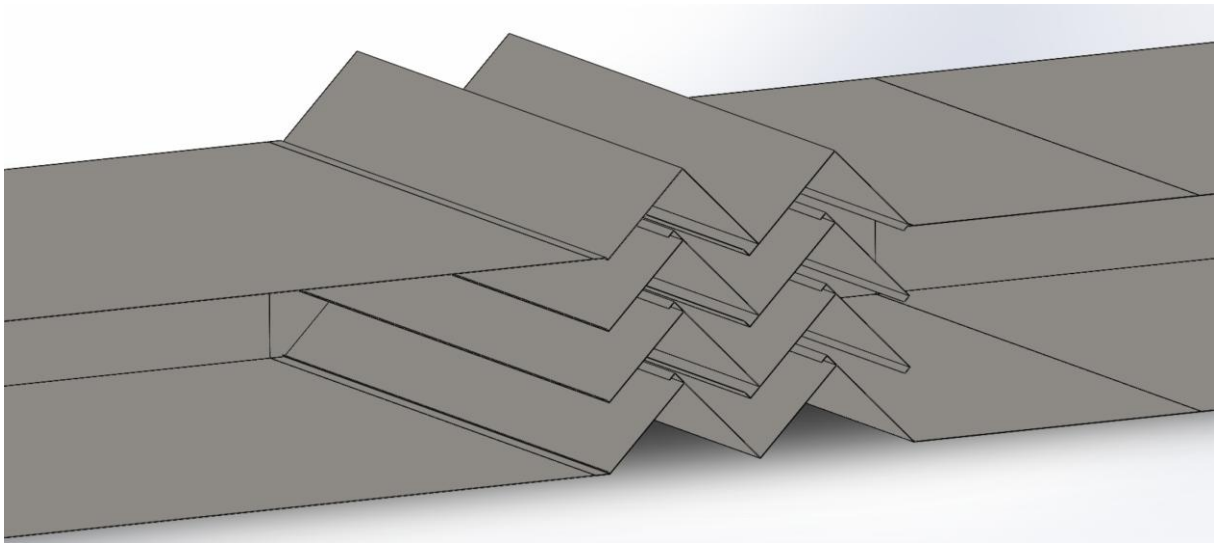

Figure 9.2. Wave-plate mist eliminator's geometry with drainage channels – visualisation [80]

Figure 9.3 shows the analysed geometries' dimensions, and Table 9.1 lists the investigated parameters for every geometry variant.

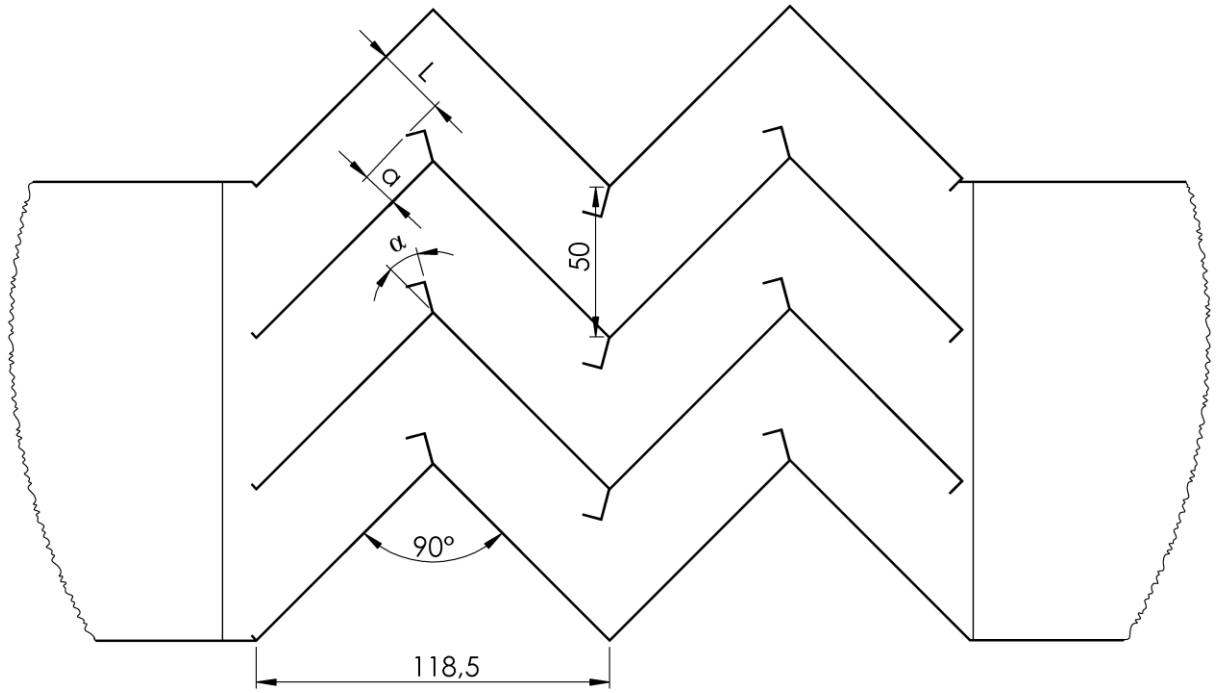

Figure 9.3. Dimensions (in millimetres) of the investigated wave-plate mist eliminators [80]

Table 9.1. Geometrical differences between investigated wave-plate mist eliminators [80]

Geometry variant	*Drainage channels' presence*	*a [mm]*	*L [mm]*	*α [°]*
A	No	-	35.5	-
B_10_0	Yes	10.5	25	0
B_10_30	Yes	10.5	25	30
B_10_60	Yes	10.5	25	60
B_10_90	Yes	10.5	25	90
B_15_0	Yes	15.5	20	0
B_20_0	Yes	20.5	15	0
B_25_0	Yes	25.5	10	0
B_30_0	Yes	30.5	5	0

9.2. Parameters and assumptions

Several assumptions were considered to model the discrete phase, such as:

- Air and water are considered to be continuous and dispersed phases, respectively
- Negligible gravitation and lift forces acting on droplets
- Lack of coalescence and droplet-droplet interaction
- Droplets behave as hard spheres, do not form film on the walls, nor affect the gas flow
- The mass fraction of the dispersed phase is below 0.1
- Droplets are removed immediately after hitting a wall

The above assumptions are commonly used in literature to investigate the influence of geometry on system efficiency [24,53,54,81]. Assuming air and water as continuous and dispersed media allows for relatively easy model validation, and the mass fraction of dispersed water below 0.1 excludes liquid film formation or droplet coalescence. The applied simplifications do not affect the simulations' accuracy, which is validated in Section 9.7 of this work. It should be noted that some of those assumptions are also general requirements for using the discrete phase model (DPM), which is applied to model droplet motions in Ansys Fluent. The DPM model was described in Section 4.3.7.

In calculations, the gas phase is considered air; if not stated otherwise, the discrete phase is in the form of water droplets. The parameters of both phases were specified at a constant

temperature equal to 15°C, listed in Table 9.2. In Section 9.9.5, this work also investigated the influence of different discrete-phase materials on the process.

Table 9.2. Parameters of the continuous and dispersed phase [80]

Parameter	*Unit*	*Value*
gas' density	$kg\ m^{-3}$	1.225
gas' dynamic viscosity	$m^2\ s^{-1}$	$1.461 \cdot 10^{-5}$
droplets' density	$kg\ m^{-3}$	999

9.3. Computational setup

The computational domain contains a planar, two-dimensional geometry shown in Figure 9.1. The inlet and outlet boundary conditions are at the outermost ends. In the wave-plate region, walls between solid and fluid are set as stationary walls without slip. Since the CFD model does not consider heat transfer, only fluid bodies are meshed. The rest of the boundaries outside the wave-plate region are set as symmetry conditions. For the discrete phase, the "trap" conditions were set on the mist eliminator's walls and "escape" on the rest of the boundaries of the computational domain. Computational meshes contain approximately 850000 quadrilateral cells, with the densest region in the wave-plate region. Figure 9.4 presents the mesh for the Geometry B_10_0.

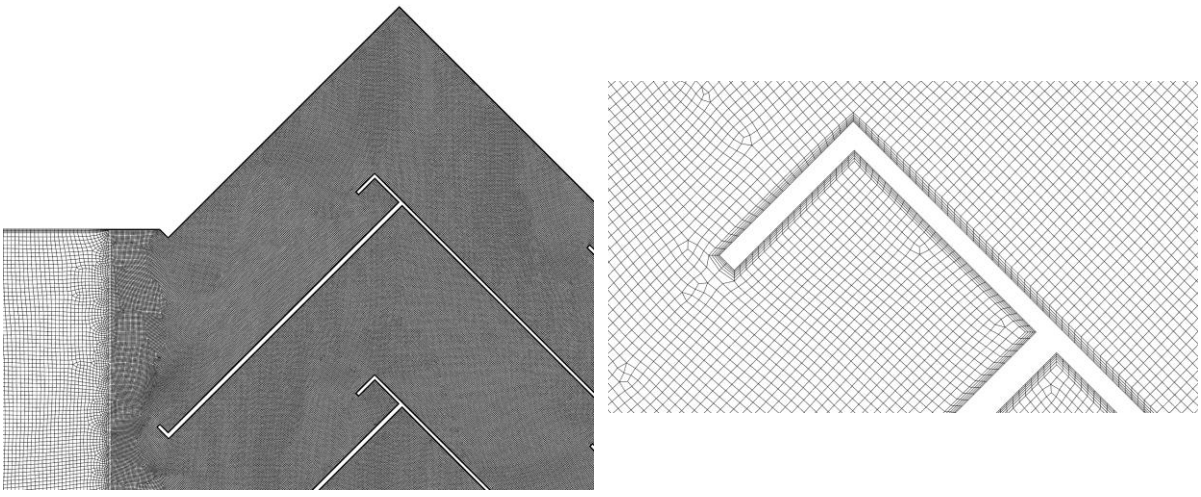

(a) (b)

Figure 9.4. Computational mesh of the Geometry B_10_0 variant: wave-plate region (a) and drainage channel enlargement (b) [80]

Second-order discretisation schemes were used for all variables, and the SIMPLE method was used for the pressure–velocity coupling. Calculations were conducted in steady-state mode without applied gravity force.

In a broad part of wave-plate mist eliminators, the gas-phase velocity has relatively high values with turbulence flow occurring, suggesting that k-ε could be accurate. However, the flow can be less turbulent in the narrow channels of the wave-plate section, making the SST k-ω model more precise. The SST k-ω is also accurate for simulating near-wall conditions since it includes turbulence shear stress transport. This work also tested the Reynolds Stress Model (RSM) for modelling turbulence as a reference. To select an appropriate turbulence model for further calculations, the above turbulence models were investigated and validated using the experimental data published by Galletti et al. [24]. To sum up, the following turbulence models based on Reynolds-averaged Navier-Stokes (RANS) were compared and validated using the experimental data [24]:

- standard k-ε with standard wall treatment
- standard k-ε with enhanced wall treatment
- SST k-ω
- Reynolds stress model (RSM) with enhanced wall treatment

In the literature, there are many examples of using more advanced turbulence models, such as large eddy simulation (LES) used in industrial CFD simulations [82–84], enabling simulations in a wide range of Reynolds numbers. However, LES simulations often increase the demand for computational resources and calculation time, and Ruiz et al. [85] conducted calculations comparing RANS and LES models. The differences in pressure drop were no higher than 3%, and droplet removal efficiency differed by 7% on average. This indicates that the RANS turbulence modelling approach can successfully use a turbulent dispersion model of droplets.

9.4. Droplet motion modelling

The droplet trajectories are modelled using the discrete phase model (DPM) described in Section 4.3.7. In this work, two approaches of the DPM model were tested and validated with the experimental data [24]:

- without turbulent dispersion
- with turbulent dispersion affecting the discrete phase motion (Equation (98))

9.5. Boundary conditions

Calculations were conducted for typical parameters used in industrial conditions [24,54,81], and they are used as boundary conditions in this work. Table 9.3 lists the values of boundary conditions in the CFD model. The outlet boundary condition was set as "Outflow", which does not require any values since it is calculated from the fully developed flow pattern.

Table 9.3. Wave-plate mist eliminator's CFD model's boundary conditions [80]

Parameter	*Unit*	*Value*
inlet velocity	m s^{-1}	2–4
inlet overpressure	MPa	5
injected droplet diameter	μm	1–40

Calculations were conducted for two different inlet velocities: 2.0 m s^{-1} and 4.0 m s^{-1}. The dispersed phase entered the domain through the inlet injections, which were calculated separately. The droplets were injected separately for every diameter from the investigated range (1 to 40 μm, every 3 μm). The droplets' velocity is the same as the gas phase, and the total mass flow rate is 0.00355 kg s^{-1}.

9.6. Droplet removal efficiency

Droplet removal is a primary function of the wave-plate mist eliminators, and its efficiency (percentage of injected droplets removed by the mist eliminator) is a critical parameter of this process. Droplet sizes from 1 μm to the size when the calculated efficiency equals 100% were considered for efficiency calculations. In the CFD models, droplets were injected perpendicularly into the inlet. Droplet removal efficiency is defined as the ratio of the number of droplets removed from the gas phase ($C_{in} - C_{out}$) to the total number of droplets injected into the system (C_{in}), which can be written as:

$$\eta = \frac{C_{in} - C_{out}}{C_{in}} \cdot 100 \tag{124}$$

9.7. Validation

The validation is presented before the primary results (Section 9.9) since it is connected to the proper turbulence model of the continuous phase and the turbulent dispersion model of the discrete phase selection. The calculations were compared with the experimental data published by Galletti et al. [24]. The Geometry B_10_0 was selected for calculations since it covers the geometry used by Galletti et al. [24] in experiments.

9.7.1. Continuous phase's turbulence model selection

In Section 9.4, the investigated RANS turbulence models were described. To select and validate the proper model, simulations were performed for each one and compared with experimental data [24]. Since Ruiz et al. [85] claim that a turbulent dispersion model of droplets improves the accuracy of the results, it was implemented for calculations in the present section. The influence of including a turbulent section will be presented in the next section. Figure 9.5 plots the obtained results as a function of droplet removal efficiency to the droplet diameter, and Tables 9.4–9.7 present a summary of results and relative errors.

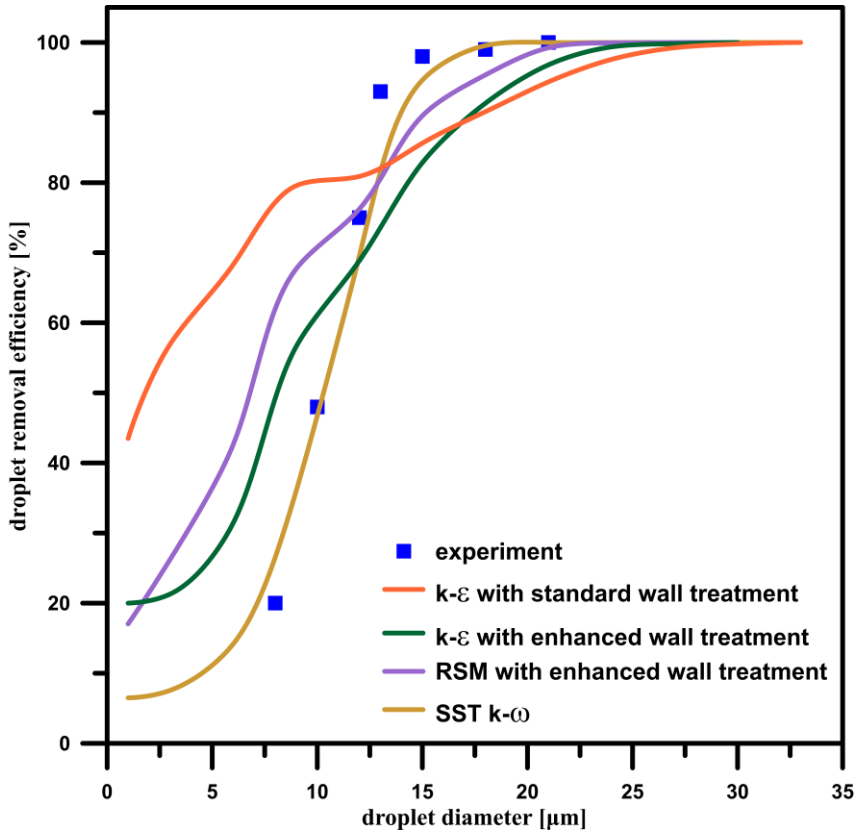

(a)

Figure 9.5. Cont.

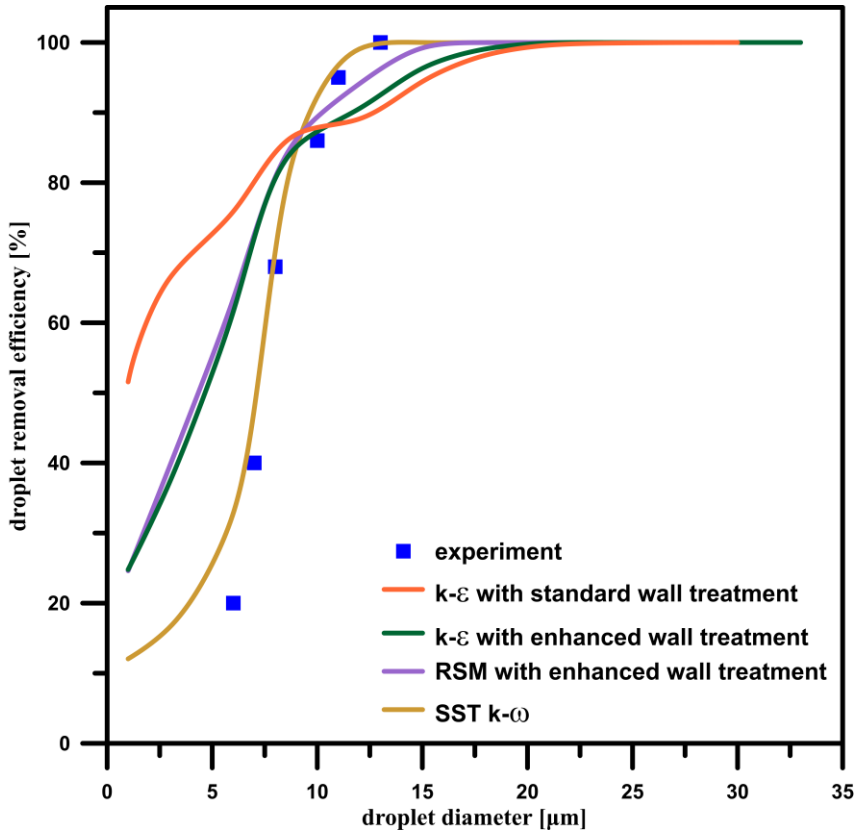

(b)

Figure 9.5. Comparison of the experimental [24] and calculated droplet removal efficiency in relation to droplet diameter for inlet velocity of 2 m s^{-1} (a) and 4 m s^{-1} (b) (Geometry B_10_0) [80]

Table 9.4. Comparison of the experimental [24] and calculated efficiencies (inlet velocity 2 m s^{-1}, Geometry B_10_0) [80]

Droplet diameter [µm]	*Experiment [%]*	*k-ε, std. wall. tr. [%]*	*k-ε, enh. wall. tr. [%]*	*RSM, enh. wall. tr. [%]*	*SST k-ω [%]*
8	20	76.6	48.7	60.5	27.0
10	48	80.7	61.9	71.7	46.8
12	75	80.9	68.8	76.2	69.5
13	93	81.9	73.2	80.2	79.8
15	98	85.6	82.8	89.5	94.6
18	99	90.1	91.3	95.4	99.6
21	100	94.4	96.8	99.2	100.0

Table 9.5. Relative errors between the experimental [24] and calculated results (inlet velocity 2 m s^{-1}, Geometry B_10_0) [80]

Droplet diameter [μm]	*k-ε, std. wall. tr. [%]*	*k-ε, enh. wall. tr. [%]*	*RSM, enh. wall. tr. [%]*	*SST k-ω [%]*
8	283.0	143.4	202.3	34.9
10	68.2	28.9	49.4	2.6
12	7.9	8.3	1.6	7.3
13	11.9	21.3	13.8	14.2
15	12.7	15.5	8.7	3.5
18	9.0	7.8	3.6	0.6
21	5.6	3.2	0.8	0

Table 9.6. Comparison of the experimental [24] and calculated efficiencies (inlet velocity 4 m s^{-1}, Geometry B_10_0) [80]

Droplet diameter [μm]	*Experiment [%]*	*k-ε, std. wall. tr. [%]*	*k-ε, enh. wall. tr. [%]*	*RSM, enh. wall. tr. [%]*	*SST k-ω [%]*
6	20	75.9	61.6	63.4	32.8
7	40	79.7	70.7	71.9	49.3
8	68	83.7	78.9	79.9	68.6
10	86	88.3	88.3	90.2	94.4
11	95	88.7	89.7	92.4	98.2
13	100	90.4	92.2	95.9	99.5

Table 9.7. Relative errors between the experimental [24] and calculated results (inlet velocity 4 m s^{-1}, Geometry B_10_0) [80]

Droplet diameter [μm]	*k-ε, std. wall. tr. [%]*	*k-ε, enh. wall. tr. [%]*	*RSM, enh. wall. tr. [%]*	*SST k-ω [%]*
6	279.50	208.0	217.0	64.0
7	99.13	76.7	79.8	23.4
8	23.14	16.1	17.5	0.9
10	2.68	2.7	4.8	9.8
11	6.66	5.6	2.7	3.3
13	9.57	7.8	4.1	0.5

All investigated turbulence models can predict the trend of increasing efficiency with a droplet size. However, there are significant differences between calculated values. The SST k-ω model provides undeniably the most accurate results. Furthermore, only this model predicted almost 100% efficiency for the cases with droplet diameters of 18 μm (inlet velocity 2 m s^{-1}) and 12 μm (inlet velocity 4 m s^{-1}). It should be noted that those cases are the minimal droplet sizes that still achieve 100% removal efficiency in experiments, so it is highly desired for the CFD model to identify those cases accurately. The SST model was found to be the most appropriate to use in further calculations.

9.7.2. Influence of turbulent dispersion model in discrete phase

This section compared the experimental data [24] to the simulation variants with and without turbulent dispersion. Since validation from Section 9.7.1 proved that the SST k-ω turbulence model is the most accurate, other turbulence models were not compared in the present section. Figure 9.6 presents the obtained results as a function of droplet removal efficiency to the droplet diameter, and Tables 9.8–9.11 list a summary of results and relative errors.

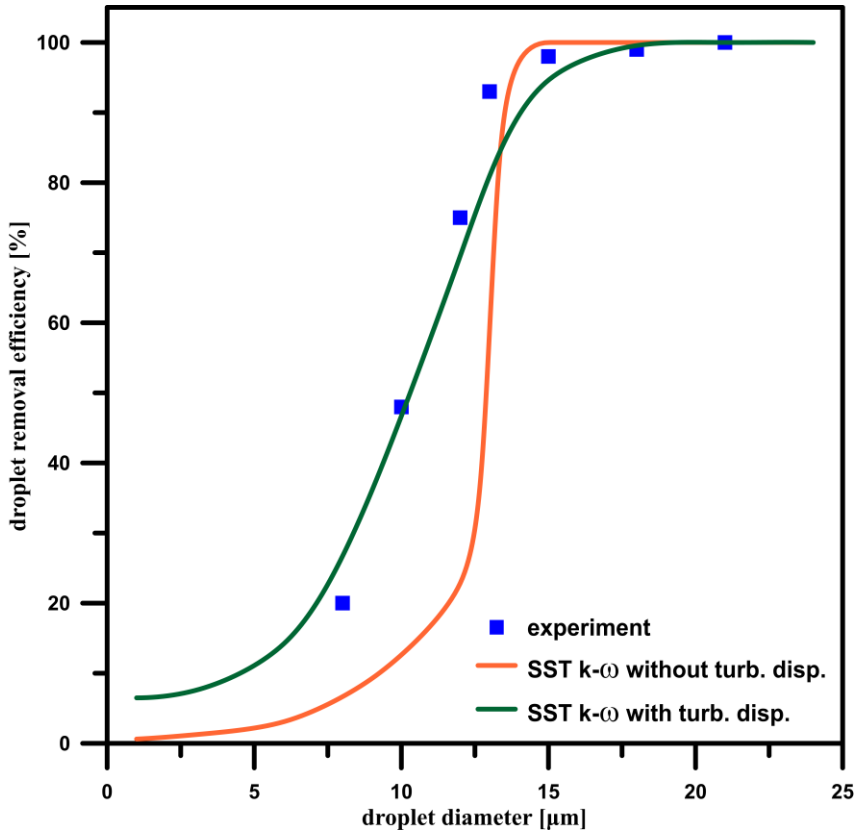

(a)

Figure 9.6. Cont.

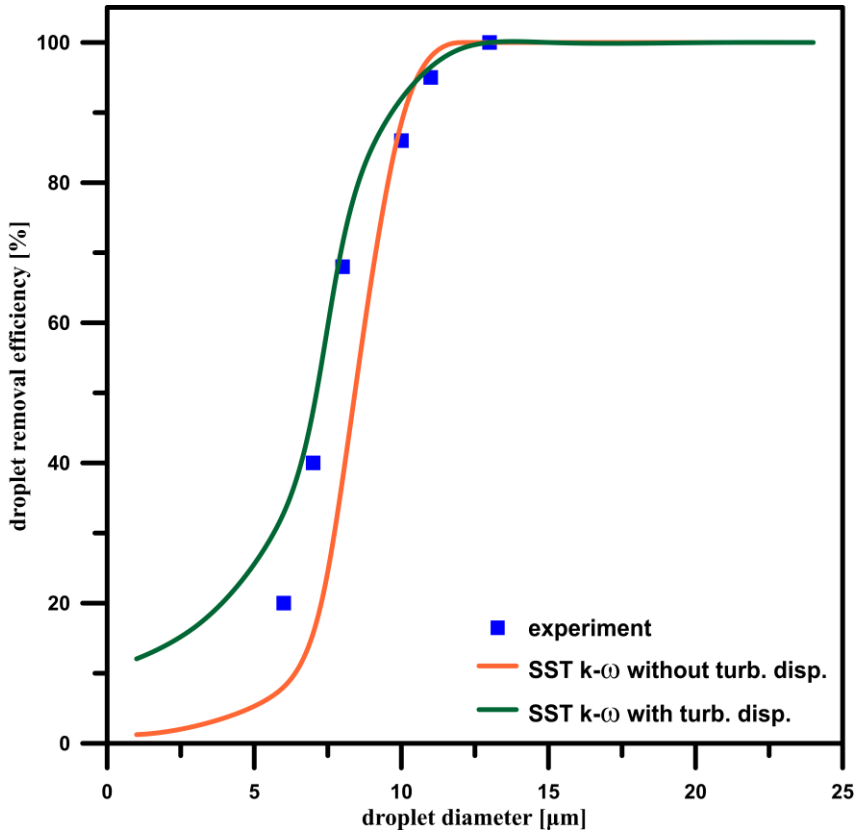

(b)

Figure 9.6. Comparison of the experimental [24] and calculated droplet removal efficiency in relation to droplet diameter for the cases with and without using turbulent dispersion for inlet velocity of 2 m s^{-1} (a) and 4 m s^{-1} (b) (Geometry B_10_0) [80]

Table 9.8. Comparison of the experimental [24] and calculated efficiencies for the cases with and without using turbulent dispersion (inlet velocity 2 m s^{-1}, Geometry B_10_0) [80]

Droplet diameter [µm]	*Experiment [%]*	*SST k-ω without turbulent dispersion [%]*	*SST k-ω with turbulent dispersion [%]*
8	20	7.2	27.0
10	48	13.8	46.8
12	75	22.8	69.5
13	93	48.5	79.8
15	98	100.0	94.6
18	99	100.0	99.6
21	100	100.0	100.0

Table 9.9. Relative errors between the experimental [24] and calculated results for the cases with and without using turbulent dispersion (inlet velocity 2 m s^{-1}, Geometry B_10_0) [80]

Droplet diameter [μm]	*SST k-ω without turbulent dispersion [%]*	*SST k-ω with turbulent dispersion [%]*
8	63.8	34.9
10	71.3	2.6
12	69.6	7.3
13	47.8	14.2
15	2.0	3.5
18	1.0	0.6
21	0.0	0.0

Table 9.10. Comparison of the experimental [24] and calculated efficiencies for the cases with and without using turbulent dispersion (inlet velocity 4 m s^{-1}, Geometry B_10_0) [80]

Droplet diameter [μm]	*Experiment [%]*	*SST k-ω without turbulent dispersion [%]*	*SST k-ω with turbulent dispersion [%]*
6	20	8.0	32.8
7	40	27.6	49.3
8	68	47.1	68.6
10	86	77.8	94.4
11	95	88.9	98.2
13	100	100.0	99.5

Table 9.11. Relative errors between the experimental [24] and calculated results for the cases with and without using turbulent dispersion (inlet velocity 4 m s^{-1}, Geometry B_10_0) [80]

Droplet diameter [μm]	*SST k-ω without turbulent dispersion [%]*	*SST k-ω with turbulent dispersion [%]*
6	60.0	64.0
7	31.1	23.4
8	30.7	0.9
10	9.5	9.8
11	6.4	3.3
13	0.0	0.5

The SST k-ω model with turbulent dispersion provides noticeably more accurate results, with good agreement with the experimental data. This is particularly visible for the smaller droplet range. The turbulent dispersion term predicts a higher acceleration of small-diameter droplets, impacting fluctuations in the gas phase. Based on the validation results, all subsequent simulations were performed using the SST model with turbulent dispersion.

9.8. Non-dimensional numbers

The Reynolds number is the most crucial non-dimensional number for wave-plate mist eliminators. This dimensionless quantity predicts fluid flow patterns using the ratio of inertial and viscous forces. Reynolds number is the basis for selecting the proper turbulence model for CFD calculations. Calculated values of the Reynolds number using the hydraulic diameter (d_h = 0.68 m) are listed in Table 9.12.

Table 9.12. Reynolds number values for different variants of calculation [80]

Inlet velocity [m s^{-1}]	*Reynolds number [-]*
2.0	94114
4.0	188277

Another non-dimensional number describing the wave-plate mist eliminators is the Stokes number, representing the ratio between droplet relaxation time and gas characteristic time. According to Galletti et al. [24], Stokes number is loosely related to droplet removal efficiency, although it is not associated with turbulent dispersion effects. Since in wave-plate mist eliminators, the characteristic length is the channel's width, the Stokes number can be written in the form of Equation (125).

$$St = \frac{\rho_p {d_p}^2 \left(\frac{u_{in}}{\sin \alpha_c}\right)}{18\mu(L \sin \alpha_c)} \tag{125}$$

where u_{in} is inlet gas velocity, and α_c is the bend angle between wave plates. This work investigated the relation between Stokes number and droplet removal efficiency, plotted in Figure 9.7. It can be observed that the efficiency-Stokes number plot has a similar pattern to the efficiency-droplet diameter plot, suggesting a connection between the two functions. Since Stokes' number is unrelated to turbulent dispersion, those similarities are visible in cases with and without turbulent dispersion.

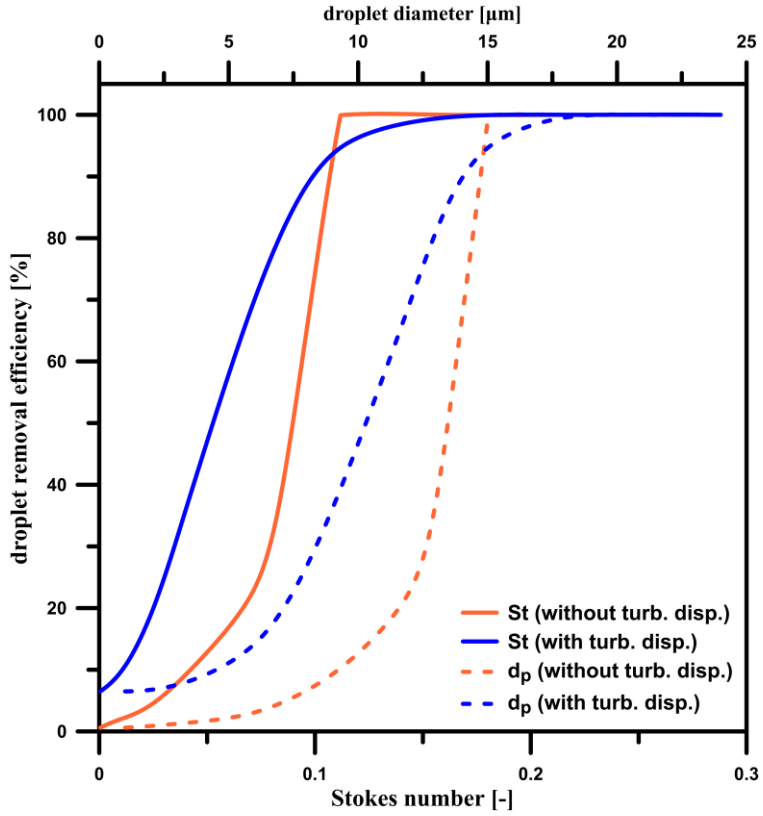

(a)

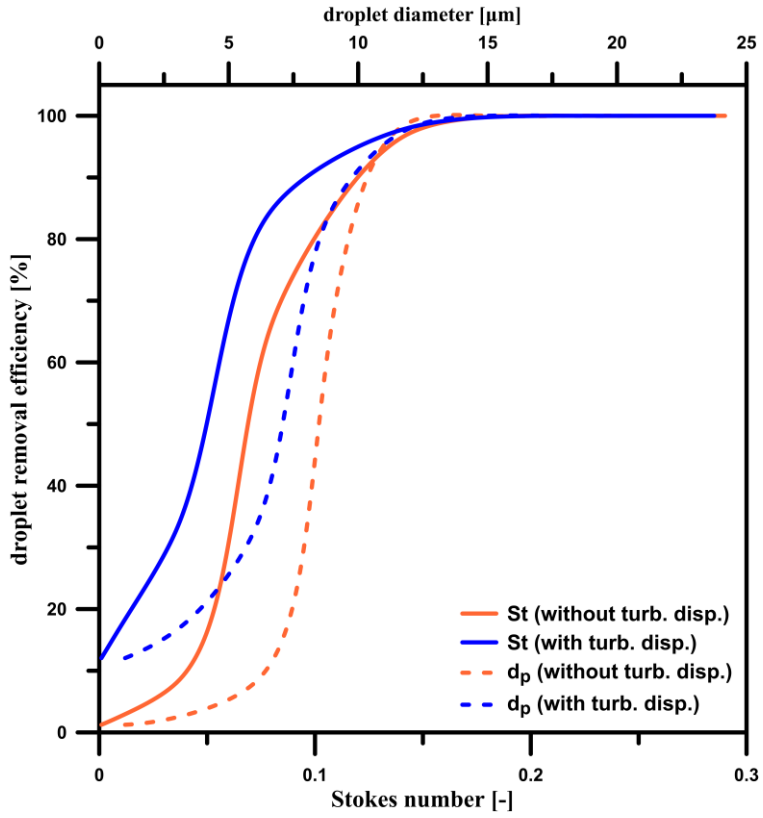

(b)

Figure 9.7. Comparison of efficiency-Stokes number and efficiency-droplet diameter functions for the cases with SST k-ω model with and without turbulent dispersion for inlet velocity of 2 m s^{-1} (a) and 4 m s^{-1} (b) (Geometry B_10_0) [80]

9.9. Results

The CFD model was used to calculate three crucial industry parameters:

- Pressure drop on the wave-plate mist eliminator
- Mean force acting on the single drainage channel
- Droplet removal efficiency

9.9.1. Influence of gas inlet velocity on pressure drop and mean force acting on the drainage channel

Pressure drop and mean force acting on the drainage channels are directly associated with running costs, and their low values are desired, especially within high-pressure installations. This parameter was calculated as a difference between pressure values at the inlet and outlet of the system. The mean force acting on the single drainage channel was computed as an arithmetic average from all forces acting on drainage channels. Figure 9.8. show the pressure drop and mean force acting on the single drainage channel in relation to geometrical parameters.

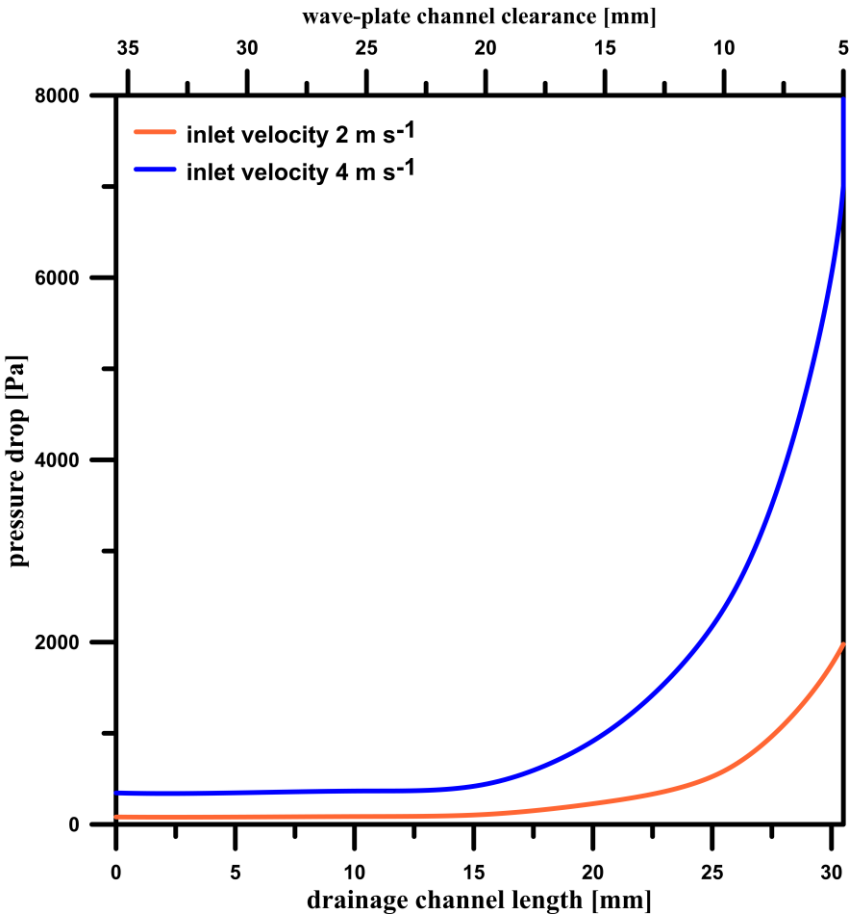

(a)

Figure 9.8. Cont.

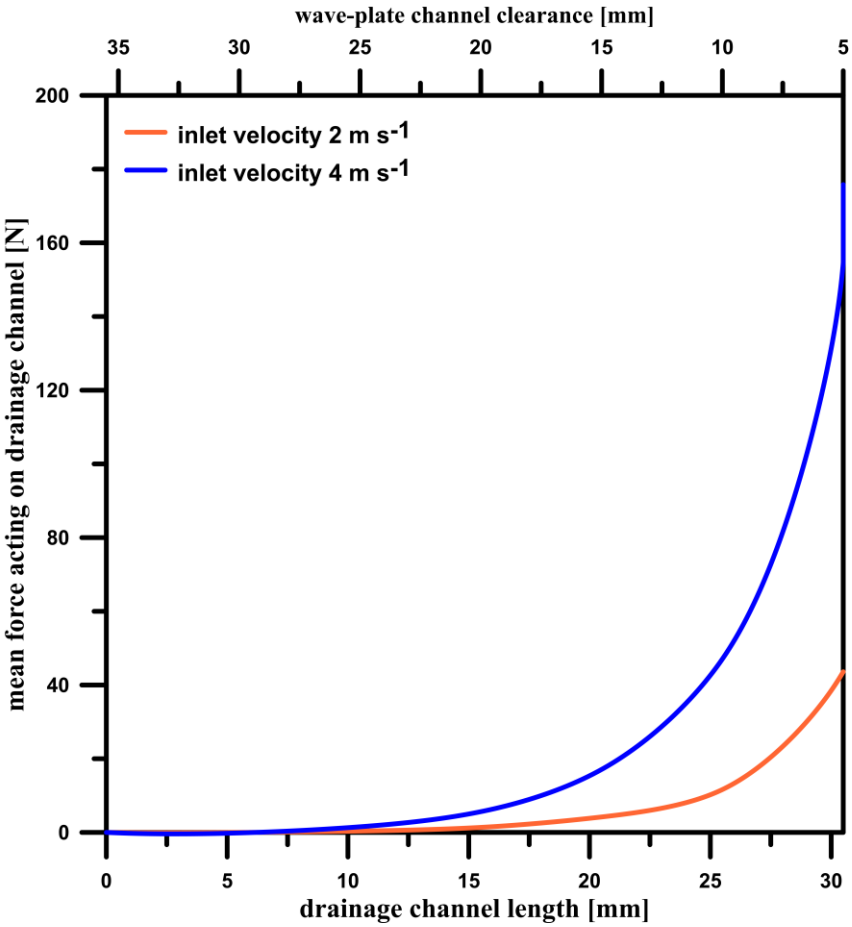

(b)

Figure 9.8. Pressure drop (a) and mean force acting on the single drainage (b) in relation to drainage channel length and wave-plate channel clearance [80]

Tables 9.13 and 9.14 list the pressure drop and mean force acting on the single drainage channel values calculated for each investigated case.

Table 9.13. Pressure drop and the mean force acting on drainage channel in wave-plate mist eliminators (inlet velocity 2 m s^{-1}) [80]

Geometry variant	A	B_10_0	B_10_30	B_10_60	B_10_90	B_15_0	B_20_0	B_25_0	B_30_0
Pressure drop [Pa]	82	87	106	151	205	109	246	587	1977
The mean force acting on drainage channel [N]	-	0.38	0.48	0.63	0.78	1.38	4.20	11.64	43.61

Table 9.14. Pressure drop and the mean force acting on drainage channel in wave-plate mist eliminators (inlet velocity 4 m s^{-1}) [80]

Geometry variant	A	B_10_0	B_10_30	B_10_60	B_10_90	B_15_0	B_20_0	B_25_0	B_30_0
Pressure drop [Pa]	346	367	446	643	872	442	1000	2371	7960
The mean force acting on drainage channel [N]	-	1.53	1.96	2.59	3.26	5.62	17.11	47.07	175.81

Based on the obtained results, it can be assumed that pressure drop increases proportionally to the square of the medium inlet velocity, which is consistent with the Darcy–Weisbach law:

$$\Delta p \sim u^2 \tag{126}$$

The results agree with the literature data [26]. It can be observed that the force acting on the single drainage channel is proportional to the total pressure drop on the wave-plate mist eliminator. Both drainage channels and velocity have a significant influence on those parameters. The pressure drop is almost constant for shorter drainage channels while increasing drainage channel length (and reducing the clearance). However, the pressure drop starts to rise at some point, and this change is considerably sharper for the higher velocities. This suggests that there is a borderline value of drainage channel length for each velocity, after which the pressure drop starts to increase.

9.9.2. Influence of gas inlet velocity on droplet removal efficiency

Droplet removal efficiency is a reference parameter in this section and the following sections. It is crucial from an industrial and practical point of view since the amount of potentially remaining droplets determines the reasonableness of using the wave-plate mist-eliminator. Figure 9.9 presents droplet removal efficiency as a function of droplet diameter for investigated velocities in geometries without channels (Geometry A) and with channels of 10 mm length (Geometry B_10_0).

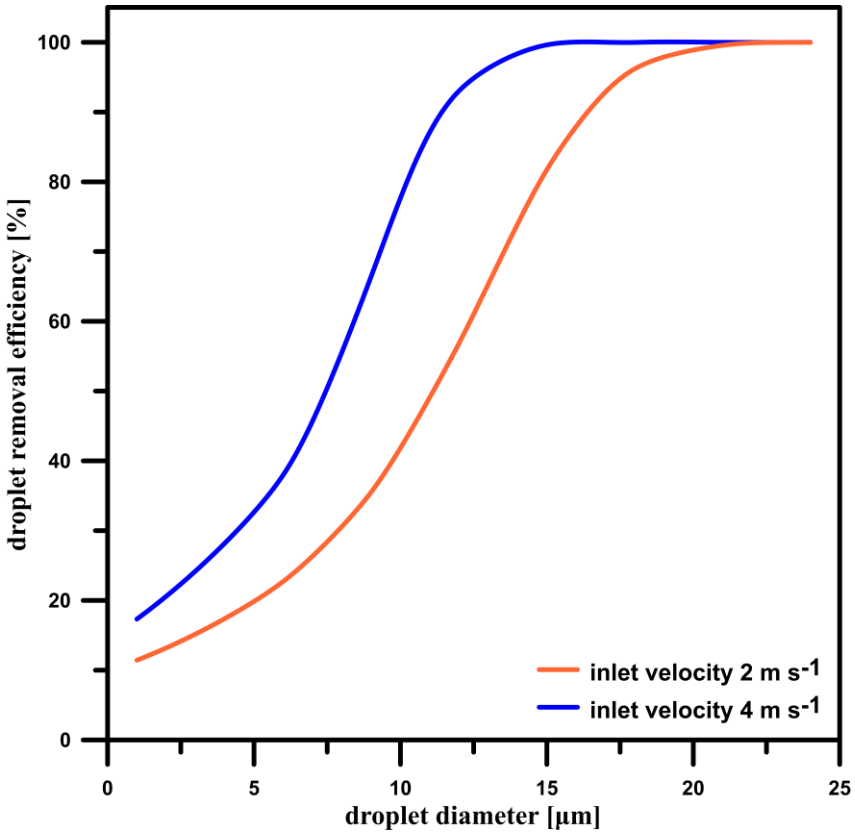

(a)

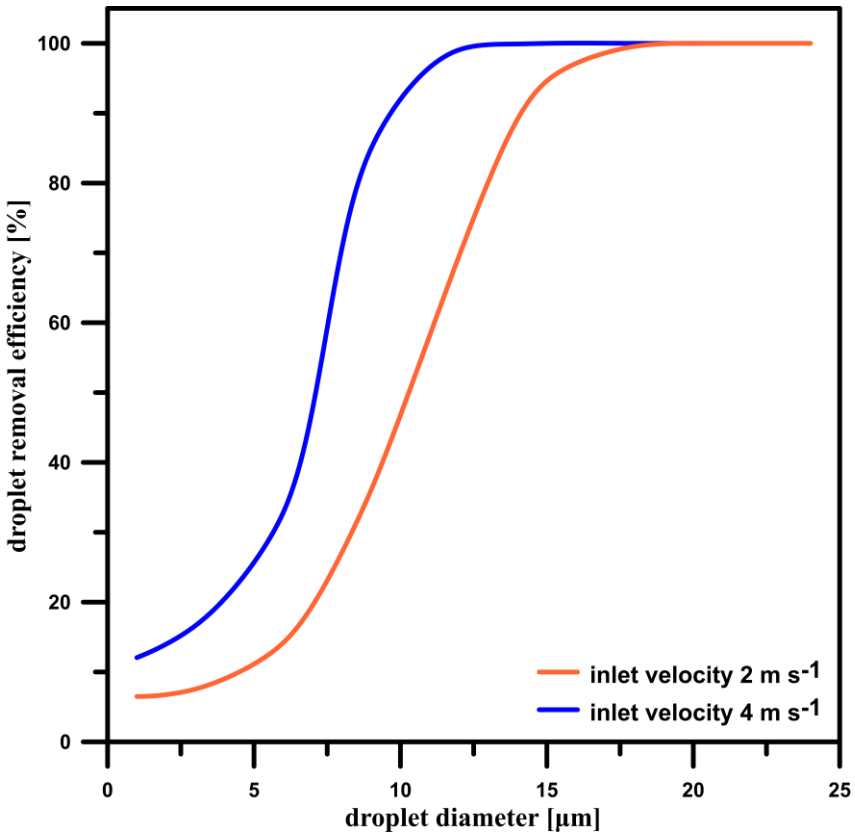

(b)

Figure 9.9. Comparison of droplet removal efficiency in relation to droplet diameter for different inlet velocities for Geometry A (a) and Geometry B_10_0 (b) [80]

It can be observed that the increased gas velocity increases the droplet removal efficiency, and this difference is more significant for higher droplet diameters for both geometries with and without drainage channels. In Geometry B_10_0, almost 100% efficiency is obtained for the droplet diameter of 12 μm for velocity 4 m s^{-1} (18 μm for velocity 2 m s^{-1}). However, higher velocity causes more than four times higher pressure drop on the mist eliminator. The channels positively affect droplet separation efficiency, described in the next section.

9.9.3. Influence of drainage channels' length on droplet removal efficiency

This section investigates the influence of the presence and length of the drainage channel, which is crucial to both efficiency and running costs (pressure drop). Figure 9.10 shows the droplet removal efficiencies as functions of droplet diameters.

The results confirm that, in most cases, the drainage channels positively affect the separation efficiency. Interestingly, short drainage channels (Geometry B_10_0) can reduce the removal efficiency in the small droplet diameter range. For droplet diameters smaller than 9 μm for 2 m s^{-1} (7 μm for 4 m s^{-1}), the droplet removal efficiency is higher for a mist eliminator without channels, which is likely due to the increased inertia forces acting on the droplets caused by the reduced wave-plate channels' clearance. In this range, smaller droplets tend to follow the gas rather than depose on walls. Nevertheless, even for the B_10_0 geometry variant, the efficiency of the larger droplet separation is increased by about 20–30%, and for the cases with more extended drainage channels, this parameter is higher.

It should be noted that geometries with channels of 15.5 in length (Geometry B_15_0) have increased efficiency compared to the system without drainage channels for all droplet size ranges, suggesting that larger drainage channels overcompensate for the efficiency loss caused by the increased droplet inertial forces. This phenomenon is caused by the increased velocity of the gas phase, decreased flow area, and increased area of the drainage channels. However, it should be noted that it comes at the cost of increased pressure drop.

Figures 9.11–9.15 present velocity contours and vectors of investigated geometries of wave-plate mist eliminators. The highest gas velocities are visible in the close vicinity of the drainage channels. It can be observed that the velocity increases after the subsequent bends within the wave-plate zone, which suggests that self-similarity flow conditions for the subsequent clearances near the channel have not been achieved. This phenomenon was also reported by Galletti et al. [24], and the increase is higher for larger drainage channels (smaller clearances). Along the areas of high velocity, stagnation and recirculation zones occur just behind drainage

channels, as seen in Figures 9.11–9.15. All observed phenomena cause the larger drainage channels to provide better separation efficiency at the cost of the increased pressure drops.

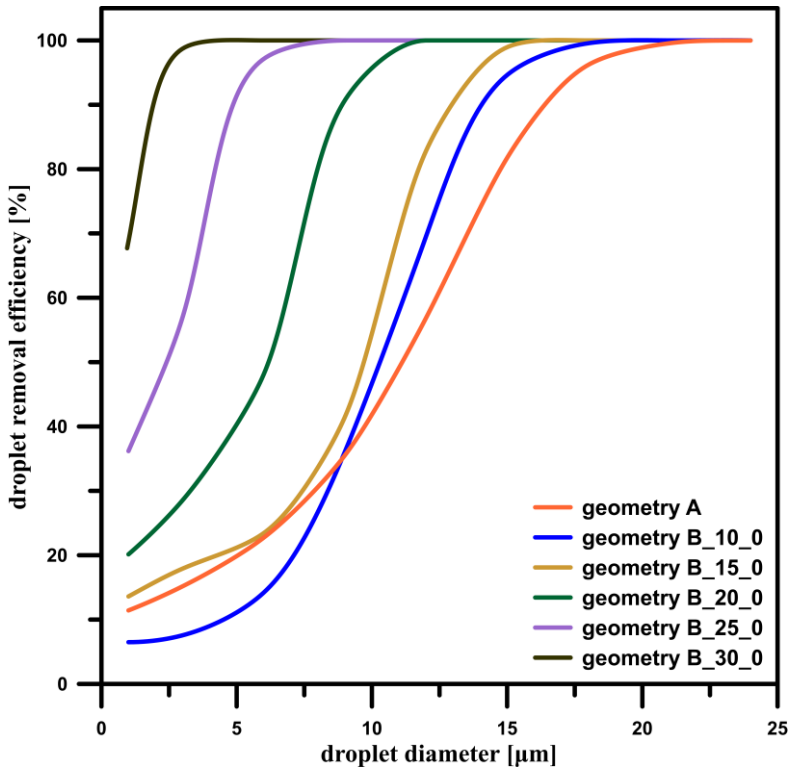

(a)

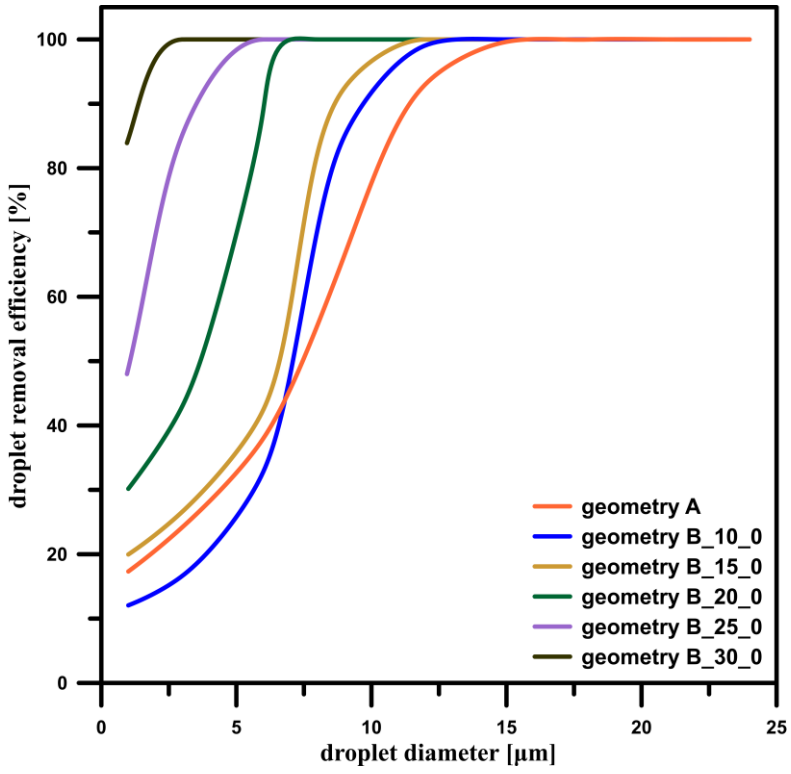

(b)

Figure 9.10. Comparison of droplet removal efficiency in relation to droplet diameter for different wave-plate mist eliminator geometries for inlet velocity of 2 m s^{-1} (a) and 4 m s^{-1} (b) [80]

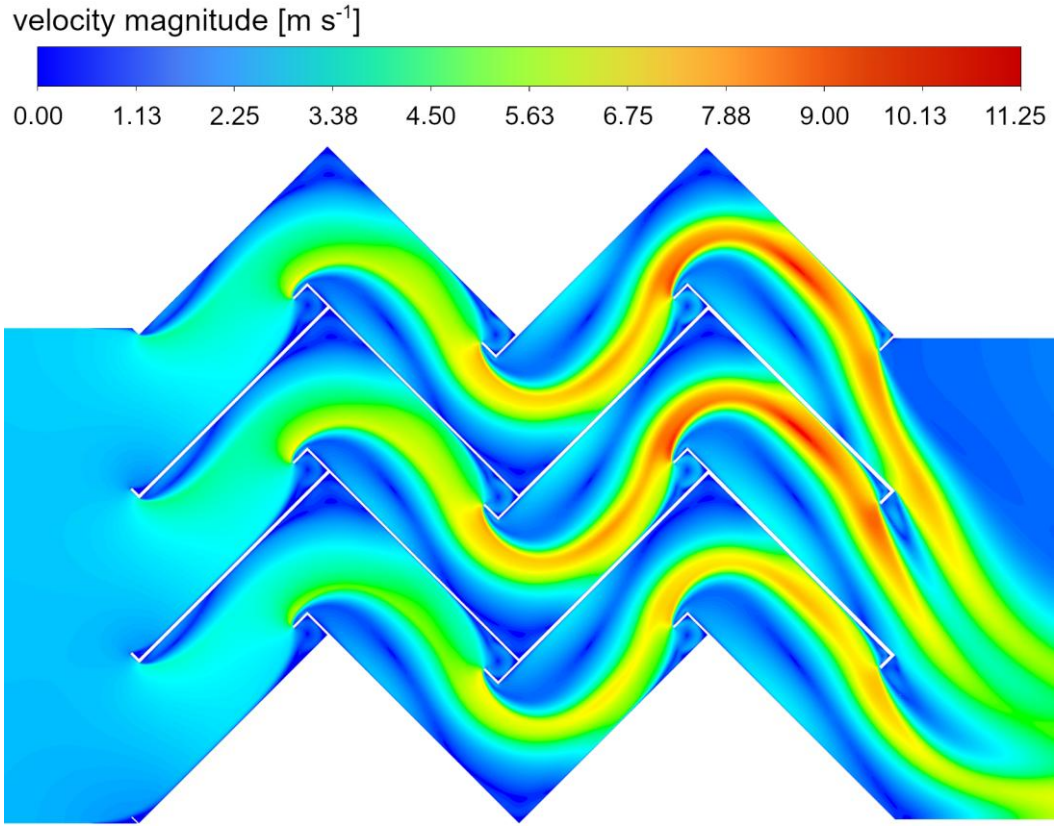

(a)

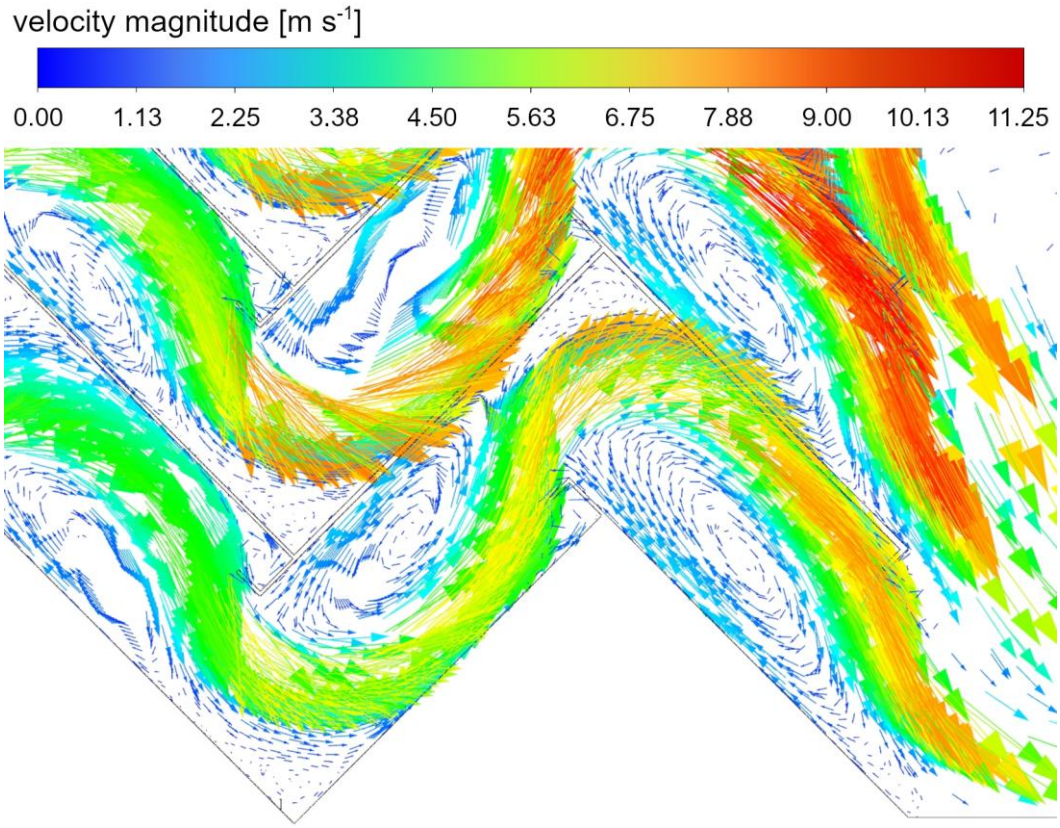

(b)

Figure 9.11. Velocity contours (a) and vectors (b) of Geometry B_10_0 (drainage channels' length of 10.5 mm, inlet velocity 2 m s^{-1}) [80]

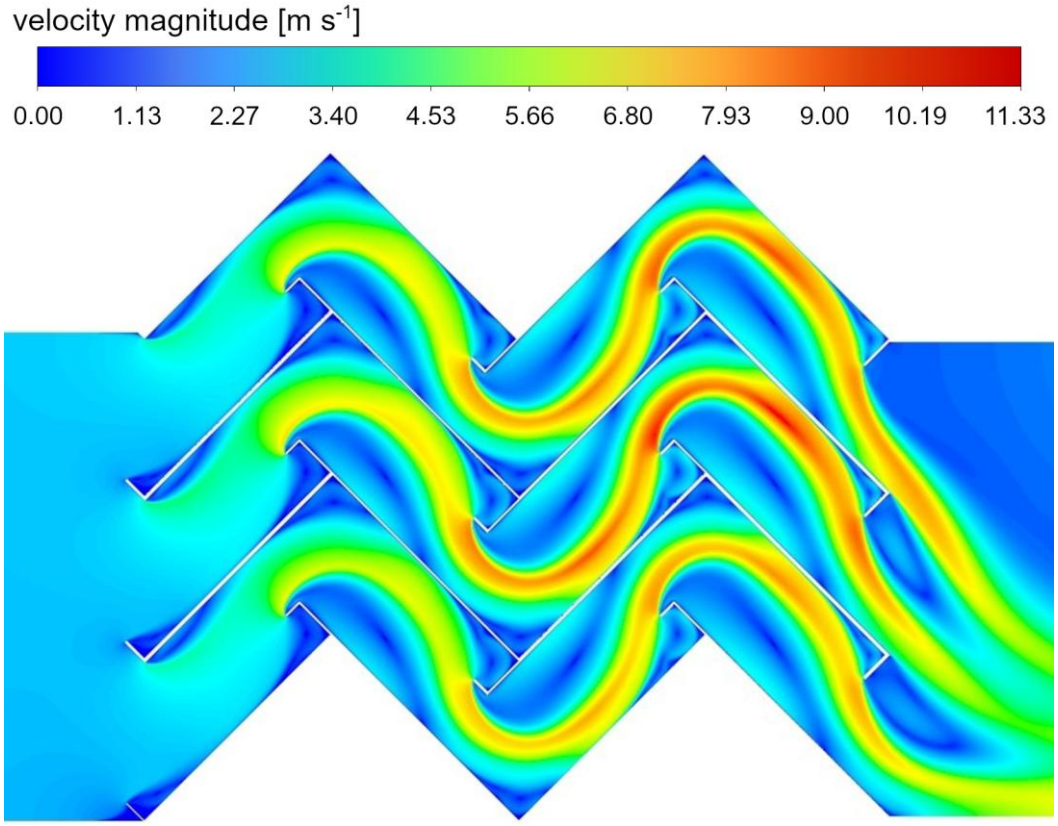

(a)

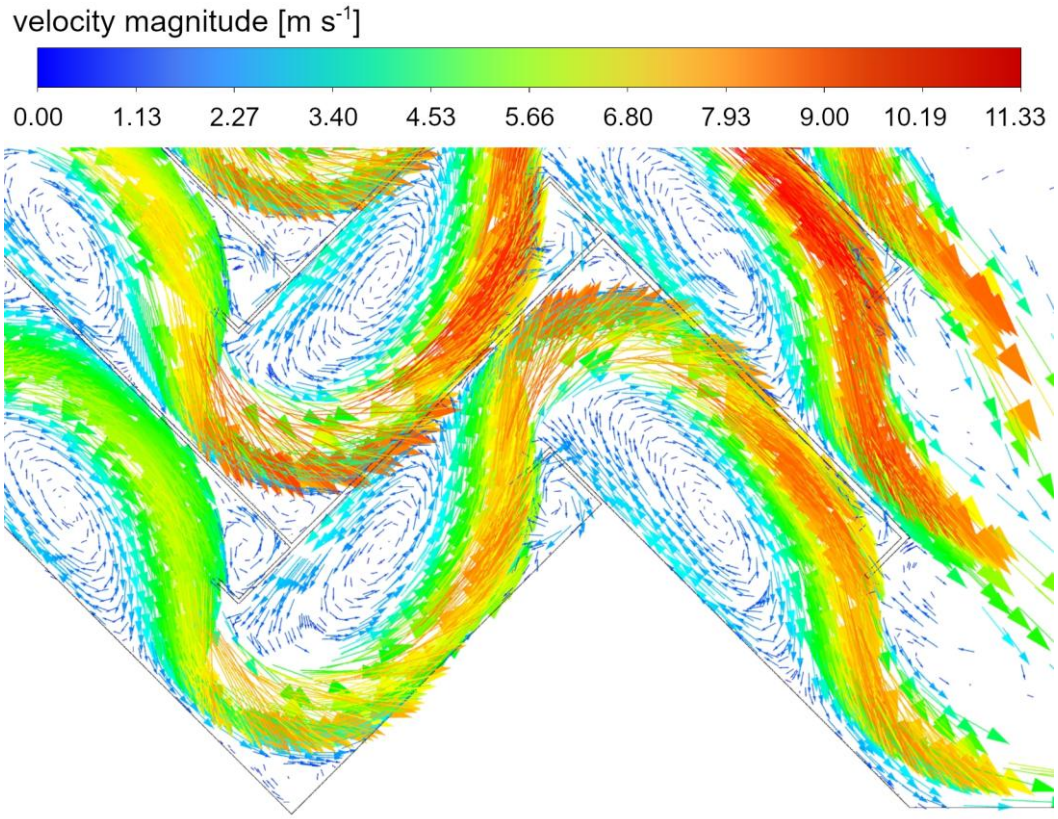

(b)

Figure 9.12. Velocity contours (a) and vectors (b) of Geometry B_15_0 (drainage channels' length of 15.5 mm, inlet velocity 2 m s^{-1}) [80]

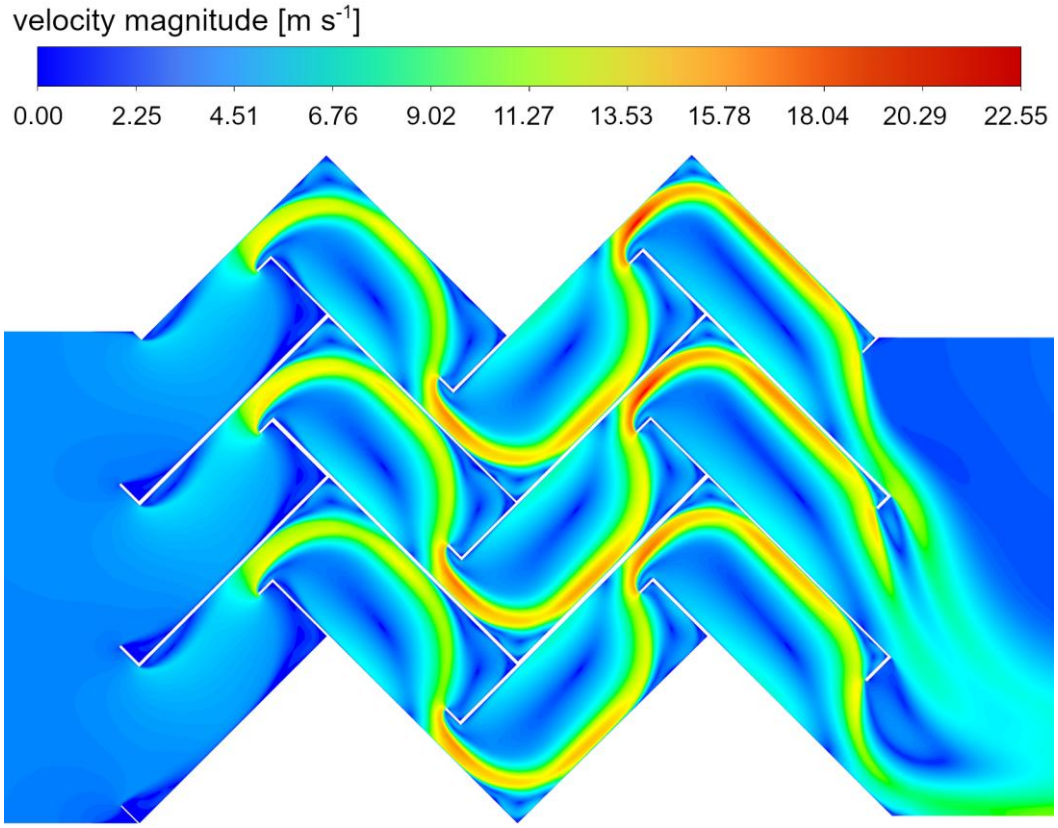

(a)

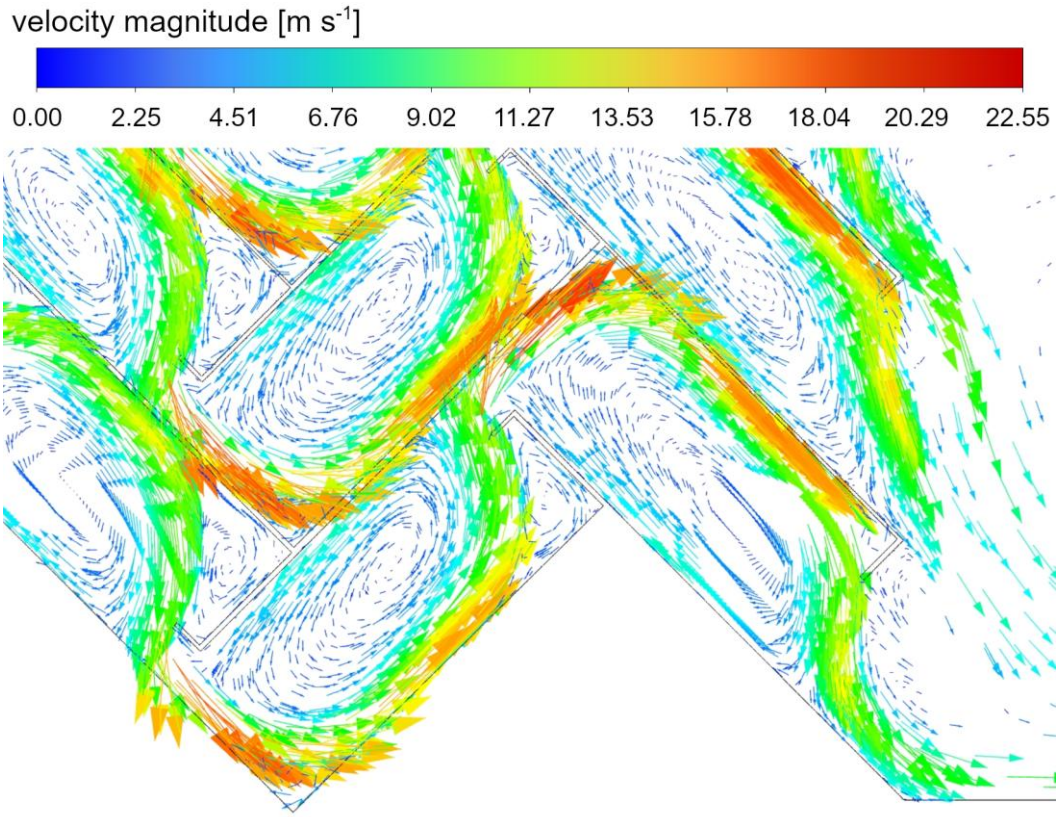

(b)

Figure 9.13. Velocity contours (a) and vectors (b) of Geometry B_25_0 (drainage channels' length of 25.5 mm, inlet velocity 2 m s^{-1}) [80]

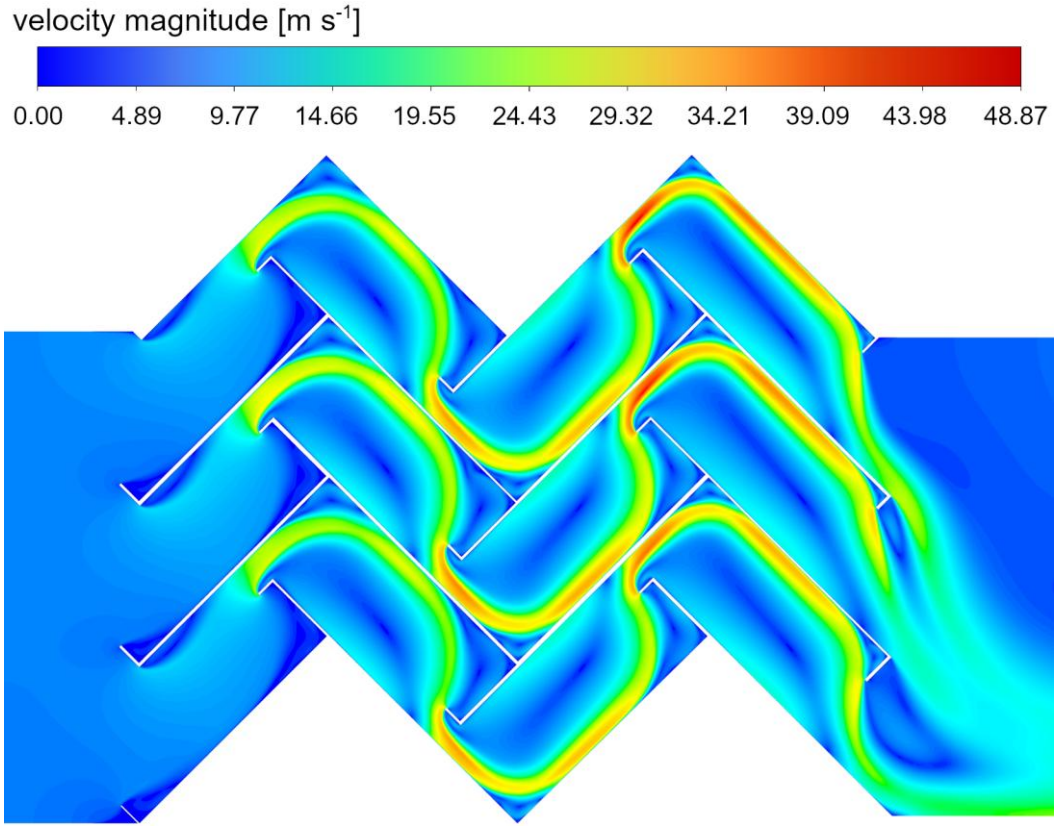

(a)

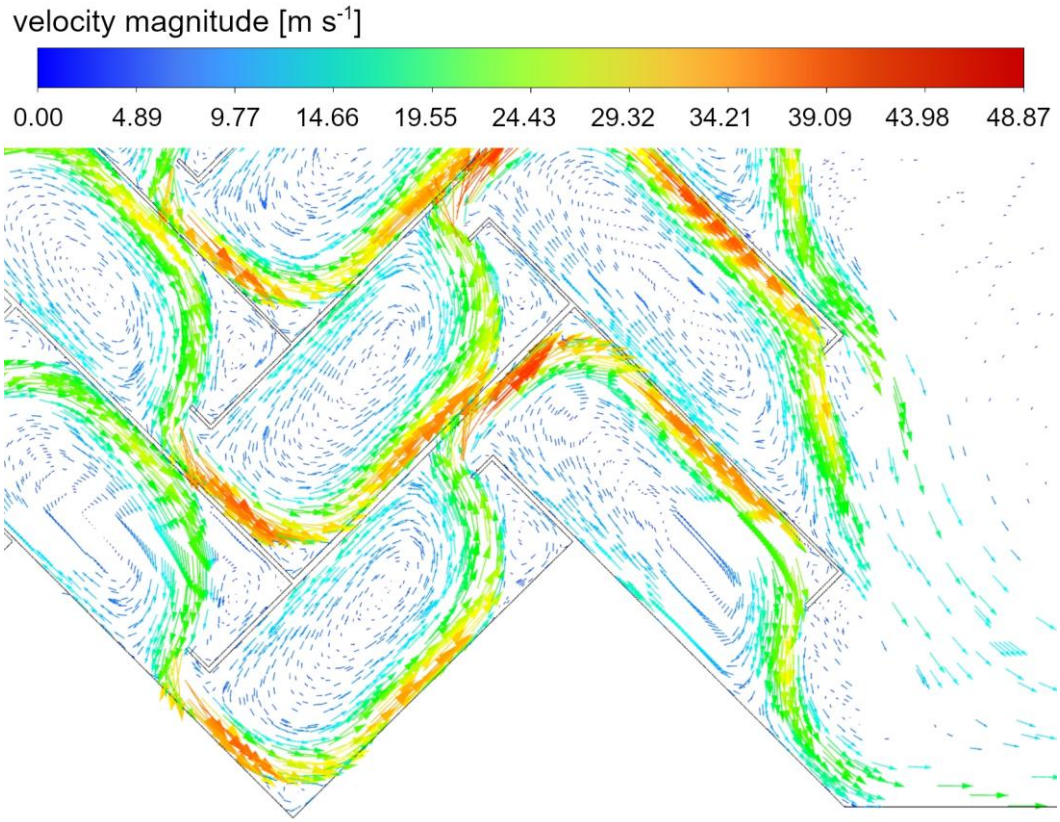

(b)

Figure 9.14. Velocity contours (a) and vectors (b) of Geometry B_25_0 (drainage channels' length of 25.5 mm, inlet velocity 4 m s^{-1}) [80]

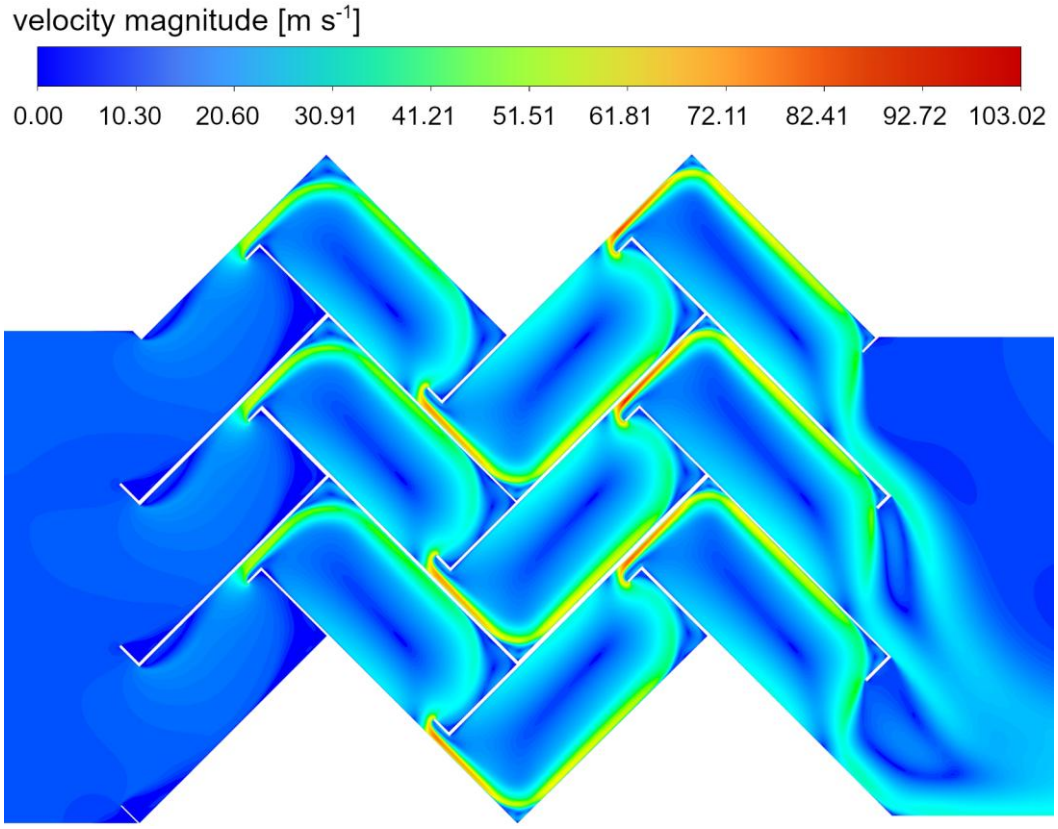

(a)

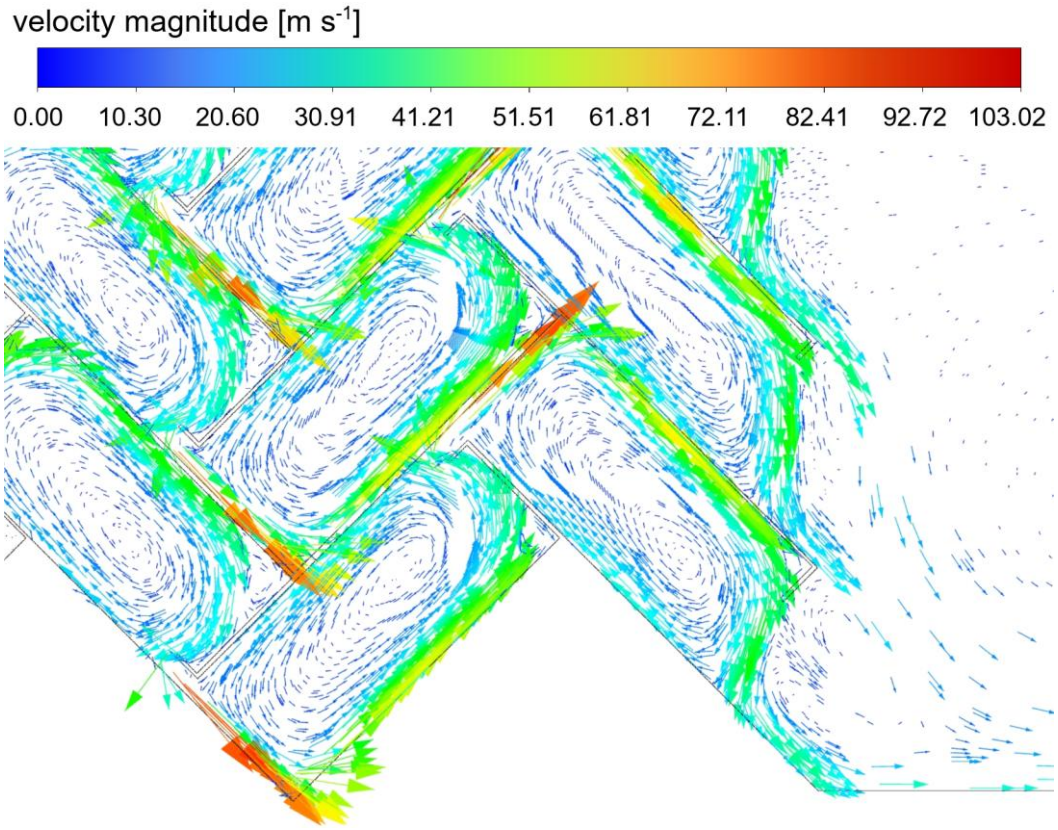

(b)

Figure 9.15. Velocity contours (a) and vectors (b) of Geometry B_30_0 (drainage channels' length of 30.5 mm, inlet velocity 4 m s^{-1}) [80]

9.9.4. Influence of drainage channels' angle on droplet removal efficiency

The drainage channel angle is another crucial parameter in this work. Table 9.1 lists the different angles of drainage channels in the geometry variants with 10.5 mm channels (geometries: B_10_0, B_10_30, B_10_60, B_10_90).

Figure 9.16 presents the droplet removal efficiency as a function of droplet diameter for investigated velocities in Geometry B_10_0 variants with different drainage channels' angles. It can be noted that separation efficiency tends to increase with the drainage channel angle (α), especially for the lower velocity (2 m s^{-1}). This phenomenon may result from moving drainage channels to higher velocity zones, causing higher inertial forces acting on droplets and higher local pressure drops.

Figure 9.17 shows velocity contours and vectors of investigated geometries of wave-plate mist eliminators with different drainage channels' angles. It can be observed that the maximum local velocity increases with the channels' angles. In the Geometry B_10_0, the local maximum velocity value is about 5.5 times higher than the mean velocity at the system's inlet. In Geometry B_10_90, the local maximum velocity is about 8.5 times higher. The separation efficiency for drainage channels' angles of 0° and 30° increases by about 40%, with the pressure drop increasing by about 25%. It should be noted that higher angles may increase secondary droplet entrainment; however, the CFD model does not include this phenomenon.

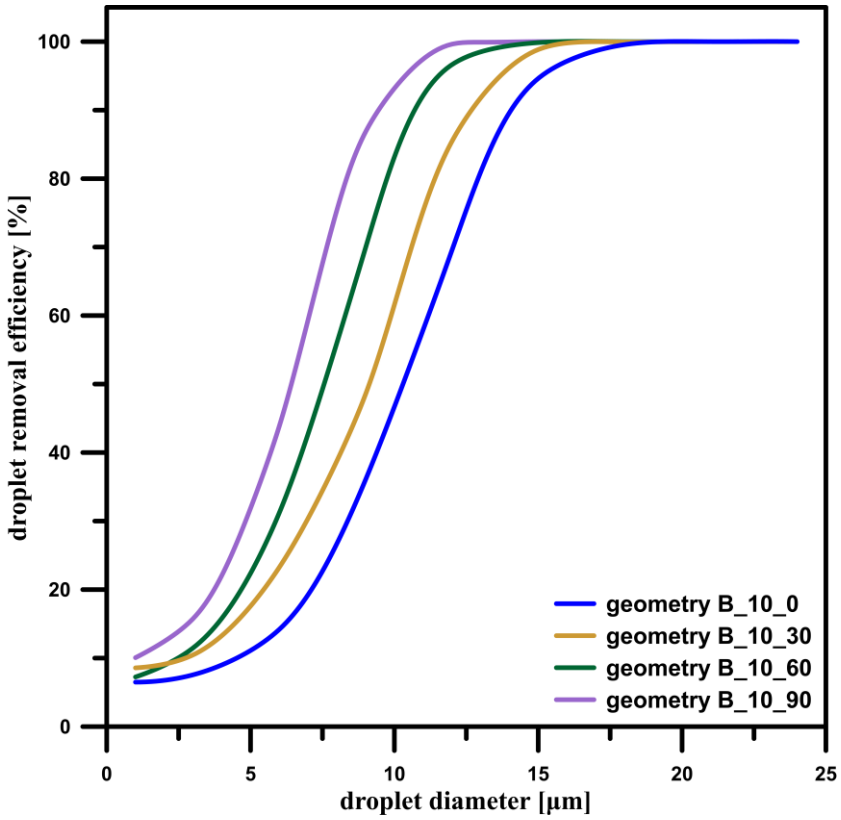

(a)

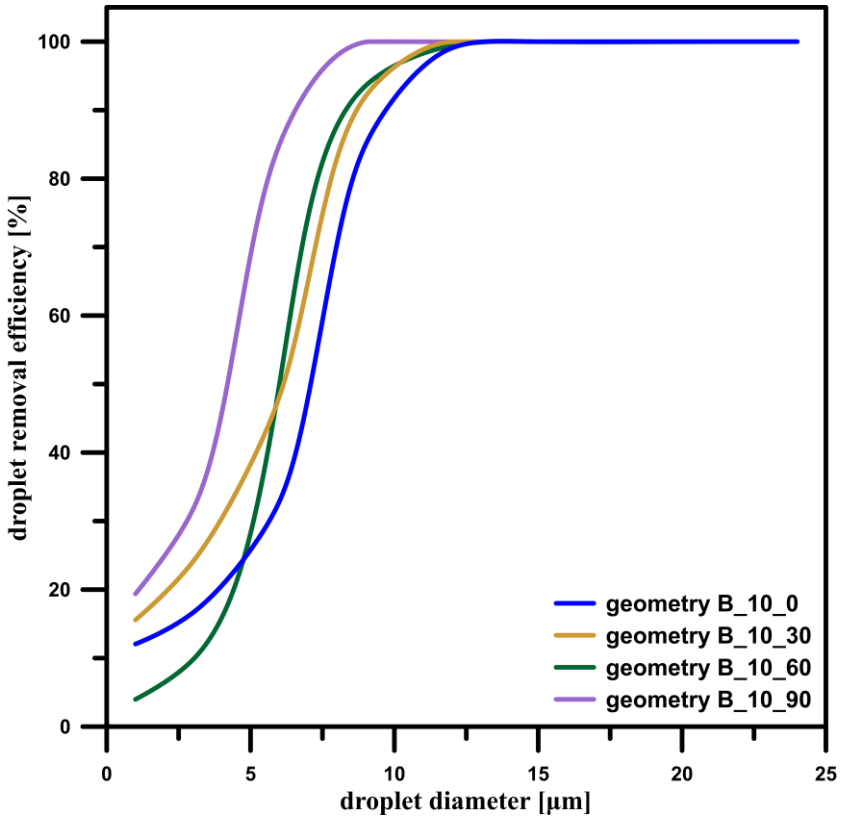

(b)

Figure 9.16. Comparison of droplet removal efficiency in relation to droplet diameter for different drainage channels' angles in different wave-plate mist eliminator geometries for inlet velocity of 2 m s^{-1} (a) and 4 m s^{-1} (b) [80]

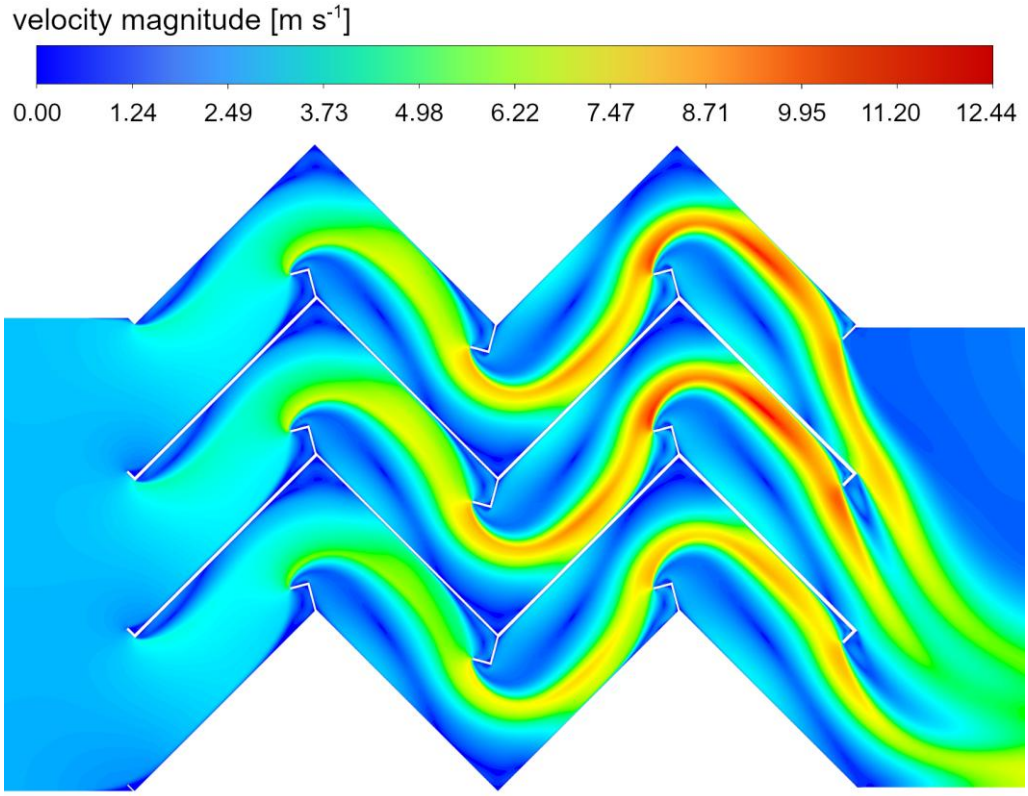

(a) drainage channels' angle 30°, u_{in} 2 m s^{-1}

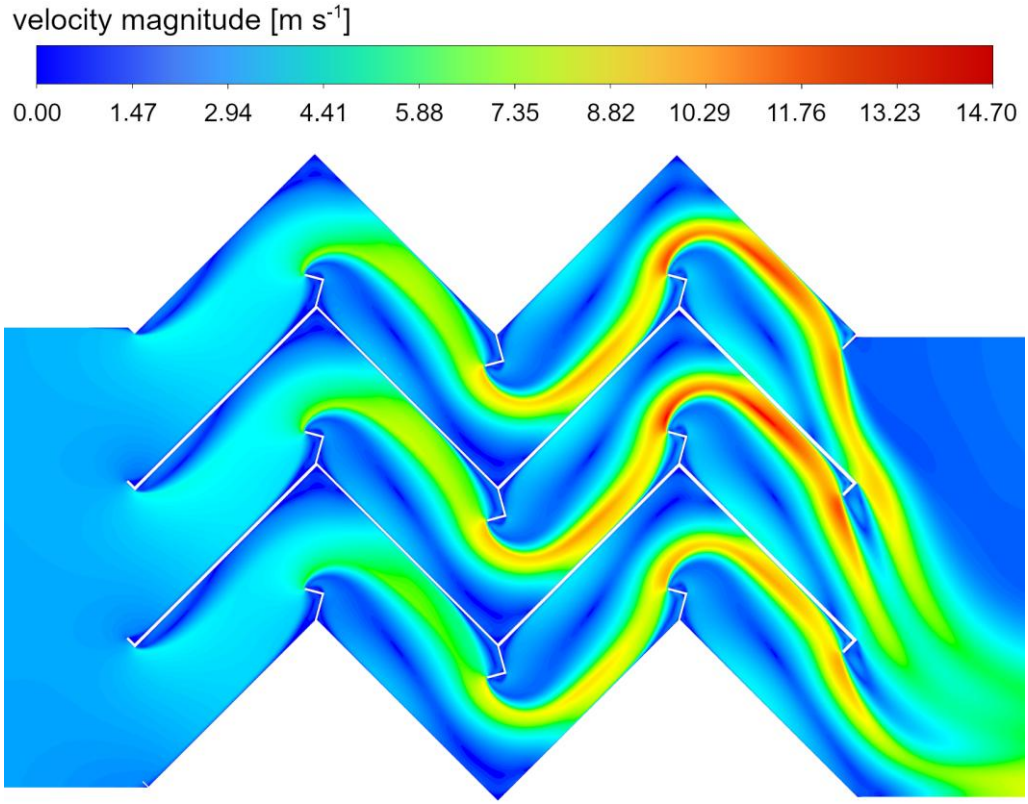

(b) drainage channels' angle 60°, u_{in} 2 m s^{-1}

Figure 9.17. Cont.

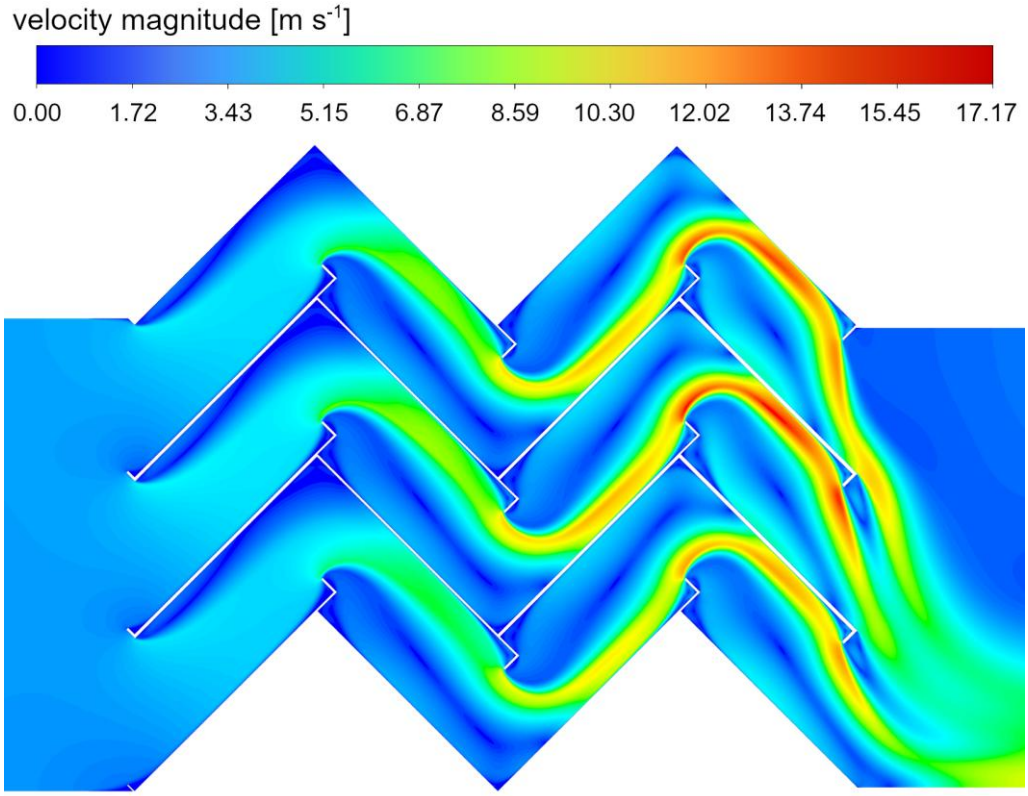

(c) drainage channels' angle 90°, u_{in} 2 m s^{-1}

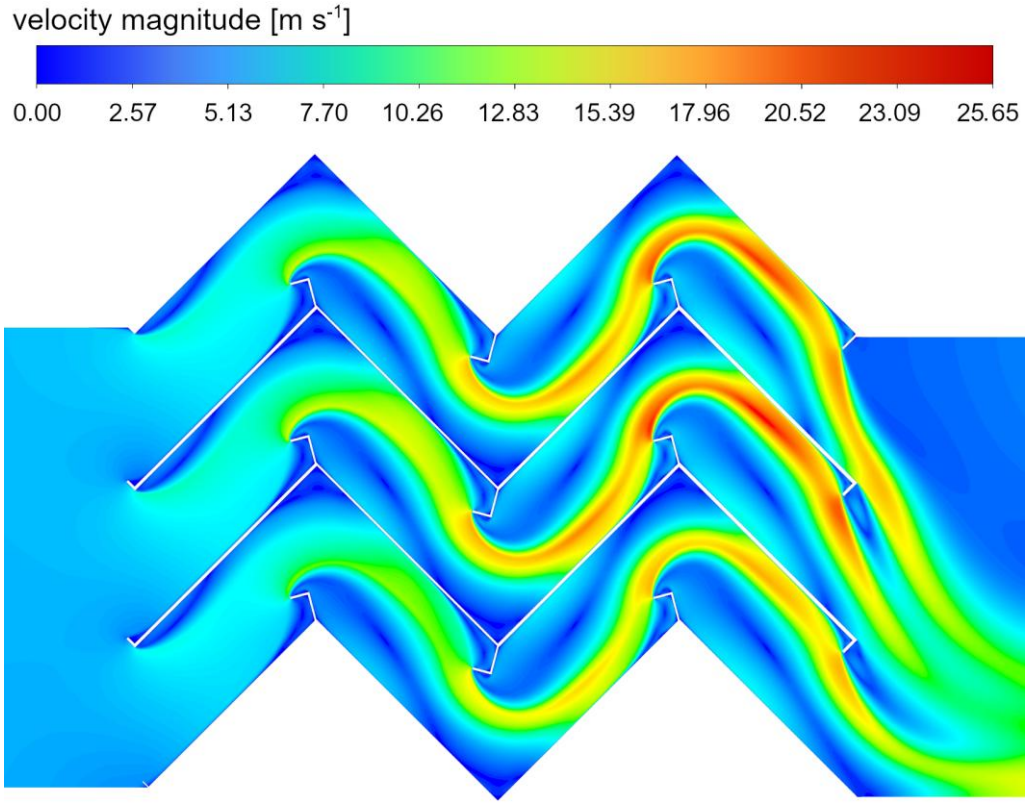

(d) drainage channels' angle 30°, u_{in} 4 m s^{-1}

Figure 9.17. Cont.

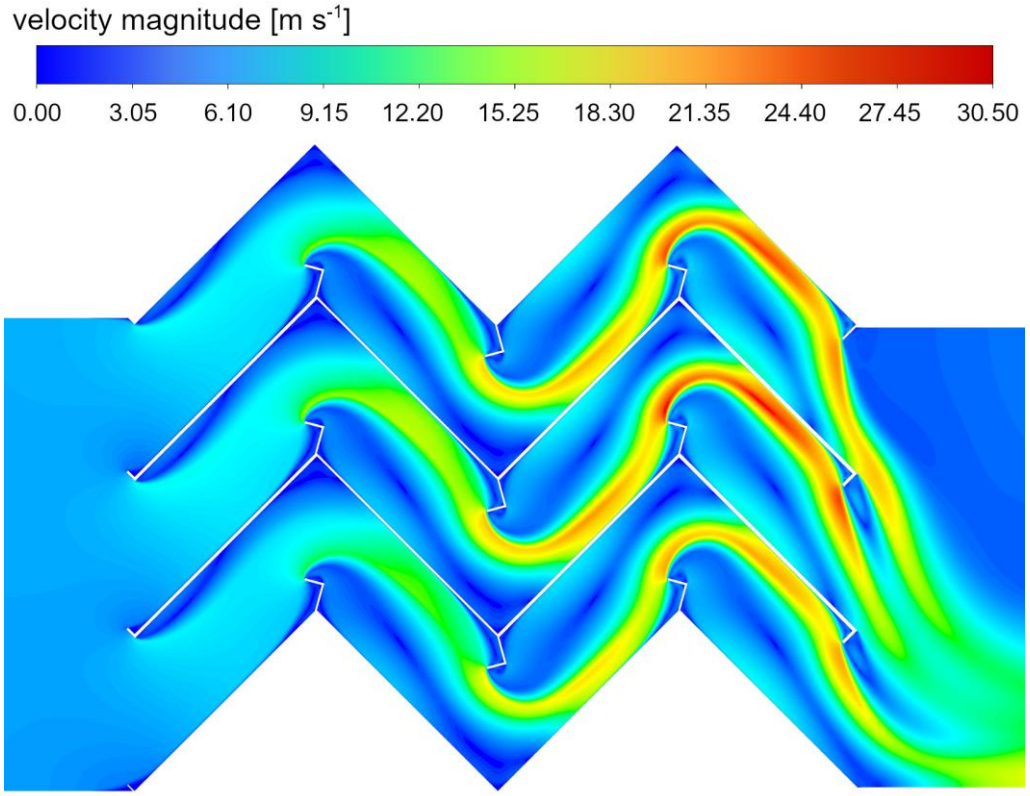

(e) drainage channels' angle 60°, u_{in} 4 m s^{-1}

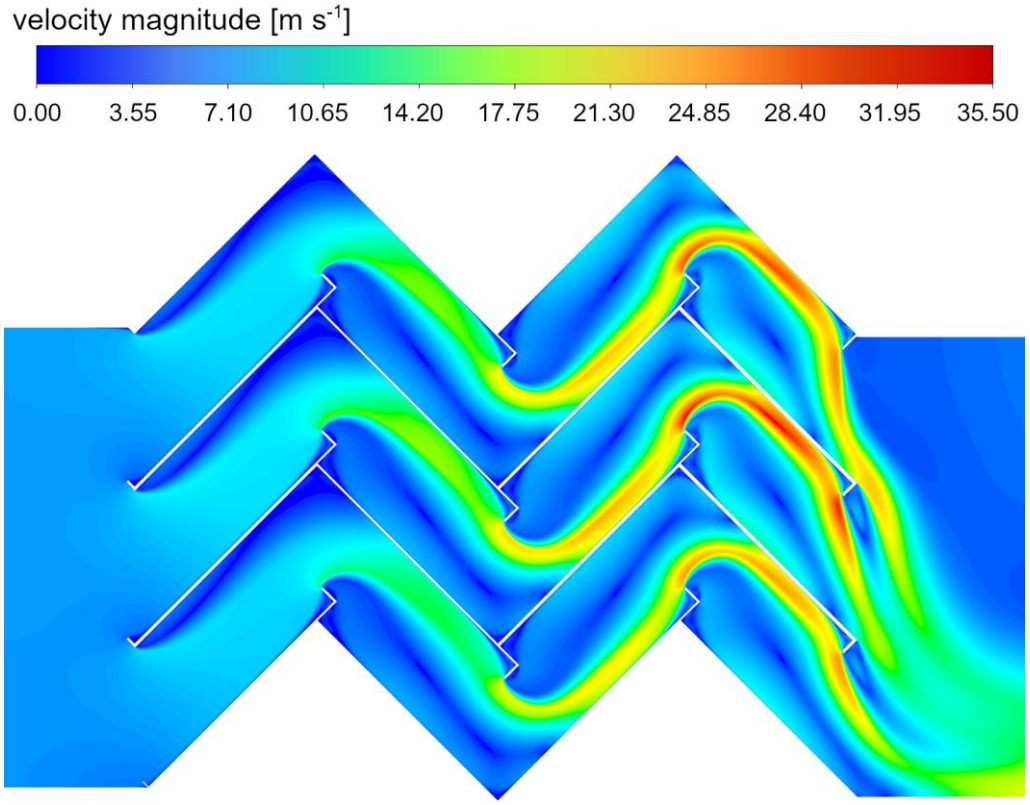

(f) drainage channels' angle 90°, u_{in} 4 m s^{-1}

Figure 9.17. Velocity contours of geometries with drainage channels angles of 30° (Geometry B_10_30) (a, d), 60° (Geometry B_10_60) (b, e) and 90° (Geometry B_10_90) (c, f) (drainage channels' length of 10.5, inlet velocity values of 2 m s^{-1} (a–c) and 4 m s^{-1} (d–f)) [80]

9.9.5. Influence of droplets' material on droplet removal efficiency

This section investigated the influence of different droplet materials on the separation efficiency. Table 9.15 lists the analysed droplet materials and their densities.

Table 9.15. Droplets' materials and their densities applied in calculations [80]

Droplet material	*Density [kg m^{-3}]*
water	999
n-octane	720
diesel fuel	830
95% sulphuric acid	1834
25% aqueous ammonia solution	865

Since, according to assumptions (Section 9.3), droplets are considered hard spheres, density is the most critical physicochemical parameter influencing separation. Figures 9.18 and 9.19 present the separation efficiency functions of droplet diameters for different droplet materials for geometries A (Figure 9.18) and B_10_0 (Figure 9.19).

The results show that the density of the droplet medium strongly influences the separation efficiency. The lower droplet densities increase the entrainment probability, while higher densities strengthen inertia forces due to the higher droplet mass, making them easier to remove. As expected, the presence of drainage channels provides better removal efficiency with an increase of about 20%. However, this happens at the cost of about 6% of pressure drop increase.

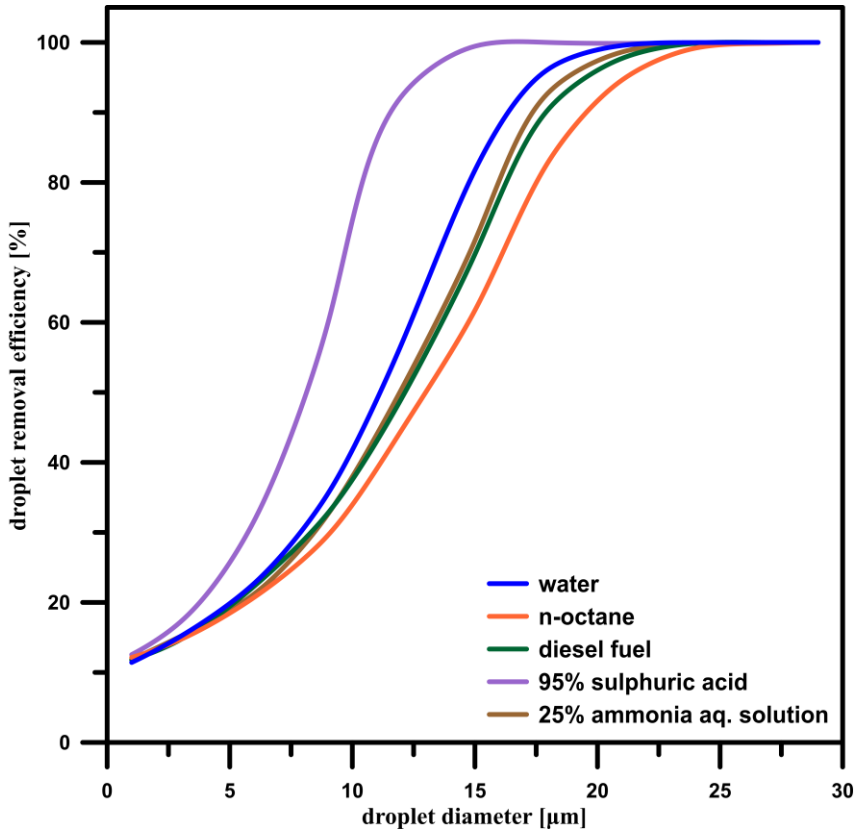

(a)

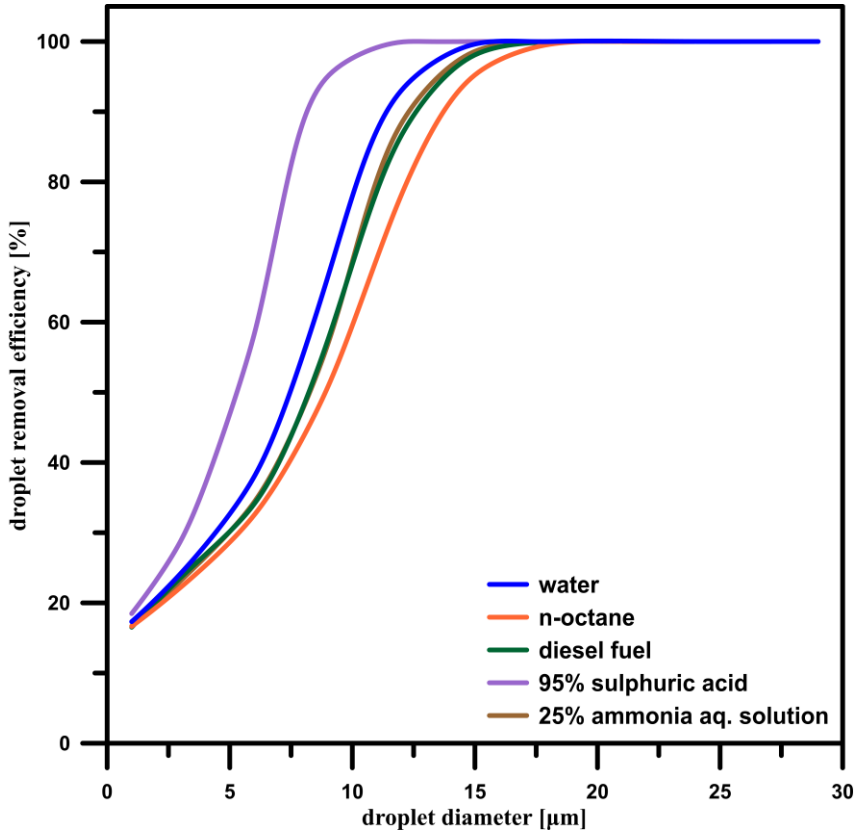

(b)

Figure 9.18. Comparison of droplet removal efficiency in relation to droplet diameter for different droplet materials in Geometry A for inlet velocity of 2 m s^{-1} (a) and 4 m s^{-1} (b) [80]

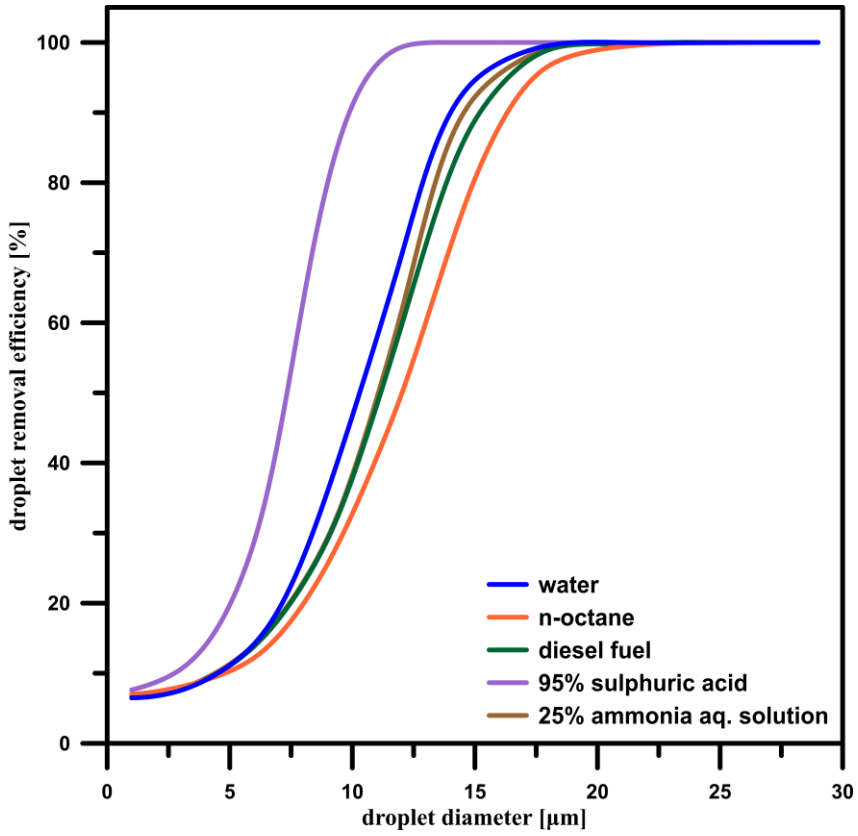

(a)

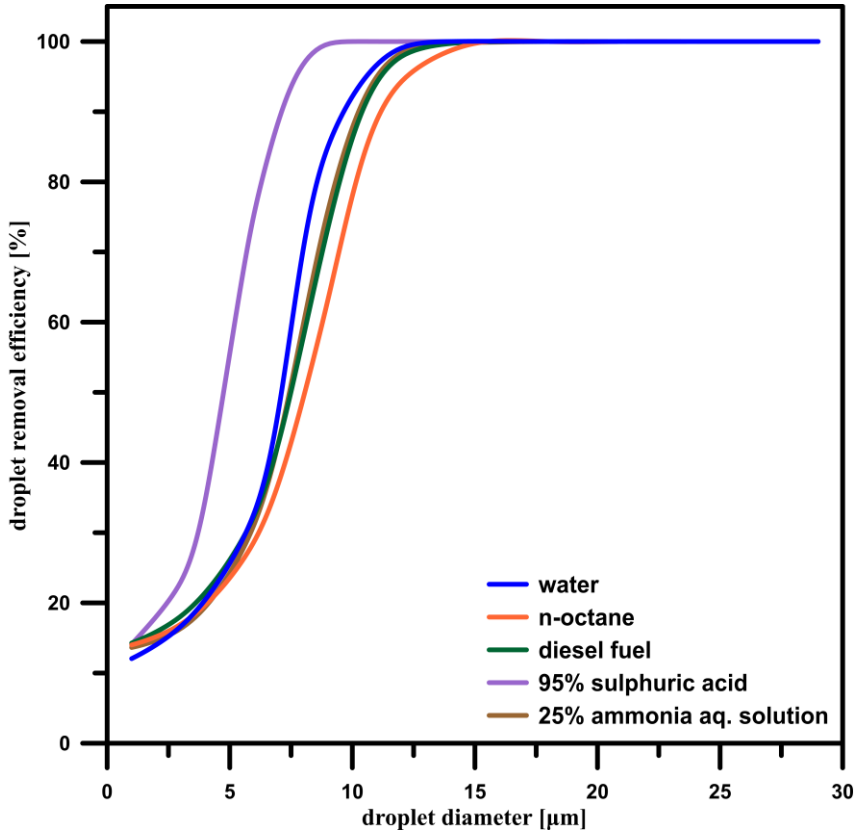

(b)

Figure 9.19. Comparison of droplet removal efficiency in relation to droplet diameter for different droplet materials in Geometry B_10_0 for inlet velocity of 2 m s^{-1} (a) and 4 m s^{-1} (b) [80]

9.10. Improvement proposal

The results and experimental validation show that the CFD model correctly predicts the droplets' behaviour in different geometries and operating parameters of wave-plate mist eliminators, allowing for a novel system modification. As a reference Geometry, B_15_0 was chosen since, according to Figure 9.8, it is still in the range of low pressure and has the best droplet removal efficiencies of all cases within this range. Figure 9.20 presents the pressure field in the Geometry B_15_0.

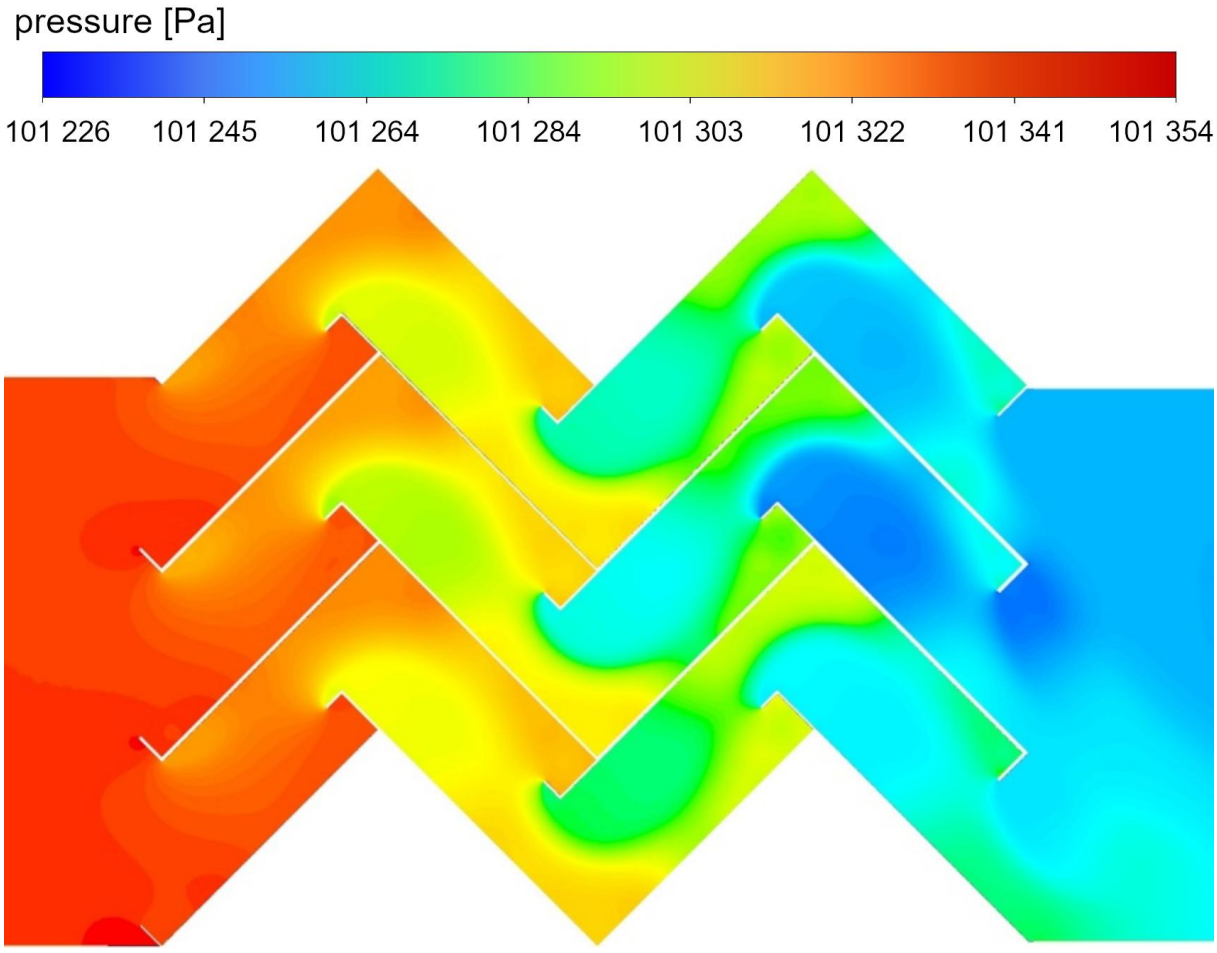

Figure 9.20. Pressure contours of Geometry B_15_0 (drainage channels' length of 15.5 mm, inlet velocity 2 m s^{-1}) [80]

In Figure 9.20, one can observe that zones of high-pressure drop values appear near the sharp edges of the drainage channels, predominately perpendicular to the flow direction. This effect is even more visible for more extended drainage channels. Therefore, a new, streamlined drainage channel was proposed to achieve high process efficiency with a slight pressure drop. Figure 9.21 presents the new system's geometry, further referenced as Geometry C_15_0, and Table 9.16 lists its dimensions.

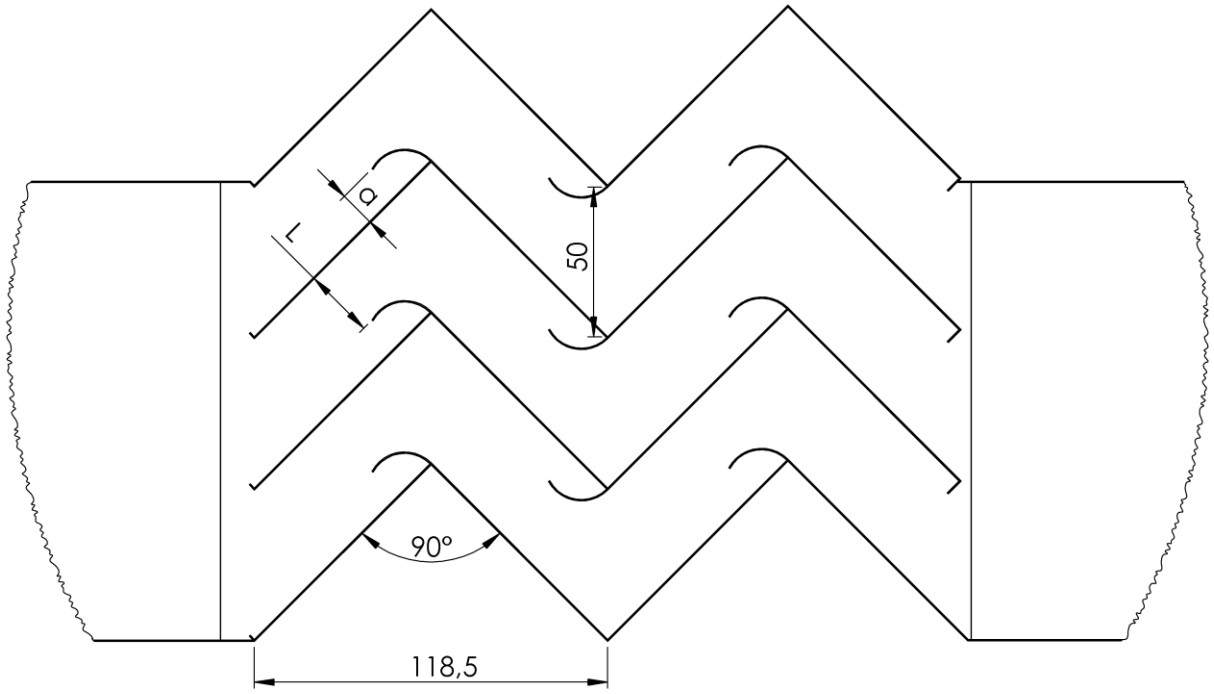

Figure 9.21. Dimensions (in mm) of the Geometry C_15_0 [80]

Table 9.16. Geometrical details of novel wave-plate mist eliminator geometry variant [80]

Geometry variant	*Drainage channels' presence*	*a [mm]*	*L [mm]*
C_15_0	Yes	15.5	18.5

Figure 9.22 compares the droplet removal efficiency functions of droplet diameters for Geometries B_15_0, C_15_0, and with the B_10_0 as a reference. It can be observed that the Geometry C_15_0 provides the highest droplet separation efficiency.

Figures 9.23 and 9.24 show the velocity contours and vectors of the Geometry C_15_0.

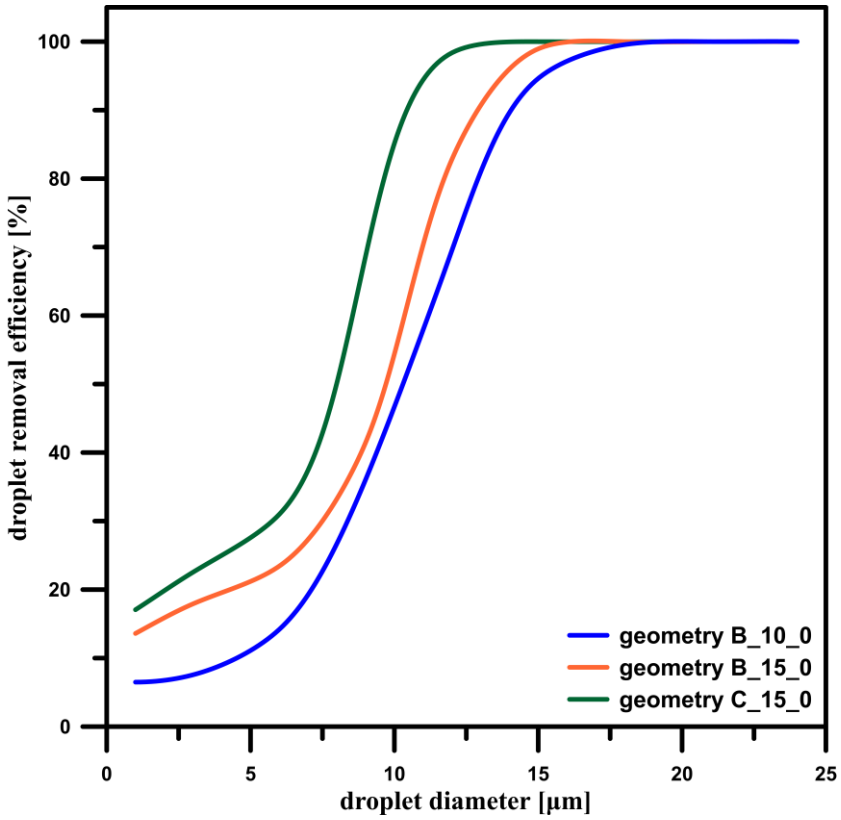

(a)

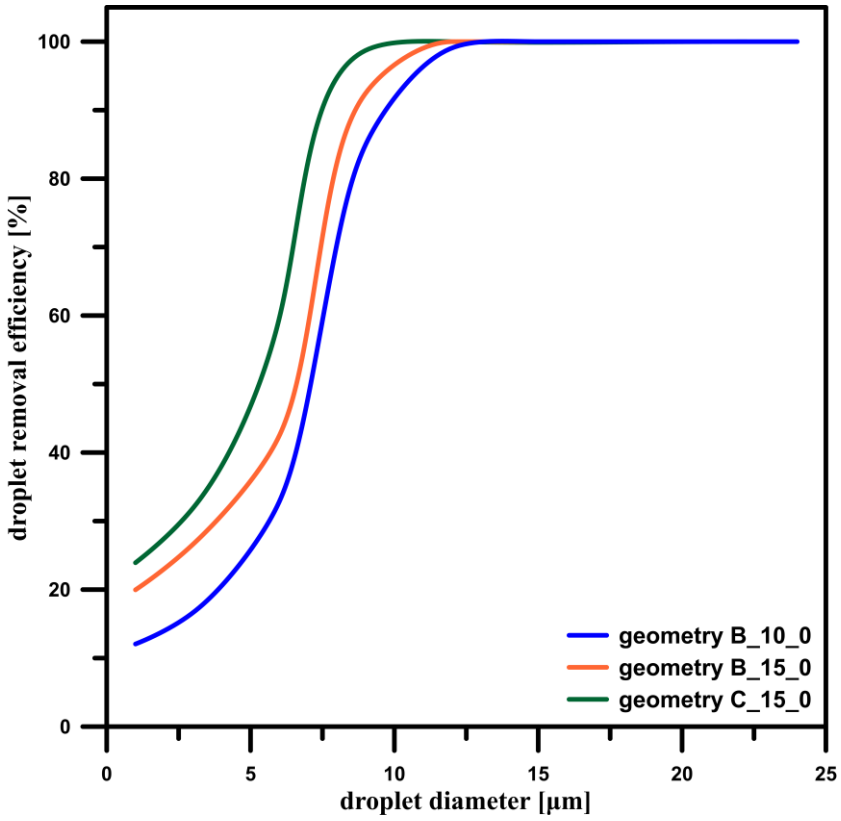

(b)

Figure 9.22. Comparison of droplet removal efficiency in relation to droplet diameter for wave-plate mist eliminator geometries with rectangular and streamlined drainage channels for inlet velocity of 2 m s^{-1} (a) and 4 m s^{-1} (b) [80]

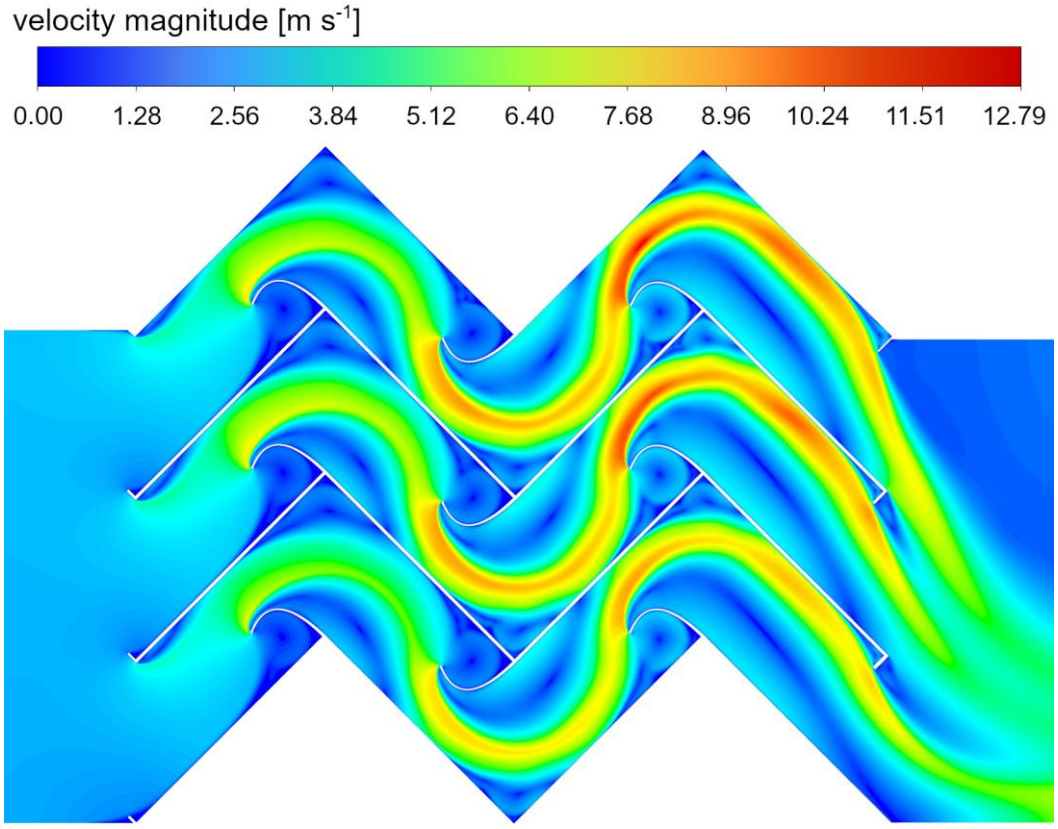

(a)

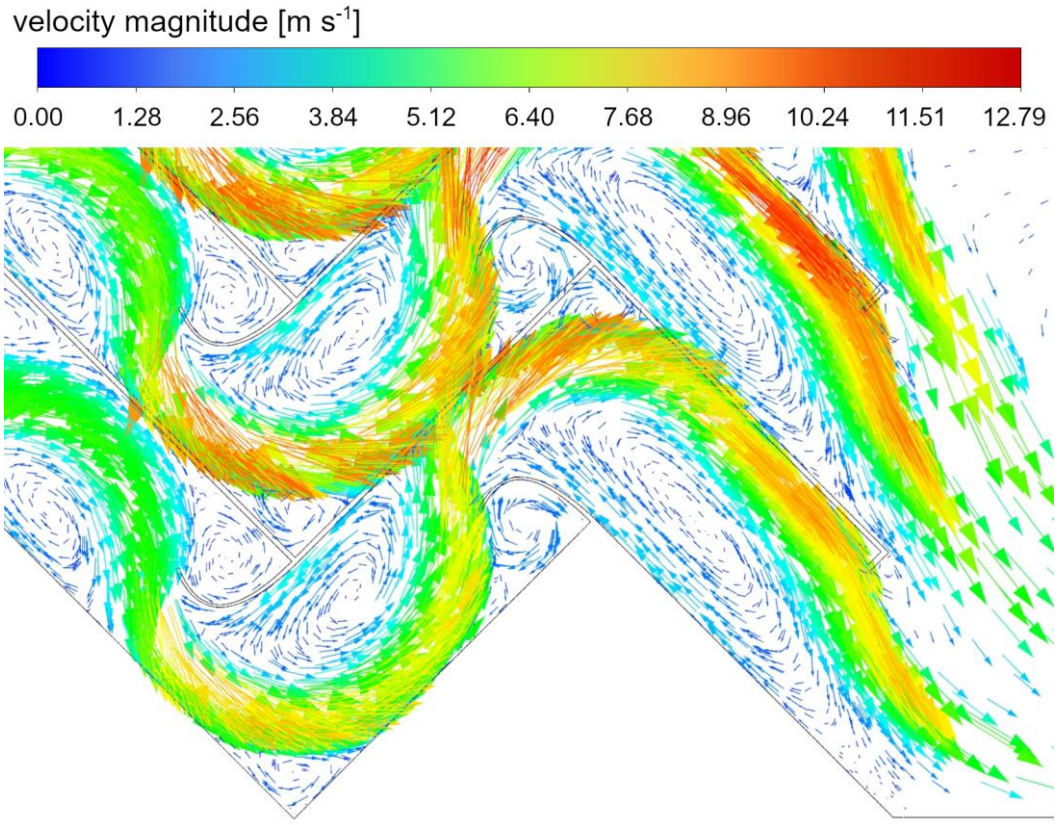

(b)

Figure 9.23. Velocity contours (a) and vectors (b) of Geometry C_15_0 (drainage channels' length of 15.5 mm, inlet velocity 2 m s^{-1}) [80]

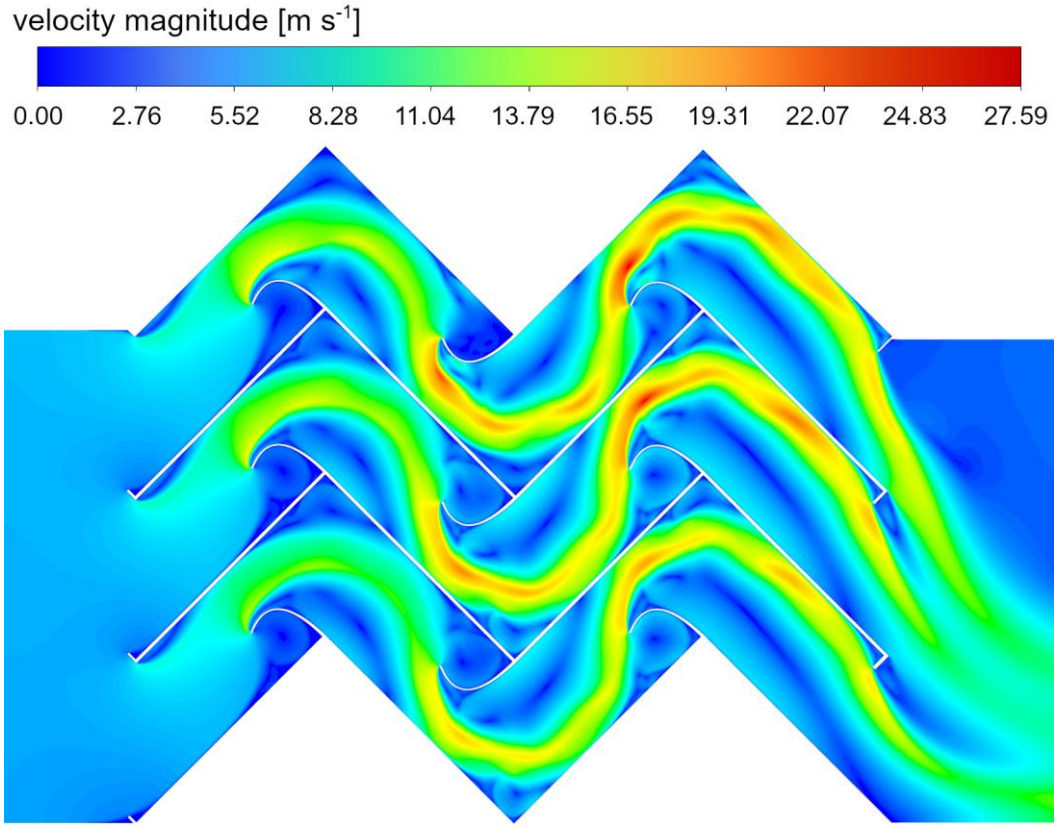

(a)

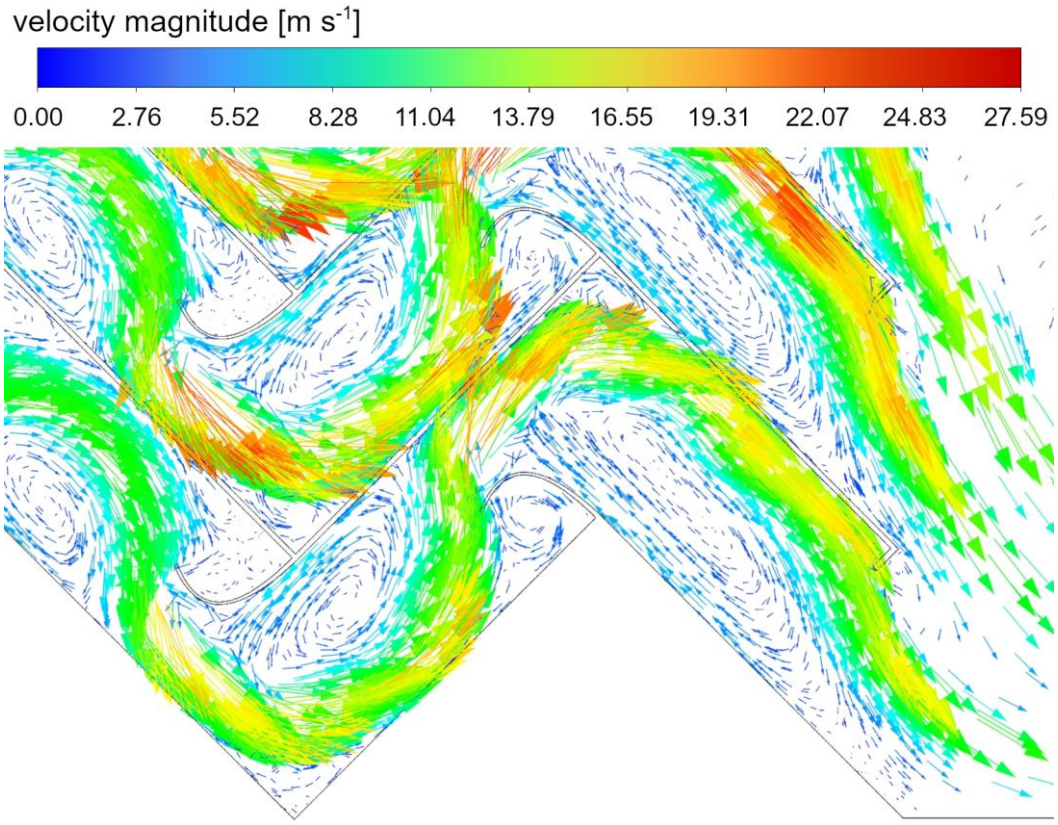

(b)

Figure 9.24. Velocity contours (a) and vectors (b) of Geometry C_15_0 (drainage channels' length of 15.5 mm, inlet velocity 4 m s^{-1}) [80]

Tables 9.17 and 9.18 present the values of pressure drops and the mean force acting on drainage channels for the novel and reference geometries.

Table 9.17. Pressure drop and the mean force acting on drainage channel geometry variants of B_10_0, B_15_0 and C_15_0 (inlet velocity 2 m s^{-1}) [80]

Geometry variant	B_10_0	B_15_0	C_15_0
Pressure drop [Pa]	87	109	107
The mean force acting on drainage channel [N]	0.38	1.38	1.40

Table 9.18. Pressure drop and the mean force acting on drainage channel geometry variants of B_10_0, B_15_0 and C_15_0 (inlet velocity 4 m s^{-1}) [80]

Geometry variant	B_10_0	B_15_0	C_15_0
Pressure drop [Pa]	367	442	406
The mean force acting on drainage channel [N]	1.53	5.62	6.20

The velocity patterns of the considered cases for 2 m s^{-1} suggest that the new geometry (Geometry C_15_0) obtains higher maximum velocity values than the corresponding variant with rectangular drainage channels (Geometry B_15_0). This phenomenon results from the shape of the external drainage channels' walls. The Geometry C_15_0 variant flattens the continuous phase stream, which is especially visible after the third bend of the wave-plate region. The critical role plays the phenomenon of vortexes inside the channels. Rectangular channels flatten the vortex into an oval shape, causing the fluid from inside to come in contact with agas with almost maximum velocity. However, streamlined channels cause the forming vortex to be round in shape, and their edges disturb the gas flow to a lesser extent. This substantially influences the entrapment of deposited droplets, presented in Figures 9.25–9.32, which show droplet trajectories in the investigated systems.

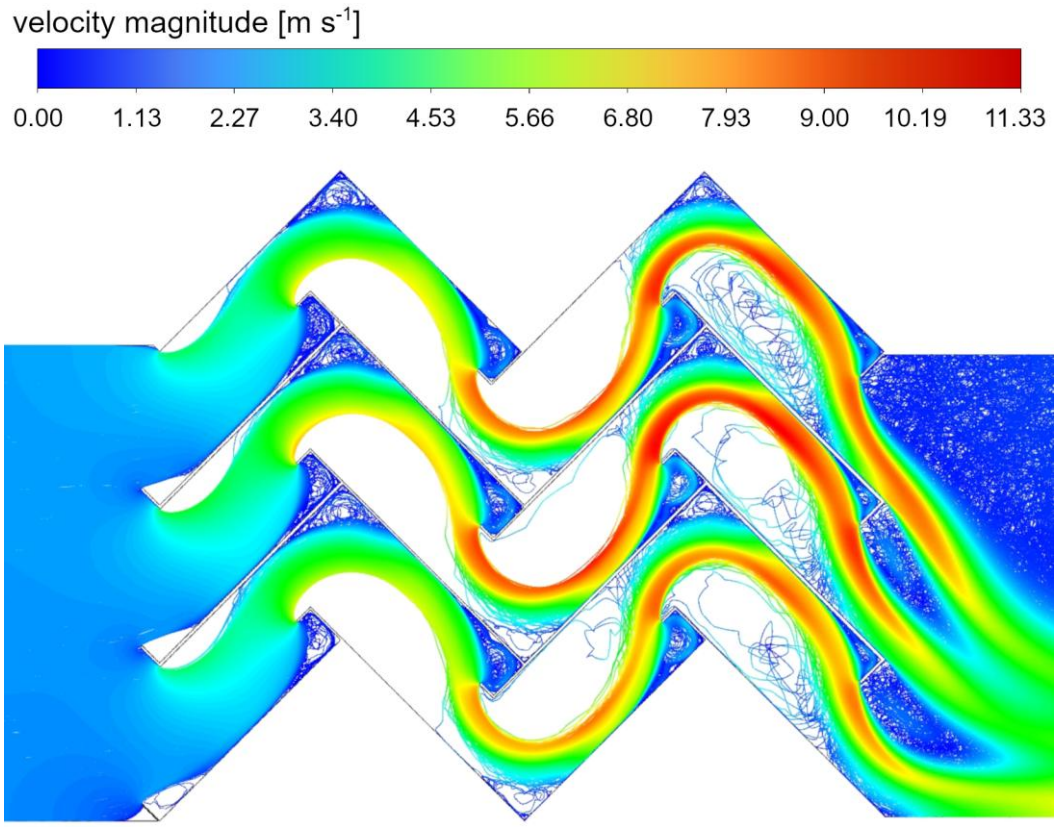

(a)

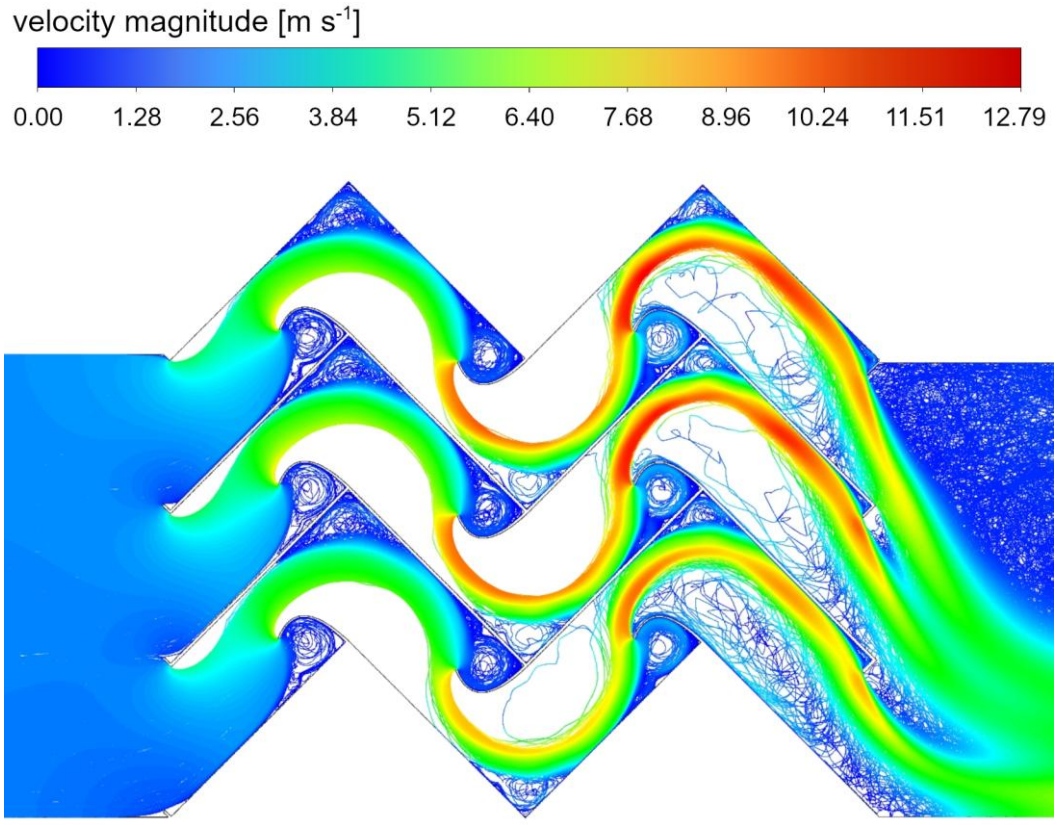

(b)

Figure 9.25. Comparison of droplet trajectories between geometries B_15_0 (a) and C_15_0 (b) (droplet diameter 8 µm, drainage channels' length of 15.5 mm, inlet velocity 2 m s^{-1}) [80]

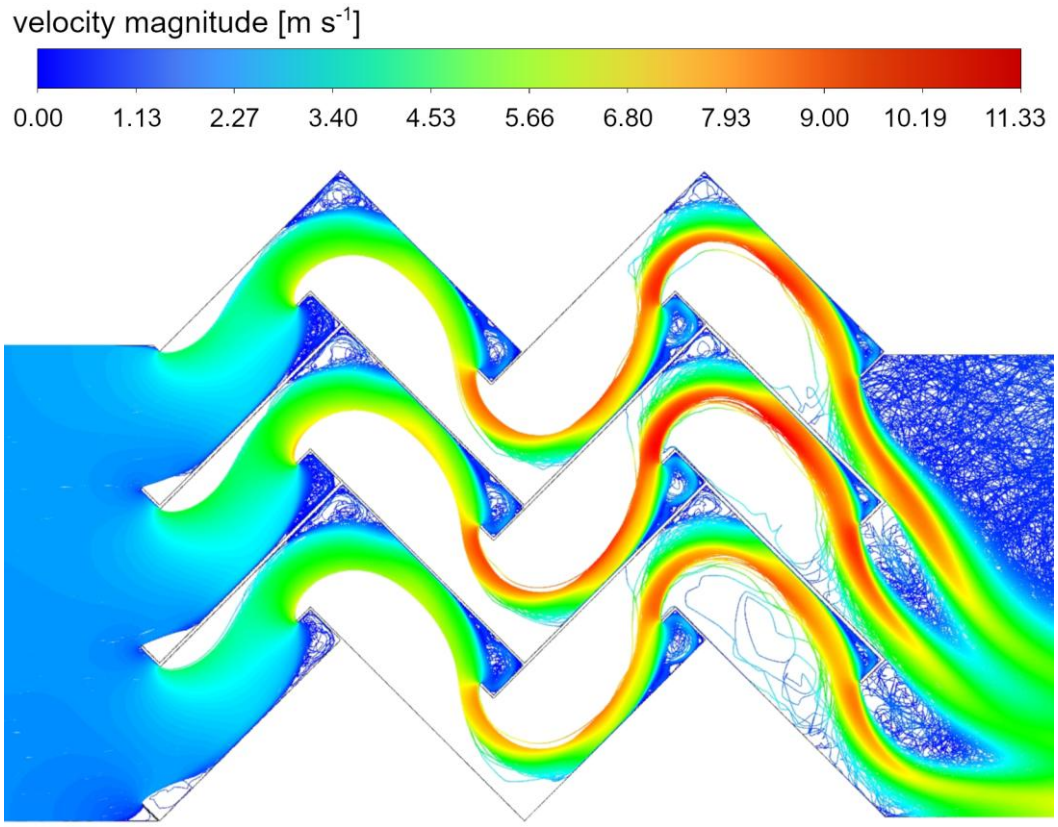

(a)

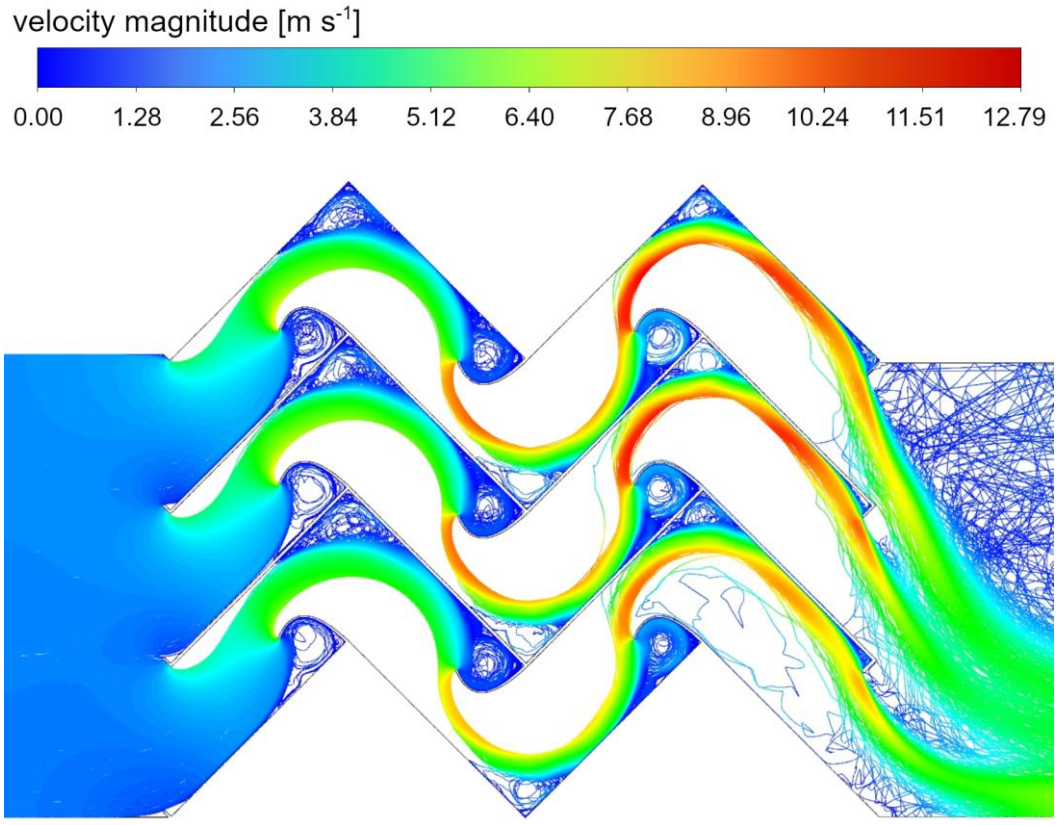

(b)

Figure 9.26. Comparison of droplet trajectories between geometries B_15_0 (a) and C_15_0 (b) (droplet diameter 10 µm, drainage channels' length of 15.5 mm, inlet velocity 2 m s^{-1}) [80]

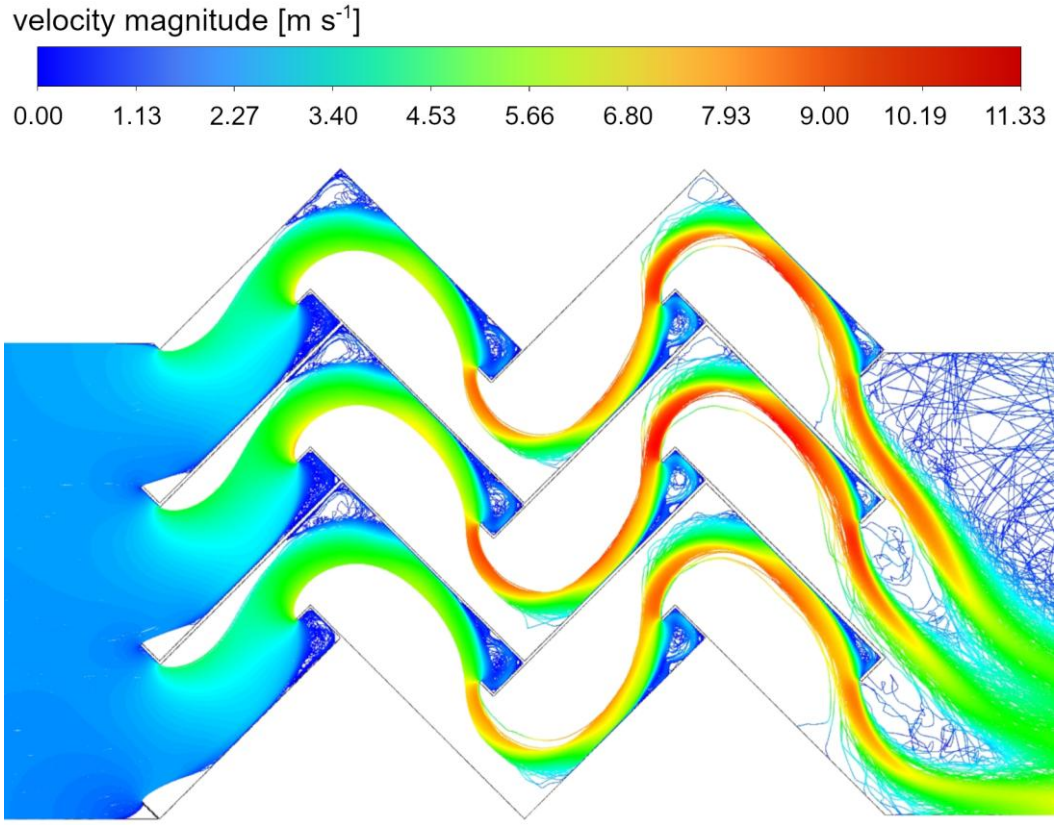

(a)

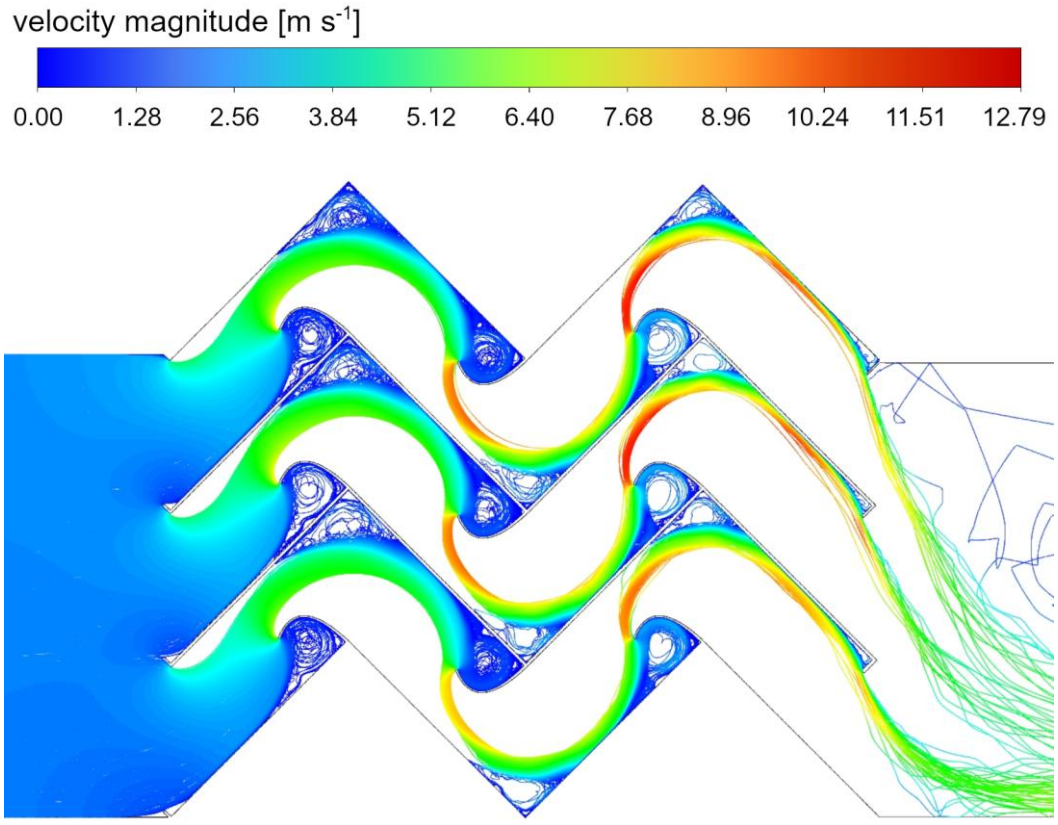

(b)

Figure 9.27. Comparison of droplet trajectories between geometries B_15_0 (a) and C_15_0 (b) (droplet diameter 12 µm, drainage channels' length of 15.5 mm, inlet velocity 2 m s^{-1}) [80]

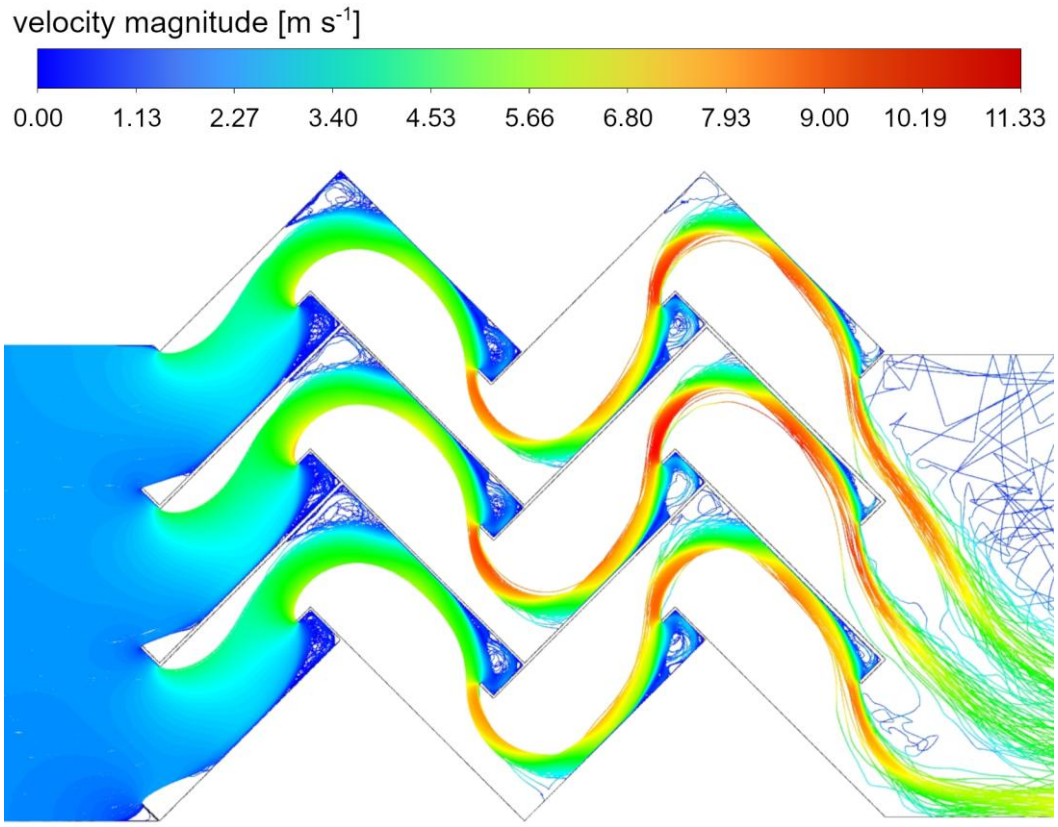

(a)

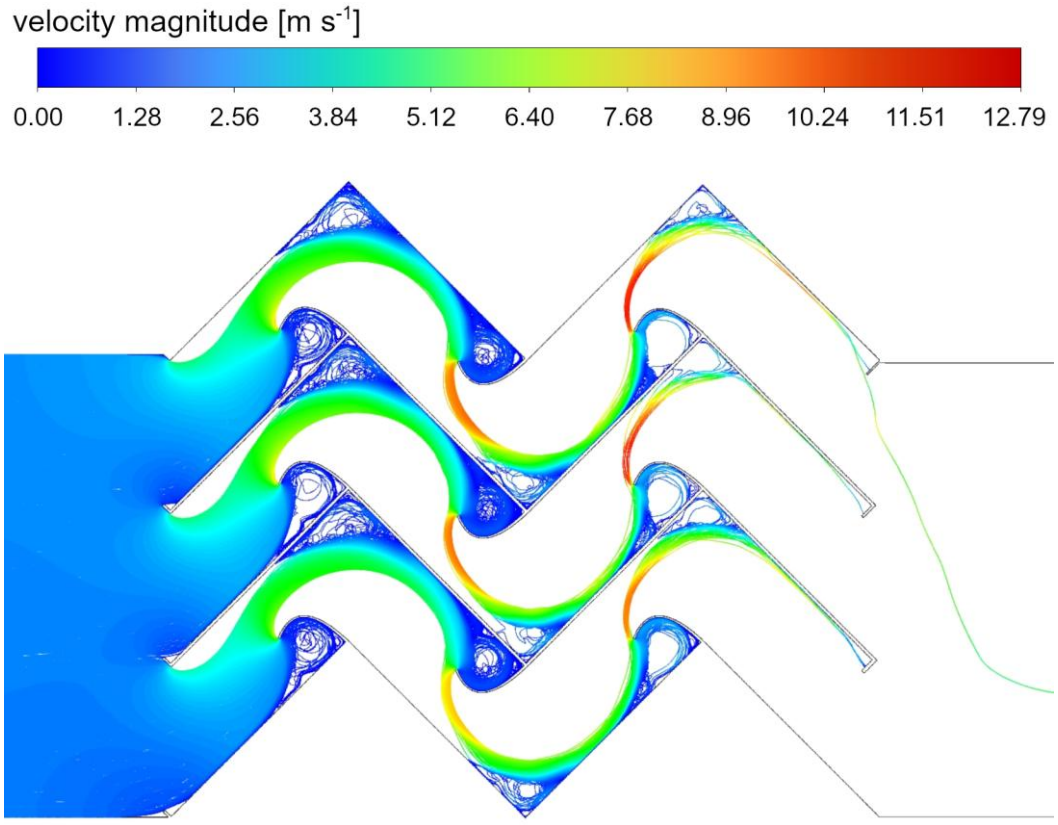

(b)

Figure 9.28. Comparison of droplet trajectories between geometries B_15_0 (a) and C_15_0 (b) (droplet diameter 14 µm, drainage channels' length of 15.5 mm, inlet velocity 2 m s^{-1}) [80]

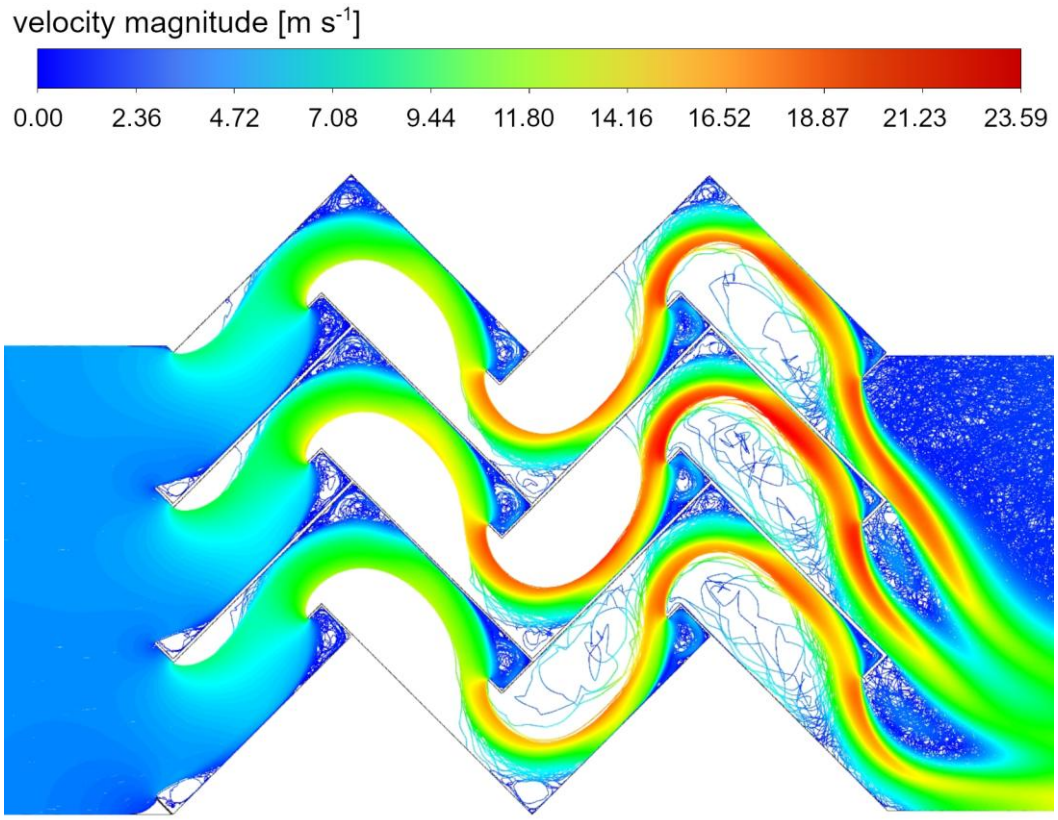

(a)

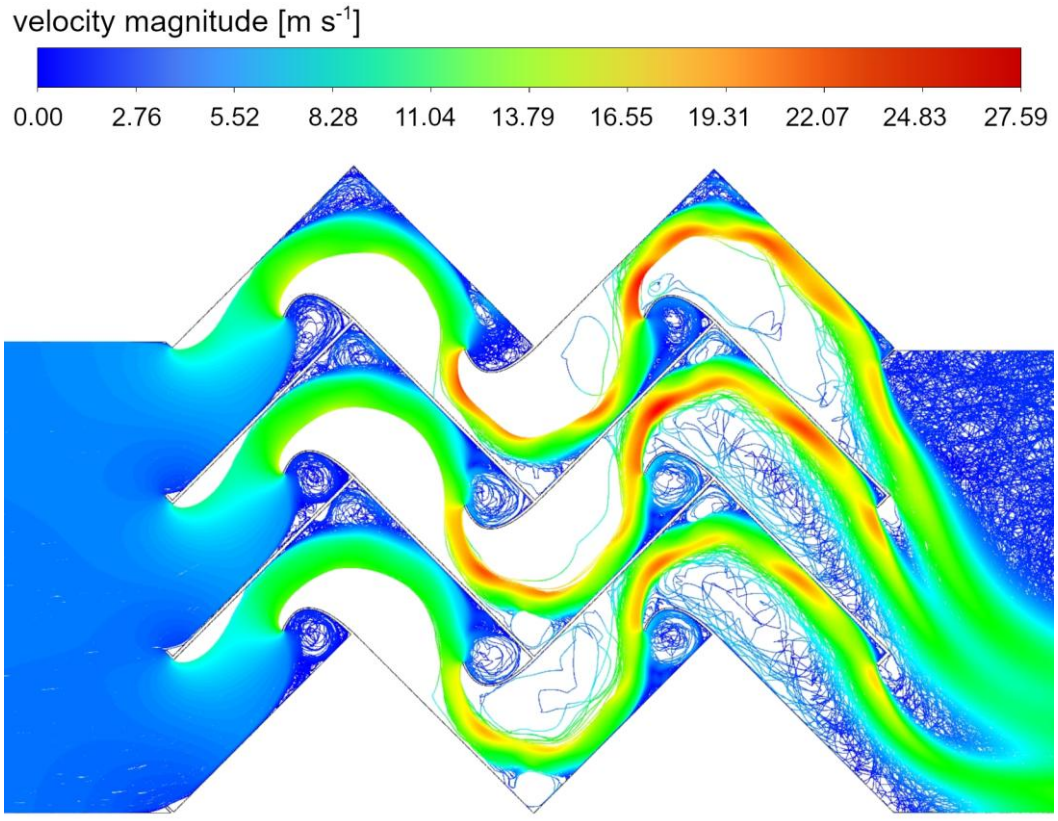

(b)

Figure 9.29. Comparison of droplet trajectories between geometries B_15_0 (a) and C_15_0 (b) (droplet diameter 6 µm, drainage channels' length of 15.5 mm, inlet velocity 4 m s^{-1}) [80]

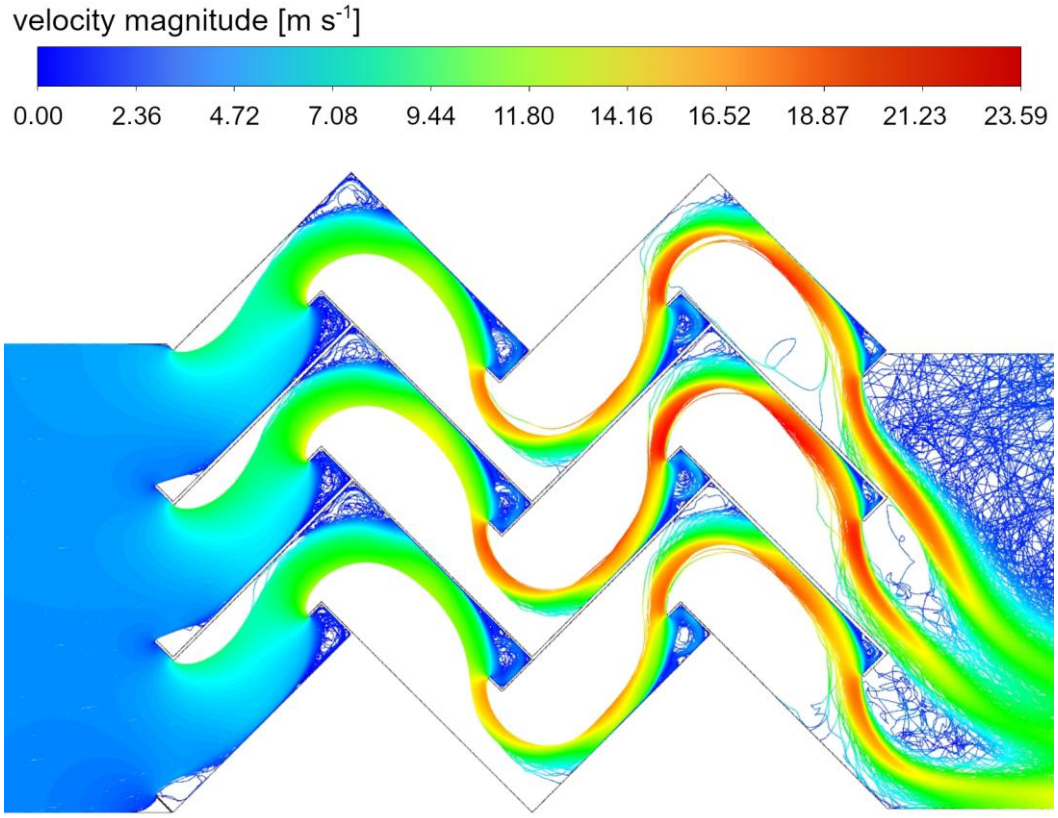

(a)

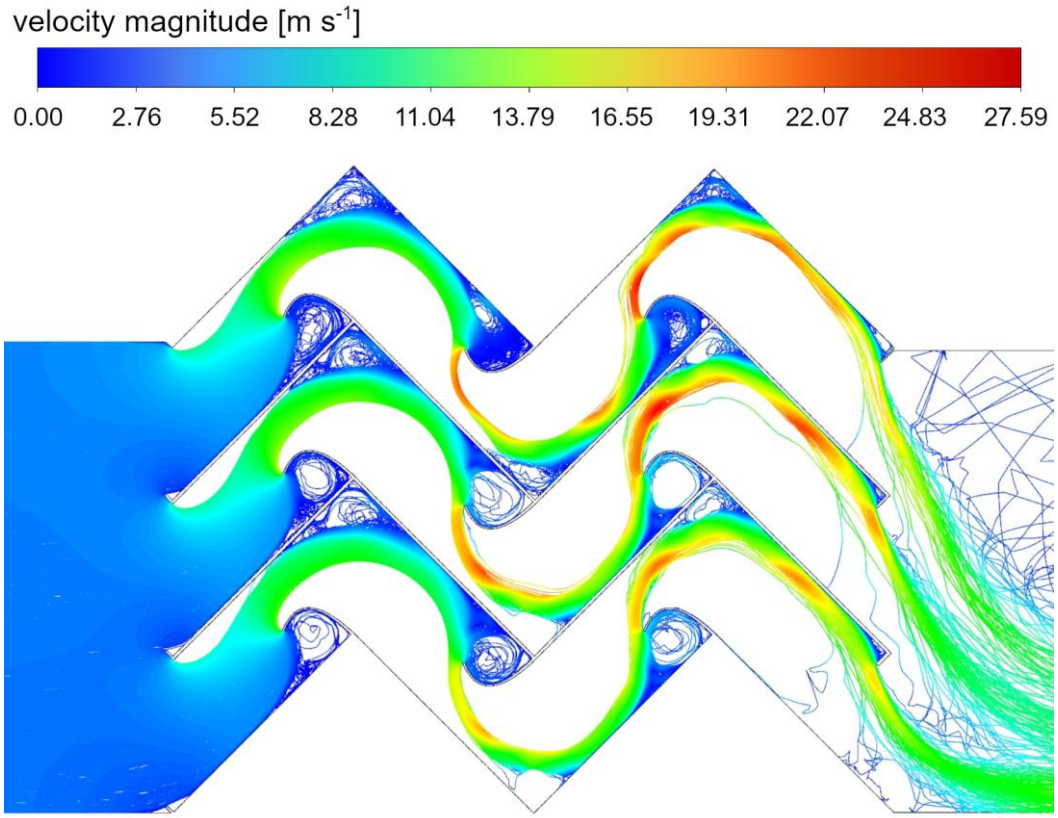

(b)

Figure 9.30. Comparison of droplet trajectories between geometries B_15_0 (a) and C_15_0 (b) (droplet diameter 8 µm, drainage channels' length of 15.5 mm, inlet velocity 4 m s^{-1}) [80]

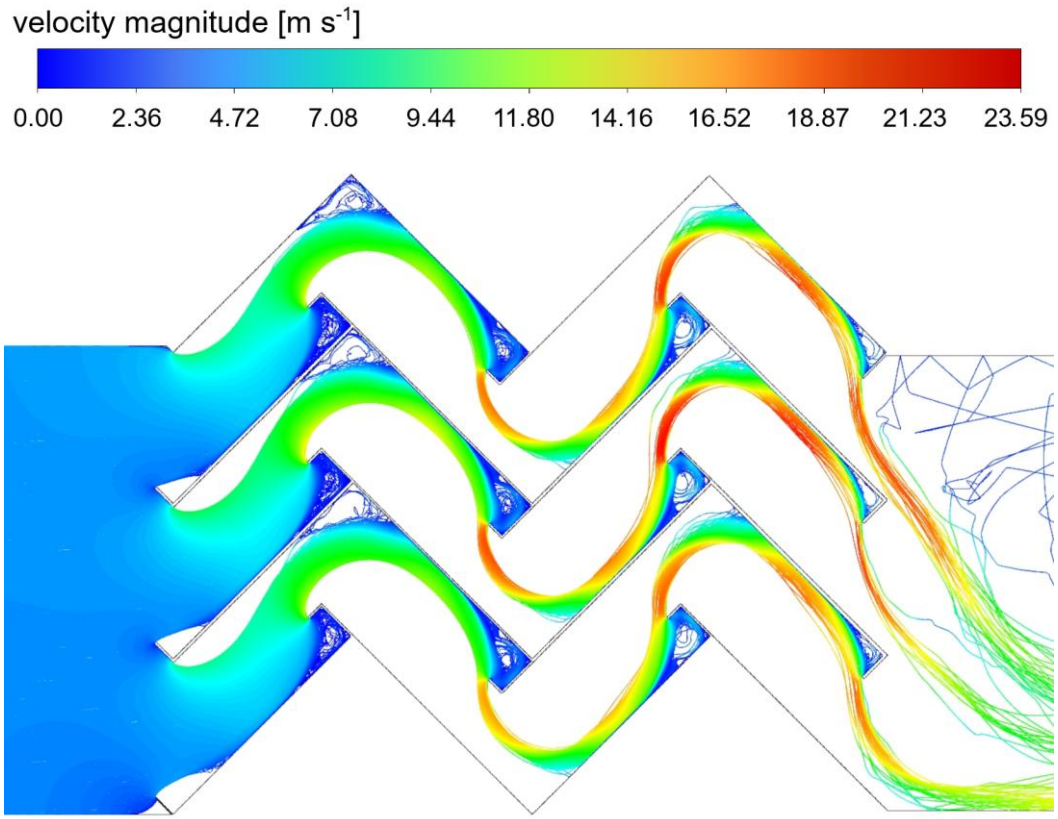

(a)

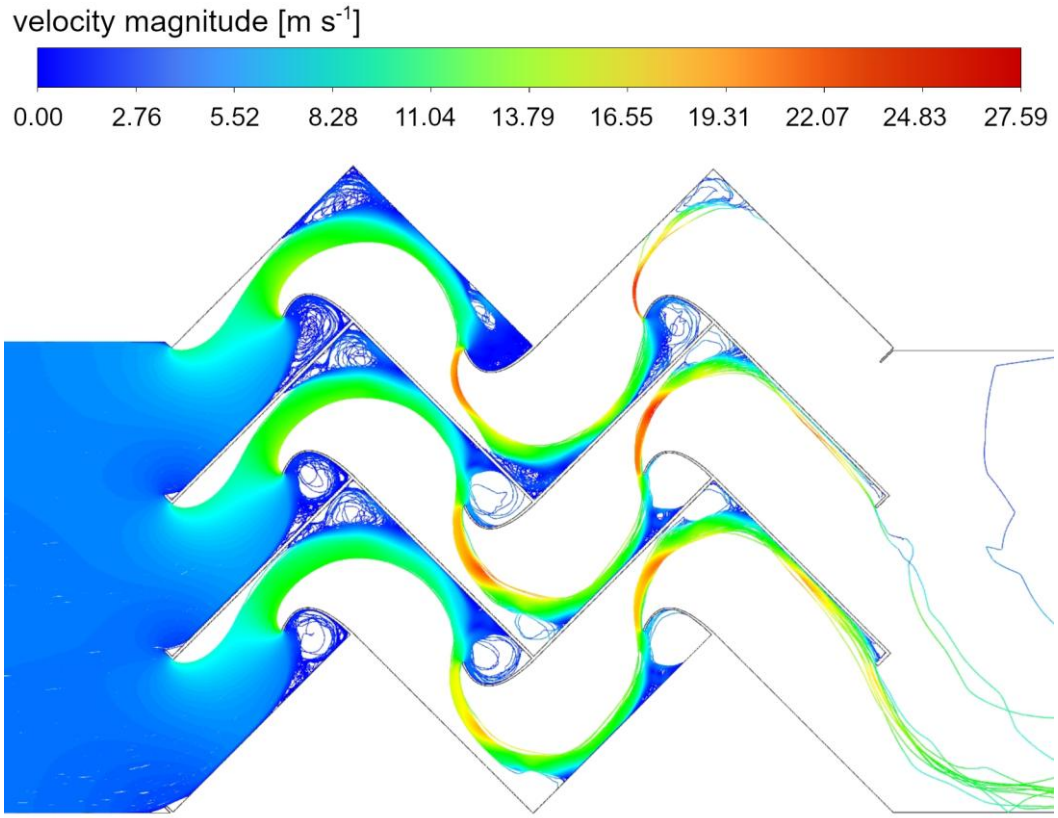

(b)

Figure 9.31. Comparison of droplet trajectories between geometries B_15_0 (a) and C_15_0 (b) (droplet diameter 10 µm, drainage channels' length of 15.5 mm, inlet velocity 4 m s^{-1}) [80]

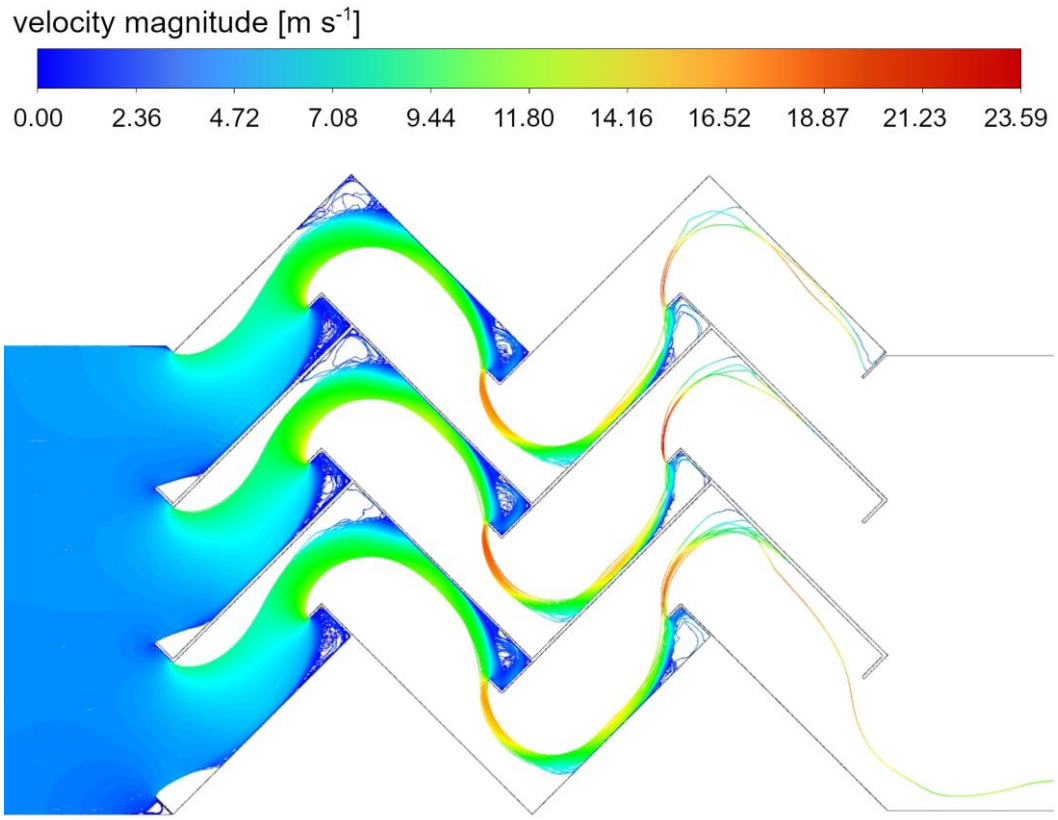

(a)

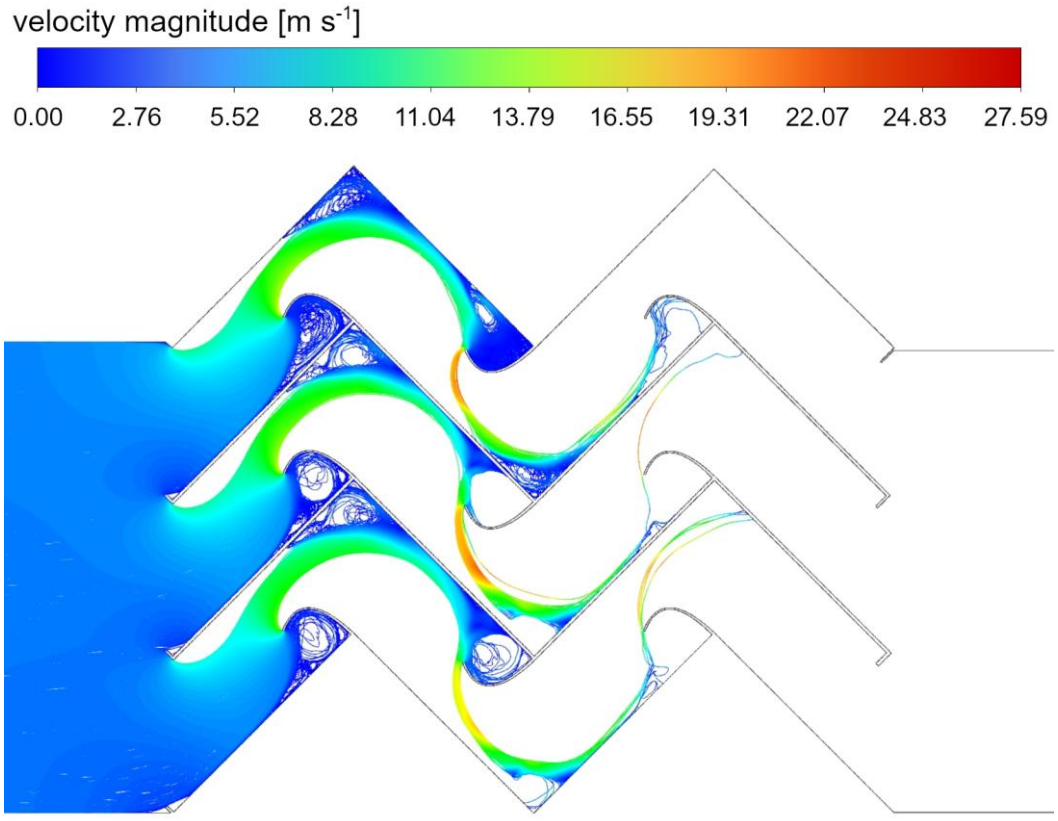

(b)

Figure 9.32. Comparison of droplet trajectories between geometries B_15_0 (a) and C_15_0 (b) (droplet diameter 12 µm, drainage channels' length of 15.5 mm, inlet velocity 4 m s^{-1}) [80]

The separation efficiency of novel geometry is about 100% for droplets over the size of 14 μm. Geometry C_15_0 also has over two times higher droplet separation efficiency than Geometry B_10_0 in the case with droplets of 6 μm and 80% higher droplet removal than Geometry B_15_0. For the inlet velocity of 2 m s^{-1}, the pressure drop of the Geometry C_15_0 is about 23% higher than that of Geometry B_10_0, although the pressure drop is almost the same as that of the Geometry B_15_0 variant. The results are even better for higher velocity. The streamlined drainage channels should also minimise the secondary drop entrainment. However, more experiments and simulations are needed to investigate it through validated simulation.

9.11. Conclusions

In this work, the CFD model simulating the inertial droplet separator was created. It allowed to investigate the influence of practical, crucial parameters of wave-plate mist eliminators, such as continuous phase velocity, droplet size and drainage channel presence and length, on the droplet removal efficiency and pressure drop. The obtained results show that the presence of drainage channels causes an increase in the pressure drop, which is undoubtedly an undesired phenomenon in inertial droplet separators. However, the drainage channels highly increase the droplet removal efficiency. Drainage channels capture the droplets and cause the gas flow velocity, improving separation efficiency. It should be noted, though, that the droplet entrainment effect was not included in the model, and it may be higher in the separator without drainage channels, which further reduces the usefulness of this variant.

Three turbulence models and two variants of turbulent dispersion modelling were tested to create a CFD model. The results were compared with the literature data in the validation section. On this basis, the most appropriate variants of those models were chosen: the SST k-ω turbulence model with turbulent dispersion modelling within the discrete phase. These models provided consistent results with the available literature data and were used to calculate further cases with different drainage channel sizes, slopes and shapes. The results show that even minor changes in geometry can significantly improve the droplet removal efficiency with a relatively small pressure drop increase. The obtained CFD model allowed for the proposal of a new geometry of streamlined drainage channels. This solution caused a significant rise in droplet separation efficiency, maintaining comparable pressure drops compared to analogical geometry with rectangular drainage channels for lower velocities and even reducing pressure drops for higher velocities. Still, these results should be confirmed by extending the theoretical models with the effects of liquid film on the wall and secondary entrainment of droplets by the continuous phase and comparing them to experimental results.

10. Summary and concluding remarks

This thesis was dedicated to investigating and improving unit operations of the fertiliser industry using computational fluid dynamics methods at the design or re-designing level. Two primary unit operations in fertiliser production lines were investigated: the Haber-Bosch and Ostwald processes. The droplet removal through a wave-plate mist eliminator was analysed as a supporting process. Due to the large-scale industrial character of those processes, even minor improvements can lead to significant increases in production and reduce energy consumption by increasing the process efficiency. This work aimed to create CFD models that can be used as support while designing or modifying the existing unit operations.

For the industrial-scale ammonia synthesis, the Topsoe converter was selected for analysis. The CFD model contained the two-dimensional geometry of the first catalyst bed. The reaction kinetics was modelled using the modified Temkin-Pyzhev expression [35] and implemented using the UDF function. The results were focused on the influence of the catalyst bed's parameters on the process, mainly the catalyst particle size, which substantially affects the results. Calculated reaction rate and concentration fields allowed to identify zones with negligible reaction rates (close-to-equilibrium state). Based on those results, new variants of the catalyst bed's geometry were proposed that maintain the same efficiency with about twice the smaller volume of catalyst capacity. The obtained model can be used to predict the effects of the catalyst bed's geometry or parameter changes. However, it does not include factors like catalyst poisoning and ageing, which should be considered for simulating cases with their significant influence on the process.

The next part of this work concerned creating a CFD model of a pilot-scale ammonia synthesis reactor. The cooperation with Yara Technology and Projects – Technology (Yara International ASA) provided access to experimental data and detailed geometry of the physical pilot-scale ammonia converters. This data allowed to create a domain covering the entire geometry of the converter and create a model validated by two independent experimental runs. Analogically to the Topsoe reactor simulation, the modified Temkin-Pyzhev expression [35] was implemented to model the reaction kinetics. The detailed catalyst data allowed the modification of the implemented kinetic model to improve the CFD simulation's accuracy, and validation proved an exceptional coverage with experimental data with the concentration error compared to experiments not exceeding 2.3% and temperature error lower than 6.61% for all validation measurements. The obtained model allows easy identification of the zones with high or low

values of critical parameters, such as reaction rate or concentration, and has excellent potential as a "virtual prototype" replacement for further computer-aided experimental research. The model can be used to test parameters or geometry changes without the need to alter the physical equipment and can be used to guide the designing process of new physical prototype variants. It should be noted that significant parameter changes, such as modelling an industrial-scale converter, may need additional validation and potential modification to maintain the model's high accuracy.

Another section refers to the modelling of the Ostwald process. The first step was creating the detailed geometry of the 3-layer catalyst gauze clipping and CFD model with the surface reaction model implemented. The simulation used the microkinetic model developed by Kraehnert and Baerns [38]. The obtained CFD models investigated the influence of contact time and catalyst gauze's wall temperature on surface parameters such as reaction rate and local selectivity, as well as outlet concentration and overall process efficiency. The simulations track changes in the surface parameters in the subsequent layers, giving insight into how their number affects the process. However, since the investigated gauze has three layers, the potential parameter values on the following layers of gauze with more than three layers may need to be extrapolated or simulated with expanded geometry. The CFD model allows to calculate and visualise surface parameters and identify areas of higher and lower reaction rate values, selectivity and temperature, which is crucial to investigating the gauze degradation process. It should be noted that the kinetic model created by Kraehnert and Baerns [38] concerns ammonia oxidation on pure platinum wires. Increasing the accuracy of simulating cases with platinum-rhodium wires may require more experimental work to develop proper correction factors to the currently implemented kinetic model and validate it.

The second part concerned ammonia oxidation, using the obtained CFD model to investigate the degradation process. Computed temperature gradients on catalyst gauze allowed to estimate the spots with increased catalyst particle release on the first layer of the gauze. Those spots were the basis for calculating the trajectories of that particle using the discrete phase model and estimating the amount of the recapture rate of subsequent layers, and computed deposition gradients allowed to estimate the initial spots of "cauliflower structures" growth. Two geometry variants were simulated and compared: the typical industrial-used gauze and the modified with alternated geometry of the second layer. The results show how the preceding layer's geometry affects platinum particles' deposition by directly influencing the gas flow. This effect varies for different contact times, and proper geometry selection can reduce the catalyst loss for the

specific process conditions. However, geometry changes also affect the efficiency of the process, and potential losses should be considered before applying those changes.

The last investigation subject is an example of a supporting process, which is droplet removal through wave-plate mist eliminators, commonly used in many industry branches, including fertiliser production, to protect the sensitive apparatus and recover valuable substances. Numerous configurations of this separator's CFD model were created to investigate cases with different lengths, angles and types of drainage channels. The influence of crucial parameters such as gas phase velocity, droplet sizes and materials, and drainage channel geometry on separation efficiency and pressure drop were investigated. The different turbulence and discrete phase turbulent dispersion models were tested to improve the accuracy of the results, and the most suitable were chosen for simulations. The results proved that drainage channels have a primary role in the separation process in wave-plate mist eliminators, affecting both droplet removal efficiency and pressure drop. Even minor geometrical changes can vastly improve the process. Based on the results, novel, streamlined drainage channels were proposed, which increased the separation efficiency, maintaining similar pressure drop values. It should be noted that the results obtained do not include the effects of liquid film on the wall and the secondary entrainment of droplets.

It should be noted, however, that although computational fluid dynamics is an excellent tool for modelling and investigating industrial-scale processes, each numerical model has its limitations. Due to the entrepreneur's secrets regarding most industries, data available in the literature is limited and incomplete, which applies especially to the geometrical details of the chemical reactors and experimental measurements. Excluding the pilot-scale ammonia synthesis reactor case (Chapter 6), every CFD model in this work was created and validated from the available literature, including the experimental data used for validation. In those cases, the simulations were performed using the most accurate accessible data, although several parameters, such as geometrical dimensions, had to be estimated, potentially generating errors. It is recommended that every CFD model should be appropriately validated using experiments to achieve excellent results and accuracy. Nevertheless, CFD models can provide accurate and unique data that can be used for computer-guided research and engineering.

Summarising, the contribution of this work was to investigate and improve the primary and supporting pilot- and large-scale unit operations in the fertiliser industry. To achieve this, the author used computational fluid dynamics as a way of computer-aided engineering support. This dissertation shows that this approach has an excellent application in the fertiliser industry,

allowing it to assist experimental research by providing a relatively inexpensive prototype replacement using precise geometries and detailed reaction kinetics. Obtained CFD models offer a unique potential to take advantage of the in-depth insight into the process, providing access to parameters unavailable to measure experimentally and the possibility to plot every needed parameter in the form of contours inside the considered geometry of the modelled apparatus. Obtained models allow for identifying problems such as geometry flaws or dead zones, granting a better understanding and control of the process and testing new parameters or geometrical variants. In conclusion, they have a unique potential to guide the experimental research and designing processes, significantly reducing the investigation time and costs.

References

[1] M. Roser, H. Ritchie, Hunger and Undernourishment, Our World in Data (2019). https://ourworldindata.org/hunger-and-undernourishment (accessed September 14, 2022).

[2] K. Karume, J.M. Mondo, J.C.K. Kiyala, Drought, the War in Europe and Its Impacts on Food Insecurity in Sub-Saharan Africa, East Africa, in: J.C.K. Kiyala, N. Chivasa (Eds.), Climate Change and Socio-Political Violence in Sub-Saharan Africa in the Anthropocene: Perspectives from Peace Ecology and Sustainable Development, Springer Nature Switzerland, Cham, 2024: pp. 91–111. https://doi.org/10.1007/978-3-031-48375-2_4.

[3] H. Ritchie, To protect the world's wildlife we must improve crop yields – especially across Africa, Our World in Data (2021). https://ourworldindata.org/yields-habitat-loss (accessed May 9, 2023).

[4] Global Market Insights, Fertilizer Market Size, Share & Forecasts 2022-2030, Global Market Insights Inc. (2022). https://www.gminsights.com/industry-analysis/fertilizer-market (accessed May 11, 2023).

[5] Maximize Market Research, Water Soluble Fertilizer market: increasing acceptance of micro-irrigation practices is expected to drive the market, Maximize Market Research (2023). https://www.maximizemarketresearch.com/market-report/global-water-soluble-fertilizer-market/33171/ (accessed May 11, 2023).

[6] Research and Markets ltd, Fertilizer Market: Global Industry Trends, Share, Size, Growth, Opportunity and Forecast 2023-2028, (2023). https://www.researchandmarkets.com/reports/5768989/fertilizer-market-global-industry-trends (accessed May 11, 2023).

[7] Statista, Fertilizer industry worldwide, Statista (2022). https://www.statista.com/study/106183/global-fertilizer-industry/ (accessed May 9, 2023).

[8] M. Haas, Modeling of industrial NH3 oxidation on Pt catalysts: The effect of local mass transfer on N2O selectivity, Ph.D. Thesis, Technische Universität Darmstadt, 2022. https://doi.org/10.26083/tuprints-00021594.

[9] International Energy Agency (IEA), International Council of Chemical Associations (ICCA), DECHEMA, Technology Roadmap - Energy and GHG Reductions in the Chemical Industry via Catalytic Processes – Analysis, IEA (2013). https://www.iea.org/reports/technology-roadmap-energy-and-ghg-reductions-in-the-chemical-industry-via-catalytic-processes (accessed October 14, 2024).

[10] The Essential Chemical Industry - online, Ammonia, (2016). https://www.essentialchemicalindustry.org/chemicals/ammonia.html (accessed October 14, 2024).

[11] T. Johansson, A. Patwardhan, N. Nakicenovic, L. Gomez-Echeverri, Global Energy Assessment: Toward a Sustainable Future, 2012. https://doi.org/10.1017/CBO9780511793677.

[12] A. Jess, P. Wasserscheid, Chemical Technology, Wiley-VCH, 2013.

[13] K. Tamaru, The History of the Development of Ammonia Synthesis, in: Catalytic Ammonia Synthesis: Fundamentals and Practice, Springer US, Boston, MA, USA, 1991. https://doi.org/10.1007/978-1-4757-9592-9.

[14] R. Schlögl, Ammonia Synthesis, in: Handbook of Heterogeneous Catalysis, 8 Volume Set, 2nd Edition | Wiley, New York, NY, USA, 2008: pp. 2501–2575.

[15] C.W. Hooper, Ammonia Synthesis: Commercial Practice, in: Catalytic Ammonia Synthesis: Fundamentals and Practice, Springer US, Boston, MA, USA, 1991. https://doi.org/10.1007/978-1-4757-9592-9.

[16] E. Cussler, A. McCormick, M. Reese, M. Malmali, Ammonia Synthesis at Low Pressure, JoVE (2017) 55691. https://doi.org/10.3791/55691.
[17] M. Warner, The kinetics of industrial ammonia combustion, PhD, The University of Sydney, 2013.
[18] J. Pérez-Ramírez, F. Kapteijn, K. Schöffel, J.A. Moulijn, Formation and control of N2O in nitric acid production, Applied Catalysis B: Environmental 44 (2003) 117–151. https://doi.org/10.1016/S0926-3373(03)00026-2.
[19] S.T. Hatscher, T. Fetzer, E. Wagner, H.-J. Kneuper, Ammonia Oxidation, in: Handbook of Heterogeneous Catalysis, 8 Volume Set, 2nd Edition | Wiley, 2008: pp. 2575–2592.
[20] M. Thiemann, E. Scheibler, K.W. Wiegand, Nitric Acid, Nitrous Acid, and Nitrogen Oxides, in: Wiley-VCH Verlag GmbH & Co. KGaA (Ed.), Ullmann's Encyclopedia of Industrial Chemistry, Wiley-VCH Verlag GmbH & Co. KGaA, Weinheim, Germany, 2000: pp. 177–225. https://doi.org/10.1002/14356007.a17_293.
[21] M. Argyle, C. Bartholomew, Heterogeneous Catalyst Deactivation and Regeneration: A Review, Catalysts 5 (2015) 145–269. https://doi.org/10.3390/catal5010145.
[22] A. Wiser, Investigation of the industrial NH3 oxidation by CFD simulations including detailed surface kinetics, Ph.D. Thesis, Technische Universität, 2020. https://doi.org/10.25534/tuprints-00017208.
[23] A.R. McCabe, G.D.W. Smith, The Mechanism of Reconstruction of Rhodium-Platinum Catalyst Gauzes, (1986) 9.
[24] C. Galletti, E. Brunazzi, L. Tognotti, A numerical model for gas flow and droplet motion in wave-plate mist eliminators with drainage channels, Chemical Engineering Science 63 (2008) 5639–5652. https://doi.org/10.1016/j.ces.2008.08.013.
[25] Del Ministro Carlotta, Bosio Federica, Spreafico Stefano, Brunazzi Elisabetta, The gx fiber bed - a novel mist eliminator with improved aerosol removal performances, Chemical Engineering Transactions 69 (2018) 811–816. https://doi.org/10.3303/CET1869136.
[26] S. Yuan, Y. Fan, J. Li, S. Zhou, Y. Cao, Influence of droplet coalescence and breakup on the separation process in wave-plate separators, Can. J. Chem. Eng. 96 (2018) 1627–1636. https://doi.org/10.1002/cjce.23089.
[27] C.P.P. Singh, D.N. Saraf, Simulation of Ammonia Synthesis Reactors, Ind. Eng. Chem. Proc. Des. Dev. 18 (1979) 364–370. https://doi.org/10.1021/i260071a002.
[28] S.S.E.H. Elnashaie, A.T. Mahfouz, S.S. Elshishini, Digital simulation of an industrial ammonia reactor, Chemical Engineering and Processing: Process Intensification 23 (1988) 165–177. https://doi.org/10.1016/0255-2701(88)80013-8.
[29] M.R. Panahandeh, J. Fathikaljahi, M. Taheri, Steady-State Modeling and Simulation of an Axial-Radial Ammonia Synthesis Reactor, Chemical Engineering & Technology 26 (2003) 666–671. https://doi.org/10.1002/ceat.200390101.
[30] N. Kasiri, A.R. Hosseini, M. Moghadam, Dynamic simulation of an ammonia synthesis reactor, in: Computer Aided Chemical Engineering, Elsevier, Amsterdam, The Netherlands, 2003: pp. 695–700. https://doi.org/10.1016/S1570-7946(03)80197-9.
[31] A. Dashti, K. Khorsand, M. Ahmadi Marvast, M. Kakavand, Modeling and simulation of ammonia synthesis reactor, Petroleum & Coal 48 (2006) 15–23.
[32] M.J. Azarhoosh, F. Farivar, H. Ale Ebrahim, Simulation and optimization of a horizontal ammonia synthesis reactor using genetic algorithm, RSC Adv. 4 (2014) 13419–13429. https://doi.org/10.1039/C3RA45410J.
[33] D.S.S. Jorqueira, A.M.B. Neto, M.T.M. Rodrigues, Modeling and Numerical Simulation of Ammonia Synthesis Reactors Using Compositional Approach, ACES 08 (2018) 124–143. https://doi.org/10.4236/aces.2018.83009.

[34] A. Mirvakili, Z. Eksiri, P. Biniaz, N. Mohaghegh, Two-dimensional mathematical modeling of an industrial ammonia synthesis reactor with CFD analysis, Journal of the Taiwan Institute of Chemical Engineers 121 (2021) 1–19. https://doi.org/10.1016/j.jtice.2021.03.032.
[35] D.C. Dyson, J.M. Simon, Kinetic Expression with Diffusion Correction for Ammonia Synthesis on Industrial Catalyst, Ind. Eng. Chem. Fund. 7 (1968) 605–610. https://doi.org/10.1021/i160028a013.
[36] D.A. Hickman, L.D. Schmidt, Modeling catalytic gauze reactors: ammonia oxidation, Ind. Eng. Chem. Res. 30 (1991) 50–55. https://doi.org/10.1021/ie00049a008.
[37] L.M. Aparicio, J.A. Dumesic, Ammonia synthesis kinetics: Surface chemistry, rate expressions, and kinetic analysis, Top Catal 1 (1994) 233–252. https://doi.org/10.1007/BF01492278.
[38] R. Kraehnert, M. Baerns, Kinetics of ammonia oxidation over Pt foil studied in a micro-structured quartz-reactor, Chemical Engineering Journal 137 (2008) 361–375. https://doi.org/10.1016/j.cej.2007.05.005.
[39] G. Novell-Leruth, J.M. Ricart, J. Pérez-Ramírez, Pt(100)-Catalyzed Ammonia Oxidation Studied by DFT: Mechanism and Microkinetics, J. Phys. Chem. C 112 (2008) 13554–13562. https://doi.org/10.1021/jp802489y.
[40] A. Scheuer, M. Votsmeier, A. Schuler, J. Gieshoff, A. Drochner, H. Vogel, NH3-Slip Catalysts: Experiments Versus Mechanistic Modelling, Top Catal 52 (2009) 1847–1851. https://doi.org/10.1007/s11244-009-9351-9.
[41] M. Rafti, J.L. Vicente, A. Albesa, A. Scheibe, R. Imbihl, Modeling ammonia oxidation over a Pt (533) surface, Surface Science 606 (2012) 12–20. https://doi.org/10.1016/j.susc.2011.08.014.
[42] J. Otomo, M. Koshi, T. Mitsumori, H. Iwasaki, K. Yamada, Chemical kinetic modeling of ammonia oxidation with improved reaction mechanism for ammonia/air and ammonia/hydrogen/air combustion, International Journal of Hydrogen Energy 43 (2018) 3004–3014. https://doi.org/10.1016/j.ijhydene.2017.12.066.
[43] M. Haas, T.-W. Nien, A. Fadic, J.P. Mmbaga, M. Klingenberger, D. Born, B.J.M. Etzold, R. Hayes, M. Votsmeier, N2O selectivity in industrial NH3 oxidation on Pt-gauze is determined by interaction of local flow and surface chemistry: A simulation study using mechanistic kinetics, Chemical Engineering Science 260 (2022) 117832. https://doi.org/10.1016/j.ces.2022.117832.
[44] J. Pottbacker, S. Jakobtorweihen, A.S. Behnecke, A. Abdullah, M. Özdemir, M. Warner, M. Menon, J.M. Bujalski, D. Waller, O. Korup, R. Horn, Resolving gradients in an ammonia oxidation reactor under industrial conditions: A combined experimental and simulation study, Chemical Engineering Journal 439 (2022) 135350. https://doi.org/10.1016/j.cej.2022.135350.
[45] S. Das, M.E. Stuckelberger, J. Pottbacker, S. Jakobtorweihen, C.G. Schroer, R. Horn, T.L. Sheppard, Quantitative Chemical Mapping of Pt/Rh Gauze Catalysts for Ammonia Oxidation using Resonant X-ray Tomography, J. Phys. Chem. C 128 (2024) 5053–5063. https://doi.org/10.1021/acs.jpcc.4c00041.
[46] O. Nilsen, A. Kjekshus, H. Fjellvåg, Reconstruction and loss of platinum catalyst during oxidation of ammonia, Applied Catalysis A: General 207 (2001) 43–54. https://doi.org/10.1016/S0926-860X(00)00615-3.
[47] L. Hannevold, O. Nilsen, A. Kjekshus, H. Fjellvåg, Reconstruction of platinum–rhodium catalysts during oxidation of ammonia, Applied Catalysis A: General 284 (2005) 163–176. https://doi.org/10.1016/j.apcata.2005.01.033.

[48] H. Houghton, W. Radford, Measurement on eliminators and the development of a new type for use at high gas velocities, Transactions of the American Institute of Chemical Engineers 35 (1939) 427–433.
[49] Y.I. Wang, P.W. James, The calculation of wave-plate demister efficiencies using numerical simulation of the flow field and droplet motion, Chemical Engineering Research and Design 76 (1998) 980–985. https://doi.org/10.1205/026387698525630.
[50] Y.I. Wang, P.W. James, Assessment of an eddy-interaction model and its refinements using predictions of droplet deposition in a wave-plate demister, Chemical Engineering Research & Design - CHEM ENG RES DES 77 (1999) 692–698. https://doi.org/10.1205/026387699526827.
[51] B. Azzopardi, K. Sanaullah, Re-entrainment in wave-plate mist eliminators, Chemical Engineering Science - CHEM ENG SCI 57 (2002) 3557–3563. https://doi.org/10.1016/S0009-2509(02)00270-1.
[52] P.W. James, Y. Wang, B.J. Azzopardi, J.P. Hughes, The role of drainage channels in the performance of wave-plate mist eliminators, Chemical Engineering Research and Design 81 (2003) 639–648. https://doi.org/10.1205/026387603322150499.
[53] M.H.H. Estakhrsar, R. Rafee, Effect of drainage channel dimensions on the performance of wave-plate mist eliminators, Korean J. Chem. Eng. 30 (2013) 1301–1311. https://doi.org/10.1007/s11814-013-0032-9.
[54] Y. Liu, D. Yu, J. Jiang, X. Yu, H. Yao, M. Xu, Experimental and numerical evaluation of the performance of a novel compound demister, Desalination 409 (2017) 115–127. https://doi.org/10.1016/j.desal.2017.01.022.
[55] J.R. Jennings, ed., Catalytic Ammonia Synthesis: Fundamentals and Practice, Springer US, Boston, MA, 1991. https://doi.org/10.1007/978-1-4757-9592-9.
[56] J.R. Jennings, S.A. Ward, Ammonia Synthesis, in: Catalyst Handbook, 2nd Edition, 2nd ed., Routledge, New York, 1989.
[57] P. Davies, R.T. Donald, N.H. Harbord, Catalytic Oxidations, in: Catalyst Handbook, 2nd Edition, 2nd ed., Routledge, New York, 1989.
[58] E.P. Perman, The direct synthesis of ammonia, Proceedings of the Royal Society of London. Series A, Containing Papers of a Mathematical and Physical Character 76 (1905) 167–174. https://doi.org/10.1098/rspa.1905.0016.
[59] G. Gramatica, N. Pernicone, Kinetics of Ammonia Synthesis and Influence on Converter Design, in: Catalytic Ammonia Synthesis: Fundamentals and Practice, Springer US, Boston, MA, USA, 1991. https://doi.org/10.1007/978-1-4757-9592-9.
[60] L.B. Hunt, The Ammonia Oxidation Process for Nitric Acid Manufacture: Early Developments with Platinum Catalysts, Platinum Metals Review 2 (1958) 129–134. https://doi.org/10.1595/003214058X24129134.
[61] M. Stewart, K. Arnold, Gas-liquid and liquid-liquid separators, Gulf Professional, Amsterdam Heidelberg, 2009.
[62] M.-W. Kim, S.-Y. Noh, M.Z. Zahir, S.-J. Yook, Performance improvement of a horizontal zigzag type mist eliminator using slit plates, J Mech Sci Technol 35 (2021) 2229–2236. https://doi.org/10.1007/s12206-021-0439-x.
[63] H.V. den Akker, R.F. Mudde, Mass, Momentum and Energy Transport Phenomena: A Consistent Balances Approach, De Gruyter, 2023. https://doi.org/10.1515/9783111246574.
[64] Ansys® Fluent, Release 2024 R1, Help System, Fluent Theory Guide, ANSYS, Inc: Canonsburg, PA, USA.
[65] R.B. Bird, W.E. Stewart, E.N. Lightfoot, Transport Phenomena, Revised 2nd Edition, 2nd edition, John Wiley & Sons, Inc., New York, 2002.

[66] Ansys® Fluent, Release 2024 R1, Help System, Fluent User's Guide, ANSYS, Inc: Canonsburg, PA, USA.
[67] A.D. Gosman, E. Ioannides, Aspects of Computer Simulation of Liquid-Fueled Combustors, Journal of Energy 7 (1983) 482–490. https://doi.org/10.2514/3.62687.
[68] M. Tyrański, J.M. Bujalski, W. Orciuch, Ł. Makowski, Computational Fluid Dynamics of Ammonia Synthesis in Axial-Radial Bed Reactor, Energies 16 (2023) 6680. https://doi.org/10.3390/en16186680.
[69] S.R. Tennison, Alternative Noniron Catalysts, in: Catalytic Ammonia Synthesis: Fundamentals and Practice, Springer US, Boston, MA, USA, 1991. https://doi.org/10.1007/978-1-4757-9592-9.
[70] A. Araújo, S. Skogestad, Control structure design for the ammonia synthesis process, Computers & Chemical Engineering 32 (2008) 2920–2932. https://doi.org/10.1016/j.compchemeng.2008.03.001.
[71] A. Nielsen, J. Kjaer, B. Hansen, Rate equation and mechanism of ammonia synthesis at industrial conditions, Journal of Catalysis 3 (1964) 68–79. https://doi.org/10.1016/0021-9517(64)90094-6.
[72] L.J. Gillespie, J.A. Beattie, The Thermodynamic Treatment of Chemical Equilibria in Systems Composed of Real Gases. I. An Approximate Equation for the Mass Action Function Applied to the Existing Data on the Haber Equilibrium, Phys. Rev. 36 (1930) 743–753. https://doi.org/10.1103/PhysRev.36.743.
[73] M. Tyrański, J.M. Bujalski, E. Nilsen, O. Bestul, W. Orciuch, Ł. Makowski, Pilot Plant Reactor for Ammonia Synthesis – Computational Fluid Dynamics Analysis with Experimental Validation, Chemical Engineering Journal, Manuscript in Review, Date of Submission 31.08.2024.
[74] M. Tyrański, I. Pasik, J.M. Bujalski, W. Orciuch, Ł. Makowski, Computational Fluid Dynamics of Influence of Process Parameters and the Geometry of Catalyst Wires on the Ammonia Oxidation Process and Degradation of the Catalyst Gauze, Energies 15 (2022) 8123. https://doi.org/10.3390/en15218123.
[75] M. Tyrański, J.M. Bujalski, W. Orciuch, Ł. Makowski, Study of the Ammonia Oxidation Process on Platinum Gauze and Catalyst Degradation Phenomenon – CFD Simulation with Surface Reaction Kinetics and Catalyst Entrained Particles Motion and Deposition Tracking, Chemical Engineering Research and Design, Manuscript in Review, Date of Submission 19.12.2024.
[76] M. Haas, A. Wiser, A. Drochner, C. Hasse, B.J.M. Etzold, M. Votsmeier, Multiscale CFD model for the catalyzed ammonia oxidation: From a detailed surface kinetic model to an industrial reactor. In Proceedings of the 25th International Conference on Chemical Reaction Engineering, ISCRE25, in: Florence, Italy, 2018.
[77] S.L. Handforth, J.N. Tilley, Catalysts for Oxidation of Ammonia to Oxides of Nitrogen, Ind. Eng. Chem. 26 (1934) 1287–1292. https://doi.org/10.1021/ie50300a016.
[78] J. Pura, P. Kwaśniak, P. Wiecinski, H. Garbacz, J. Zdunek, Z. Laskowski, M. Gierej, Investigation of the Degradation Mechanism of Platinum-Rhodium Catalytic Wires during Oxidation of Ammonia Process, SSP 227 (2015) 229–232. https://doi.org/10.4028/www.scientific.net/SSP.227.229.
[79] J. Pura, P. Wieciński, P. Kwaśniak, M. Zwolińska, H. Garbacz, J. Zdunek, Z. Laskowski, M. Gierej, Investigation of the degradation mechanism of catalytic wires during oxidation of ammonia process, Applied Surface Science 388 (2016) 670–677. https://doi.org/10.1016/j.apsusc.2016.05.071.
[80] Ł. Makowski, J. Łaskowski, M. Tyrański, Influence of Modification of the Geometry of the Wave-Plate Mist Eliminators on the Droplet Removal Efficiency—CFD Modelling, Processes 9 (2021) 1499. https://doi.org/10.3390/pr9091499.

[81] J. Gharib, M.K. Moraveji, Determination the factors affecting the vane-plate demisters efficiency using CFD modeling, J Chem Eng Process Technol 01 (2011). https://doi.org/10.4172/2157-7048.S1-003.
[82] V. Michalcová, K. Kotrasová, The Numerical Diffusion Effect on the CFD Simulation Accuracy of Velocity and Temperature Field for the Application of Sustainable Architecture Methodology, Sustainability 12 (2020) 10173. https://doi.org/10.3390/su122310173.
[83] Ł. Makowski, W. Orciuch, J. Bałdyga, Large eddy simulations of mixing effects on the course of precipitation process, Chemical Engineering Science 77 (2012) 85–94. https://doi.org/10.1016/j.ces.2011.12.020.
[84] Ł. Makowski, J. Bałdyga, Large eddy simulation of mixing effects on the course of parallel chemical reactions and comparison with k–ε modeling, Chemical Engineering and Processing: Process Intensification 50 (2011) 1035–1040. https://doi.org/10.1016/j.cep.2011.06.003.
[85] J. Ruiz, A.S. Kaiser, B. Zamora, C.G. Cutillas, M. Lucas, CFD analysis of drift eliminators using RANS and LES turbulent models, Applied Thermal Engineering 105 (2016) 979–987. https://doi.org/10.1016/j.applthermaleng.2016.01.108.